Outer Continental Shelf Environmental Assessment Program

Final Reports of Principal Investigators

Volume 40 **June 1986**

U.S. DEPARTMENT OF COMMERCE
National Oceanic and Atmospheric Administration
National Ocean Service
Office of Oceanography and Marine Assessment
Ocean Assessments Division
Alaska Office

U.S. DEPARTMENT OF THE INTERIOR
Minerals Management Service
OCS Study, MMS 86-0054

"Outer Continental Shelf Environmental Assessment Program Final Reports of Principal Investigators" ("OCSEAP Final Reports") continues the series entitled "Environmental Assessment of the Alaskan Continental Shelf Final Reports of Principal Investigators."

It is suggested that sections of this publication be cited as follows:

Martin, S. 1982. Interaction of oil with sea ice. U.S. Dep. of Commer., NOAA, OCSEAP Final Rep. 40 (1986):1-214

Appendices 1 through 4 of the above report may be cited as follows:

Muench, R. 1981. Physical oceanographic investigations in the Bering Sea marginal ice zone. In: S. Martin. Interaction of oil with sea ice. U.S. Dep. Commer., NOAA, OCSEAP Final Rep. 40(1986):1-214

Martin, S., P. Kauffman, and C. Parkinson. 1983. The movement and decay of ice edge bands in the winter Bering Sea. Journal of Geophysical Research 88C:2803-2812

Muench, R. D., P. H. LeBlond, and L. E. Hachmeister. 1982. On some possible interactions between internal waves and sea ice in the marginal ice zone. In: S. Martin. Interaction of oil with sea ice. U.S. Dep. Commer., NOAA, OCSEAP Final Report 40(1986):1-214

Martin, S. and S. L. McNutt. 1982. The Bering Sea ice cover during March 1979: Comparison of surface and satellite data with the Nimbus-7 SMMR. In: S. Martin. Interaction of oil with sea ice. U.S. Dep. Commer., NOAA, OCSEAP Final Report 40(1986):1-214

Nummedal, D. 1980. Persistence of spilled oil along the Beaufort Sea coast. U.S. Dep. of Commer., NOAA, OCSEAP Final Rep. 40 (1986):215-294

Thomas, D. R. 1983. Potential oiled ice trajectories in the Beaufort Sea. U.S. Dep. of Commer., NOAA, OCSEAP Final Rep. 40 (1986):295-402

Thomas, D. R. 1983. Interaction of oil with Arctic Sea ice. U.S. Dep. of Commer., NOAA, OCSEAP Final Rep.40 (1986):403-406

Warner, J. S. and W. L. Margard. 1979. Activity-directed fractionation of petroleum samples. U.S. Dep. of Commer., NOAA, OCSEAP Final Rep. 40 (1986):437-503

OCSEAP Final reports are published by the U.S. Department of Commerce, National Oceanic and Atmospheric Administration, National Ocean Assessments Division, Alaska Office, Anchorage, and primarily funded by the Minerals Management Service, U.S. Department of the Interior, through interagency agreement.

Requests for receipt of OCSEAP Final Reports on a continuing basis should be addressed to:

NOAA-OMA-OAD
Alaska Office
701 C Street
P. O. Box 56
Anchorage, AK 99513

OUTER CONTINENTAL SHELF

ENVIRONMENTAL ASSESSMENT PROGRAM

FINAL REPORTS OF PRINCIPAL INVESTIGATORS

Volume 40

June 1986

U.S. DEPARTMENT OF COMMERCE
National Oceanic and Atmospheric Administration
National Ocean Service
Office of Oceanography and Marine Assessment
Ocean Assessments Division
Alaska Office

U.S. DEPARTMENT OF THE INTERIOR
Minerals Management Service
Alaska OCS Region
OCS Study, MMS 86-0054

Anchorage, Alaska

The facts, conclusions, and issues appearing in these reports are based on research results of the Outer Continental Shelf Environmental Assessment Program (OCSEAP), which is managed by the National Oceanic and Atmospheric Administration, U.S. Department of Commerce, and funded (wholly or in part) by the Minerals Management Service, U.S. Department of the Interior, through an Interagency Agreement.

Mention of a commercial company or product does not constitute endorsement by the National Oceanic and Atmospheric Administration. Use for publicity or advertising purposes of information from this publication concerning proprietary products or the tests of such products is not authorized.

Content of these reports has not been altered from that submitted by the Principal Investigators. In some instances, minor grammatical, spelling, and punctuation errors have been corrected to improve readability; some figures, charts, and tables have been enhanced to improve clarity in reproduction.

Outer Continental Shelf Environmental Assessment Program

Final Reports of Principal Investigators

VOLUME 40 JUNE 1986

CONTENTS

INTERACTION OF OIL WITH SEA ICE

by

Seelye Martin

School of Oceanography
University of Washington

Final Report
Outer Continental Shelf Environmental Assessment Program
Research Unit 87

May 1982

TABLE OF CONTENTS

LIST OF FIGURES

Final Report of NA81RAC00013; "The Interaction of Oil with Sea Ice"

ABSTRACT

This document constitutes the final report of contract number NA81RAC00013. The document is composed of a summary introduction, plus four Appendices. Appendix 1 is a report entitled "Physical oceanographic investigations in the Bering Sea Marginal Ice Zone," by Robin Muench. Appendix 2 is a manuscript titled "The movement and decay of ice edge bands in the Bering Sea," by Martin, Kauffman, and Parkinson. Together, these two manuscripts describe the oceanographic and sea ice conditions during the mid-winter 1981 SURVEYOR cruise. We also include copies of two related reports in Appendices 3 and 4. The first, a paper entitled "On some possible interactions between internal waves and sea ice in the marginal ice zone," by Muench, LeBlond, and Hachmeister, uses the data described in Appendix 1 and 2 to describe possible interactions between internal waves and ice bands in the Bering Sea. The second, "The Bering Sea ice cover during March 1979: comparison of surface and satellite data with the NIMBUS-7 SMMR" describes an all-weather satellite technique for following the evolution of the Bering Sea ice cover.

1. Introduction

The following short report provides both an overview and a drawing together of the material in the Appendices. Within this section, we will repeat several of the figures in the Appendices; and all references will be to work cited in the Appendices. In the following, we first discuss the Bering Sea oceanography, with particular reference to a salinity-temperature front which we feel strongly interacts with the ice edge. We then discuss the nature of the ice edge as revealed from our February-March 1981 cruise; and finally discuss the relevance of our observations to the interaction of oil with the ice edge.

2. Ocean and Ice Processes

Appendix 1 shows in November 1980 and February-March 1981 that a hydrographic structure which was two-layered in temperature, salinity, and density, characterized the water of the central Bering Sea shelf. In November, this structure covered the central Bering shelf. In February-March, the structure was confined to an 80 km wide front which coincided approximately with the ice edge. The cruise results show that the cold, low-salinity upper layer water in the front was continuous in its T-S properties with the homogenous water to the north beneath the ice. Similarly, the warmer, more-saline lower layer water was continuous with the Pacific water farther south near the shelf break. To illustrate this front, Figure 1 shows our observational area and the location of the moored current meter BC22; and Figure 2a shows the frontal temperature structure preceding a storm.

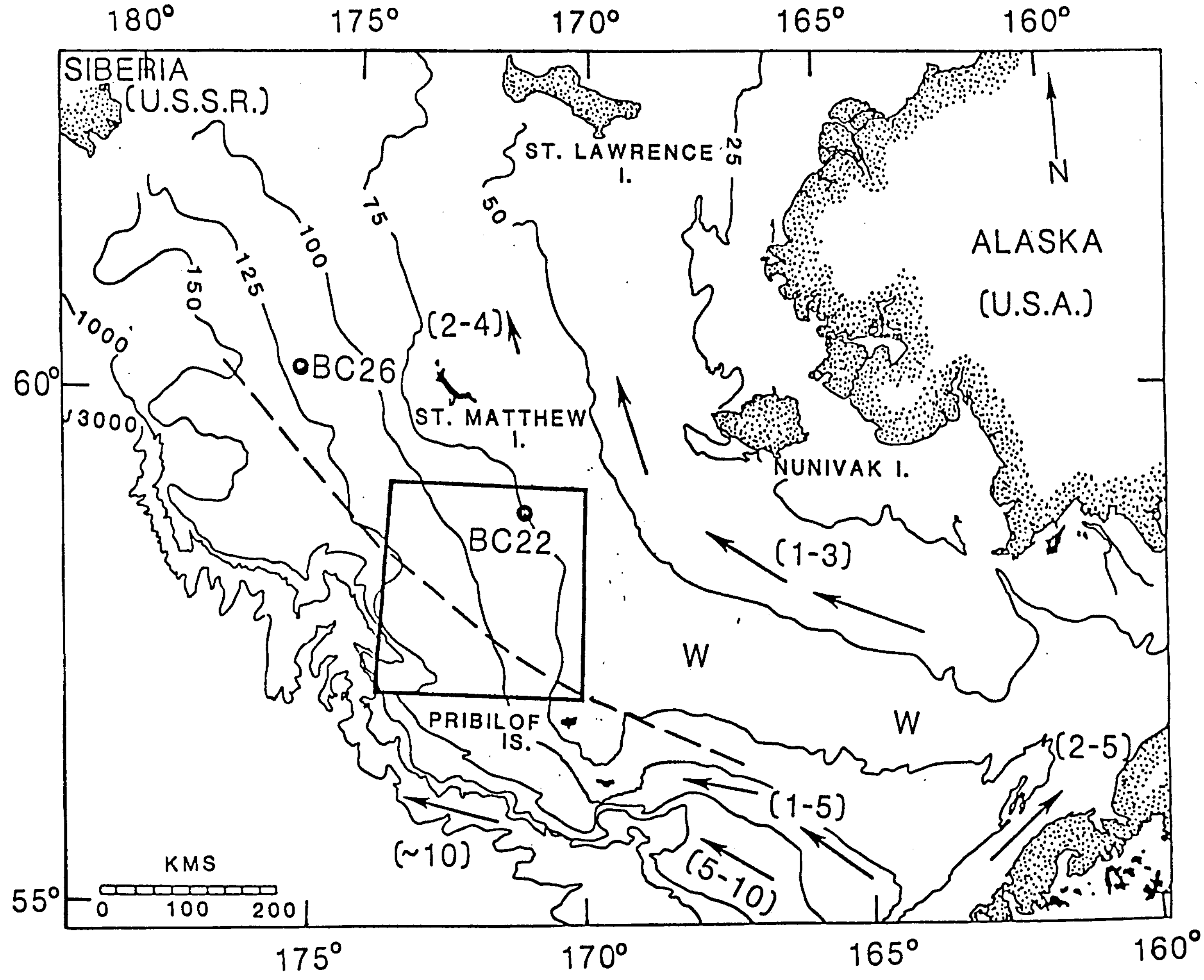

Figure 1. Observation area and location of moored current meter BC22.

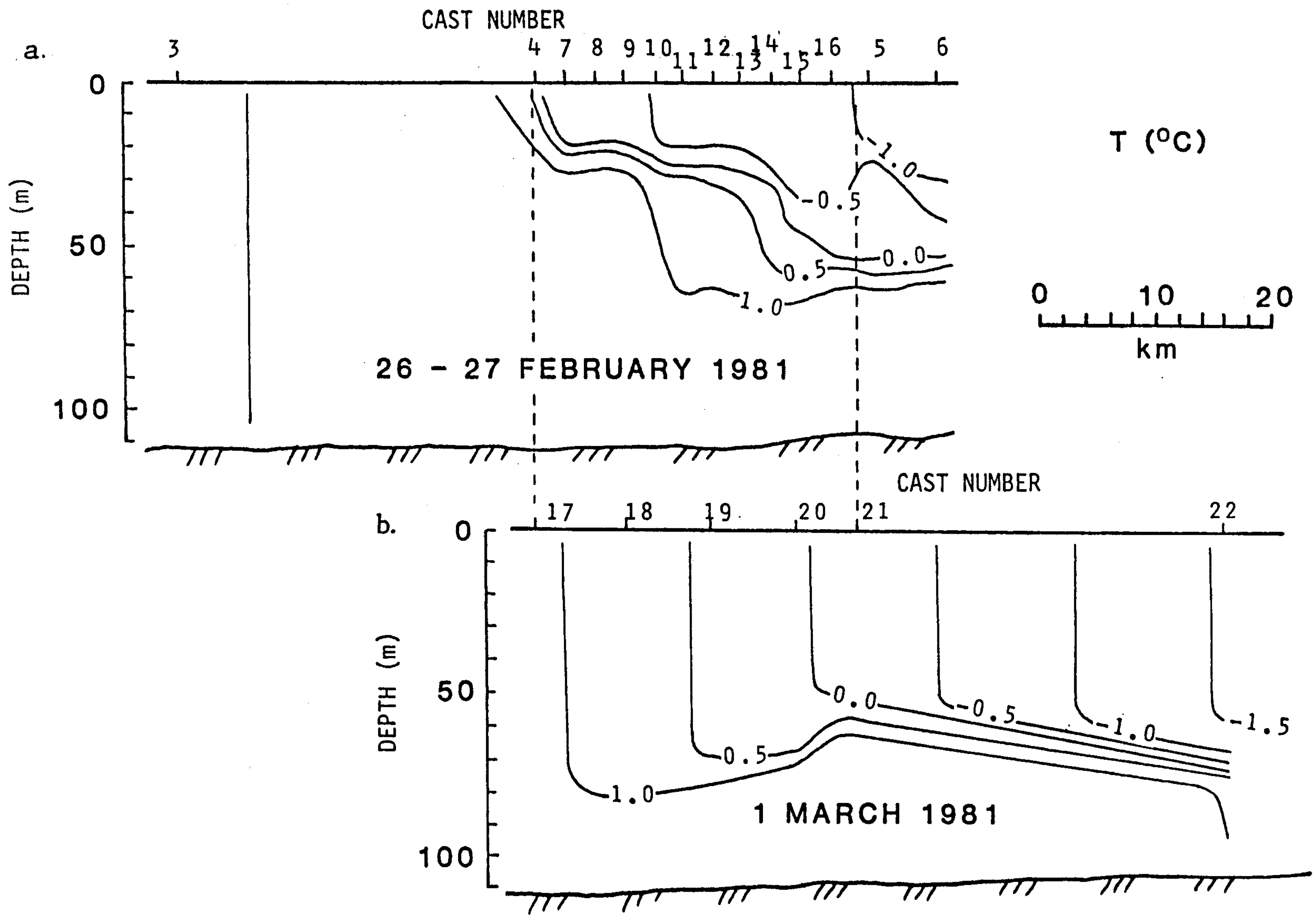

Figure 2. Vertical distribution of temperature across the central Bering Sea shelf, approximately beneath the ice edge, prior to (upper) and following (lower) a strong, southerly wind event in mid-winter 1981. Figure 2-2 in Appendix 1 shows locations of stations which are included in these two transects. Numbers given are cast numbers.

Both our current meters and our geostrophic calculations show that this layered front generated a northwest baroclinic surface flow with winter surface speeds of about 7 cm s^{-1}. Observed over-winter mean currents at two locations near the ice edge were 2-3 cm s^{-1} at 50 m depth, with flow toward the northwest in qualitative agreement with the computed baroclinic surface flow and in general agreement with the conventional wisdom which presupposes a net north-northwestward flow on the Bering shelf. Fluctuations were superposed on the observed currents and led to periods of reversal. Cross-shelf flow components in particular fluctuated strongly, with the greatest on-shelf flow in mid-winter. Tidal currents were mixed, predominantly diurnal and were 20-40 cm s^{-1} east of St. Matthew Island and 10-20 cm s^{-1} west of it.

Our most interesting observation about this front was its response to a five day storm. During this storm, which caused the ice edge to retreat about 100 km, the front did not move with the ice. Rather, while the ice was pushed back into uniformly cold, low-salinity water at its freezing point, the comparison of Figure 2b with 2a, which were taken respectively after and before the storm, shows that the two-layer stratification sharpened and deepened, but suffered almost no lateral motion during the storm.

The ice edge started out well to the south on 26 February, then retreated 125 km during the storm to its maximum retreat position on 3 March. Then given the onset of northeast winds, the ice edge once again advanced southwest to the front, so that by 11 March, the ice edge had returned to its position of 25 February.

From the ship, we observed that when the ice was north of the front and floating in water at its freezing point, the ice did not melt. Instead, we observed grease ice growth in the water surrounding the floes. Then, as the northeast winds drove the ice edge back over the front and the surface water temperature rose above the freezing point, the ice began to melt. This melting cools and dilutes the surface water and thus contributes to the maintenance of the front. As Appendix 2 shows, the melting of ice over the front is greatly enhanced through the formation of ice edge bands and their movement over the front. These bands which form at the ice edge through mechanisms which we do not yet understand, lie at approximately right angles to the wind, are made up of floes measuring approximately 10 m in diameter and 2-4 m in thickness, and measure approximately 1 km wide by 10 km long. Appendix 2 describes our detailed study of a band, in which we mounted two radar transponders on a band at a distance of 4 km apart, then followed the band until it decayed.

Our analysis of the band displacement shows several important facts. First, Figure 3 shows a chart of the bottom topography in the experimental region. The point BC22 is the current meter mooring; the line "a" shows the displacement of a satellite-tracked buoy for the times listed at the end points in Julian days and GMT, and the line "b" shows the similar displacement of our band. Comparison of the line lengths demonstrate that the band moves about 30% faster than the interior ice. Also, under line "b", we give the water temperature in °C; the temperature increase along the line shows that the band is crossing the oceanic front. An ice survey described in Appendix 2 shows that the satellite-tracked buoy, which was deployed by Carol Pease and

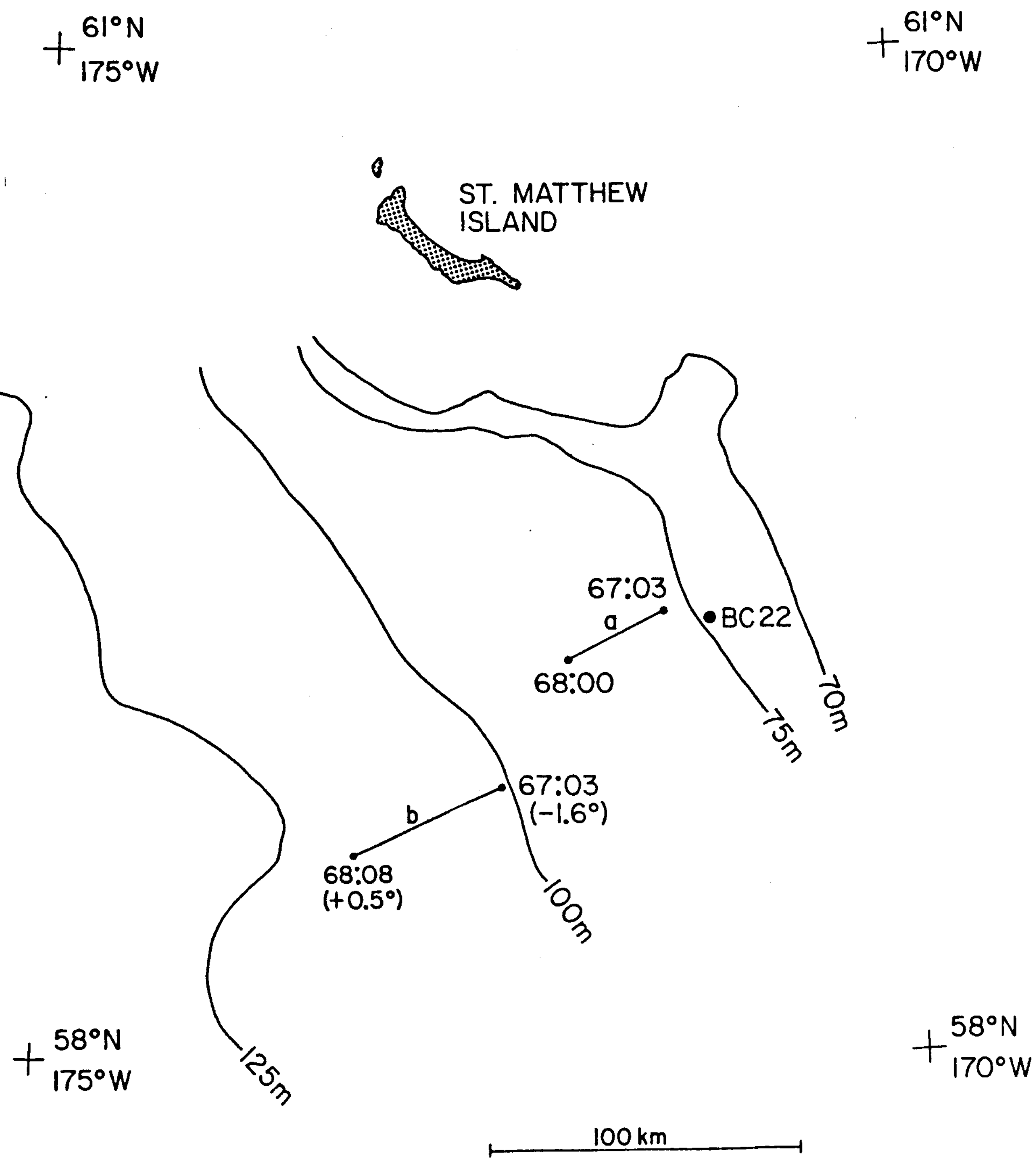

Figure 3. Bottom topography in the experimental region.

will be referred to as 'Pease's station', lay about 80 km inside of the ice edge in a region of concentrated ice pack. We show below that the cause of the ice band velocity increase relative to Pease's station is the wind-wave radiation stress acting on the band.

3. Ice Band Properties

The ice band has several important small-scale properties relevant to both the large-scale modelling of the ice edge, and the ice band behavior. The properties include the following: response of the ice band to tides; the mechanisms for band decay; the band acceleration by the wave radiation stress; and the formulation of the air, water, and Coriolis stress responsible for the ice band motion.

First, we compare in Figure 4 the band motion with the currents measured at BC22. On Figure 4, the upper two curves show the east u_C and north v_C current components from BC22; the middle two curves show the ice band velocities u_I and v_I; and the lower two curves show the velocities u_R and v_R of the ice relative to the currents. Examination of these curves shows that the rotary tides on the shelf account for most of the oscillations in the band trajectory.

Second, our field observations showed that the ice bands melted according to Figure 5. Figure 5, a schematic drawing of the band in cross section, shows in (a) the initial band configuration; and in (b) the band configuration at a later time. The figure shows that at the upwind band edge the wind-waves are reflected and absorbed, and that the wave agitation breaks up the large floes into small pieces. Then, because these small pieces are less effective wave absorbers and reflectors than the large floes, they experience a smaller wave radiation stress and thus drift upwind relative to the band to melt in

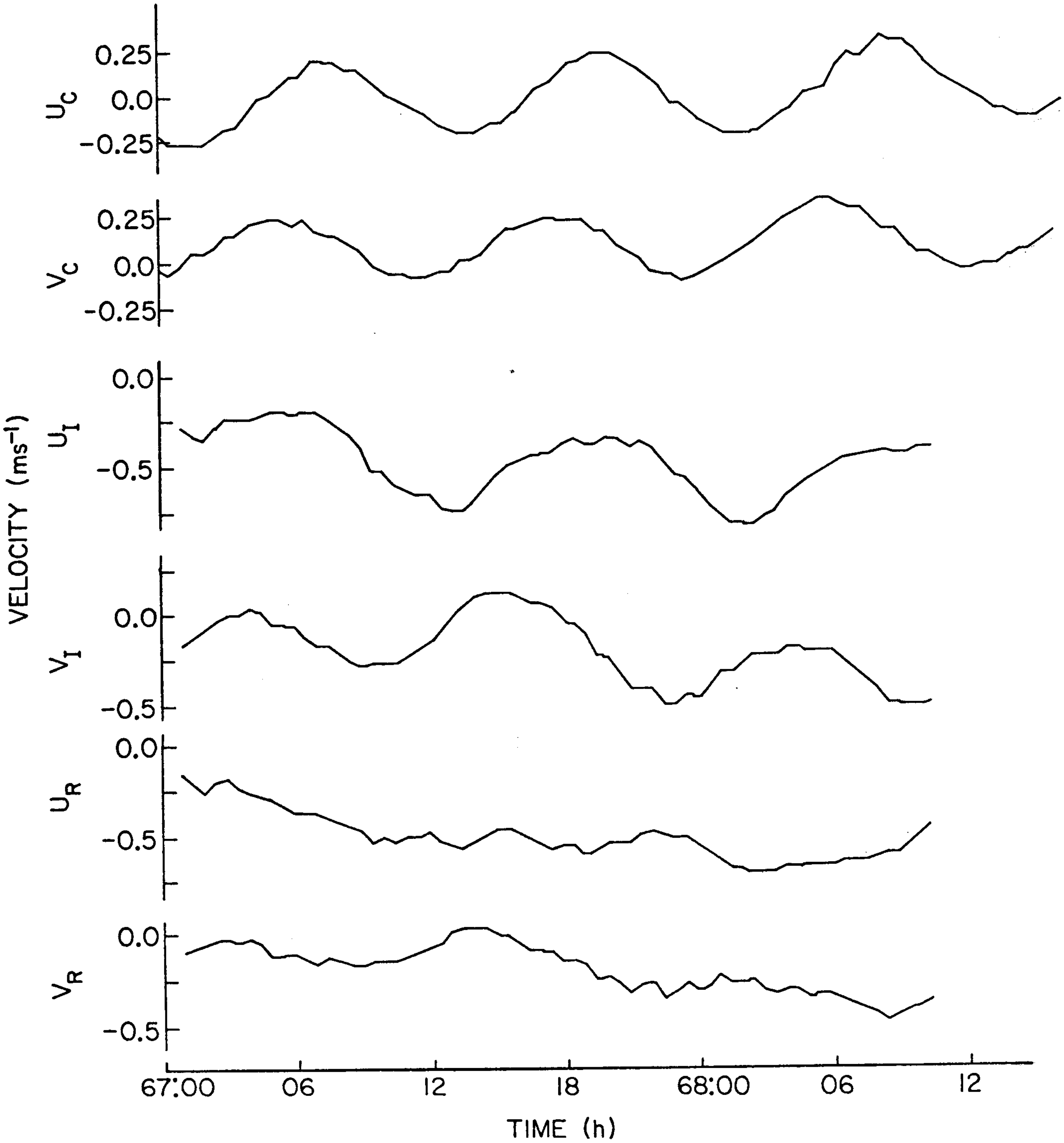

Figure 4. Comparison of band motion with currents measured at BC22.

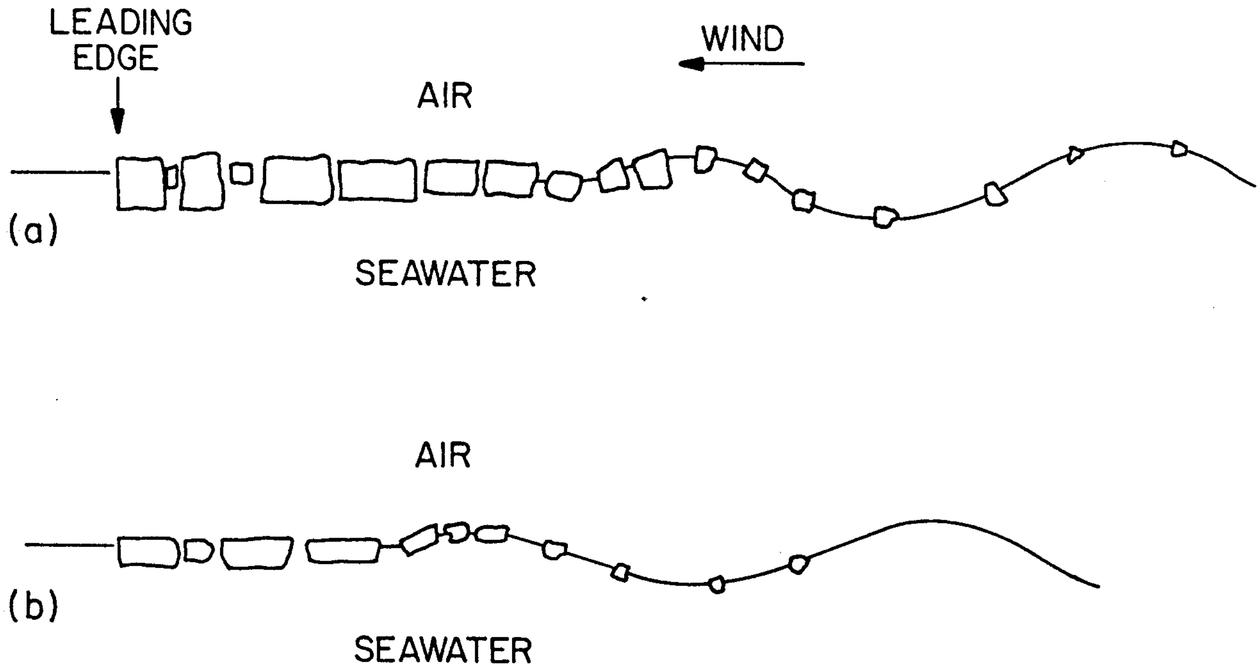

Figure 5. Schematic drawing of the band in cross section.

the surrounding warm water associated with the front. Although the ice also melts below, our field experiment suggests that the lateral erosion rate of the band is about 20 m hr^{-1}, or 0.5 km dy^{-1}. Third, Appendix 2 shows from a momentum balance on the band that the wave radiation stress, which is that stress exerted by the absorption and reflection of waves from the band, is the cause of the band acceleration relative to Pease's interior station.

Fourth, the Appendix also shows that the mean band motion can be modelled by a momentum balance among the air, water, Coriolis, and wave radiation stresses acting on the band. We also indirectly show that the AIDJEX water drag formulation is too large to describe the band motion; a better drag formulation is to use McPhee's (1982) sixth drag law described in Appendix 2.

Therefore, the physics of the ice response to wind and currents is very different in the MIZ than in the ice interior. There are three reasons for this.

1. Once the ice bands form, the internal ice stress term is unimportant.

2. The radiation stress term, which is the excess wave momentum flux exerted on the ice by the wind-waves generated in the fetch between the band and the next upwind obstacle, becomes on the same order as the wind stress.

3. The water stress term as described in the AIDJEX model is too large for the observed range of band velocities (0.4 - 0.6 m s^{-1}). A better water drag formulation is McPhee's sixth drag law. The use of the AIDJEX drag in calculation of the band motion yields 20% slower band velocities than the McPhee law.

The use of this new information will permit modelling of these ice edge features.

4. Oil in the MIZ

When considering the presence of oil in the MIZ, our most important observations are as follows: The oceanography of the region is characterized by a nearly stationary front, which responds to storms through a sharpening of the pycnocline. This front has a temperature transition of about 5 deg over 100 km, so that the front should be clearly visible on the high resolution IR channel on the TIROS satellite. Since the location of this front determines the ice edge position, we should be able to tell from satellite observations where an oil spill will melt out.

Second, the above observations on band translation and decay give us further information on oil impact in the MIZ. We have already discussed in earlier reports the translation of oil south from Norton Sound within large floes, and that as these floes approach the MIZ, the incident waves fracture, raft, and ridge them into small, thick, oily floes. Then, the formation of these floes into bands will lead to the translation of oil away from the ice edge. Just as the small floes lag behind the bands as the bands decay from the upwind edge, so will oil lag behind the bands as the floes containing oil break up and melt. Therefore, the bands will leave a trail of oil sheen and slick, depending on the amount of entrained oil. Finally, an oil slick within the frontal region will be overrun by the bands, and thus transported at a greater speed until the bands melt away.

APPENDIX 1:

PHYSICAL OCEANOGRAPHIC INVESTIGATIONS IN THE BERING SEA MARGINAL ICE ZONE

by

Robin D. Muench
Science Applications, Inc.

December 1981

TABLE OF CONTENTS

2.1. INTRODUCTION

2.1.1. Summary

A physical oceanographic field program has been carried out in the Bering Sea marginal ice zone (MIZ) as part of an integrated research effort addressing air-ice-water interactions in the MIZ and relating these interactions to fate and transport of OCS-related pollutants. As part of this field program, water temperature and salinity observations have been obtained from the Bering Sea MIZ during autumn (November) 1980 and mid-winter (February-March) 1981. Moored current observations were also obtained from two locations in the MIZ during the corresponding over-winter (November 1980 - June 1981) period. This report describes and discusses the temperature, salinity and current observations and relates the conditions summarily to past work and to current hypotheses concerning regional processes.

2.1.2. Background

Little information was available, prior to this study, concerning physical oceanographic processes in the Bering Sea MIZ. This lack of information was due in large part to logistical difficulties inherent in winter field activities in the region. Rigorous speculation on physical oceanographic processes in the Bering MIZ was initiated by Muench and Ahlnäs' (1976) observation that the MIZ was the locus of ice melting for the Bering Sea. This realization led in turn to speculation concerning methods by which heat to melt the ice might be supplied to the MIZ; a crude regional heat budget was computed by Muench and Ahlnäs. The realization also pointed out that the MIZ was the receiving area for a considerable quantity of ice-melt-derived, very low salinity water. It has generally been accepted that the approximate coincidence of the Bering ice edge, during its winter period of maximum southward extent, with the shelf break suggests an interaction between ice edge-related and shelf break oceanographic processes. This interaction has not been, however, rigorously explored.

Temperature-salinity data were obtained along the Bering Sea MIZ in midwinter 1979 and reported on by Pease (1980). She noted that the ice edge was underlain by a two-layered water structure wherein a warmer, more saline lower layer underlay a colder, lower salinity upper layer. Similar water structures underlying the ice edge were noted using mid-late winter data from 1975 and 1976 (Niebauer et al., 1981). Finally, Newton and Andersen (1980) noted the same structure associated with the Bering ice edge in winter 1980 temperature-salinity data. These data, obtained prior to the present study, supported the concept of a water structure two-layered in temperature and salinity underlying the ice edge.

A theoretical argument for presence along the ice edge of wind-driven upwelling similar in nature to coastal upwelling was advanced by Clarke (1978). More recent work with numerical modeling techniques has suggested, however, that the off-ice winds which would lead to upwelling also lead to breakup of a discrete ice edge into bands, which in turn destroys the tendency toward upwelling (L.P. Rød, personal communication, 1981). At the present time, it therefore appears unlikely that wind-induced upwelling at the ice edge is a significant factor in the dynamics there. Hypotheses concerning the process have not yet, however, been fully developed.

Development of additional speculations or hypotheses concerning Bering Sea MIZ processes awaits further analysis of existing data or acquisition of new data. This report, by providing a summary analysis of newly obtained data, will further the development of knowledge on such processes.

2.1.3. Objectives

The overall objective of the Bering Sea MIZ physical oceanographic program is to derive information on oceanographic processes associated with the MIZ which exert control over the fate and effects of OCS-related pollutants. Specific program objectives include:

- Definition of the large-scale (i.e. of order hundreds of km) fields of temperature and salinity (and derived density) and relating of these to regional oceanographic advective (transport) and diffusive (mixing) processes.
- Observation of small-scale (1-10 km) features (such as low salinity lenses and frontal structures) in the temperature and salinity distributions along the ice edge during winter and relating these where possible to regional oceanographic features, ice motion and distribution, and the wind field.
- Estimation, in conjunction with sea ice and meteorological data, of regional heat and salt balances.
- Estimation of the effects upon the water column of convective processes associated with local winds and with ice freezing.
- Estimation of the effects of both large- and small-scale water circulation features upon ice motion and distribution in the MIZ.

2.2. FIELD PROGRAM

2.2.1. Temperature and Salinity Observations

Two field activities involving temperature and salinity observations have been carried out under this program: an autumn (November 1980) observation program of regional temperature and salinity distributions combined with current meter mooring deployments, and a mid-winter (February-March 1981) program of detailed temperature and salinity observations along the ice edge. The mid-winter program was carried out simultaneously with intensive observations of meteorological and sea ice features. Recovery of the current meters which had been deployed in November 1980 was carried out in June 1981.

During the November 1980 program, 25 CTD casts were occupied in the portion of the Bering Sea normally occupied by the MIZ during winter (Figure 2-1). These CTD data were acquired from the NOAA vessel DISCOVERER using a Plessey Model 9040 CTD system with calibration and processing procedures carried out as per OCSEAP specifications. These November CTD data provide two transects extending across the shelf normal to the isobaths from about the shelf break to the 50-meter isobath and give a good representation of conditions over the central Bering Sea shelf including the MIZ. The observed distributions are discussed in the following section of this report. A listing of the autumn 1980 CTD stations is given in Table 2-1.

During the February-March 1981 field program, 64 CTD casts (2-65, Figure 2-2) were taken in the Bering Sea MIZ near the ice edge. (The initial single cast (1) was taken in the Gulf of Alaska near Unimak Pass for equipment calibration purposes.) These CTD data were taken from the NOAA vessel SURVEYOR using a Plessey Model 9040 CTD system; calibration casts were taken every third station. The geographical location of the winter field work within the overall study region

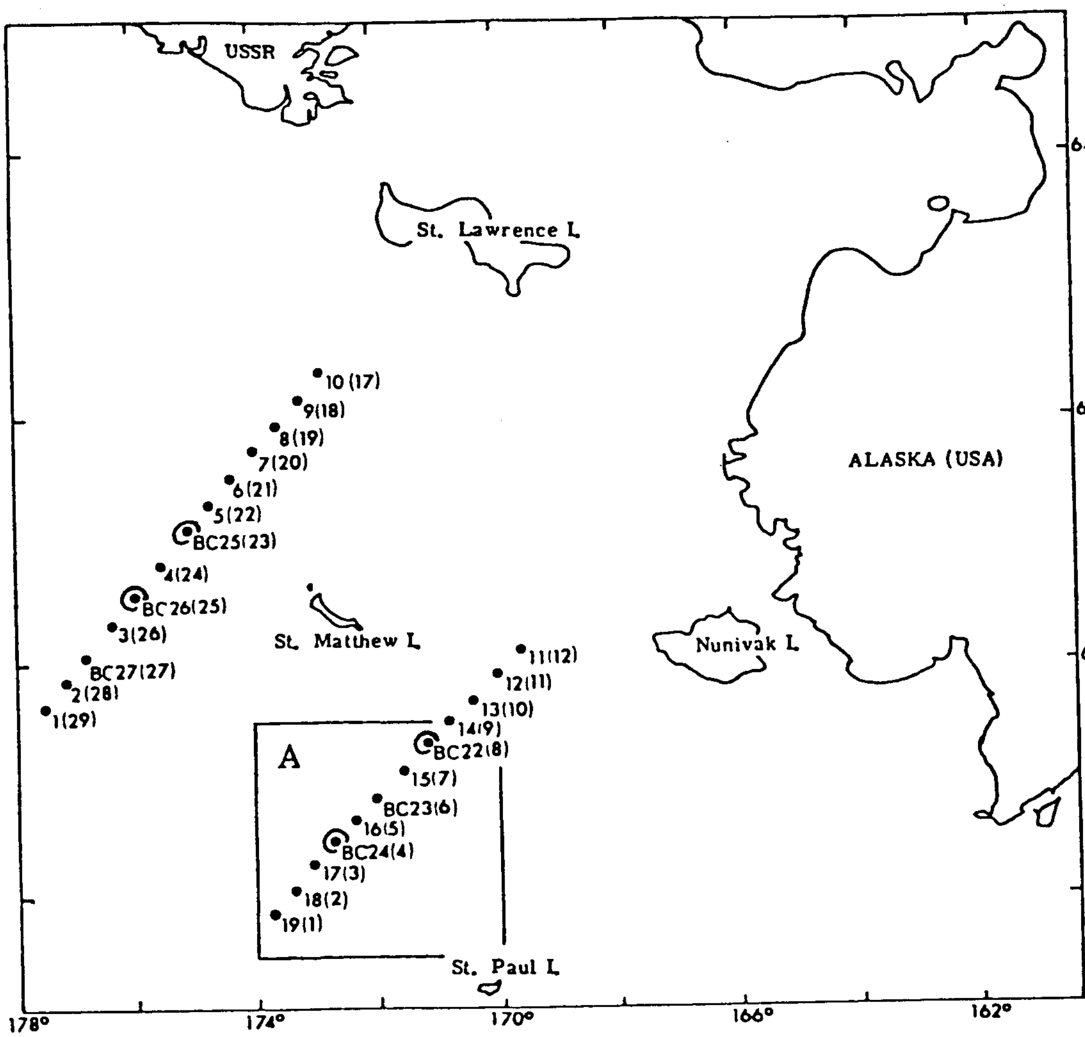

Figure 2-1. Geographical locations in the study region, showing positions of CTD stations occupied in November 1980 (•) and current meter moorings deployed from November 1980 - June 1981 (◉). First number at each station gives the station designation, while the second (parenthesized) number is the cast number. Geographical locations, depths and other information for stations are given in Table 2-1. The rectangular area "A" indicates the location of the February-March 1981 winter field program which is shown in greater detail on Figure 2-2.

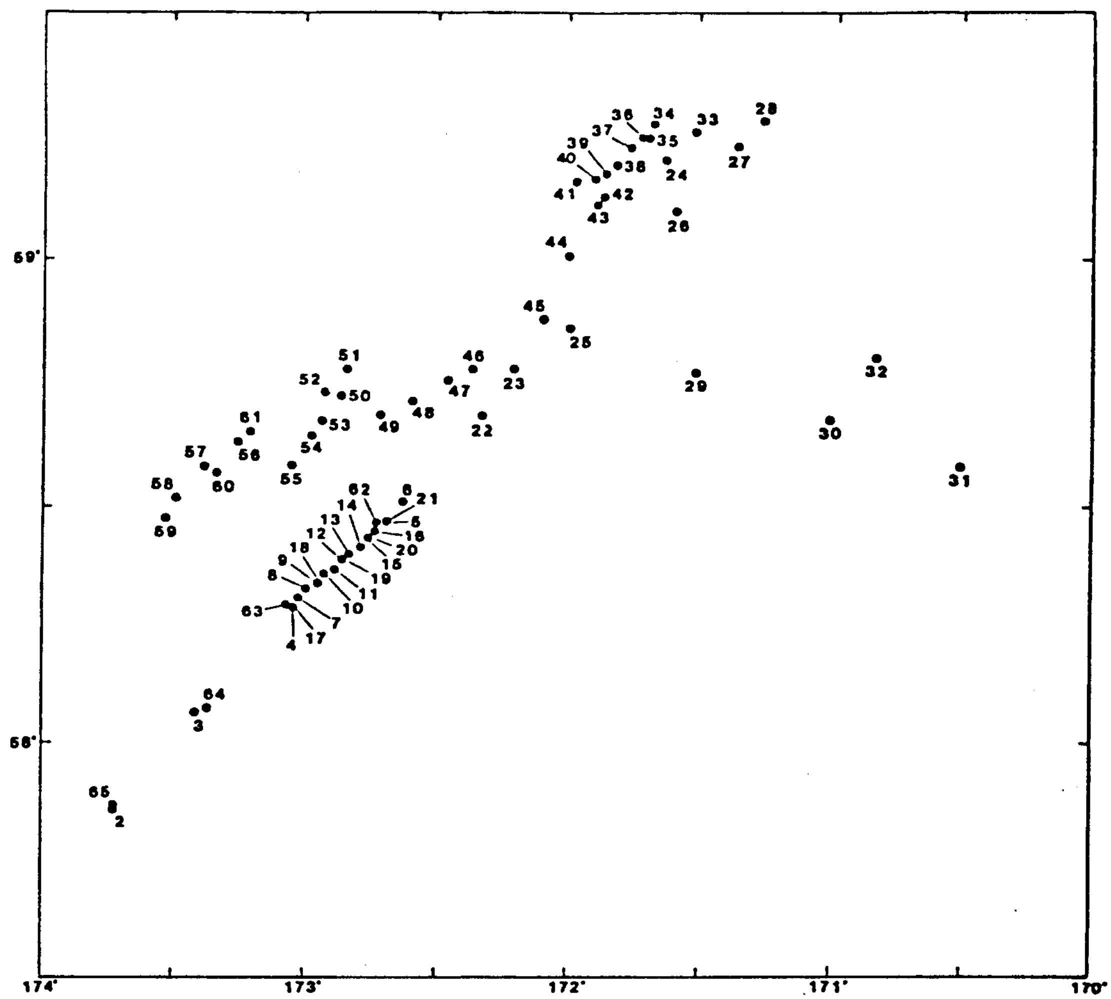

Figure 2-2. Locations of CTD stations occupied in the Bering Sea MIZ during February-March 1981. Numbers are cast numbers. Detailed information on each station is provided in Table 2-2. Geographical location of study region is indicated on Figure 2-1.

Table 2-1. Listing of CTD stations occupied in November 1980 in the central Bering Sea shelf region.

Consecutive Cast No.	Latitude (N)	Longitude (W)	Date (GMT)	JD (GMT)	Hour (GMT)	Bottom Depth (m)	Assigned Sta. No.
1	57-51.5	173-43.2	11-10	315	1440	137	19
2	58-03.8	173-21.7	11-10	315	1623	111	18
3	58-17.1	173-02.7	11-10	315	1759	110	17
4	58-28.1	172-41.1	11-10	315	1935	107	BC24
5	58-41.1	172-20.7	11-10	315	2159	97	16
6	58-51.8	171-59.3	11-10	315	2331	91	BC23
7	59-05.7	171-35.8	11-11	316	0154	82	15
8	59-18.0	171-12.7	11-11	316	0327	76	BC22
9	59-31.1	170-50.8	11-11	316	0526	73	14
10	59-42.1	170-27.1	11-11	316	0658	65	13
11	59-55.9	170-02.9	11-11	316	0823	53	12
12	60-08.1	169-38.8	11-11	316	1013	48	11
17	62-21.0	172-50.1	11-13	318	0207	58	10
18	62-08.9	173-12.6	11-13	318	0334	60	9
19	61-57.0	173-37.0	11-13	318	0509	65	8
20	61-45.1	173-58.9	11-13	318	0635	73	7
21	61-32.1	174-20.7	11-13	318	0759	80	6
22	61-19.9	174-44.0	11-13	318	0931	86	5
23	61-08.0	175-05.7	11-13	318	1057	92	BC25
24	60-51.2	175-34.3	11-13	318	1316	106	4
25	60-34.1	176-01.5	11-13	318	1503	119	BC26
26	60-19.7	176-24.9	11-13	318	1707	128	3
27	60-04.3	176-49.8	11-13	318	1858	142	BC27
28	59-52.2	177-09.8	11-13	318	2103	135	2
29	59-39.2	177-30.3	11-13	318	2238	207	1

is indicated on Figure 2-1; the winter CTD station work included occupation of the outer (southern) eight stations on the southeastern transect shown on Figure 2-1, multiple occupation of a portion of this transect, and time series taken along the ice edge. A listing of the winter 1981 CTD stations is given in Table 2-2.

2.2.2. Current Observations

Six current meter moorings were deployed in November 1980 at the locations indicated on Figure 2-1. Four of the six moorings were recovered in June 1981. Of those recovered, two malfunctioned so that only two current records were obtained. The current meter moorings are summarized in Table 2-3.

Current data were obtained using Aanderaa Model RCM-4 current meters deployed in a standard taut-wire mooring configuration such as described by Muench and Schumacher (1980). The current meters recorded at 30-minute intervals. Translation of the data from the current meter tapes onto 9-track tape was carried out at the Department of Oceanography, University of Washington. The data were filtered using a 35-hour running-average type filter and subsampled every 6 hours to provide de-tided data.

Table 2-2. Listing of CTD stations occupied in February-March 1981 in the central Bering Sea shelf region along the ice edge.

Consecutive Cast No.	Latitude (N)	Longitude (W)	Date (GMT)	JD (GMT)	Hour (GMT)	Bottom Depth (m)	Assigned Sta. No.
1	55-36.3	158-59.7	2-23	54	2333	114	
2	57-51.7	173-43.0	2-26	57	1315	136	19
3	58-03.8	173-24.7	2-26	57	1610	113	18
4	58-17.1	173-02.9	2-26	57	1921	112	17
5	58-27.9	172-41.1	2-26	57	2116	109	BC24
6	58-30.6	172-37.6	2-26	57	2255	108	
7	58-18.4	173-01.5	2-27	58	0642	111	
8	58-19.4	172-59.7	2-27	58	0724	111	
9	58-20.1	172-57.3	2-27	58	0811	111	
10	58-21.3	172-55.5	2-27	58	0857	112	
11	58-21.9	172-53.1	2-27	58	0937	111	
12	58-23.2	172-51.7	2-27	58	1023	112	
13	58-23.9	172-49.8	2-27	58	1054	110	
14	58-24.8	172-47.2	2-27	58	1135	110	
15	58-25.9	172-45.9	2-27	58	1235	108	
16	58-26.8	172-43.8	2-27	58	1323	108	
17	58-17.2	173-02.6	3-01	60	0916	111	
18	58-20.2	172-56.6	3-01	60	1012	112	
19	58-23.1	172-50.9	3-01	60	1059	110	
20	58-26.1	172-45.1	3-01	60	1146	108	
21	58-28.2	172-41.1	3-01	60	1224	108	
22	58-41.1	172-19.6	3-01	60	1846	104	16
23	58-47.0	172-12.6	3-01	60	2200	101	BC23
24	59-11.9	171-37.9	3-02	61	2237	82	
25	58-52.0	171-59.2	3-03	62	0631	96	BC23
26	59-05.7	171-35.3	3-03	62	0827	83	
27	59-13.3	171-21.4	3-03	62	1048	81	
28	59-16.6	171-15.7	3-03	62	2037	78	BC22
29	58-46.5	171-30.8	3-04	63	0619	91	
30	58-40.6	171-00.7	3-04	63	0817	82	
31	58-34.9	170-30.7	3-04	63	1011	79	
32	58-48.3	170-49.9	3-04	63	1151	79	
33	59-15.5	171-31.2	3-04	63	1505	81	
34	59-16.4	171-40.7	3-05	64	0244	81	
35	59-14.7	171-41.8	3-05	64	0603	80	
36	59-14.7	171-43.1	3-05	64	0637	80	
37	59-13.4	171-45.4	3-05	64	0842	80	
38	59-11.4	171-49.0	3-05	64	1030	83	
39	59-10.3	171-51.4	3-05	64	1232	84	
40	59-09.6	171-54.0	3-05	64	1448	85	
41	59-09.3	171-58.1	3-05	64	1648	85	
42	59-07.5	171-51.9	3-05	64	2045	86	
43*	59-06.7	171-53.2	3-06	65	0049	79	
44*	59-00.4	171-59.8	3-06	65	0449	93	
45*	58-52.9	172-05.6	3-06	65	1244	97	
46	58-46.9	172-22.1	3-08	67	0037	102	
47	58-45.4	172-27.7	3-08	67	0442	104	
48	58-42.8	172-35.6	3-08	67	0915	106	

*Temperature record only, due to icing of conductivity cell.

Table 2-2. (continued)

Consecutive Cast No.	Latitude (N)	Longitude (W)	Date (GMT)	JD (GMT)	Hour (GMT)	Bottom Depth (m)	Assigned Sta. No.
49	58-41.3	172-43.0	3-08	67	1230	108	
50	58-43.6	172-51.8	3-08	67	1654	112	
51	58-47.0	172-50.5	3-08	67	1913	110	
52	58-44.0	172-55.5	3-08	67	2029	112	
53	58-40.6	172-56.1	3-08	67	2200	112	
54	58-38.7	172-58.6	3-08	67	2340	113	
55	58-35.1	173-03.0	3-09	68	0100	114	
56	58-37.8	173-15.3	3-09	68	0438	119	
57	58-34.9	173-23.1	3-09	68	0845	122	
58	58-31.1	173-29.6	3-09	68	1232	123	
59	58-28.7	173-31.5	ABORTED - Surface values only				
60	58-34.1	173-20.3	3-10	69	1940	121	
61	58-39.1	173-12.8	3-10	69	2348	119	
62	58-28.1	172-43.7	3-11	70	0236	108	BC24
63	58-17.4	173-04.1	3-11	70	0513	112	17
64	58-04.3	173-22.2	3-11	70	0703	113	18
65	57-52.1	173-43.3	3-11	70	0851	137	19

Table 2-3. Listing of mooring deployments in the central Bering Sea shelf region during the over-winter 1980-1981 period.

Assigned Mooring ID	Latitude (N)	Longitude (W)	Deployment Date (GMT)	Deployment JD (GMT)	Deployment Hour (GMT)	Bottom Depth (m)	Meter Depth (m)	Meter Serial No.	Record Length (days)
BC22	59-10.4	171-11.4	11-11	316	0357	76	51	1813	207
BC23*	58-51.8	172-01.0	11-11	316	0007	95	52	3130	---
BC24**	58-28.3	172-42.4	11-10	315	2021	107	59	3128	110
BC25**	61-08.3	175-05.9	11-13	318	1128	95	52	3177	205
BC26	60-34.2	176-02.1	11-13	318	1531	119	52	3135	203
BC27*	60-04.6	176-49.6	11-13	318	1927	142	61	3131	---

*Not recovered.
**T and C records only due to malfunction.

2.3. TEMPERATURE, SALINITY AND DENSITY DISTRIBUTIONS

2.3.1. November 1980

Vertical distributions of temperature, salinity and density along the two CTD transects occupied in November 1980 are shown in Figure 2-3 through 2-8. The following features were common to both transects:

- The water column was two-layered vertically in temperature, salinity and density, with the interface between layers occurring at 50-60 m. The water was vertically well mixed above and below the interface. The interface between layers was 5-10 m shallower at the northwest than at the southeast transect, and was about 10-m thick.

- There was a relatively constant northeastward decrease in temperature, salinity and density in both the upper and lower layers in both transects. The ensuing horizontal gradients in either layer were approximately 0.01 °C/km, 0.003 ^{o}/oo/km and 0.003 sigma-t units/km, respectively.

- There was a tendency for slightly increased horizontal temperature and salinity gradients in both layers at the 80-90 m isobaths. However, this was not true for density due to the cancelling effects exerted by the opposing temperature and salinity gradients on the density gradient.

- At about the 80-m isobath, there was a 50-km wide "bolus" of water which was about 1 °C colder than the surrounding water. This feature appeared on both transects, though the temperature of the bolus was about 2.5 °C lower on the northwest transect.

While the major feature of the comparison between the two transects was the similarity in distributions, overall water temperatures at the northwest transect were about 2^{o}C lower than those in the southeast transect. Salinity and density were similar along the two transects. In the southeast section, there was some indication of salinity finestructure at the interface between layers (stations 3, 4 and 8, Figure 2-4); such finestructure was not evident anywhere in the transect to the northwest.

The tendency for water temperature to be lower along the northwest section is evident in the horizontal distributions of temperature in the upper and lower layers (Figures 2-9 and 2-10). The upper layer distribution shows maximum

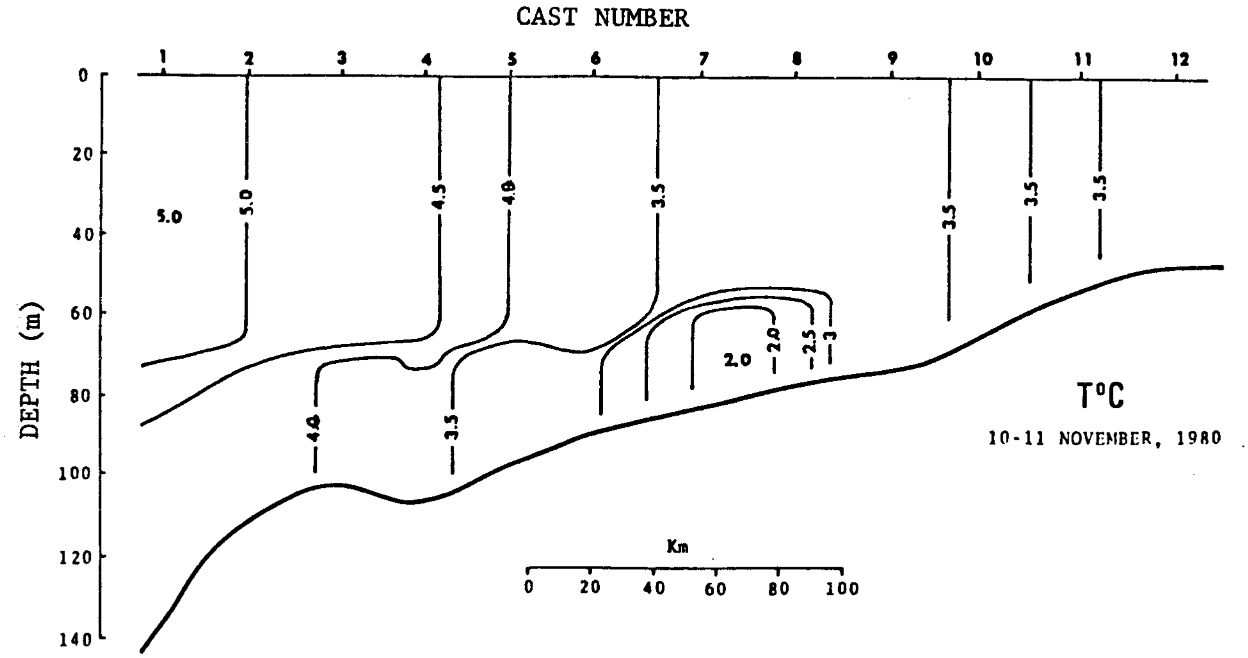

Figure 2-3. Vertical distribution of temperature across the central Bering Sea shelf in autumn 1980. Figure 2-1 shows locations of stations included in the transect. Numbers are cast numbers.

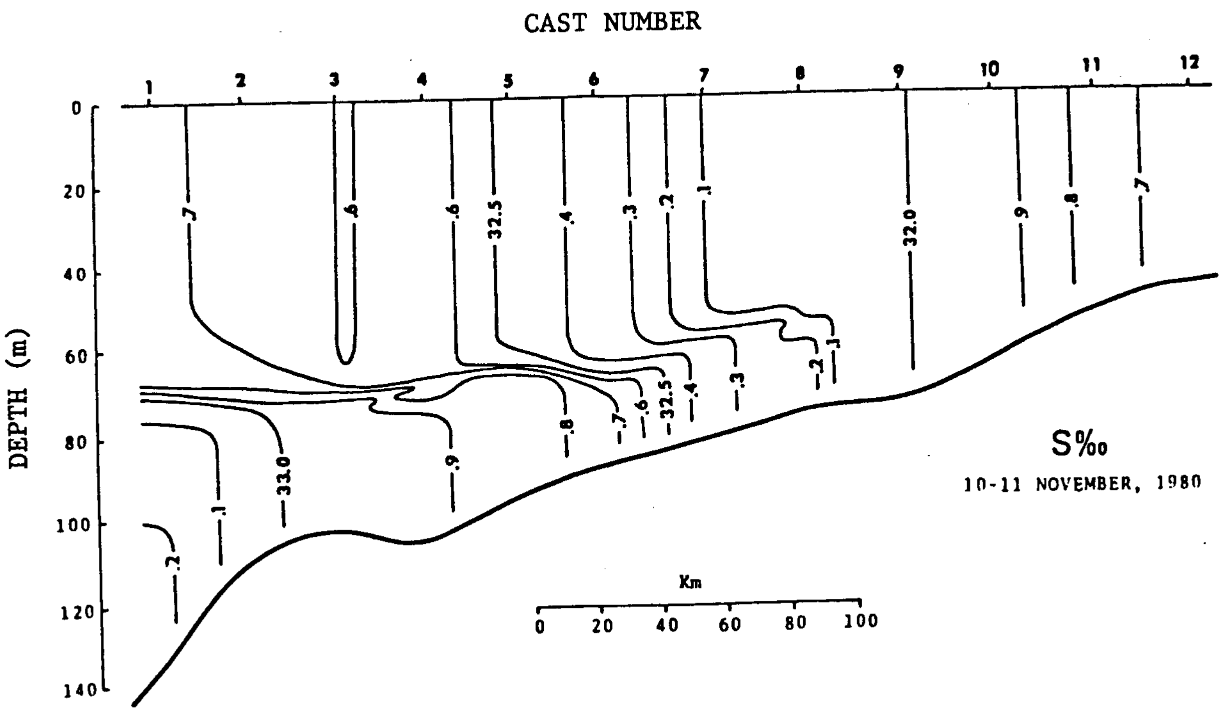

Figure 2-4. Vertical distribution of salinity; same transect as Figure 2-3.

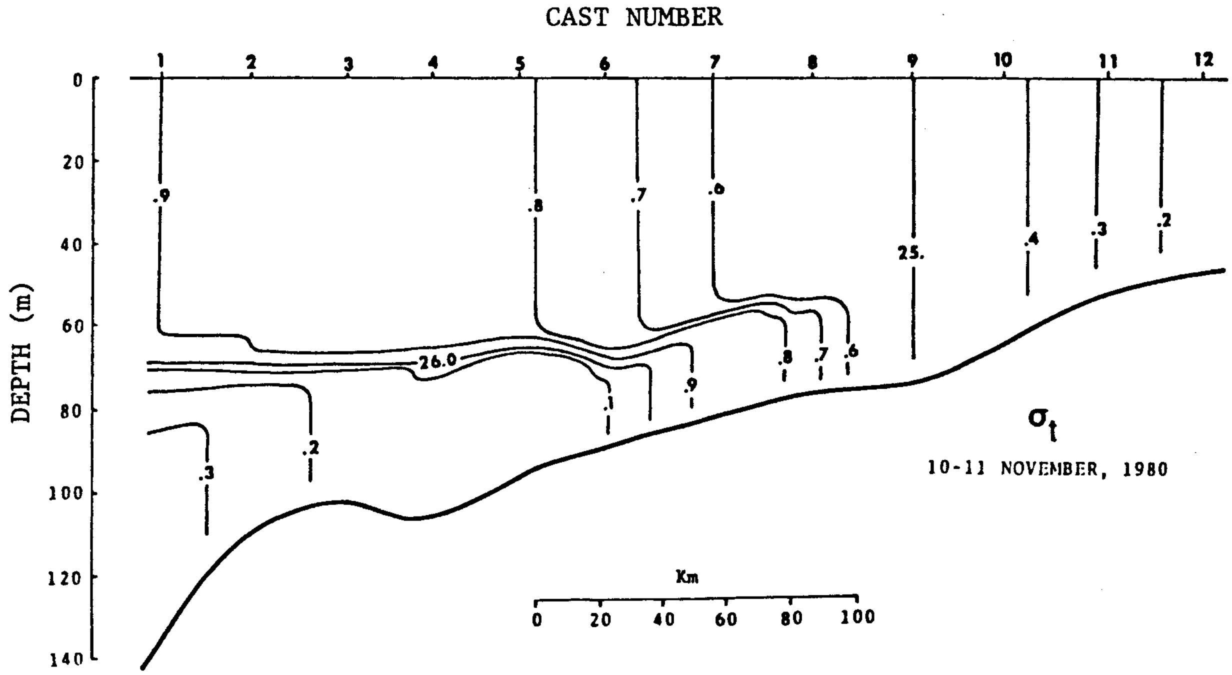

Figure 2-5. Vertical distribution of density (as sigma-t); same transect as Figure 2-3.

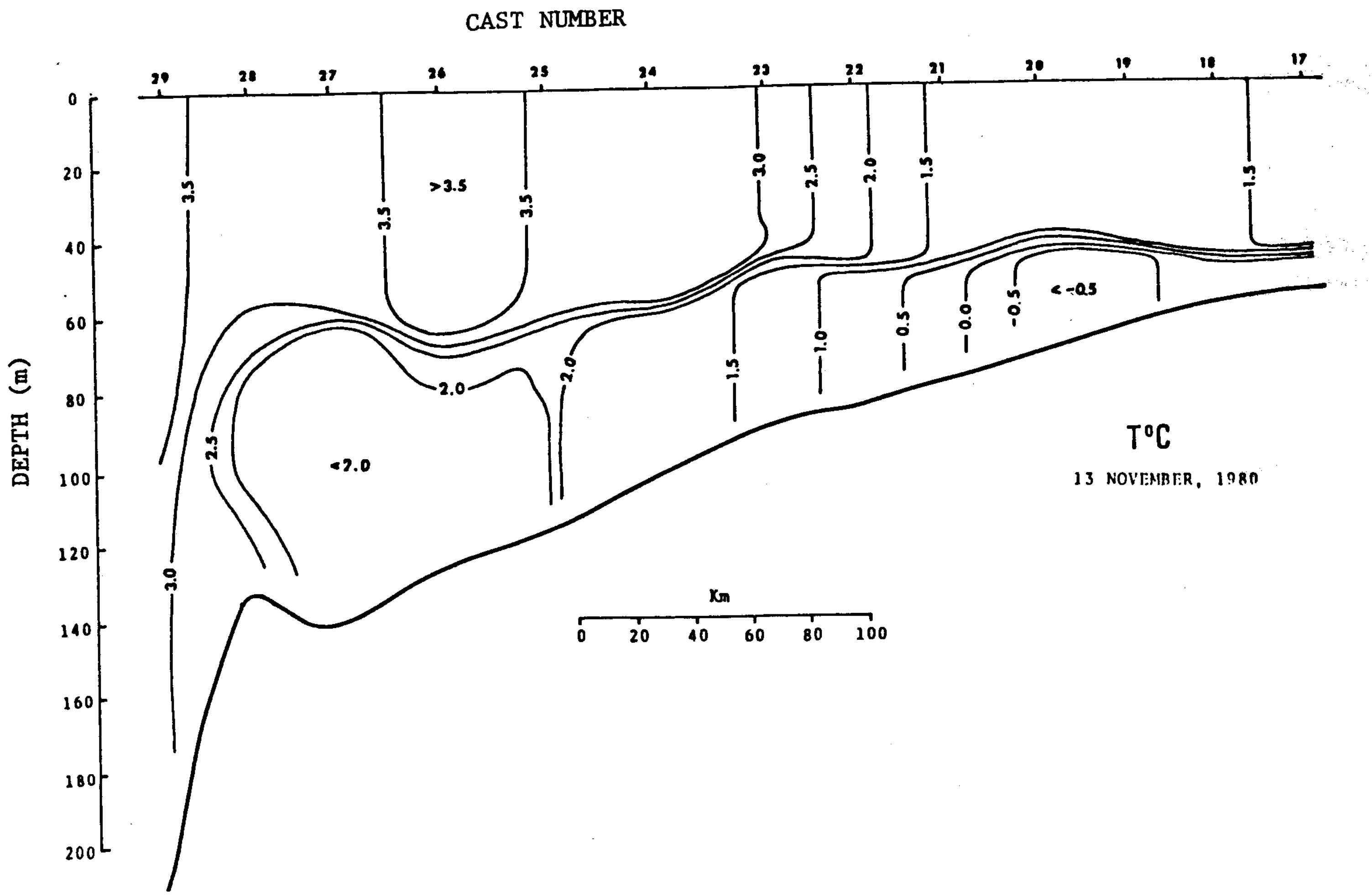

Figure 2-6. Vertical distribution of temperature across the central Bering Sea shelf in autumn 1980. Figure 2-1 shows locations of stations included in the transect. Numbers used are cast numbers.

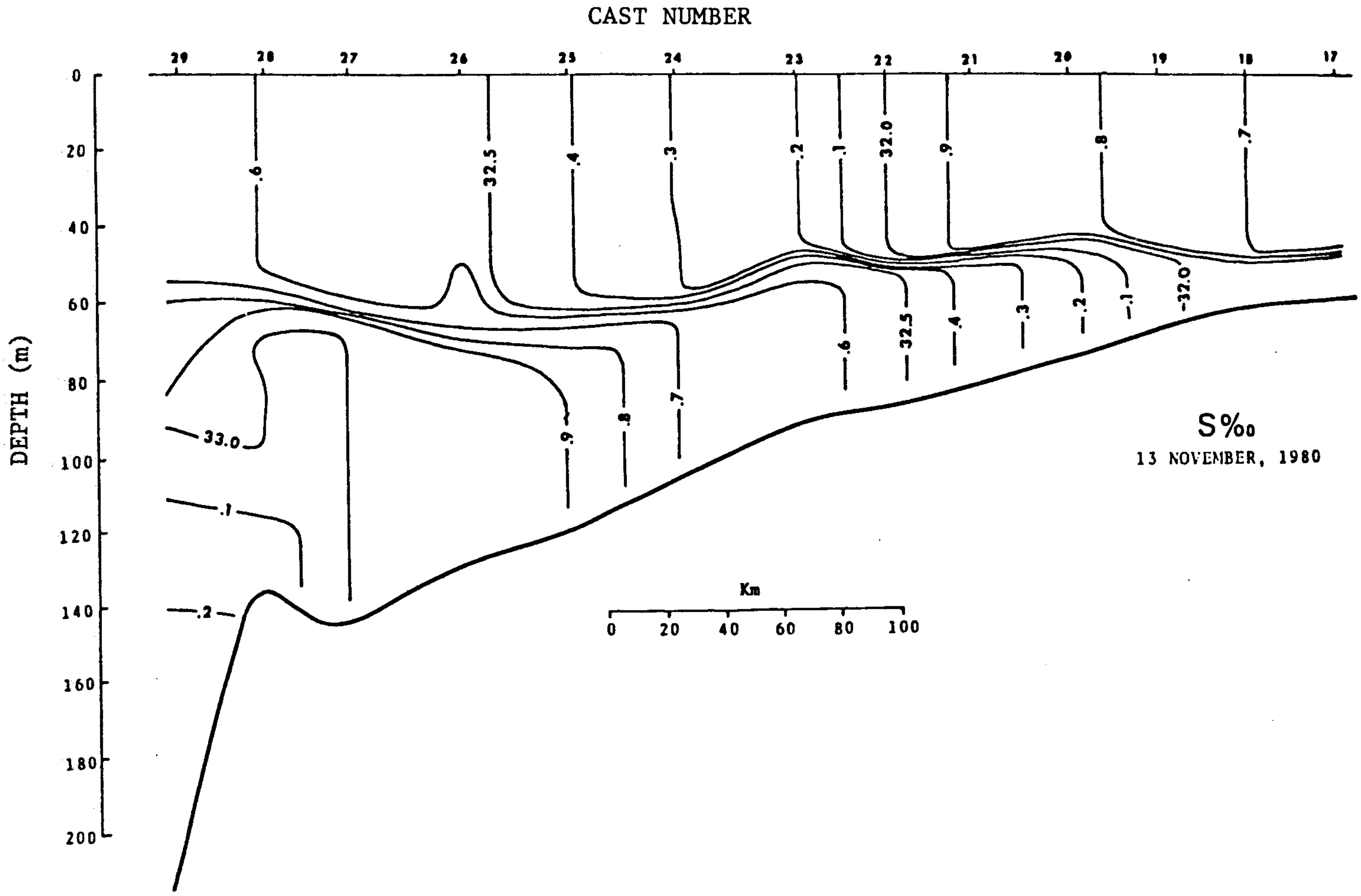

Figure 2-7. Vertical distribution of salinity; same transect as Figure 2-6.

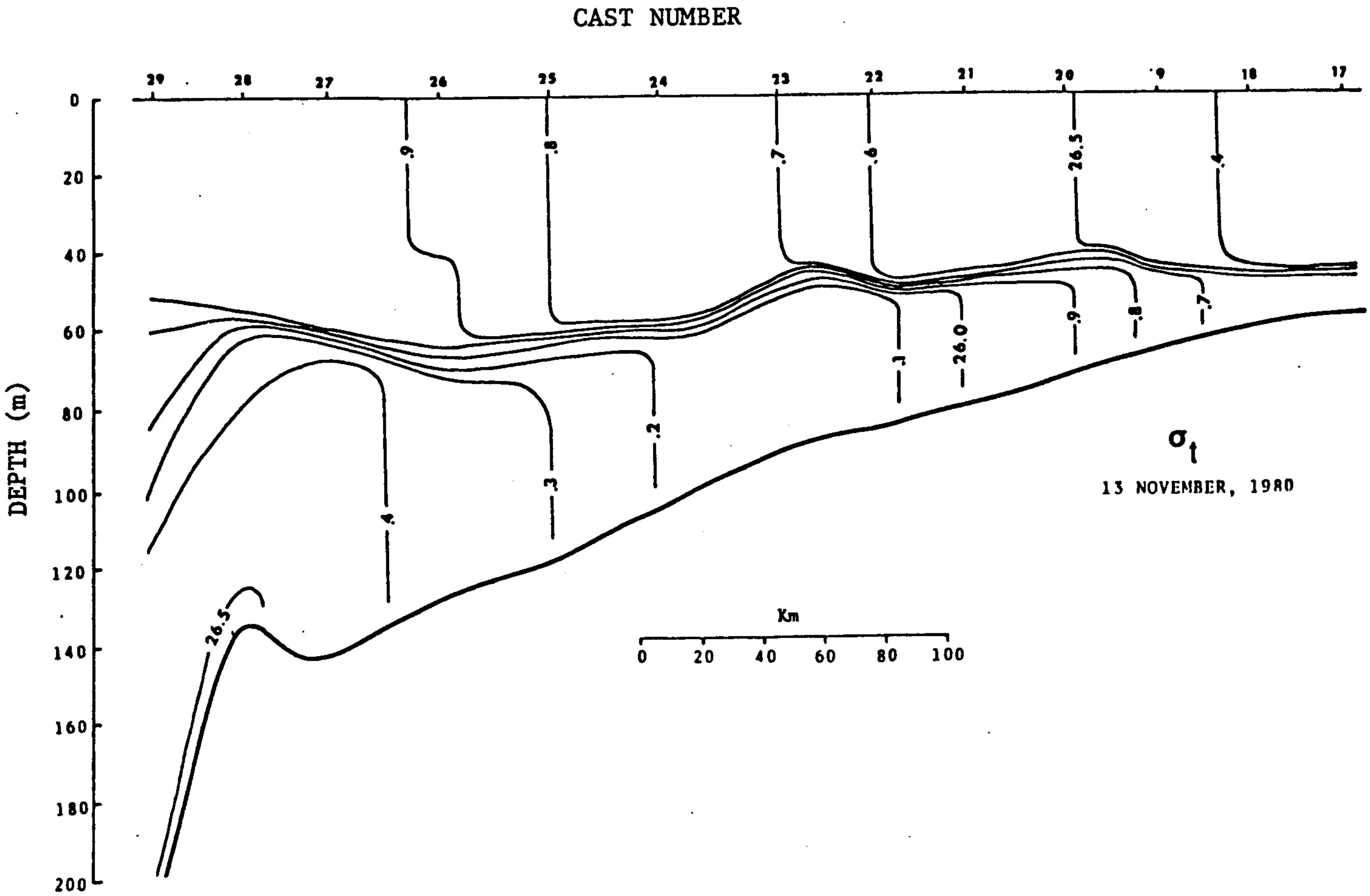

Figure 2-8. Vertical distribution of density (as sigma-t); same transect as Figure 2-6.

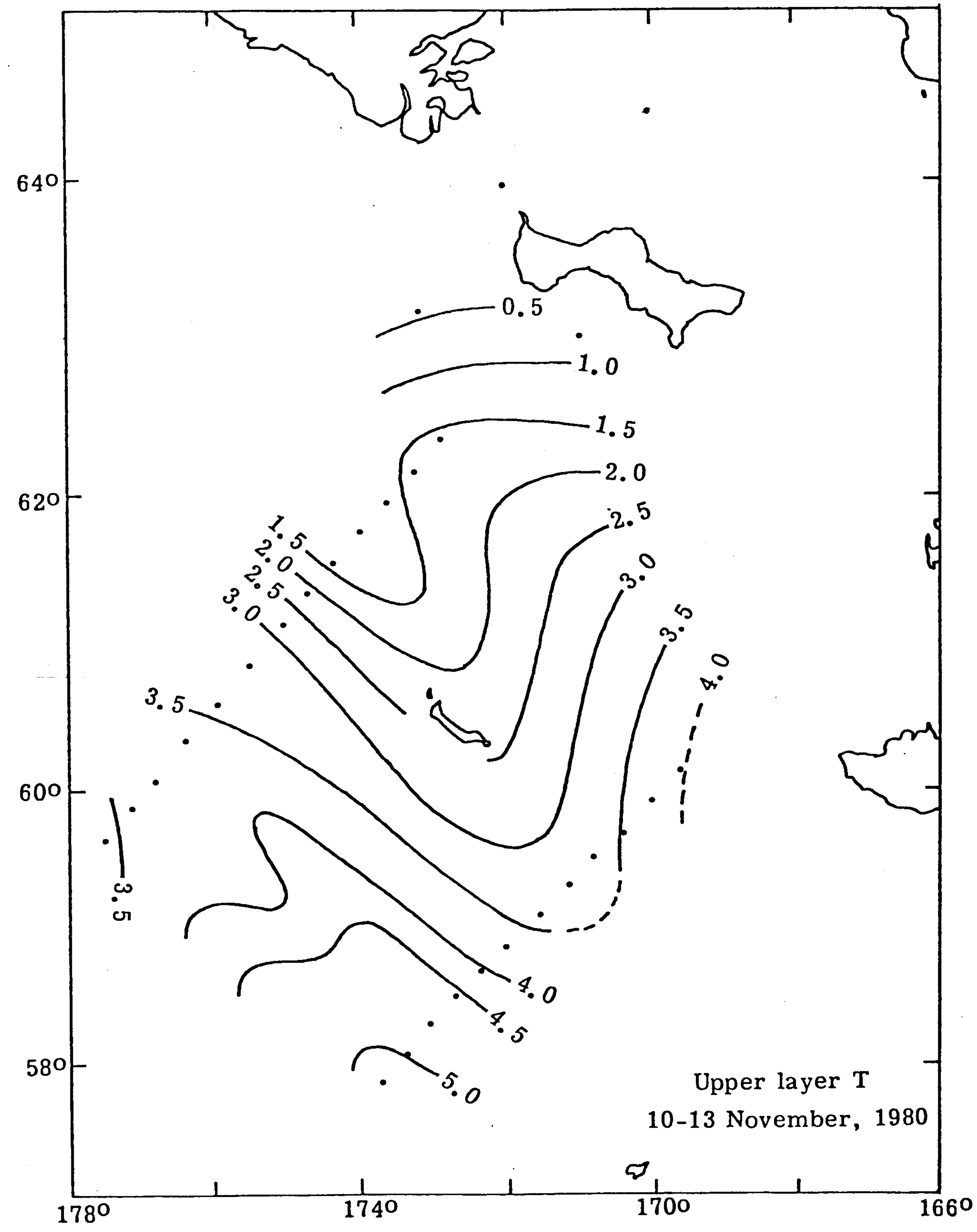

Figure 2-9. Horizontal distribution of temperature in the upper water layer during autumn, 1980.

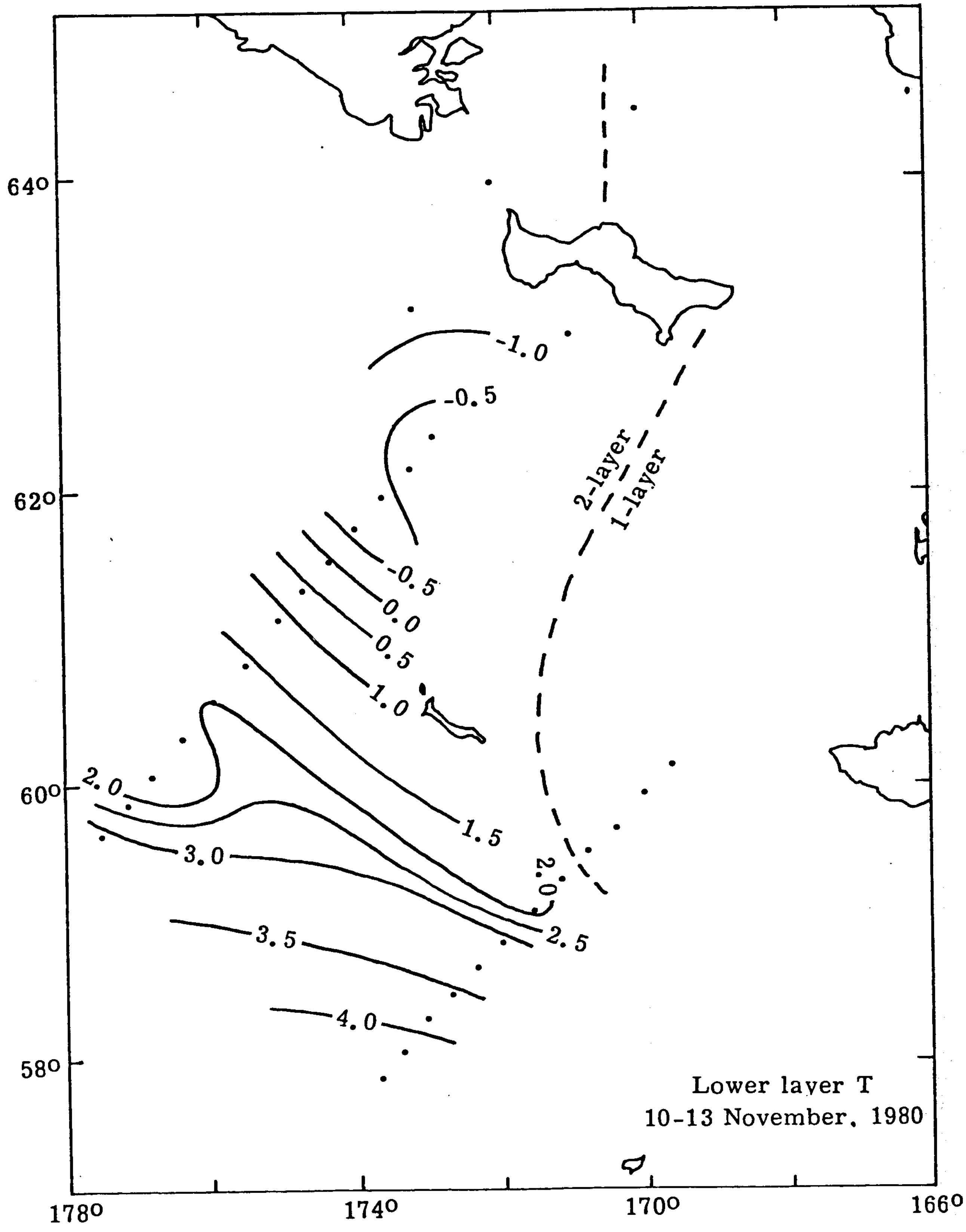

Figure 2-10. Horizontal distribution of temperature in the lower water layer during autumn 1980. Dashed line indicates boundary between water characterized by two-layered structure and vertically homogeneous water.

temperatures higher than 5 °C in the southern portion, with temperatures down to less than 0.5 °C in the north. The distribution shows a "tongue"-like, low-temperature (< 3.5 °C) feature extending toward the southeast from the northwest, with higher temperatures to the east along the Alaskan coast (4.0 °C) and to the southwest toward the shelf break (3.5-5.0 °C).

Lower layer temperatures (Figure 2-10) showed a similar pattern, except that temperatures were lower than in the upper layer. Minimum temperatures (< -1.0 °C) occurred to the north, with the highest temperatures (> 4.0 °C) to the south near the shelf break.

Upper- and lower-layer distributions of salinity (Figure 2-11) show maximum salinity in both layers near the shelf break and lowest values toward the northeast.

The cross-shelf horizontal density gradient evident in Figures 2-5 and 2-8 suggests that baroclinic northwestward flow may have been present. Dynamic topographies of the surface relative to both 50 dbar and 100 dbar (Figure 2-12) confirm presence of a weak northwestward baroclinic flow tendency, in agreement with conventional wisdom concerning circulation on the Bering Sea shelf. The weak southeasterly counterflow at the southern end of the northwest transect is probably connected with a bolus of relatively cold (< 2.0 °C) water located in the lower layer (stations 25-28, Figure 2-6).

2.3.2. February-March 1981

Temperature-salinity data were acquired, during February-March 1981, along a transect which coincided with the southeastern of the two transects occupied

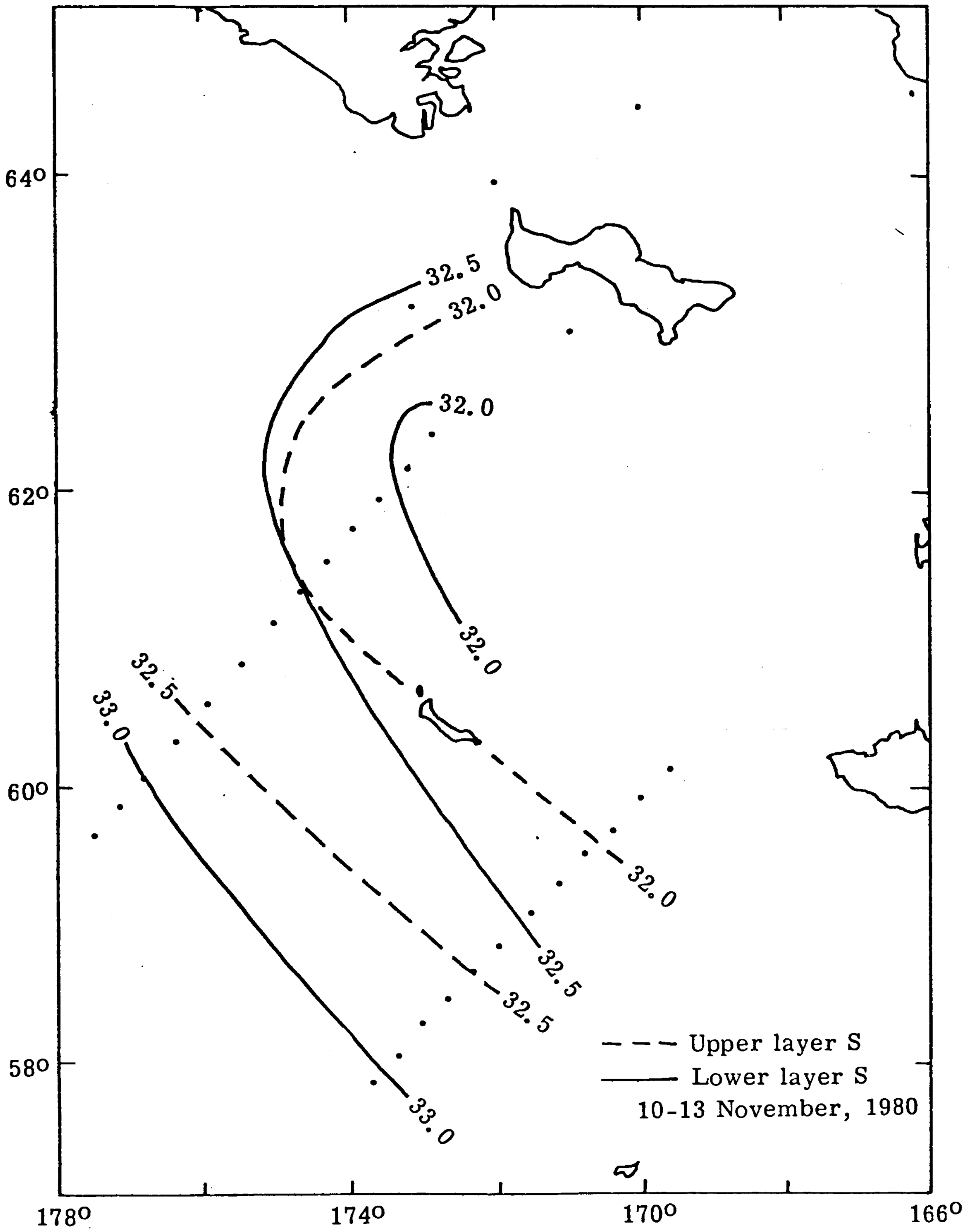

Figure 2-11. Horizontal distributions of salinity ($^{0}/oo$) in both the upper and lower water layers during autumn 1980.

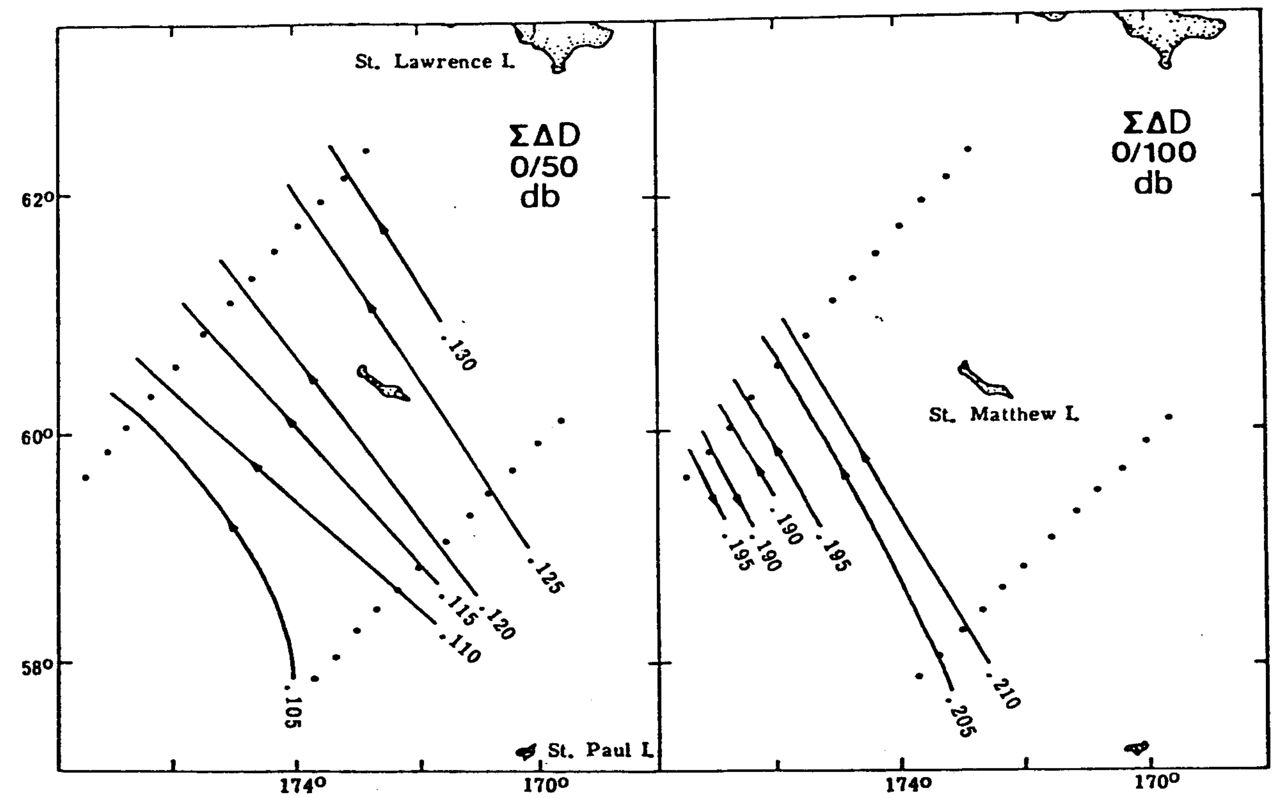

Figure 2-12. Dynamic topographies of the water surface relative to the 50 db (left) and 100 db (right) levels during autumn 1980. Arrowheads on contours indicate direction of baroclinic surface flow, relative to the reference levels, as implied by the dynamic topography. Contours are in dynamic meters, with contour interval of 0.5 dynamic centimeter.

in November 1980 (see Figure 2-1). The vertical distributions of temperature, salinity and density along the transect are shown on Figures 2-13 to 2-15. Stations 1-20 along this transect were south of the ice edge, while the remaining stations were occupied after the ice had been forced northward by strong south winds associated with a storm system. The temperature, salinity and density were near-homogeneous in the vertical in the southern part of the transect. In its northern portion, the water was vertically homogeneous, at or near the freezing point and had a salinity of about 31.9 $^{o}/oo$. A region about 80-km wide underlay the southern extreme location of the ice edge and was characterized by two-layered water structure. The lower layer was warmer (> 1.0 °C) and more saline (32.5-32.7 $^{o}/oo$) than the upper layer (< 0.5 °C and 32.1-32.6 $^{o}/oo$). The temperature and salinity of the lower layer were continuous with those of water to the south. Temperature and salinity of the upper layer were continuous with those of water to the north.

Two separate occupations were obtained along part of the transect shown in Figures 2-13 to 2-15. These separate occupations documented variation in the water column during passage over the region of a severe storm having south winds which forced the ice edge northward. Temperature is well correlated with salinity and density (Figures 2-13 to 2-15) and may be used as a tracer of water properties. Figure 2-16 illustrates this relationship, showing the water structure before and after passage of the storm along the southern portion of the two-layered structure which underlay the ice edge. Prior to the storm, on 27 February, the lower layer was well-mixed and the upper layer was stratified. After the storm, on 1 March, both layers were well-mixed and the upper layer had been considerably deepened at the southern extreme of the two-layered structure. Despite the

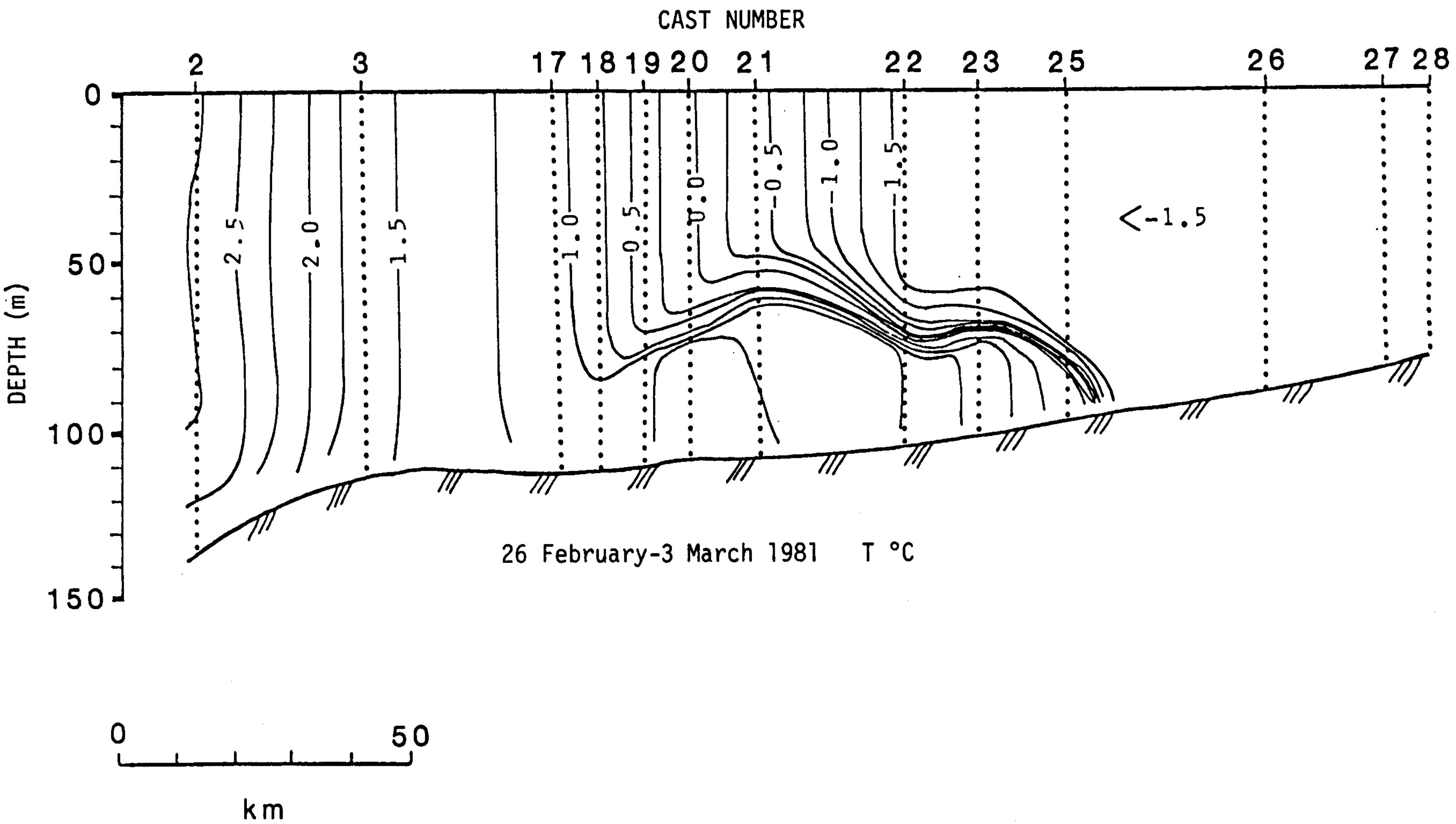

Figure 2-13. Vertical distribution of temperature across the central Bering Sea shelf in mid-winter 1981. Figure 2-2 shows locations of stations which are included in this transect. Numbers given are cast numbers.

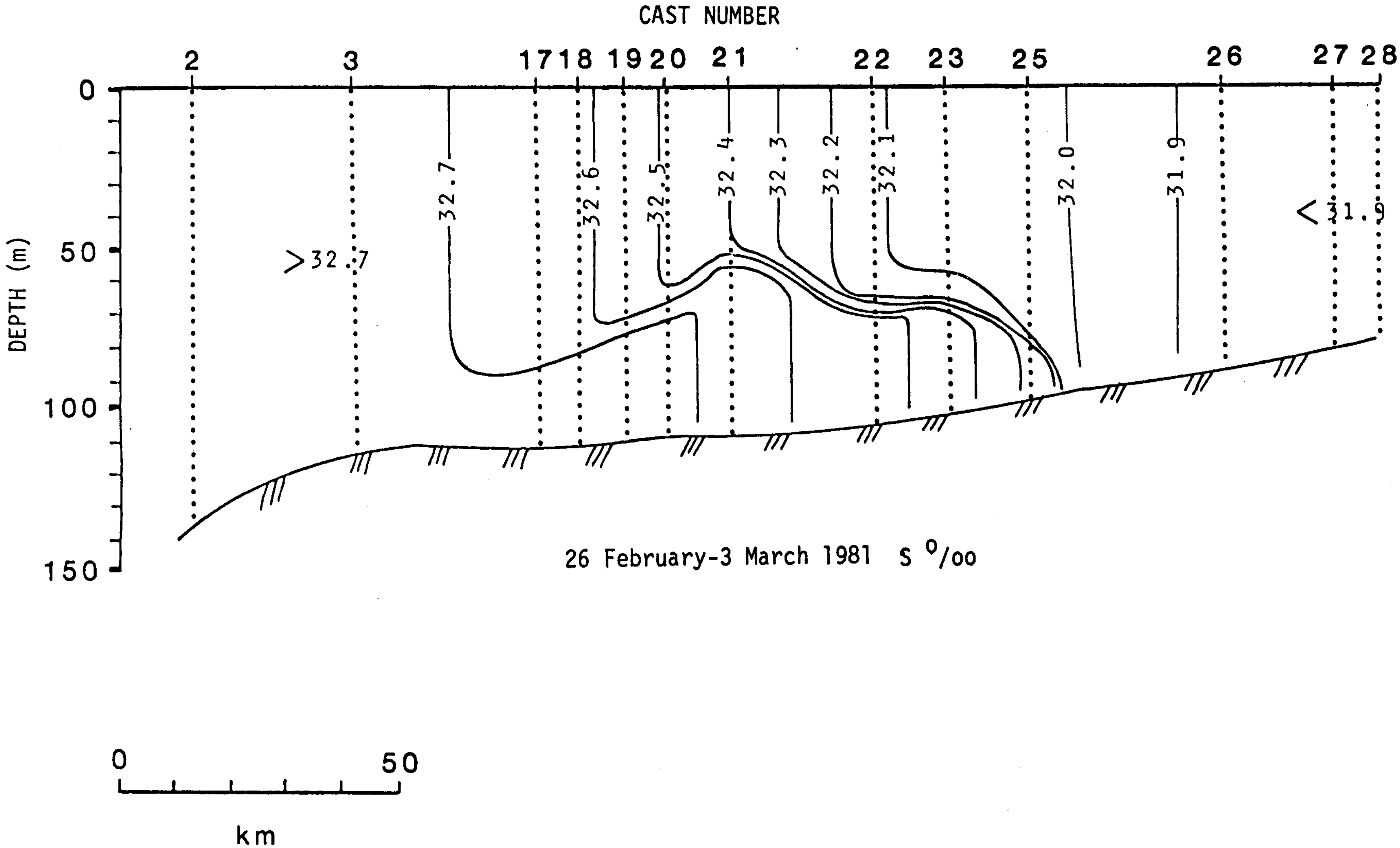

Figure 2-14. Vertical distribution of salinity; same transect as Figure 2-13.

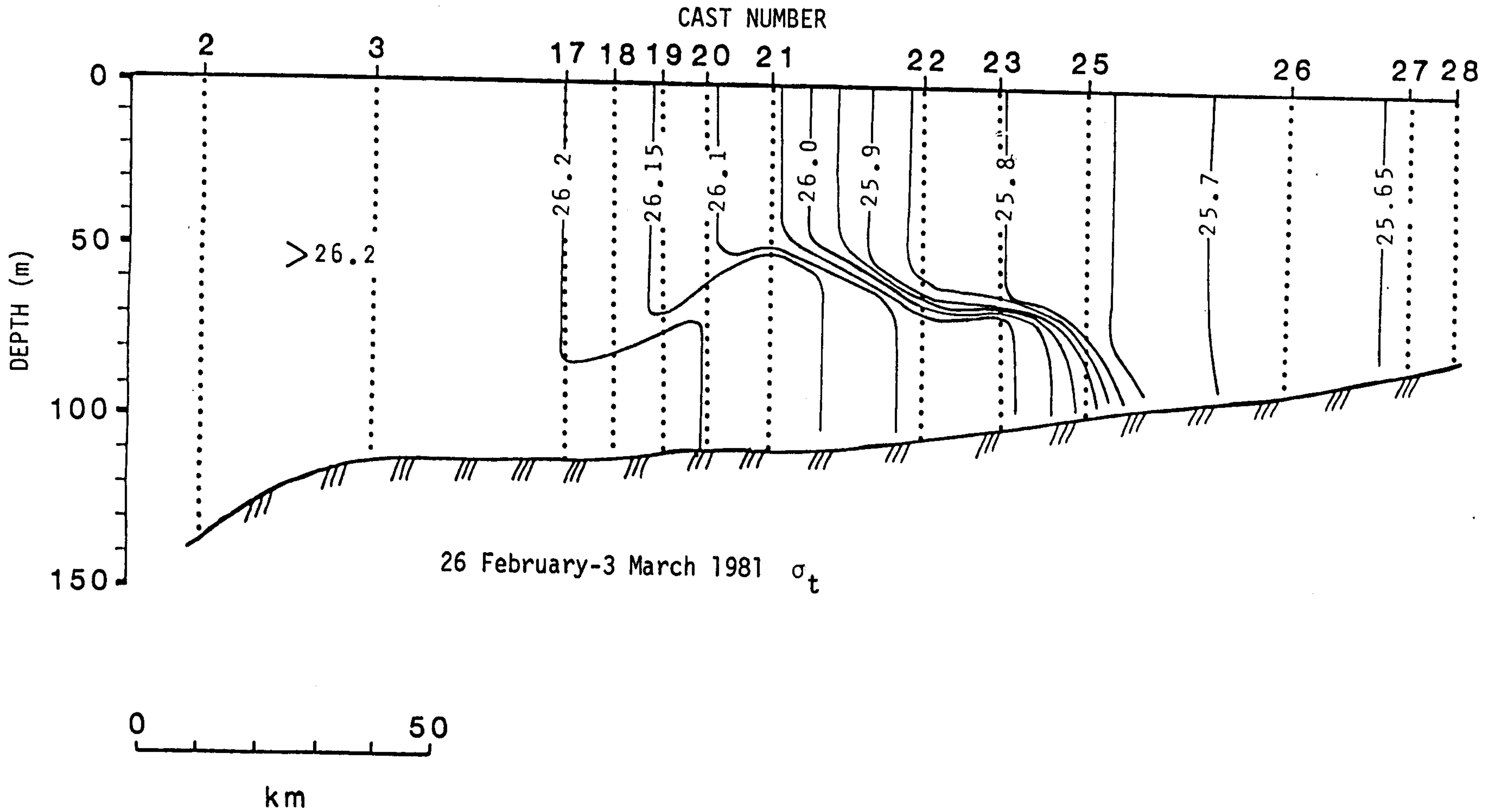

Figure 2-15. Vertical distribution of density (as sigma-t); same transect as Figure 2-13.

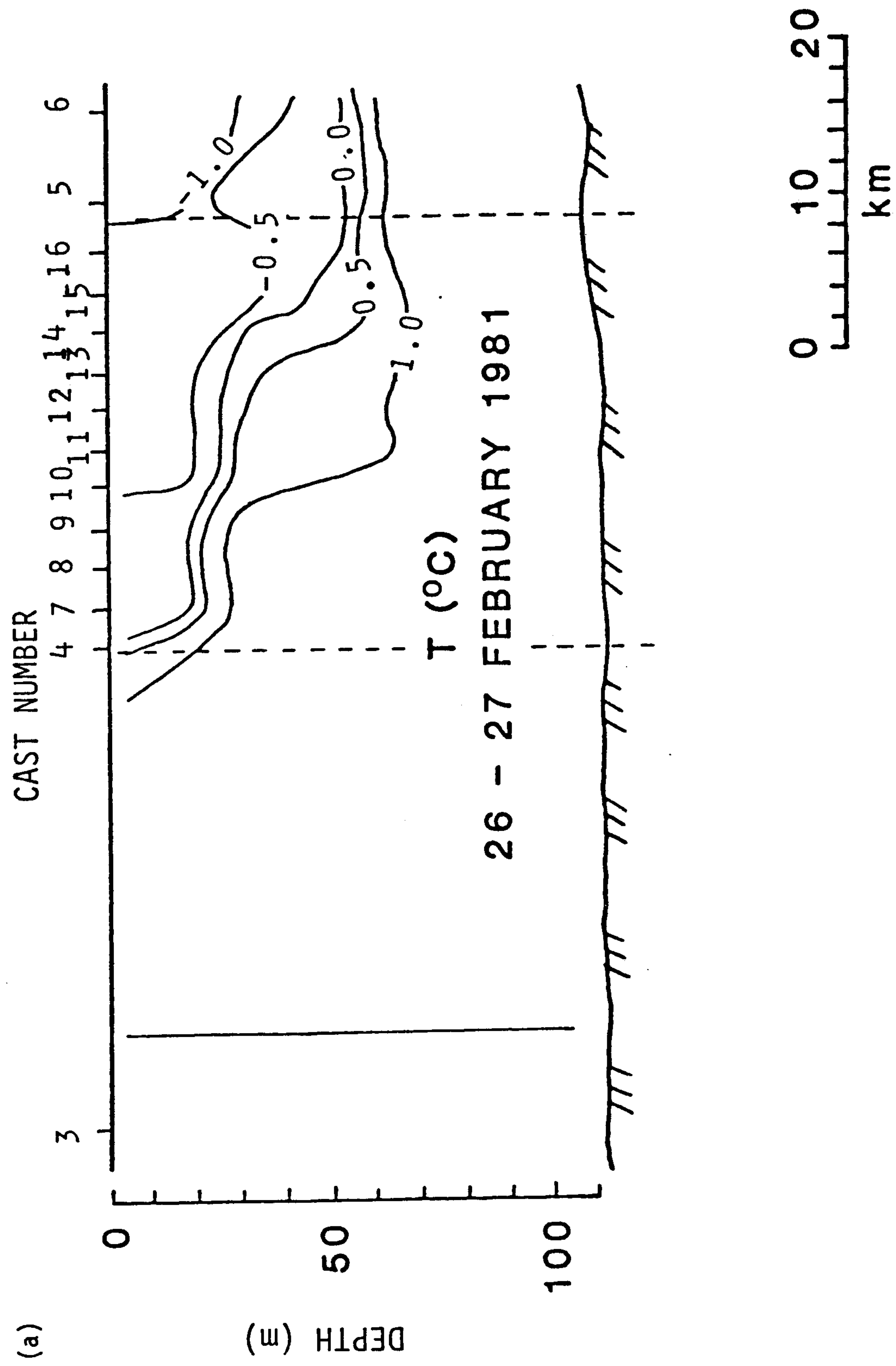
(a)
DEPTH (m)
0
50
100
CAST NUMBER
3
4
7
8
9
10
11
12
13
14
15
16
5
6
-1.0
-0.5
0.0
0.5
1.0
T (°C)
26 - 27 FEBRUARY 1981
0
10
20
km

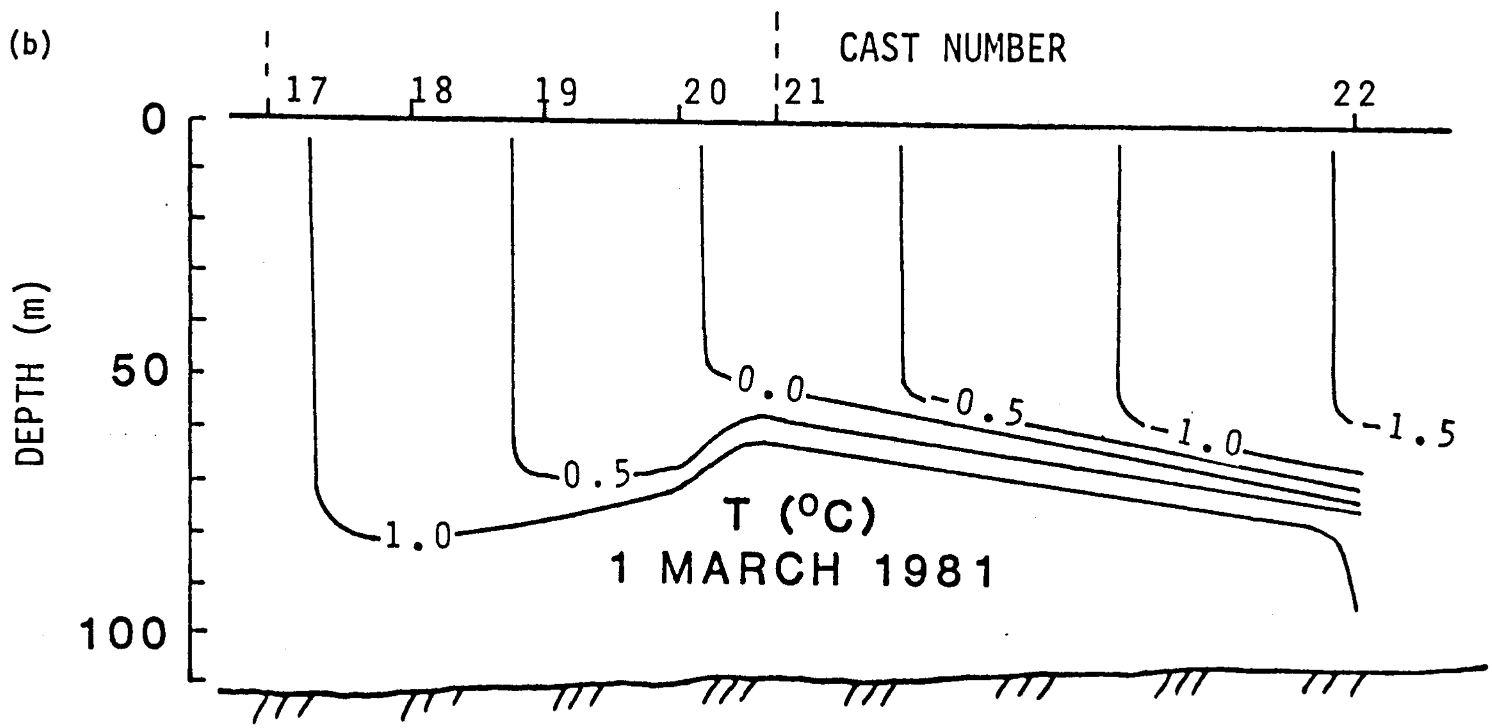

Figure 2-16. Vertical distribution of temperature across the central Bering Sea shelf, approximately beneath the ice edge, prior to (a) and following (b) a strong, southerly wind event in mid-winter 1981. Figure 2-2 shows locations of stations which are included in these two transects. Numbers given are cast numbers.

obvious change in structure, however, the locations where isotherms intersected the surface at the south edge (the 1.0 °C isotherm) did not shift more than about 20 km northward during the period when the ice edge itself was forced about 100 km to the north. Moreover, the vertical heat content of the water column did not change significantly during the storm event. It is concluded that the change in structure between 27 February and 1 March was due to wind mixing of the upper layer and its subsequent deepening due to erosion of the pycnocline.

The transitions between vertically homogeneous water (to the north) and near-homogeneous water (to the south) and the two-layered structure are compared in Figure 2-17 with ice edge locations. This figure shows the spatial relation of the two-layered structure to the ice edge at the various ice edge locations observed from 26 February-11 March 1981.

A final example of the observed short-term variability in vertical water structure is given in Figure 2-18. This shows vertical density profiles at a station south of the ice "edge" on three separate occupations. The 20 February structure preceded the storm event, while the 1 March profile directly followed it and shows wind-mixing of the upper layer. The 11 March profile shows the upper layer returning toward its original (i.e. as observed on 26 February) stratified state. The change in density in the lower layer was probably advective in origin, which suggests that some portion of the upper layer variability was, also, advective rather than due entirely to wind-mixing. Presence to the southwest of denser lower-layer water suggests that a northward current pulse might have led to such an increase in density. Data are, however, inadequate to test this speculation.

Finally, as for the November density structure, that observed in February-March suggests a baroclinic flow to the northwest. This is confirmed by the

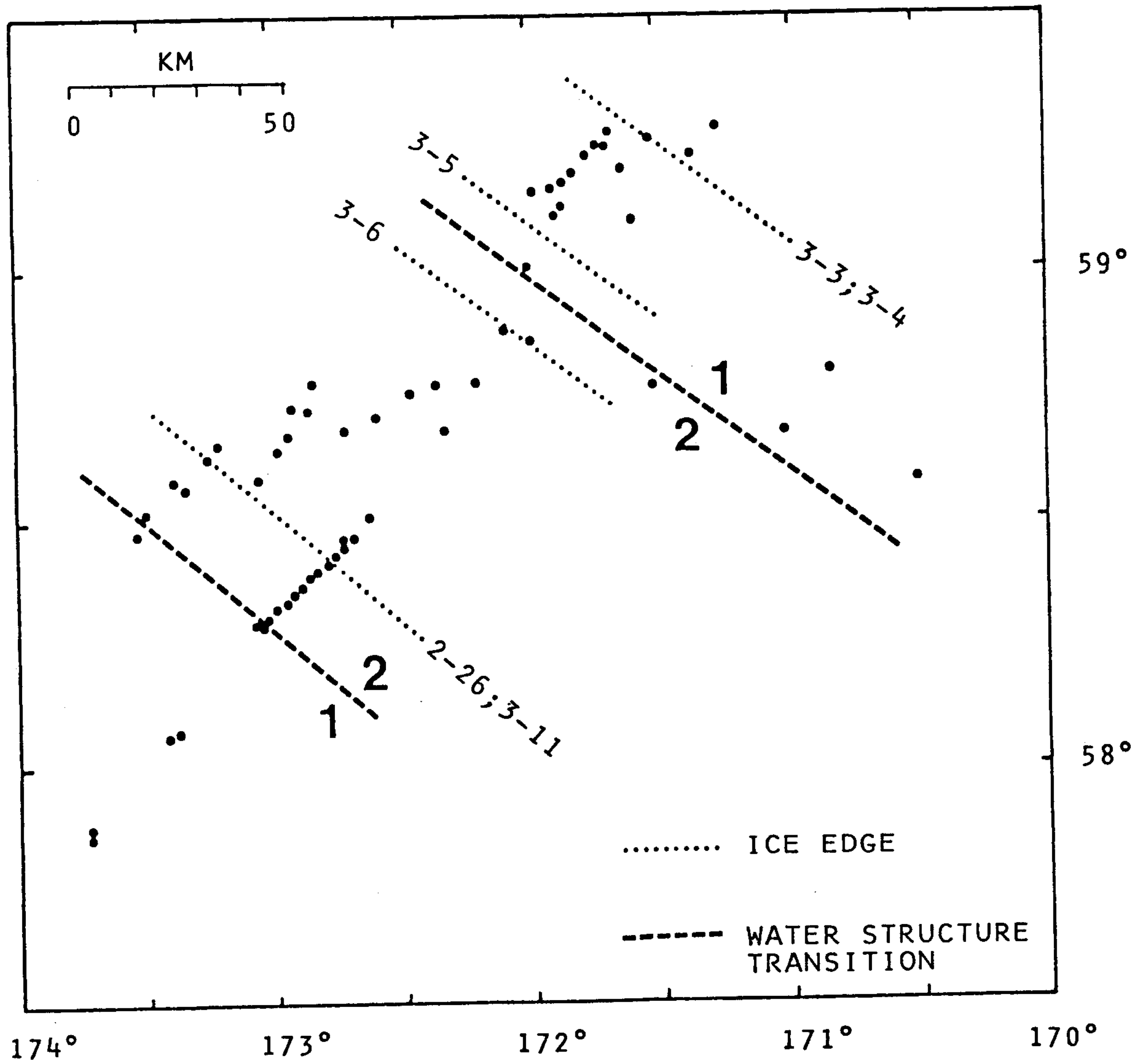

Figure 2-17. Horizontal plan view indicating schematically the fluctuations in ice edge location (dotted lines, with numbers indicating month-day of location), and position of two-layered water structure which was associated with the ice edge region (between two heavy, dashed lines) observed during mid-winter, 1981. Two-layered structure is indicated by the numeral "2", whereas homogeneous or nearly homogeneous water is indicated by "1".

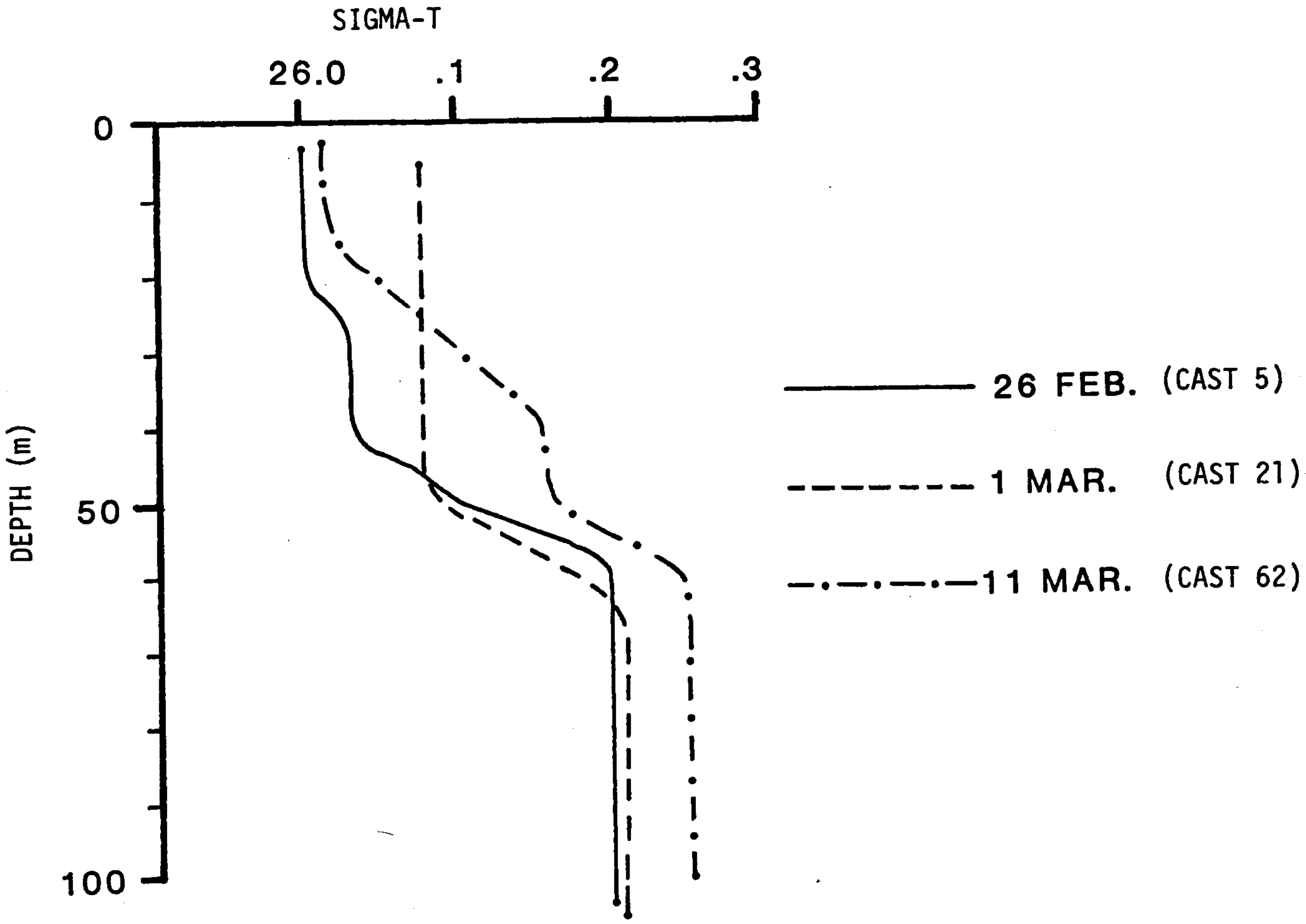

Figure 2-18. Vertical density profile (as sigma-t) on the central Bering Sea shelf during mid-winter preceding (26 February), directly following (1 March) and following by several days (11 March) a strong, southerly wind event. Figure 2-2 shows locations of stations from which these profiles were derived. Numbers given are cast numbers.

dynamic topography of the surface relative to 75 db (Figure 2-19). The computed surface current speed, assuming 75 db as a level of no motion, was about 7 cm/sec toward the northwest and was confined to the area bounded by the two-layered structure. This baroclinic flow will be discussed at greater length in Sections 2.4 and 2.5 below.

2.3.3. Temperature-Salinity Characteristics

The central Bering Sea shelf region was characterized, both in autumn 1980 and mid-winter 1981, by a vertical structure which was two-layered in temperature and salinity. In autumn, this structure covered the shelf from the shelf break to north of the 50-m bottom isobath. In mid-winter, this layered structure was confined to a "band" approximately 100 km in width which underlay the location of the ice edge.

The observed temperature and salinity characteristics can be compared with those elsewhere in the Bering Sea region by plotting them superimposed on the diagram constructed by Kinder and Schumacher (1981) to illustrate Bering Sea temperature-salinity relationships (Figure 2-20). It is readily apparent that observed salinities were, for both seasons during which data were obtained, more characteristic of Alaska Stream/Bering Sea Water than Bering Shelf Water. Temperatures were lower than those typical of Alaska Stream/Bering Water, but our data were obtained later in the season than that analyzed by Kinder and Schumacher and so would have been subject to greater cooling. The February-March data were similar in salinity to the November 1980 data, but minimum observed temperatures were lower (-1.7 °C) as would be expected for winter as compared to autumn data.

In summary, temperature and salinity data obtained during autumn 1980 and mid-winter 1981 suggest that water on the central Bering Sea shelf has characteristics

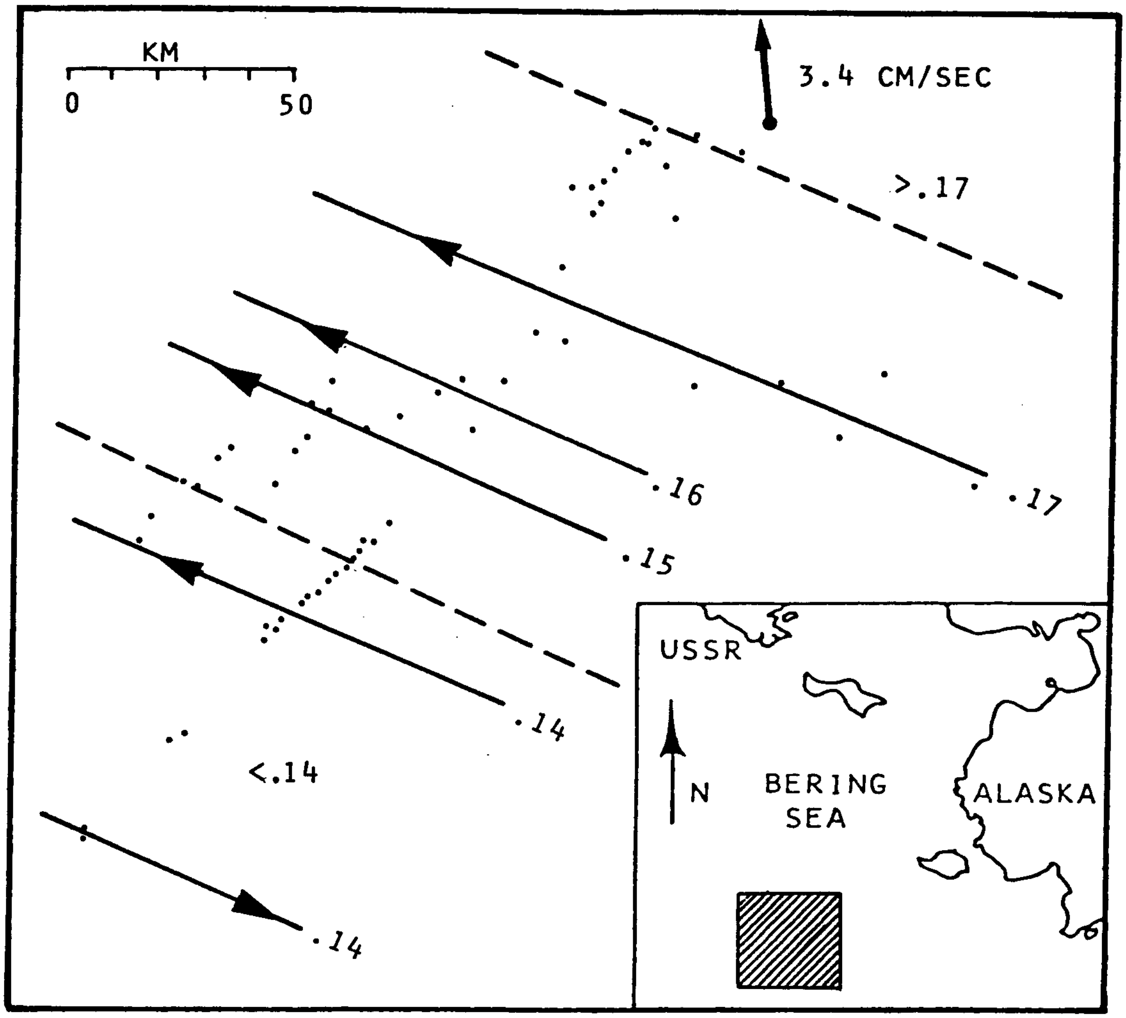

ΣΔD 0/75 db.

23 FEB. - 11 MAR. 1981

Figure 2-19. Dynamic topography of the water surface relative to the 75 db level during mid-winter 1981. Arrowheads on contours indicate direction of baroclinic surface flow, relative to the reference level, as implied by the dynamic topography. Contours are in dynamic meters, with contour interval of 1 dynamic centimeter. Arrow indicates vector-averaged February-March flow at 50 m, as observed from mooring BC22. Inset map shows general location on the central Bering Sea shelf region (shaded rectangle).

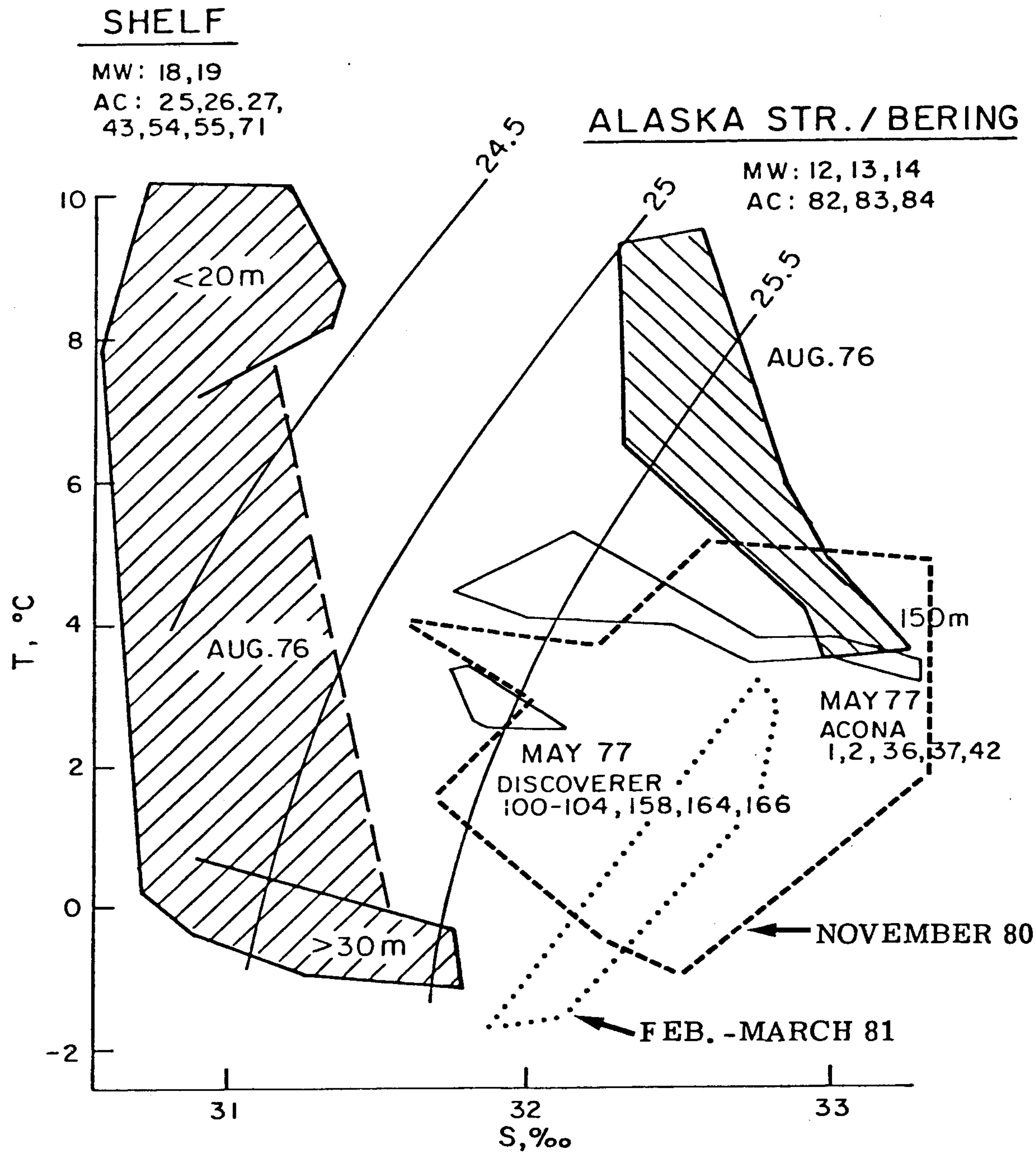

Figure 2-20. Comparison between temperature-salinity characteristics observed in autumn 1980 and mid-winter 1981 on the central Bering Sea shelf, and those compiled for the southeastern Bering Sea shelf by Kinder and Schumacher (1981).

more typical of Alaska Stream/Bering Sea Water than of that classified by Kinder and Schumacher (1981) as Shelf Water farther to the southeast. This difference was due to a large (1-1.5 $^{o}/oo$) salinity difference between waters on the southeast and on the central Bering Sea shelf. Speculation concerning this observation is presented in Section 2.5 below.

2.4. CURRENT OBSERVATIONS

Two current records, each more than 200 days in length, were obtained from 50-m depths on the central Bering Sea shelf between November 1980 and June 1981. Geographical locations of these current records are shown on Figure 2-1; other pertinent information is listed in Table 2-3.

Both of the overwinter 1980-81 current records supported the concept of a mean northwesterly flow along the central Bering Sea shelf. The vector-averaged current for the entire record at mooring BC22 was 2.3 cm/sec, directed toward 340 °T. That from mooring BC26 was 3.3 cm/sec, directed toward 347 °T. These directions closely approximated the local trend of the isobaths. Speeds were somewhat higher than the approximately 1 cm/sec means given by Kinder and Schumacher (1981b) for the mid-shelf regime farther southeast.

The high-frequency components of flow at both moorings BC22 and BC26 were heavily dominated by tidal currents which were mixed, predominantly diurnal. These show clearly in the time-series segment of raw current data presented in Figures 2-21 (for BC22) and 2-22 (for BC26). Visual inspection of these time series reveals tidal currents varying between about 20 to 40 cm/sec at BC22 and 10 to 30 cm/sec at BC26. This decrease in tidal current speeds between BC22 and BC26 is in qualitative agreement with Pearson _et al._ (1981), who indicate that diurnal tidal currents decrease in magnitude toward the western Bering Sea shelf.

While the tidal currents were the highest speed components, lower frequency (1 to 10 day period) fluctuations in speed and direction were evident throughout the observation period. The tidal signal has been removed from the current vectors in Figure 2-23 in order to illustrate these fluctuations. Time scales were of order 7 to 10 days, and reversals to southeastward flow occurred and were more

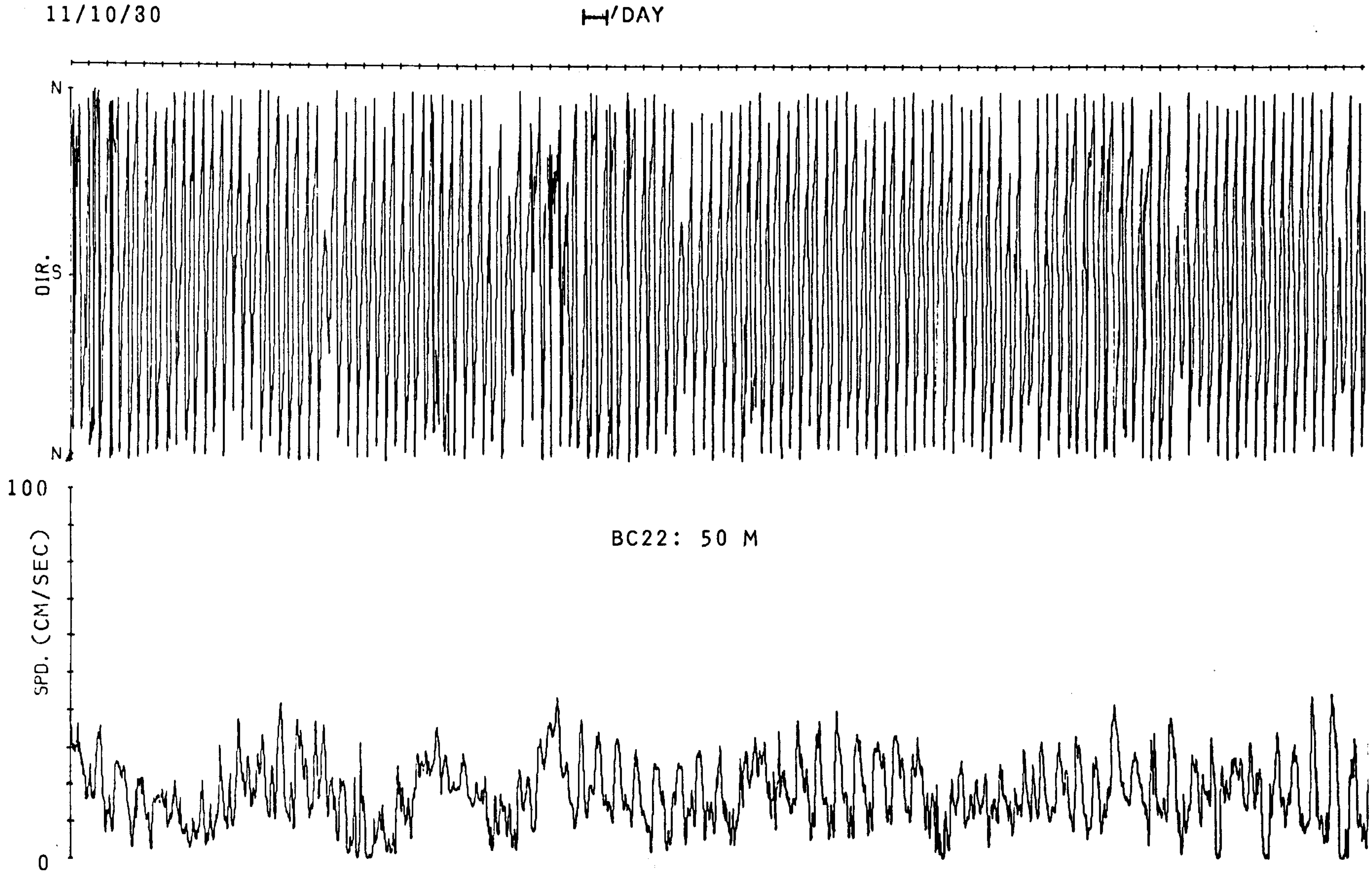

Figure 2-21. 70-day segment of raw current speed (lower) and direction (upper) as observed at 50-m depth at mooring BC22. Start date for this plot is 10 November 1980 and each time mark represents 1 day.

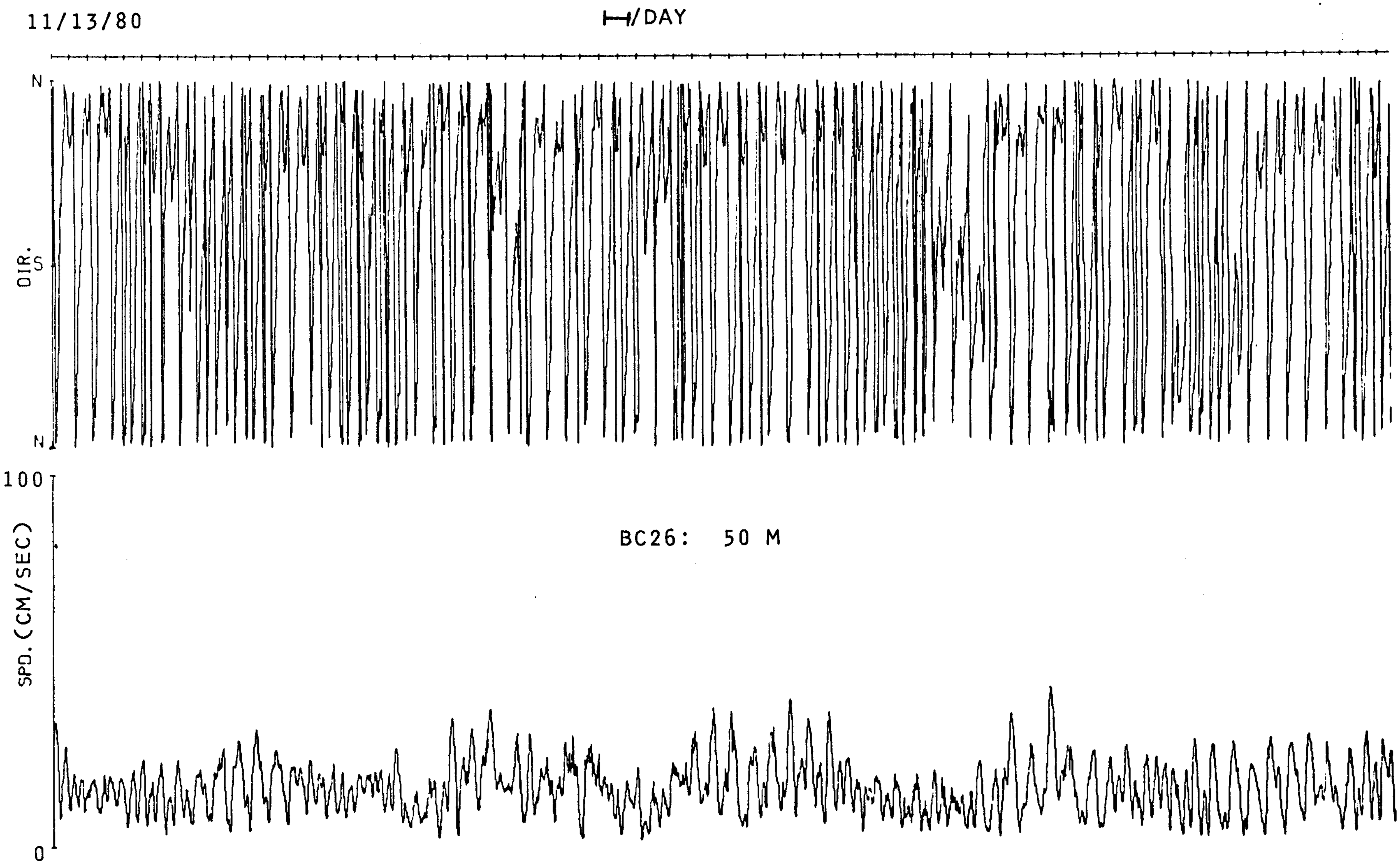

Figure 2-22. Same as for Figure 2-21, except that this record was from mooring BC26. The start date for the plot is 13 November 1981 and the segment plotted is 73 days in length.

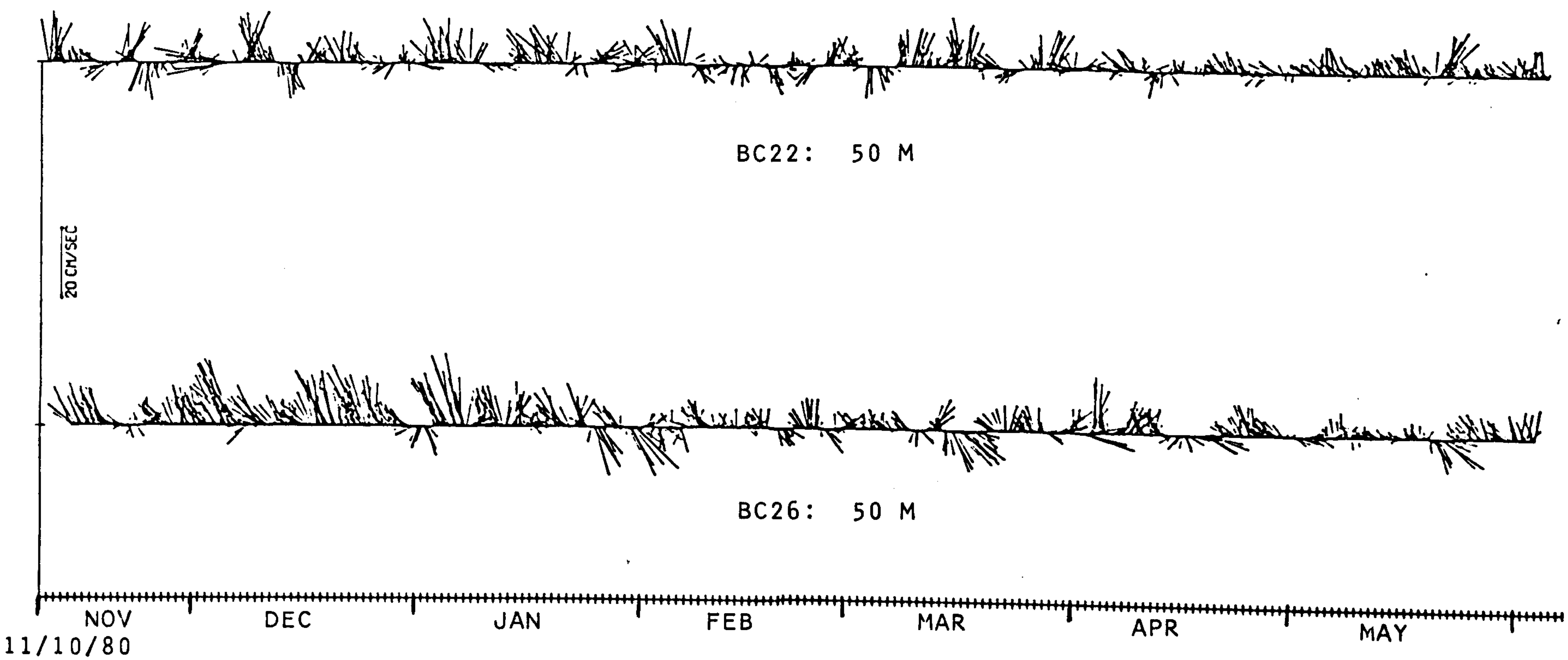

Figure 2-23. 35-hour filtered current speed vectors plotted every six hours as a function of time for the 50-m deep records from moorings BC22 (upper) and BC26 (lower). Locations of moorings are shown on Figure 2-1 and geographical coordinates and other information are listed in Table 2-3.

frequent later in the record than near its beginning. These fluctuations are also apparent on the raw speed records (Figures 2-21 and 2-22), with the tidal currents appearing as high-frequency "noise" superimposed on the lower-frequency pulse.

In an attempt to estimate the significance of low-frequency (periods of 10 days or longer) flow fluctuations, monthly vector-averaged currents were computed for both moorings and are presented in Figure 2-24. While flow was northerly during all months, significant variations in east-west flow occurred from month to month. Comparison with the local bathymetry (shown as the local isobath direction at each mooring on Figure 2-24) indicates that the flow most strongly paralleled the bathymetry in November, December and May at both locations. The greatest deviation occurred at BC26 in March, when flow was completely across-isobath, onshore. These time-variations in along- and cross-shelf flow can also be depicted as plots versus time of the monthly mean along- and cross-shelf flow (Figure 2-25). Along-shelf flow was to the northwest for all months, though it was minimum through the mid-winter period February-April. Cross-shelf flow showed a clear tendency at both moorings to be off-shelf (to the southwest) early and late during the observation period, while flow was onshelf (toward the northeast) in mid-winter.

Temperature and salinity data obtained during February-March allowed qualitative comparison between the observed February-March currents at mooring BC22 and the internal density field. Figure 2-26 compares the computed baroclinic surface current with both the February-March and over-winter observed currents at 50-m depth. The computed surface flow parallelled the ice edge, while the observed current approximately parallelled the bathymetry. Since no current observations were obtained closer to the surface, it is impossible to rigorously compare magnitudes of the computed baroclinic and observed currents. The component

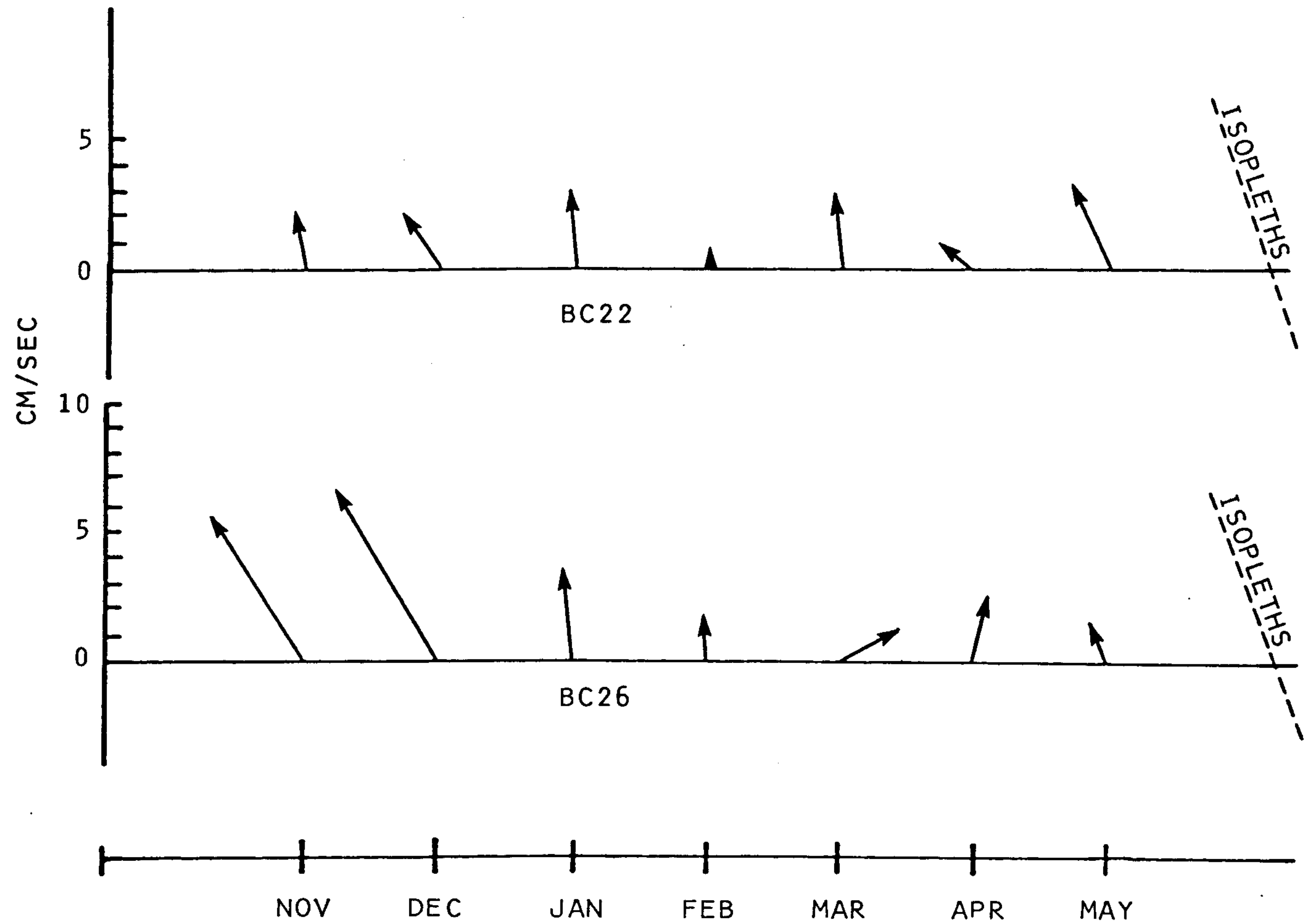

Figure 2-24. Monthly vector-averaged currents plotted as a function of time for the 50-m deep records from moorings BC22 (upper) and BC26 (lower). Dashed lines indicate direction of bottom isobaths at each mooring.

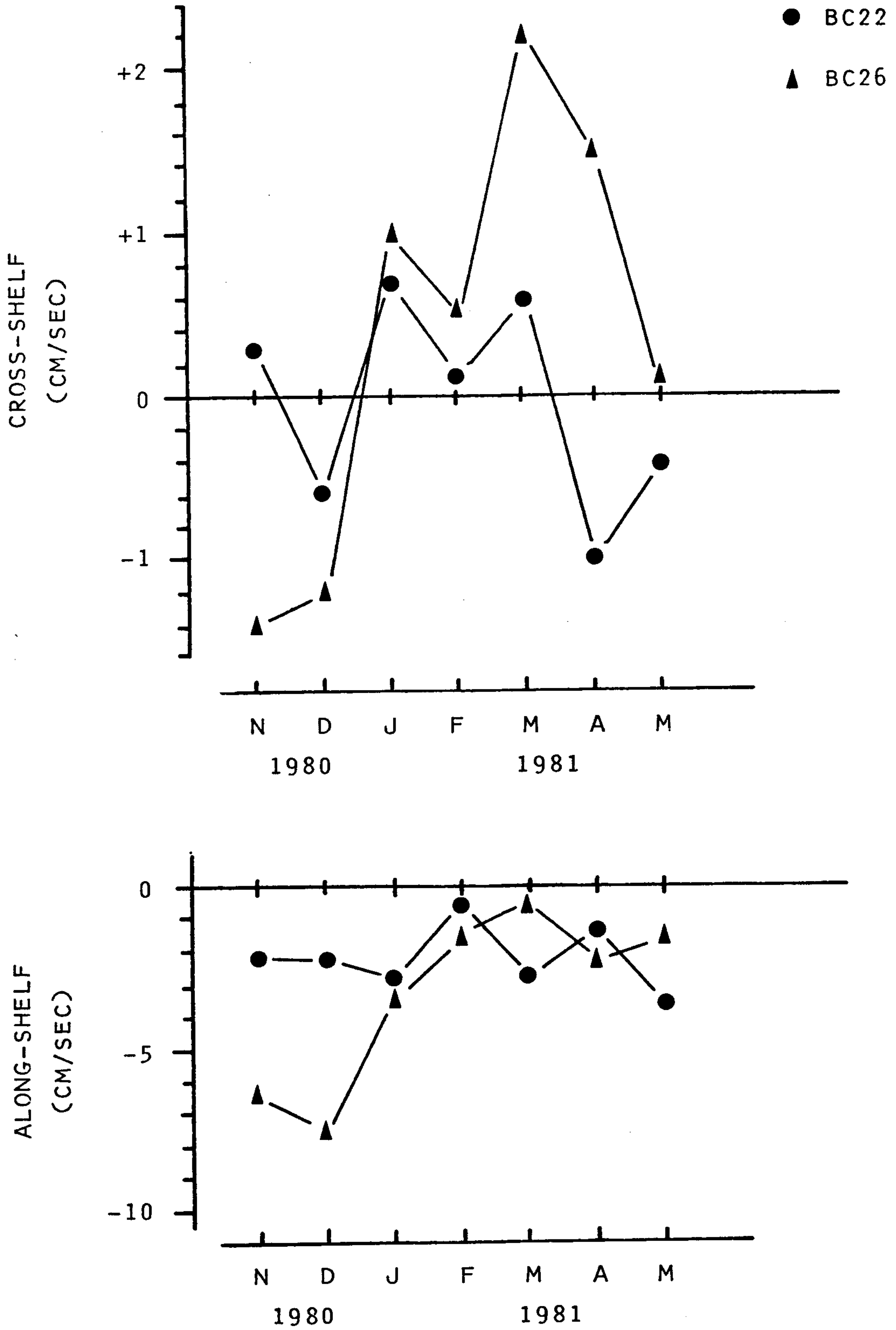

Figure 2-25. Plot as a function of time of the monthly mean cross-shelf (upper) and along-shelf (lower) current components derived from the 50-m deep current records at moorings BC22 and BC26.

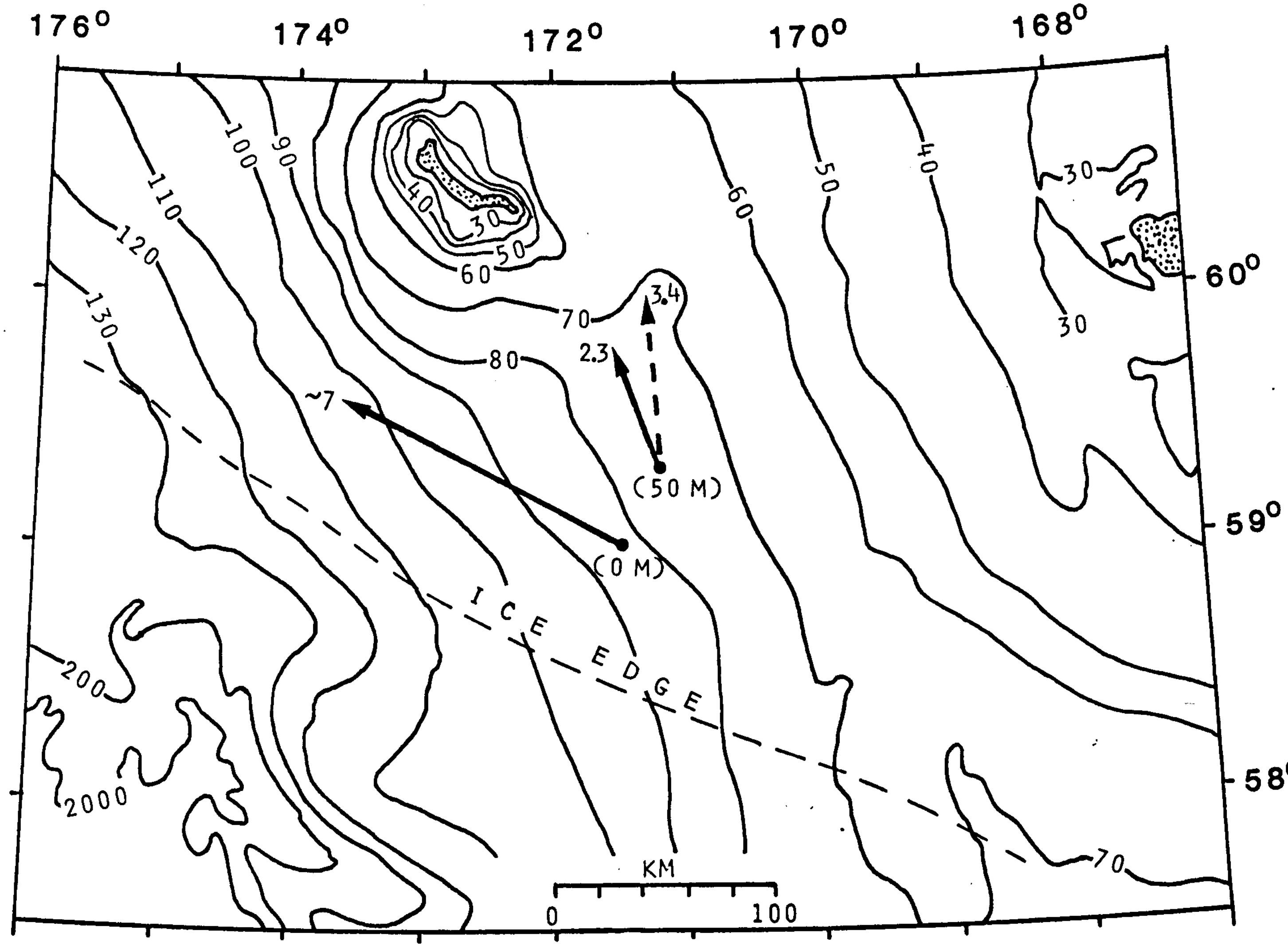

Figure 2-26. Comparison between implied mid-winter baroclinic surface current (arrow labeled "0 M"), vector-averaged over-winter current observed at 50-m depth at mooring BC22 (solid arrow labeled "50 M"), vector-averaged February-March current observed at 50-m depth at mooring BC22 (dashed arrow labeled "50 M"), and directional trend of local isobaths. Numbers at arrowheads refer to speed in cm/sec.

of the observed 50-m current parallel to the ice edge, hence, to the computed surface current, was about 1 cm/sec for February-March. Since this is of the same order as the computed surface current <u>at the mooring</u> (not shown on the figure), but was at 50-m depth rather than at the surface, the actual surface flow may have been somewhat larger than computed due to presence of a barotropic mode. Further discussion of these currents, within the context of regional oceanographic processes, is presented below in Section 2.5.

2.5. CONCLUSIONS

2.5.1. Discussion

The most significant contributions resulting from this program have been improved definition of the two-layered temperature and salinity structure associated with the ice edge in mid-winter, and the implications of this structure with respect to time-mean circulation and the ice edge location on the central Bering Sea shelf. This section will focus primarily upon these aspects of the results.

A schematic illustration of the extent of the two-layered structure on the Bering Sea shelf during mid-winter has been constructed using data obtained in March 1980 and March 1981 (Figure 2-27). The three crossings of the ice edge show, even though they were obtained during separate winters, a progressive divergence toward the west between the actual ice edge and the northern extent of the two-layered, subsurface water structure. The latter is seen, west of the Pribilofs, to approximately parallel the 100-m isobath. The ice edge, conversely, does not parallel the isobaths but extends farther south toward deep water over the western shelf. Historical analyses of the Bering Sea midwinter ice extent indicate that this is normally the case (Muench and Ahlnäs, 1976; Pease, 1980; Niebauer, 1981). The ice edge is well north of the shelf break in the eastern Bering Sea, whereas in the western Bering it extends well south of the shelf break and overlies deeper water.

The currents observed at 50 m during winter 1980-1981 parallelled isobaths, whereas the computed baroclinic surface currents parallelled the ice edge rather than the isobaths. This suggests that the location of the northern edge of the two-layered structure is controlled by the tendency for local currents to parallel isobaths, as observed. On the other hand, the computed baroclinic surface flow

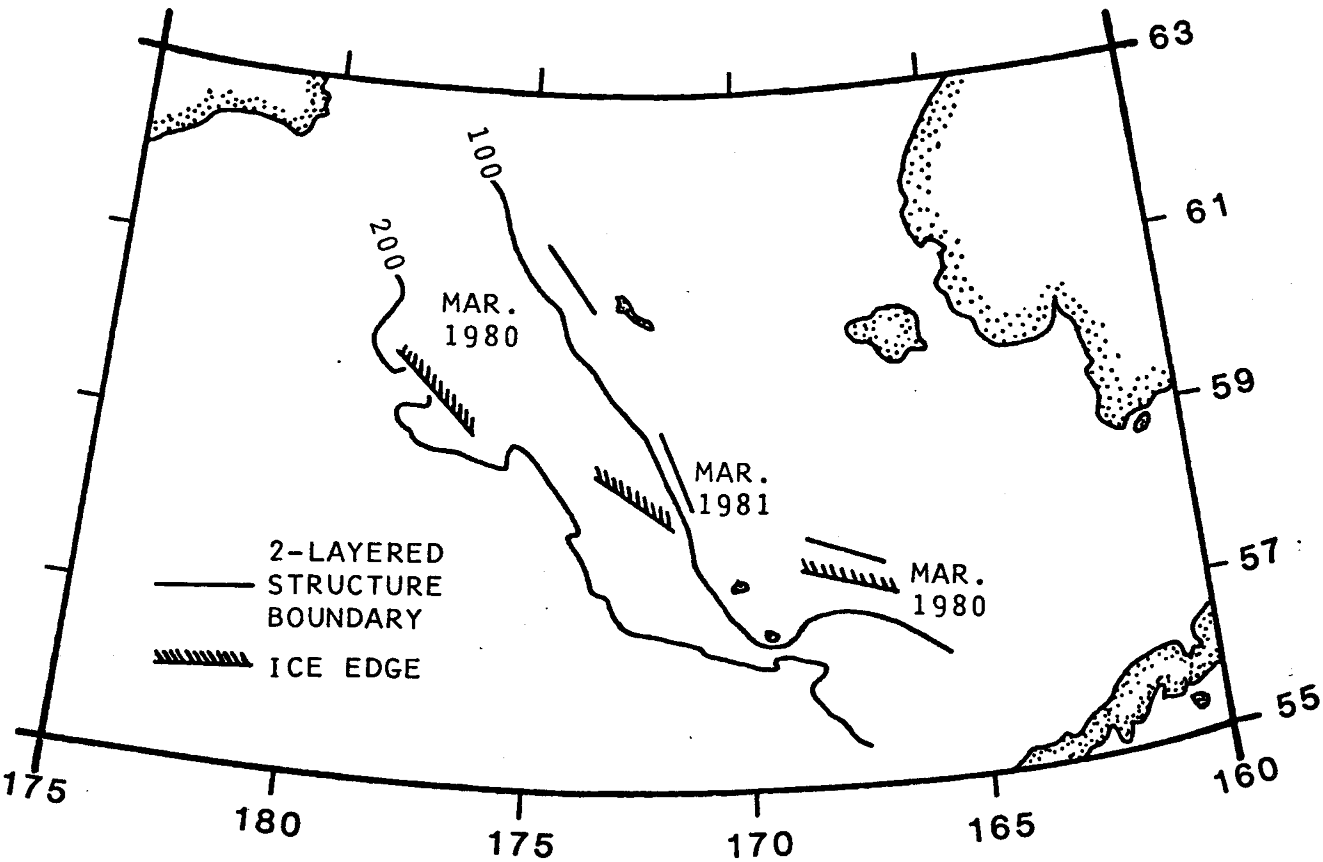

Figure 2-27. Schematic diagram comparing relationships between approximate ice edge locations and northern boundaries of two-layered water structure at three locations along the central Bering Sea shelf. The March 1981 data were obtained from this program, while the March 1980 data were derived from Newton and Andersen (1980). Bottom contour depths are in meters, with the 200-m isobath coinciding approximately with the shelf break.

would be somewhat decoupled from the bathymetry by the stratification between the layers, and would tend to follow a path related to the source of the baroclinic field: the melting of ice along the ice edge.

At this point, it is necessary to speculate on processes which might control the location of the ice edge. In mid-winter, when air temperatures are generally below freezing, the time mean ice edge location must be controlled primarily by availability of heat from the underlying water column. This heat can be supplied by advection, or through horizontal and vertical turbulent diffusion. Presence of a 1-2 cm/sec current component, at 50-m depth, northward normal to the ice edge suggests one mechanism for advecting heat beneath the ice. The warm lower layer is, however, separated from the ice by a colder (approaching the freezing point at its northern edge), lower salinity upper layer. The interface between these layers is about 10-m thick. The density difference between layers varies from about 0.2 sigma-t units (observed in March 1981) on the central shelf up to more than 0.5 sigma-t units (observed by Newton and Andersen in March 1980) at the westernmost section on Figure 2-27. We hypothesize that, as the upper layer flows toward the northwest beneath the ice edge, its salinity is decreased by continual addition of low-salinity water derived from ice melt. This decrease in upper layer salinity increases the strength of the between-layer density interface, thus decreasing the upward flux of heat from the relatively warm, lower layer. This decreased upward heat flux allows the ice to extend farther southward before melting, as observed. Assuming a mean southward ice advection rate of 20 cm/sec, which is reasonable based both upon data obtained during winter 1981 and upon historical data (Muench and Ahlnäs, 1976; Pease, 1980), about 0.5 x 10^6 m^3/sec of meltwater derived from sea ice is added to the upper layer between the easternmost and westernmost sections shown on Figure 2-27. This is of the same order as the computed baroclinic flow through the winter 1981 section and, clearly, is sufficient to strongly impact the regional salinity (hence density) field.

The westward baroclinic flow associated with the ice edge appears to be a consequence of the local input of low-salinity water due to ice melting. It is this consistent westward flow which leads to the above mechanism allowing the ice to extend into deeper and deeper water toward the western side of the Bering shelf. Presence of this baroclinic field and its associated flow also suggest a reason for the relatively constant location of the two-layered structure, despite large north-south excursions of the ice edge. The ice edge excursions occur over time scales of a few days, as was graphically demonstrated during February-March 1981 (see Figure 2-17). The baroclinic response time of the water column is, however, longer. It is not likely that the two-layered structure would respond to single storm events. While it is generally recognized that the year-to-year variability in maximum southward extent of the ice edge is a function of the severity of the winter, and that short-term fluctuations in ice extent may occur in response to discrete storms, it now appears that fluctuations of ice edge location over time scales of several weeks are probably damped by the combined response time of the baroclinic field associated with the ice edge and the vertical density structure associated with this field. If ice is advected rapidly southward over the higher temperature water in the southern part of the two-layered structure, it will melt and soon return to its original location. On the other hand, a short term retreat of the ice would place it over water at or near the freezing point. Northeasterly winds, which prevail over the Bering Sea in winter, could then rapidly advect it southward to its equilibrium location without appreciable melting. Freezing of ice in the region overlying the layered structure would release salt into the water and decrease the density difference across the interface. This would allow, in turn, increased upward heat flux which would act to slow the freezing process. Increased melting, conversely, would add low salinity water to the upper layer, increase the strength of the interface and decrease upward heat flux available to melt the ice.

It was noted above (Section 2.3.3) that water on the central Bering shelf had temperature-salinity characteristics similar to those of Alaska Stream/Bering Sea Water rather than the Bering Shelf Water defined by Kinder and Schumacher (1981) using data obtained farther to the southeast. This difference was due to the salinity, which was 1-1.5 $^{o}/oo$ higher on the central than on the southeastern shelf. Part of this difference may have been seasonal, since Kinder and Schumacher used spring and summer data which would have included maximum freshwater admixture from terrestrial sources. It also seems reasonable, however, that the flow of deep layer, oceanic water beneath the ice edge as observed would, through admixture with the upper layers, increase the salinity of the shelf water over that observed to the southeast.

The above discussion qualitatively relates the observed ice edge location, currents and the temperature, salinity and density fields on the central Bering Sea shelf. Quantification and rigorous testing of these hypotheses require additional field data, particularly with respect to the vertical and horizontal definition of the observed currents, and are beyond the scope of the present treatment.

2.5.2. Summary

The results of the physical oceanographic investigations carried out in support of the overall Bering Sea MIZ program may be summarized as follows:

- The central Bering Sea shelf region was characterized in November 1980 and February-March 1981 by a water structure vertically two-layered in temperature, salinity and density. In November, this structure covered the entire shelf. In February-March, the structure was restricted to a band about 80-km wide which underlay the ice edge.
- Associated with the two-layered structure in winter was a northwesterly baroclinic surface current having maximum speeds of about 7 cm/sec relative to the 75 db level. Northwestward baroclinic volume transport relative to the same level was of order 0.5×10^6 m^3/sec.

- Observed over-winter mean currents at two locations on the central Bering Sea shelf at 50-m depth were 2-3 cm/sec, with flow along-isobath to the northwest in agreement with conventional wisdom on Bering shelf circulation. These mean flow speeds were somewhat higher than those which have been previously reported farther to the southeast on the shelf.

- Fluctuations, having time scales of 7-10 days, were present in both speed and direction at both current moorings, and led in several instances to reversals to southeastward flow.

- Monthly mean observed currents were all alongshelf toward the northwest; however, cross-shelf components fluctuated from month-to-month with maximum on-shelf flow in mid-winter.

- Tidal currents were 20-40 cm/sec east of St. Matthew Island and were 10-30 cm/sec west of it. Tides were mixed, predominantly diurnal.

- Overall temperature-salinity characteristics on the central shelf in both November 1980 and February-March 1981 were similar to those of Alaska Stream and Bering Sea Water, rather than to Bering Shelf Water as defined farther to the southeast.

- A hypothesis is developed which qualitatively interrelates the ice edge location and the observed temperature, salinity and current fields in terms of stability of a baroclinic current which is maintained by the ice edge, under-ice heat advection by near-bottom flow and control over vertical heat exchange by a density interface.

Acknowledgement

This study was supported by the Bureau of Land Management through interagency agreement with the National Oceanic and Atmospheric Administration, under which a multiyear program responding to needs of petroleum development of the Alaskan continental shelf has been managed by the Outer Continental Shelf Environmental Assessment Program (OCSEAP) Office.

References

Clarke, A.J. 1978: On wind-driven quasi-geostrophic water movements near fast-ice edges. Deep-Sea Res. 25, 41-51.

Kinder, T.H. and J.D. Schumacher 1981: Hydrographic structure over the continental shelf of the southeastern Bering Sea. Chapter 4 in The Eastern Bering Sea Shelf: Oceanography and Resources, Volume One (D.W. Hood and J.A. Calder, eds.), Univ. of Wash. Press, Seattle, 31-52.

Kinder, T.H. and J.D. Schumacher 1981b: Circulation over the continental shelf of the southeastern Bering Sea. Chapter 5 in The Eastern Bering Sea Shelf: Oceanography and Resources, Volume One (D.W. Hood and J.A. Calder, eds.), Univ. of Wash. Press, Seattle, 53-75.

Muench, R.D. and K. Ahlnäs 1976: Ice movement and distribution in the Bering Sea from March to June 1974. J. Geophys. Res. 81, 4467-4476.

Muench, R.D. and J.D. Schumacher 1980: Physical oceanographic and meteorological conditions in the northwest Gulf of Alaska. NOAA Tech. Memo. ERL PMEL-22, 147 pp.

Newton, J.L. and B.G. Andersen 1980: MIZP AC 80A; USCG Polar Star (WAGB-10) Arctic West Operations. March 1980: Bering Sea, Cruise report and preliminary oceanographic results. Science Appl. Inc. Report SAI-202-80-460-LJ, La Jolla, Calif., 32 pp. (unpub. man.).

Niebauer, H.J. 1981: Recent fluctuations in sea ice distribution in the eastern Bering Sea. Chapter 9 in The Eastern Bering Sea Shelf: Oceanography and Resources, Volume One (D.W. Hood and J.A. Calder, eds.), Univ. of Wash. Press, Seattle, 133-140.

Niebauer, H.J., V. Alexander and R.T. Cooney 1981: Primary production at the eastern Bering Sea ice edge: The physical and biological regimes. Chapter 44 in The Eastern Bering Sea Shelf: Oceanography and Resources, Volume Two (D.W. Hood and J.A. Calder, eds.), Univ. of Wash. Press, Seattle, 763-772.

Pearson, C.A., H.O. Mofjeld and R.B. Tripp 1981: Tides of the Eastern Bering Sea Shelf. Chapter 8 in The Eastern Bering Sea Shelf: Oceanography and Resources, Volume One (D.W. Hood and J.A. Calder, eds.), Univ. of Wash. Press, Seattle, 111-130.

Pease, C.A. 1980: Eastern Bering Sea ice processes. Mo. Wea. Rev. 108, 2015-2023.

APPENDIX 2:

THE MOVEMENT AND DECAY OF ICE EDGE BANDS IN THE WINTER BERING SEA

by

Seelye Martin and Peter Kauffman

School of Oceanography
University of Washington

and

Claire Parkinson

NASA/Goddard Space Flight Center

Submitted to Journal of Geophysical Research

April 1982

TABLE OF CONTENTS

LIST OF FIGURES

Figure 11. Schematic drawing in cross-section of the evolution of a band in a wave field. (a) Initial band configuration; (b) some time later. See text for additional discussion

Figure 12. Seawater temperature versus time for the band experiment

Figure 13. Details of an upwind band edge, following 9 March 0000 GMT. (a) The upwind edge; (b) the floes behind the band; (c) small floes melting in open water. See text for further description.

Figure 14. A chart of the experimental region. The point 'BC22' shows the current meter position; the line 'a' shows the net translation of Pease's station for the times shown at the endpoints; line 'b' shows the net band translation. The numbers in parentheses under the times are water temperatures in degrees.

Figure 15. Comparison of the band velocity with the currents measured at BC22. The upper two curves show the east u_C and north v_C current components from BC22; the middle two curves show the ice band components u_I and v_I; the lower two curves show the relative velocities u_R and v_R. See text for additional description.

Figure 16. Observed wind speed and direction for the band experiment as measured on the ship at one-hour intervals

Figure 17. Sketch of ice band made on 11 March 0400 GMT while leaving the ice edge (courtesy Scott Ferguson).

LIST OF TABLES

ABSTRACT

During periods of off-ice winds, the winter Bering Sea ice edge consists of ice bands which measure 1 - 10 km in length, 0.1 - 1 km in width, and are oriented at approximately right angles to the wind. The bands are made up of small floes 10 - 20 m in diameter and 1 - 5 m in thickness. In March 1981 working from the NOAA ship SURVEYOR, we mounted two radar transponders 4 km apart on such a band, then tracked them for 46 hr over an 80 km distance as the band moved into warmer water and melted. Comparison of the band position with that of a satellite-tracked ARGOS station deployed in the ice interior shows that the band moved 30% faster than the interior ice. Both our observations and analysis strongly suggest that the cause of this speed increase is the wind-wave radiation stress on the upwind side of the band. We also observed that wind-waves contribute to band ablation by the following mechanism: At the upwind edge, these waves break up the floes into small pieces. Because these pieces are no longer good wave reflectors or absorbers, they drift relatively upwind to melt, so that the band width, as well as the individual floe thicknesses, decrease with time. In summary, because the bands provide an efficient way for the export and ablation of sea ice, the bands play a major role in the maintenance of the ice edge position.

THE MOVEMENT AND DECAY OF ICE EDGE BANDS IN THE WINTER BERING SEA

1. Introduction

At the winter Bering Sea ice edge during periods of off-ice winds, the pack ice forms into long bands of ice measuring 1 - 10 km in length, and 0.1 - 1 km in width, with their long axes at right angles to the wind. After formation, these long bands move away from the interior ice and melt in the warmer southerly waters.

From a satellite study, Muench and Charnell (1977) show that these bands extend over a 50 - 100 km distance downwind of the pack ice, and have a regular spacing in the wind direction of 6 - 12 km. In a subsequent field study, Bauer and Martin (1980) show that the ice which makes up the bands comes from the outer 5 - 10 km of the pack ice, and consists of small thick floes measuring approximately 10 - 20 m in diameter, and 1 - 5 m in thickness. The reason these floes occur is that the propagation of ocean swell into the pack fractures, rafts, and ridges the large interior floes into the observed small floes. Bauer and Martin also observed from the tracking of visual targets in a band, that the band moved southwest at the higher velocity than the originally adjacent pack ice; they attribute this speed increase to the wind-wave radiation stress generated in the fetch between the band and the pack ice acting on the upwind side of the band.

The present paper describes a study of the movement and decay of these bands carried out in March 1981 from the NOAA ship SURVEYOR. In this study, we tracked a pair of radar transponders mounted on ice floes within a band. We also compared the band motion to that of a satellite-tracked buoy deployed by Pease (1982) in the ice interior. The study showed the following: first, that the bands moved away from the interior pack ice at speed 30% greater than that of the interior ice; second, that the cause of this band acceleration was very likely the wind-wave radiation stress on the upwind side of the band; third, that as the bands moved into warmer water, they decayed both by wind-wave erosion of the upwind edge and by bottom melting.

In the following, Section 2 describes how the buoys work and our method of deployment. Then, Section 3 describes the band shape and trajectory, and Section 4 describes how the band decays. Finally, Section 5, through a calculation of the steady state stress balance on the band, shows that the radiation stress can account for the velocity increase of the band relative to the ice interior.

2. How the Buoys Work

Figure 1 is a schematic drawing of the radar transponder buoy, and Figure 2 is a photograph of a buoy deployed in an ice floe. We built these buoys from 3 m lengths of PVC pipe with an 8 mm wall thickness and a 0.17 m outer diameter. The pipes, which were sealed at the top and bottom with stock end caps, fitted into a standard 0.2 m diameter auger hole. We designed the buoys both to transmit from the ice and to float upright in and transmit from open water. So that the buoy fulfilled both these functions, inside the tube we mounted the radar transponder at the top with a timing circuit just beneath it, additional flotation in case of leaks in the middle, and the batteries at the bottom. Outside of the tube we fastened styrofoam flotation around the middle, and suspended 17 kg of chain from the tube bottom. This allowed the buoy to float upright in open water with 1.3 m of freeboard. We also fastened a wire harness above and below the flotation to which we attached a 50' length of 3/8" polypropylene line looped through a VINY-FLOAT. This line and float allowed us to recover the buoy from open water with a grappling hook. The transponder had a current consumption of 0.5 amps, and the lead-acid batteries had a 10 amp-hr lifetime. Therefore to stretch our

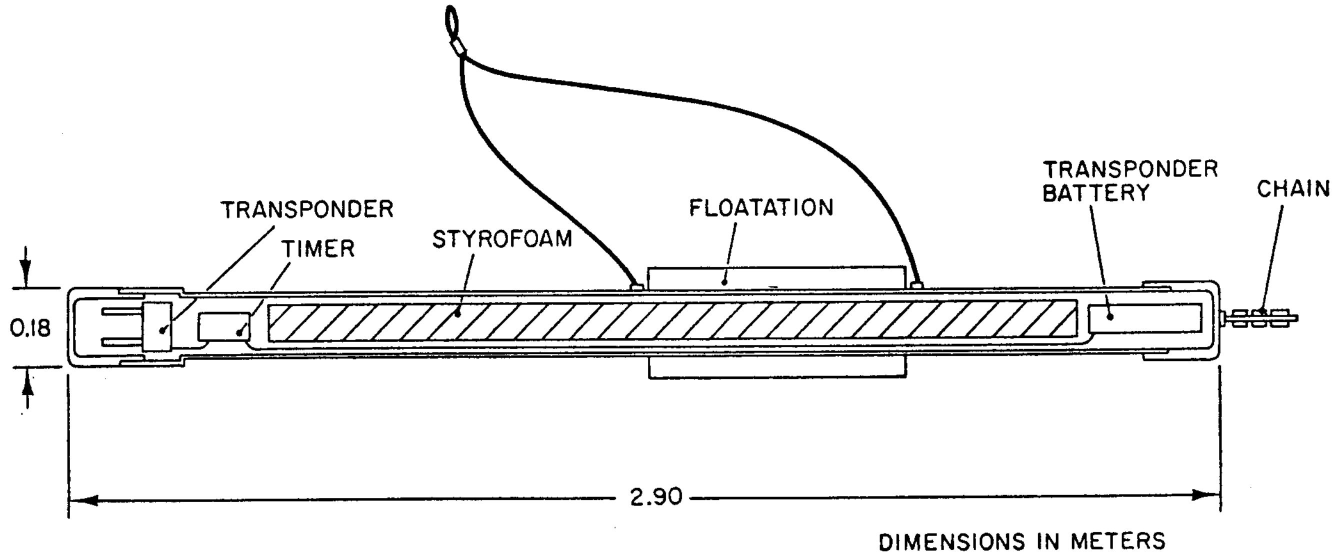

Figure 1. A schematic drawing of the radar transponder buoy. See text for additional description.

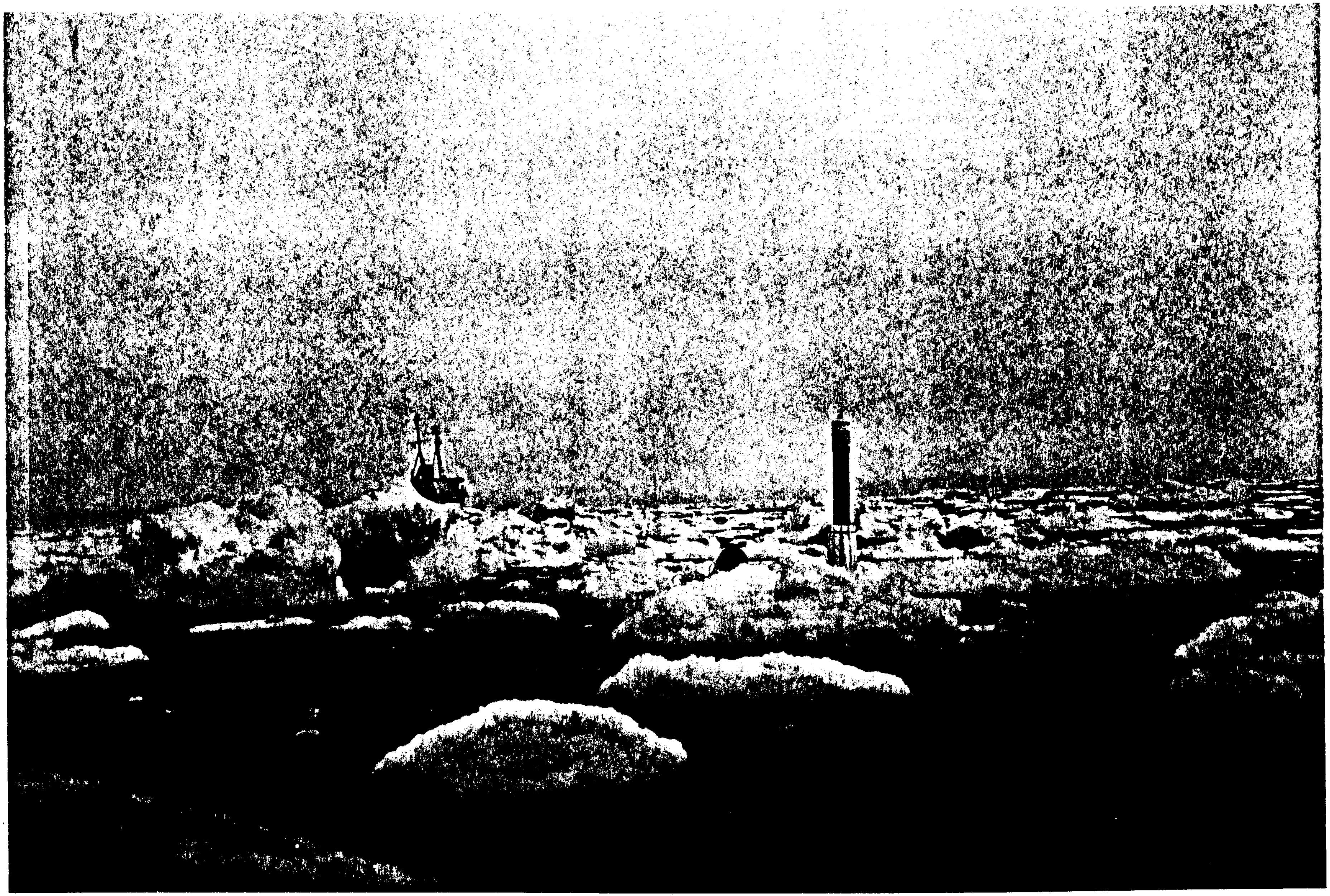

Figure 2. The radar transponder buoy deployed on a floe in the pack ice with the SURVEYOR in background.

operational time to 60 hr, we added the timer shown on Figure 1 below the transponder, which turned the transponder on for one minute, then off for two.

To install the buoy on an ice floe, we tied the ship against a suitable floe, went down on the ice, cored an auger hole, dropped the buoy in this hole, and attached the VINY-FLOAT. The entire procedure took about 1 hr. Once the buoys were deployed, we tracked them with the X-Band radar on the ship. We then recorded their range and bearing from the radar and the ship's position from the Loran-C at 0.5 hr intervals. We estimate that our position accuracy from the radar was about 1° in bearing, and 100 m in range. Off the ship, we reduced the data to absolute buoy position, which we estimate is accurate to within 100 m.

3. Description of the Band Experiment

In the experiment, we deployed the two buoys, named 'KURT' and 'JERAL' after two crew members, from the ship around 1200 local time (2200 GMT) on 7 March 1981 along a north-south line about 4 km apart. We deployed the buoys within the outer-most pack ice; Figure 3 shows the approximate ice appearance during the deployment as seen from the ship. Although the SURVEYOR was equipped with a helicopter, a combination of fog, high winds, and rotor icing prohibited our flying and viewing the ice from above throughout the band study.

In the deployment region, the ice consisted of floes with diameters ranging from 1 - 15 m. The floe JERAL was about 5 m in diameter and 1.2 m thick; the floe KURT was about 6 m in diameter and again 1.2 m thick. The maximum pressure ridge height within the region was about 1 m, which implies a ice keel depth of about 5 m. As Figure 3 shows, initially the ice containing the buoys did not appear to be a band; rather it had a north-south length scale greater than 6 km, and an east-west scale of order 1 - 2 km. Following deployment the ice advanced southwest in response to the 10 m s^{-1} northeast winds.

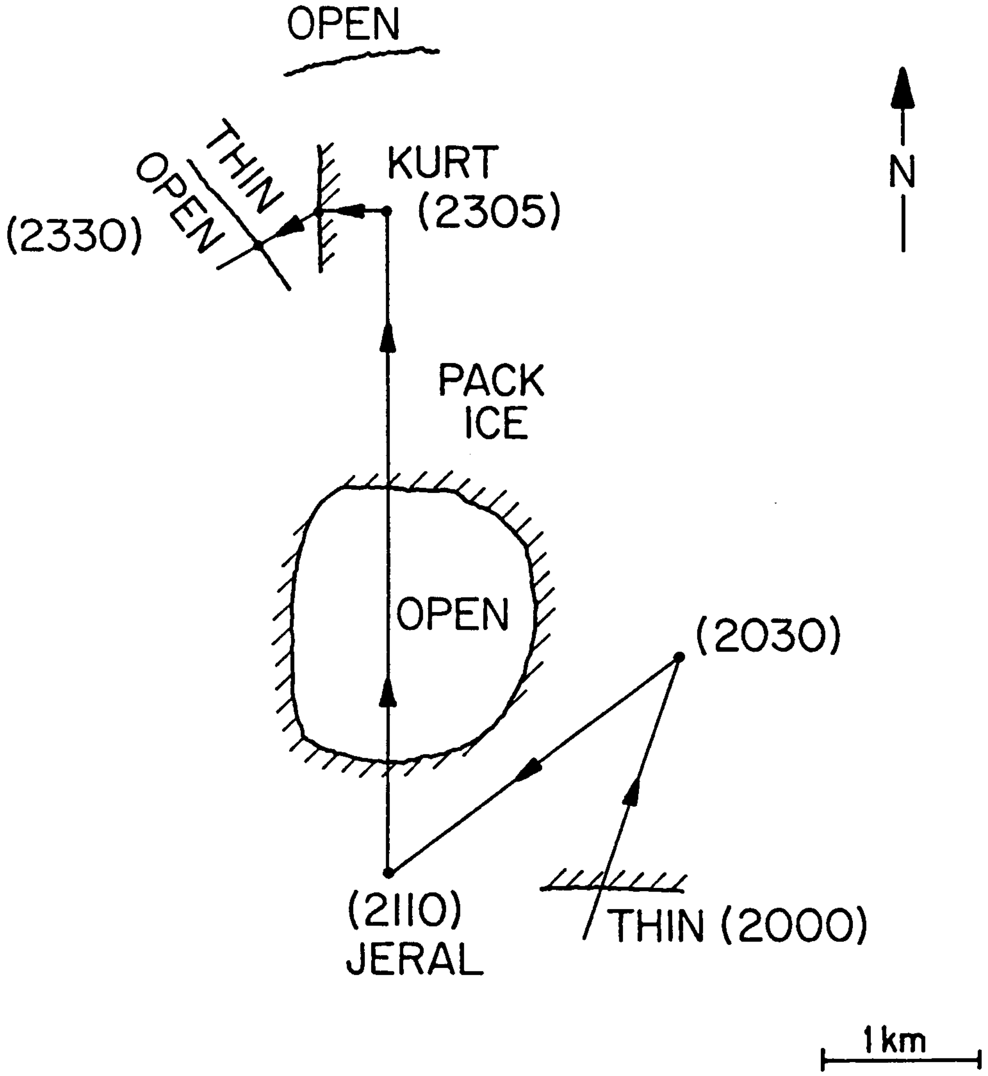

Figure 3. The ship track and buoy deployment for the band experiment. The numbers in parentheses show Greenwich Mean Time on 7 March; the plot is uncorrected for relative ice motion except for the relative position of JAREL to KURT which was determined at 2305 from the radar.

The following day, the wind velocity remained from the northeast and increased to 20 m s^{-1}. To show that the ice floes were now organized into a band, Figure 4 shows a sketch of the band appearance made from the ship on 9 March, 0000 GMT; and Figure 5 shows a composite photograph made at the same time with arrows indicating the approximate buoy positions. As the figures show, the band was long and narrow with a curve in the middle; the band maintained this appearance throughout the day. To avoid disturbance of the band, we deliberately kept the ship downwind and at least a km away. We continued tracking the band through the evening of 8 March, while the northeast wind velocity remained high. At 0230 local, we noted that KURT was not transponding regularly; at 0530, JERAL stopped transponding completely. At 0630, the ship moved against the ice band to take a CTD observation, at which time KURT was weakly transponding 1.5 km away to the northeast.

Therefore, at first light we decided to recover KURT; we steamed through the band which was now no more than 50 m wide, and picked up KURT at 0830 local in open water well upwind of the band. At pick-up, we found that the floatation collar on KURT had slipped upward so that it was adjacent to the expansion section at the top of the buoy. This lower buoy freeboard explained the signal attenuation. We then steamed on a dead-reckoning course for JAREL, and picked it up at 0900 local, again well away from any ice. The flotation had not slipped on JAREL; however, the high winds had blown the hull over so that the buoy lay nearly horizontal in the water. Because of this, we assumed that JAREL ceased transponding after breaking out of the ice.

The buoy trajectories for the entire 46 hr deployment are shown in Figure 6. The upper curve shows buoy KURT; the lower curve, JAREL. The dots on the curves show our position fixes at 0.5 hr intervals. The broken vertical arrows between the two trajectories show the position and relative orientation of the two buoys at 6

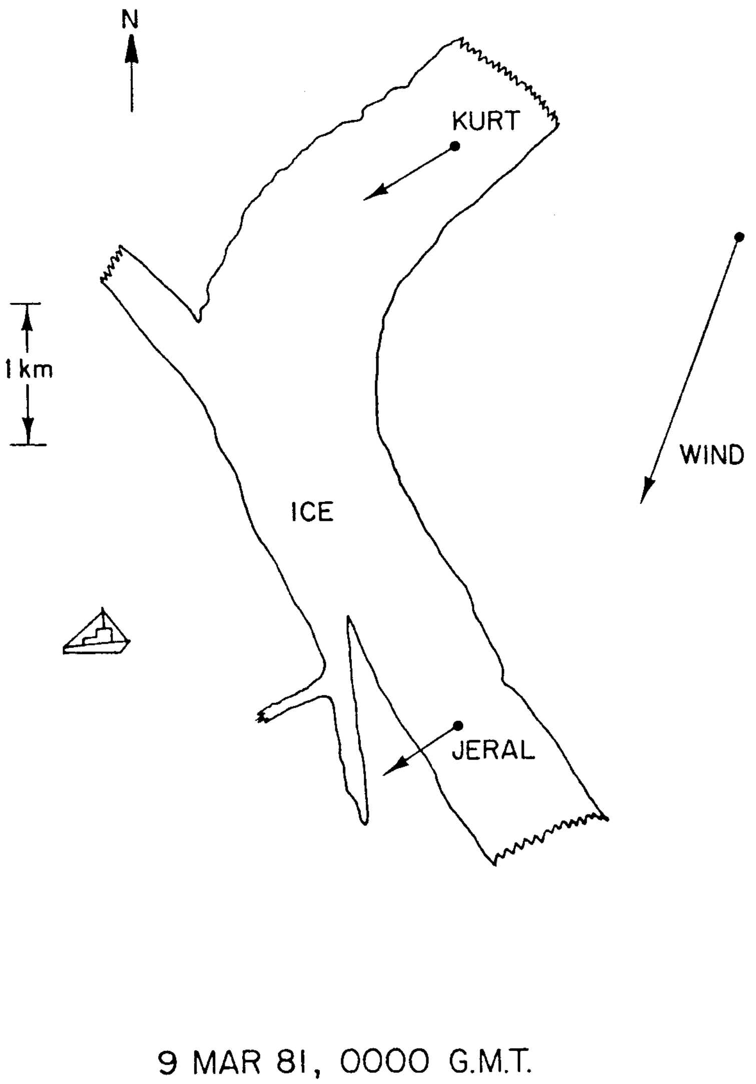

Figure 4. A schematic drawing of the band appearance on 9 March 1981, 0000 GMT. Except for the radar-derived distance between the buoys, the sketch is qualitative. The arrows show the direction of buoy motions; the symbol shows the ship position.

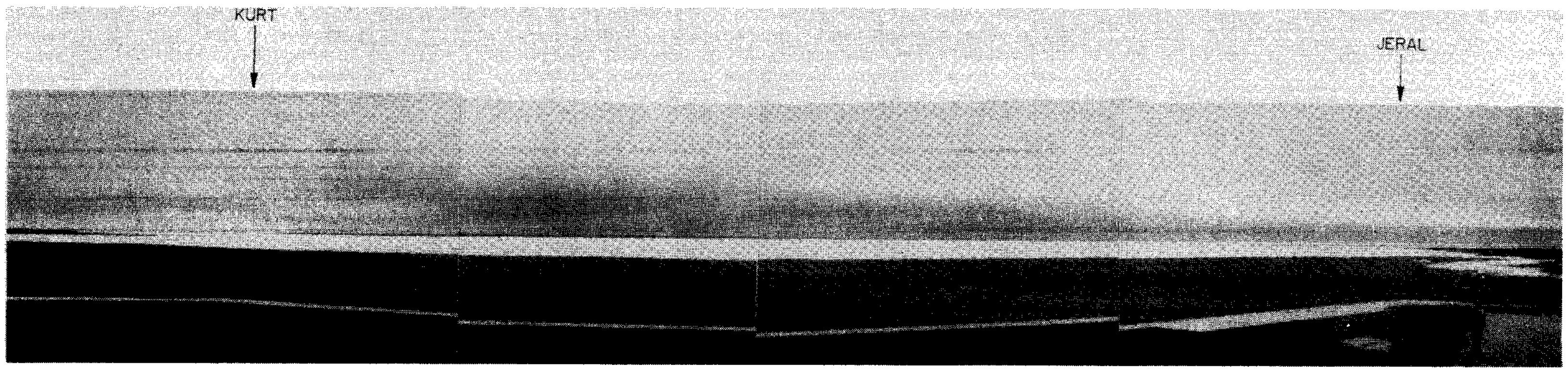

Figure 5. A composite photograph of the band made at the same time as Figure 4. The ship is downwind of the band; the arrows mark the approximate buoy positions.

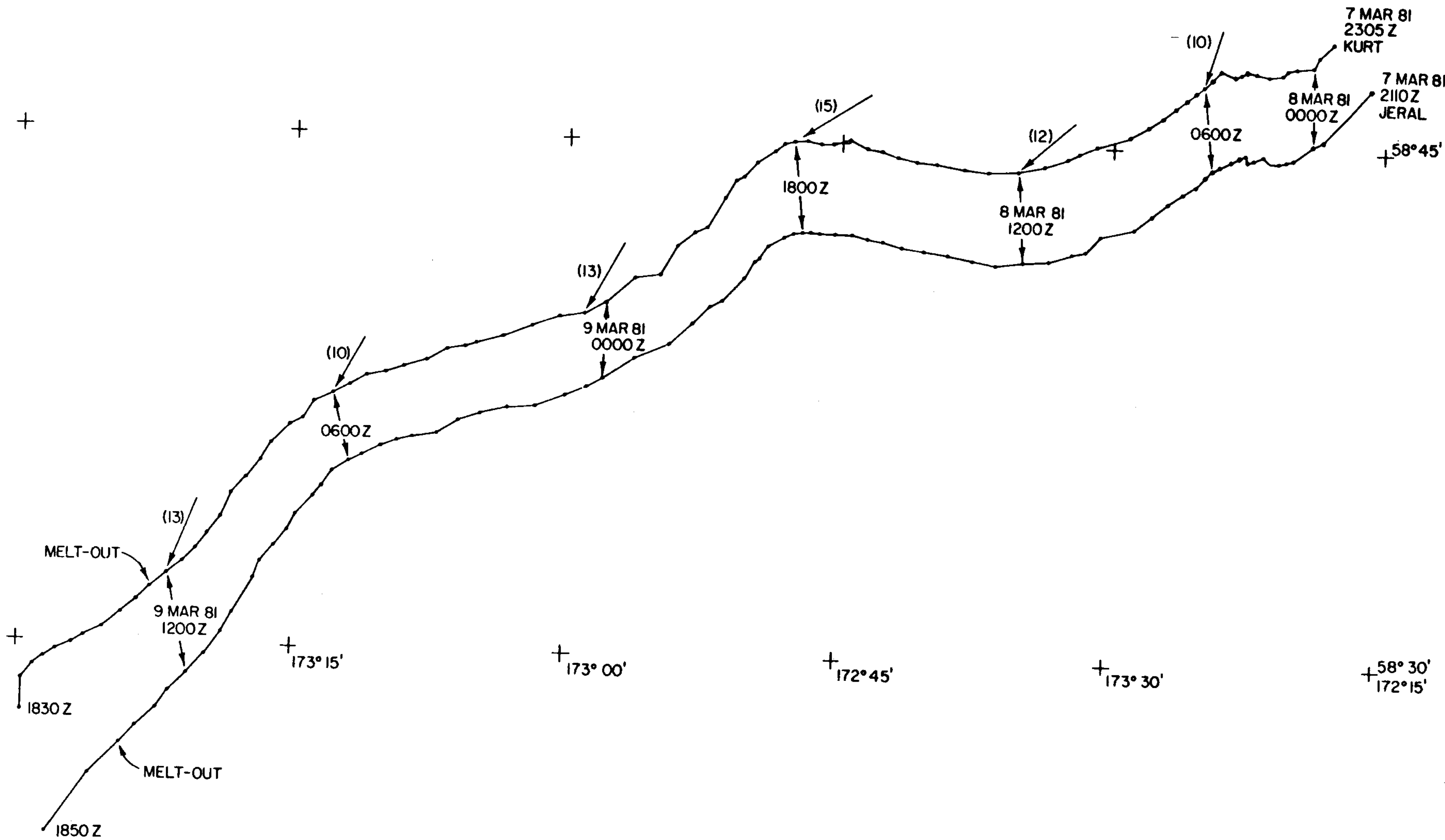

Figure 6. The buoy trajectories over the entire deployment period. The last point on 'KURT' is from the ship's log, not our records. See text for additional description.

hr intervals for the times listed in GMT in the arrow gaps. The sloping arrows above the trajectories show the wind direction; the numbers in parentheses beside the arrows show the wind velocity in m s^{-1}. Finally, the points labeled 'melt-out' are where we observed the transponder signal strength to diminish. The figure shows that over the deployment period, the wind advected the buoys to the west, with a mean speed of about 2 km hr^{-1}. The figure also shows the oscillations on the trajectories caused by the diurnal and semi-diurnal tides discussed below and that the buoys maintained approximately the same orientation and distance apart.

To discuss the relative positions of the two buoys in more detail, Figure 7 is a plot of buoy separation and angle versus time. Our original hypothesis for the reason that the bands became thinner as they moved downwind was that the incident ocean swell caused them to stretch out in length. Both Figures 6 and 7 however, clearly show that before the transponders melted out of the ice, the distance between them only varied between 4 and 5 km and their relative angle remained between 340°-360°. In addition, Figure 7 shows that before melt-out, as the band moved west, it neither appreciably stretched nor rotated, while after melt-out the buoys diverged rapidly. As we will show below, the cause of the band growing thinner as it moved downwind was wave erosion of the upwind edge.

Next, in order to compare the band velocity with that of the ice interior, we use data from a station deployed by Pease (1982) in the pack ice interior approximately 100 km upwind of the band. At her station, Pease measured position from a satellite-tracked ARGOS buoy, the air stress from an anemometer mast, and the water stress from a current meter suspended 3 m below the ice. From her measurements, we are able to compare both the relative velocities of and the stresses acting on the band and the ice interior.

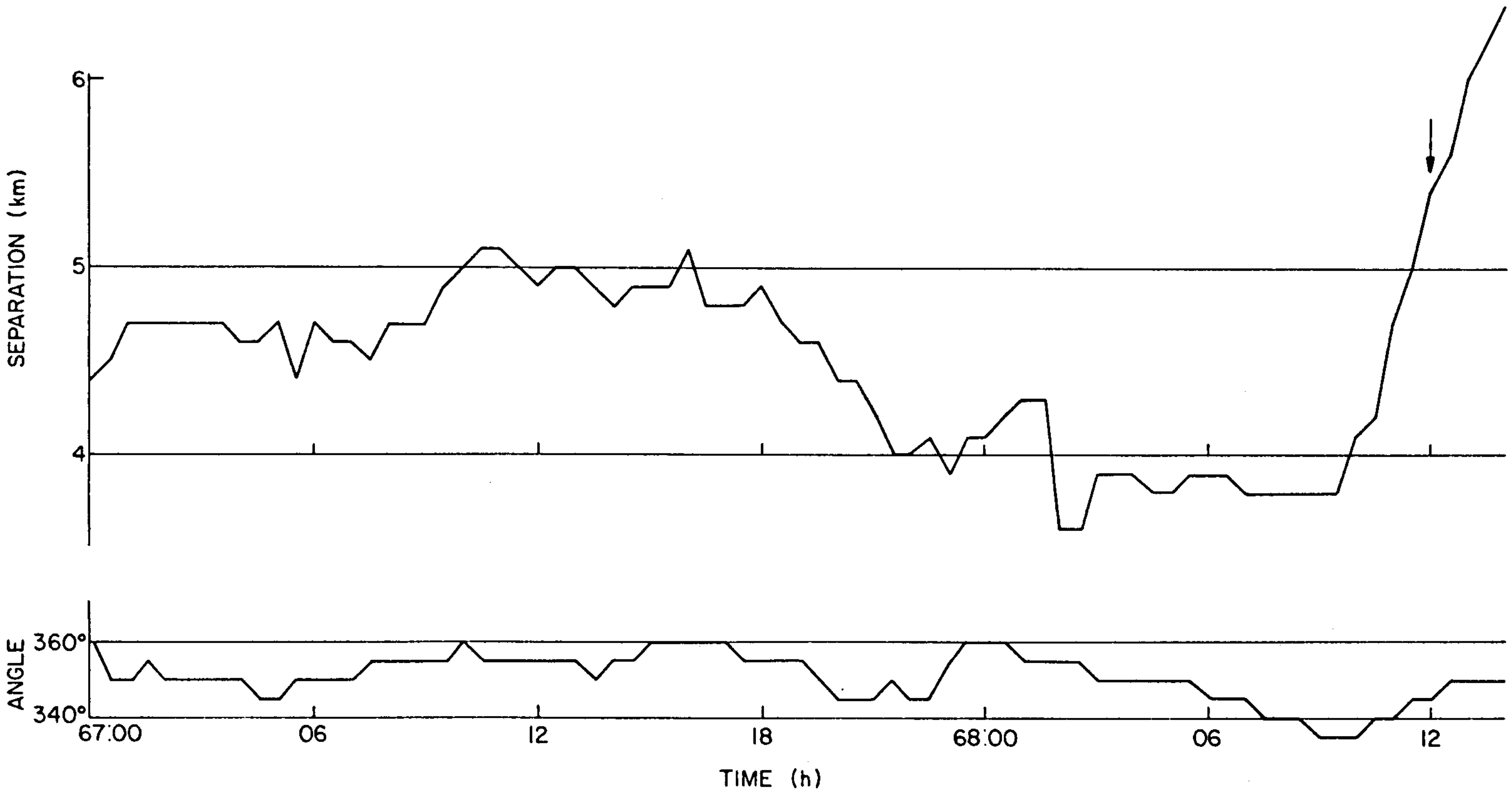

Figure 7. The relative separation and angle between the two buoys. The vertical arrow on the upper curve marks the logged melt-out time for KURT; the times are in Julian days and hours, where day 67 is 8 March.

Before comparison of the band and station velocities, we first describe the ice which lay between the band and Pease's interior station. In the local afternoon of 9 March, after recovery of a meteorological buoy in open water south of our band, we returned to the ice edge to recover Pease's station. Figure 8 shows a sketch of the ice features encountered along the cruise track, where the ship traveled 37 km over the 3 hr period 0100-0400 GMT, 10 March. During this cruise, we recorded the position of the observed bands from the LORAN-C, and the ice band orientation from the S-band radar. The figure shows that we encountered 5 bands during the traverse, the widest of which was 2 km, and that the band spacing varied between 5-10 km. We also observed that the swell was in the wind direction and decreased in magnitude as we moved northwest through the bands. The traverse ended when we encountered ice which was too heavy to steam through; at this point, Pease's station was a further 81 km at 44°T inside of the pack ice. The following day during an overflight to recover her station, Pease found that the pack ice between the ship and the station had the following structure: In the outer 10-20 km, the ice was organized into compact zones of broken ice, which were interspersed with occasional large leads and polynyas, where the leads were approximately oriented at right angles to the wind. Further into the pack, the ice concentration was greater, with many of the small floes refrozen into km-sized aggegates. The leads were sparser and still ran at approximately right angles to the wind. The station was located in a region of high concentration on a floe which was quasi-rectangular and measured about 10 by 20 m.

Figure 9 shows the relative displacement of KURT from Pease's station. The station was initially 80 km northeast of KURT; we assume that approximately the same tidal currents and winds acted on the two buoys. The figure shows, however, that KURT moves away from the station at a mean speed of 0.48 km hr^{-1} or 0.13 m s^{-1}, so that the band moves 30% faster than the interior ice. Section 5 shows that

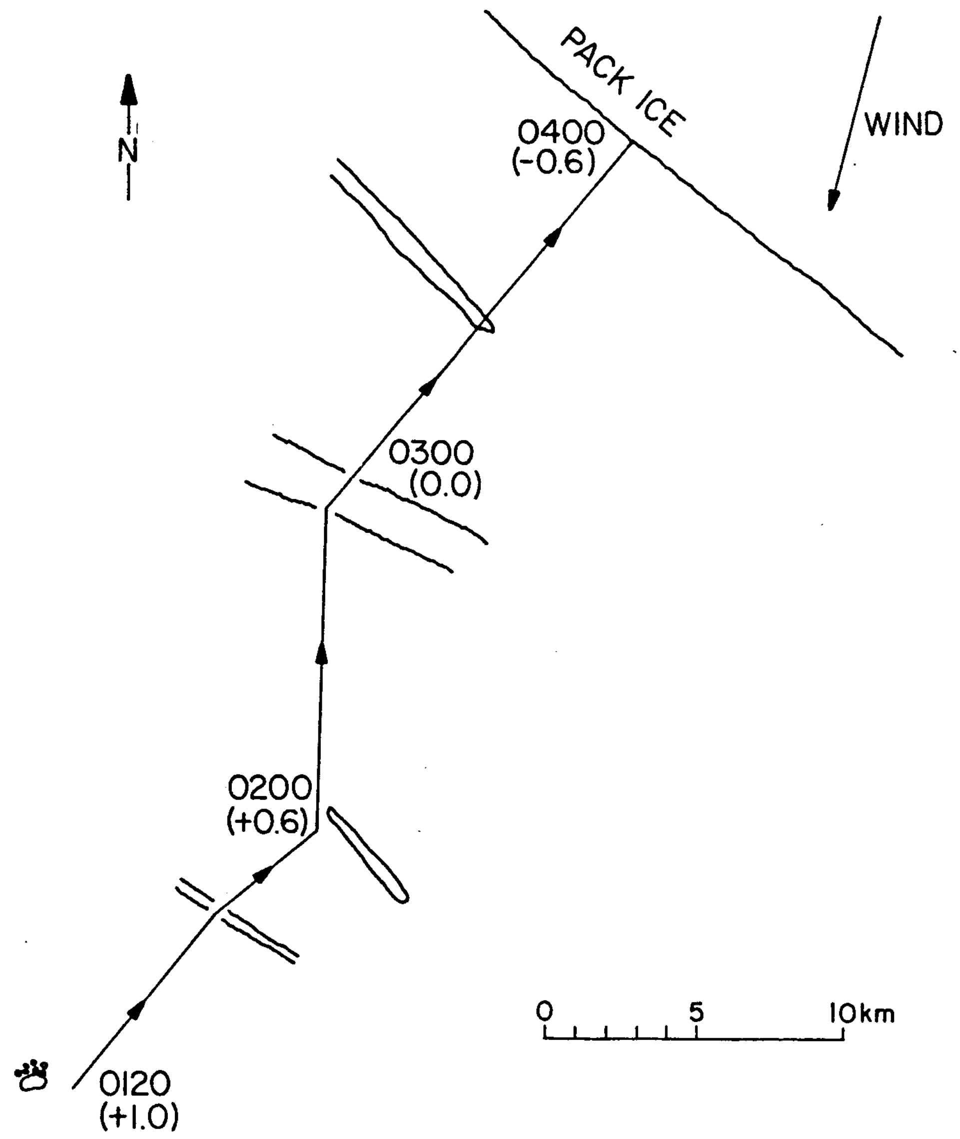

Figure 8. A schematic drawing of the ice features encountered during the return to the ice edge on 10 March, 0100 - 0400 GMT. The solid line shows the cruise trajectory; the adjacent numbers give times in GMT; the numbers in parentheses are the water temperatures in degrees. The arrow shows the mean wind direction; the mean wind speed was 15 m s^{-1}.

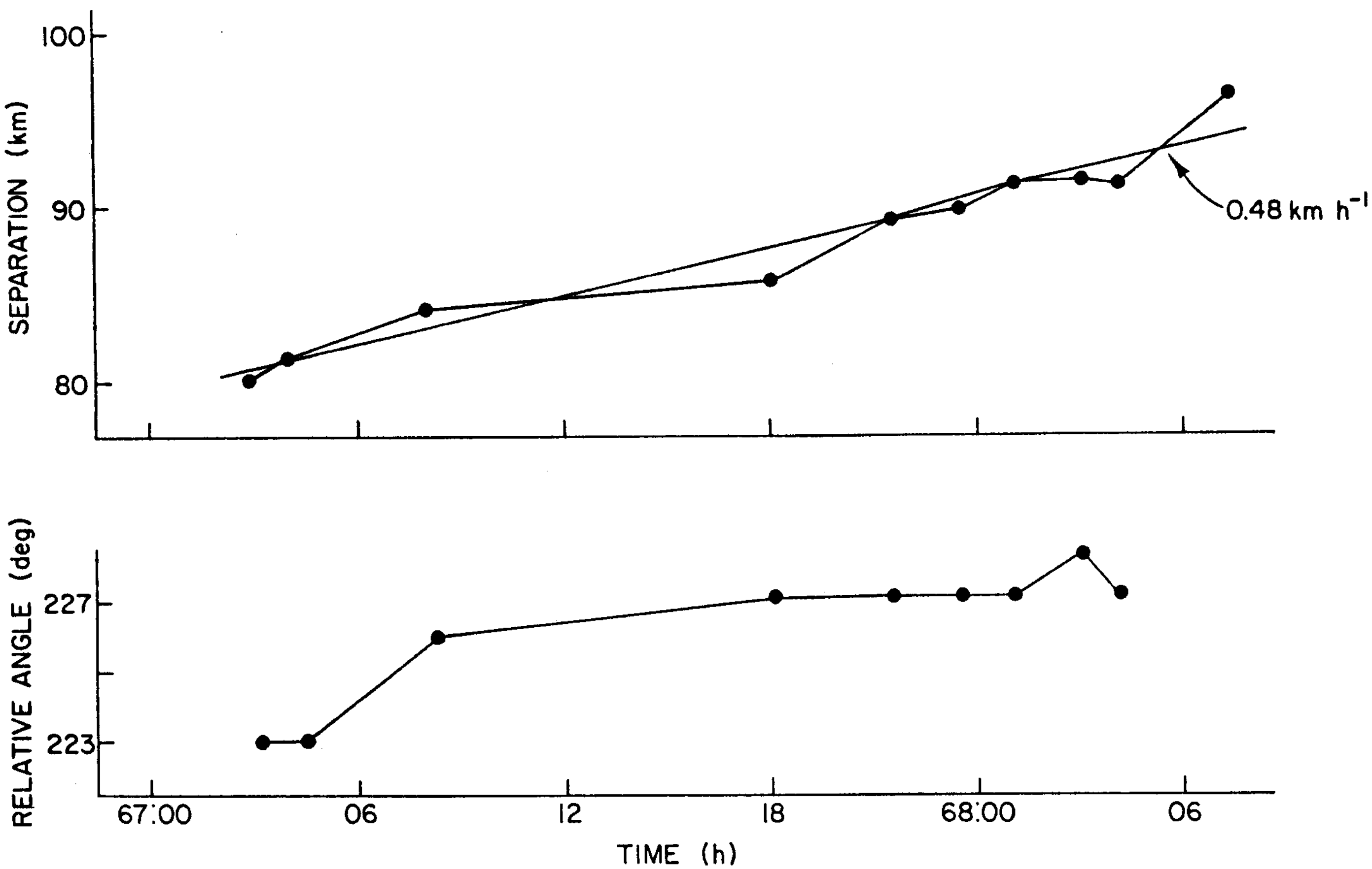

Figure 9. Relative displacement of KURT from Pease's station. The dots show the separation, the solid straight line is a least-squares fit showing that KURT moved away from Pease's station at a speed of 0.48 km hr^{-1} or 0.13 m s^{1}

the cause of this speed increase is the radiation stress on the band exerted by the wind waves generated in the fetch between the band and the ice margin. Before discussing of the band momentum balance, however, we first discuss how wind-waves contribute to the band structure and erosion.

4. Wave Erosion of the Band

To illustrate first the band structure, Figure 10 is a composite photograph of the cross-section of a small band, made 2 hr after the photograph in Figure 5. As determined from the LORAN-C, the band is approximately 100 m wide. The photograph shows that the band consists of 3 - 5 m diameter floes downwind, with a sharp water-ice boundary at the leading edge. Although it is not apparent on the photograph, the seawater surface downwind of the band is also smooth. In contrast, the ice on the upwind edge is diffuse and consists of small ice pieces which are strongly wave-agitated.

Figure 11, a schematic drawing of a band in cross-section, shows that at the upwind band edge, the wind waves are reflected and absorbed. Further, the wave agitation breaks up the larger floes into small pieces. These small floes then drift upwind relative to the larger floes in the consolidated band for the following reason: For an ice floe to be a good wave reflector, the floe diameter must be greater than half the incident wavelength, so that for the same incident wave, large floes are good reflectors and small floes are bad reflectors. Therefore, the small floes experience less of a radiation stress than the large floes so that once the small floes form, they drift upwind relative to the consolidated band. This physical process, where the broken-up floes experience a smaller radiation stress and then drift upwind relative to the band, explains the diffuse nature of the trailing band edge. Because of this process, small floes constantly break off the upwind band edge, drift relatively upwind, and melt in

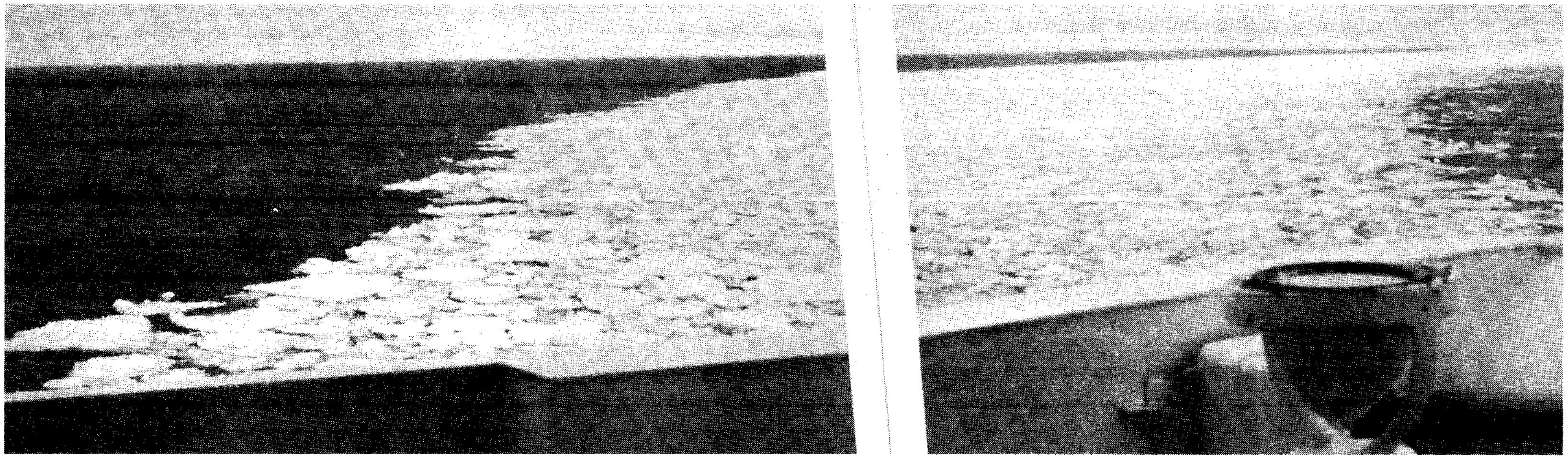

Figure 10. Composite photograph of a small 100 m wide band; downwind is to the left, upwind is to the right.

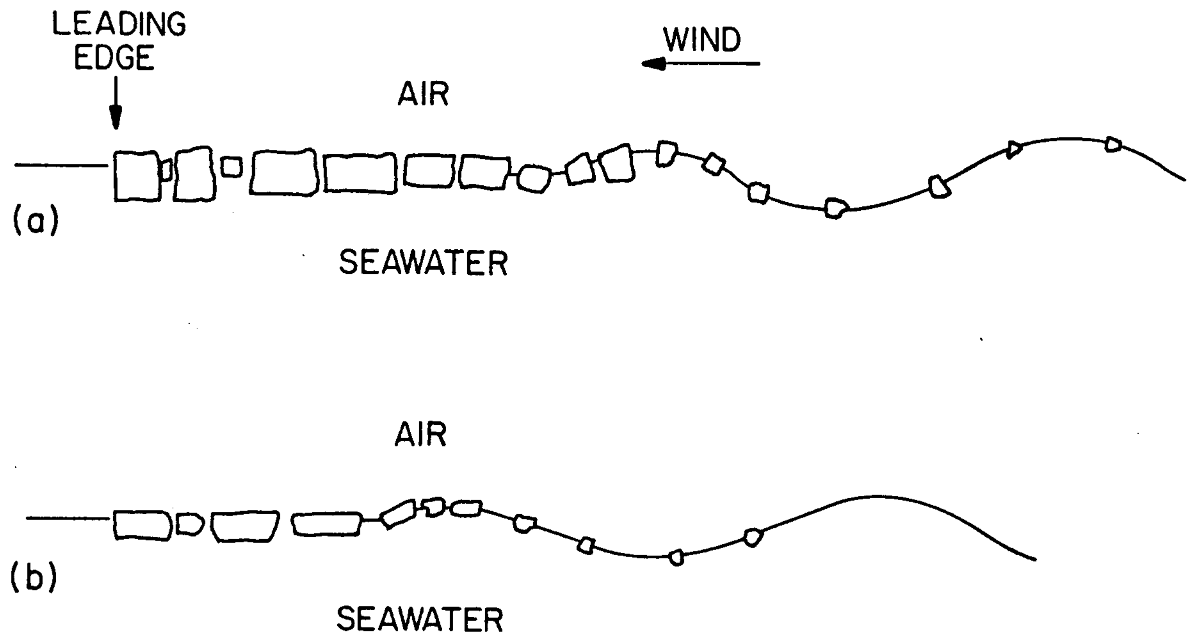

Figure 11. Schematic drawing in cross-section of the evolution of a band in a wave field. (a) Initial band configuration; (b) some time later. See text for additional discussion.

the surrounding warm water. The new ice thus exposed to the wind-waves also breaks up, drifts away, and melts so that the erosive process continues. Therefore as Figure 11 shows, the band melts both by the interior floes growing thinner in the vertical and by the horizontal erosion of the upwind edge.

For an additional detailed look at this melting process, Figure 12 shows the seawater temperature taken at 1 hr intervals from the ship while following the ice band, plotted versus time. The figure shows that the temperature began at the seawater freezing point, then had a nearly step increase of 2 degrees between 1800 - 2400 hr, 8 March. The following three photographs (Figures 13a, b, c) show details of the deterioration of the upwind band edge in the warm seawater following 0000 hr, 9 March (day 68). In Figure 13a the entire band is visible with the upwind edge to the right. Although it is not apparent on the photograph, the small floes upwind of the band tend to collect into Langmuir rolls formed at right angles to the band. Figure 13b next shows the individual floes upwind of the band, with diameters of 0.2 - 0.3 m; and Figure 13c shows the small floes well upwind of the band melting in the surrounding warm water.

This discussion shows that the wind waves cause the width decrease of the band. For our band, which had an initial width of order 1 km, and a final width of order 50 m, the rate of ice ablation is on the order of 20 m hr^{-1}. Figures 10 and 11 also show that following Wadhams (1982), the wave radiation stress exerts a compressive force which aside from the upwind edge, maintains the band integrity. In the next section, we further show that the radiation stress is of the right magnitude and direction to cause the observed band velocity increase over the ice interior.

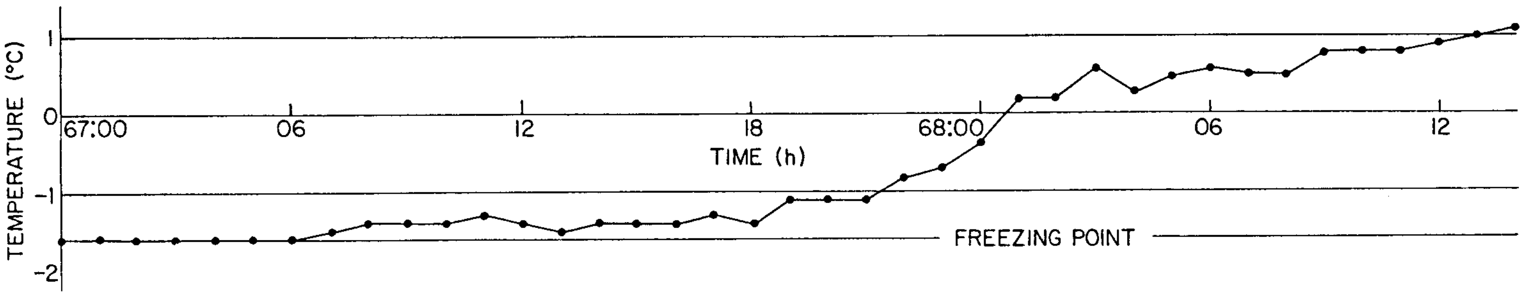

Figure 12. Seawater temperature versus time for the band experiment.

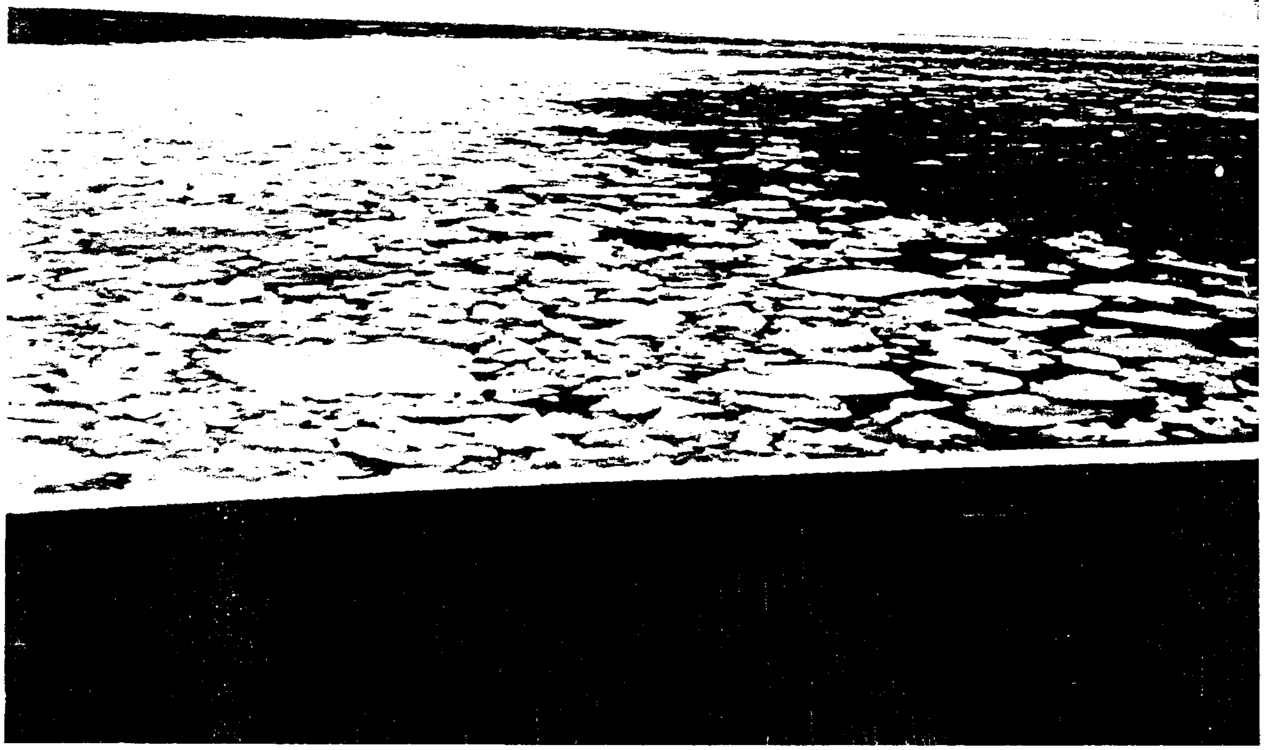

(a)

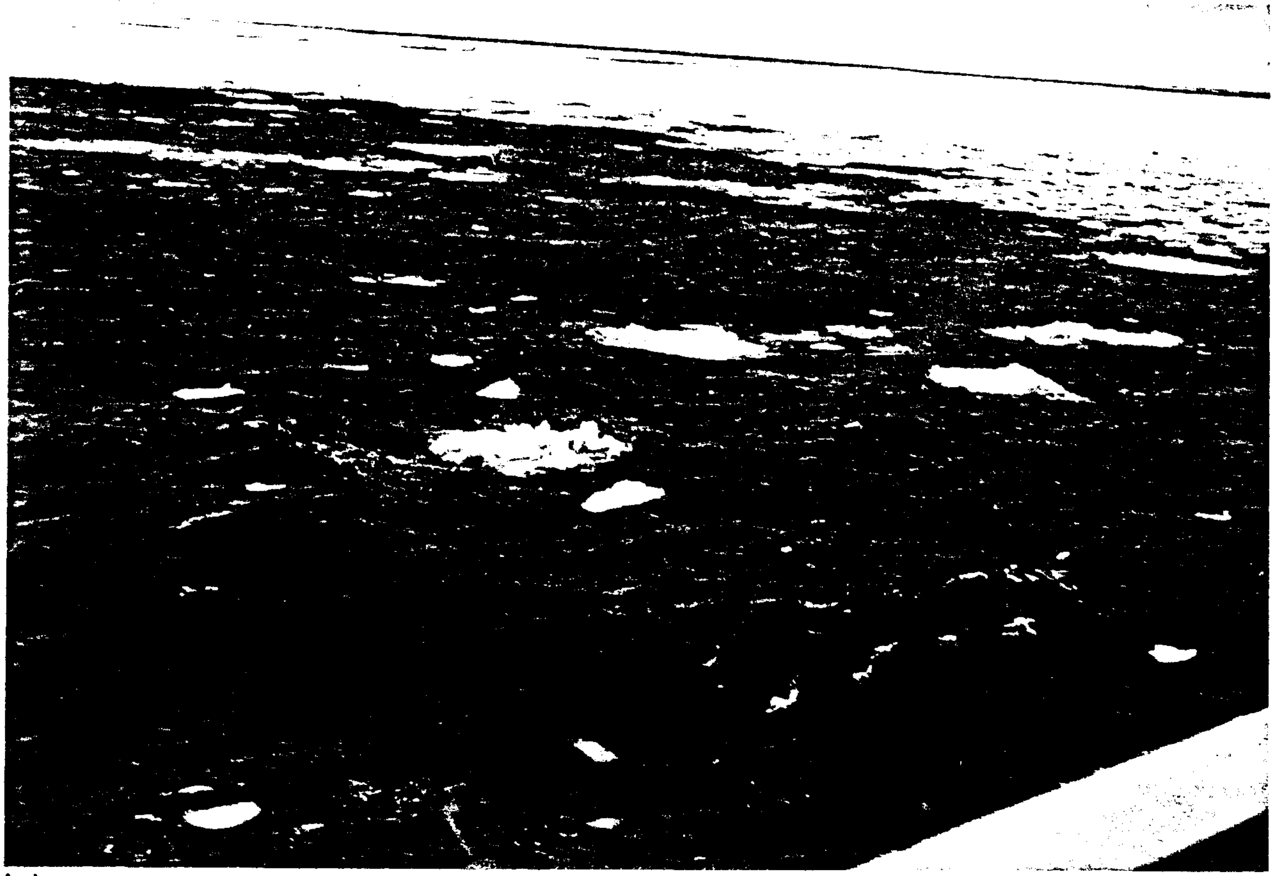

(b)

Figure 13. Details of an upwind band edge, following 9 March 0000 GMT. (a) The upwind edge; (b) the floes behind the band; (c) small floes melting in open water. See text for further description.

(c)

Figure 13.(c) small floes melting in open water.

5. The Stress Balance on the Band

In this section, we first identify and discuss the terms in the steady momentum balance, then qualitatively show that the tides cause the oscillations on the buoy trajectories, and finally apply the steady momentum balance to the ice band.

In application of the momentum balance, our major uncertainty is regarding water stress. Therefore we derive this stress in two ways: first, through use of the relative velocity observed at the band; second, by a scaling-up of the water stress measured at Pease's station. The use of these two stresses at the band gives a range of additional stress required for the band to move faster than the interior ice. Finally, for bands with widths of the same order as ours, we show that the radiation stress calculated from the observed wind speeds and fetches can account for both the direction and magnitude of the additional stress, so that the radiation stress can cause the increased band velocity.

To model the band motion, McPhee (1979, 1982) gives the following equation for the steady-state momentum balance on an ice floe relative to a barotropic geostrophic current:

$$\rho_w \underline{\tau}_w = \rho_a \underline{\tau}_a - i\, m\, f\, \underline{u}_R, \tag{1}$$

where $\underline{\tau}_w$ and $\underline{\tau}_a$ are respectively the water and air stress, ρ_w and ρ_a are the water and air density, m is the ice density per-unit-area, f is the Coriolis parameter, and the under-bar denotes a vector. In our analysis, we take ρ_a = 1.2 kg m^{-3} and ρ_w = 1030 kg m^{-3}. The relative ice velocity $\underline{u}_R$ is given by

$$\underline{u}_R = \underline{u}_I - \underline{u}_G, \tag{2}$$

where $\underline{u}_I$ is the absolute ice velocity, and $\underline{u}_G$ is the geostrophic flow due to sea surface tilt.

For the wind stress $\underline{\tau}_a$, McPhee uses

$$\underline{F}_a \equiv \rho_a \underline{\tau}_a = \rho_a C_{10} |U_{10}| \, \underline{U}_{10} \tag{3}$$

where $C_{10} = 2.7 \times 10^{-3}$, and $\underline{U}_{10}$ is the 10 m wind velocity. To simplify our notation, we define $V = |u_R|$. Then for the water stress, McPhee derives $\underline{\tau}_w$ from 60 days of summer Beaufort sea ice drift data, for $0.08 < V < 0.22$ m s^{-1}. McPhee's (1982) best-fit theoretical formulation (his sixth model) gives

$$\tau_w = 0\ 0128\ V^{1.70 \pm 0.00}, \tag{4}$$

and the best fit to his observed data from McPhee (1979) is

$$\tau_w = 0.0104\ V^{1.78 \pm 0.12} \tag{5}$$

for V in cm s^{-1}. In both cases, $\underline{\tau}_w$ is directed in the opposite direction and about 20° to the right of V.

Before application of the above steady-state momentum balance to the ice band, we first show that the cause of the oscillations in the buoy trajectories is the rotary tidal currents. For simplicity, and because of the close correlation between the two trajectories, we work only with buoy KURT. In this comparison we take the ocean currents from a current meter (BC22) discussed in Muench (1982). Figure 14, a simplified chart of the experimental region, shows the position of the current meter, which was moored at 50 m depth, and the net

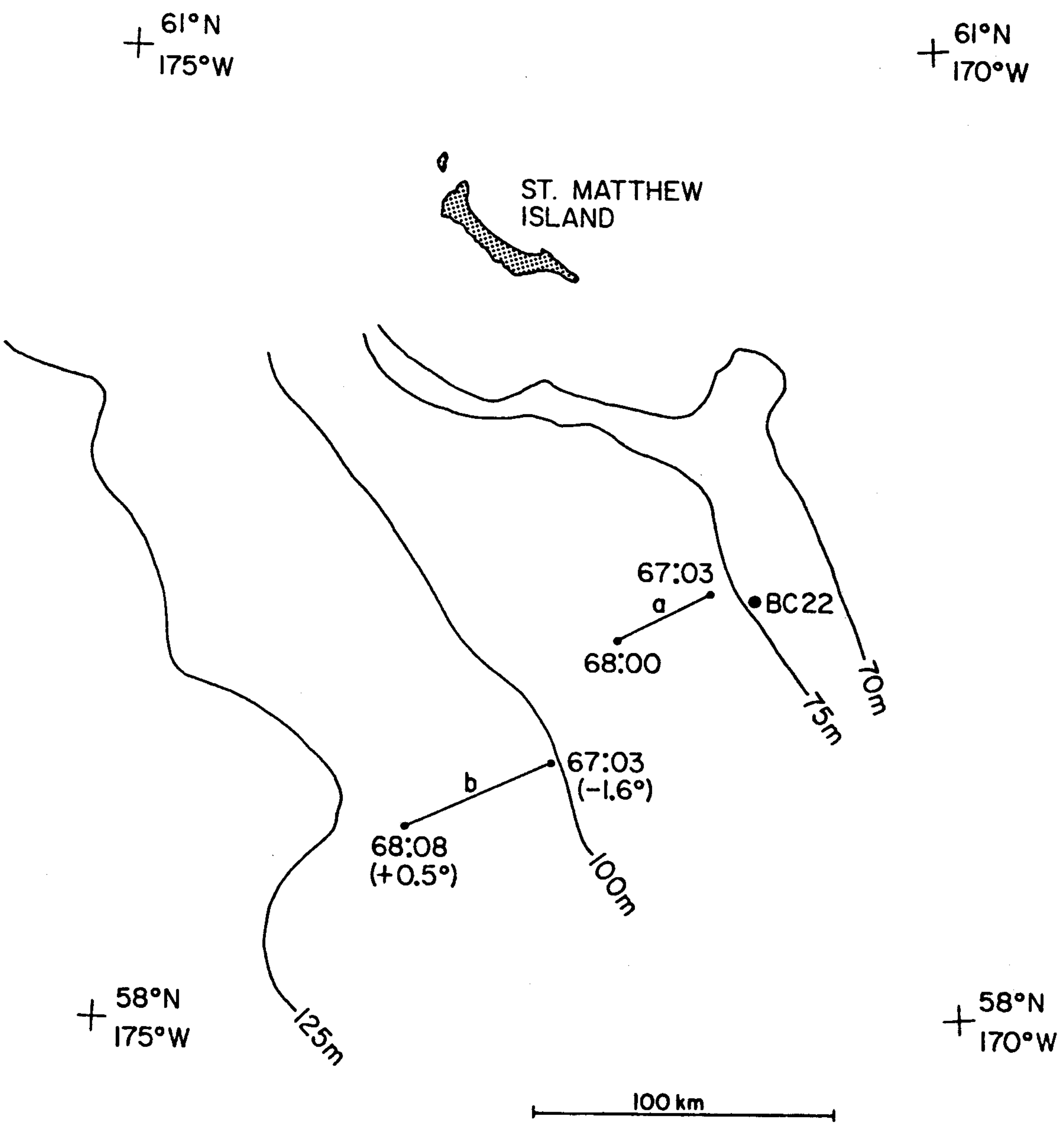

Figure 14. A chart of the experimental region. The point 'BC22' shows the current meter position; the line 'a' shows the net translation of Pease's station for the times shown at the endpoints; line 'b' shows the net band translation. The numbers in parentheses under the times are water temperatures in degrees.

southwest translation of Pease's station on line 'a' and KURT on line 'b', for the times shown at the line endpoints.

The figure shows that the band is between 90 - 140 km southwest of BC22 in water depths of 100 - 125 m. From a CTD survey during the cruise, Muench (1982) shows that the seawater at BC22 is nearly homogenous, while the rising temperatures along the band trajectory correspond to a 100 km wide region of two-layered stratification in both temperature and salinity with an average interface depth of 30 m, with the two-layer structure running approximately parallel to the isobaths. Because of the change in depth and oceanic stratification at the band relative to BC22, application of the BC22 currents to the band may be complicated by amplitude and phase shifts. Even with these potential changes, it can be seen from Figure 15 that the BC22 currents account for most of the oscillations in the band trajectory. On the figure, the top 2 curves show the north u_C and west v_C current components from BC22; the middle two curves, u_I and v_I, show the ice band velocity components, which are filtered with a 2.5 hr running average; and the lower two curves show the relative velocities $\underline{u}_R = \underline{u}_I - \underline{u}_C$. Examination of the lower curves shows that the rotary tide accounts for most of the oscillatory motion on the trajectory. The remaining slight oscillations are either caused by the band position change relative to BC22, or by inertial oscillations.

Next, to average out the diurnal and semi-diurnal tides from the band data, and to derive the steady state force balance on the band, we average all relevant quantities over the 25 hr period beginning at 8 March, 0600 GMT. For the currents, Table 1 lists the mean components of $\underline{u}_I$, $\underline{u}_C$, and $\underline{u}_R$. We assume that the mean current $\underline{u}_C$ is due to the sea surface tilt. Then, using $|\underline{u}_R|$ and the wind velocity observed on the ship, we calculate the terms in (1) which make up the steady state stress balance. We then sum these stresses to derive the magnitude and direction of the residual stress $\underline{F}_R$.

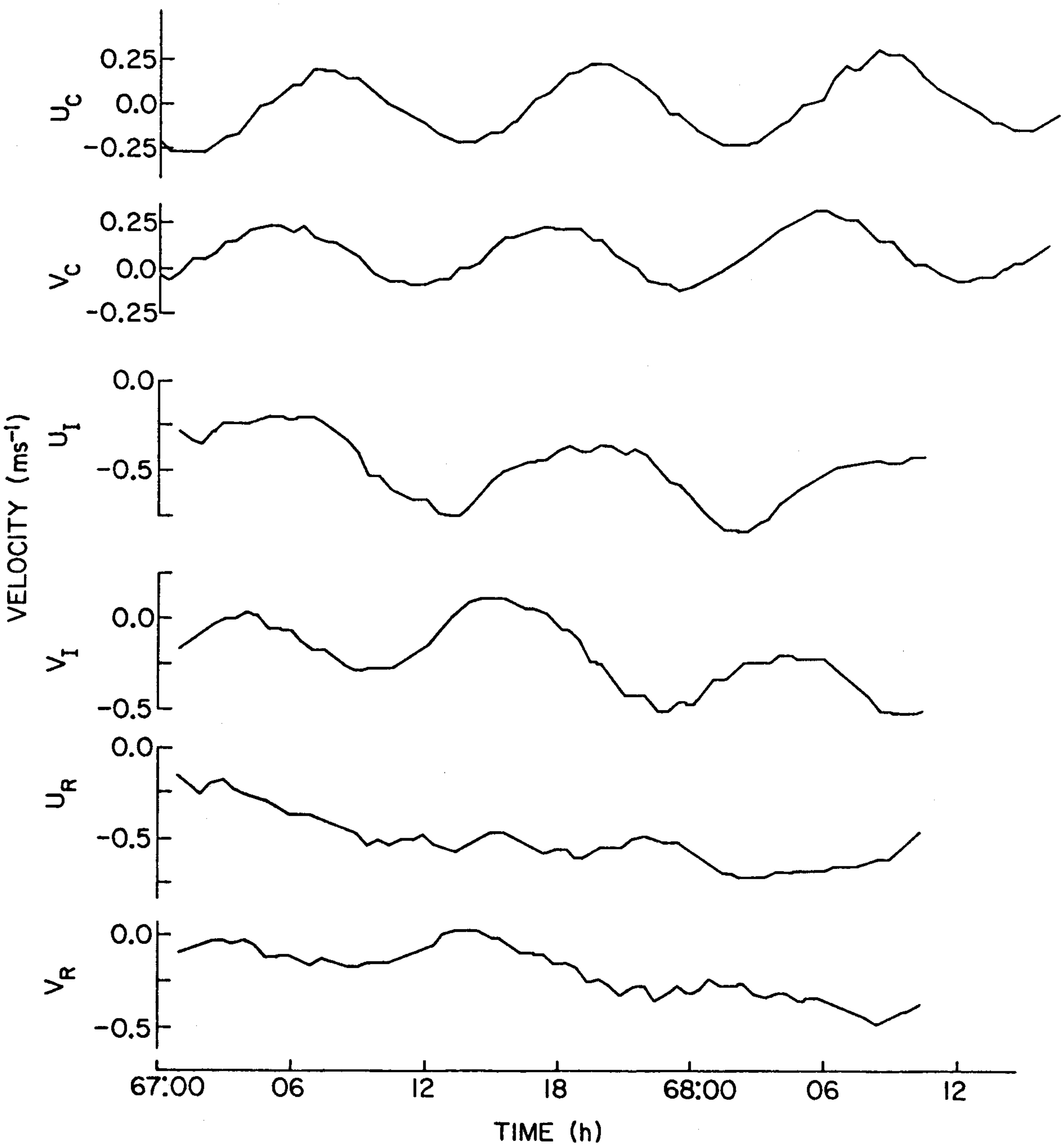

Figure 15. Comparison of the band velocity with the currents measured at BC22. The upper two curves show the east u_C and north v_C current components from BC22; the middle two curves show the ice band components u_I and v_I; the lower two curves show the relative velocities u_R and v_R. See text for additional description.

Table 1. Average velocities used in the calculation of the ice momentum balance. $\underline{u}_I$, absolute ice velocity; $\underline{u}_C$, currents at BC22; $\underline{u}_R$, relative ice velocity. '$\hat{x}$' , east direction; '$\hat{y}$' , north direction, 'mag', magnitude, 'deg', current direction in true degrees.

velocity	$\hat{x}$	$\hat{y}$	mag	deg
$\underline{u}_I$	-0.529	-0.179	0.56	251°
$\underline{u}_C$	-0.002	+0.093	0.09	359°
$\underline{u}_R$	-0.527	-0.272	0.59	243°

Table 2 lists the values of the stresses acting on the band. To calculate the air stress, we use the hourly wind speed and direction shown in Figure 16 as recorded from a cup anemometer and a wind vane mounted on a mast above the bridge. For $\underline{F}_a$, we substitute these winds into equation (3), then average (3) over the 25 hr period. To calculate the Coriolis stress $\underline{F}_c$, we use $f = 1.25 \times 10^{-4}\ s^{-1}$ corresponding to 59° N, $m = 1.9 \times 10^3\ kg\ m^{-2}$ corresponding to an average ice thickness of 2 m, and the value of $\underline{u}_c$ given in Table 1. To calculate the magnitude of the water stress F_w, we substitute $V = 59\ cm\ s^{-1}$ into equation (4) giving the mean water stress as $1.34\ N\ m^{-2}$. For the direction of F_w we follow the formulation of the sixth drag law in McPhee (1982, Table 1) which gives the stress direction α, as

$$\alpha_1 = \alpha_2 - 180^{\circ} - \beta$$

where α_2 is the ice velocity direction, and we calculate β as 19°. We then use these values to calculate the vector components of $\underline{F}_w$ listed in Table 2. Finally, the last line in Table 2, which gives the values of $\underline{F}_R$ necessary to complete the stress balance, shows that $\underline{F}_R$ has a magnitude of $0.8\ N\ m^{-2}$ in the wind stress direction. The additional stress required for balance then, is both of the same order and in the same direction as the wind stress.

There are several problems with the formulation in Table 2. First, our ice velocity of $0.59\ m\ s^{-1}$ is 2.5 times the largest velocity measured in McPhee's field data. This leads to a large range of error. For example, substitution of $0.59\ m\ s^{-1}$ into equation (5), which is McPhee's least-square best fit empirical equation, gives a stress range of $0.9 - 2.5\ N\ m^{-2}$. Substitution of these magnitudes alone in the stress balance gives that $\underline{F}_R$ ranges between $0.5 - 2\ N\ m^{-2}$. Second, with regard to the wind stress, we felt when the quartermasters measured

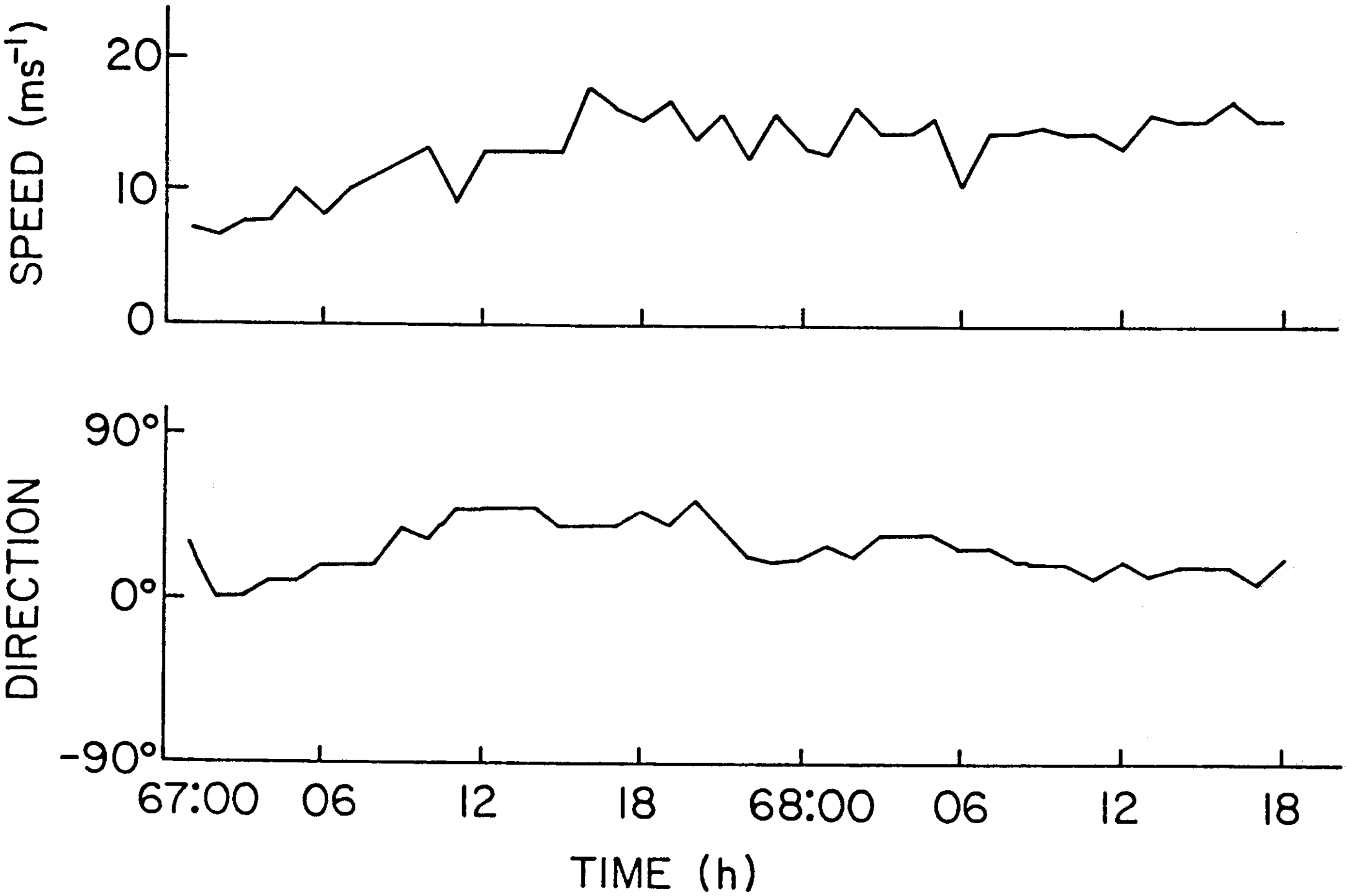

Figure 16. Observed wind speed and direction for the band experiment as measured on the ship at one-hour intervals.

Table 2. Stresses on the ice band. F_w, water stress; F_a, air stress; F_x Coriolis stress; F_R, residual stress required for balance; all in N m^{-2}. See caption of Table 1 for notation.

Stress	$\hat{x}$	$\hat{y}$	mag	deg
F_w	0.93	0.96	1.34	44°
F_a	-0.36	-0.49	0.61	216°
F_c	-0.06	+0.13	0.14	333°
F_R	-0.51	-0.60	0.79	220°

the hourly wind speed on the ship, they underestimated the effect of gusts. An increase of the mean wind speed by 10% yields a 20% increase in the wind stress, which reduces $\underline{F}_R$ to 0.6 N m^{-2}. Finally, our assumption of a 2 m average ice thickness is only an estimate. Reduction of this value from 2 to 1 m, however, only reduces $\underline{F}_R$ by a negligible amount.

Our second method for calculation of the ice band water stress is to scale up the water stress measured at Pease's station, where the radiation stress is negligible, by the ratio of the band and station velocities raised to the 1.7 power. From her drag and position measurements, Pease calculated for the same 25 hr period the average station velocity and stress balance. First, the relative velocity $\underline{u}'_R$ of her station is as follows:

$$u'_R = -0.37 \text{ m s}^{-1}, \qquad v'_R = -0.27 \text{ m s}^{-1}, \tag{6}$$

$$\text{or} \quad V' = 0.45 \text{ m s}^{-1}, \qquad \alpha' = 234^\circ,$$

where V' and α' are the current magnitude and direction. Comparison of the station and band velocities shows that, consistent with Figure 8, the station moves 0.14 m s^{-1} slower than the band.

Second, Table 3, which lists the measured stress balance for 1 m thick ice at Pease's station, shows that as a first approximation the air and water stress are in balance. Further the table shows that, although the wind stress at the station approximately equals the wind stress on the band, the station water stress is only 38% of the stress derived for the band. Therefore, an alternative method for calculation of the water stress on the band is to scale up the stress measured at Pease's station by the ratio

Table 3. Stress balance at Pease's station. See caption of Table 1 for notation.

Stress	$\hat{x}$	$\hat{y}$	mag	deg
F_w	0.32	0.38	0.50	40°
F_a	-0.35	-0.41	0.54	220°
F_c	-0.03	+0.04	0.05	324°
F_R	+0.06	-0.01	0.06	260°

$$\left(\frac{V}{V^1}\right)^{1.7} = 1.58 \quad ,$$

which yields a stress of 0.8 N m^{-2} in magnitude acting on the band. Table 4, which lists for this water stress the new band stress balance shows that the residual stress is now 0.3 N m^{-2} and still directed approximately in the wind direction. In summary, Tables 2 and 4 show that depending on which method we use for calculation of the water stress, F_R is in the range 0.3 - 0.8 N m^{-2}, and is directed approximately in the wind direction.

We next show that the wind-wave radiation stress can provide F_R. Following Longuet-Higgins (1977), if the ice band totally absorbs the wave energy with no transmission or reflection, then the radiation stress S in N m^{-1} is

$$S = \frac{1}{4} \rho_w g\, a^2 = \frac{1}{2} \varepsilon \qquad (7)$$

where g is the gravity acceleration 9.8 m s^{-2}, a is a characteristic incident wave amplitude, and ε is the incident wave energy density.

Hasselmann et al (1973) give ε as the following function of fetch X (in km) and wind velocity U_{10}:

$$\varepsilon = 1.6 \times 10^{-4} \rho_w\, X\, U_{10}^2 \quad , \qquad (8)$$

so that

$$S = 8.2 \times 10^{-2} X\, U_{10}^2 \quad . \qquad (9)$$

For the same formulation, the dominant wave frequency ω_o is given by

Table 4. Recalculation of the stress balance on the ice band, using Pease's water stress scaled up from Table 3. See caption of Table 1 for notation.

Stress	$\hat{x}$	$\hat{y}$	meg	deg
F_w	0.51	0.60	0.79	40°
F_a	-0.36	-0.49	0.61	216°
F_c	-0.06	+0.13	0.14	333°
F_R	-0.09	-0.24	0.26	200°

$$\omega_o = 2.2 \left[\frac{g^2}{U_o X} \right]^{1/3} \tag{10}$$

We next calculate S for the observed range of wind speeds (10-20 m s^{-1}) and fetches (5-10 km). Our choice of fetches is consistent with both Figure 8 and the observations of Muench and Charnell (1977). Because our unknown in the force balance is the band width, we then use S to calculate the range of band widths for F_R = 0.3 and 0.8 N m^{-2}. Table 5 shows the dependence of S on X and U_{10}, and the resultant band widths. In the table, the first number in each of the four blocks is S; the two lower numbers in parentheses are the band widths for the two cases 0.3 and 0.8 N m^{-2}. To show that for each case the no-transmission assumption is valid, for the case X = 10 km and U_{10} = 20 m s^{-1}, we calculate from equation (10) the dominant frequency ω_o = 1.7 s^{-1} which corresponds to a wavelength of 20 m. The general requirement for total reflection of the wave energy from a floe is that the floe diameter be greater than half the incident wavelength. Since our floe diameters are about 10 m, this criterion is met for the longest fetch, highest wind speed case.

The table shows that for total energy absorption, that the band widths range from 0.1 - 1 km. On the further assumption of total wave reflection, all of the widths in the table would be doubled, so that even for 0.8 N m^{-2} case, for 10 km of fetch a band made up of deep wide floes can be 1 km wide. We also note that as the bands move downwind and thin out by the mechanism described above, the bands will begin to transmit the longer incident wavelengths. This leakage of energy through the band will reduce the incident radiation stress and explains why the bands do not continue to accelerate with increasing fetch.

Table 5. Radiation stress (N m^{-1}) and resultant band widths (m) as a function of fetch X, and wind speed U_{10}. The top number in each block is the stress; the lower two numbers in parentheses are the band widths for the two cases.

X (km) / U_{10} ($m\ s^{-1}$)	10	20
5	40 (50, 140)	160 (200, 530)
10	80 (100, 270)	330 (400, 1,100)

6. Concluding Remarks

The present study shows that the wind waves account for both a large part of the band decay and the band velocity increase relative to the ice interior. Because the long axes of the bands lie approximately at right angles to the wind, the bands serve as line wave absorbers and reflectors, so that the processes of band decay and acceleration are more efficient than for randomly-oriented bands. The problems which are unsolved include the question of how the bands initially form, the exact nature of the water stress on the bands, and the dependence of the rate of band ablation on wind, waves, and water temperature.

Also, not all bands are linear; some of them occur as complicated sinuous patterns. Figure 17 shows an example of a band observed as we left the ice edge on 11 March, 0000 GMT, where the only noticeable ocean waves were from the wind direction. At present, we have no idea as to how these complicated structures form and evolve. In summary, the bands are efficient structures for the absorption and reflection of wave energy where the energy and radiation stress go into increased band velocities and the band ablation. Thus, the ice bands are probably strong contributors to the maintenance of the ice edge position through rapid ice export and melting.

Acknowledgments

We are grateful to Captain Bruce I. Williams and the officers and crew of the NOAA ship SURVEYOR. Without their help and patience, we could never have done this experiment. We also thank Carol Pease, for her role as chief scientist, for allowing us to use the data from her ice interior station, and for many useful conversations about stress balance. We also thank Dr. Robin Muench for the use of his current meter data, John Gunn and Patricia Fogle for help with the data processing, Jane Bauer for conversations about radiation stress, Cathie

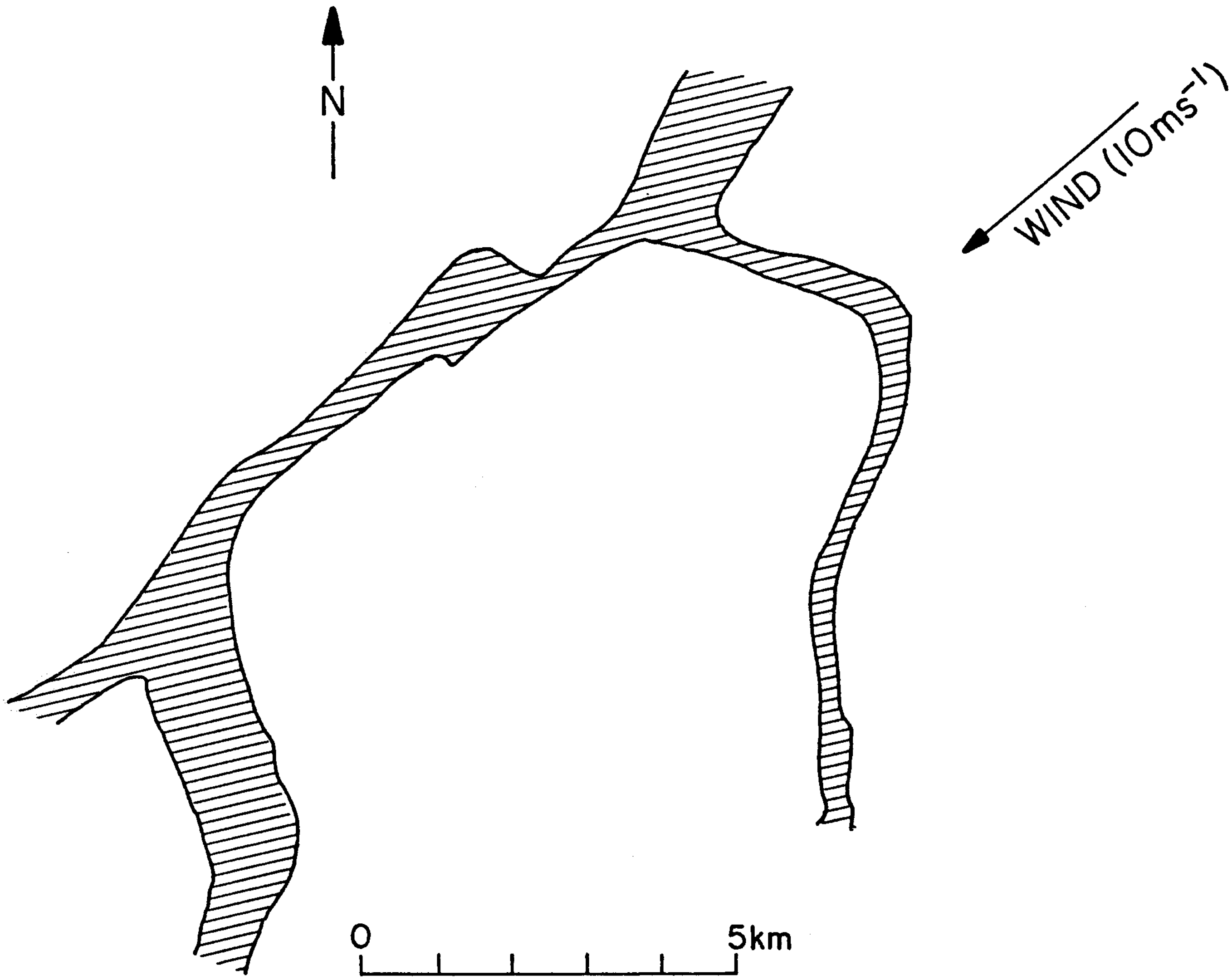

Figure 17. Sketch of ice band made on 11 March 0400 GMT while leaving the ice edge (courtesy Scott Ferguson).

Boyd for typing this manuscript, Scott Ferguson for providing the sketch shown in Figure 17, and Jeral Turay and Kurt Zaverson for the loan of their names. This work was primarily supported by the BLM/NOAA Outer Continental Shelf Program through Contract NA81RAC000-13; we are very grateful for their support. We also acknowledge the support of the Office of Naval Research under Project NR307-252 and Contract N00014-76-C-0234, which supported the radar buoy development and the manuscript preparation. This is contribution No. 0000 of the School of Oceanography, University of Washington.

References

Bauer, B.J. and S. Martin, Field observations of the Bering Sea ice edge properties during March 1979, Mon. Wea. Rev. 108, 2045-2056, 1980.

Hasselman, K. et XV al., Measurements of wind wave growth and swell decay during the Joint North Sea Project (JONSWAP), Herausgegeben vom Deutsch. Hydrograph. Institut., Reihe A, no. 12, 95 pp., 1973.

Longuet-Higgins, M.S., The mean force exerted by waves on floating or submerged bodies with applications to sand bars and wave power machines, Proc. Roy. Soc. Long. A. 352, 463-480, 1977.

McPhee, M.G., The effect of the oceanic boundary layer on the mean drift of pack ice: application of a simple model, J. Phys. Ocean. 9, 388-400, 1979.

McPhee, M.G., Sea ice drag laws and simple boundary layer concepts, Rev. Geophys. and Space Phys. (in press), 1982.

Muench, R.D. and R.L. Charnell, Observations of medium-scale features along the seasonal ice edge in the Bering Sea, J. Phys. Ocean. 7, 602-606, 1977.

Pease, C.H. S.A. Salo, and J.E. Overland, Drag measurements for first-year sea ice over a shallow sea, J. Geophys. Res. (submitted), 1982.

Wadhams, P., A mechanism for the formation of ice edge bands, J. Geophys. Res. (submitted), 1982.

APPENDIX 3:

ON SOME POSSIBLE INTERACTIONS BETWEEN INTERNAL WAVES AND SEA ICE IN THE MARGINAL ICE ZONE

by

Robin D. Muench and Lon E. Hachmeister

Science Applications, Inc.

and

Paul H. LeBlond

Department of Oceanography
University of British Columbia

March 1982

TABLE OF CONTENTS

LIST OF FIGURES

ABSTRACT

The ice edges of the world ocean are generally the site, at times when winds are blowing off the ice, of regularly-spaced surface bands of ice floes. These bands have size scales of order 1-10 km, and their long axes are oriented approximately normal to the wind direction. Available oceanic temperature and salinity data from the Bering and Greenland Sea ice edge regions suggest that these ice bands are commonly underlain by a two-layered density structure which is maintained by net melting along the ice edges. Linear internal wave theory is applied to these data to compute first-mode interfacial wave phase speeds. A simple analytical model is developed which demonstrates the feasibility of generation of such interfacial internal waves by the stress discontinuity due to off-ice winds blowing over either a stationary or a moving ice edge. It is qualitatively shown that the computed internal wave phase speeds and wavelengths are, under many conditions, compatible with the speeds and spacings of the surface ice bands. This compatibility suggests, in turn, that coupling between internal waves and ice bands may commonly occur. Some possible implications of the generation and presence of these internal waves upon other ice edge processes, such as air-sea heat and momentum transfer, are qualitatively discussed.

1. INTRODUCTION

The ice-covered regions of the world ocean provide a surface tracer which both responds to and exerts an influence over the underlying water motion. This tracer, floating sea ice, is active rather than passive because it affects the local air-sea heat and momentum transfers as well as responding to them. These interactions are most pronounced along an ice edge where the ice cover is unbounded to seaward and has considerable freedom to respond to and interact with the local water motions.

This paper discusses possible interactions between interfacial oceanic internal waves and the floating ice "bands" or "streamers" along an ice edge. Additionally, a new hypothesis is advanced for a mechanism for internal wave generation along an ice edge. The internal wave interactions contribute to explaining the initial divergence of ice near the edge prior to its formation into bands and are consistent with the observed features of the bands and of the regional oceanography.

Section 2 below describes the nature of the ice edge bands and the background oceanic density distribution which has been observed to be associated with ice edges. Section 3 presents a theoretical development of some possible interactions between ice and water, including a mechanism for generation of internal waves by wind action over an ice-water interface. Section 4 discusses the degree to which the theoretical model is consistent with the field observations, and also points out some possible implications of the results with respect to overall air-ice-water interactions along an ice edge.

2. BACKGROUND

With the advent of remote sensing techniques and increased scientific and practical interest in the ice edge regions, a variety of mesoscale and small-scale features have been identified along the ice edges. Of these features, the regularly spaced ice "bands" or "streamers" which occur during off-ice local wind events appear to be universal in occurrence. These features have been documented and studied in the Bering Sea along the winter ice edge [Muench and Charnell, 1977; Bauer and Martin, 1980]. They have been documented along the East Greenland Sea ice edge [Wadhams, 1981] and are mentioned by LeBlond [1982] as being evident on satellite imagery of the Labrador Sea winter ice edge. Finally, they have been identified on unpublished satellite images of the Weddell Sea ice edge.

Descriptions of Ice Bands

Descriptions of the ice bands will focus primarily upon those observed in the Bering Sea along the winter ice edge, because the observations from that region are far more complete than those from other regions. A location chart for the Bering Sea shows the location from which data presented here were obtained (Figure 1).

Using satellite imagery, statistics on ice-band spacing for the winter 1974-75 period were compiled by Muench and Charnell [1977]. Examination of satellite imagery for the period between 1975 and the present time has suggested that their observations are valid over the longer time period. They observed a mean band spacing of 8.7 km, with a standard deviation of 1.6 km and a variation between 6 and 12 km. These bands were observed to be roughly normal to the wind direction. Their general appearance is shown on Figure 2.

Shipboard observations obtained more recently than Muench and Charnell's work have revealed bands more closely-spaced along the ice edge than were visible on the satellite images. Resolution of these bands, spaced about 1 km apart, by the satellite was impossible because of the relatively coarse (1 km) resolution of the satellite imagery used. Bauer and Martin [1980], Hachmeister and Muench [1981], Martin and Kauffman [1981] and Martin [this volume] have all reported the widespread presence, during off-ice winds, of these bands spaced about 1 km apart and oriented with their long axes approximately normal to the wind direction. An example of this band configuration obtained from shipboard in March 1981 and reported on by Hachmeister and Muench [1981] is shown in Figure 3. During the transect which yielded the ice distribution shown on Figure 3, the wind was off-ice and steady at about 6 m/sec. The computed mean downwind extent of the open water areas between ice bands was 1 km, and the standard deviation was 0.5 km; mean width of the ice bands was 0.5 km and the standard deviation was 0.3 km.

Translation speeds for the ice bands are harder to estimate because adequate time-series information is not available. Because of the impossibility of tracking the 10-km spaced bands from day to day using satellite imagery, no estimates of these relatively widely-spaced band speeds are available. Speeds of the more closely-spaced bands which were observed from shipboard varied widely [Martin and Kauffman, 1981; Martin, this volume]. At the start of an off-ice wind event, ice speed was near zero at the time when the bands were first separated from the main body of the ice. Speeds then passed through a wide range, with speeds as high as about 70 cm/sec being observed through use of radar-tracked buoys deployed in specific bands to study their motions. In the absence of more rigorous data, speeds of 20-30 cm/sec are considered typical translation speeds for the bands. Band motion was always in the downwind (seaward) direction, and band formation has never been observed during periods of on-ice wind.

Oceanic Parameters Associated with Ice Edges

Ice edge regions are typically areas of melting. This has been documented, based upon ice distribution and motion, for the Bering Sea by Muench and Ahlnäs [1976] and Pease [1980]. This observation has been supported more recently by oceanic temperature and salinity data [Muench and Pease, 1981; Muench, this volume]. Wadhams [1981] has characterized the East Greenland Sea ice edge as a region of ice melting. A. Gordon [personal communication, 1981] has characterized the Weddell Sea ice edge also as a region of net melting.

A primary effect of ice melting along the edge is to create a strongly two-layered salinity -- hence, density -- structure. The vertical distribution of density underlying the Bering Sea ice edge region in February-March 1981, about mid-winter or during the time of maximum southward ice extent reflects this and is shown on Figure 4. The location of this density transect coincides approximately with that of the ice-band transect illustrated on Figure 3; hence, the density distribution shown was that which underlies the banded structure. Density differences of 0.01-0.3 sigma-t units over a 10-20 m layer were typical, and the interface depth varied from about 30 to 60 m. The two-layered density structure appears to be a regular winter oceanic feature associated with the Bering Sea winter ice edge [Muench and Pease, 1981; Muench, this volume]. A set of vertical density profiles, obtained at different times from a single location along the Bering Sea ice edge in February-March 1981, illustrates a range of stratifications which appears to be typical for the region (Figure 5).

Vertical density stratification in the Greenland Sea ice edge region is greater, at least during summer, than in the Bering Sea. A vertical profile of density in the Greenland Sea ice edge region during summer is shown on Figure 6. The interface between upper and lower layers is extremely strong and sharp.

A second basic difference between the Bering and Greenland Sea ice edge regions, in addition to the degree of stratification, is that between the characteristic bottom depths. Depths underlying the Bering Sea ice edge are typically 80-110 m. Beneath the Greenland Sea ice edge, on the other hand, the bottom falls on the continental slope so that depths vary from 500 to 1000 m and more to seaward.

3. PROPOSED MECHANISM FOR BAND FORMATION AND MAINTENANCE

The mechanisms which form and maintain the ice edge bands are not well understood. Muench and Charnell [1977] hypothesized, based upon analyses of satellite imagery of the Bering Sea winter ice edge, that the larger-scale (10-km wide) bands were due to interactions between sea ice at the edge and the atmospheric roll vortices which are ubiquitous along the edge during off-ice wind conditions [Walter, 1980]. Bauer and Martin [1980] used results from a 1979 mid-winter field program along the Bering Sea ice edge to hypothesize that band formation was due to a combination of wind stress acting differentially upon the rougher ice along the edge so that a line of ice divergence formed along the edge parallel to it, and radiation stress (due to surface water waves generated in the leads between the bands) which would tend to accelerate the bands away from the main ice pack. Overland and Pease [this volume] present additional evidence that the initial divergence of ice along the edge may be due to wind drag, with accentuation of the divergence through a "sea-breeze" effect. Further arguments in favor of radiation stress as a causative mechanism for the divergence are presented by Wadhams [this volume]. Finally, Hachmeister and Muench [1981] hypothesized, based upon laboratory model results and field data, that the ice edge bands coincide with surface convergences which are associated with interfacial internal waves beneath the ice edge. They maintained, in addition, that formation of the interfacial waves is due either to interaction of ice keels (in regions where the ice is thick enough to have a ridged structure) with the oceanic stratification or to response of the stratified ocean to a nonuniform wind stress where the nonuniformity is due to the surface presence of the ice edge.

Of the mechanisms for ice band formation listed above, only that involving interaction with internal waves provides a satisfactory explanation for the observed regular spacing of the bands. This paper explores some possible interactions between ice edge bands and oceanic internal waves in more detail, with the intention of clarifying the dynamic processes involved and demonstrating compatibility between the observed ice features and internal waves.

The development presented here follows two avenues of approach. First, linearized theory is used to estimate ranges for the first-mode interfacial internal-wave phase speeds appropriate to the density differences observed in the Bering and Greenland sea ice edge regions. Second, an analytical solution is derived for the generation of internal waves by a wind stress acting across the surface discontinuity presented by an ice edge.

Estimation of Representative Interfacial Wave Phase Speeds

In the simplest physical sense, the oceanic regimes underlying the Bering and Greenland Sea ice edges may be considered as two-layered systems separated by a horizontal density interface. In order to establish ranges for parameters to be used in the following analytical development, and also as a prelude to establishing compatibility between internal wave and ice band parameters, it is useful to compute representative values of interfacial internal-wave phase speeds which might be expected given the oceanic conditions observed in association with ice edges. The upper- and lower-layer densities, interface depth, and bottom depths used in the computations include the ranges which we would expect, based upon available data, to occur in the Bering or Greenland Sea ice edge regions (see, for example, Figures 4-6).

The computations used for arriving at the first-mode interfacial wave speeds are based upon a two-layered fluid model given in Turner [1973]. The basic equation for the phase speed c is

$$c^2 = \frac{g\Delta\rho}{k} (\rho_1 \coth kh_1 + \rho_2 \coth kh_2)^{-1} \qquad (1)$$

where h_1 = upper layer thickness, h_2 = lower layer thickness, ρ_1 = upper layer density, ρ_2 = lower layer density, and $\Delta\rho$ = density difference between layers. In the shallow-water long-wave case appropriate to the Bering Sea ice edge region, kh_1 and kh_2 both approach zero and Equation (1) can be approximated by

$$c^2 = \frac{g\Delta\rho}{\rho_2} \frac{h_1 h_2}{(h_1 + h_2)} .$$

For waves which are at least as long as the lower layer depth, this approximation is also appropriate to the Greenland Sea ice edge region; now, since $h_2 >> h_1$, Equation (1) becomes, for the Greenland Sea,

$$c^2 = \frac{g\Delta\rho}{\rho_2} h_1 .$$

Table 1 gives the computed values for c using varying upper layer thicknesses and density differences between the layers.

The above computations assumed small-amplitude waves, allowing use of linear theory. Even if the waves were of large enough amplitude to violate this assumption, the results would not be greatly different. Holyer [1979] has demonstrated, using theoretical arguments, that at the largest amplitudes the phase speeds of long waves are only about 20% higher than those for infinitesimal waves. Given the approximate nature of the estimated band speeds presented above, a 20% error in computed wave phase speeds would not substantially alter the conclusions which are presented below.

A Mechanism for Wind-Generation of Internal Waves

A theoretical development is presented here of a mechanism for generation at an ice edge of internal waves by the nonuniform wind stress due to off-ice winds. This proposed mechanism is schematically illustrated on Figure 7. It is assumed, in concert with observations, that the wind is blowing in the off-ice direction and that the ice edge is underlain by an oceanic structure two-layered in density. Location "A" on Figure 7 indicates the region where divergence in the ice cover first occurs. In a region referred to on the figure as the "generation" region, the wind blowing off-ice either across a band or off the main mass of ice causes a localized upwelling tendency due to surface divergence. This is illustrated by the upward-bulging of the interface in the middle of the generation region. This bulge will then propagate in both directions, as shown, as trains of interfacial waves. Point "B" signifies the boundary between the generation region and the propagation region through which the ensuing internal wave train moves. Those waves travelling in the off-ice direction at phase speed c will tend to collect floating ice in the convergences overlying the wave troughs, as shown. Waves travelling in the opposite direction, beneath the ice edge, might contribute to surface divergence of the ice pack there.

Internal wave generation at the seaward edge of a moving ice cover may be analyzed in a simple model. The vertical density distribution is approximated in terms of a two-layered structure with linear phase speed c as estimated above. With x measured positively from the uniformly moving (at speed V) ice edge and y along it, two-dimensional ($\partial_y = 0$) perturbations of the stratified fluid from its equilibrium state are governed by the long-wave equations

$$\frac{\partial u_1}{\partial t} - V\frac{\partial u_1}{\partial x} - fv_1 = -g\frac{\partial \eta}{\partial x} + \frac{\tau}{\rho_1 h_1} \tag{2a}$$

$$\frac{\partial v_1}{\partial t} - V\frac{\partial u_1}{\partial x} + fu_1 = 0 \tag{2b}$$

$$h_1\frac{\partial u_1}{\partial x} = -\left(\frac{\partial}{\partial t} - V\frac{\partial}{\partial x}\right)(\eta - \zeta) \simeq \left(\frac{\partial}{\partial t} - V\frac{\partial}{\partial x}\right)\zeta \tag{2c}$$

$$\frac{\partial u_2}{\partial t} - V\frac{\partial u_2}{\partial x} - fv_2 = -g\frac{\rho_1}{\rho_2}\frac{\partial \eta}{\partial x} - g\frac{\Delta\rho}{\rho_2}\frac{\partial \zeta}{\partial x} \tag{3a}$$

$$\frac{\partial u_2}{\partial t} - V\frac{\partial u_2}{\partial x} + fu_2 = 0 \tag{3b}$$

$$h_2\frac{\partial u_2}{\partial x} = -\left(\frac{\partial}{\partial t} - V\frac{\partial}{\partial x}\right)\zeta \ . \tag{3c}$$

Subscripts 1 and 2 refer to the upper and lower layers, respectively. The surface displacement η is assumed of order $\zeta\Delta\rho/\rho_2$ and neglected, as appropriate for internal waves. The stress τ changes value at the ice edge (x=0). For $x < 0$, the surface stress is applied to the water as $\tau_- = \rho_1 c_w(V-u_1)^2$ with c_w the ice-water drag coefficient; for $x > 0$, the wind stress is exerted directly on the water surface, i.e. $\tau_+ = \rho_{air}c_D(U-u_1)^2$, with c_D the air-water drag coefficient and U the wind speed. This discontinuity in stress generates the internal waves.

Eliminating all variables but ζ from (2) and (3), we find

$$\zeta_{tt} - 2V\zeta_{xt} - (c^2 - V^2)\zeta_{xx} + f^2\zeta = \frac{c^2}{\rho_1 h_1}\tau_x \ , \tag{4}$$

where c is the long-wave speed, i.e. $c^2 = g(\Delta\rho/\rho_2)[h_1h_2/(h_1+h_2)]$. Free-plane wave solutions of the homogeneous form of Equation (4) are shortened when they travel against V, i.e. in the +x direction, and lengthened when they travel under the ice away from the edge in the -x direction. Near resonance ($V \simeq c$) the wavelength ahead of the ice becomes

$$\lambda \simeq \frac{\pi c}{\omega}\left(1 - \frac{V^2}{c^2}\right) \ . \tag{5}$$

Measured seaward ice speeds V are comparable to the calculated internal wave speeds c, so that even for rather long-period forcing ($T = 2\pi/\omega \sim 1$ day, as for sea-breeze winds, for example) λ can approach the observed ice band spacing near resonance. The alternation on a scale λ of surface flow divergence and convergence, as given by $\partial u_1/\partial_x$, would then contribute to the sum of forces (wind, waves) which determine ice band spacing.

As a more specific extension of the above case, we may consider the forced initial value case wherein internal waves are produced from rest by a wind stress of the form

$$\tau = F(t)[\tau_o + \Delta\tau\, H(x)] \ , \tag{6}$$

where H(x) is the Heaviside step function, $\Delta\tau$ is the stress discontinuity across $x = 0$, and F(t) describes the time-dependence of the stress with $F(0) = 0$. Taking the Laplace transform of Equation (4) ($\partial_t \rightarrow P$) and applying the matching conditions

$$\lim_{x\to 0} \bar{\zeta}(x < 0) = \lim_{x\to 0} \bar{\zeta}(x > 0) \tag{7a}$$

$$\left(1 - \frac{V^2}{c^2}\right) \left[\lim_{x\to 0} \bar{\zeta}_x\ (x > 0) - \lim_{x\to 0} \bar{\zeta}_x\ (x < 0)\right] = -\frac{\bar{F}(P)\Delta\tau}{\rho_1 h_1} \tag{7b}$$

across $x = 0$ on the transformed variables (denoted by overbars), we find that

$$\bar{\zeta}_{\pm}(x,P) = \frac{c\Delta\tau\ \bar{F}(P)}{2\rho_1 h_1 \left[P^2 + \left(1 - \frac{V^2}{c^2}\right) f^2\right]^{1/2}} \exp\left\{\frac{-VPx}{(c^2 - V^2)} - \left[P^2 + \left(1 - \frac{V^2}{c^2}\right)f^2\right]^{1/2} \frac{|x|}{c}\right\}. \tag{8}$$

The surface layer divergence is obtained from (2c) as

$$h_1\bar{u}_{1_x} = \frac{c\Delta\tau\ \bar{F}(P)}{2\rho_1 h_1}\left(\frac{c^2 P/(c^2 - V^2)}{\left[P^2 + (1 - \frac{V^2}{c^2})\ f^2\right]^{1/2}} \pm \frac{V}{c}\right)\ \exp\left\{\ldots\right\}\ . \tag{9}$$

The argument of the exponential in Equation (9) is the same as in Equation (8) and is not repeated. Near resonance, $V \to c$ and the first term in Equation (9) will dominate for $P^2/(1-\frac{V^2}{c^2})f^2 \simeq O(1)$. For a step-function wind stress, $\bar{F}(P) = 1/P$, and a tabulated inverse is found for $h_1\bar{u}_{1_x}$ [Abramowitz and Stegun, 1965, Ch. 29],

$$h_1 u_{1_x}(x,t) = \frac{c\Delta\tau}{2\rho_1 h_1 (1 - \frac{V^2}{c^2})}\ J_o\left((1 - \frac{V^2}{c^2})^{1/2}\ f\sqrt{\left(t - \frac{|x|V}{c^2 - V^2}\right)^2 - \frac{x^2}{c^2}}\right) H\left(t - \frac{|x|V}{(c^2V^2)} - \frac{|x|}{c}\right) \tag{10}$$

As we would expect, the response becomes singular at resonance, i.e. as soon as the ice field velocity approaches the internal wave speed, a strong pattern of surface divergence is set up with spatial dependence given by Equation (10) for an impulsive wind stress or by the convolution of Equation (10) with the appropriate transform for a different stress history. The position of the first zero of the Bessel function gives an estimate of the scale from the ice edge to the first zone of maximum divergence (or convergence, depending on the sign of $\Delta\tau$). For $x > 0$, this first zero occurs at

$$\left(t - \frac{xV}{c^2 - V^2}\right)^2 = \frac{3.8}{f^2(1 - \frac{V^2}{c^2})} + \frac{x^2}{c^2}\ . \tag{11}$$

The scale length of the Bessel function decreases as its argument, which is roughly proportional to t, increases. We then seek to know, using Equation (11), whether a scale $x \sim 10^3$ m which is of the order of the observed band spacing can arise in a reasonable value of the time elapsed since the wind began to blow. With $x \simeq 10^3$ m, $c \simeq 50$ cm/sec, and $V \simeq 0.9\ c$, then $t \simeq 5 \times 10^4$ sec $\simeq 0.5$ day, which is short enough to respond to a diurnal sea-breeze type of forcing.

4. DISCUSSION

The field data available from the Bering and Greenland Sea ice edge regions have been obtained for use primarily in analyses of mesoscale processes. Consequently, the spatial and temporal resolutions of these data make them inadequate to rigorously determine whether internal wave mechanisms such as discussed above (Section 3) are in fact significant in those regions. Nevertheless, reference to the computed first-mode internal wave speeds c presented in Table 1 reveals that ice speeds of up to about 35 cm/sec would be compatible with the internal wave phase speeds computed using the stratification observed along the Bering Sea ice edge. Computed first-mode internal wave speeds for the Greenland Sea ice edge are higher than those for the Bering (Table 1). We therefore expect that interfacial waves along the Greenland Sea ice edge would have a much greater range of propagation speeds than in the Bering. While no data are available on ice band motion along the Greenland Sea ice edge, it seems reasonable that the speeds of these bands would tend to fall within the range of possible speeds shown in Table 1 and that their interaction with internal waves would be consistent with physical reasoning. This supposition is supported by the consistency between computed internal wavelength λ and observed ice band spacing.

A single time series of current and temperature, obtained from the Bering Sea winter ice edge region, revealed oceanic features which are consistent with the presence of internal waves. This record was obtained at 50-m depth and was sampled at 30-minute intervals (Figure 8). During the January-February 1981 period, the interface between the upper and lower oceanic layers beneath the ice edge (see Figure 4) moved toward the south-southwest past this mooring as the ice cover advanced toward its annual maximum southward extent. Temperature variations coincide with density variations because the upper lower-density layer is colder than the denser lower layer [Muench, this volume]. The temperature record from the mooring revealed rapid (i.e. of the same order as or having shorter period than the 30-minute sampling intervals of the instruments) temperature fluctuations while the density/temperature interface was passing by the current meters (Figure 8). Current speed fluctuations were present at the same time. The maximum recorded temperatures, which occurred early in the portion of the record shown and were about +1.3 °C, were those in the warmer lower layer of water. The minimum temperature (-1.7 °C), which occurred later in the record segment shown on Figure 8, was typical of the colder upper-layer water. The lower- and upper-layer water temperatures therefore provided an "envelope" of maximum and minimum temperatures. Presence of the fluctuations between these maximum and minimum values, superposed upon the overall trend toward lower temperature as the current meter was surrounded by the colder upper-layer water, suggest that vertical oscillations of the interface between the upper and lower layers were occurring. These oscillations were sufficient to vertically move the entire temperature gradient region past the current meter. Reference to the profiles shown on Figure 5 suggests that vertical oscillations of 10-20 m amplitude would have been necessary to achieve this.

High-frequency oscillations in current speed were also present. They were superposed upon a tidal current signal and were less obvious than the corresponding temperature oscillations. Because of the relatively widely-spaced sampling interval (30 minutes), it was not possible to examine phase relations between the current and temperature fluctuations in the frequency range of interest. Visual inspection of the current fluctuations shown on Figure 8 suggests that peak associated speeds were about 5 cm/sec.

Although these data are clearly inadequate for a rigorous analysis, they nevertheless demonstrate that vertical motions of the interface between layers were present and had time scales of about 30 minutes. Such time scales would be consistent with interfacial waves phase-locked with surface ice bands.

In addition to providing a physically satisfying explanation for one of the more widespread medium-scale ice edge features, the results presented above can be expected to have significant consequences for other ice-edge processes. A major factor would be the additional "form drag" term due to interaction of the ice bands with the internal waves. This term must be considered when using observed winds, ice speeds, and oceanic currents to compute the air-sea-ice momentum transfer. Sea ice moves across the ocean surface under the influence of both internal stresses in the ice and coupling with the wind and upper layers of the ocean. Coupling between ice and ocean affects both ice motion and the dynamics of the upper ocean layer, and more than one such coupling mechanism exists between the ice and ocean. In the absence of oceanic stratification, drag forces between the ice and the water result from a combination of skin friction (applied over the entire underside of the ice) and form drag exerted by irregularities on the lower side of the ice cover. In a stratified fluid an additional coupling mechanism exists: as demonstrated by Ekman [1906], internal waves generated by a large obstacle can contribute a significant wave resistance to the total drag on an obstacle moving in a stratified fluid. Hachmeister and Rigby [1980] modeled this mechanism in a laboratory tow tank and detected drag increases of nearly 150% due to the internal wave-sea ice coupling. The internal wave/ice band interactions suggested here would tend to limit the off-ice translation speed of ice bands to the internal-wave phase speed. Since the rate of ice melting at the edge is dependent to some extent on the ambient water temperature, and the water temperature increases away from the ice edge, the speed with which the bands move into warmer water is critical to estimation of melting rates. The results of this investigation therefore impact on both air-sea-ice momentum transfer and the melting rates of ice along the edge.

Finally, the internal waves generated by a stress discontinuity at the ice edge set up surface layer divergence bands behind as well as ahead of the ice edge and contribute to opening up of leads as well as to compacting of ice bands ahead of the ice edge. Of course, as soon as the original ice edge becomes accompanied both fore and aft by other ice edges, the simple conditions of the above analysis no longer prevail. For example, surface wave radiation stress would then tend to compact the ice bands from the rear and accelerate them to seaward. However, the above arguments should be sufficient to demonstrate that coupling between ice bands and internal waves is possible on the scales observed in nature.

Rigorous testing of the hypotheses presented above awaits the acquisition of new field and laboratory data. It is hoped that the current growing interest in marginal ice zone problems will enable such a testing program to be carried out.

5. ACKNOWLEDGEMENTS

The satellite image used in the manuscript was kindly supplied by Dr. Seelye Martin of the University of Washington. This work has been funded by the Office of Arctic Programs, Office of Naval Research, under contract N00014-82-C-0064 and by the Bureau of Land Management through interagency agreement with the National Oceanic and Atmospheric Administration, under which a multi-year program responding to needs of petroleum development of the Alaskan continental shelf is managed by the Outer Continental Shelf Environmental Assessment Program (OCSEAP) office.

REFERENCES

Abramowitz, M., and I. Stegun, Handbook of Mathematical Functions, Dover, New York, 1965.

Bauer, J., and S. Martin, Field observations of the Bering Sea ice edge properties during March 1979, Mo. Wea. Rev., 108, 2045-2056, 1980.

Ekman, V.M., On dead-water, in The Norwegian North-Polar Expedition, 1893-96, Scientific Results, Vol. 5 (ed., F. Nansen), Christiana, Norway, 1-152, 1906.

Hachmeister, L.E., and F.A. Rigby, Laboratory studies of stratified flow interaction with topography, Proc. Second IAHR Symp. on Strat. Flows, Vol. II, Trondheim, Norway, 623-635, 1980.

Hachmeister, L.E., and R.D. Muench, Interactions between internal waves and ice bands in the marginal ice zone, Eos, 62, 895, 1981.

Holyer, J.Y., Large amplitude progressive interfacial waves, J. Fluid Mech., 93, 433-448, 1979.

LeBlond, P.H., Satellite observations of Labrador Current undulations, Atmos.-Ocean., in press, 1982.

Martin, S., The movement and decay of ice edge bands in the winter Bering Sea, J. Geophys. Res., this volume.

Martin, S., and P. Kauffman, The movement and decay of ice edge bands in the winter Bering Sea, Eos, 62, 895, 1981.

Muench, R.D., Some circulation and hydrographic features associated with the Bering Sea ice edge region, J. Geophys. Res., this volume.

Muench, R.D., and K. Ahlnäs, Ice movement and distribution in the Bering Sea from March to June 1974, J. Geophys. Res., 81, 4467-4476, 1976.

Muench, R.D., and R.L. Charnell, Observations of medium-scale features along the seasonal ice edge in the Bering Sea, J. Phys. Oceanogr., 7, 602-606, 1977.

Muench, R.D., and C.H. Pease, Mid-winter interactions between a two-layered hydrographic structure and the ice edge on the central Bering Sea shelf, Eos, 62, 890, 1981.

Overland, J.E., and C.H. Pease, Local acceleration of the wind as a mechanism for divergence in the marginal ice zone, J. Geophys. Res., this volume.

Pease, C.H., Eastern Bering Sea ice processes, Mo. Wea. Rev., 108, 2015-2023, 1980.

Turner, J.S., Buoyancy Effects in Fluids, Cambridge Univ. Press, Cambridge, England, 1973.

Wadhams, P., The ice cover in the Greenland and Norwegian seas, Rev. Geophys. and Space Phys., 19, 345-393, 1981.

Wadhams, P., A mechanism for formation of ice edge bands, J. Geophys. Res., this volume.

Walter, B.A., Wintertime observations of roll clouds over the Bering Sea, Mo. Wea. Rev., 108, 2024-2031, 1980.

Table 1. Computed first-mode internal wave speed c in cm/sec for the Bering Sea and Greenland Sea cases. $\Delta\rho$ is the density difference in g/cm^3 across the interface between the upper and lower layers; h is the depth of the interface in meters.

CASE	$\Delta\rho \rightarrow$ / h $\downarrow$	0.00010	0.00025	0.00050	0.00100	0.00500
Bering Sea						
(bottom depth ∿ 100 m)	25	14	22	30	42	96
	50	16	26	36	51	114
	75	15	24	34	48	107
E. Greenland Sea						
(bottom depth > 1000 m)	25	15	24	35	49	109
	50	22	35	49	69	155
	75	27	42	60	85	189

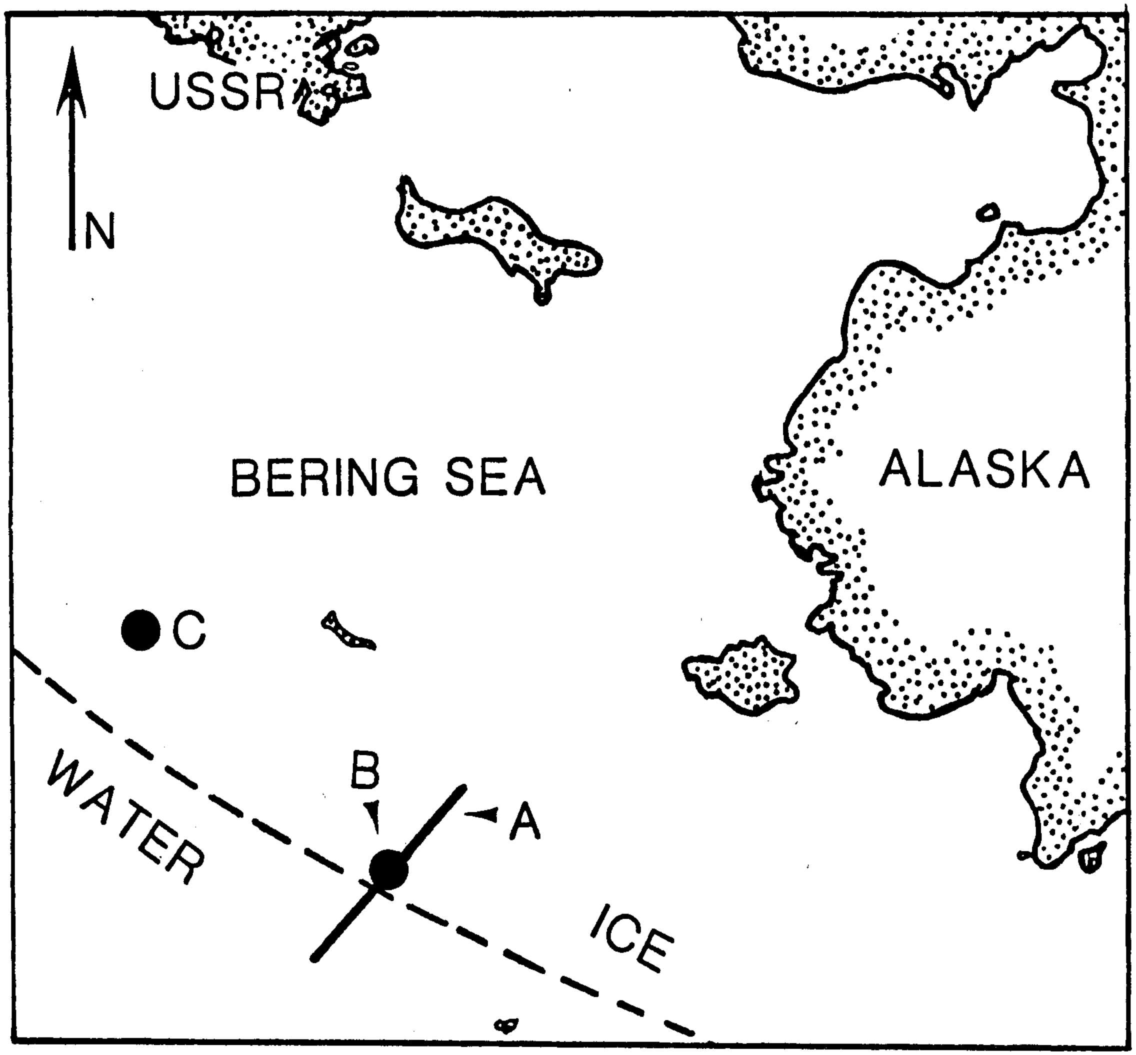

Figure 1. Location figure for data shown which were obtained from the Bering Sea ice edge region. Letter designations "A", "B" and "C" are explained in the appropriate figure legends.

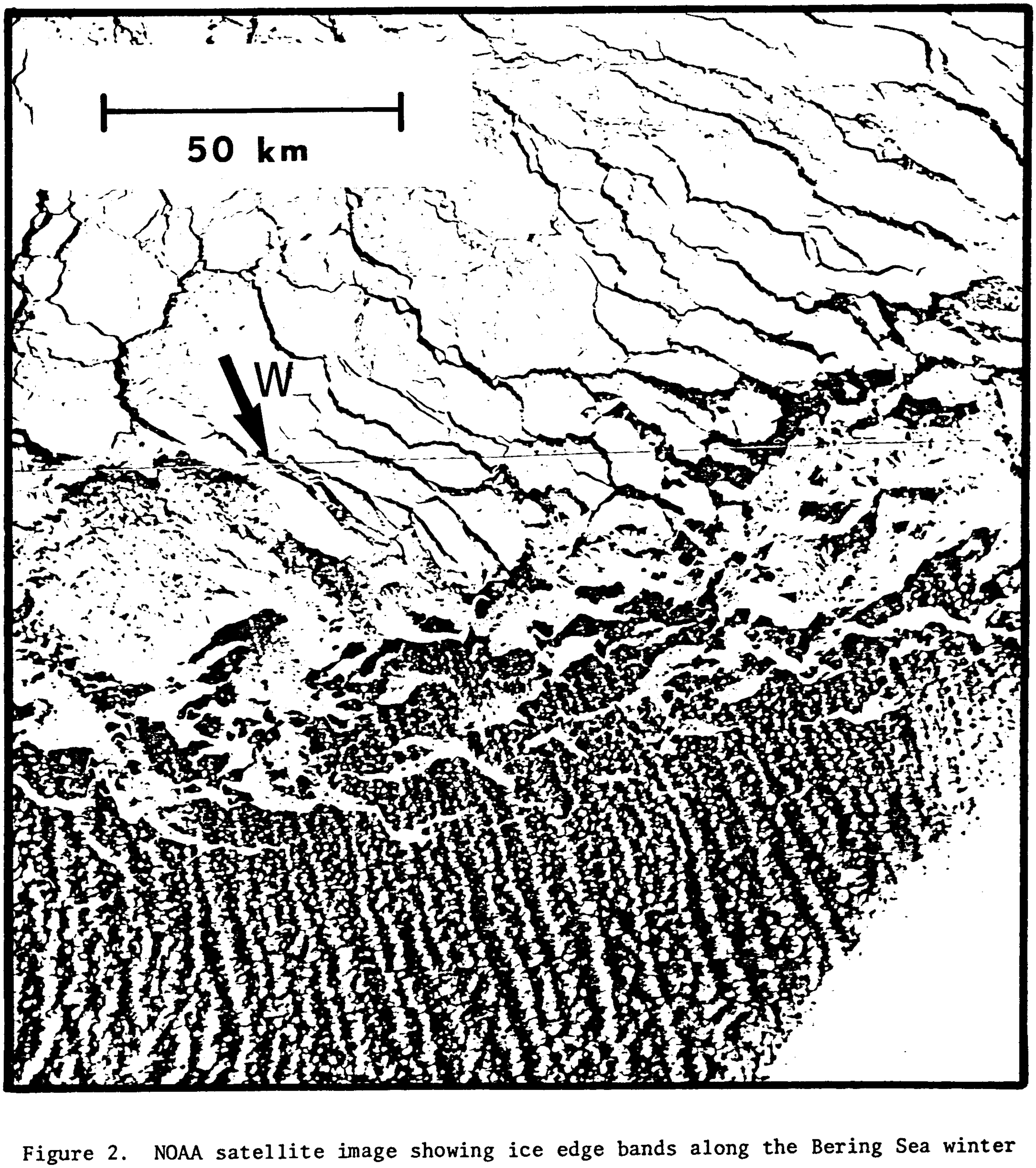

Figure 2. NOAA satellite image showing ice edge bands along the Bering Sea winter ice edge. Arrow "W" indicates approximate wind direction.

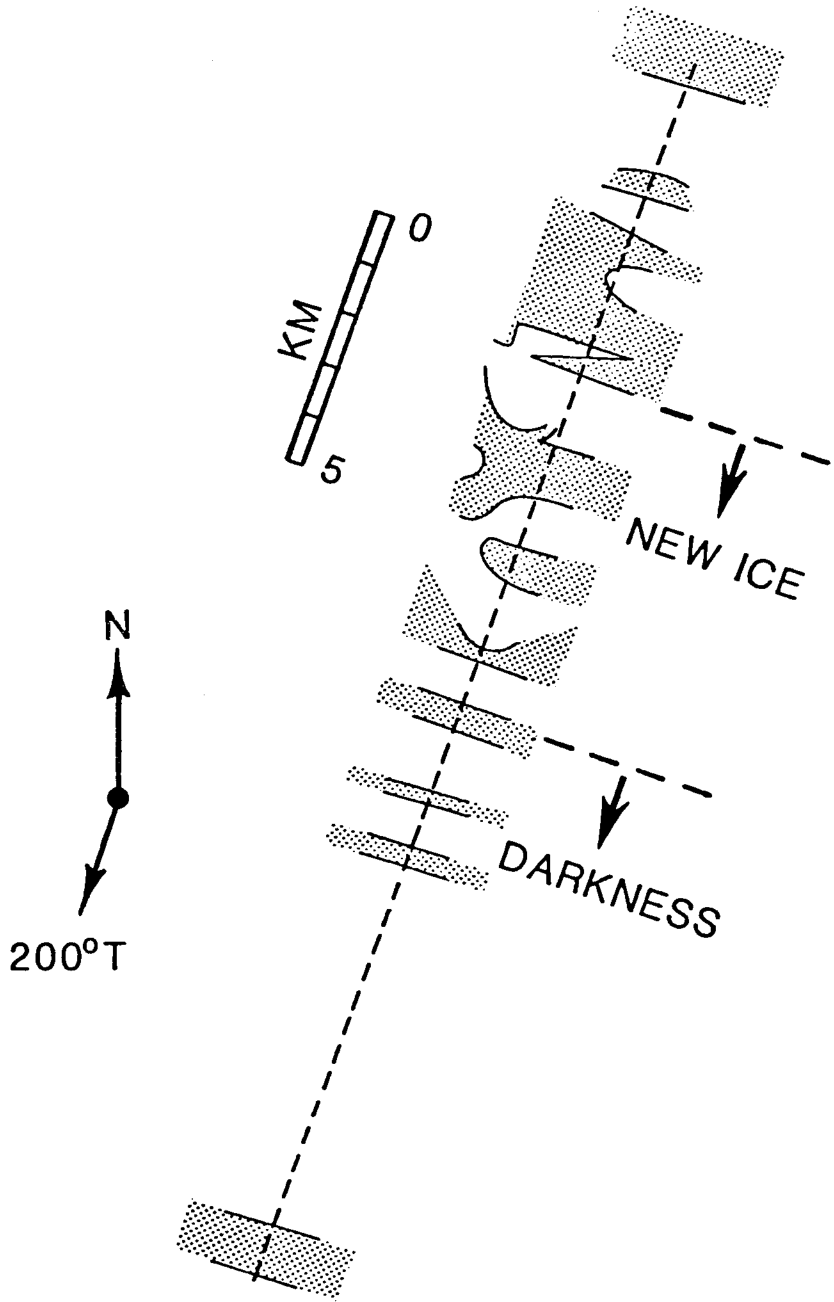

Figure 3. Schematic of ice bands along the Bering Sea ice edge late on 7 March 1981. Observations were obtained from a surface vessel traveling toward 200 °T along the dashed line. South of the border "new ice", no rafting or ridging was evident and most ice appeared to be only a few days old. After dark it became impossible to discern details of the ice. The wind was steady at about 6 m/sec toward 200 °T throughout the transect. Approximate location of transect is shown as southern part of line "A" on Figure 1.

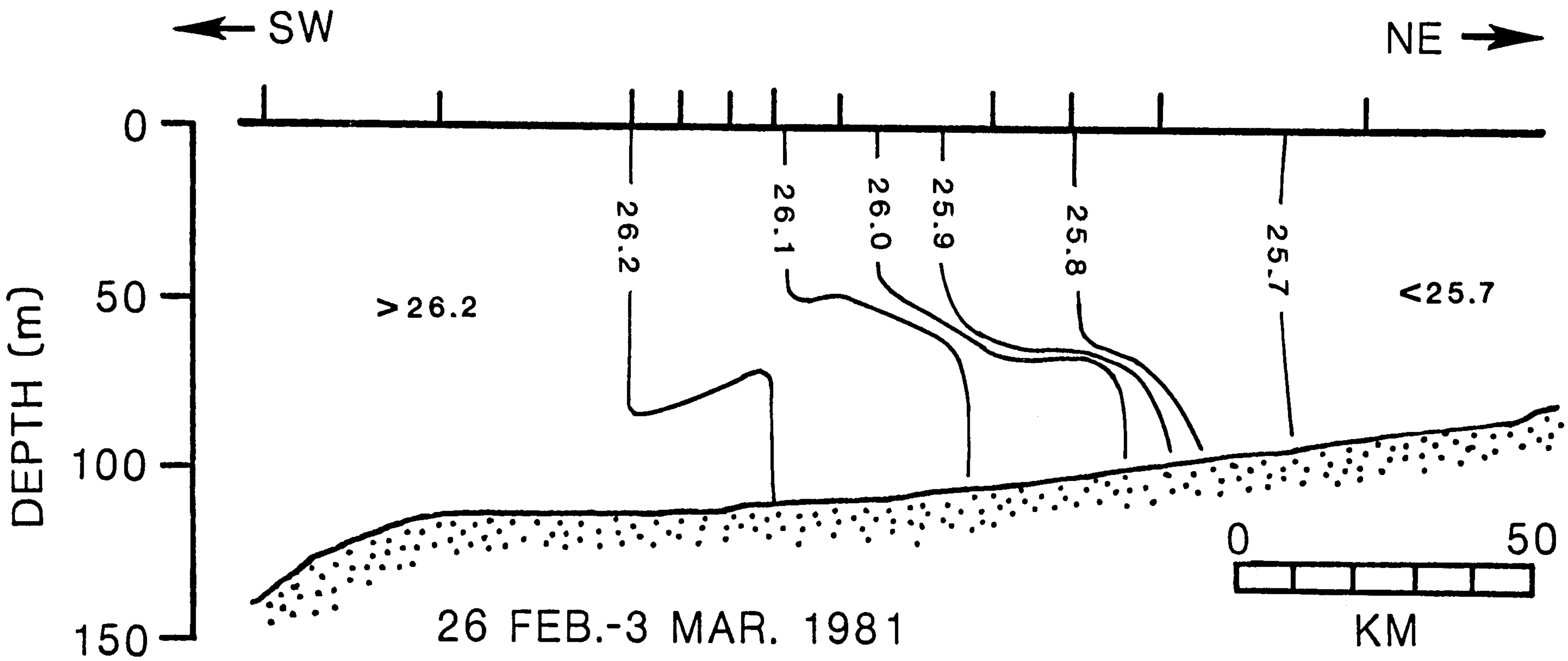

Figure 4. Vertical distribution of density (as sigma-t) along a transect across the Bering Sea ice edge in mid-winter 1981. Approximate location of transect is shown as line "A" on Figure 1.

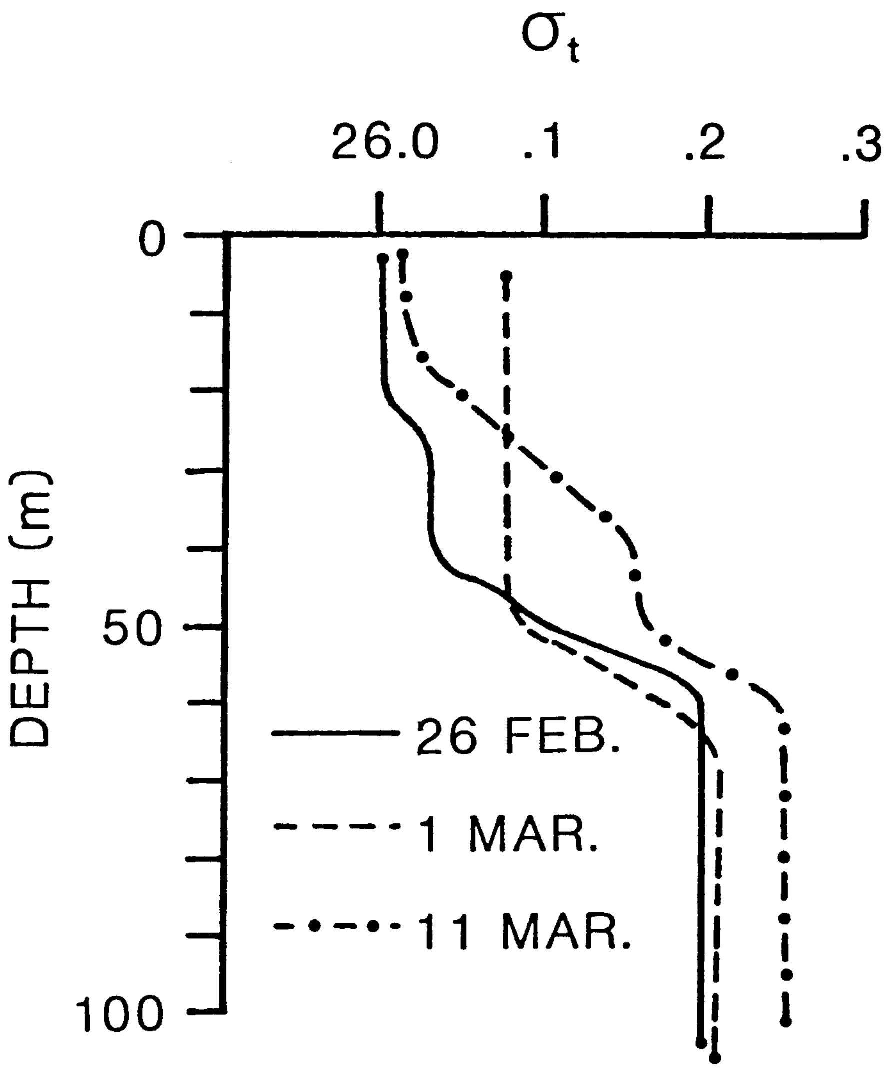

Figure 5. Illustration of variability in vertical density (as sigma-t) distribution at a single position near the Bering Sea ice edge over a 14-day period in mid-winter 1981. Bottom depth was 109 m. Approximate location of station is shown as point "B" on Figure 1.

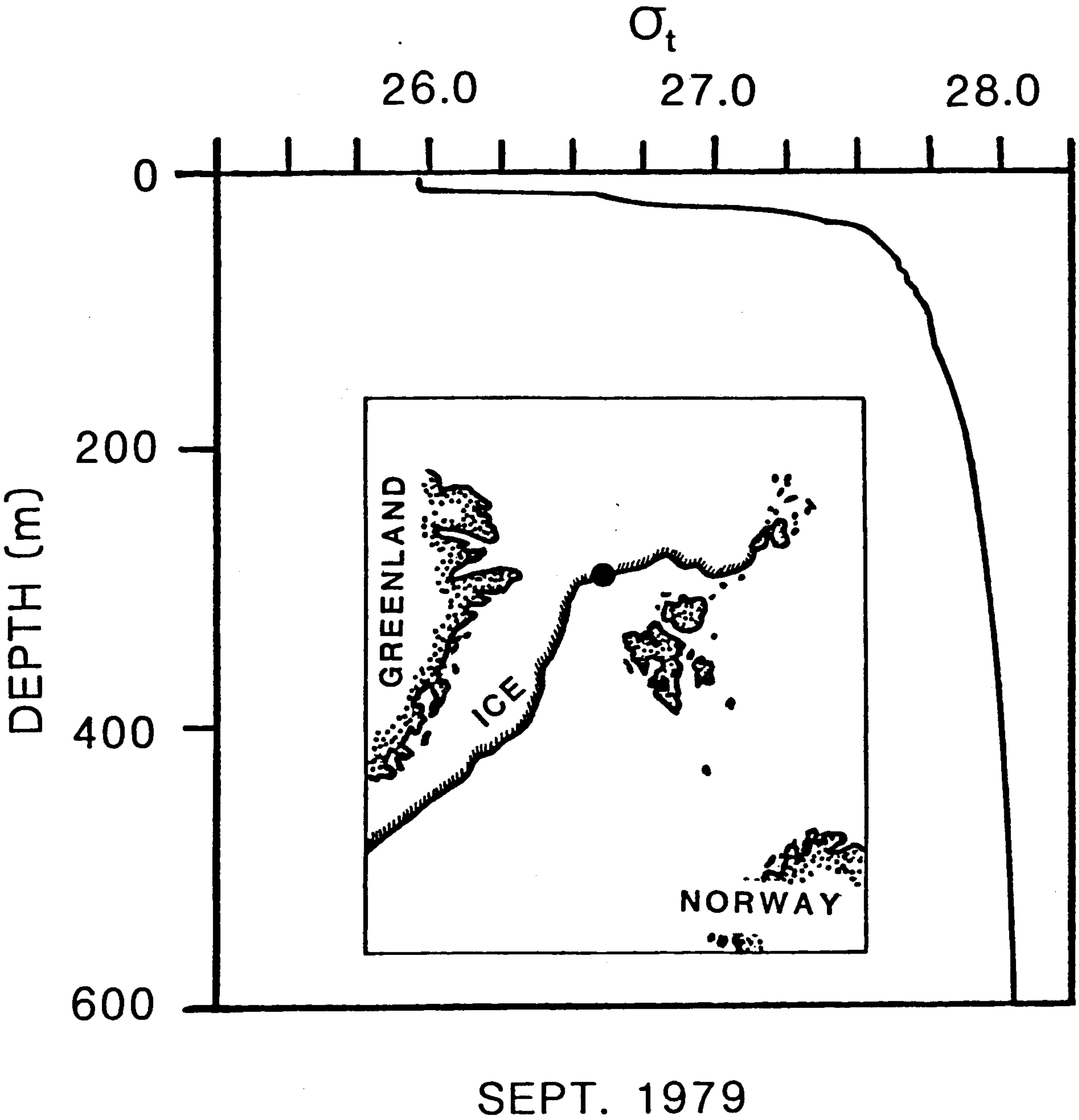

Figure 6. Example of vertical density (as sigma-t) distribution at a location near the Greenland Sea ice edge in late summer 1979. Bottom depth was greater than 700 m. Inset map shows approximate location of station.

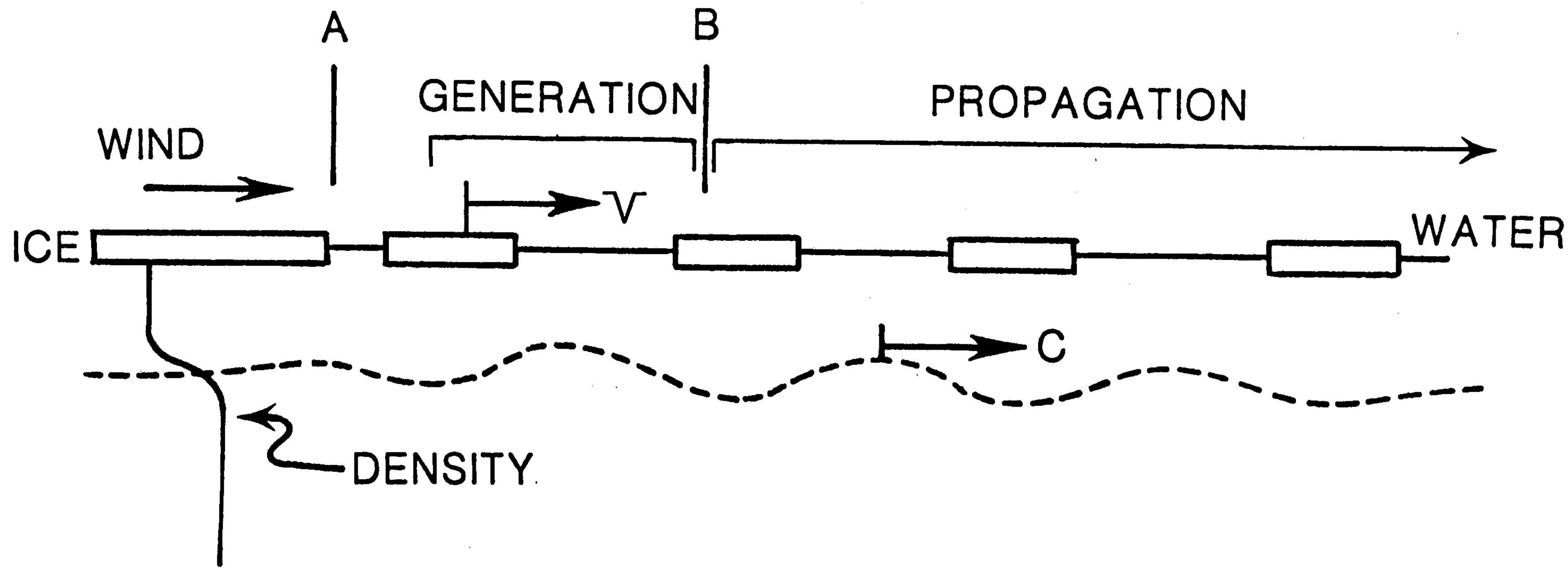

Figure 7. Schematic diagram illustrating the conceptual model discussed in the text.

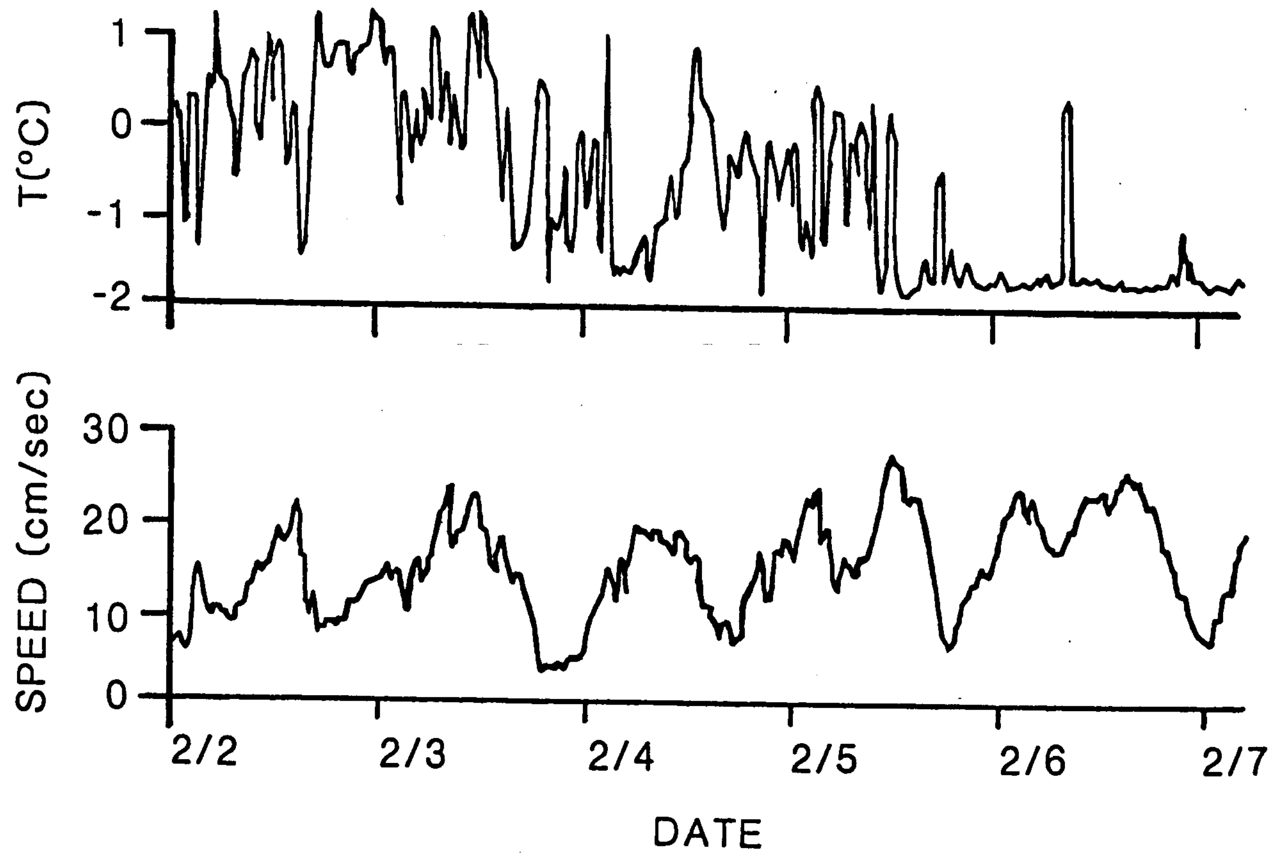

Figure 8. Time-series of temperature (upper) and current speed (lower) obtained in the density interface at 50-m depth below the Bering Sea ice edge in early February 1981. Approximate location of mooring from which data were obtained is shown as point "C" on Figure 1.

APPENDIX 4:

THE BERING SEA ICE COVER DURING MARCH 1979: COMPARISON OF SURFACE AND SATELLITE DATA WITH THE NIMBUS-7 SMMR

by

Seelye Martin and S. Lyn McNutt

School of Oceanography
University of Washington

and

Donald J. Cavalieri and Per Gloersen

NASA/Goddard Space Flight Center

January 1982

TABLE OF CONTENTS

1. INTRODUCTION

During March 1979, field operations were carried out in the Marginal Ice Zone (MIZ) of the Bering Sea. The field measurements which included oceanographic, meteorological, and sea ice observations were made nearly coincident with a number of Nimbus-7 and Tiros-N satellite observations.

This report presents the results of a comparison between surface and aircraft observations, and images from the Tiros-N satellite, with ice concentrations derived from the microwave radiances of the Nimbus-7 Scanning Multichannel Microwave Radiometer (SMMR). Following a brief discussion of the field operations, including a summary of the meteorological conditions during the experiment, we describe the satellite data with emphasis on the Nimbus-7 SMMR and the physical basis of the algorithm used to retrieve ice concentrations. We then carry out a detailed comparison for four days in March of the SMMR imagery with all available surface, satellite, and meteorological data. The results of this study show that the SMMR-derived ice concentrations provide nearly all-weather information on both the ice edge position and the location of low and high ice concentrations within the Bering Sea pack ice.

2. SUPPORT OBSERVATIONS

The present section describes the surface, aircraft, weather, and satellite data used for comparison with the results of the SMMR algorithm. Specifically, §2.1 summarizes the data sources and §2.2 gives an overview of the weather and the general ice behavior. Then, because the Bering Sea ice edge is not an abrupt transition from open ocean to solid ice, but rather a gradual transition which affects the SMMR ice edge resolution, §2.3 gives a physical description of the ice edge. Next, §2.4 describes the Tiros images, and the way in which we prepared the ice charts from these images. Finally, throughout the report, we give all dates in terms of Julian days and Greenwich Mean Time, so that 2 March, 1200 G.M.T., for example, is Julian day 62:1200.

2.1 Data Sources

As part of the Bureau of Land Management/National Oceanic and Atmospheric Administration (NOAA) Outer Continental Shelf Program, the NOAA ship SURVEYOR carried out a survey of the properties of the Bering Sea Marginal Ice Zone (MIZ) in the region between Nunivak and St. Matthew Islands from 1 - 14 March 1979 (Figure 1). Several papers and reports describe the results of this cruise. Pease (1980) gives an overview of meteorology and oceanography of the Bering Sea, with particular reference to the region surveyed by the cruise.

Second, Salo et al. (1980) list all of the oceanographic and meteorological data taken during the cruise, and give maps of both surface level pressure and air temperature, and surface level pressure and winds at 12 hour intervals for 1 - 31 March. Third, Squire & Moore (1980) give the results of their ocean swell attenuation by pack ice experiment. Fourth, Bauer & Martin (1980) give a complete description of the ice edge properties at distances of up to 50 km into the pack, and also describe the formation and movement of the ice edge bands. Fifth, Martin & Kauffman (1979) give descriptions of all ice cores taken during the cruise plus core photographs and surface and aerial site photographs. Finally, from a related study, McNutt (1980) gives a detailed ice description based on satellite and aircraft observations.

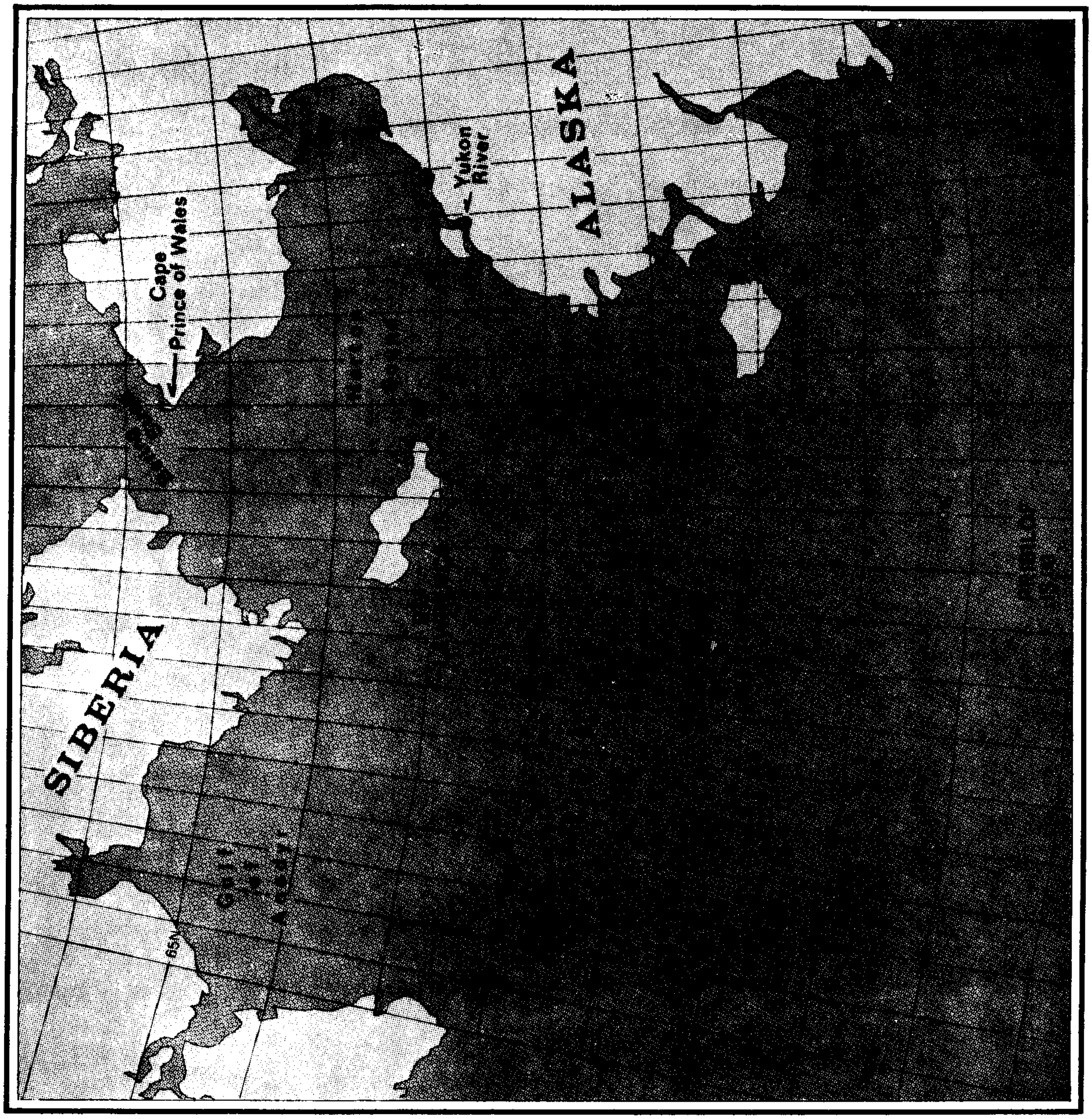

Figure 1. Base Map.

The data used to verify the SMMR output then, consists of the following:

1. Surface observations of ice thickness and concentration carried out by helicopter from the NOAA ship SURVEYOR are described in Bauer & Martin (1980) and Martin & Kauffman (1979).

2. P-3 ice reconnaissance overflights on 3 and 9 March give ice edge position and the location of some interior features from visual and classified radar observations. Appendices A and B give the verbatum ice reconnaissance messages.

3. Surface level pressure and winds are from Appendix C of Salo *et al*. (1980). This data is re-analyzed from maps produced by the National Weather Service Field Office in Anchorage, Alaska.

4. Tiros Imagery was made available by the the NOAA Environmental Satellite Services Field Office in Anchorage.

5. Ice Charts are prepared from the Tiros images by the method described in §2.4.

2.2 The Weather

We take our weather analysis from the maps and discussion of Salo *et al* (1980). Following their Appendix 3, the weather in the southern Bering Sea divides into two parts during March 1979. First, from 1 - 19 March (60:0000 - 78:1200), the Siberian high pressure system dominated the Bering Sea. During this period, the winds were cold and from the north to northeast direction, with only a few 12 hour interruptions caused by lows moving along the Aleutians (Figures 2a - 2c). Beginning 20 March (79:0000) through the end of the month, a large low pressure system centered over the western Aleutians caused warm southerly winds to flow up into the Bering (Figure 2d). The predominant winds in the eastern Bering Sea were then from the southwest, and the ice retreated.

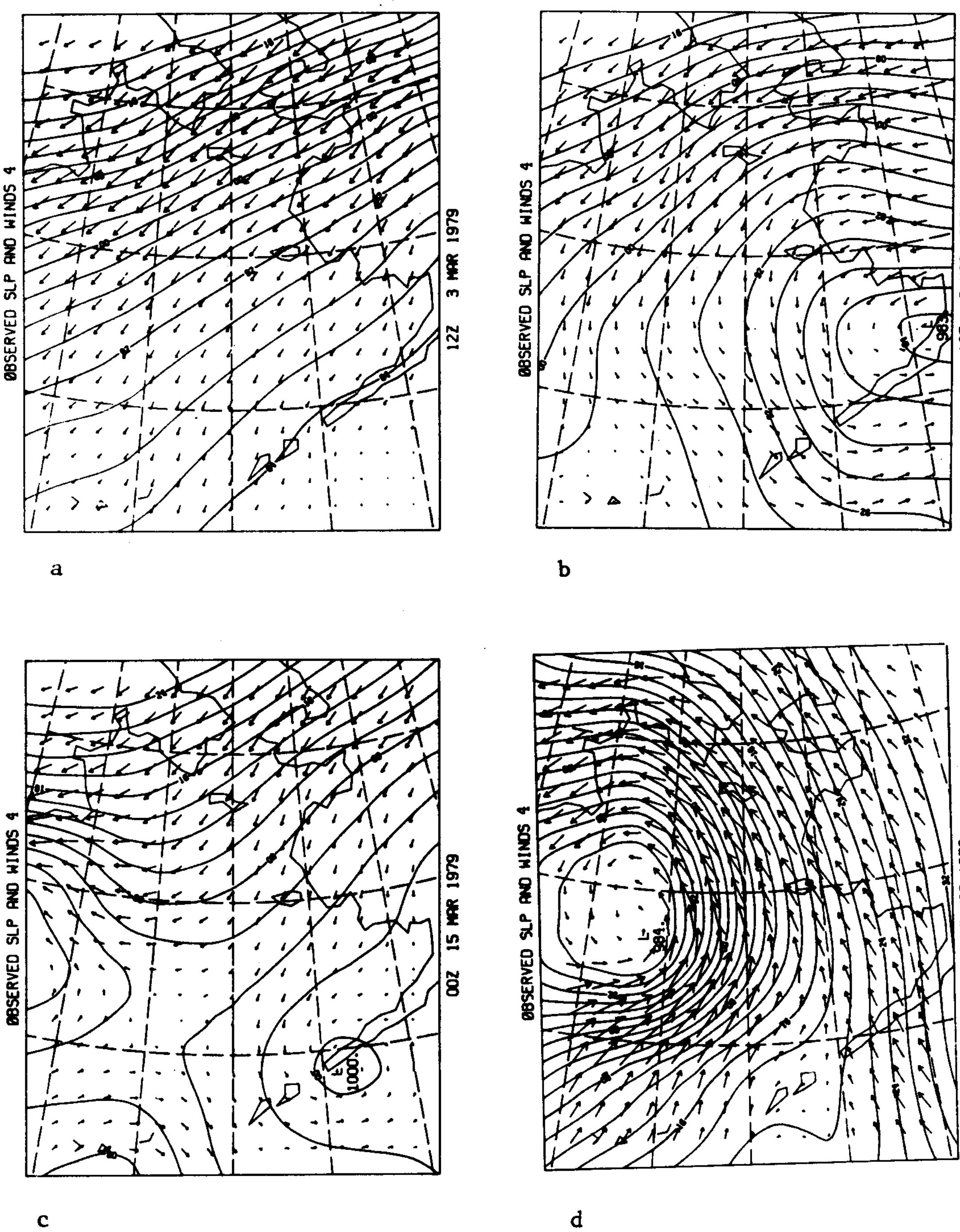

Figure 2. Observed surface level pressure and winds for March 1979 [from Salo et al. (1980)]. The longest wind vector is 20 m s^{-1}. (a) 62:1200; (b) 68:1200; (c) 74:0000; (d) 84:1200.

Because of partially clear weather during 1 - 19 March, Tiros satellite imagery of the ice was available, although the oblique satellite orbit caused bad distortion on some images. From 20 - 25 March, the Bering Sea was completely cloud covered, with the first clear image on 25 March (day 84) showing a dramatic ice retreat. During this first period of north to northeast winds, the ice which moved to the right of the wind in general advanced southwest away from the Alaska mainland and the islands. During the southerly wind period the ice retreated dramatically up into Norton Sound.

2.3 The Nature of the Ice Edge

During the cruise period, Bauer & Martin (1980) describe the ice edge appearance as observed along three section lines. Figure 3 gives an idealized picture of the ice edge. Because of both the propagation of ocean swell into the pack, and its attenuation by the pack ice, Squire & Moore (1979) show that the MIZ divides into three distinct zones called respectively the 'edge', 'transition', and 'interior' zones.

In the edge zone, the ocean swell fractures the floes and causes them to raft and ridge into irregularly shaped floes with diameters of about 20 m and thicknesses of 1-4 m (Figure 4). In the transition zone the swell fractures the floes, but does not raft and ridge them, so that the ice has a regular rectangular pattern with the long axis of the rectangle at right angles to the swell propagation direction (Figure 5). In the interior zone, the swell amplitude is sufficiently reduced such that it propagates through the floes without fracturing them, so that the floes have widths of order km, and thicknesses of 0.2 - 0.3 m (Figure 6). We observed some form of this idealized ice distribution on

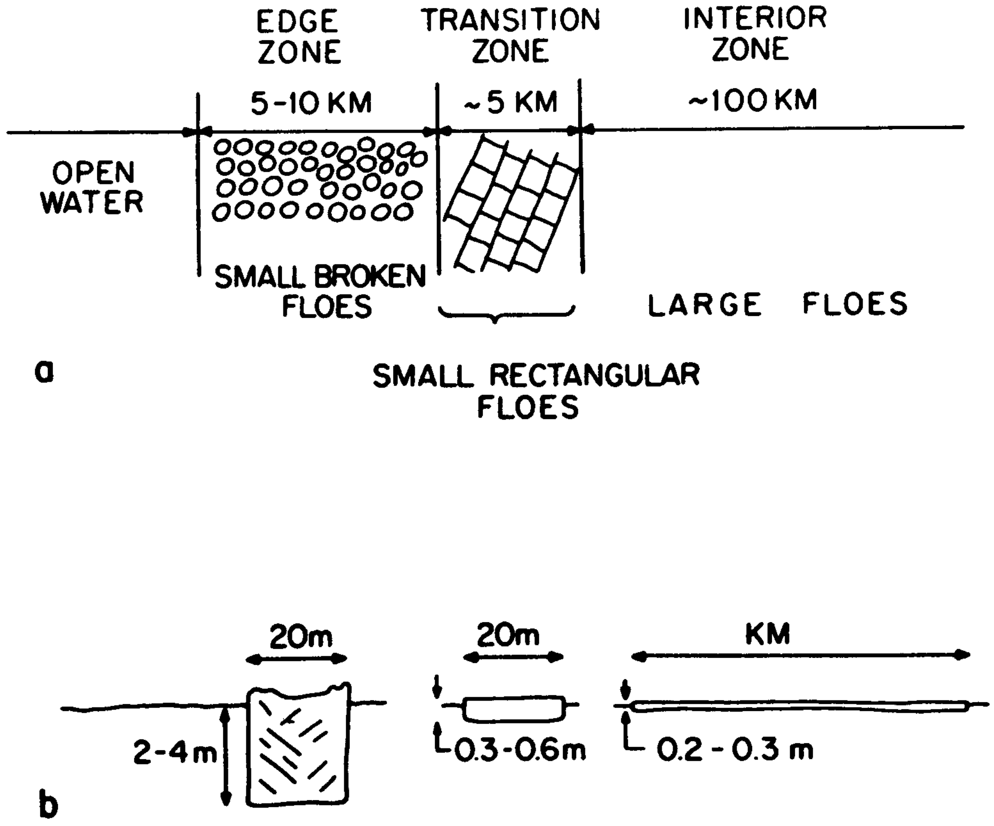

Figure 3. A schematic diagram of the three kinds of ice which occur near the ice edge, proceeding inward from open water. The upper part of the figure shows the ice in plan view; the lower part, in side view ([from Bauer & Martin (1980, Figure 2)].

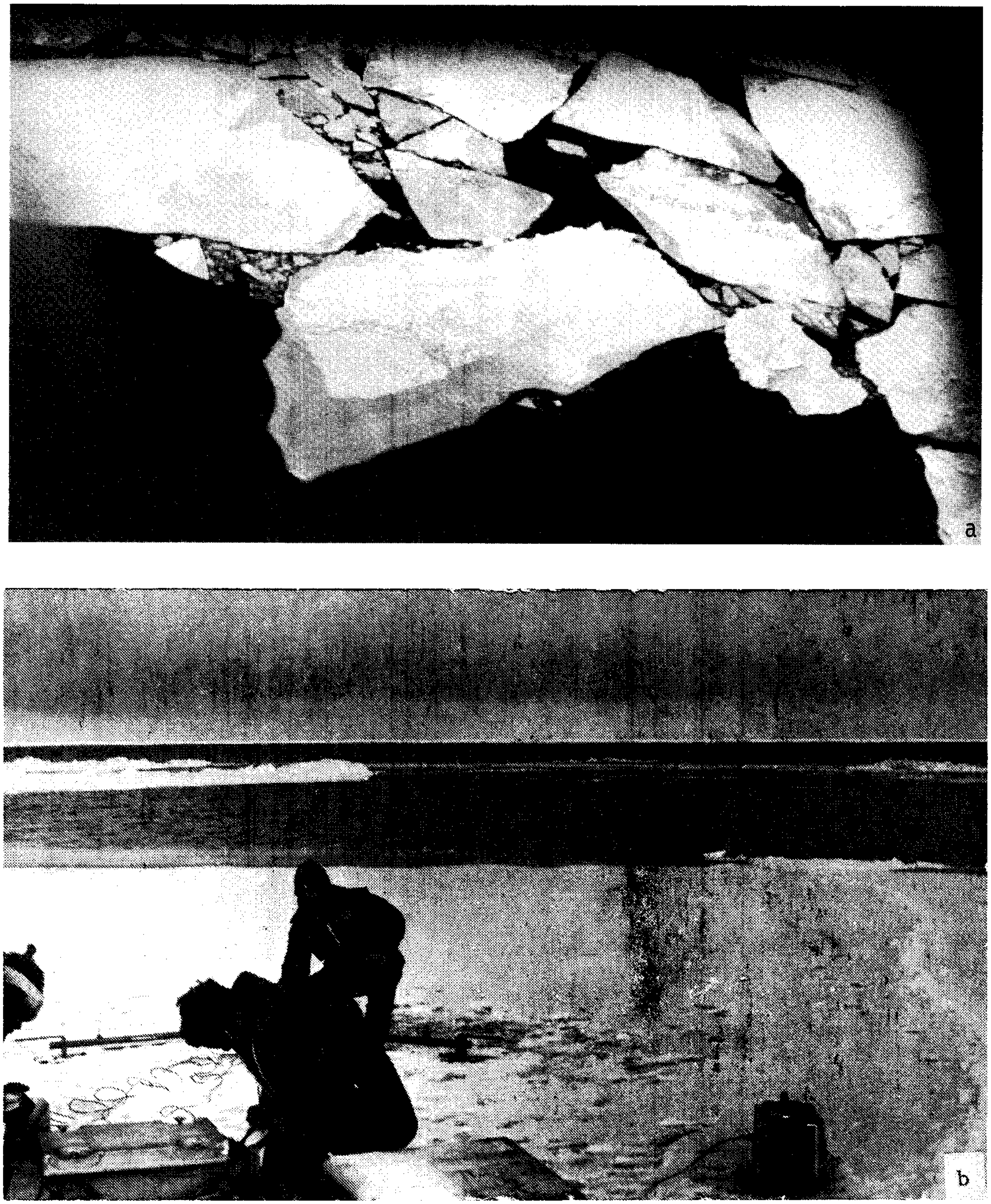

Figure 4. Floes in the edge zone on 6 March 1979 (day 65). (a) Aerial view from 60 m; large floe in foreground measures 20 by 40 m^2; (b) surface view of large floe looking toward dark area in foreground of (a); seal is in water. From divers' observations, this floe is 1-5 m thick [from Bauer & Martin (1980) and Martin & Kauffman (1979)].

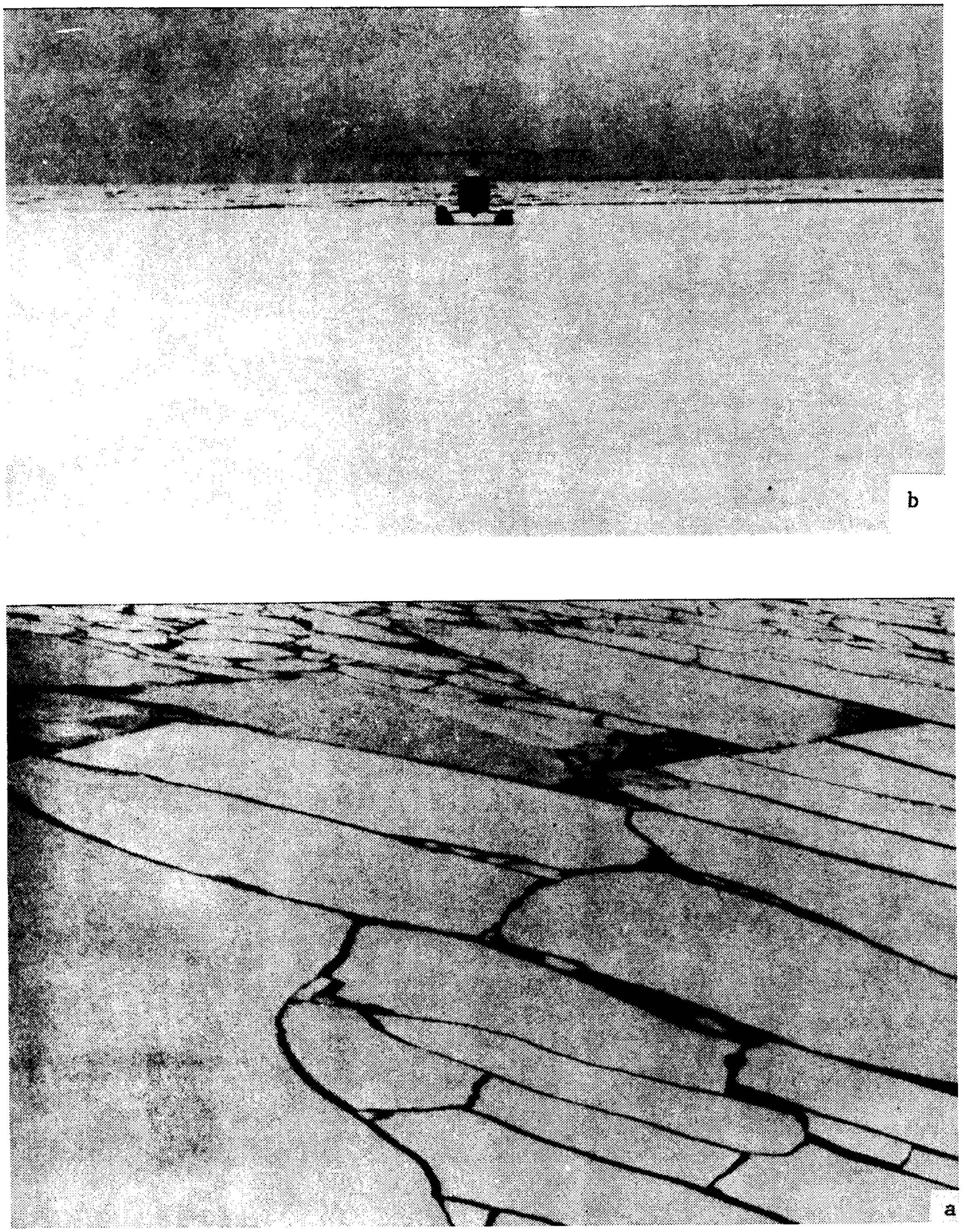

Figure 5. Floes in the transition zone on 9 March 1979 (day 68); (a) Aerial view from 150 m showing ocean swell fracturing large floe into small floes measuring 20 m across. (b) Surface view, where helicopter is on the large floe in lower left of (a). Its thickness is 0.33 m.

our three traverses, where in each case the thickest ice occurred at the edge.

We also observed that during periods of off-ice winds, the transition between the open water and solid ice cover was complicated by the formation of ice edge bands. These long thin bands, which form from ice divergence, measured about 1 - 10 km in length and 0.1 - 1 km in width, were oriented perpendicular to the wind direction, and moved away from the solid ice cover with a higher velocity than the interior pack. Figure 15a shows these bands streaming off south of the solid pack. Bauer and Martin (1980) show that these bands continue to move away from the pack until they melt in the surrounding warmer water. Therefore, the change from open water to solid ice in the Bering Sea is not abrupt, but rather is a gradual transition over about 50 km changing from open water to ice bands with a 10 - 20% large area concentration, into the edge zone which has 40 - 70% ice concentration, then into the higher concentration transition and interior zones.

2.4 The Tiros Ice Charts

For comparison with the SMMR results, one of us (S.L.M.) prepared ice charts from the Tiros images (see Figures 8a, 14, 15a, and 17a for examples). To avoid bias, the ice charts (Figures 8b, 11, 15b, and 17b) were prepared independently and without knowledge of the SMMR charts.

The Tiros imagery, which is available in both the visible and infra red wavelengths, has two problems. First, clouds frequently obscured the image; second, the satellite orbit often produced extremely oblique images. Because both these factors prohibited daily coverage of the Bering Sea, when coverage was not available we extrapolated the ice cover from a combination of previous or subsequent images. To transfer

Figure 6. Aerial view of large ice floes in the interior zone from 150 m on 6 March 1979 (day 65). Ice thickness is 0.24 m.

the Tiros data to a standard map base, we used a Zoom Transfer Scope (ZTS). The ZTS permits correction of the image distortion and the hand drawn transfer of the adjusted image to a base map. In this transfer, the resolution and scale of the original image limits the practicability of gaining information from the enlarged image. The location of land areas gives the best geometric control, so that our data plots are on a small-scale polar stereographic projection. Comparisons with Landsat imagery show that the error induced is in the rotational shift of the location of a feature and not in its shape or area (McNutt, 1981).

On the charts we classify the ice in terms of both ice type and concentration. The different shadings on the ice chart divide the ice into the six categories of fast ice, new-young ice, first year-young ice, medium first year ice, thick first year ice, and the diffuse ice bands at the edge. These qualitative ice types do not imply an ice thickness; the identification is made in terms of the gray scale on each image. Second, ice concentration is expressed in terms of percentages, which are expressed to an accuracy of 25%. The cause of this low accuracy is the small scale of the Tiros image and the presence of low clouds over the ice, in particular over open water regions.

In summary, the accuracy of the charts depends on the clarity of the original image, the amount of cloud cover, and the distortion inherent in the satellite photo. Since the locational error increases away from land, the most accurate portions of these images occur near land.

3. THE SMMR IMAGERY

3.1 SMMR Radiances

The study of sea ice by means of microwave remote sensing from space has evolved from the use of the single wavelength measurements of the Electrically Scanning Microwave Radiometer (ESMR) aboard Nimbus-5 [Gloersen *et al*. (1974), Zwally & Gloersen (1977), and Gloersen *et al*. (1978)] to the multispectral measurements of the Scanning Multichannel Microwave Radiometer (SMMR) on Nimbus-7 [Gloersen & Barath (1977)]. The Nimbus-7 SMMR measures microwave radiances at five wavelengths (4.55, 2.81, 1.67, 1.43 and 0.81 cm) for both horizontal and vertical polarizations providing ten channels of radiometric brightness temperatures. The spatial resolution of the instrument as defined by the integrated field-of-view (FOV) ranges from 148 x 151 kilometers at 4.55 cm to 27 x 32 kilometers at 0.81 cm. Gloersen & Barath (1977) give a complete summary of the instrument operating characteristics.

The usefulness of microwave measurements results from the high contrast in emitted radiances between open ocean and sea ice. The microwave radiation can be expressed as a brightness temperature through the application of the Rayleigh-Jeans approximation and written as a product of emissivity and physical temperature. The brightness temperature within a spacecraft instrument FOV is a composite of contributions from the surface of the earth, the atmosphere, and reflected components at the surface of both the atmospheric radiation and free space radiation [Gloersen & Barath (1977)]. With the assumption that the contribution from both the atmospheric and space components are negligible, the brightness temperature, T_B, observed by the satellite is simply

$$T_B = eT_S \,, \tag{1}$$

where e and T_S are respectively the emissivity and surface physical temperature.

In the discussion to follow the sea surface will be considered either to be ice free, open ocean or to be covered only by first-year ice corresponding to the Bering Sea. Finer distinctions of ice type, as for example, new, young, and thin first-year ice, are not made since discrimination between thin ice and water within a given FOV of the instrument remains ambiguous. Figure 7a presents typical emissivity values for both calm open ocean and first-year sea ice at each of the SMMR wavelengths and polarizations. The calm open ocean values are optical model results corresponding to a thermodynamic temperature of 271 K while the ice emissivities are derived from observed Nimbus-7 SMMR brightness temperatures and physical surface temperature measurements made during nearly-coincident aircraft flights over first-year ice in Baffin Bay. The ice emissivities for both horizontal and vertical polarizations are greater than 0.9 at all wavelengths and exhibit little spectral variation. On the other hand, the water values are considerably lower, decrease with increasing wavelength, and have a much greater degree of polarization. Differences between vertical and horizontal ice emissivities range from 0.02 at 4.55 cm to 0.08 at 0.81 cm, whereas those for water fall within the range 0.26-0.29 at all wavelengths. This difference in the degree of polarization between water and ice is used below to retrieve ice concentration information.

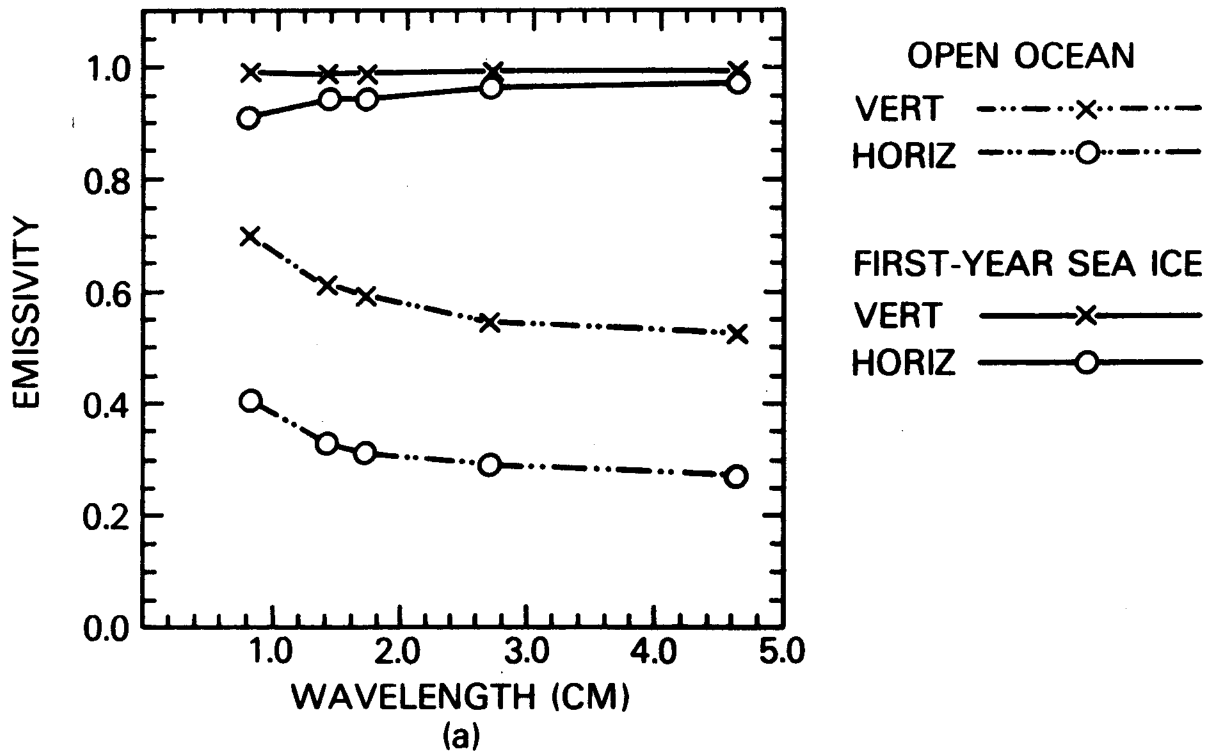

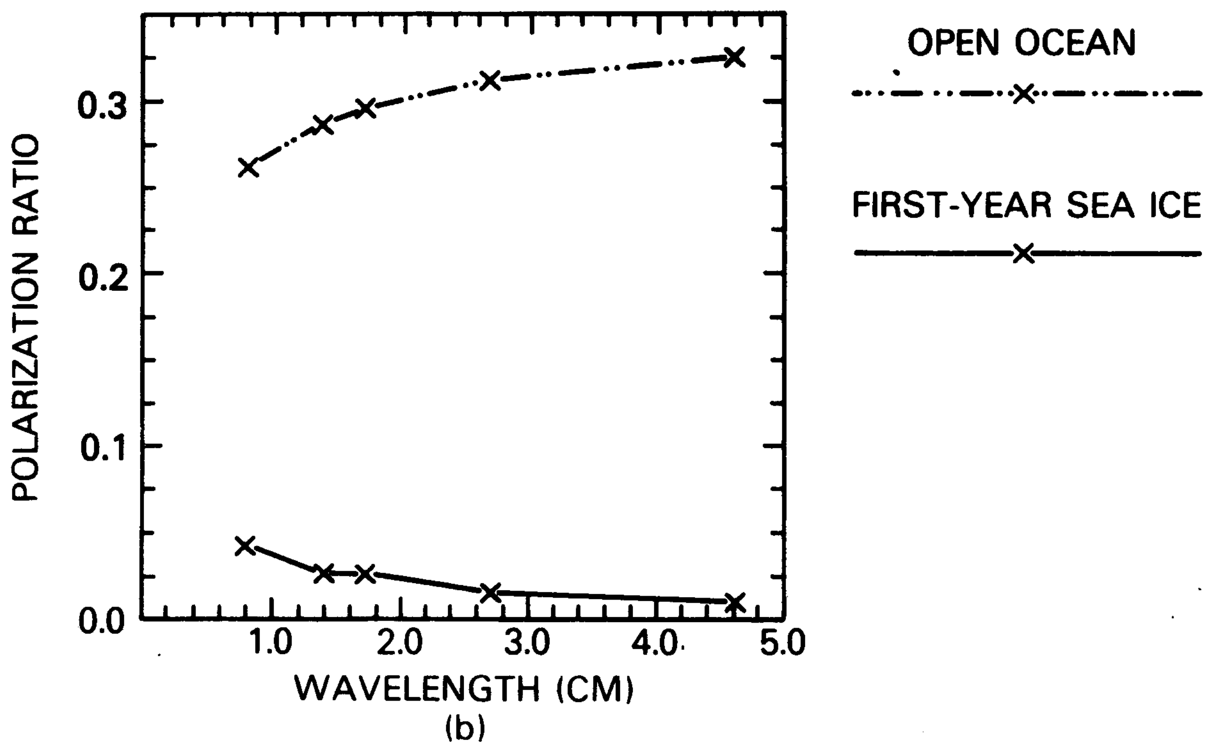

Figure 7. Microwave emissivities and polarization ratios at each SMMR wavelength for calm open ocean and first year sea ice. (a) Emissivity values. (b) Polarization ratios.

The polarization ratio PR, a measure of the degree of polarization, is defined in terms of observed SMMR brightness temperatures for a given wavelength as follows:

$$PR = \frac{T_B(\text{vert}) - T_B(\text{horz})}{T_B(\text{vert}) + T_B(\text{horz})} \quad . \qquad (2)$$

Figure 7b plots PR for each SMMR wavelength; the advantages of using this brightness temperature ratio are 1) the surface temperature dependency is largely removed and 2) any residual instrument gain variations will be reduced. From Figure 7b the difference between PR for water and ice varies from 0.32 at 4.55 cm to 0.22 at 0.81 cm. This large water-ice contrast and the near-independence of PR on physical temperature variations makes PR suitable for computing sea ice concentration.

3.2 Ice Algorithm

In the case when the instrument FOV is filled by a mixture of first-year ice and water, the surface emissivity is

$$e = e_W (1-C) + e_I C \quad , \qquad (3)$$

where e_W and e_I are the emissivities of water and ice respectively and C is the ice concentration, or the areal fraction of the field of view that is ice-covered. For this simple single ice species case, the brightness temperature equation becomes:

$$T_B = e_W T_W (1-C) + e_I T_I C \quad , \qquad (4)$$

where T_W and T_I represent the physical temperature of the sea surface and ice respectively. Our purpose here is to show that even with this crude model variations in ice cover are observed which, as will be seen below, agree well with analyses based on both visible satellite imagery and near-surface observations.

Equation (2) can now be used with the simplified expression for brightness temperature within an FOV [Equation (4)] to derive a relationship between C and PR for each of the five SMMR wavelengths. The resulting expression is

$$C = \frac{1}{1-R} \quad , \tag{5a}$$

where

$$R = \frac{T_{BI}(\text{horz}) - \left(\frac{1 - PR}{1 + PR}\right) T_{BI}(\text{vert})}{T_{BW}(\text{horz}) - \left(\frac{1 - PR}{1 + PR}\right) T_{BW}(\text{vert})} \quad . \tag{5b}$$

$T_{BI(horz)}$ and $T_{BI(vert)}$ are horizontal and vertical brightness temperatures of consolidated first-year ice and $T_{BW(horz)}$ and $T_{BW(vert)}$ are the corresponding brightness temperatures of calm open ocean. In equation (5b) we set the ice and water brightness temperature values to those observed in the Bering Sea. In this report, we use only the 0.81 cm channel to obtain the highest spatial resolution. For the 0.81 cm wavelength, these values are

$$T_{BI}(\text{horz}) = 215\text{ K}, \qquad T_{BW}(\text{horz}) = 120\text{ K},$$
$$T_{BI}(\text{vert}) = 242\text{ K}, \qquad T_{BW}(\text{vert}) = 192\text{ K}, \tag{6}$$

which were obtained from orbit 1966 (day 74:1202), an orbit coinciding with a period of relatively clear atmospheric conditions. This tuning of the algorithm was done in lieu of in situ Bering Sea measurements of ice emissivity and physical temperature on scales comparable to the SMMR FOV's. The polarization ratios derived from (6) differ slightly from those presented in Figure 1b. The Bering Sea water ratio of 0.23 is 0.03 less than the model value for calm ocean (Figure 7b) indicating a wind roughened surface or an atmospheric effect or both. The Bering Sea first-year ice polarization ratio is 0.06 while that of Baffin Bay ice is 0.04 reflecting real differences in the physical properties of the ice as, for example, increased surface roughness which would tend to depolarize the received microwave radiances.

Equation (5) with the values from (6) is used to compute ice concentrations from the polarization ratios calculated from the observed SMMR brightness temperatures. Because the algorithm translates emissivity variations into concentration variations, the accuracy of the concentration retrievals depends primarily on the observed ice having an emissivity close to the tuned value. Since thin ice species have emissivities between those of open water and thick first-year ice, areas of thin ice translate into areas of lower ice concentration. As an example, actual radiance and sensible surface temperature measurements made during AIDJEX [Gloersen et al. (1978)] show that the emissivity difference between thick snow-covered first-year ice and thin ice without snow cover at 0.81 cm is 0.01 for the vertical polarization and 0.08 for the horizontal. In the algorithm, the ice concentration noise amplification factor for variations in ice emissivity is approximately 3, so that the error in ice concentration caused by an emissivity variation of 0.05 is approximately 15 percent. Therefore, based on the AIDJEX data, we expect for the Bering a maximum concentration error of up to 24 percent. Because of this limitation on accuracy, it is the relative position of high and low ice concentration regions and concentration gradients which are of prime importance. In fact, we show in §4 that these features correspond well with patterns of thin and thick ice in the ice charts.

3.3 Spatial Resolution of Data

As previously mentioned, the FOV size of each SMMR channel decreases with decreasing wavelength. The FOV or footprint of the instrument is elliptical in shape with the long axis in the direction of spacecraft motion because of spatial smearing due to both the integration time and the spacecraft velocity. The 0.81 cm channel has the highest resolution, or an integrated FOV of approximately 27 x 32 kilometers. We use this channel below in the ice algorithm to obtain information on the smallest possible scale. The resolution has been degraded somewhat by "binning" the brightness temperatures from each individual FOV into cells approximately 30 km x 30 km in order to accommodate existing software packages for producing the contour plots.

The maps on which the SMMR data have been contoured were generated from the Wolfplot package[1] of routines and have an accuracy of 0.1 degrees latitude (11 km) in both latitude and longitude. Examination of these maps shows, however, that landfall may be in error by as much as 0.2 degrees latitude. Part of this may be due to inaccuracies resulting from the plotting of the land boundaries themselves. In any case, the

[1]The Wolf Plotting and Contouring Package by G.T. Masaki 1972 (Revised Ed. 1976) Computer Sciences Corporation, Silver Spring, MD.

mapping errors are within the microwave resolution size and should not significantly affect the results of the comparison.

4. COMPARISON OF DATA

This section compares the surface, aircraft, and Tiros data described in §2 with the SMMR algorithm results. Table 1 summarizes the data used in the comparison. Specifically, we examine in the following sub-sections the ice behavior for 3, 9, 15, and 25 March, and show that the SMMR algorithm gives a good description of both the ice edge and the observed ice interior properties.

4.1 3 March (day 62)

Figure 8a shows the Tiros image, and 8b shows the ice chart prepared from 8a. Examination of these figures shows that the northeast winds shown on Figure 2a drove the ice away from the Alaska mainland, from the south coast of Nunivak, St. Lawrence, and St. Matthew Islands, and from the northern part of the Gulf of Anadyr, thus creating lee-shore regions of both thin ice and low ice concentrations. The southwest advection of ice is also responsible for the thick plume of ice extending southwest from Norton Sound to the ice edge, and for the high concentration region in the southern Gulf of Anadyr.

For comparison with the ice chart and aircraft and helicopter data, Figure 9 shows the SMMR ice concentration chart. On the chart we plot contours of constant ice concentration at intervals of 10% up to 95%. To simplify the presentation and to minimize the effects of roughened seas and atmospheric liquid water, the lowest concentration shown is 25%. On the chart, the solid white line is the P-3 ice edge, the symbols S1 and S2 show our helicopter core locations, and the letters "A-F" show regions of comparison with the Tiros ice chart. As Table 1 shows,

Table 1. Summary of the research platforms and the times of their observations

Mode	Orbit	Julian Day	GMT
3 March			
Tiros		62	0020
Helicopter		62	00-02
P-3		62	00-03
SMMR	1806	62	2202
9 March			
P-3		68	00-03
HELO		68	18-21
SMMR	1889	68	2202
Tiros		(average of day 67, 69)	
15 March			
HELO		74	00-01
SMMR	1966	74	1202
Tiros		75	0127
25 March			
SMMR	2110	84	2149
Tiros		85	0124

Figure 8a. Tiros image for 3 March (62:0020); see text for further description.

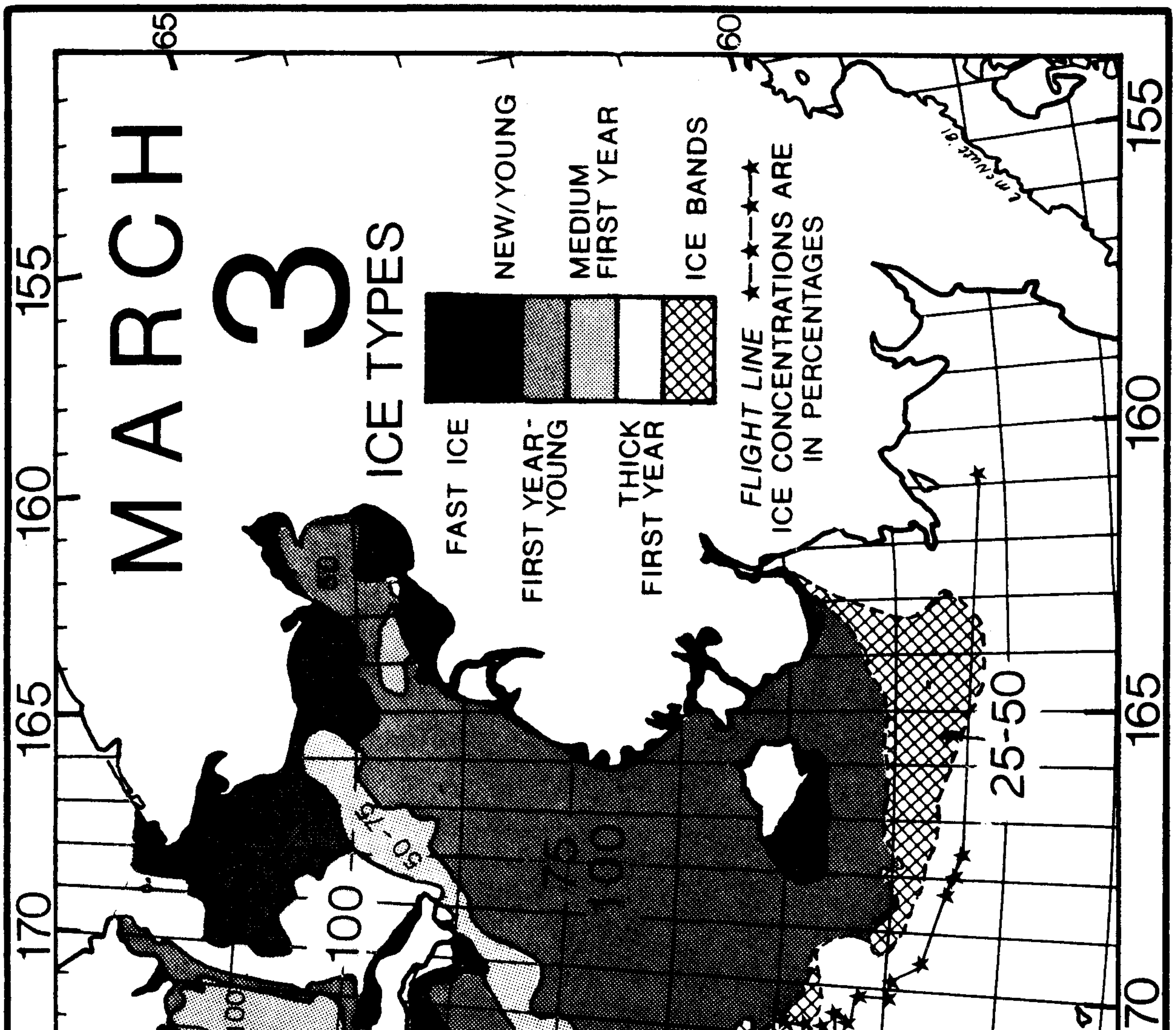

Figure 8b. Ice chart derived from Figure 8a.

the data used in the comparison was taken about 20 hr before the SMMR image.

Examination of Figure 9 shows that the ice edge is defined by a concentration gradient ranging from 25 to 55% over a distance of about 50 km. The cause of this 50 km width is partly the SMMR FOV, and partly the width of the physical transition from open water to the ice interior described in §2.2. Along this gradient region, the white line shows the P-3 ice edge position, where Appendix A gives a copy of the reconnaissance report. Because the ice observer took this line in part from a classified radar, we are unable to check independently the ice position; however, examination of the figure shows that the line lies within 1/4° latitude of the SMMR edge, or within one SMMR cell.

Second, the two points S1 and S2 lying below Nunivak Island show the location of the ice cores taken by helicopter. Figure 10a shows an aerial view of the field of 10 m diameter floes from which core S2 was taken and 10b shows a surface view. We measured this floe thickness as 0.80 m; the ice appearance in the photograph is similar to that at S1 where we measured a 0.60 m floe thickness. From the pictures, the ice at S1 and S2 consists of small thick floes, floating in a layer of about 0.1 m thick grey ice. Examination of our photographs from this region supports the algorithm result of a 50-60% concentration.

Finally, the letters on Figure 9 mark regions of comparison between the SMMR data, the ice chart, and the Tiros image. First, "A" marks the broad region of young uniform ice filling the eastern Bering Sea. As we expect from the predominantly northeast winds, the concentration decreases toward the Alaskan coast. Also, the 65% contour to the left of "A" outlines approximately the boundary between the young and medium

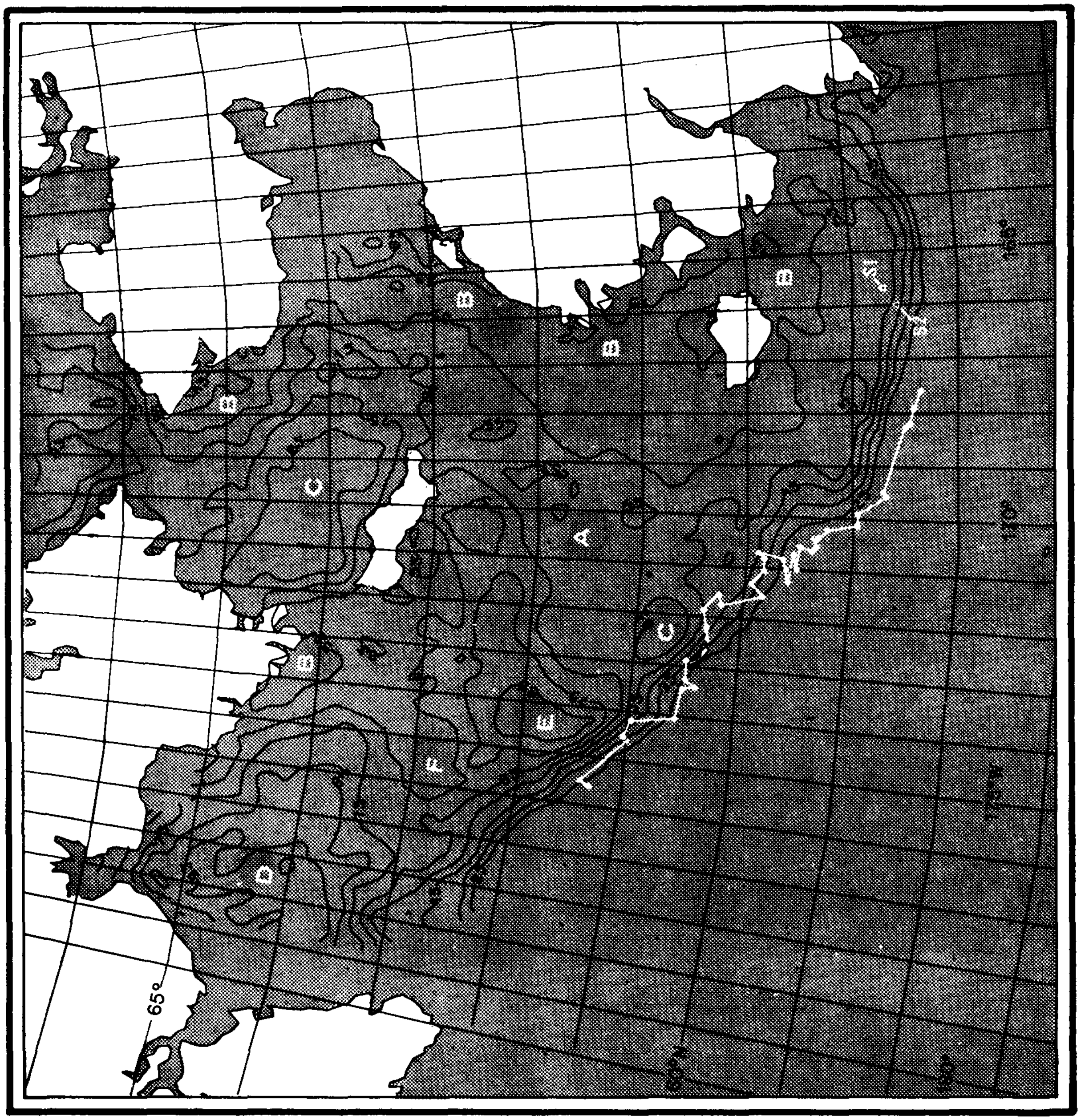

Figure 9. The SMMR ice chart showing contours of ice concentration in intervals of 10% computed from the 0.81 cm wavelength for day 62:2200. See text for further description.

first year ice shown on the ice chart. There is a discrepancy in concentration, however, between 45-65% ice concentrations in the region marked by "A", and the 75-100% concentrations in the same region on the ice chart.

The cause of part of this discrepancy may have occurred in the transfer of the ice concentration data from the Tiros image to the ice chart. With thin or medium first-year ice appearing dark grey on the image, thicker ice as white, and open water as black, to the ice observer open water shows up better in white ice than in dark grey ice, so that the thin ice concentration can be easily overestimated. The second cause of this discrepancy, as Section 3.2 discusses, is that for the same concentration of thin and thick ice, the present algorithm shows the thin ice as having a lower concentration than thick ice. We suspect that a combination of ice observer and algorithm error causes the above discrepancy.

To continue with the letters on the chart, the regions "B" show the coastal ice-generation regions, which are physically characterized by both thin ice and low concentrations. Because of land contamination in the algorithm, the contouring for these regions breaks down within a SMMR FOV or approximately 1/4° latitude of land. Next, the "C's" mark the regions of thick ice and high concentration to the north of St. Lawrence and to a lesser degree north of St. Matthew Island, where the winds drive the ice against the coasts. The concentration decrease immediately north of both islands is again caused by land contamination. Fourth, in good agreement with the ice chart, "D" marks the region of older, thicker ice in the Gulf of Anadyr.

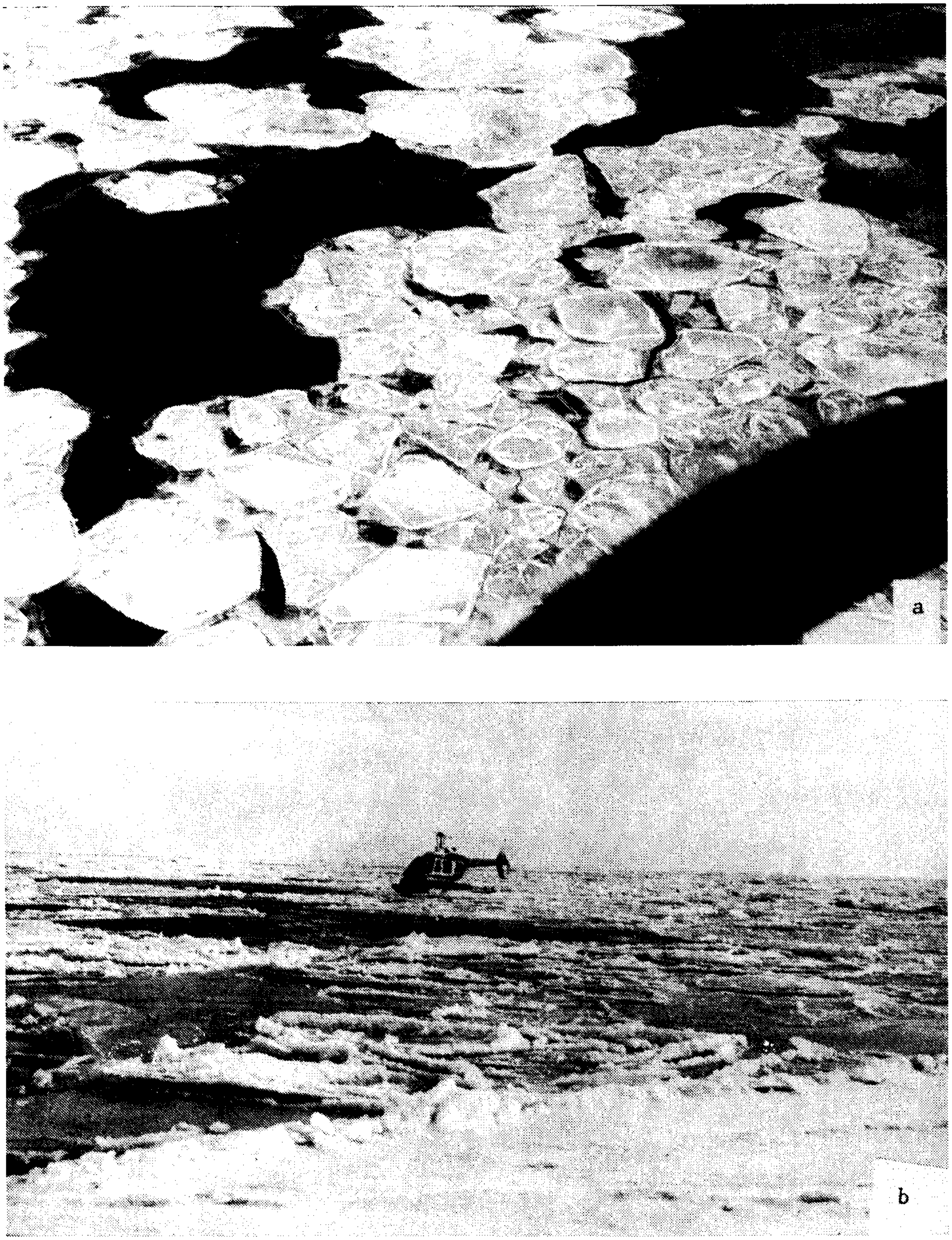

Figure 10. Aerial and surface view of site S2. (a) Aerial view from about 150 m; floe S2 is white floe at lower left measuring about 10 m across and 0.8 m thick. (b) Surface view of area from S2 showing 0.2 m thick grey ice beyond S2.

Fifth, "E" marks the region of older, thicker ice clearly shown on the Tiros image and with a SMMR concentration of 65-85% and an ice chart concentration of 50-75%, where this ice was probably advected down to the edge from Norton Sound. Finally, "F" marks the region of younger thinner ice in the western Bering Sea, which was generated both south of St. Lawrence and in the Gulf of Anadyr. Again for this case, the SMMR and ice chart concentrations agree.

In summary, comparison of the ice and SMMR charts show that the SMMR output gives good results for first, the ice edge; second, the low concentration, thin ice regions adjacent to the coasts; and third, the high concentration regions north of the islands, in the Gulf of Anadyr, and the plume center "E". The ambiguities in the algorithm results, which may be caused by errors in reading the Tiros ice concentrations, occur in discrimination of the thin ice concentrations. We feel, however, that comparison of the two methods shows that, except within 1/4° latitude of land, the SMMR ice algorithm gives as good results as the ice chart in the interior, and a better definition of the ice edge.

4.2 9 March (day 68)

Between day 62 and 68, the Siberian high pressure system continued to dominate the weather so that as Figure 2b shows, the winds continued out of the northeast. Because of problems with clouds, we prepared the ice chart for this day (Figure 11) from an average of Tiros images on days 67 and 69.

In addition to the ice chart, Table 1 shows that we also had a helicopter ice survey and a P-3 overflight preceding the SMMR image, where the P-3 preceded the SMMR by about 20 hr, while the ice survey was nearly simultaneous. Examination of the Tiros ice chart, on which we

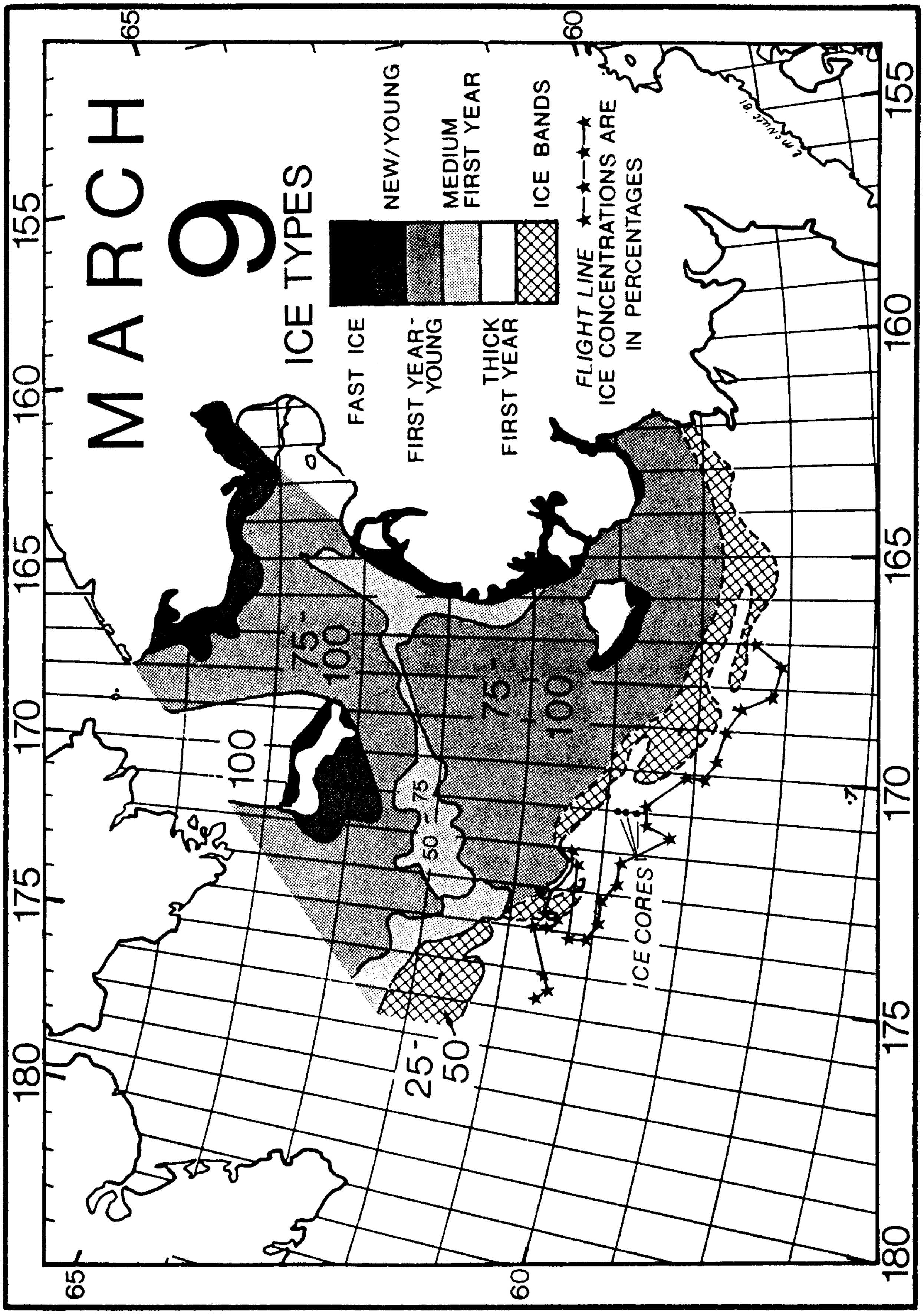

Figure 11. Ice chart for 9 March 1979 from Tiros images on day 67 and 69. See text for further description.

plot the aircraft ice edge and ice core positions, clearly shows that the ice chart and the physical ice edge do not agree. The ice chart shows, however, many of the same physical features described for 3 March, specifically the thin ice and low concentration regions southwest of the coasts and islands.

For comparison, Figure 12 shows the SMMR ice concentration plot. On this figure, the solid white lines show the aircraft flight lines from Appendix B; one at the ice edge, and another in the ice interior northwest of St. Matthew Island. The figure shows that except in the immediate vicinity of St. Matthew Island, the P-3 ice edge is well correlated with the SMMR ice edge. The interior line, following and paraphrasing slightly the P-3 report, marks the "vicinity of the heaviest, thickest ice," and the circle marks the regions of "greatest concentration within a 10 nm radius". Although the circle is not identified with any particular concentration feature, the interior track line follows the 85-95% concentration lines. Again the aircraft and SMMR results are in good agreement.

Second, the point C shows the ship location,,and C1-C4 show the line along which we took four ice cores. Along this line, Martin & Kauffman (1979) reported that the sky was heavily overcast, while the P-3 (Appendix B) also reported "undercast between 169.5°W and 171.75°W". The figure shows that, in spite of the overcast, the traverse line lies across both the SMMR and physical ice edge. Figure 13 shows a schematic of the ice concentrations and types observed along this traverse, and Figure 5 shows station C3. From Martin & Kauffman (1979) the ice thicknesses along this line are as follows: C1 is 0.25 m thick, C2 is 0.33 m thick, C3 is 0.33 m thick, and C4 is 0.15 m thick. Further, from our

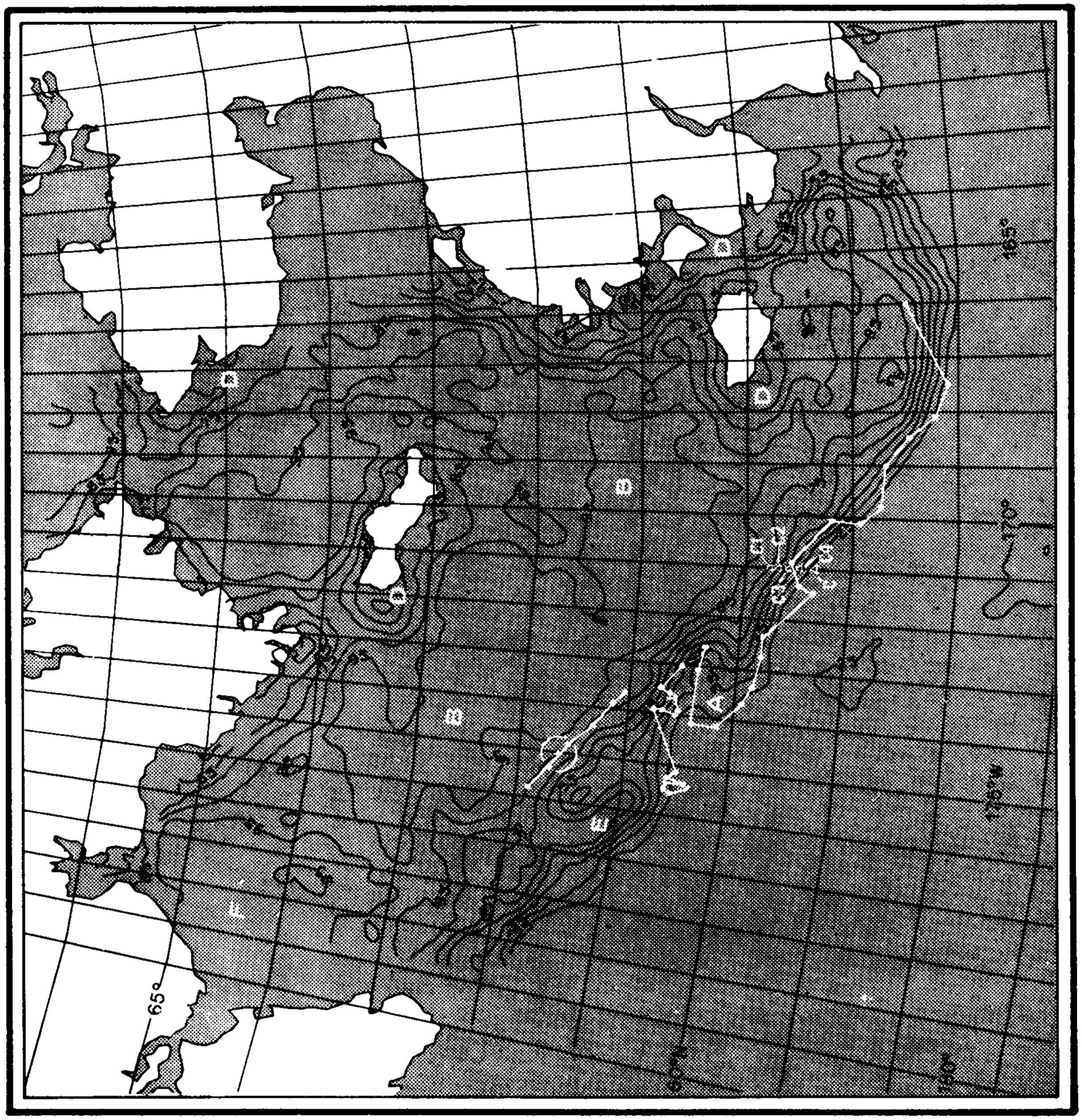

Figure 12. SMMR ice chart for 9 March (68:2200). See text for further description.

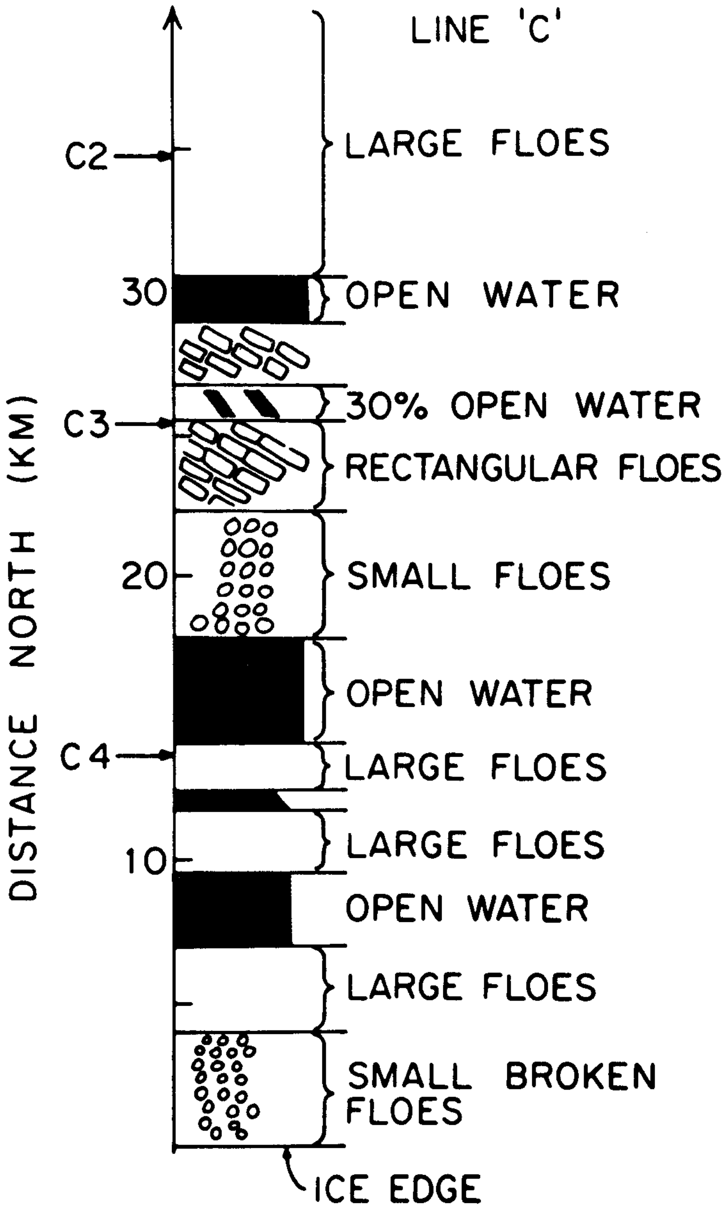

Figure 13. A diagram of the ice types along Line C [from Bauer & Martin (1980)]. Region above C3 marked "30% open water" consists of large floes in 30% open water; conditions at C1 (not shown) are similar to those at C2.

previous days' work from the ship, the small broken floes near the edge had thicknesses of 1-5 m. This complicated mixture of small broken floes, open water, and very large floes is a specific example of a traverse line in the ice transition region.

The capital letters on the SMMR chart again mark regions of comparison with the ice chart. "A" shows the open water southwest of St. Matthew Island, which is marked by a dip toward the island of the concentration lines. The cause of the lack of agreement between this dip and the aircraft line may be the time difference between the two observations. "B" marks the broad interior regions of high concentration, "D" the regions of new ice production southwest of the coasts and islands, and "F" the high concentration region in the Gulf of Anadyr. These regions are in general agreement with the ice chart. Finally, the letter "E", which marks a feature not shown on the ice chart, is a local high concentration region, separated from the main pack by a low. To show that this local high probably represents a physical feature rather than a computer artifact, Figure 14 shows the closest clear Tiros image of this region at day 66:0119, or almost three days before the SMMR image. The white arrow points to a large ice mass west of St. Matthew Island which is slightly separated from the main pack. This ice mass, which may be the advection southwest of the high-concentration feature also marked by "E" on Figure 9 at day 62, is probably the cause of the feature "E" on Figure 12.

4.3 15 March (day 74, 75)

As the weather charts in Section 2.1 show, between day 68 and 74 the winds continued out of the northeast. Figure 15a shows the Tiros image for day 75:0127, and Figure 15b shows the resultant ice chart. On

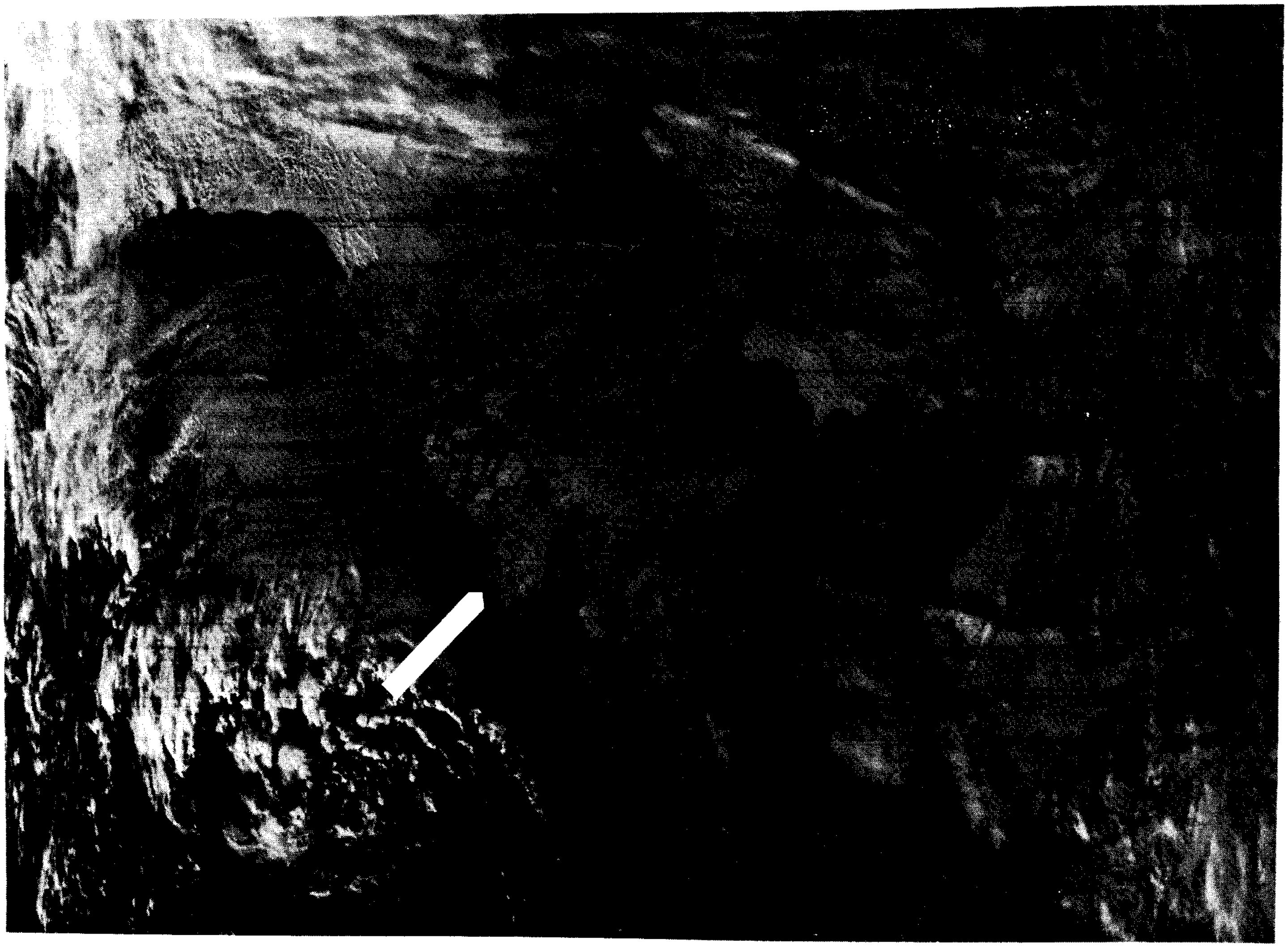

Figure 14. Tiros image for day 66:0119; white arrow points to large detached ice mass.

the Tiros image to the west of St. Matthew Island there is a cloud line over the ice parallel to the edge where the cloud shadow is visible on the ice cover. Comparison of these two images again shows the difficulty of making concentration estimates from the Tiros images. On Figure 15b the ice tongue to the east of Nunivak Island was mapped from the day 73 Tiros image. Figures 15a and b show that the ice is again characterized by thin ice and low concentration regions southwest of the major landmasses.

Figure 16 shows the SMMR ice chart for day 74:1202, where the letters N1,N2 show our core positions, and the other letters refer to significant ice features. For this case the SMMR swath covered only the eastern Bering Sea. The SMMR image again shows that the ice edge gradient region goes from 25% to 65-75% over approximately 50 km, again in agreement with the diffuse nature of the ice edge shown on the Tiros image.

To discuss next the regions marked by capital letters on the SMMR image, "A" marks the dip in the concentration lines caused by the polynya southwest of St. Matthew Island, and "B" marks the region of low ice concentration associated with the polynya southwest of St. Lawrence Island. In the ice interior the "C's" mark the high concentration, broad region of thick and medium first-year ice shown on the ice chart, although comparison with the chart suggests that the concentration at the "C" immediately to the west of Nunivak Island is too large by 20%. "D" marks the low ice concentration region southwest of Nunivak Island, where a lower 65% concentration corridor extending from the island to the ice edge separates the high concentration regions "E" and "C". This low concentration corridor is clearly visible on both the ice chart and the satellite photograph.

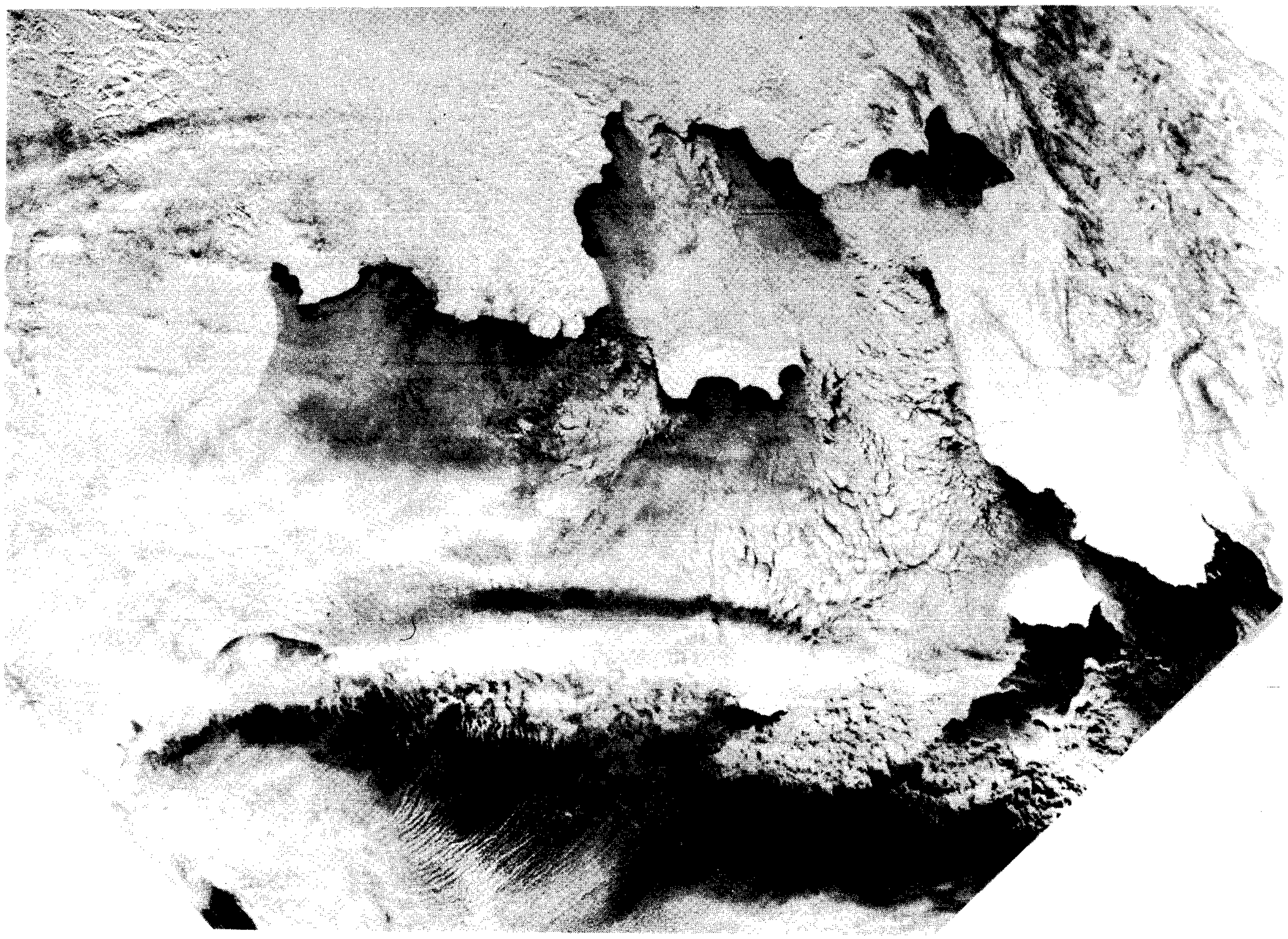

Figure 15a. Tiros image for 15 March (75:0127).

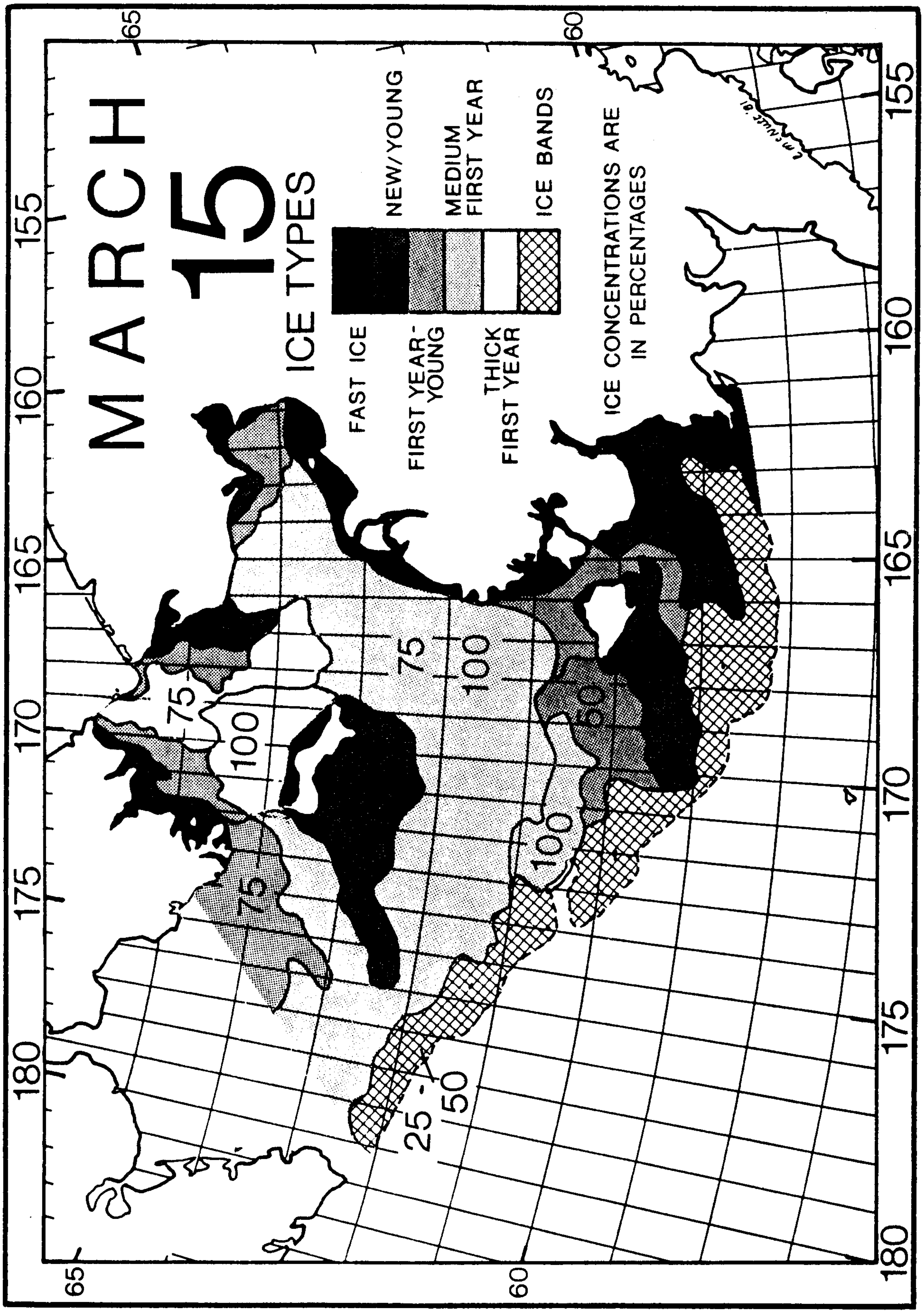

Figure 15b. Ice chart derived from Figure 15a.

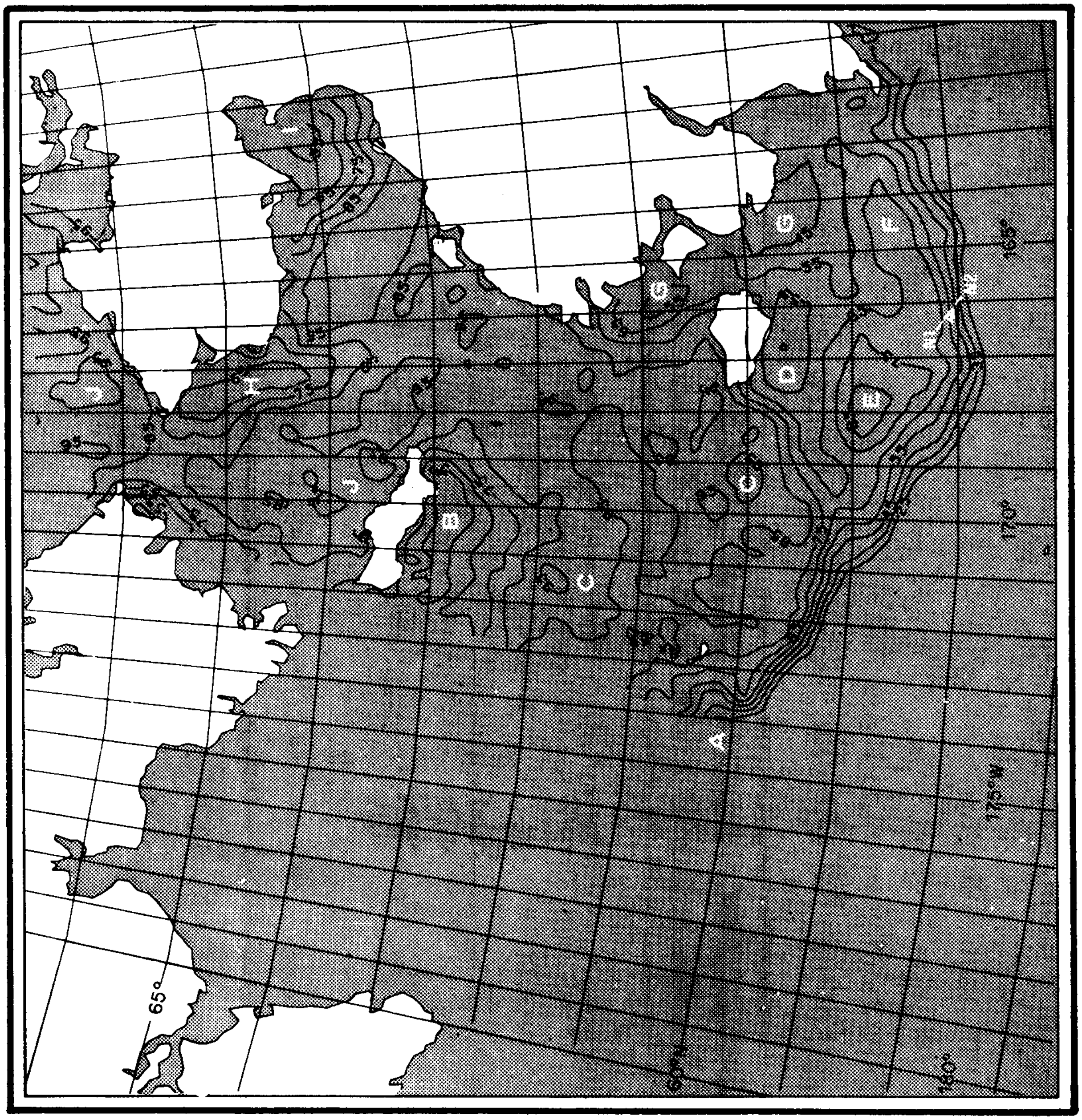

Figure 16. SMMR ice chart for 15 March (74:1202). See text for further description.

To the east of Nunivak Island, "F" marks the ice tongue that extends over into Kuskokwim Bay, and "G" marks the low concentration regions adjacent to the coast. Finally, in the northern Bering Sea, "H" and "I" respectively mark the low ice concentration regions off Cape Prince of Wales and in Norton Bay. Also north of both St. Lawrence Island and the Bering Strait, the 85-95% ice concentrations marked by "J's" show the wind-driven ice pile-ups.

Finally, the "N1" and "N2" which lie on the 55% contour line mark the core locations described in Martin & Kauffman (1979). From our helicopter overflights, the ice in this region was diffuse and divergent. The floes were generally broken, with diameters of 20-100 m and with little pressure ridging. The ice consisted of a mixture of two broad types: grey-white ice with a 0.2 m thickness, and white ice with a 0.6 m thickness. From our aerial photographs we estimate the ice concentration here at 60%, which is consistent with the SMMR results.

4.4 25 March (days 84, 85)

As section 2.1 describes, beginning 20 March a large low pressure system in the southern Bering Sea caused a weather pattern shift from cold northeast to warm southerly winds (Figure 2d). Because of this change, the Tiros imagery from 20 to 25 March showed only clouds. Figure 17a (75:0124) shows the first clear image of the ice during this weather condition. Figure 17a and the derived ice map in Figure 17b show that the warm southerly winds during this period caused a large melt-back of the sea ice, so that an open water region now extends almost into Norton Sound.

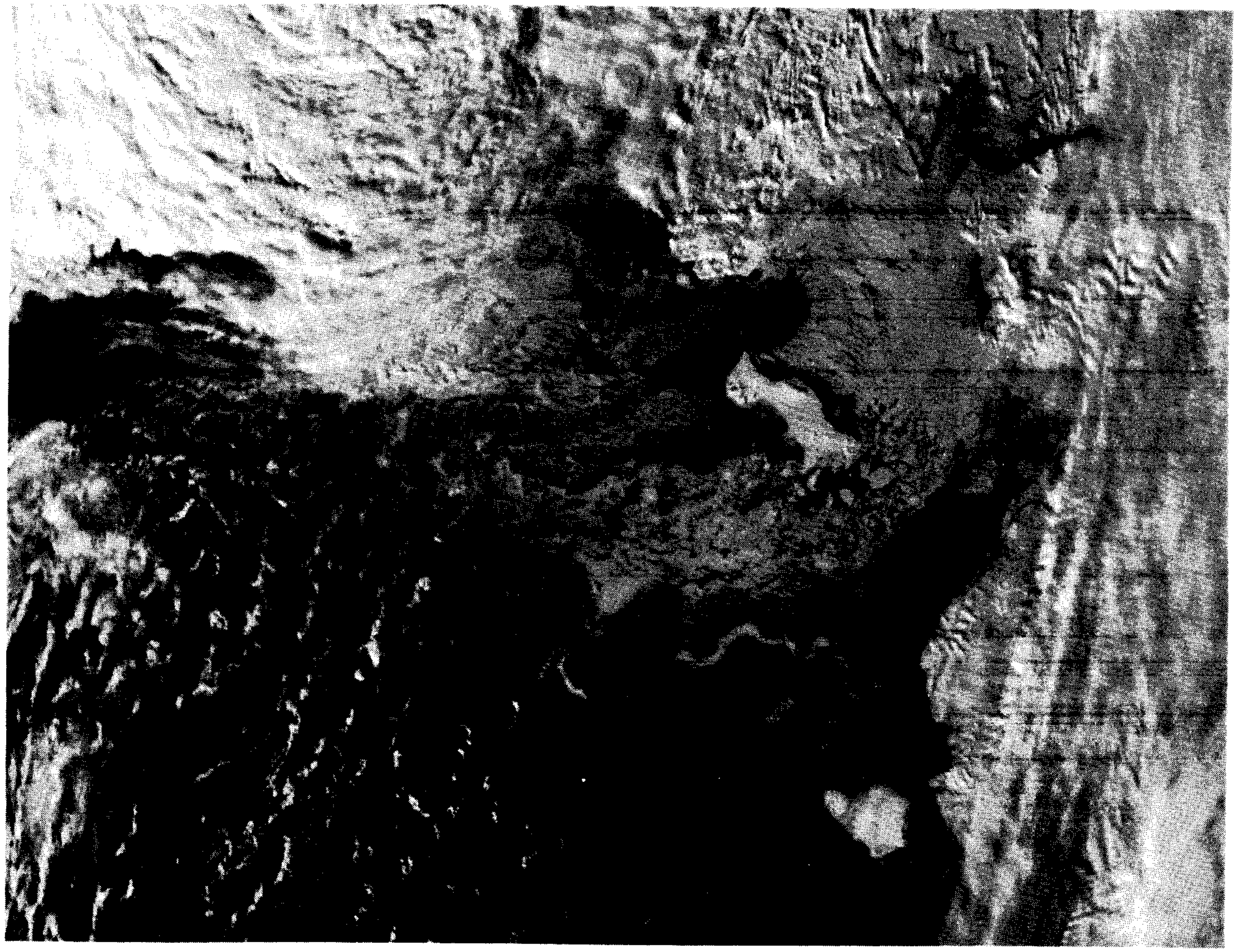

Figure 17a. Tiros image for 25 March (85:0124).

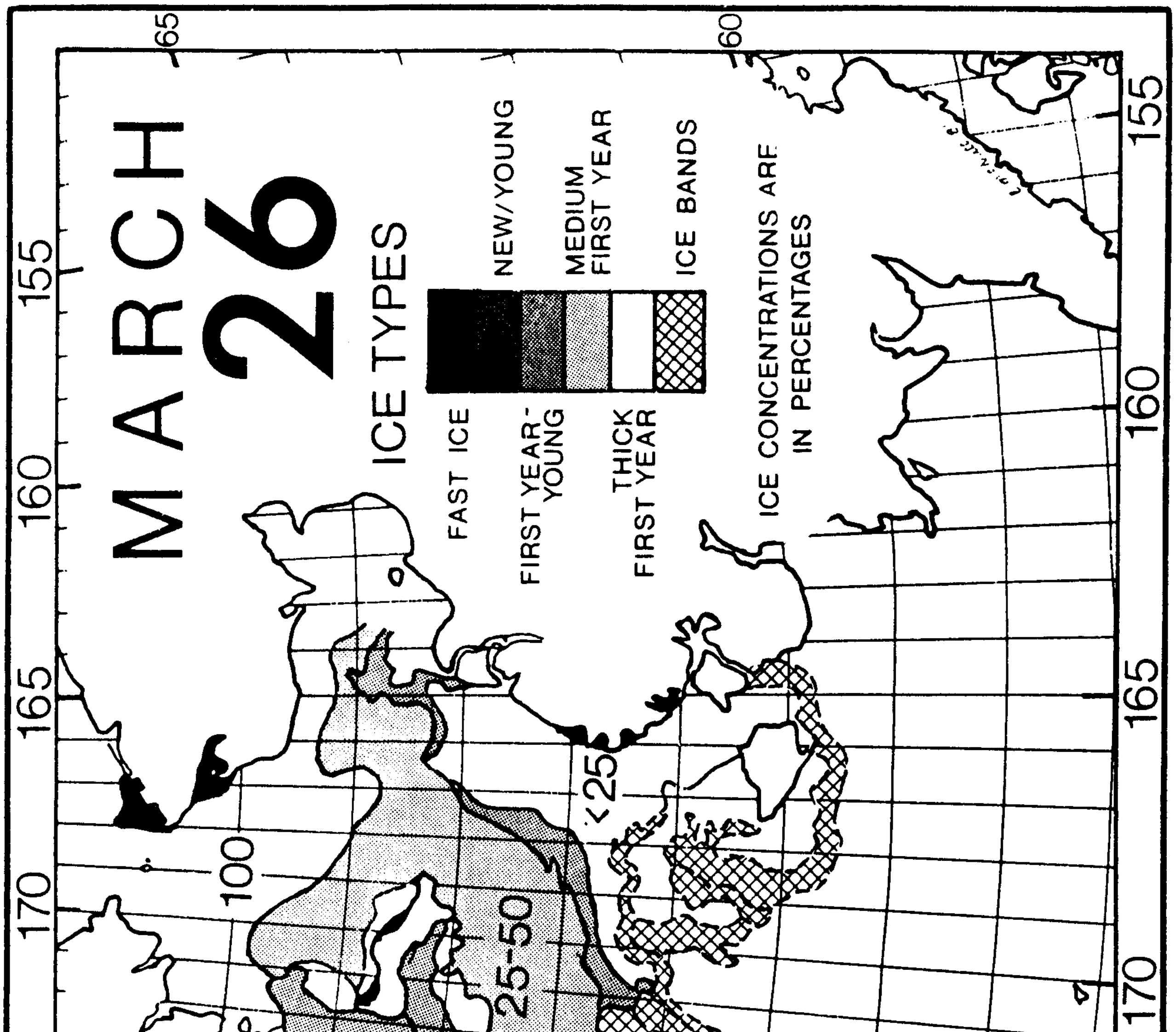

Figure 17b. Ice chart derived from Figure 17a.

Figure 18 shows the SMMR ice chart. As Table 1 shows, the SMMR image precedes the Tiros image by only 3.5 hr, so that the two are nearly simultaneous. The letters on the SMMR image again mark areas of correspondence between the two images. First, the main ice edge "A", as shown by the location of the high gradient region, now extends north into Norton Sound. Second, "B" marks the open water region adjacent to the coast shown in Figure 17a where, because of land contamination, the contours adjacent to the coast show an unobserved ice concentration increase. Third, continuing with the open water regions, "C" marks the open water area north of Nunivak Island, and the elliptical 45% minimum contour marked by "D" is centered on the long narrow open water feature southwest of St. Lawrence Island. The long axis of the ellipse is nearly parallel to the axis of the open water feature, where the small lateral scale of the physical feature increases the apparent SMMR concentration. Similarly, "E" marks a more rectangular polynya north of the west end of St. Lawrence Island; and the concentration decrease marked by "F" shows the cloud-obscured coastal polynya in the Gulf of Anadyr.

Fifth, "G" marks the 95% concentration region immediately south of the Bering Strait, where the southerly winds have created a high concentration ice jam. Also in this region, the 85% contour approximately follows the boundary between the thick and medium first-year ice shown in Figure 18. Finally, the 45-55% contour lines to the northwest of Nunivak Island correspond to the diffuse ice features in this region.

5. CONCLUDING REMARKS

The preceding discussion shows that, for the case of the Bering Sea in March, the high resolution SMMR channel produces uniformly good data

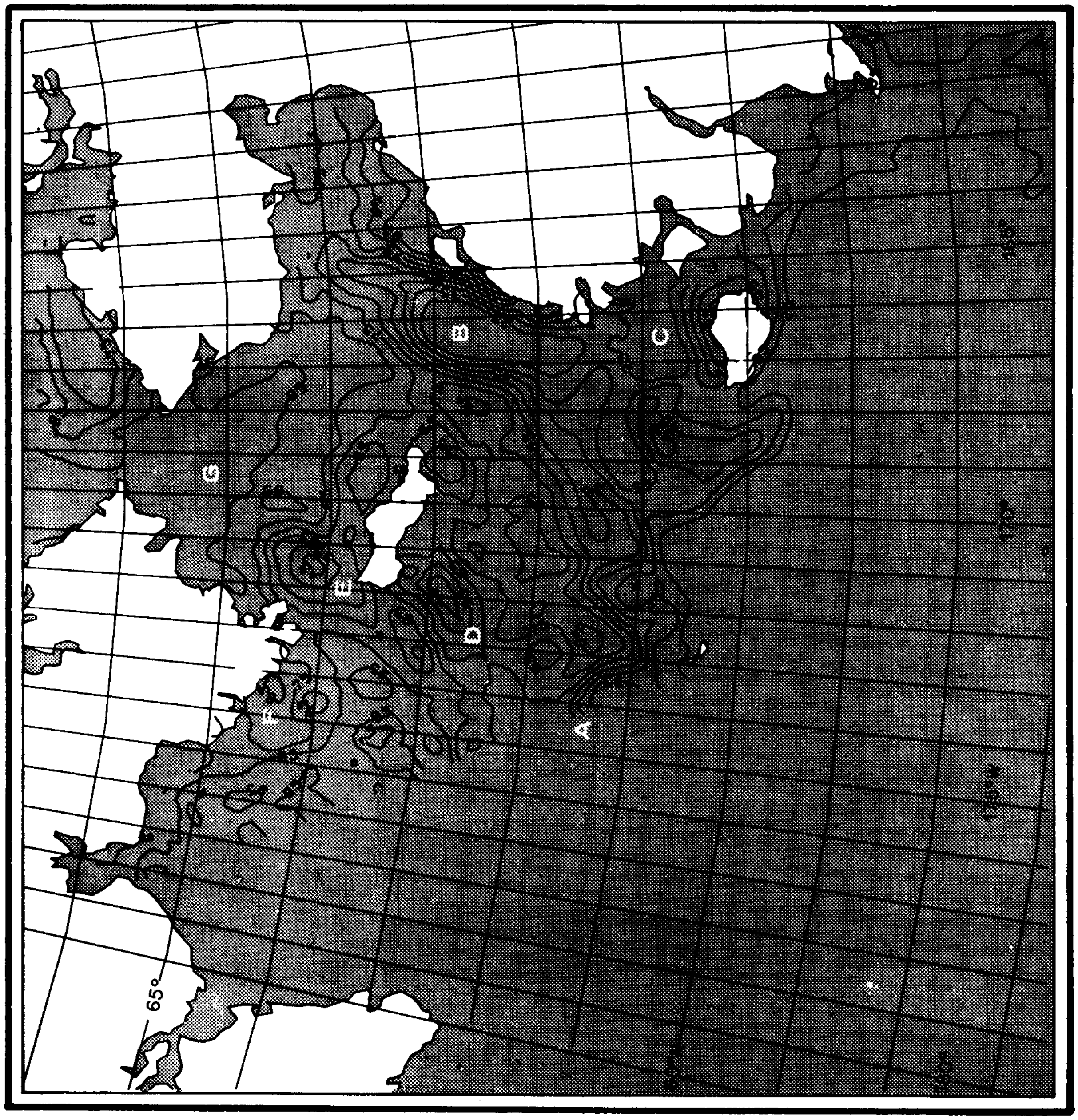

Figure 18. SMMR ice chart for day 84:2149. See text for further description.

regardless of weather. For each case, the SMMR mapped out the ice edge and the low and high concentration interior regions with an accuracy equal to that of the derived ice charts. The only major difficulty in this algorithm comes from our lack of knowledge about thin ice emissivities, a lack which may produce some of the unrealistically low concentration values observed for thin ice. The other difficulty is that of land contamination, which can be anticipated. Finally, we hope that this work stimulates future work on both the measurement of thin ice emissivities and the application of this algorithm to other regions of first year sea ice such as the Labrador Sea and the Antarctic Ocean.

6. ACKNOWLEDGMENTS

This report received help and support from numerous sources. In particular, we thank Mr. William Abbott of NASA-Goddard for his help with the numerical work, Mr. K. F. Huemmrich of the Computer Sciences Corporation for implementing the SMMR ice algorithm, and Mr. Hugh Powell of Sigma Data Corporation for overcoming many of the technical difficulties in generating the final SMMR ice contour plots. We are also very grateful to the P-3 ice observer Lieutenant (jg) Daniel E. Munger and the pilot and crew of the Navy P-3, and to Captain James G. Grunwell and the officers and crew of the NOAA ship SURVEYOR. We also thank Ms. Carol Pease, who organized the weather data compilation cited in the text, arranged for the ice observer overflights, and provided help and encouragement in our analysis of the Bering Sea field data, and Dr. William Campbell, who provided valuable help with the early stages of this work. We further thank Ms. Frances Parmenter-Holt of the National Environmental Satellite Services field office in Anchorage for providing the satellite imagery, and Mr. Bruce Webster, who is the Alaska Regional

Ice Forecaster at the National Weather Service in Anchorage for providing ice advisories during the cruise.

During the period of this research, S. Martin gratefully acknowledges the support of the Department of Commerce Spacecraft Oceanography (SPOC) Group under contract MO-A01-00-4335, and thanks Dr. John Sherman and Mr. Henry Yotko for their encouragement and support. For the field portion of this work, he also acknowledges the support of the BLM/NOAA Outer Continental Shelf Program through Contract NA81RAC000-13. S. L. McNutt also acknowledges both the support of the SPOC group through Contract MO-A01-78-00-4335, and the support of NASA Contract NAG5-161. Finally, D. Cavalieri acknowledges support received from the NASA Oceanic Processes Branch under RTOP 146-40-08.

7. BIBLIOGRAPHY

Bauer, B.J. and S. Martin. 1980. Field observations of the Bering Sea ice edge properties during March 1979. Mon. Wea. Rev. 108:2045-56.

Gloersen, P. and F. Barath. 1977. A scanning multichannel microwave radiometer for Nimbus G and Seasat. IEEE J. Oceanic Engr. OE-2:172-78.

Gloersen, P., Wilheit, T.T., Chang, T.C., and W. Nordberg. 1974. Microwave maps of the polar ice of the earth. Bull. Am. Meteorol. Soc. 55:1442-48.

Gloersen, P., Zwally, H.J., Chang, A.T.C., Hall, D.K., Campbell, W.J. and R.O. Ramseier. 1978. Time-dependence of sea ice concentration and multiyear ice fraction in the Arctic Basin. Bdry. Layer Met. 13:339-59.

Martin, S. and P. Kauffman. 1979. Data Report on the Ice Cores taken during the March 1979 Bering Sea ice edge field cruise on the NOAA ship SURVEYOR. Special Report Number 89, Department of Oceanography (Department of Oceanography WB-10, University of Washington, Seattle WA 98195).

McNutt, S.L. 1981. Remote sensing analysis of ice growth and distribution in the Eastern Bering Sea. In: The Eastern Bering Sea Shelf: Oceanography and Resources, Volume One (Ed: Hood, D.W. and Calder, J.A.), National Oceanic and Atmospheric Administration, United States Department of Commerce, 141-66.

Pease, C.H. 1980. Eastern Bering Sea processes. Mon. Wea. Rev. 108:2015-23.

Salo, S.A., Pease, C.H. and R.W. Lindsay. 1980. Physical Environment of the Eastern Bering Sea, NOAA Technical Memorandum ERL PMEL-21, Pacific Marine Environmental Laboratory, Seattle WA, 119 pp.

Squire, V.A. and S.C. Moore. 1980. Direct measurement of the attenuation of ocean waves by pack ice. Nature, 283, No. 5745, 365-68.

Zwally, H.J., and P. Gloersen. 19771 Passive microwave images of the polar regions and research applications. Polar Record 18:431-50.

Appendix A. Verbatim Report of the P-3 Ice Reconnaissance Flight on 3 March 1979 (day 62)

AERIAL ICE RECON BERING SEA

1. RADAR ICE EDGE FM 6120N/17540W, TO 6124/17536, TO 6100/17440, TO 6102/17435, TO 6059/17415, TO 6033/17406, TO 6032/17330, TO 6024/17328, TO 6030/17320, TO COAST 6030N/17255W.

CONTINUING EDGE AT 6020N/17215W, TO 6024/17155, TO 6015/17135, TO 6012/17148, TO 5955/17135, TO 5958/17120, TO 6110/17112, TO 5950/17102, TO 5950/17050, TO 5955/17045, TO 5940/17050, TO 5938/17101, TO 5936/17115, TO 5934/17045, TO 5932/17102, TO 5931/17035, TO 5924/17040, TO 5921/17035, TO 5922/17025, TO 5920/17025, TO 5915/17015, TO 5858/17008, TO 5858/16958, TO 5840/16935, TO 5842/16930, TO 5830/16815, TO 5828/16812, TO 5826/16755, TO 5822/16735, TO END OF TRACK AT 5814N/15950W.

2. TRACK FEATURES - SOUTHEAST TO NORTHWEST PORTION OF FLIGHT TRACK STRESSED VISUAL OBSERVATION OF PACK ICE GENERALLY 10-1 NM WITHIN THE ICE EDGE. NORTHWEST TO SOUTHEAST LEG WAS FOR DETAILED POSITIONING OF THE ICE EDGE BY VISUAL/RADAR OBSERVATION. THE FOLLOWING REPRESENTS A SYNOPOSIS OF SIG FEATURES ALONG, AND 10-1 5NM WITHIN THE BERING SEA ICE EDGE BETWEEN 16615W AND 17550W:

A) PREDOMINANT CONCENTRATION OF SURFACE COVERAGE OBSERVED -05-06 OKTAS

B) PREDOMINANT STAGES OF DEVELOPMENT - (BY PERCENT)

55 - GREY/GREY WHITE

40 - NEW/YNG

05 - FIRST YEAR THIN (IN EXCESS OF 12 INCHES IN THICKNESS)

C) PREDOMINANT FORM OF ICE TOPOGRAPHY - (BY PERCENT)

70 - RAFTING

30 - NEW RIDGES

MAXIMUM OBSERVED RIDGES - 1 METER

D) PREDOMINANT FORMS OF ICE - (BY PERCENT)

40 - NEW ICE

30 - SMALL/MEDIUM FLOE

25 - BRASH/CAKE

05 - BIG, VAST, GIANT FLOE

3. SIGNIFICANT AREAS OF INTEREST -PARA 2 REPRESENTS THE GENERAL DESCRIPTION OF ICE ALG TRACK/WITHIN EDGE. FOLLOWING GIVES SPECIAL INTEREST AREAS DURING FLT:

A) HEAVIEST/THICKEST ICE WITHIN 10NM RADIUS OF 5952F/170W. FIRST YR THIN WITH 30 PERCENT 1M NEW RIDGES

B) AREA OF LARGEST OBSERVED FLOES -WITHIN EDGE BETWEEN 16850W AND 16950W -25 PERCENT BIG/VAST FLOES.

C) AREA OF GREATEST CONCENTRATION - WITHIN EDGE BETWEEN 17245W AND 17530W - GENERALLY 07-08 OKTAS.

D) YOUNGEST/THINNEST ICE -01-05 NM ADJACENT EDGE ALG ENTIRE TRACK - MOSTLY NEW ICE, NILAS, PANCAKE.

4. LOCALLY HIGH SURFACE WINDS ALG TRACK CAUSED CONSIDERABLE STRINGS OF ICE 02-05NM ADJACENT HVY PACK AT SLIGHT RIGHT ANGLE TO WIND.

5. FLIGHT ADAK TO ADAK 6 PT ZERO HRS. LTJG MUNGER/AGC DAMICO SEND. NEXT SKED FLIGHT 08 OR 09 MARCH 79.

Appendix B. Verbatim Report of the P-3 Ice Reconnaissance Flight on 9 March 1979 (day 68)

AERIAL ICE RECON 08 MARCH 79

1. RADAR ICE EDGE FM 6024N/17527W TO 6033N/17535W, 6037N/17530W, 6035N/17523W, 6025N/17522W, 6033N/17518W, 6030N/17510W, 6046N/17355W, 6040N/17355W, 6037N/17400W, 6032N/17355W, 6035N/17345W, 6037N/17345W, 6037N/17335W, 6042N/17330W, TO COAST 6031N/17303W, RESUMING COAST 6019N/17237W, 6022N/17305W, 6024N/17410W, 6009N/17410W, 5956N/17340W, 5951N/17318W, 5947N/17245W, 5947N/17220W, 5920N/17127W, 5928N/17120W, 5933N/17055W, 5912N/17002W, 5855N/17005W, 5842N/16948W, 5839N/16900W, 5827N/16828W, 5812N/16805W, 5804N/16730W, 5828N/16600W END EDGE.

2. TRACK FEATURES; SOUTHEAST TO NORTHWEST PORTION OF FLIGHT TRACK STRESSED VISUAL OBSERVATION OF PACK ICE GENERALLY 15-50NM WITHIN THE ICE EDGE. NORTHWEST TO SOUTHEAST LEG WAS FOR DETAILED POSITIONING OF ICE EDGE BY RADAR OBSERVATION. THE FOLLOWING REPRESENTS A SYNOPSIS OF SIG FEATURES ALONG AND 15-50NM WITHIN THE BERING SEA ICE EDGE BETWEEN 167W AND 176W.

A) PREDOMINANT CONCENTRATION ALONG TRACK 15-25NM WITHIN ICE EDGE BTWN 167W AND 16930W 07-08 OKTAS. UNDERCAST ALONG TRACK BTWN 16930W AND 17145W. ALONG TRACK GENERALLY 25-50NM WITHIN EDGE BTWN 17145W AND 176W GENERALLY 08 OKTAS WITH SCTD FRACTURES BTWN FLOES.

B) PREDOMINANT STAGES OF DEVELOPMENT (BY PERCENT) ALONG TRACK 15-25NM WITHIN ICE EDGE BTWN 167W AND 16930W: 80 GREY/GREY WHITE
10 FIRST YR THIN
10 NEW

ALONG TRACK 25-50NM WITHIN ICE EDGE BTWN 16930W AND 176W:

(BY PERCENT): 30 FIRST YR THIN/MEDIUM

15 GREY/GREY WHITE

05 NEW

C) PREDOMINANT FORM OF ICE TOPOGRAPHY ALONG TRACK WEST OF 16930W-NEW AND WEATHERED RIDGES - MAX HEIGHT 2M. ALONG TRACK EAST OF 16930W - NEW RIDGES AND RAFTED ICE - MAX HEIGHT 1M.

D) PREDOMINANT FORMS OF ICE 15-50NM WITHIN ICE EDGE 9BY PERCENT

15 NEW ICE

15 BRASH/CAKE

40 SMALL/MEDIUM FLOE

30 BIG/VAST/GIANT FLOE

3. SIGNIFICANT AREAS OF INTEREST-PARA 2 REPRESENTS THE GENERAL DESCRIPTION OF ICE ALONG TRACK EAST AND WEST OF 16930W. FOLLOWING GIVES SPECIAL INTEREST AREAS DURING FLIGHT.

A) HEAVIEST/THICKEST ICE VICINITY FOLLOWING LINE: 6103N/17338W, TO 6109N/17353W, 6120N/17423W, 6133N/17452W, 6144N/17520W, TO 6155N/17548W. ICE GENERALLY FIRST YR MEDIUM (IN EXCESS 28 INCHES).

B) AREA OF LARGEST OBSERVED FLOES VICINITY LINE DESCRIBED PARA ABOVE-MOSTLY BIG/VAST/GIANT FLOE WITH RIDGING 1-2M.

C) AREA OF GREATEST CONCENTRATION WITHIN 10NM RADIUS OF 6139N/17509W FIRST YR MEDIUM, COMPACT PACT, 9/8 CONCENTRATION, WITH 2M RIDGING THRUOUT.

5. FLIGHT ADAK TO ADAK SIX PT NINE HRS. SEVERE ICING AT LO LVL PRECLUDED LOITER FOR VISUAL OBSERVATION ALONG SOUTHERN ICE EDGE. HI LVL RADAR ANALYSIS INDICATES LARGE OPEN WATER AREAPTO WEST-SOUTHWEST OF ST MATHEW ISLAND. CONTINUED SUCCESS DURING YOUR SURVEY.

PERSISTENCE OF SPILLED OIL ALONG THE BEAUFORT SEA COAST

by

Dag Nummedal

Department of Geology
Louisiana State University

Final Report
Outer Continental Shelf Environmental Assessment Program
Research Unit 540

April 1980

TABLE OF CONTENTS

LIST OF TABLES

1. INTRODUCTION

1.1 Objectives

The research project for which this is the final report was initiated in 1977 with the following three major objectives:

1. Assess the retention potential for spilled oil within the coastal environments of Alaska's Beaufort Sea.

2. Characterize the morphology and sediments of the Beaufort coast.

3. Determine, as precisely as possible, the annual longshore sediment transport rate.

1.2 Oil spill retention potential

This final report presents an assessment of the oil spill problem. The results are presented in the form of 30 maps prepared at an original scale of about 1:50,000 and then reduced for presentation in this report to a scale of approximately 1:125,000.

To compile these maps the entire Alaskan coast from Pt. Barrow to Demarcation Pt. was sampled, photographed and described during the summers of 1977 and 1978. The primary data sources used in the compilation consisted of ground sample stations, spaced about 5 NM apart, nearly continuous oblique aerial photography obtained by the investigators from low-flying aircraft, detailed descriptions read on tape while flying, vertical aerial photography from commmercial sources, coastal charts from the National Ocean Survey, and U.S. Geological Survey topographic maps.

The chosen map scale permits the differentiation of shoreline categories at a spatial resolution of 200 meters. In addition to delineating the spatial distribution of different shoreline categories, the maps also present the frequency distribution of the eight retention classes within each area. These frequency distributions provide a useful summary of the regional variability in oil spill sensitivity along the Beaufort coast.

1.3 Coastal morphology and sediments

As demonstrated in the discussion of oil spill retention, both grain size and profile of the beach significantly influence the potential for oil entrapment. Both parameters are directly incorporated into the classification scheme used for the maps. Additionally, all the profile and grain size data are enclosed as data appendices to this report. An interpretation of the grain size statistics was presented in the 2nd quarterly progress report, of January 1978.

1.4 Sediment transport studies

This part of the study addresses the magnitudes and frequencies of marine events responsible for coarse sediment transport, as well as field observations and theoretical calculations on sediment transport due to wave-generated longshore currents. The results were presented at the 5th Conference on Port and Ocean Engineering under Arctic Conditions in August, 1979. A reprint of the paper published in the proceedings of that meeting is enclosed (Nummedal, 1979).

POTENTIAL IMPACT OF THE OILSPILL PROBLEM

2.1 General

During the last two decades, we have become accustomed to large oil spills in nearly all parts of the world. Spills occur as results of tanker collisions (Netherland's Antilles, July 1979), well blow-outs (Gulf of Campeche, July, 1979; North Sea, April 1977), tanker groundings (Brittany, March 1978; northwest Spain, May 1976), ruptures of shore-based tanks and pipelines and accidents at refineries and tanker terminals. Additionally, the single largest source is river and urban runoff which account for 31 percent of all spilled oil introduced into the environment (Nat. Acad. Sci. 1975). Containment and clean-up procedures are generally totally inadequate. Consequently, major oil spills have caused significant detrimental impacts on the environment, often accompanied by severe economic losses to a population dependent on marine and coastal resources.

In the arctic, in particular, the chances of effectively containing and removing sizeable portions of a spill are presently very low (Logan, in NOAA, 1978). Also because the growing season in arctic ecosystems is very short, anything which interferes with the primary productivity during this brief period can have very serious and long-lasting effects.

In recognition of the sensitivity of the arctic marine ecosystem to the consequences of both planned activities and accidents related to petroleum development along the Alaskan Beaufort coast, a wide spectrum of environmental studies have been conducted under the general auspices of the National Oceanic and Atmospheric Administration. This program has supported studies on the oceanography, geology, biology and chemistry of the arctic shelf and littoral regions. In addition, interdisciplinary aspects of the impacts of development in the arctic have been addressed both in specific studies and in discussions at the OCSEAP "synthesis meetings" held at the Naval Arctic Research Laboratory.

2.2 Environmental Impacts of Oil Development

The OCSEAP synthesis discussions identified a series of environmental implications of oil development (NOAA, 1978). Of significance in the context of this report are the possible effects of large oil spills. It was recognized that sensitivity to oil spills could be defined both in terms of species sensitivity, as when a particular species of bird or animal could be adversely affected by the spill without any significant damage to the habitat, and in terms of sensitive habitats, as when the ability of a specific geographic area to support its fauna and flora is impaired. Species sensitivity is discussed in some detail in the synthesis report (NOAA, 1978). This report will address only aspects of the concept of sensitive habitats. Such areas are considered those where biological productivity is high and where the introduction of a foreign substance like oil would directly impair the activities of many species and damage the chain of trophic interactions.

Although habitat sensitivity is a biological concept, the primary environmental controls on the habitat are provided by the geological substrate and the dominant physical process to which it is subjected. For example, the many marshes along the Beaufort coast are highly sensitive habitats. The marshes have formed in coastal locations of low topography, poor drainage and a fine-grained substrate. Generally, they are sheltered from the direct attack of waves by barrier islands, spits or tundra remnants. For this reason, a quite useful practical assessment of the sensitivity of a coastline to oil spill impact can be based on the sedimentary environments of the inter-and supratidal zone.

The primary habitat-effects of a significant oil spill in the arctic are expected to include (NOAA, 1978, p. 295):

- eventual accumulation of large amounts of oil on beaches;
- long-term re-release into the marine system from beaches and sediments;
- incorporation of non-volatile components into sediments;
- concentration of oil in leads, cracks and other openings in the sea ice;
- long-term entrapment and entrainment of oil by ice;
- long-term floating oil slick.

Of these primary effects, the first three are directly dependent on the morphology and sedimentary characteristics of the litttoral zone and the energy levels of the dominant physical processes within the individual environments (habitats).

3. OIL SPILL RETENTION CATEGORIES

3.1 General

Hayes et al. (1976) introduced the concept of shoreline classification with respect to oil spill vulnerability. In their classification each shoreline segment was assigned a vulnerability index; in part based on the physical energy level of the environment, in part based on observed longevity of hydrocarbon accumulations following the Metula spill in the Strait of Magellan, Chile (Hayes and Gundlach, 1975) and the Urquiola spill in Spain (Gundlach and Hayes, 1977). Their ten shoreline categories range form straight, rocky headlands (vulnerability index = 1, lowest) to protected estuarine salt marshes (vulnerability index = 10, highest).

The environmental classification of the coastal zone of the Beaufort Sea departed from this scheme in two respects. (1) The index is called a retention index, because it represents in fact a measure of the persistence of stranded oil; there is no assessment of the potential biological effects of that stranded oil. As discussed, the persistence of spilled oil in a given environment correlates with, but is not identical to, a biological measure of habitat sensitivity. (2) The coastal environments of the arctic differ significantly from those of temperate latitudes; therefore, a complete categorization of the Beaufort Sea coast required the consideration of shoreline types not included in the original Hayes et al.(1976) scheme.

As pointed out by Owens (1978) the environmental impact of an oil spill varies with the type of oil, the volume of stranded oil, the air/water temperature and the shoreline morphology and sediments (Table 1). There may exist a wide range of combination of these four factors; for any given spill, however, the first three are relatively constant and only shoreline type will vary significantly over the area of spill impact.

In this report shoreline types have been classified in eight categories in terms of the magnitude of the energy of the mechanical factors which tend to remove stranded oil relative to the ability of in situ factors in the environment to retain the oil.

Table 1. Persistence factors for stranded oil (from Owens, 1978, p. 58).

TYPES OF OIL	THICKNESS OF OIL ON SHORE SURFACE	DEPTH OF OIL PENETRATION	WAVE ENERGY LEVEL AT SHORELINE	AIR TEMPERATURE		EXPECTED PERSISTENCE
Light Volatile	Very thin (<1.0cm)	All oil exposed on shore surface	High energy levels; Exposed coast	High (>25°C)		Days/weeks
↓	↓	↓	↓	↓	↓ INCREASING PERSISTENCE	↓
Tarry	Thick (>10.0cm)	All oil buried below beach surface	Low energy levels; Totally sheltered coast	Low (<0°C)		Decades

A discussion of the role of each pertinent factor within any given category of Beaufort coast follows. Table 2 summarizes the applied classification scheme. Photographs illustrating the typical coastal morphology of each category are presented in Appendix A.

3.2 Steep cliffs (Retention index: 1)

Morphology. Because there are no bedrock outcrops along the Beaufort coast, steep cliffs are restricted to shoreline exposures of ice-bonded permafrost. These cliffs are thermally unstable and subject to high rates of retreat. Cliff collapse generally occurs through a combination of undercutting by wave notching, mechanical failure of the ice-bonded block, and ice melting. Along exposed shorelines the released material is immediately removed by wave action, maintaining a vertical cliff. Retreat rates can be as high as 20 m/yr (Owens et al. 1980).

Impact. Along the virtually tideless Beaufort coast the oil would, at worst, coat only a narrow band of a vertical cliff. During storms the combination of a surge and wave splash could coat the cliff a few meters above mean sea level. It is commonly observed, however, that strong wave reflection occurs in front of these steep cliffs during high wave energy conditions. The reflected waves may keep the oil offshore (Gundlach and Hayes, 1977; Owens, 1978).

Table 2. Oil spill retention potential for different environments of the Alaskan Beaufort Sea coast.

Environment	Retention Index	Level of mechanical degradation	Efficiency of retaining factors
Steep cliffs	1	High	Low
Steep beaches and bluffs of unconsolidated sediments	2	High	Moderate
Exposed non-vegetated barriers	3	High	Moderate
Vegetated low barriers	4	Moderate	Moderate
Lagoon-facing mainland shores	5	Moderate	Moderate
Peat shores	6	Low	High
Sheltered tidal flats	7	Low	High
Marshes	8	Low	High

Persistence. Oil trapped on the cliff face will rapidly flow down and re-enter the nearshore water as a result of rain wash, cliff melting and retreat. No oil would be retained over long time periods. Some oil stranded in crevices or sprayed onto the tundra mat on top of the cliff during a violent storm could persist for long periods.

Protection. In general, protection of this shoreline type would not be of high priority. If protection should be desired the only effective means would be offshore oil containment and removal.

Clean-up. As indicated, these cliffs would generally be self-cleaning. Oil accumulated in crevices and pools on the tundra surface would have to be manually collected.

3.3 Steep beaches and bluffs of unconsolidated sediments. (Retention index: 2).

Morphology. Steep, narrow beaches generally exist in front of unconsolidated cliffs of tundra. The dominant size fraction of sediment in the tundra cliff will control the nature of the beach. If silt and clay dominate there may be no beach as the fines are continuously removed in suspension. This is a common situation along the Beaufort coast west of the Kuparuk River delta where the dominantly fine-grained Gubik Formation outcrops along the shoreline. In front of sandy and gravelly bluffs, sand and gravel beaches will occur. In general, the bluffs to the east of Prudhoe Bay are composed of coarse sediment. Local pockets of Flaxman Formation outcrops (Leffingwell, 1908) generally provide a coarse beach (boulder beach) backed by steep cliffs. Leffingwell himself mapped these boulder patches almost exclusively to the east of the Kuparuk River. Subsequent investigations by Lewellen (1978), and the sampling carried out for this study, have identified numerous Flaxman boulder areas further west. The second source of coarse sediment along the eastern Beaufort coast are the numerous Pleistocene braided stream deposits now being truncated by an actively retreating shoreline. The best example of this would be the northern bluffs at Barter Island, immediately north of the DEW-line station.

Impact. The grain size of the beach will determine oil penetration. Only light oils can penetrate sand. Maximum penetration will be a few centimeters. Even medium and heavy oils can penetrate gravel, perhaps by as much as a meter. In spite of these differences, the steep shorelines are all grouped together and characterized by a low retention index because (a) the width of the coastal zone impacted by a potential oil spill will be narrow, (b) steep cliffs occur in high-energy zones where natural removal is effective, and (c) wave reflection during storms might be quite effective in keeping some oil away from the beach.

Persistence. The retreat rate of unconsolidated bluffs would not be as high as that of vertical ice-bonded permafrost cliffs. Nevertheless, a retreat rate in excess of a meter per year would be expected (Cannon, 1978). Therefore, even in the case of deep oil penetration into gravel, the oil-stained sediment would in all probability only have a residence time of one or at most, a few years. Oil on the face of the bluff would easily be removed by wave spray, rain wash or gravity slumping.

Protection. The only effective method of protection would be offshore oil containment.

Cleanup. Manual clean-up would be effective on sandy beaches. The bluff should be left to natural self-cleaning. Hydraulic flushing, which generally is recommedned for rocky cliffs and headlands (Owens, 1978), would cause erosion of the unconsolidated tundra bluffs and further mix oil and sediment on the beach face.

3.4 Exposed, Non-vegetated barriers (Retention index: 3).

Morphology. The large majority of the Holocene barrier spits and islands along the Beaufort coast are non-vegetated. The islands typically are of low relief, subject to occasional complete surface sedimentary reworking by storm tide overwash and ice push. Magnitudes and frequencies of these events are discussed in Nummedal (1979). The Beaufort barriers are gravelly, or of mixed sand and gravel composition. Most temperate and tropical barriers are sandy. Reimnitz (1979) attributes this difference to strong wind-depletion of sand from the unprotected arctic barriers. Other mechanisms are also possible. Shoreline retreat rates are high, 3 to 7 meters per year appear to be typical (Dygas et al., 1972).

Impact. The impact of a potential oil spill on an arctic barrier island would differ significally from impacts in warmer climates. The coarse sediments would permit deeper penetration for any grade of spilled oil. The low relief would generally cause a wide impact area. These are the two primary factors tending to retain the oil on arctic barriers. They are both quite effective. Economic impact would be negligible because of the non-commercial utilization of Beaufort barriers. Also, the biological impact of an oil spill on the subaerial non-vegetated barrier would be minimal, because such barriers generally have a very low species density.

Persistence. All non-vegetated barriers satisfy the impact criteria just described. Only the exposed barriers, however, are subject to high-energy wave conditions. The general absence of low-tide terraces, and protected berm top areas, further differentiate the Beaufort barriers from the mixed sand and gravel beaches of high retention potential described by Hayes et al. (1976, p. 84). The shoreline retreat rates, efficiency of overwash, and intense ice-push will make it unlikely that significant amounts of spilled oil will be retained on a Beaufort barrier more than a year. Exceptions to this may be found in local back-barrier swales.

Protection. Most Beaufort barriers form the outer boundary of large shallow-water lagoons. The critical consideration if a spill drifts toward such a barrier island chain, therefore, is to prevent oil from entering the lagoonal area. Protective efforts through the use of containment booms and skimmers should be focused on the tidal entrances. The barriers form natural "booms"; their oil-stained beaches will probably cleanse themselves within a year.

Cleanup. Given the short residence time for barrier beach oil here predicted, no large-scale cleanup can be recommended. Local manual cleanup could be effective on short sections of sandy barrier beach. For the gravelly barrier beaches, the geological and ecological damage due to large-scale sediment removal would, in most cases, far exceed the damage done by the initial impact of oil.

3.5 Vegetated low barriers (Retention index: 4).

Morphology. This category refers to those Holocene barriers with some back-barrier sections old enough to have developed a vegetative mat of mosses and grasses, and perhaps a permafrost core. Islands with Pleistocene tundra remnants would generally have a much lower retention index (1 or 2) because their exposed shores will be steep, partly ice-cored, bluffs.

Included in this category are also those low, flat beaches which grade landward into tundra, as well as perched beaches on top of the tundra. Sheltered tidal flats (generally with a retention index of 7) are included in this retention category if their margins are protected by large dunes which would limit the landward penetration of an oil spill.

Impact. The impact on a barrier in category 4 would be more severe because vegetation is generally associated with a highly productive ecological niche. Bird nesting grounds are widespread on vegetated barriers. The other impact factors would correspond to those discussed in category three.

Persistence. Oil persistence would be greatly increased over non-vegetated barriers for tow reasons: (a) the presence of vegetation would provide a greatly increased surface area to which the oil could adhere, (b) the very presence of vegetation demonstrates infrequent water flushing of ice-push. Once oil has entered a vegetated back-barrier or back-beach environment it could persist for many years until removed by processes of biological rather than mechanical degradation.

Protection. Oil could enter vegetated back-barrier environments either through storm overwash from the ocean beach, or through flooding by water from an oiled lagoon. The latter would probably be the most common occurrence. Therefore, the best protection would be to block oil entrance through the tidal passes.

Cleanup. Pools of standing oil could be pumped out. Oil-stained vegetative matter should be left to biological degradation. The use of heavy equipment should be kept to an absolute minimum, because a mechanical disruption of the tundra surface may have far more serious long-range environmental effects than the oil.

3.6 Lagoon-facing mainland shores (Retention index: 5).

Morphology. This category incorporated a wide range of shoreline morphologies, yet they are all exposed to only moderate wave action. They are assigned the relatively high retention index of 5. Numerous examples of mainland beach morphology are depicted in Appendix A.

Most commonly one finds a sand, or mixed sand or gravel, beach. The beach is a few meters wide in front of a thermally retreating tundra bluff. Retention index 5 is used on maps only where the tundra bluff is high enough to prevent oil penetration further inland. In areas of low bluffs or no bluffs a higher retention index applies.

In other areas the lagoonal mainland shore is a zone of collapsed tundra, with sod-covered blocks forming a jumbled transition from the unbroken tundra surface to the lagoon.

A third type of lagoonal mainland shore would be a flat platform, generally muddy or sandy, with a surface layer of large boulders.

The wave energy directly relates to the longshore sediment transport and shoreline retreat rates. Transport rates along the mainland shore at Oliktok Pt. (Dygas and Burrell, 1976) appear to be about one order of magnitude less than those on the exposed sections of the mainland or the barrier islands (Nummedal, 1979). Measured retreat rates of the mainland shore are highly variable. From Demarcation Point to the Colville River the rate averages about 1.6 m/yr. Further west, the retreat rate may be significally higher (NOAA, 1978).

Impact. Oil deposited on the lagoonal beaches would initially have no more impact than that on exposed beaches with a retention index of 2. Due to low wave energy the removal would be quite slow, however. Oil from lagoonal beaches could be re-released into the marine environment over a period of years after the initial impact. Furthermore, the low wave energy of the lagoon prevents the development of long, uninterrupted beaches. Along the mainland shore there is a high frequency of river mouths, small tidal inlets, marsh entrances, coves and low organic-rich bluffs. Oil re-released from lagoonal beaches at any time after the initial impact would be free to enter any of these environments in the absence of continuous human monitoring and protection.

Persistence. Because of the low transport rates, the moderate shoreline retreat rates, and the irregularly embayed nature of the lagoonal mainland beach, oil introduced into this environment would be expected to last for years. Biological and mechanical processes would be expected to play about equivalent roles in degradation of the oil.

Protection. To be effective, protective measures should be carried out in the lagoonal entrances. The persistent winds would quickly distribute the oil along wide sections of the mainland shore once it entered the lagoon. On the other hand, due to reduced wave action and a general absence of floating ice during the summer months, mechanical oil-collecting devices like skimmers and booms could operate more efficiently in lagoonal waters.

Cleanup. The narrow size of the mainland beaches would make anything but manual clean-up extremely destructive to the tundra margin. Destruction of the tundra would further greatly enhance the shoreline retreat rate.

3.7 Peat shores (Retention index: 6).

Morphology. A considerable amount of peat detritus is mixed in with inorganic sediments in the tundra bluffs. Furthermore, the surface tundra mat may be many feet thick. This abundance of organic material and low wave energy locally give rise to a uniquely arctic peat shore. Morphologically it assumes three distinct forms:

(a) Peat fragments eroded from headlands commonly accumulate in adjacent embayments where they might form a wide peat "beach-ridge" plain. Generally, the deposit grades into a thick "coffee grounds" mass of floating peat, becoming more dispersed seaward. The floating peat acts as a very efficient energy-absorbing wave attenuator. Locally, these peat deposits form spits.

(b) Subsiding mainland marsh appears in places to have come so close to sea level that frequent storm inundation has destroyed the tundra vegetation. Wide plains with in situ peat and an admixture of suspension-derived mineral matter characterize these areas.

(c) This is a variation of type (b) where some sand and gravel has been added to the system in the form of a small transgressive beach, perched on the peat surface.

Impact. Cannon (1978) has estimated that each kilometer of coastline along Simpson Lagoon contributes about 700 metric tons of peat per year. This provides a substantial nutrient input at the lowest trophic level. Schell (reported in NOAA, 1978) has estimated that between 25 and 50 percent of the fixed carbon input into Simpson Lagoon was in the form of eroded peat from the shoreline. The availability of this carbon source as detrital particulate material in winter may further increase its significance as an energy-source on a year-round basis.

Oil staining of the peat could have serious effects up the entire trophic chain. The peat would also be a very efficient oil collector, because its mechanical properties are very similar to the absorbent mats used in combating oil spills.

Persistence. The "coffee-grounds" shores appear to have very low erosion rates. In fact, in many places they are actively accreting. Furthermore, because waves are completely attenuated before reaching shore, there would be no mechanical processes of oil degradation in this environment except during major storms when the peat shore may be completely disaggregated. The peat shores would probably retain oil for many years.

Protection. Peat accumulations are of quite limited spatial extent but they are numerous along the shore. Efforts should be made to keep floating oil slicks away through the use of booms or other deflection devices.

Cleanup. Peat which has been contaminated could be physically removed in bulk. In fact, it could be used as an adsorbent. Bulk removal, in spite of the physical destruction of the immediate shoreline, might be preferable to the circulation of all the hydrocarbons through the system of trophic interactions operating in the lagoon.

3.8 Sheltered tidal flats (Retention index: 7).

Morphology. The distal margin of most major river deltas along the arctic slope consists of featureless fine sand tidal flats. Local mud drapes are common. Stream gradients are such as to drop all coarse load some distance short of the shoreline. The bifurcation of the channels downstream and the consequent reduction in effective bed shear stress is the direct control on this fining in grain size.

The arctic rivers have a distinctly seasonal hydrograph, with peak discharge associated with early summer snow melt. Only three North Slope rivers have been gauged. These are the Kuparuk, the Putuligayuk and the Sagavanirktok. These demonstrate that a large percentage of the total annual discharge occurs within a 10-day period after breakup (Carlson et al. 1977). Generally, peak discharge occurs while the nearshore zone, and indeed parts of the delta, still are ice-covered. Sediment is deposited on the ice to a distance of many kilometers offshore (Barnes and Reimnitz, 1974). Shortly after the flooding the nearshore ice generally breaks up. Sediment deposited on the delta plain ice tends to protect the ice and delay its melting. Extensive areas of mud-covered ice were found at the delta of the Kongakut River at the end of August in 1977.

Most major river deltas exist at the head of shallow embayments (Ikpikpuk, Colville) or at lagoonal shores (Kuparuk, Sagavanirktok, Canning, Jago). In both cases the nearshore wave energy is very small. The deltas are completely fluvially dominated with no wave-built spits or bars along their seaward margins. Small storm surges, therefore, cause inundation of extensive areas of these sheltered delta tidal flats. Driftwood and finer organic debris reflecting storm-surge water lines commonly litter the flats.

Impact. The fine grain size of the tidal flats prevents deep oil penetration except for the lightest grades of oil. The abundant organic debris, however, would tend to absorb large amounts. The exceptionally level topography would permit oil staining of vast areas even during a minor storm surge event. Locally, some of the tidal flats have aeolian sand dunes along the channel banks. Such areas have been assigned a retention index of four, reflecting the restricted extent of a potential oil coating on such flats.

Persistence. The tidal flats have a high retention potential primarily because of the inefficiency of mechanical oil removing processes. Wave energy is virtually zero; the heavier, sediment-laden "asphalt" left behind on the flats after a spill of heavy crude oil (the most likely spill in the arctic) will not be broken down and removed by slack-water inundation during a storm surge. Secondly, the seaward margins of the tidal flats are likely to be ice-covered during the spring flood, preventing fluvial removal of the oil. The heavier components of oil which would enter and coat the river mouth tidal flats would most likely be protected from any form of mechanical degradation. The oil would be expected to last for years.

Protection. Protection of tidal flats would be most effective through the use of booms in tidal entrances leading into the delta-front lagoon. The second line of defense would be to operate skimmers and other sea-surface oil collection equipment in the lagoon. The generally quiet water off the deltas could make such collection fairly effective.

Cleanup. The fine-grained, firm and non-vegetated tidal flats could easily be cleaned manually. Oil penetration would be generally less than that on sandy beaches. The oiled surface sediments could be removed by shovel and transported away by barge. Cleanup would generally be desirable in order to prevent oil from drifting from the tidal flats into the biologically highly productive marshes. Marshes commonly border many delta-front tidal flats.

3.9 Marshes (Retention index: 8).

Morphology. In the absence of any significant astronomical tidal range there are no true intertidal salt marshes along the Beaufort coast (Frey and Basan, 1978). However, vegetated low-lying coastal areas, subject to frequent storm-tide salt-water inundation, are brackish or saline marshes. Marshes are frequent, but individually occupy rather limited areas along the coast. There are two morphologically distinct marsh categories: (a) river bank, estuarine and delta margin marshes, and (b) areas of low-lying polygonal tundra. The former marsh type maintains generally both a high species diversity and density; probably because of high nutrient influx during spring floods in the rivers. The latter type often occupies sites of partly drained thaw-lakes. Initially, these coastal marshes may maintain the vegetation characteristic of the freshwater lake shores. With increasing frequency of storm surge inundation they gradually change into supratidal marshes.

Impact. Marshes play a significant role in the arctic ecosystem because of their high primary productivity and the fact that they are important habitats for many species of birds and smaller mammals. Oil accidentally introduced into an arctic marsh could seriously alter the biological balance. Many marsh-dwelling species already live under rather stressed conditions, due to rapid, and often dramatic, changes in water level, salinity and surface temperature. Destruction of large populations of primary producers in a coastal marsh, due to an oil spill, could have significant effects on the whole chain of trophic interactions in the arctic ecosystem.

Persistence. Studies of *Metula* oil in salt marshes of the Strait of Magellan demonstrated essentially no change in the oil 1½ years after the spill. Hayes *et al.* (1976) predicted a life span of at least 10 years for that oil. Studies by McLean and Betancourt (1973) in Cheabucto Bay, Nova Scotia, demonstrated that oil stranded in a sheltered location lost about 20 percent by weight within the first year, but thereafter degradation virtually ceased.

Some removal of oil could be expected from river bank and estuarine marshes during high river stages. The process, however, would be rendered rather ineffective due to baffling of currents by vegetation, the deposition of sediments and the infrequent floods. Mechanical degradation of oil by wave action would be equally ineffective due to the same factors. Biological degradation of oil along the Beaufort would be no more effective than that in the Strait of Magellan or Chedabucto Bay. Therefore, one would expect a residence time of at least 10 years for oil spilled into an arctic marsh.

Protection. Most arctic marshes are not only small in total areal extent, but they generally exchange water with the arctic ocean through narrow river mouths or tidal entrances, constricted by wave-built spits. Therefore, marsh protection would be a relatively inexpensive procedure. Booms across these small inlets would probably prove to be quite effective. As part of proper contingency planning booms should be kept ready for rapid deployment in areas of extensive marsh.

Cleanup. Cleanup in a marsh would generally be counterproductive.

4. SPILL RETENTION MAPS

The oil spill retention potentials for the Beaufort Coast are shown in Maps 1 through 30. The maps are arranged in spatial succession from east to west beginning at Demarcation Point. Ground truth data were collected at sites labeled BE 1 through BE 119. The ground truth data sets consist of beach profiles, sediment samples and photographs along the beach in two directions from the sample site. Each ground truth site was picked from the air as being representative of a given section of the shoreline. Based on the criteria discussed in Chapter 3, each site was then assigned an oil spill retention index. Adjacent sections of shore were classified by extending information obtained at the ground truth site to the adjacent shores by means of vertical and oblique air photos, descriptions read on tape while flying, and coastal charts and maps. In simple cases the shoreline was directly classified while flying.

The length of shoreline in each retention category was measured and calculated as a percentage of total shoreline within each map square. The results are displayed as frequency histograms on each map. Summary statistics on the retention index frequencies are given in Table 3. The maps have been identified by their NOS number (new 16-thousand series), or, where NOS charts were nonexistent, by the U.S. Geological Survey quadrangle map names and numbers.

5. CONCLUSIONS

This classification of shoreline segments of the Beaufort coast, with respect to their oil spill retention potential, is largely based on empirical findings at recent oil spills. None of these has occurred in the arctic, but spills at Chedabukto Bay and the Strait of Magellan provide good insights into processes and rates of hydrocarbon degradation in high latitude environments. These studies have demonstrated that the longevity of spilled oil in specific coastal environments depends on the energy level of the physical processes, the texture of the sediments, and the morphology and vegetative cover at the site.

TABLE 3. DISTRIBUTION OF SHORELINE RETENTION INDEX FREQUENCIES BY MAP SQUARES

	MAP	RETENTION INDEX FREQUENCY (%)							
		1	2	3	4	5	6	7	8
1.	16041, east	0	16.9	29.6	0	50.7	0	0	2.8
2.	16041, west	0	0	38.2	0	10.4	2.2	41.8	7.4
3.	16042, east	0	1.5	31.7	0	32.5	4.9	20.1	9.3
4.	16042, west	0	10.0	31.8	4.5	42.0	3.5	0	8.2
5.	16043, east	0	1.1	26.5	1.1	43.0	5.2	16.8	6.3
6.	16043, west	0	2.3	14.8	19.3	18.5	0	17.0	28.1
7.	16044, east	0	7.2	26.0	25.4	31.3	2.5	7.6	0
8.	16044, west	0	0	28.6	0	44.4	4.4	10.0	12.6
9.	16045, east	3.8	0.5	23.4	0	37.5	1.4	30.6	2.7
10.	16045, west	0	0	47.6	0	36.6	2.2	4.6	9.1
11.	Beechy Pt. & Flaxman qd.	0	0	24.1	10.9	0	13.6	48.1	3.3
12.	Beechy Pt. qd.	0	0	27.5	16.0	8.8	15.2	27.5	5.0
13.	16061, east	0	1.0	1.0	2.1	36.3	.8	58.7	0
14.	16061, west	0	6.2	25.2	8.5	22.6	1.8	20.8	14.9
15.	16062, east	0	9.4	28.4	1.6	49.4	0	0	11.2
16.	16062, west	0	8.7	26.7	0	44.6	0	0	20.0
17.	16063, east	0	0	3.1	0	14.7	0	73.4	8.8
18.	16063, west	0	0	0	0	0	0	79.8	20.2
19.	16064, east	0	0	0	0	3.2	0	65.4	31.4
20.	16064, central	0	0	0	0	53.8	0	0	46.2
21.	16064, west	0	0	.9	0	82.5	2.9	0	13.6
22.	16065, west	0	0	0	0	69.2	8.5	13.4	8.9
23.	16066, east	16.0	32.0	14.4	0	4.6	2.3	28.5	2.3
24.	16066, west	0	.9	23.0	24.2	0	1.8	6.8	43.3
25.	Teshekpuk qd. east	9.7	20.3	5.8	8.7	45.9	4.8	----	4.8
26.	Teshekpuk qd. west	0	0	0	0	13.4	0	52.5	34.1
27.	16067, west	0	11.7	25.7	10.7	7.3	1.3	32.6	10.7
28.	16081, east	0	0	47.4	0	6.4	0	39.4	6.8
29.	16081, west	0	0	26.6	6.7	40.2	18.1	3.2	5.2
30.	16082, east	0	1.2	29.0	1.3	37.8	10.4	20.3	0

LIST OF SPILL RETENTION MAPS

Map 1: East half of NOS Chart No. 16041
Map 2: West half of NOS Chart No. 16041
Map 3: East part of NOS Chart No. 16042
Map 4: West part of NOS Chart No. 16042
Map 5: East half of NOS Chart No. 16043
Map 6: West half of NOS Chart No. 16043
Map 7: East half of NOS Chart No. 16044
Map 8: West half of NOS Chart No. 16044
Map 9: East half of NOS Chart No. 16045
Map 10: West half of NOS Chart No. 16045
Map 11: U.S.G.S.Beechey Pt.(A-1,2) Quads Flaxman Is. (A-5,B-5) Quads
Map 12: U.S.G.S. Beechey Pt. (A-1,2; B-1,2) Quads
Map 13: East half of NOS Chart No. 16061
Map 14: West half of NOS Chart No. 16061
Map 15: East half of NOS Chart No. 16062
Map 16: West half of NOS Chart No. 16062
Map 17: East half of NOS Chart No. 16063
Map 18: West half of NOS Chart No. 16063
Map 19: East part of NOS Chart No. 16064
Map 20: Central part of NOS Chart No. 16064
Map 21: Western part of NOS Chart No. 16064
Map 22: Western part of NOS Chart No. 16065
Map 23: Eastern part of NOS Chart No. 16066
Map 24: Western part of NOS Chart No. 16066
Map 25: U.S.G.S. Teshekpuk (D-2,3) Quads
Map 26: U.S.G.S. Teshekpuk (D-2,3) Quads
Map 27: Western half of NOS Chart No. 16067
Map 28: Eastern part of NOS Chart No. 16081
Map 29: Western half of NOS Chart No. 16081
Map 30: Eastern half of NOS Chart No. 16082

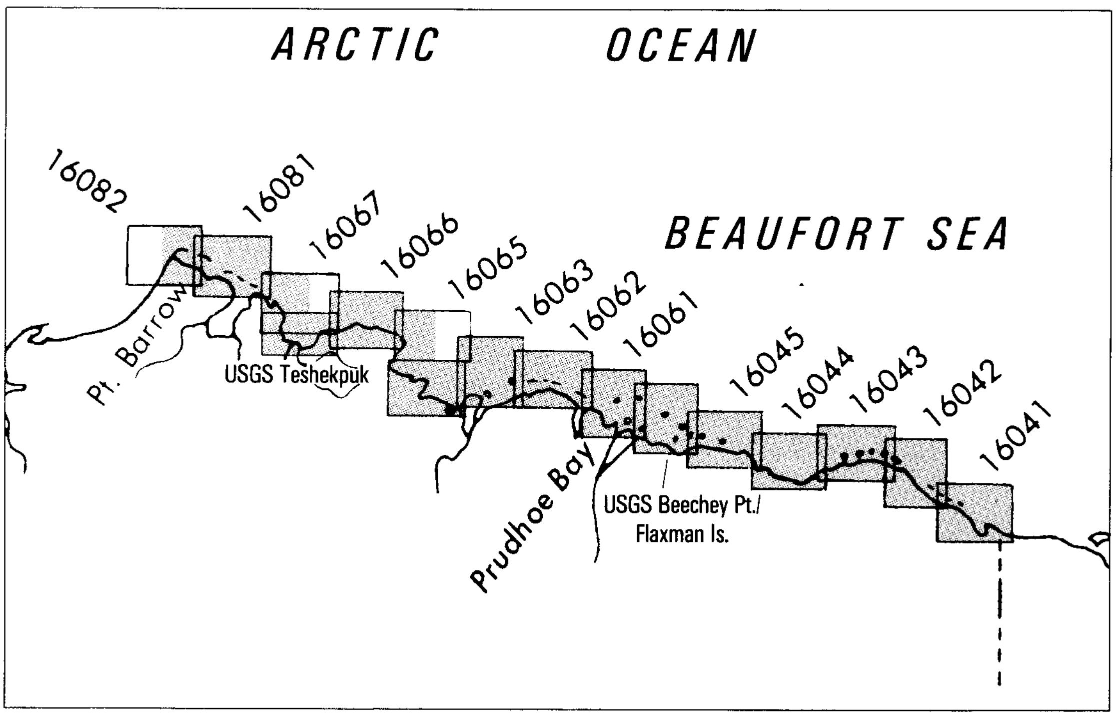

Map 1

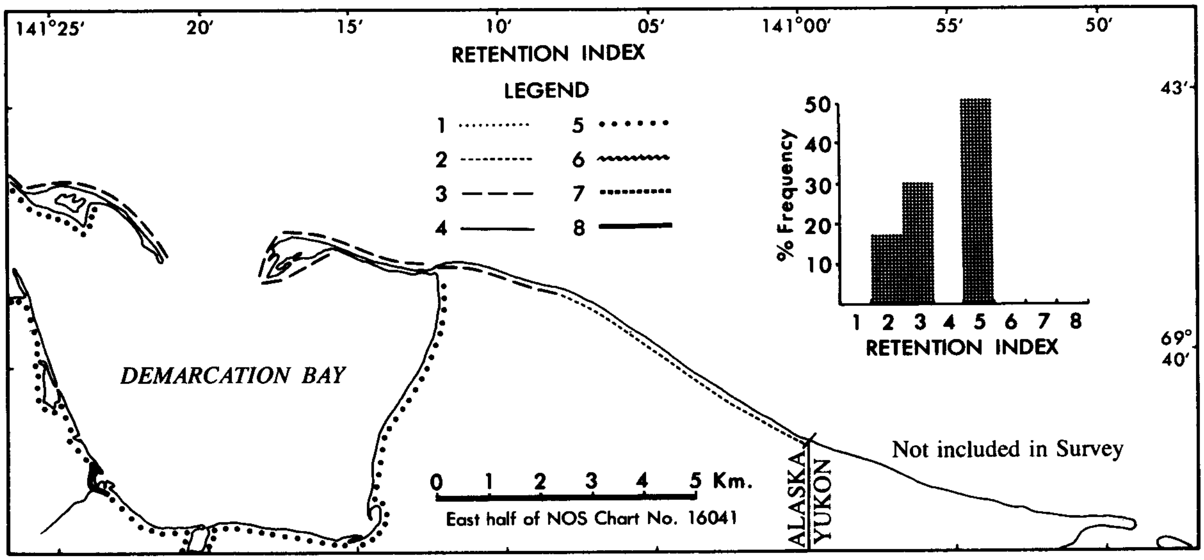

141°25'
20'
15'
10'
05'
141°00'
55'
50'
43'
69° 40'
RETENTION INDEX
LEGEND
1
2
3
4
5
6
7
8
% Frequency
50
40
30
20
10
1 2 3 4 5 6 7 8
RETENTION INDEX
DEMARCATION BAY
0 1 2 3 4 5 Km.
East half of NOS Chart No. 16041
ALASKA
YUKON
Not included in Survey

Map 2

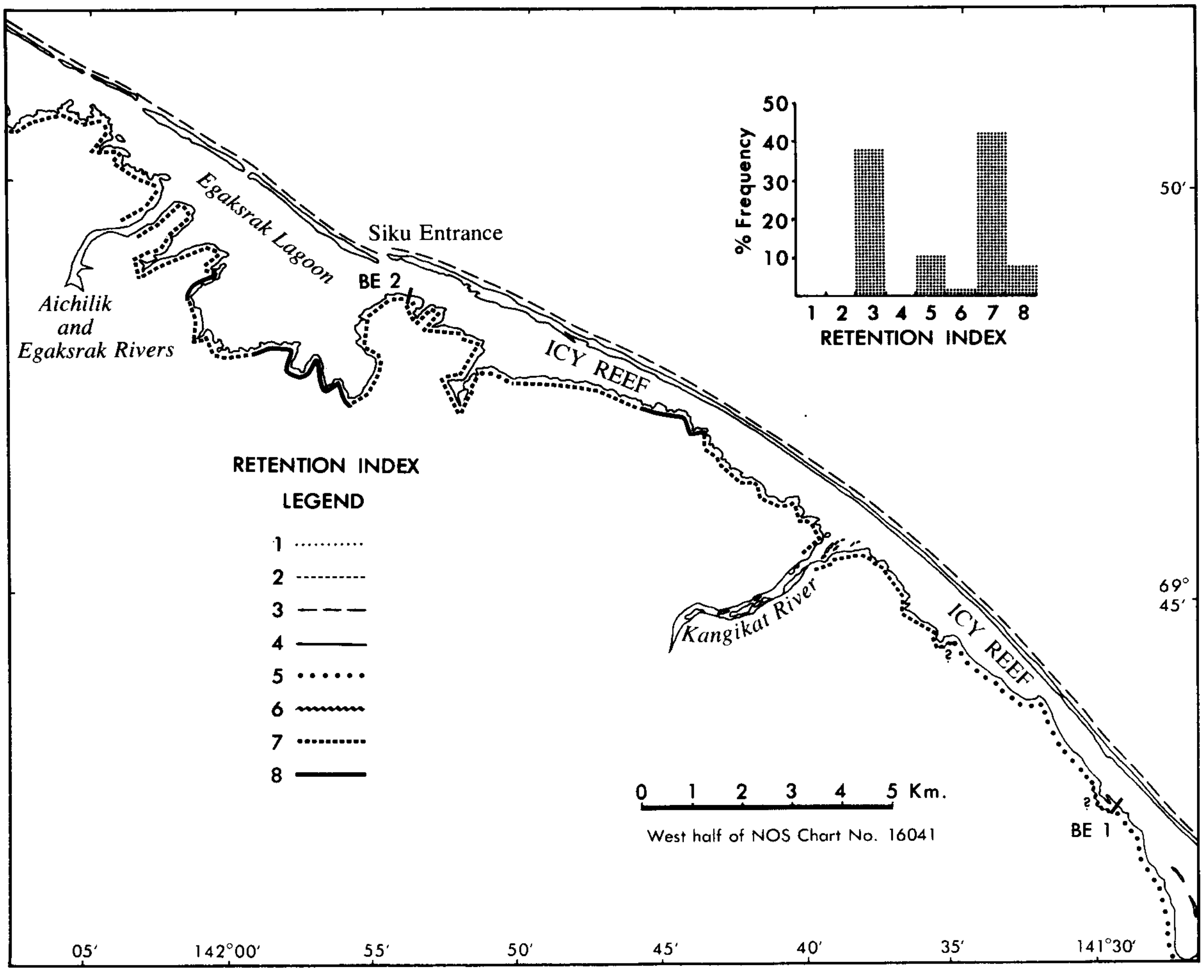

% Frequency
50
40
30
20
10
1 2 3 4 5 6 7 8
RETENTION INDEX
50'
69° 45'
Egaksrak Lagoon
Siku Entrance
BE 2
Aichilik and Egaksrak Rivers
ICY REEF
RETENTION INDEX
LEGEND
1
2
3
4
5
6
7
8
Kangikat River
ICY REEF
0 1 2 3 4 5 Km.
West half of NOS Chart No. 16041
BE 1
05'
142°00'
55'
50'
45'
40'
35'
141°30'

Map 3

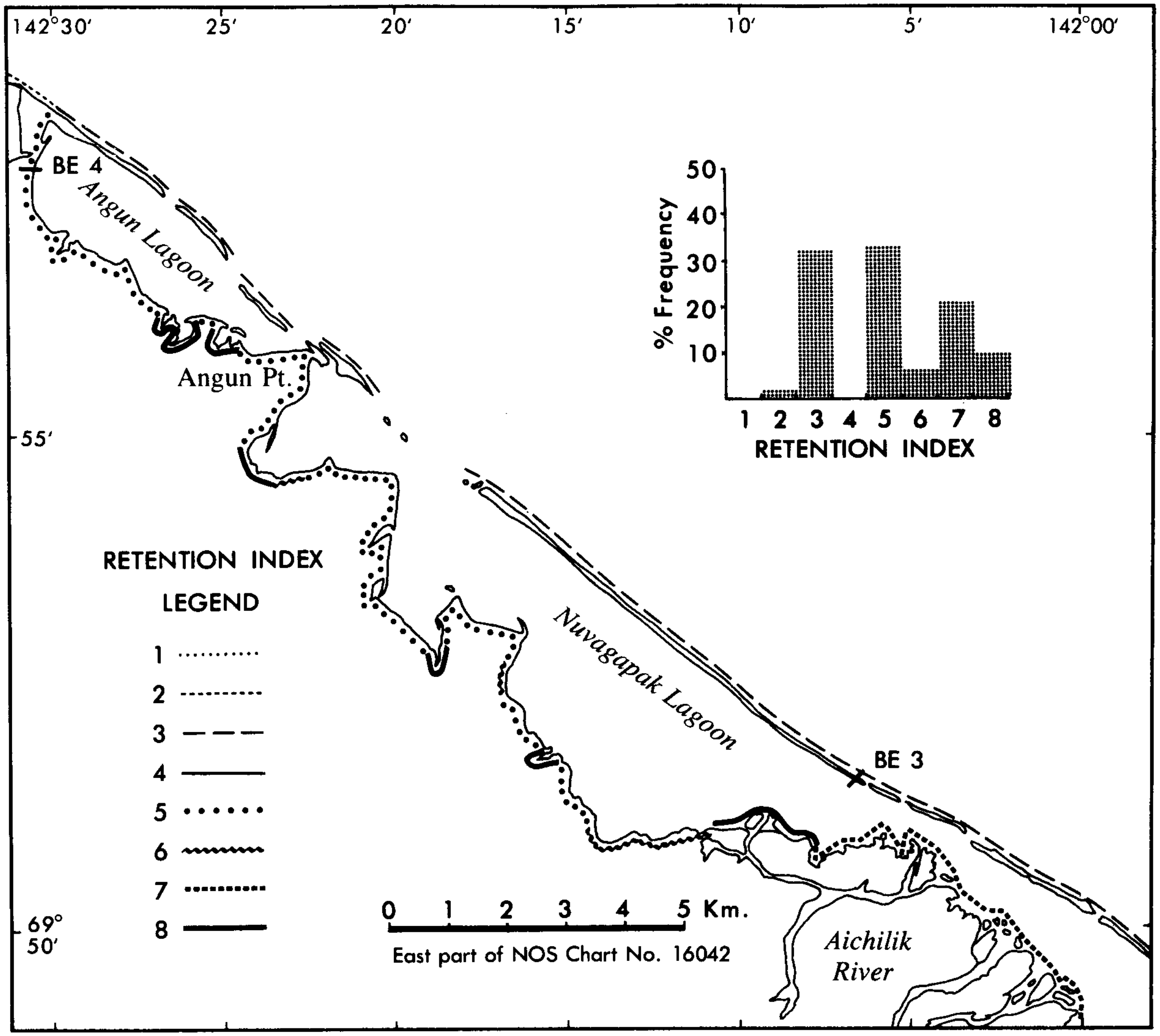
142°30′
25′
20′
15′
10′
5′
142°00′
55′
69° 50′
BE 4
Angun Lagoon
Angun Pt.
Nuvagapak Lagoon
BE 3
Aichilik River
50
40
30
20
10
% Frequency
1 2 3 4 5 6 7 8
RETENTION INDEX
RETENTION INDEX
LEGEND
1
2
3
4
5
6
7
8
0 1 2 3 4 5 Km.
East part of NOS Chart No. 16042

Map 4

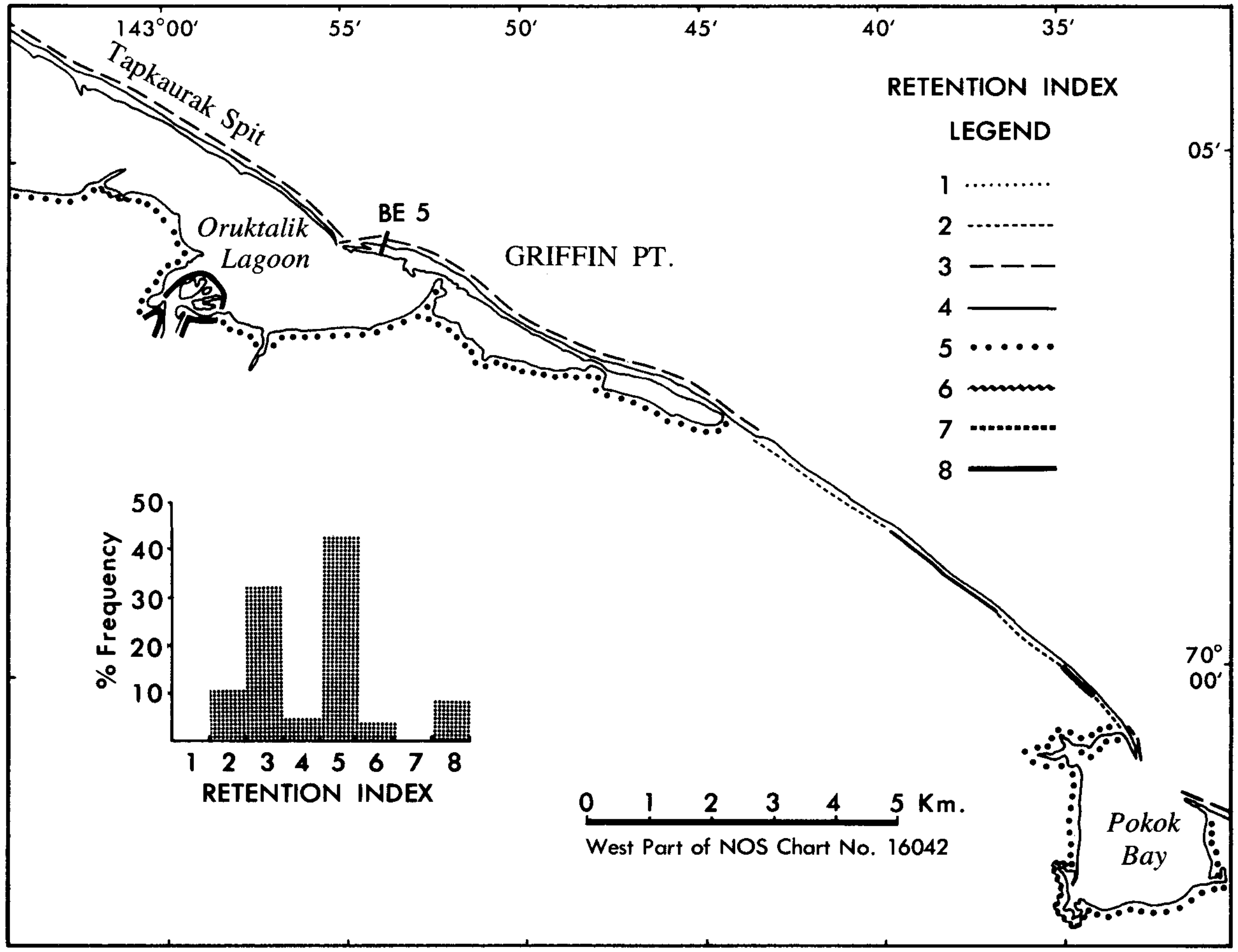

143°00′
55′
50′
45′
40′
35′
05′
70°
00′
Tapkaurak Spit
Oruktalik
Lagoon
BE 5
GRIFFIN PT.
Pokok
Bay
RETENTION INDEX
LEGEND
1
2
3
4
5
6
7
8
50
40
30
20
10
% Frequency
1 2 3 4 5 6 7 8
RETENTION INDEX
0 1 2 3 4 5 Km.
West Part of NOS Chart No. 16042

Map 5

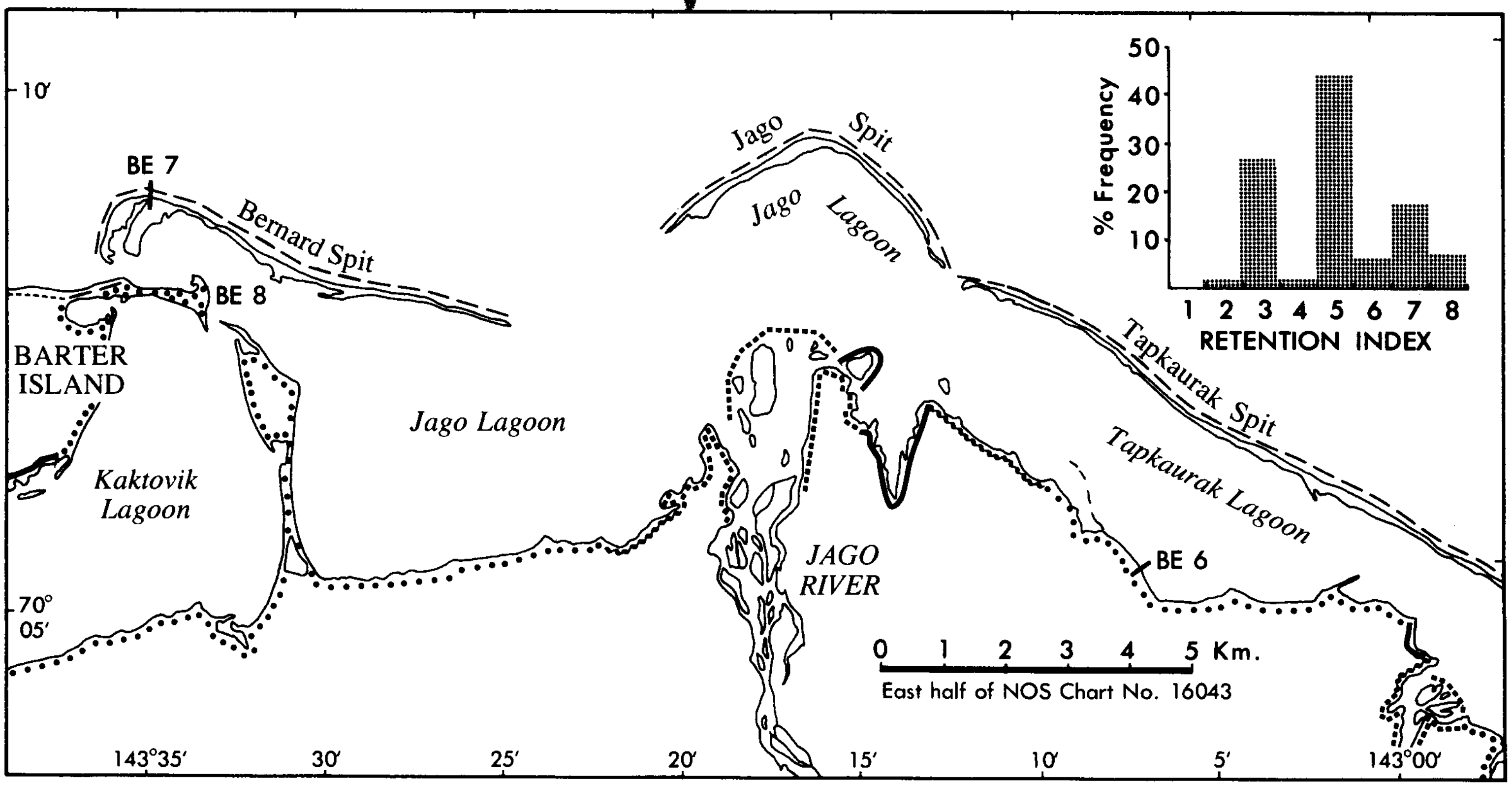

BE 7
Bernard Spit
BE 8
BARTER ISLAND
Kaktovik Lagoon
Jago Lagoon
Jago Spit
Jago Lagoon
JAGO RIVER
Tapkaurak Spit
Tapkaurak Lagoon
BE 6
10′
70° 05′
143°35′
30′
25′
20′
15′
10′
5′
143°00′
0 1 2 3 4 5 Km.
East half of NOS Chart No. 16043
% Frequency
50
40
30
20
10
1 2 3 4 5 6 7 8
RETENTION INDEX

Map 6

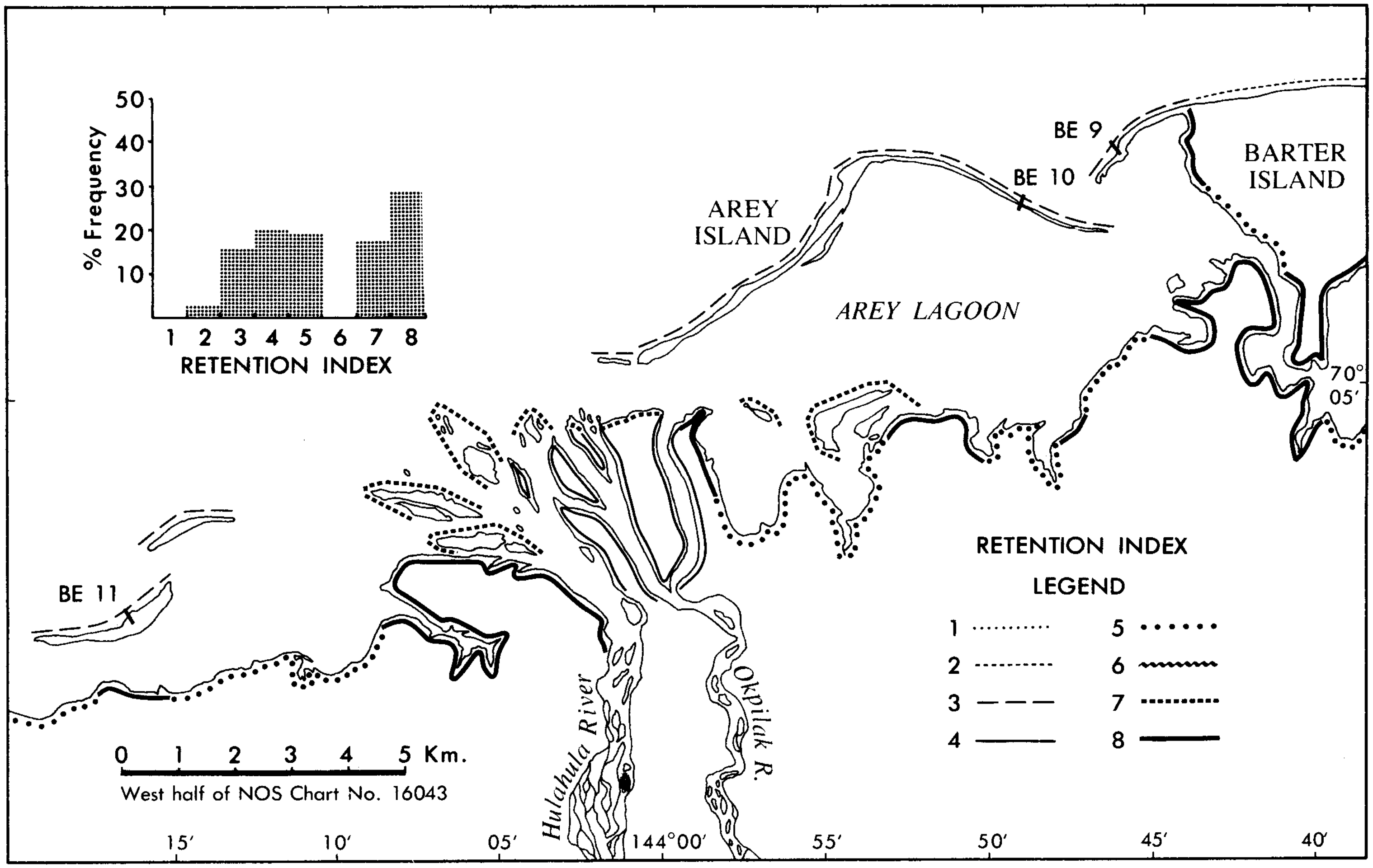

50
40
30
20
10
% Frequency
1 2 3 4 5 6 7 8
RETENTION INDEX
AREY ISLAND
AREY LAGOON
BE 9
BE 10
BARTER ISLAND
70° 05′
BE 11
Hulahula River
Okpilak R.
RETENTION INDEX
LEGEND
1
2
3
4
5
6
7
8
0 1 2 3 4 5 Km.
West half of NOS Chart No. 16043
15′
10′
05′
144°00′
55′
50′
45′
40′

Map 7

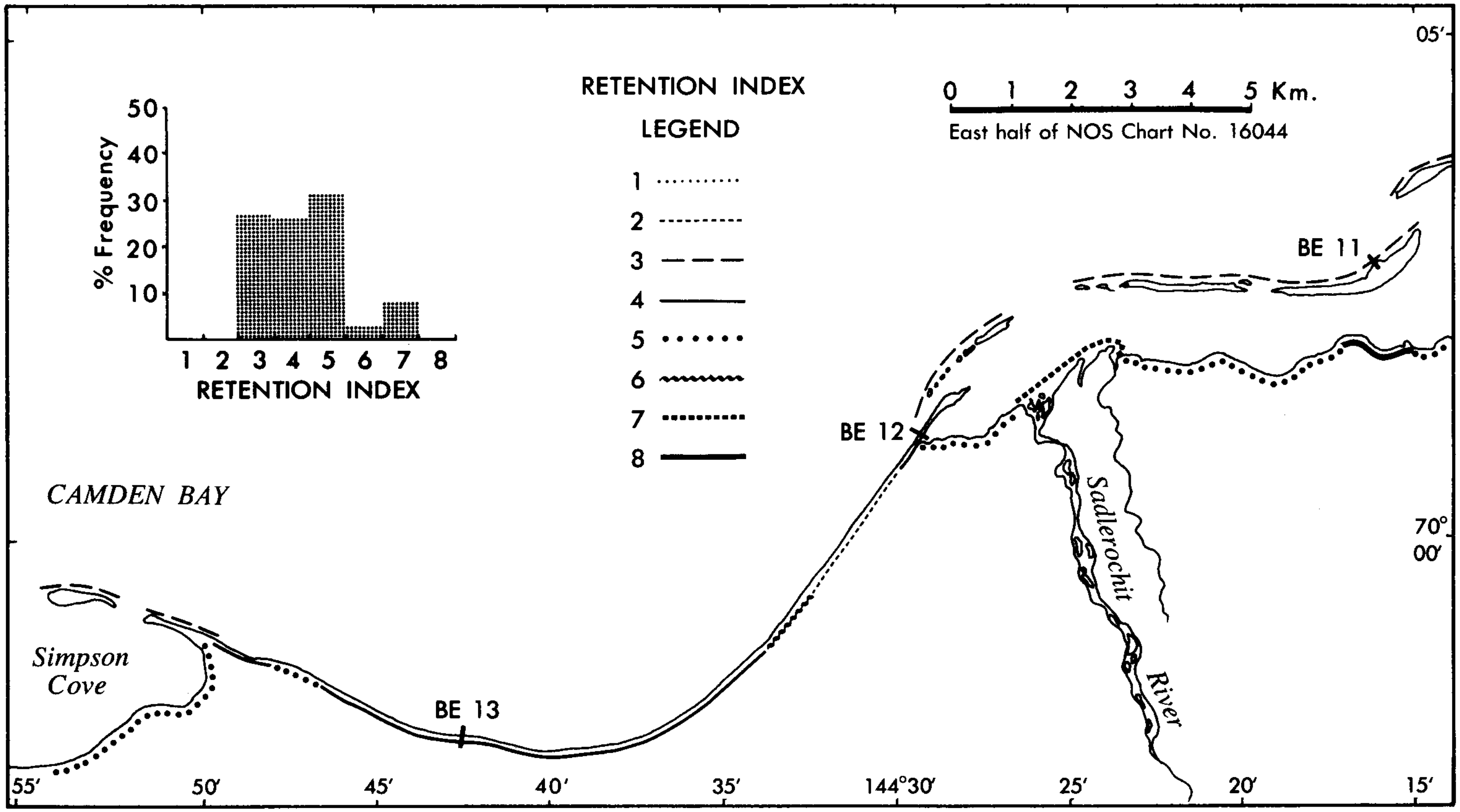
50
40
30
20
10
% Frequency
1 2 3 4 5 6 7 8
RETENTION INDEX
RETENTION INDEX
LEGEND
1
2
3
4
5
6
7
8
0 1 2 3 4 5 Km.
East half of NOS Chart No. 16044
05′
BE 11
BE 12
Sadlerochit
River
70°
00′
CAMDEN BAY
Simpson
Cove
BE 13
55′
50′
45′
40′
35′
144°30′
25′
20′
15′

Map 8

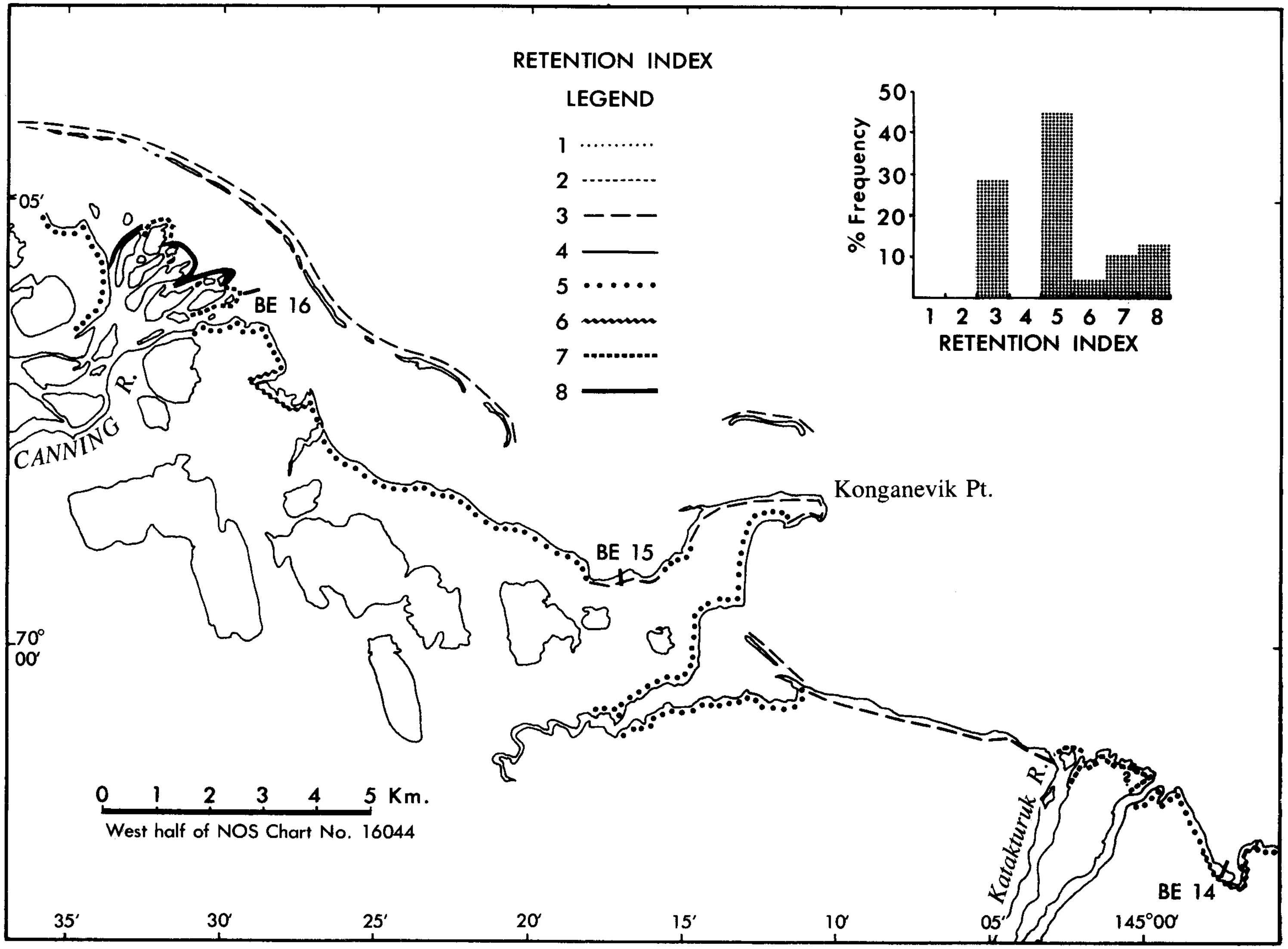
RETENTION INDEX
LEGEND
1
2
3
4
5
6
7
8
% Frequency
50
40
30
20
10
1 2 3 4 5 6 7 8
RETENTION INDEX
05′
BE 16
CANNING R.
Konganevik Pt.
BE 15
70°
00′
0 1 2 3 4 5 Km.
West half of NOS Chart No. 16044
Katakturuk R.
BE 14
35′
30′
25′
20′
15′
10′
05′
145°00′

Map 9

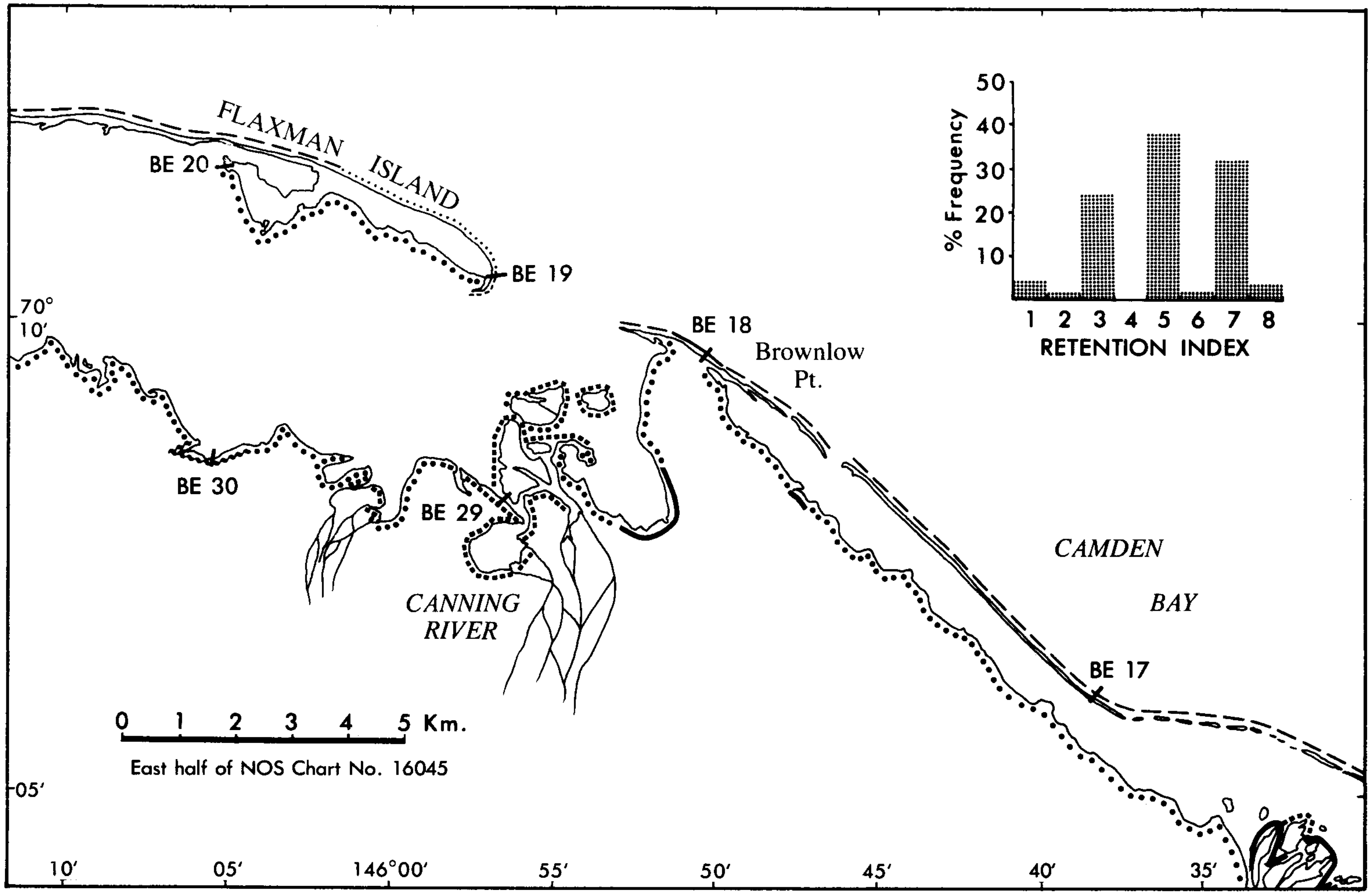
FLAXMAN ISLAND
BE 20
BE 19
70°
10′
BE 18
Brownlow
Pt.
BE 30
BE 29
CANNING
RIVER
CAMDEN
BAY
BE 17
05′
10′
05′
146°00′
55′
50′
45′
40′
35′
0 1 2 3 4 5 Km.
East half of NOS Chart No. 16045
% Frequency
50
40
30
20
10
1 2 3 4 5 6 7 8
RETENTION INDEX

Map 10

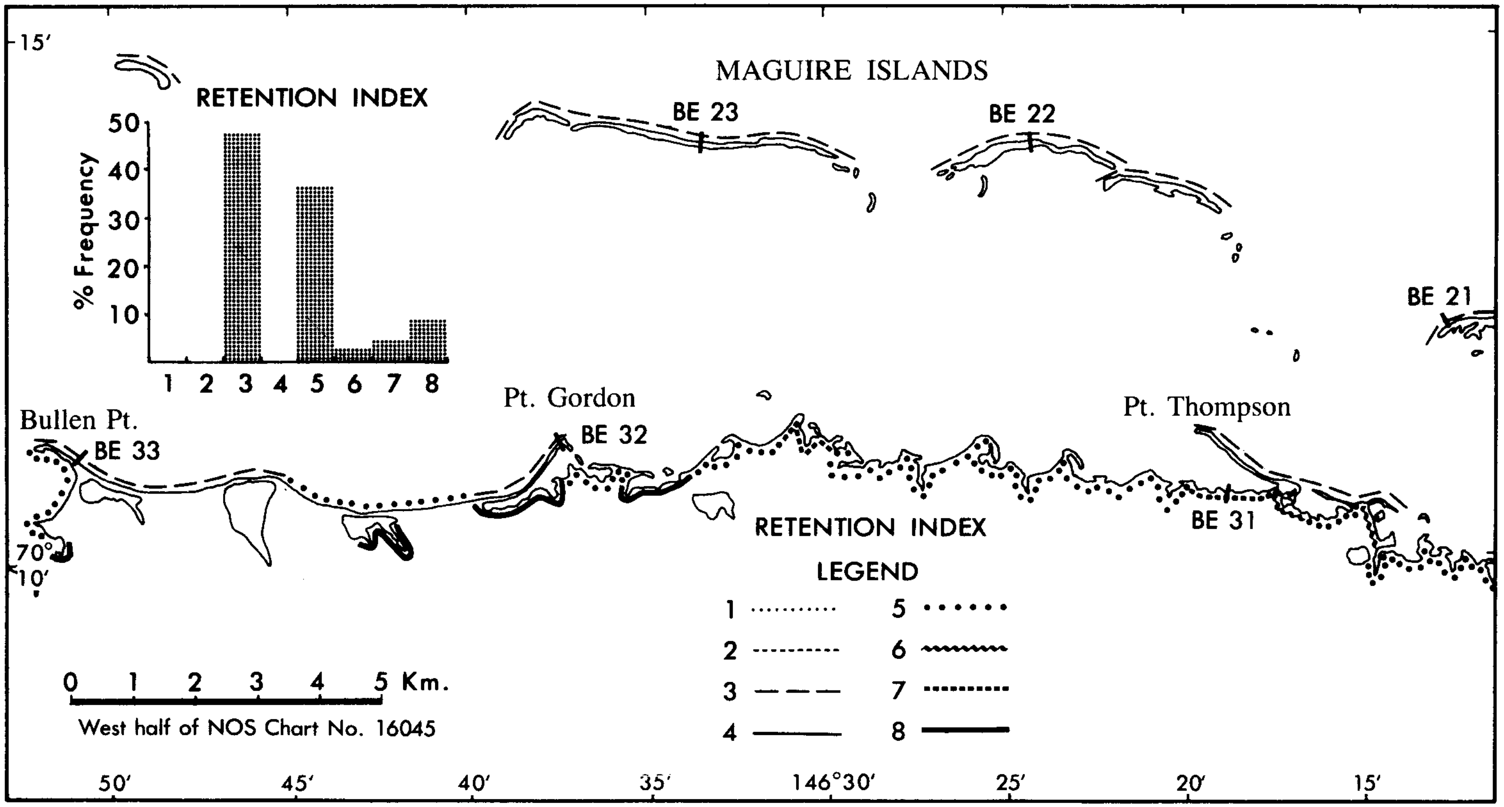
15′
MAGUIRE ISLANDS
BE 23
BE 22
BE 21
RETENTION INDEX
50
40
30
20
10
% Frequency
1 2 3 4 5 6 7 8
Bullen Pt.
BE 33
Pt. Gordon
BE 32
Pt. Thompson
BE 31
70°
10′
RETENTION INDEX
LEGEND
1
2
3
4
5
6
7
8
0 1 2 3 4 5 Km.
West half of NOS Chart No. 16045
50′
45′
40′
35′
146°30′
25′
20′
15′

Map 11

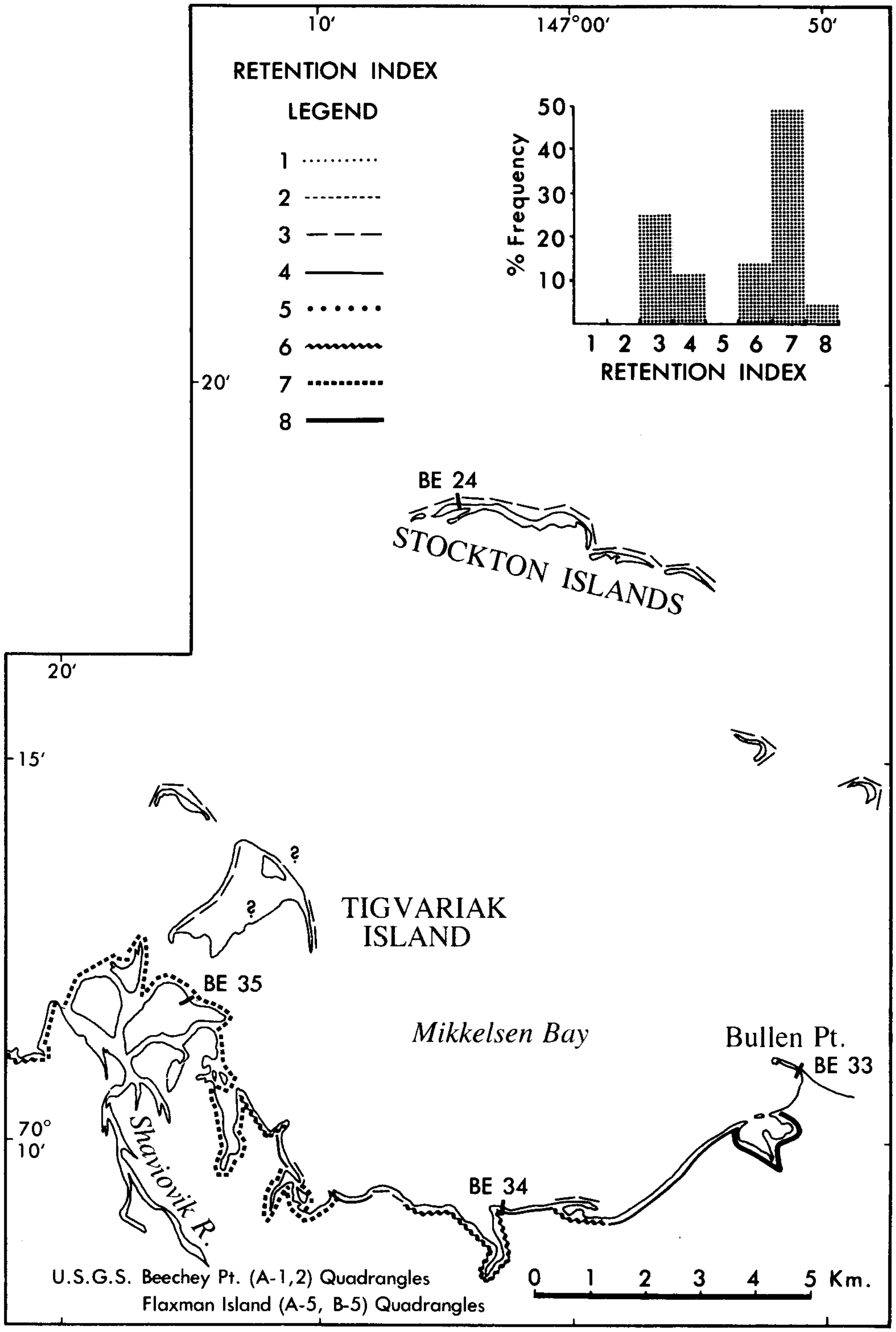

10'
147°00'
50'
RETENTION INDEX
LEGEND
1
2
3
4
5
6
7
8
50
40
30
20
10
% Frequency
1 2 3 4 5 6 7 8
RETENTION INDEX
20'
BE 24
STOCKTON ISLANDS
20'
15'
TIGVARIAK ISLAND
BE 35
Mikkelsen Bay
Bullen Pt.
BE 33
70° 10'
Shaviovik R.
BE 34
U.S.G.S. Beechey Pt. (A-1,2) Quadrangles
Flaxman Island (A-5, B-5) Quadrangles
0 1 2 3 4 5 Km.

Map 12

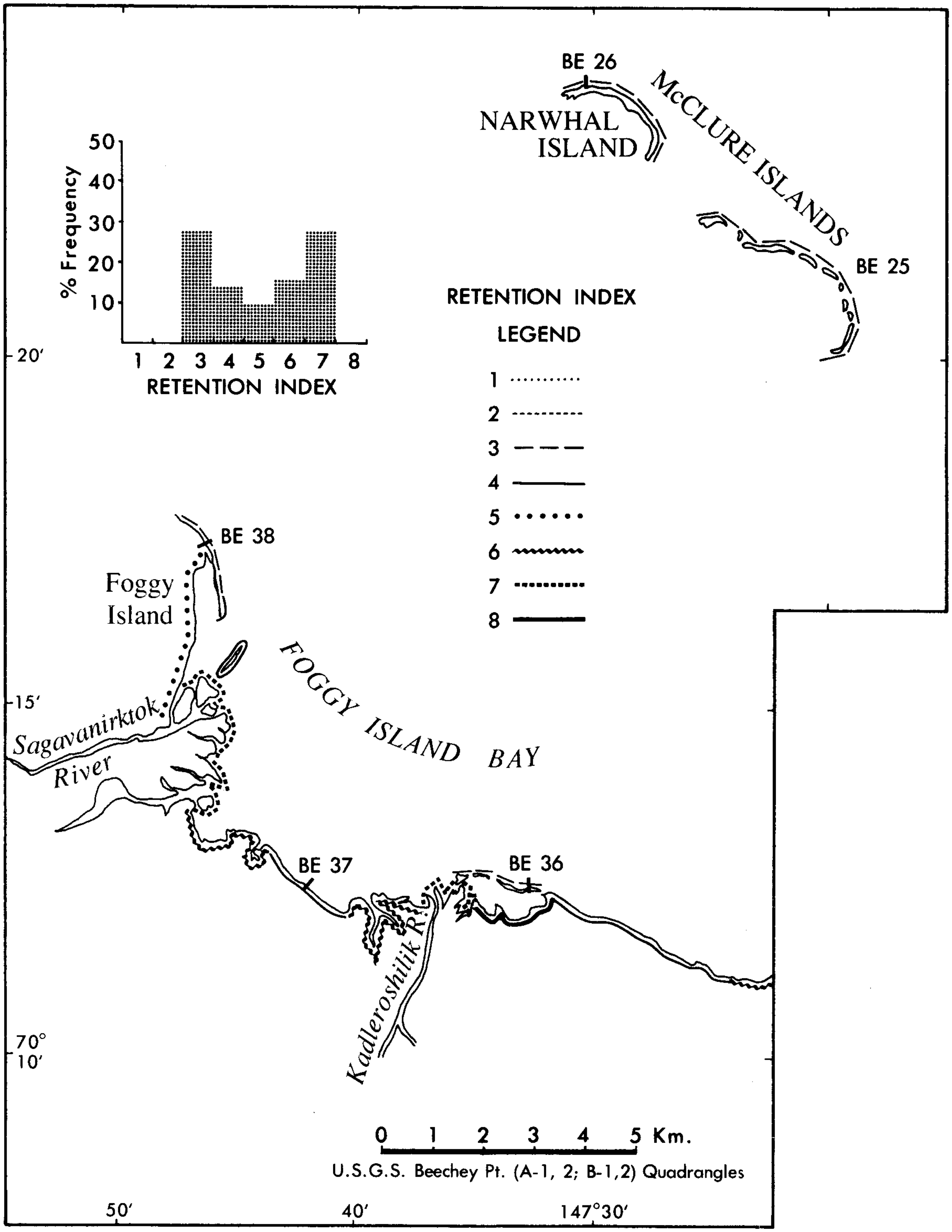

BE 26
NARWHAL ISLAND
McCLURE ISLANDS
BE 25
50
40
30
20
10
% Frequency
1 2 3 4 5 6 7 8
RETENTION INDEX
RETENTION INDEX
LEGEND
1
2
3
4
5
6
7
8
20′
BE 38
Foggy Island
FOGGY ISLAND BAY
15′
Sagavanirktok River
BE 37
BE 36
Kadleroshilik R.
70° 10′
0 1 2 3 4 5 Km.
U.S.G.S. Beechey Pt. (A-1, 2; B-1,2) Quadrangles
50′
40′
147°30′

Map 13

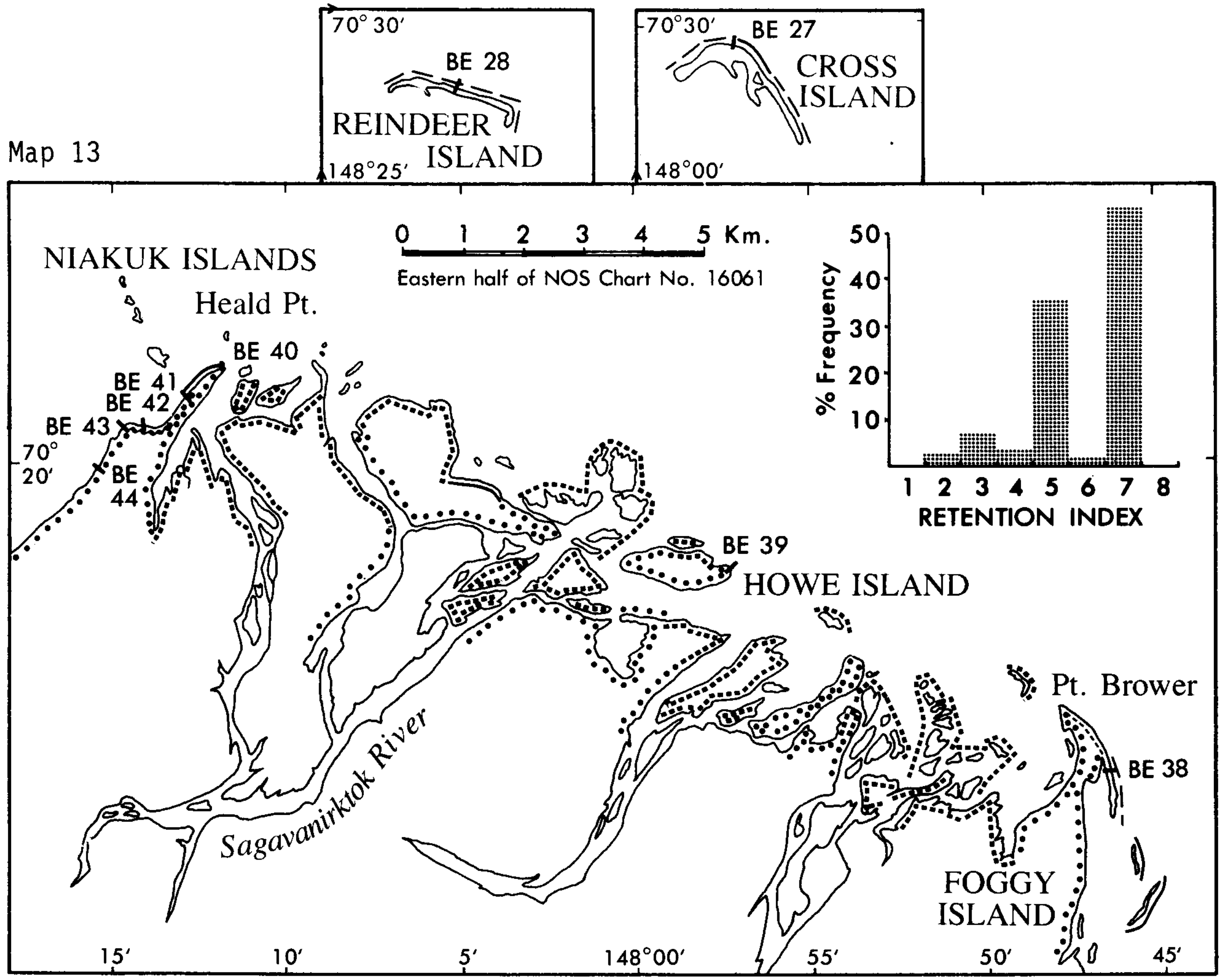
70° 30′
BE 28
REINDEER
ISLAND
148°25′
70°30′
BE 27
CROSS
ISLAND
148°00′
0 1 2 3 4 5 Km.
Eastern half of NOS Chart No. 16061
NIAKUK ISLANDS
Heald Pt.
BE 40
BE 41
BE 42
BE 43
BE 44
70° 20′
BE 39
HOWE ISLAND
Pt. Brower
BE 38
FOGGY
ISLAND
Sagavanirktok River
15′
10′
5′
148°00′
55′
50′
45′
% Frequency
10
20
30
40
50
1 2 3 4 5 6 7 8
RETENTION INDEX

Map 14

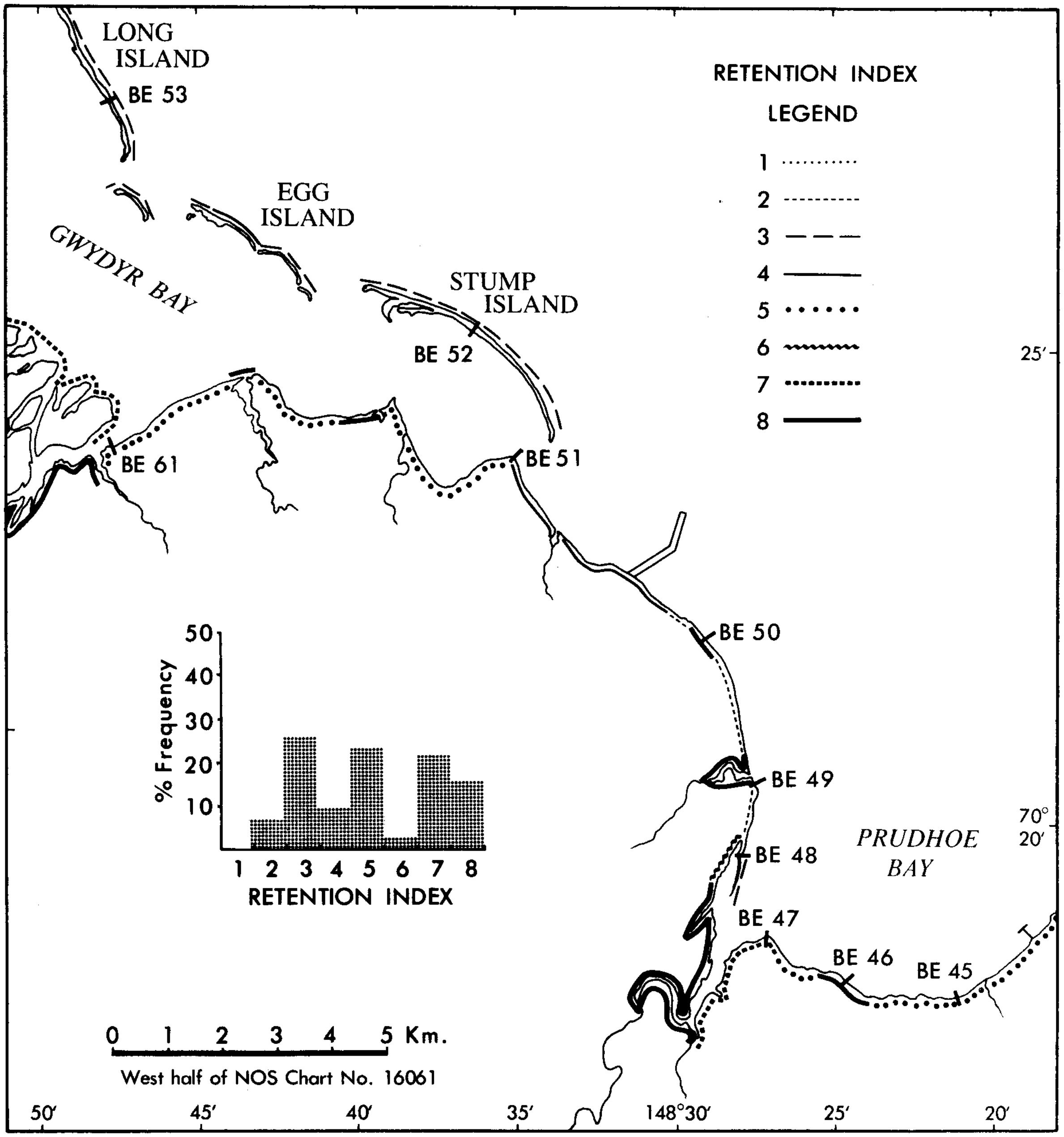
LONG ISLAND
BE 53
EGG ISLAND
GWYDYR BAY
STUMP ISLAND
BE 52
RETENTION INDEX
LEGEND
1
2
3
4
5
6
7
8
25′
BE 61
BE 51
BE 50
50
40
30
20
10
% Frequency
1 2 3 4 5 6 7 8
RETENTION INDEX
BE 49
70°
20′
PRUDHOE BAY
BE 48
BE 47
BE 46
BE 45
0 1 2 3 4 5 Km.
West half of NOS Chart No. 16061
50′
45′
40′
35′
148°30′
25′
20′

Map 15

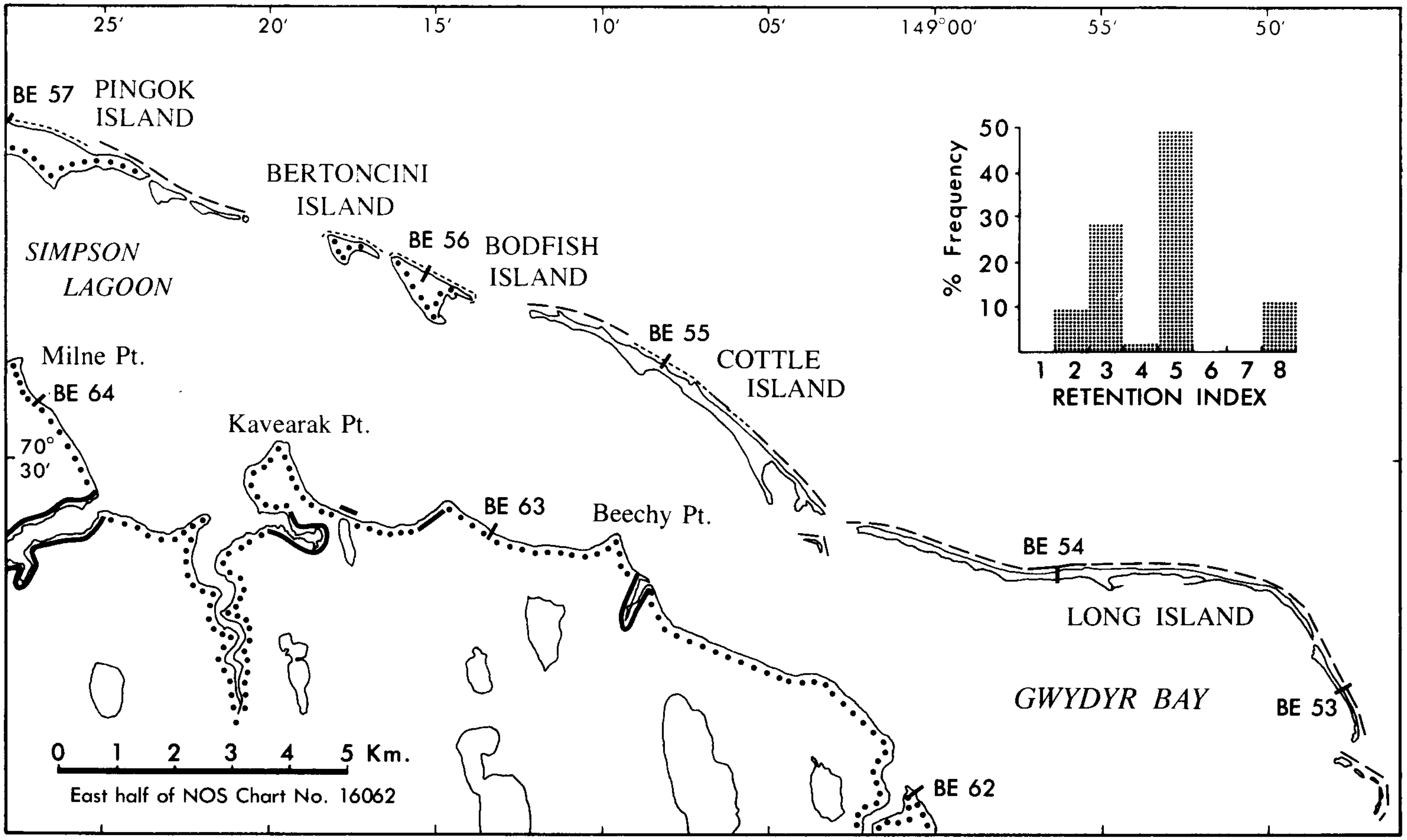
25′
20′
15′
10′
05′
149°00′
55′
50′
BE 57
PINGOK ISLAND
BERTONCINI ISLAND
BE 56
BODFISH ISLAND
SIMPSON LAGOON
BE 55
COTTLE ISLAND
Milne Pt.
BE 64
Kavearak Pt.
70° 30′
BE 63
Beechy Pt.
BE 54
LONG ISLAND
GWYDYR BAY
BE 53
BE 62
0 1 2 3 4 5 Km.
East half of NOS Chart No. 16062
% Frequency
50
40
30
20
10
1 2 3 4 5 6 7 8
RETENTION INDEX

Map 16

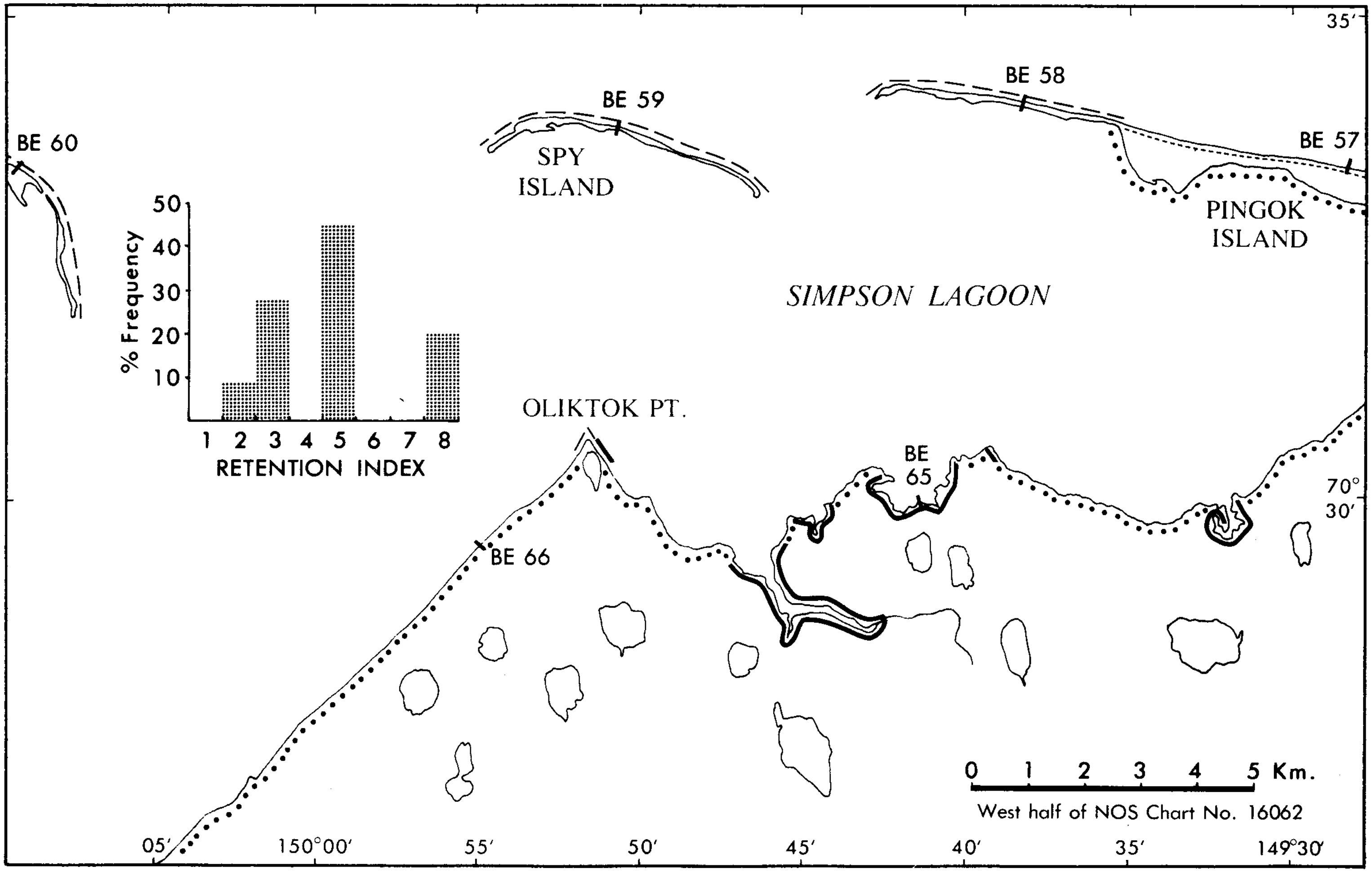

35′
BE 60
BE 59
SPY
ISLAND
BE 58
BE 57
PINGOK
ISLAND
SIMPSON LAGOON
50
40
30
20
10
% Frequency
1 2 3 4 5 6 7 8
RETENTION INDEX
OLIKTOK PT.
BE 66
BE
65
70°
30′
0 1 2 3 4 5 Km.
West half of NOS Chart No. 16062
05′
150°00′
55′
50′
45′
40′
35′
149°30′

Map 17

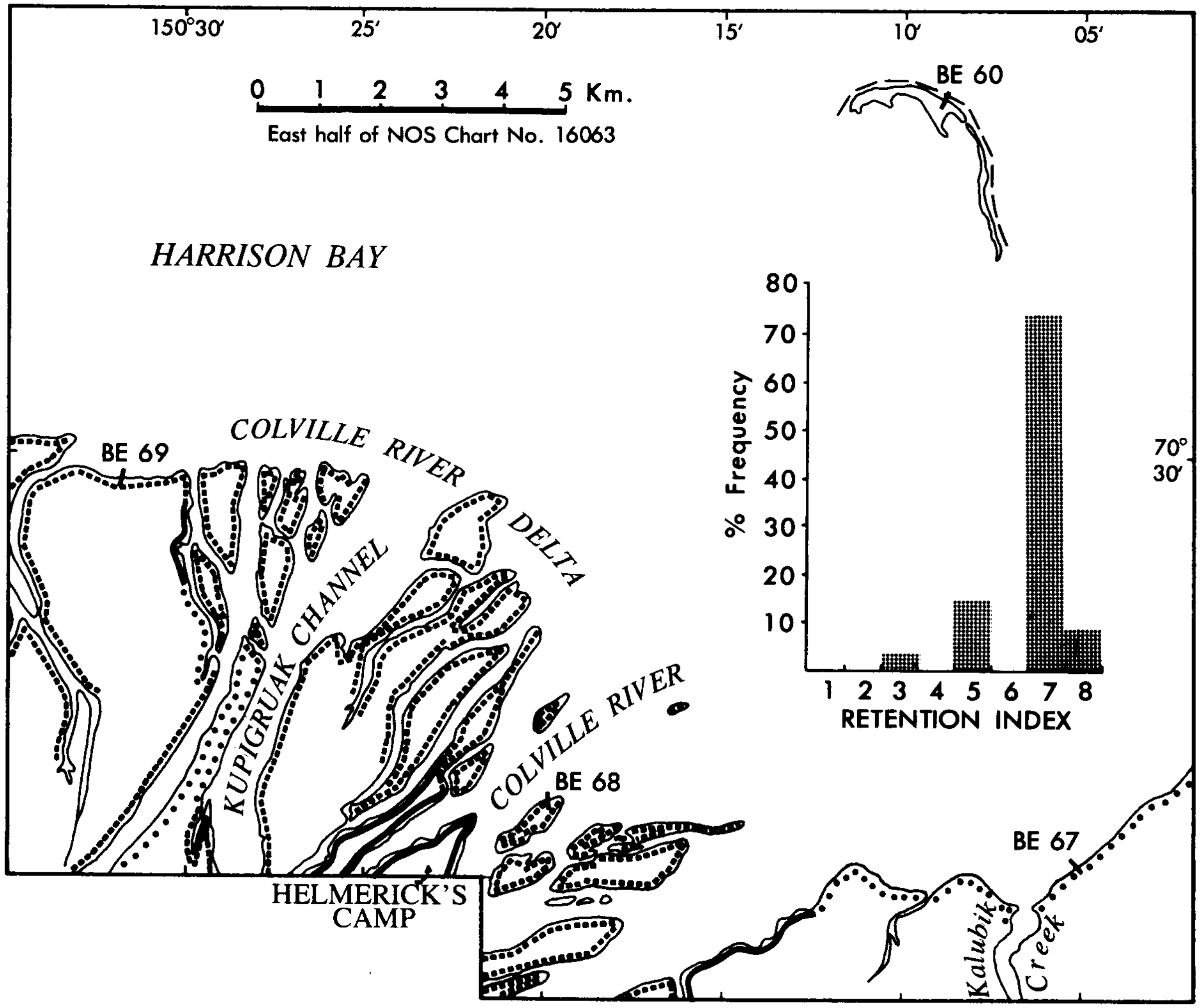

150°30′
25′
20′
15′
10′
05′
0 1 2 3 4 5 Km.
East half of NOS Chart No. 16063
BE 60
HARRISON BAY
BE 69
COLVILLE RIVER DELTA
KUPIGRUAK CHANNEL
COLVILLE RIVER
BE 68
HELMERICK'S CAMP
BE 67
Kalubik Creek
70° 30′
% Frequency
80
70
60
50
40
30
20
10
1 2 3 4 5 6 7 8
RETENTION INDEX

Map 18

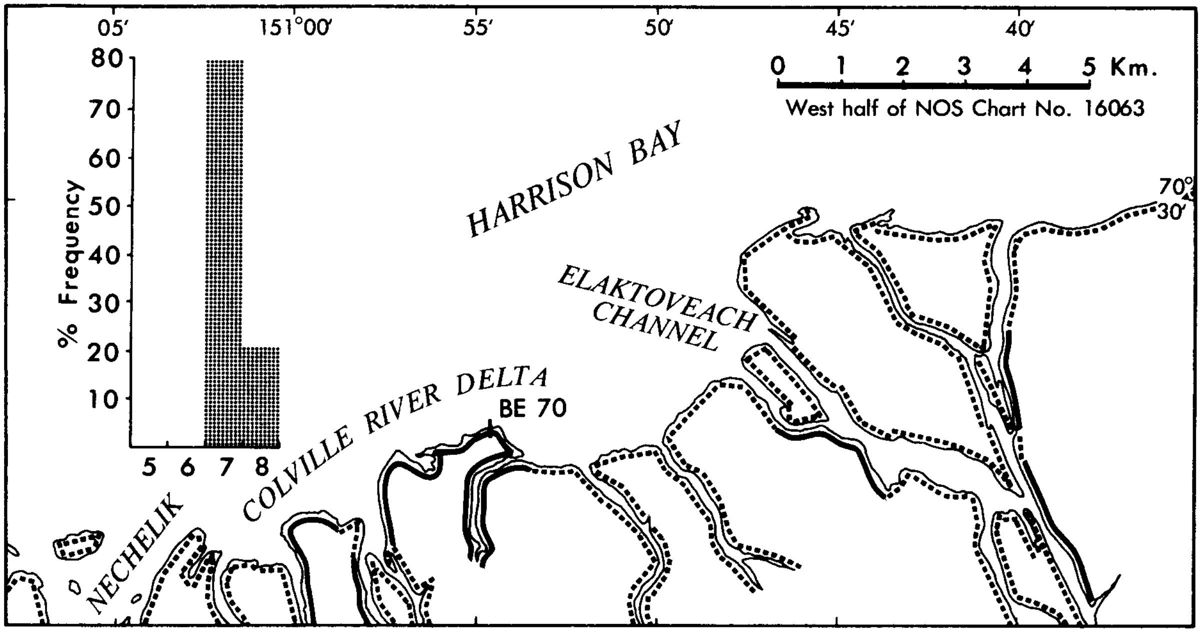
05′
151°00′
55′
50′
45′
40′
80
70
60
50
40
30
20
10
% Frequency
5 6 7 8
0 1 2 3 4 5 Km.
West half of NOS Chart No. 16063
HARRISON BAY
ELAKTOVEACH CHANNEL
COLVILLE RIVER DELTA
BE 70
NECHELIK
70°
30′

Map 19

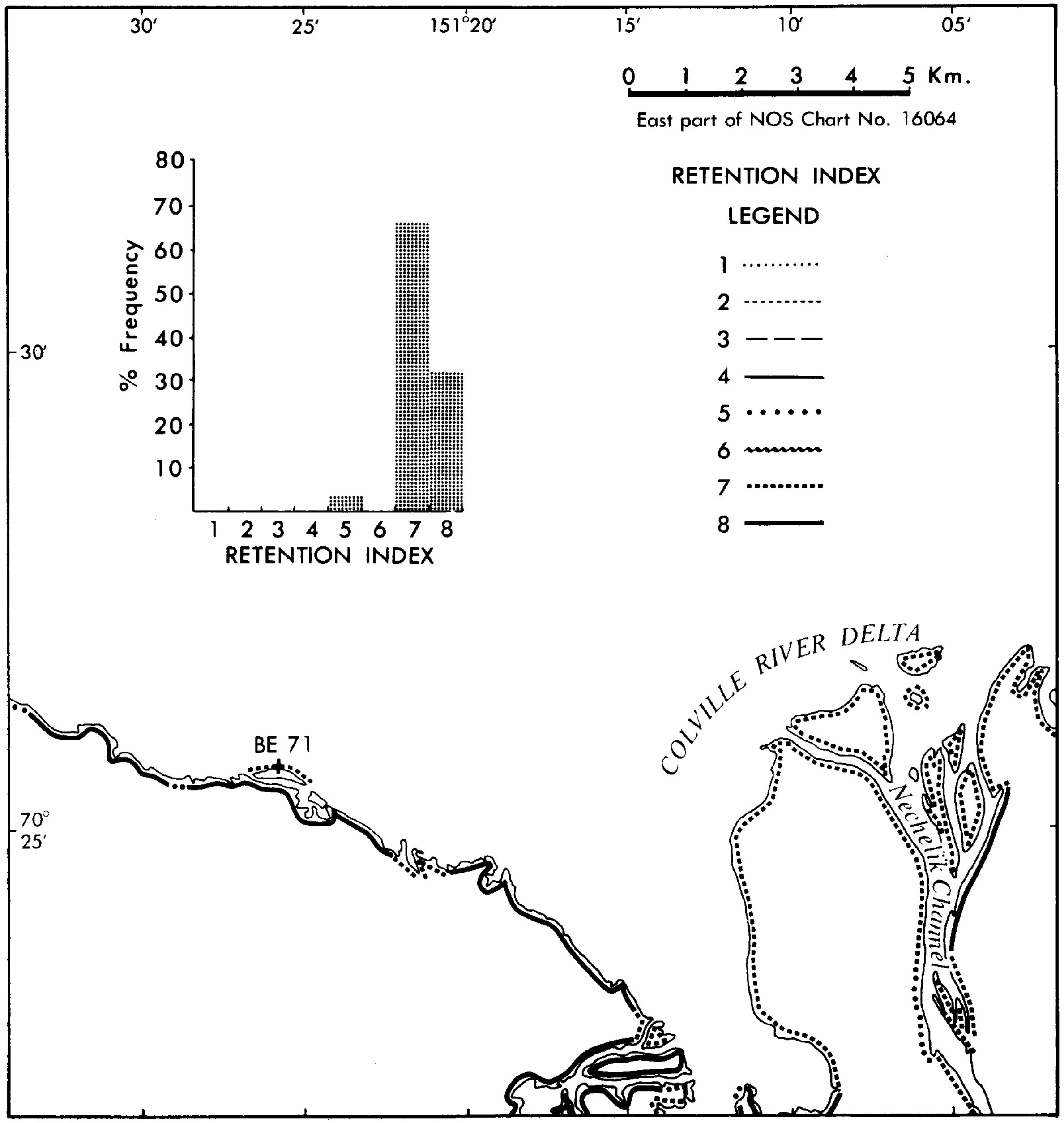
30′
25′
151°20′
15′
10′
05′
0 1 2 3 4 5 Km.
East part of NOS Chart No. 16064
80
70
60
50
40
30
20
10
% Frequency
1 2 3 4 5 6 7 8
RETENTION INDEX
RETENTION INDEX
LEGEND
1
2
3
4
5
6
7
8
30′
70°
25′
BE 71
COLVILLE RIVER DELTA
Nechelik Channel

Map 20

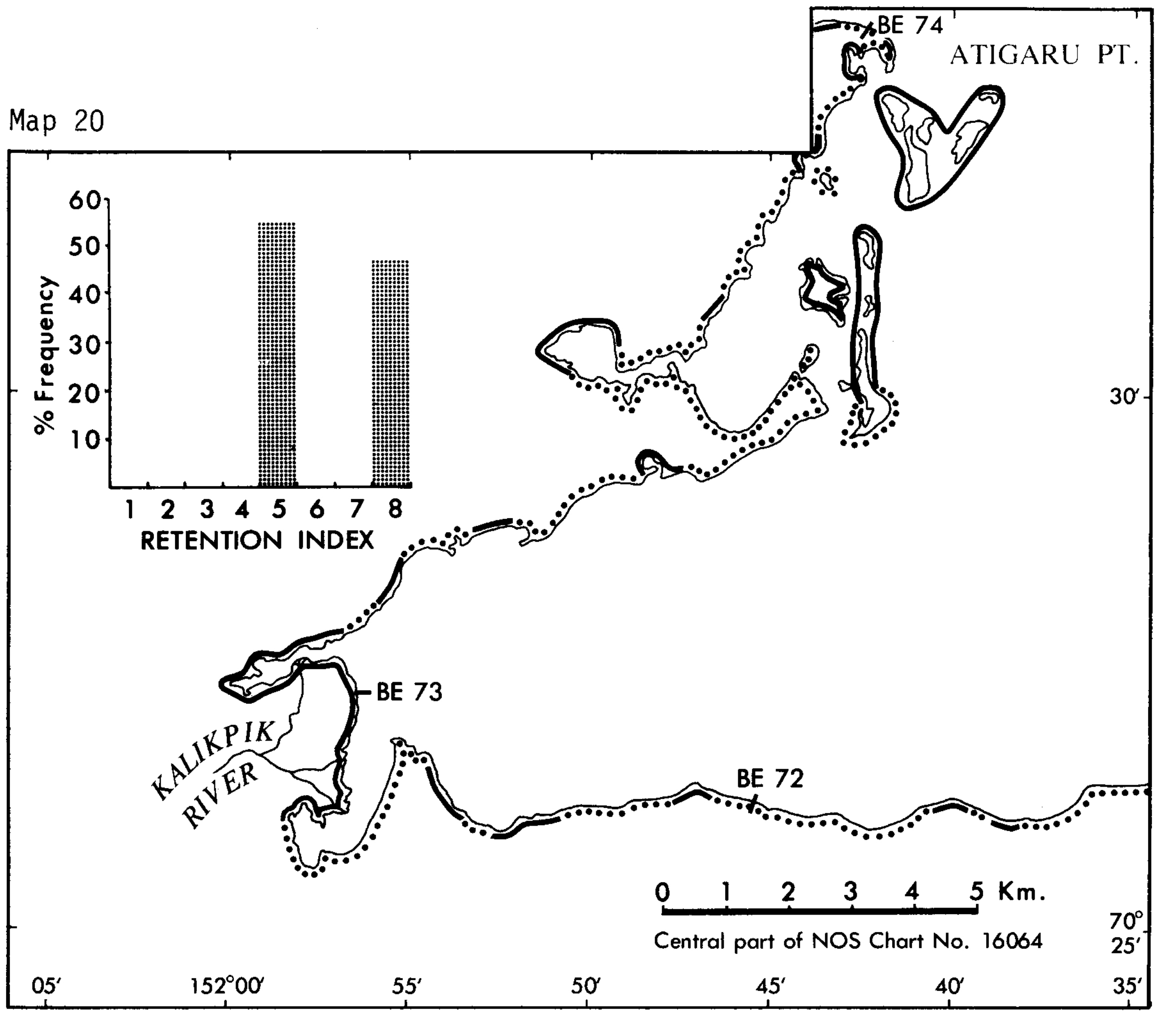

BE 74
ATIGARU PT.
60
50
40
30
20
10
% Frequency
1 2 3 4 5 6 7 8
RETENTION INDEX
30′
BE 73
KALIKPIK
RIVER
BE 72
0 1 2 3 4 5 Km.
70°
25′
Central part of NOS Chart No. 16064
05′
152°00′
55′
50′
45′
40′
35′

Map 21

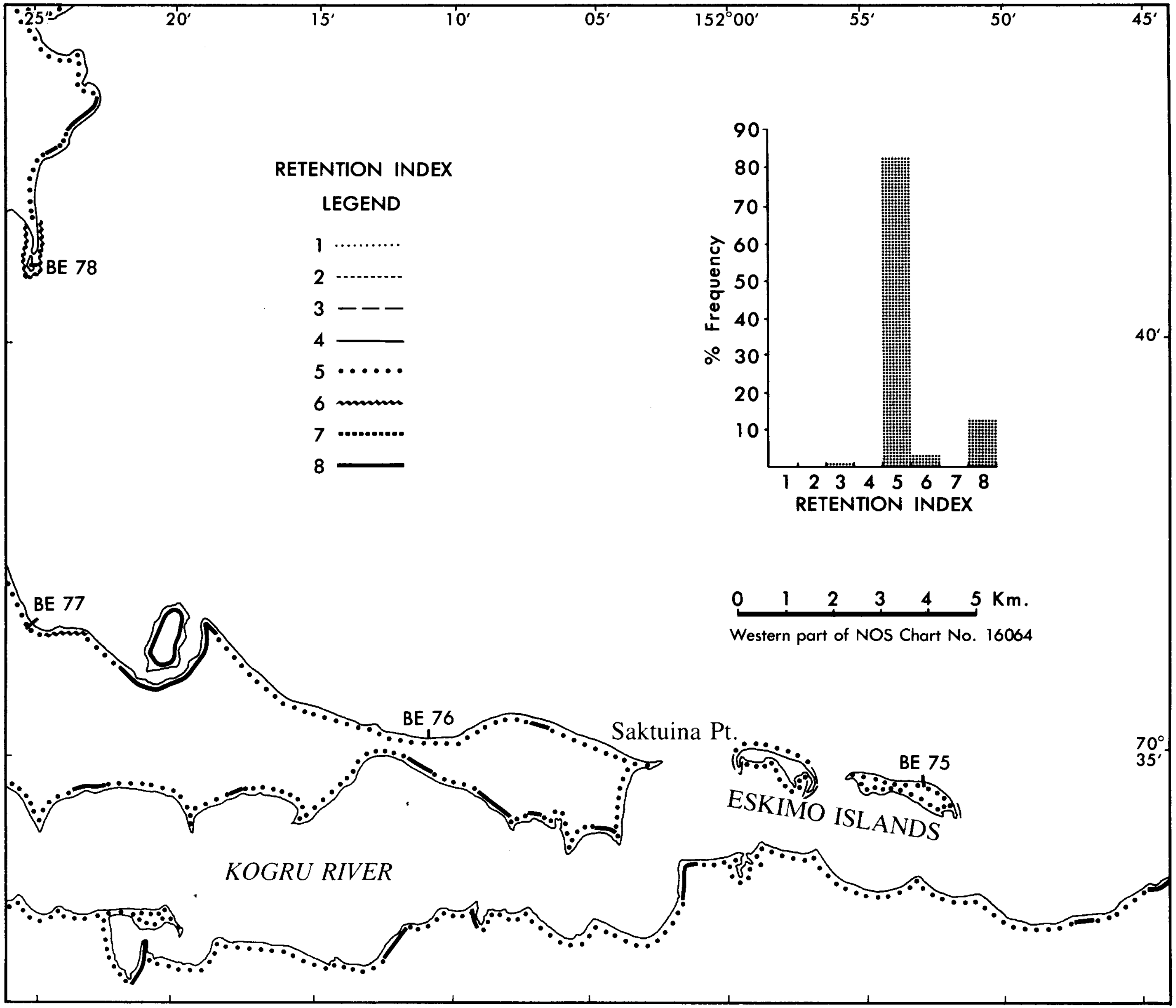
25'
20'
15'
10'
05'
152°00'
55'
50'
45'
40'
70°
35'
RETENTION INDEX
LEGEND
1
2
3
4
5
6
7
8
BE 78
BE 77
BE 76
BE 75
Saktuina Pt.
ESKIMO ISLANDS
KOGRU RIVER
90
80
70
60
50
40
30
20
10
% Frequency
1 2 3 4 5 6 7 8
RETENTION INDEX
0 1 2 3 4 5 Km.
Western part of NOS Chart No. 16064

Map 22

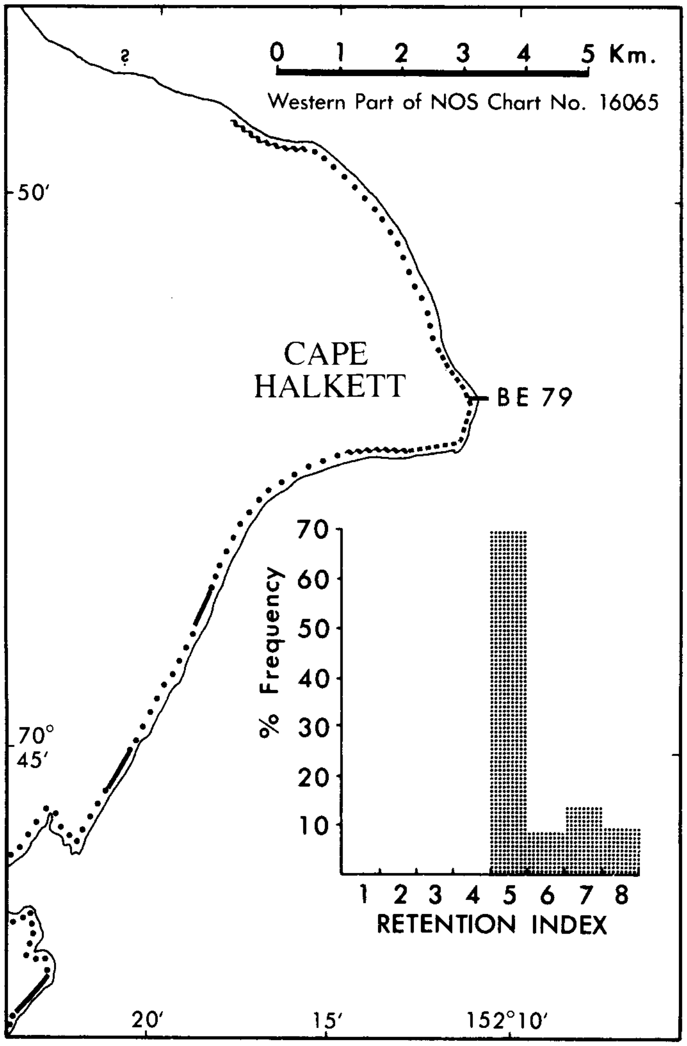

0 1 2 3 4 5 Km.
Western Part of NOS Chart No. 16065
50′
CAPE HALKETT
BE 79
70° 45′
20′
15′
152°10′
70
60
50
40
30
20
10
% Frequency
1 2 3 4 5 6 7 8
RETENTION INDEX

Map 23

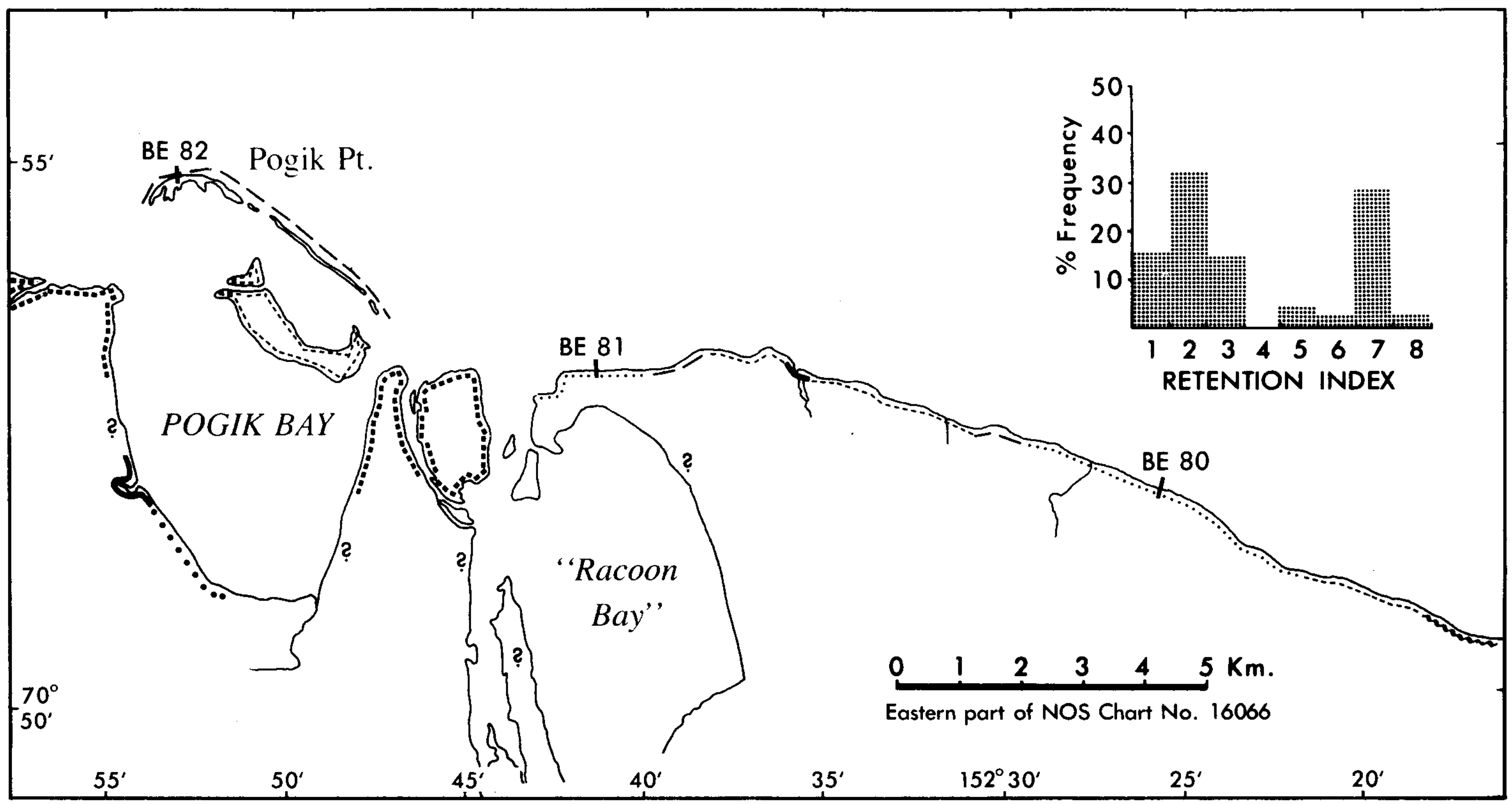

BE 82
Pogik Pt.
POGIK BAY
BE 81
"Racoon Bay"
BE 80
50
40
30
20
10
% Frequency
1 2 3 4 5 6 7 8
RETENTION INDEX
0 1 2 3 4 5 Km.
Eastern part of NOS Chart No. 16066
55′
70°
50′
55′
50′
45′
40′
35′
152°30′
25′
20′

Map 24

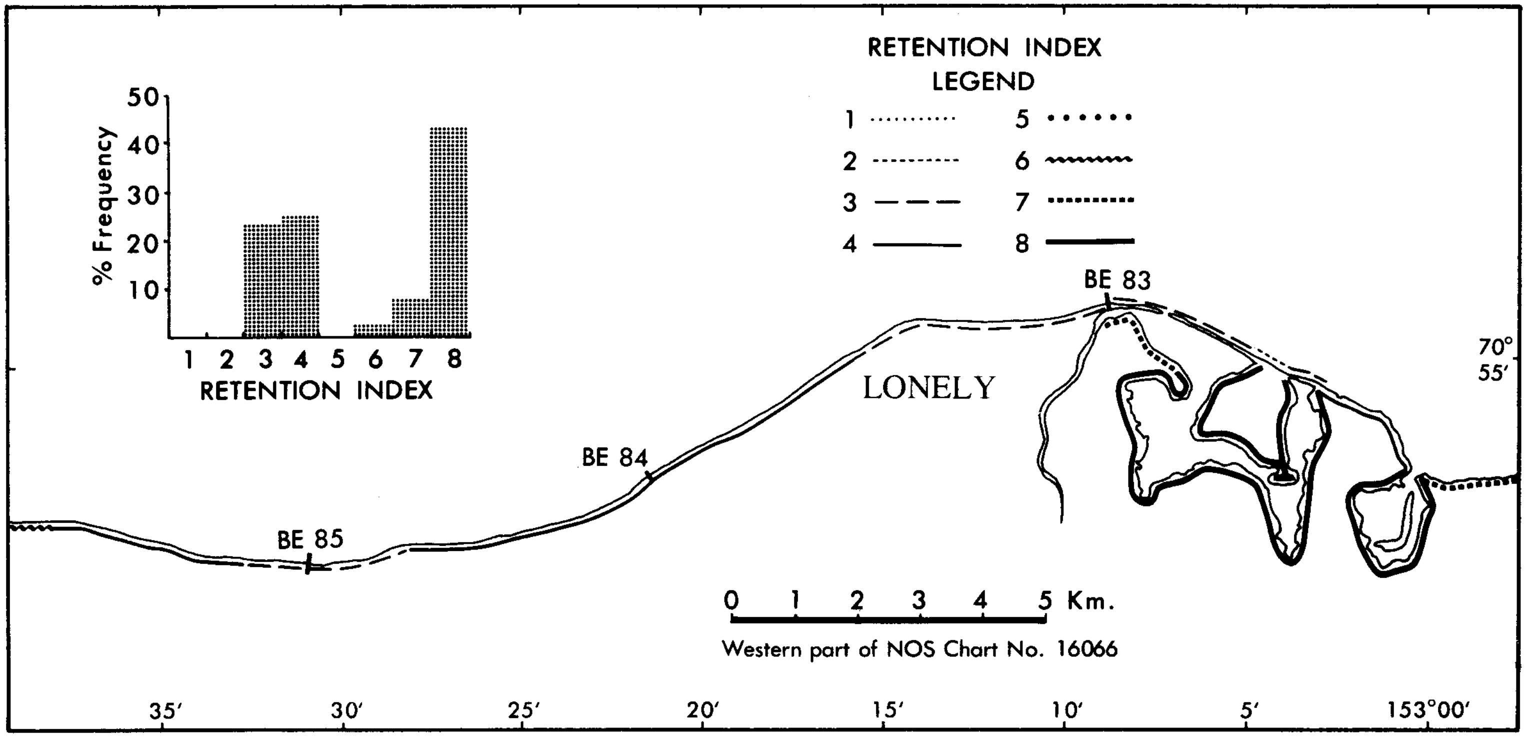
RETENTION INDEX
LEGEND
1
2
3
4
5
6
7
8
50
40
30
20
10
% Frequency
1 2 3 4 5 6 7 8
RETENTION INDEX
BE 83
BE 84
BE 85
LONELY
70°
55′
0 1 2 3 4 5 Km.
Western part of NOS Chart No. 16066
35′
30′
25′
20′
15′
10′
5′
153°00′

Map 25

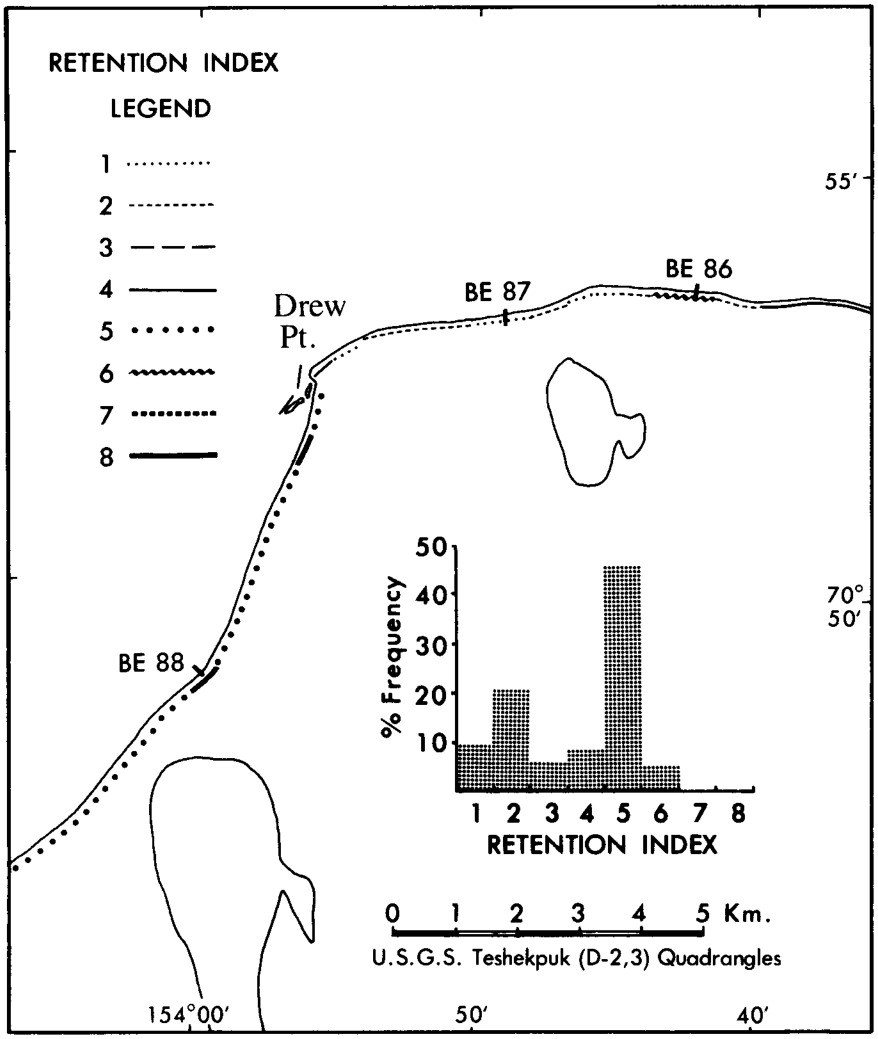

RETENTION INDEX
LEGEND
1
2
3
4
5
6
7
8
Drew
Pt.
BE 87
BE 86
BE 88
55′
70°
50′
50
40
30
20
10
% Frequency
1 2 3 4 5 6 7 8
RETENTION INDEX
0 1 2 3 4 5 Km.
U.S.G.S. Teshekpuk (D-2,3) Quadrangles
154°00′
50′
40′

Map 26

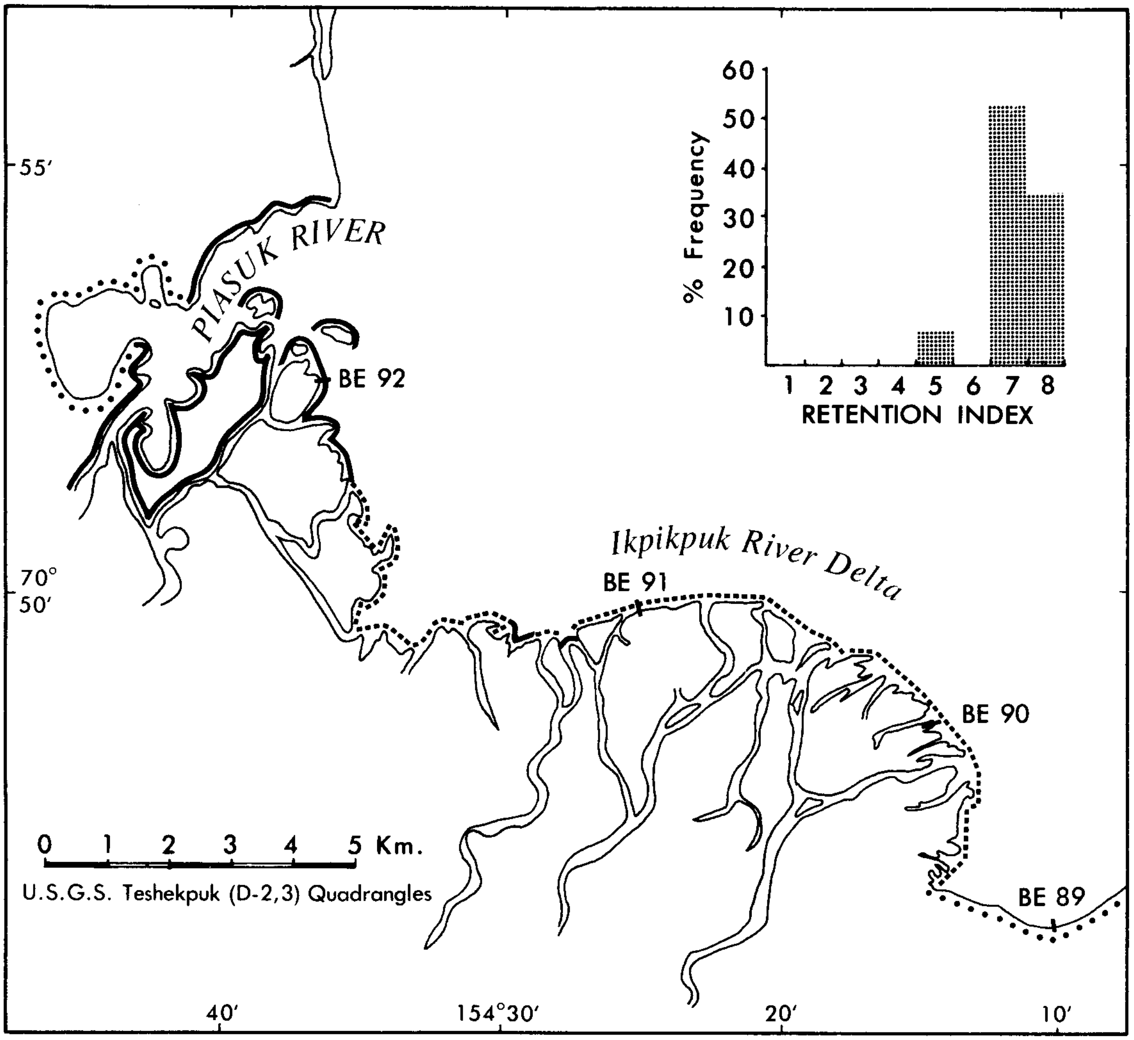

PIASUK RIVER
BE 92
Ikpikpuk River Delta
BE 91
BE 90
BE 89
55′
70°
50′
40′
154°30′
20′
10′
0 1 2 3 4 5 Km.
U.S.G.S. Teshekpuk (D-2,3) Quadrangles
% Frequency
60
50
40
30
20
10
1 2 3 4 5 6 7 8
RETENTION INDEX

Map 27

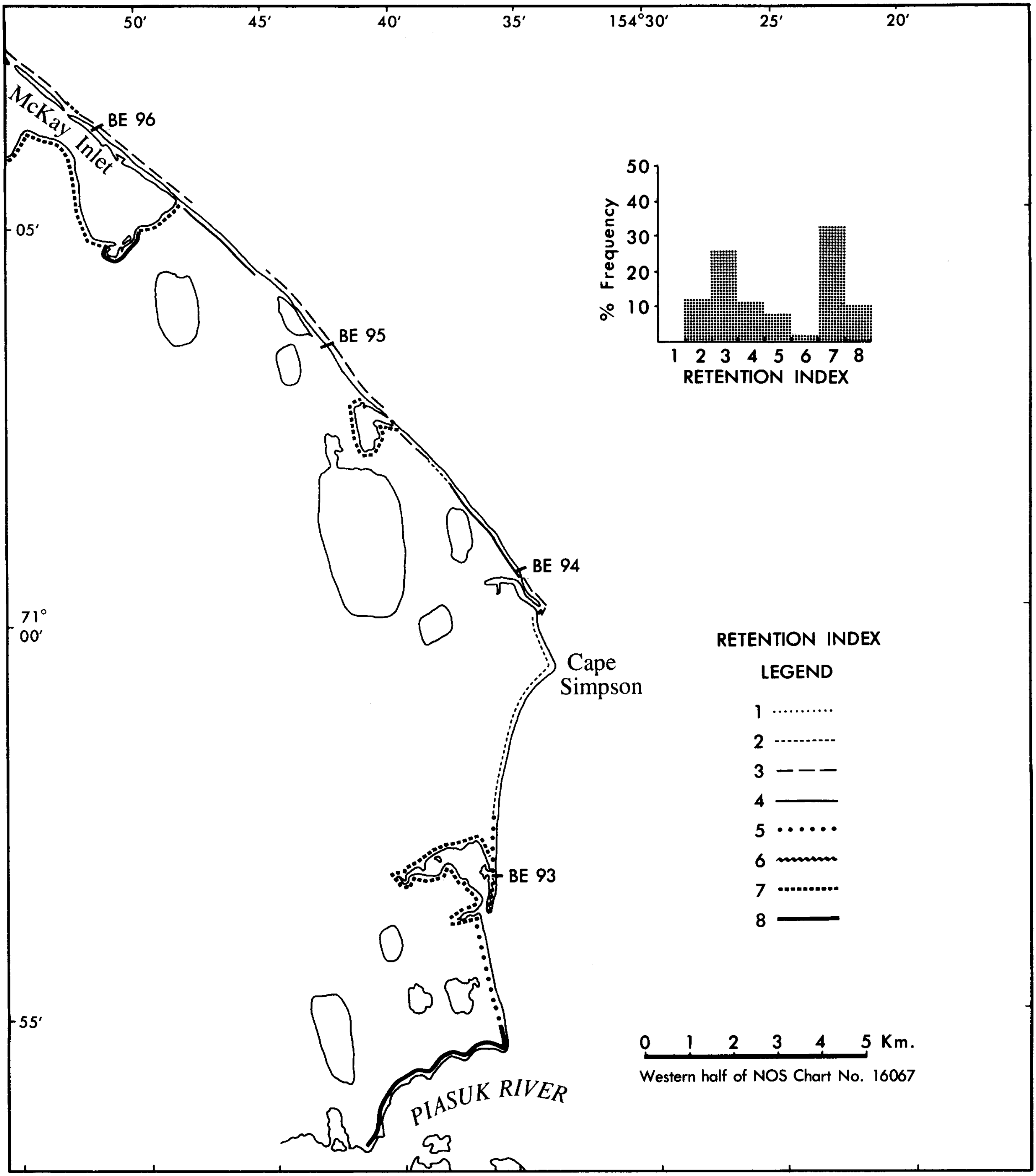

50′
45′
40′
35′
154°30′
25′
20′
05′
71°
00′
55′
McKay Inlet
BE 96
BE 95
BE 94
BE 93
Cape Simpson
PIASUK RIVER
50
40
30
20
10
% Frequency
1 2 3 4 5 6 7 8
RETENTION INDEX
RETENTION INDEX
LEGEND
1
2
3
4
5
6
7
8
0 1 2 3 4 5 Km.
Western half of NOS Chart No. 16067

Map 28

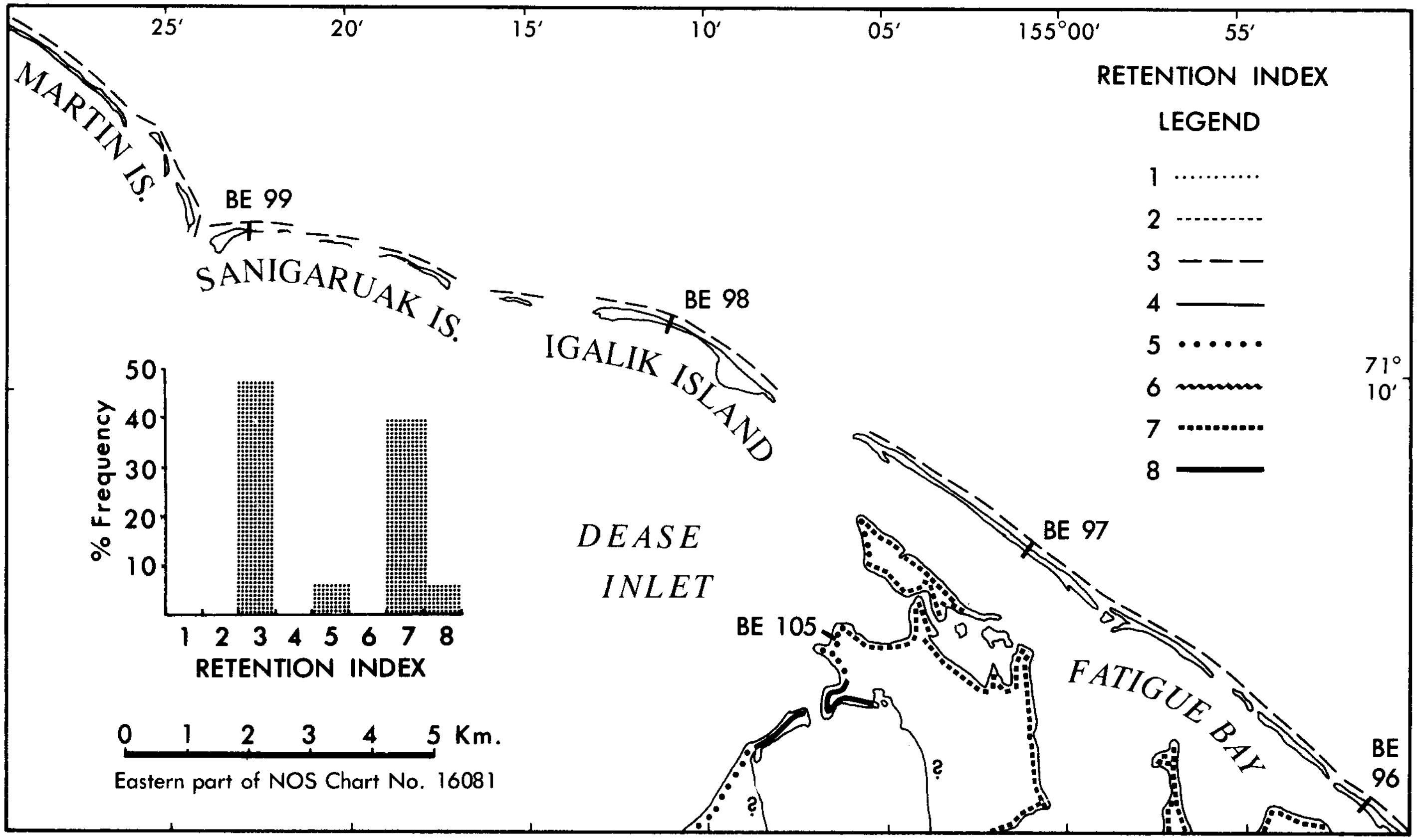
25′
20′
15′
10′
05′
155°00′
55′
71°
10′
RETENTION INDEX
LEGEND
1
2
3
4
5
6
7
8
MARTIN IS.
BE 99
SANIGARUAK IS.
BE 98
IGALIK ISLAND
DEASE
INLET
BE 97
BE 105
FATIGUE BAY
BE
96
50
40
30
20
10
% Frequency
1 2 3 4 5 6 7 8
RETENTION INDEX
0 1 2 3 4 5 Km.
Eastern part of NOS Chart No. 16081

Map 29

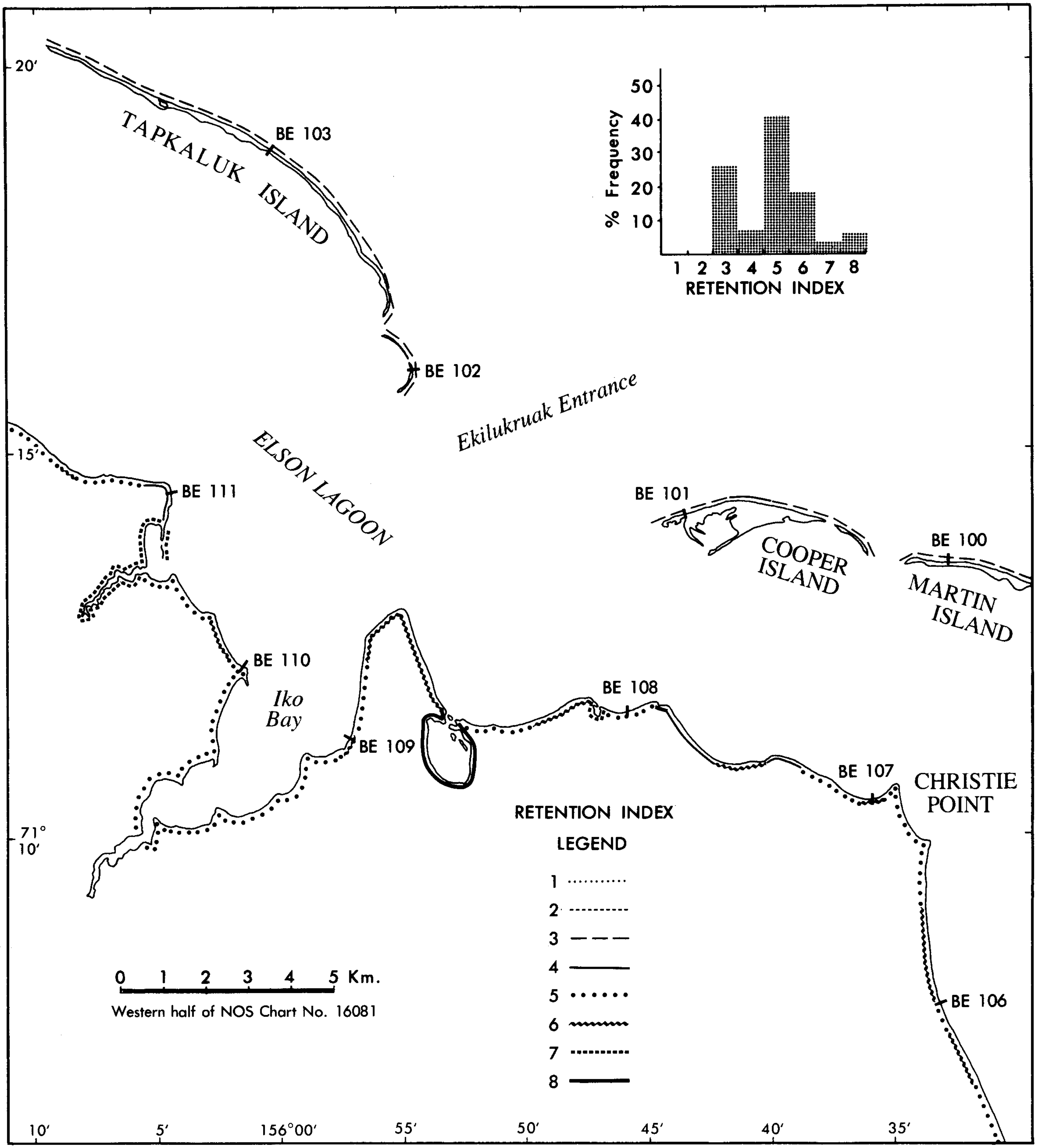
TAPKALUK ISLAND
BE 103
BE 102
Ekilukruak Entrance
ELSON LAGOON
BE 111
BE 101
COOPER ISLAND
BE 100
MARTIN ISLAND
BE 110
Iko Bay
BE 109
BE 108
BE 107
CHRISTIE POINT
BE 106
% Frequency
50
40
30
20
10
1 2 3 4 5 6 7 8
RETENTION INDEX
RETENTION INDEX
LEGEND
1
2
3
4
5
6
7
8
0 1 2 3 4 5 Km.
Western half of NOS Chart No. 16081
20′
15′
71° 10′
10′
5′
156°00′
55′
50′
45′
40′
35′

Map 30

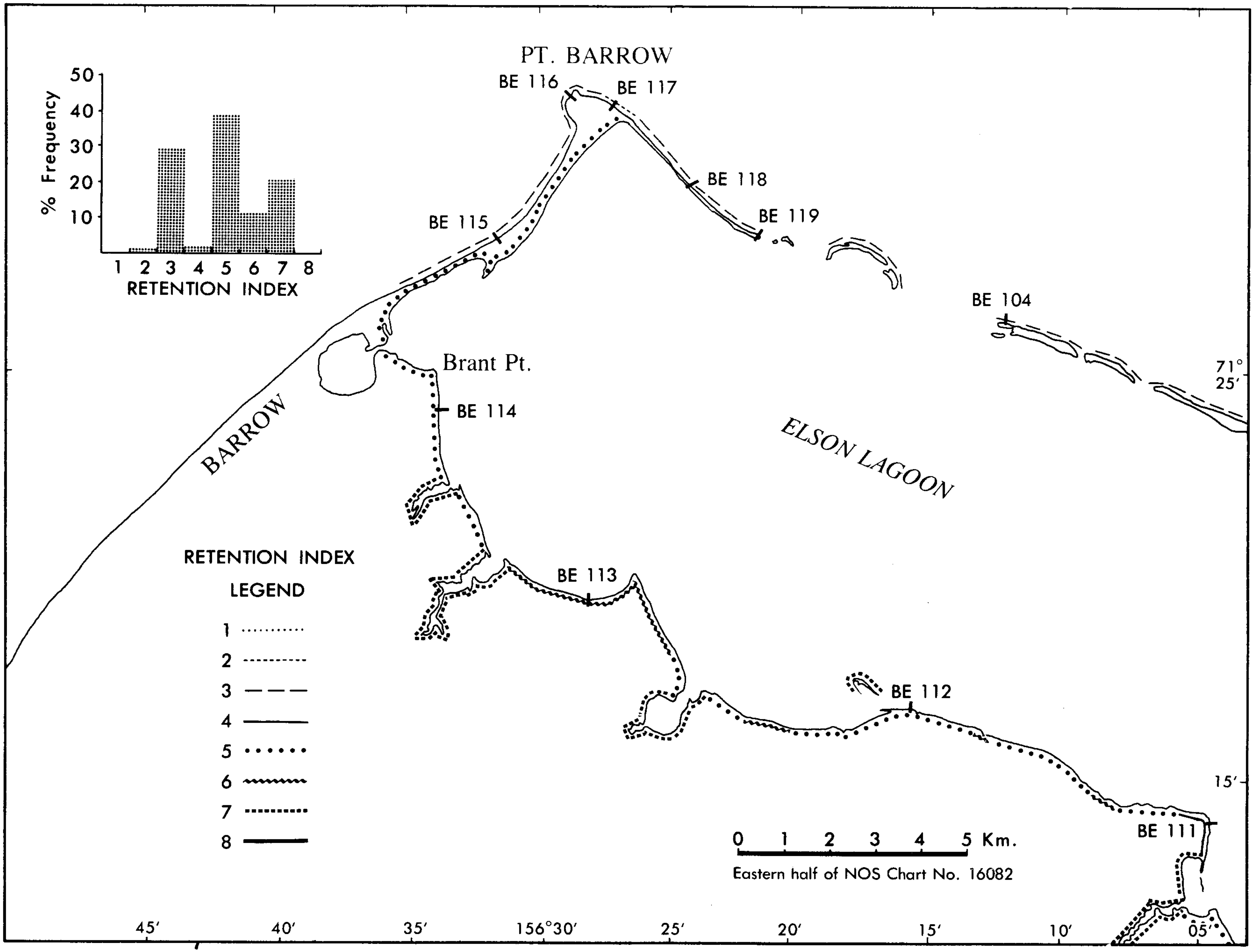
PT. BARROW
BE 116
BE 117
BE 118
BE 119
BE 115
BE 104
Brant Pt.
BE 114
BARROW
ELSON LAGOON
BE 113
BE 112
BE 111
71° 25′
15′
50
40
30
20
10
% Frequency
1 2 3 4 5 6 7 8
RETENTION INDEX
RETENTION INDEX
LEGEND
1
2
3
4
5
6
7
8
0 1 2 3 4 5 Km.
Eastern half of NOS Chart No. 16082
45′
40′
35′
156°30′
25′
20′
15′
10′
05′

Some Beaufort coast subenvironments differ from any in which earlier spills have occurred. The predicted longevity of spilled oil in these environments is somewhat speculative. Controlled arctic oil spill experiments, planned for the near future, may permit a better assessment of the retention potential of these unique arctic coasts.

The main product of this oil spill assessment of the coast of the Beaufort Sea, is a series of maps at a scale of about 1:125,000, depicting the geographic distribution of the potential for retention of oil introduced into any given environment. This is expressed as a retention index. The index ranges from 1 for an environment with low probability for oil retention to 8 for an environment with the maximum probability for retention. There is no assessment of the actual probability for oil to reach any location on the coast.

The maps in this report are prepared as aids in the development of a contingency plan for oil spill combat along the arctic coast of Alaska.

6. ACKNOWLEDGEMENTS

A large number of people have contributed to this oil spill assessment of the Beaufort coast. Many ideas and concepts were developed by Miles Hayes and colleagues at the University of South Carolina; others were generated during discussions at the OCSEAP-sponsored Beaufort synthesis meetings. Field assistance was provided by Christopher Ruby, Jeffrey Knoth, Ian Fischer, Peter Rinehart and Robert Fahnestock. Data on the morphology, sediments, and general geology of the Beaufort coast were also provided by Carter Broad and David Hopkins.

Funds for the study were provided through the Outer Continental Shelf Environmental Assessment Program by NOAA Grant no. 03-5022-82 to the University of South Carolina (Dag Nummedal, Principal Investigator). The aurthor wishes to express his sincere gratitude to Gunter Weller (Arctic Project Office, University of Alaska) for encouragement and help during the project.

As this is written the day after Fahnestock's tragic death in an aircraft accident, I would also like to express my sincere gratitude for the sense of observation and scientific inquiry he has helped develop in me and many of my colleagues over these years.

REFERENCES

Barnes P. W., and E. Reimnitz, 1974, Sedimentary processes on arctic shelves off the northern coast of Alaska: in, J.C. Reed and J.E. Sater (eds.), The Coast and Shelf of the Beaufort Sea. Proceedings of the Arctic Institute of North America, Symposium on Beaufort Sea Coast and Shelf Research, Arlington, VA, pp. 439-476.

Cannon, P.F., 1978, The environmental geology and geomorphology of the barrier island - lagoon system along the Beaufort Sea coastal plain from Prudhoe Bay to the Colville River: Annual Repts. of Principal Investigators, OCSEAP Program, NOAA, v. X, pp. 687-713.

Carlson, R.F.,R. Seifert and D. Kane, 1977, Effects of seasonability and variability of stream flow on nearshore coastal areas: Annual Repts. of Principal Investigators, OCSEAP Program, NOAA, Research Unit 111.

Dygas, J.A., and D.C. Burrell, 1976, Dynamic sedimentological processes along the Beaufort Sea coast of Alaska; in D.W. Hood and D.C. Burrell (eds.), Assessment of the Arctic Marine Environment, Institute of Marine Science, Univ. of Alaska, Occ. Publ. no. 4, pp. 189-203.

Dygas, J.A., R. Tucker and D.C. Burrell, 1972, Heavy minerals, sediment transport and shoreline changes of the barrier islands and coast between Oliktok Point and Beechy Pt.: in, P.J. Kinney et al. (eds.), Baseline Study of the Alaskan Arctic Aquatic Environment, Institute of Marine Science, Univ. of Alaska, Report no. 72-73, pp. 61-121.

Frey, R.W., and P.B. Basan, 1978, Coastal salt marshes: in, R.A. Davis (ed.), Coastal Sedimentary Environments, Springer-Verlag, N.Y., pp. 101-169.

Gundlach, E.R. and Hayes, M.D., 1977, The Urquiola oil spill: Case history and discussion of clean-up and control methods: Marine Pollution Bull., v. 8, p. 132-136.

Hayes, M.D., and Gundlach, E.R., 1975, Coastal geomorphology and sedimentation of the Metula oil spill site in the Strait of Magellan: Rept. to NSF, Washington, D.C.

Hayes, M.D., Michel, J., and Brown, P.J., 1977, Vulnerability of coastal environments of Lower Cook Inlet, Alaska, to oil spill impact: Proceedings, POAC '77, v. II, p. 832-838.

Leffingwell, E., deK., 1908, Flaxman Island, a glacial remnant: J. Geology, v. 16, p. 56-64.

Lewellen, R., 1978(?), A study of Beaufort Sea coastal erosion, northern Alaska: Final Report to the OCSEAP Program, NOAA, Research Unit 407, 24 pp.

McLean, A.Y., and O.J. Betancourt, 1973, Physical and chemical changes in spilled oil weathering under natural conditions: Proceedings of the Offshore Technology Conference, Dallas, Paper no. 1748, pp. 1250-1255.

National Academy of Sciences, 1975, Petroleum in the Marine Environment, Washington, D.C.

National Oceanic and Atmospheric Administration, 1978, Environmental Assessment of the Alaskan Continental Shelf. Interim Synthesis: Beaufort/Chukchi, NOAA, Environmental Research Laboratories, Boulder, Colo. 362 pp.

Nummedal, D., 1979, Coarse grained sediment dynamics - Beaufort Sea, Alaska: Proceedings of the 5th conference on Port and Ocean Engineering Under Arctic Conditions, Trondheim, Norway, v. II, pp. 845-858.

Owens, E.H., 1978, Oil spills, shoreline cleanup and the coasts of Prince Edward Island: Report to the Atlantic Regional Office of Environment Canada, Halifax, Nova Scotia.

Owens, E.H., J.R. Harper and D. Nummedal, 1980, Sediment transport processes and coastal variability on the Alaskan North Slope: Abstracts, 17th International Conference on Coastal Engineering, Sydney, Australia, pp. 43-44.

APPENDIX

PHOTOS OF RETENTION POTENTIAL CATEGORIES

The photos are arranged in order of increasing degree of oil spill retention potential.
Retention index 1: lowest potential
Retention index 8: highest potential

LIST OF FIGURES

Figure A.35. Retention Index: 6. "Coffee-grounds" shoreline at Simpson Cove in Camden Bay. Station BE 14

Figure A.36. Retention Index: 7(8 in areas of polygonal ground). The Ikpikupk River delta at the head of Smith Bay

Figure A.37. Retention Index: 7. This view upstream of the Konganevik River delta demonstrates the ice-covered delta with a wide-spread mud deposit from the spring flood. Photo taken on August 23, 1977

Figure A.38. Retention Index: 7. Margin of the Colville River delta at Station BE 69

Figure A.39. Retention Index: 7. Tracks and trails on recently emergent mudflat at the margin of the Colville River delta. Station BE 68

Figure A.40. Retention Index: 7. Tidal flats at the margin of the Sagavanirktok River delta

Figure A.41. Retention Index: 7. Tidal flats at the margin of the Kangikat River delta. Station BE 2

Figure A.42. Retention Index: 8. Low marsh in areas of polygonal ground at the margin of the Kuparuk River delta

Fig. A. 1. Retention Index: 1. Ice-bonded permafrost cliff west of Cape Halkett of station BE 80.

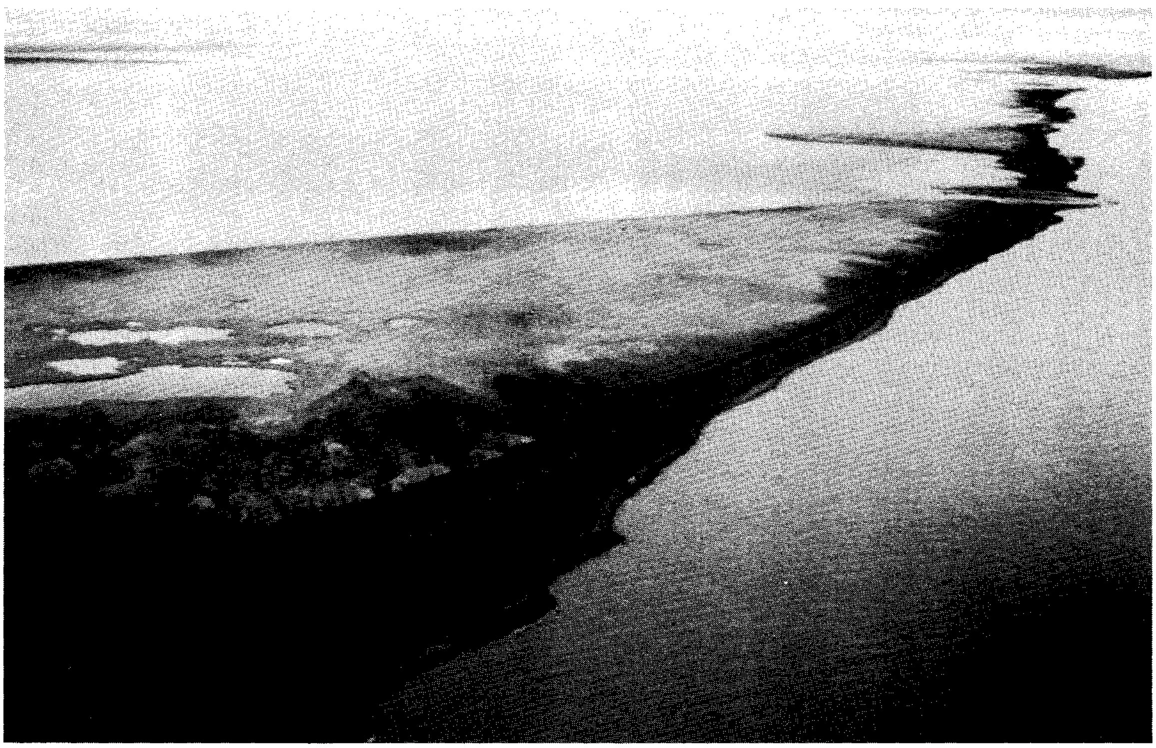

Fig. A. 2. Retention Index: 2. Westward view of Bodfish and Bertoncini islands in the Jones Islands group.

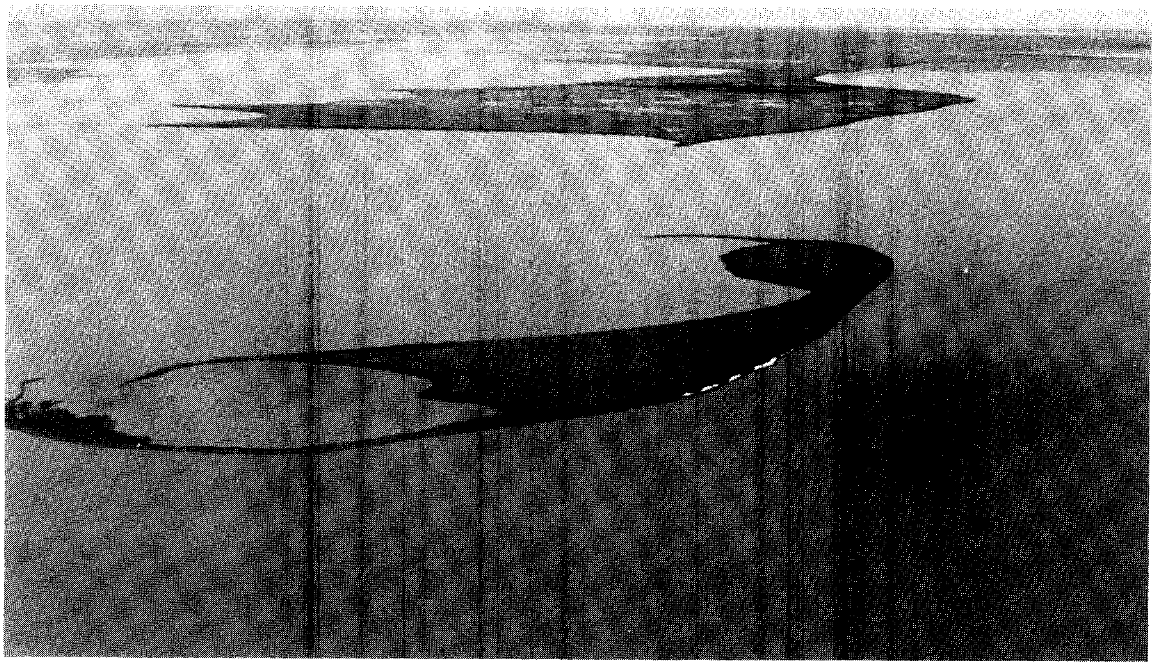

Fig. A. 3. Retention Index: 2. Westward view of Eskimo Island. Saktuina Point in the background north of Kogru River.

Fig. A. 4. Retention Index: 2. North-facing bluff at Barter Island, immediately north of the DEW-line station.

Fig. A. 5. Retention Index: 2. Bluff at Pt. Barrow.

Fig. A. 6. Retention Index: 2. Truncated sand dune and narrow beach in Harrison Bay.

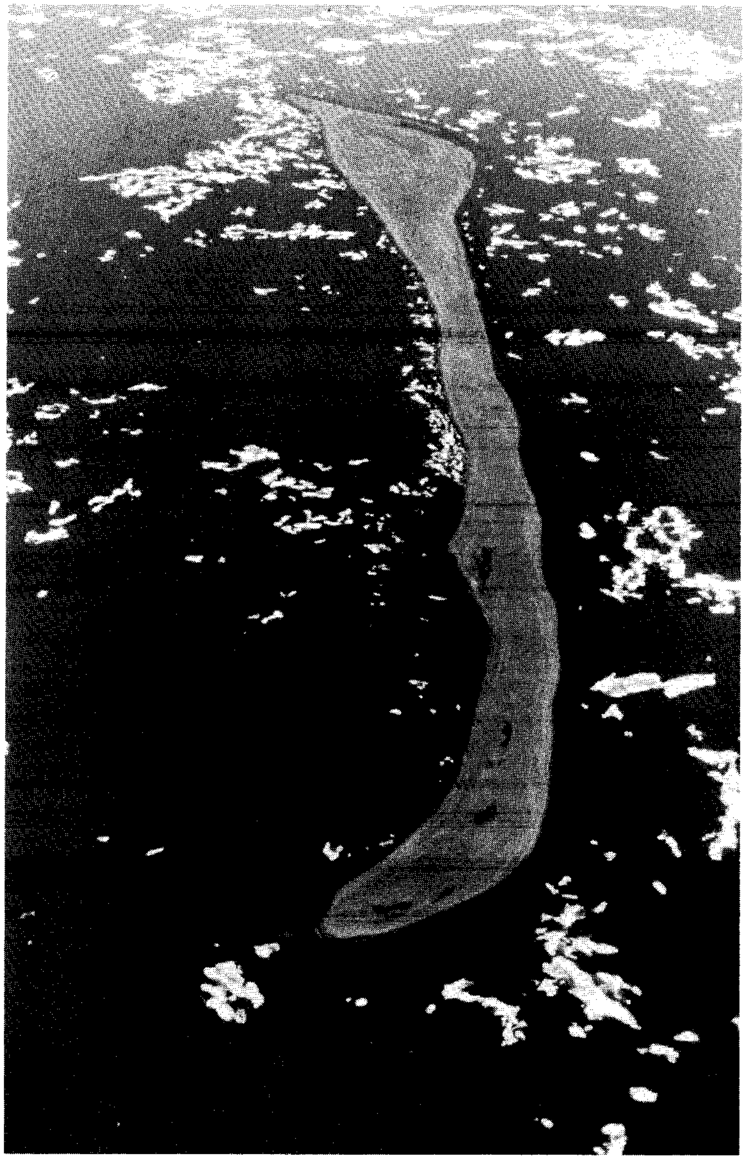

Fig. A. 7. Retention Index: 3. Small island in the Plover Islands chain, near Cooper Island.

Fig. A. 8. Retention Index: 3. Long Island in the Jones Islands group. View to the east.

Fig. A. 9. Retention Index: 3. Barriers at Pogik Pt. Pogik Bay to the right.

Fig. A. 10. Retention Index: 3(and 4). Cross Island off Prudhoe Bay. View to the west.

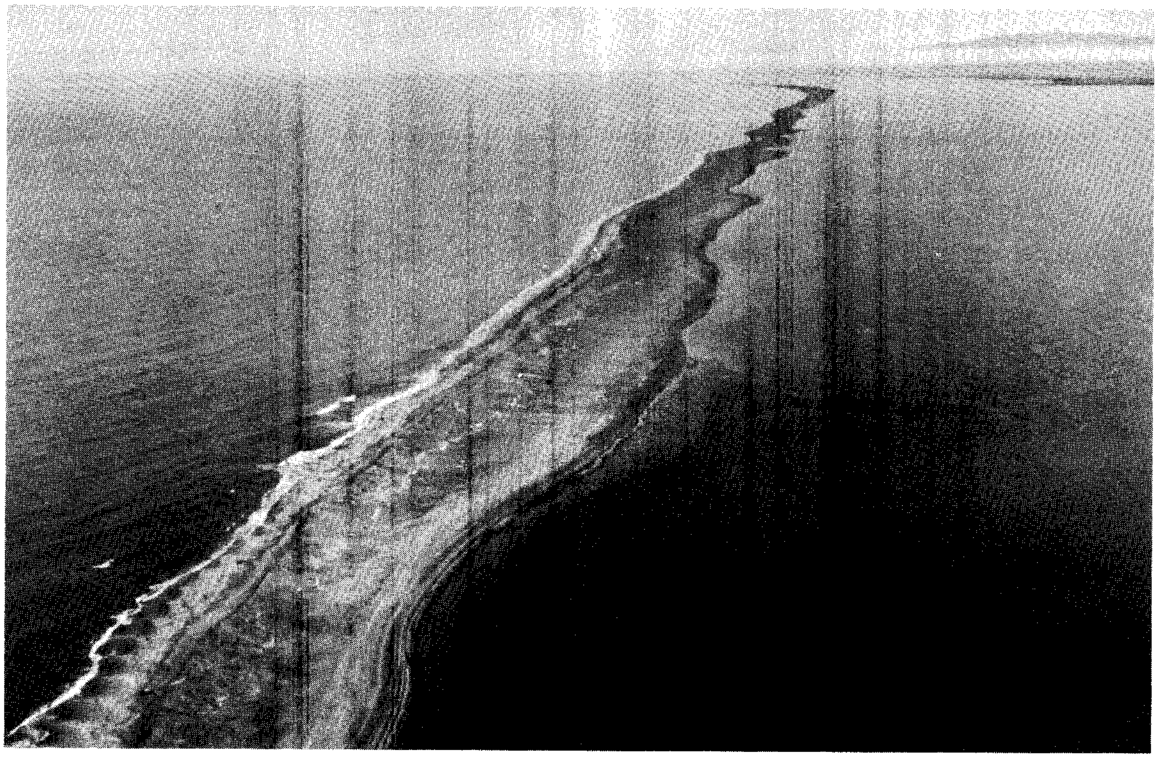

Fig. A. 11. Retention Index: 3. Barrier system in Camden Bay, near station BE 17.

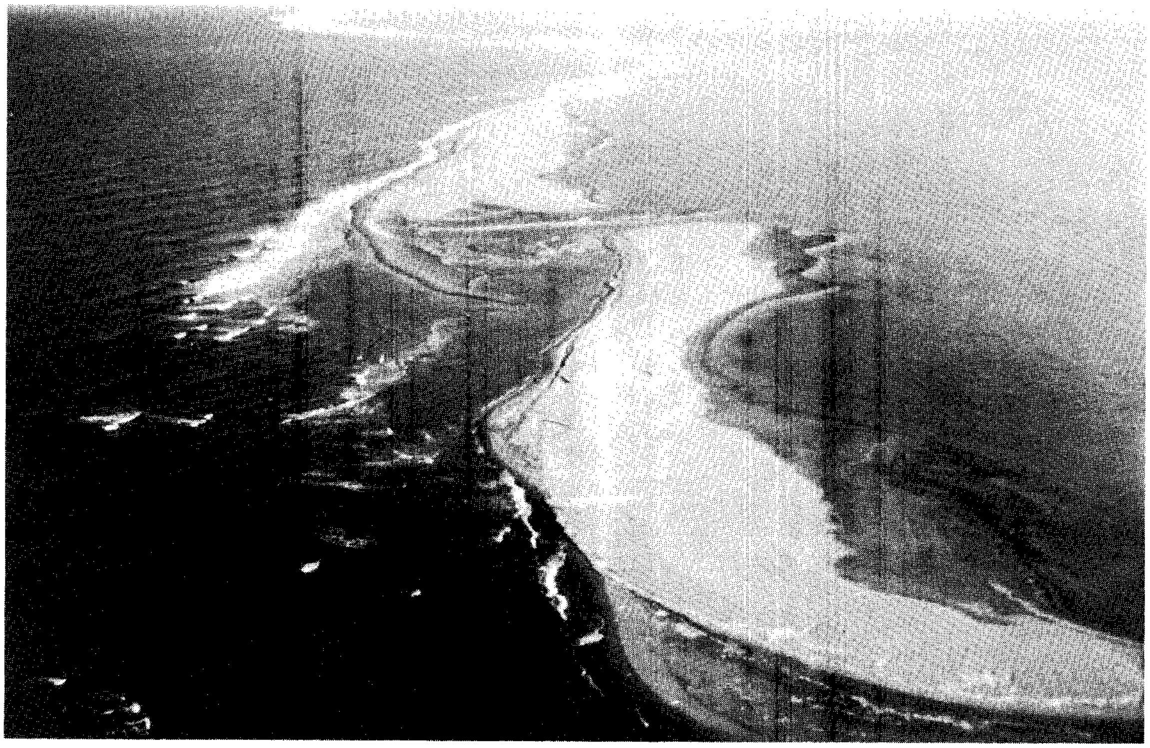

Fig. A. 12. Retention Index: 3. Barriers at Egaksrak Lagoon towards Siku Entrance. View towards the southeast.

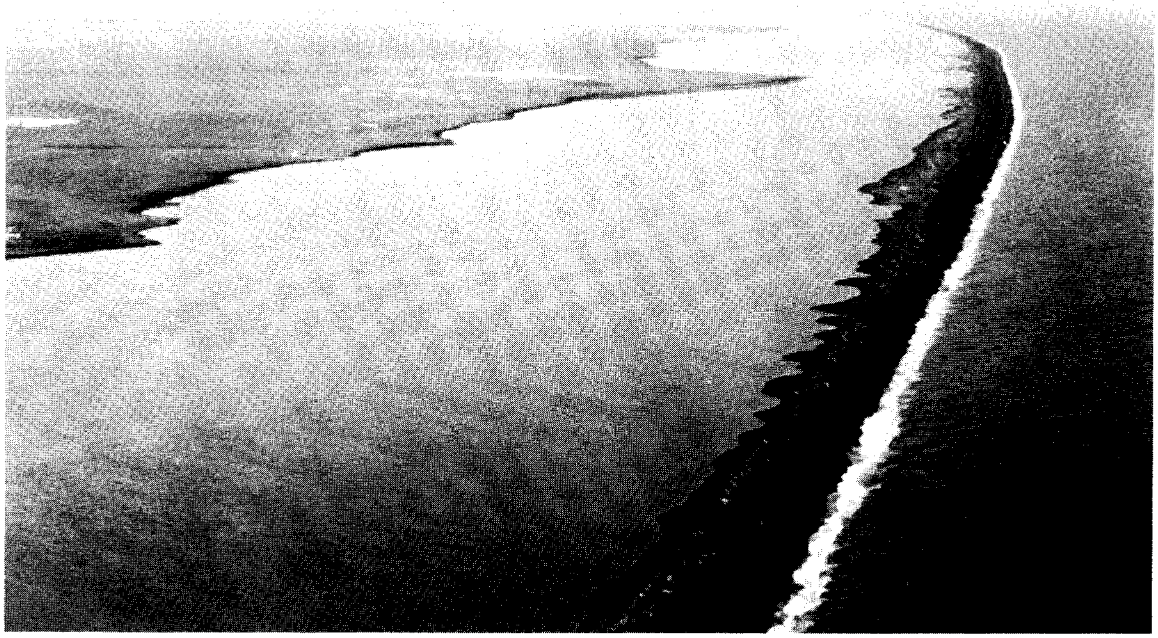

Fig. A. 13. Retention Index: 3. Barrier of Icy Reef, at Pingokraluk Point.

Fig. A. 14. Retention Index: 3. Ice-push at Long Island in the Jones Islands group.

Fig. A. 15. Retention Index: 3. Ice-push at Karluk Island in the McClure Islands group. Station BE 25.

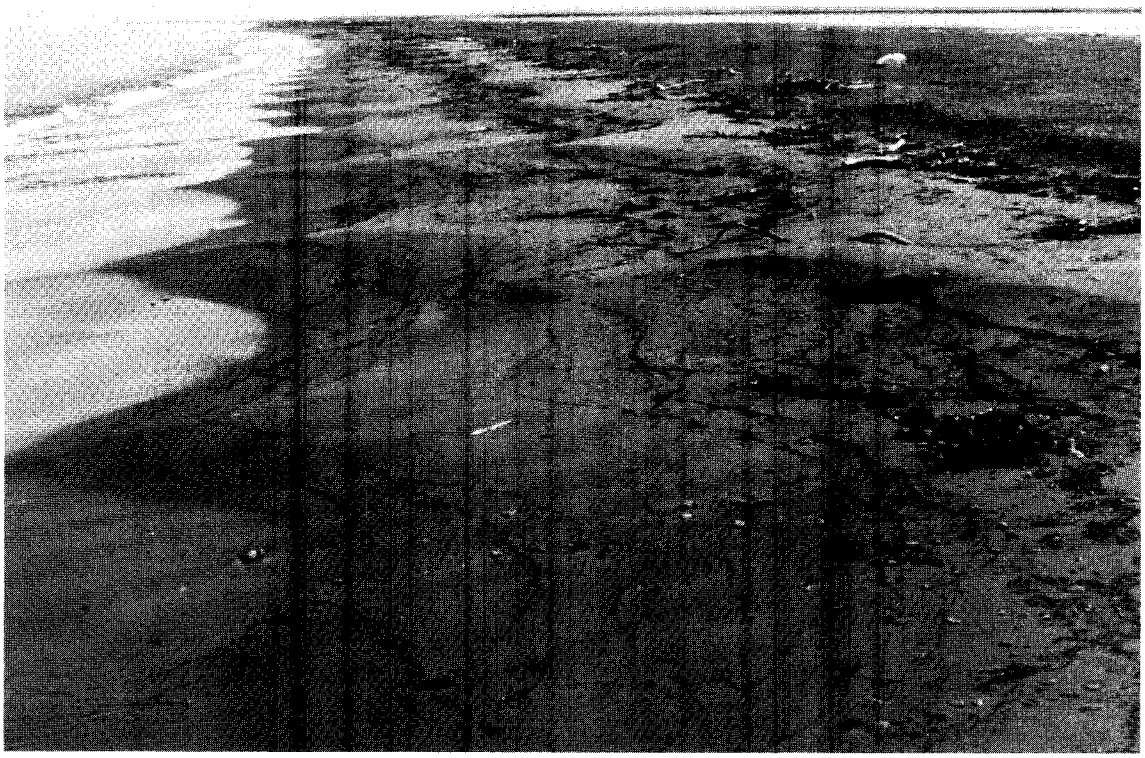

Fig. A. 16. Retention Index: 3. Cusps on a barrier beach in Camden Bay east of Brownlow Pt., at station BE 17.

Fig. A. 17. Retention Index: 3. Beach on the lagoonal side of Arey Island, at station BE 10.

Fig. A. 18. Retention Index: 3. Beach on the barrier system north of Egaksrak entrance at station BE 3.

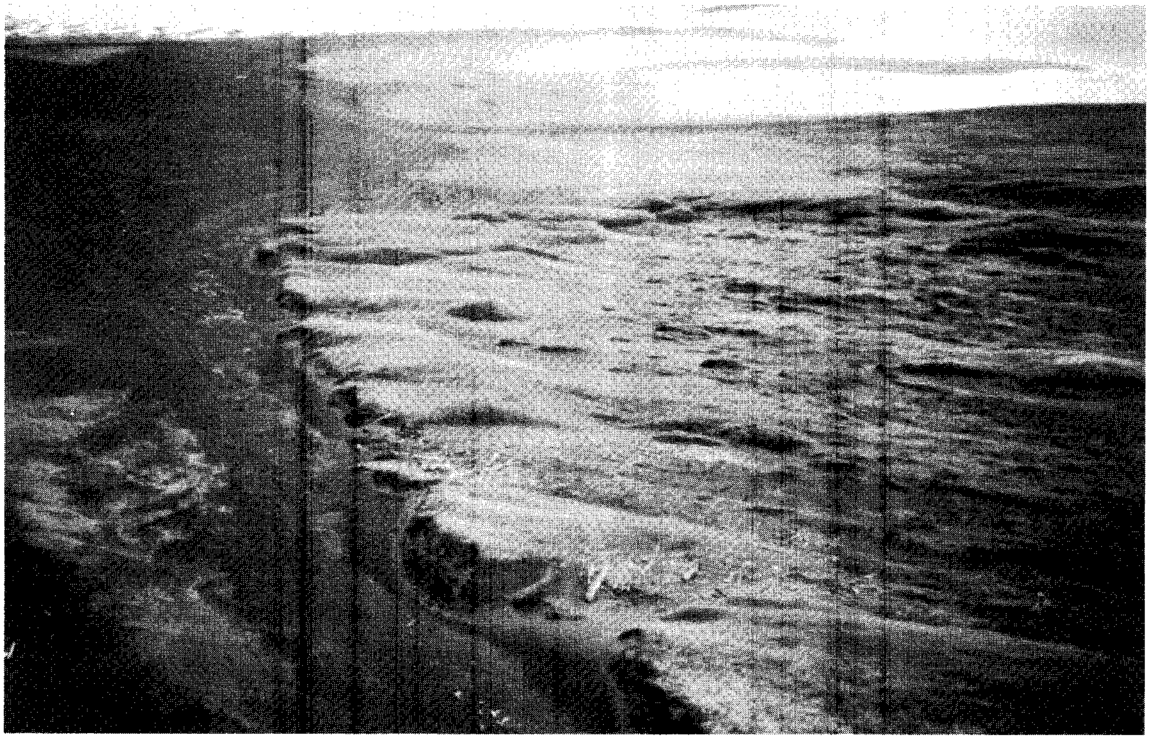

Fig. A. 19. Retention Index: 4. Sand dunes behind beach at east end of Bodfish Island in the Jones Islands group.

Fig. A. 20. Retention Index: 4. Beach at Atigaru Point in Harrison Bay. Station BE 74.

Fig. A. 21. Retention Index: 4. "Perched" gravel beach on low tundra along the east shore of Prudhoe Bay.

Fig. A. 22. Retention Index: 4. Truncated sand dunes on tidal flats of the Canning Delta at station BE 29.

Fig. A. 23. Retention Index: 4. Gravel beach grading into tundra at Brownlow Point. Station BE 18.

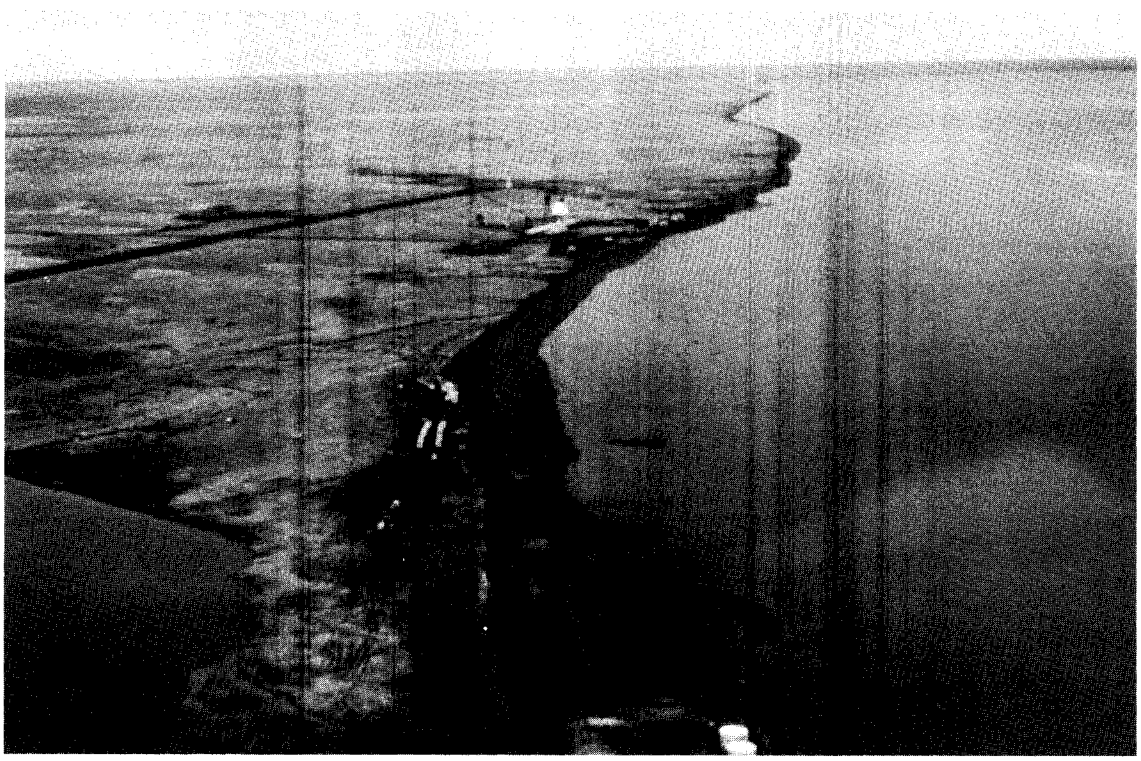

Fig. A. 24. Retention Index: 5. Southward view of Oliktok Point.

Fig. A. 25. Retention Index: 5. Lagoonal beach of central part of Flaxman Island. View to the east.

Fig. A. 26. Retention Index: 5. Northward view of the eastern shore of Harrison Bay. Station BE 67 in foreground.

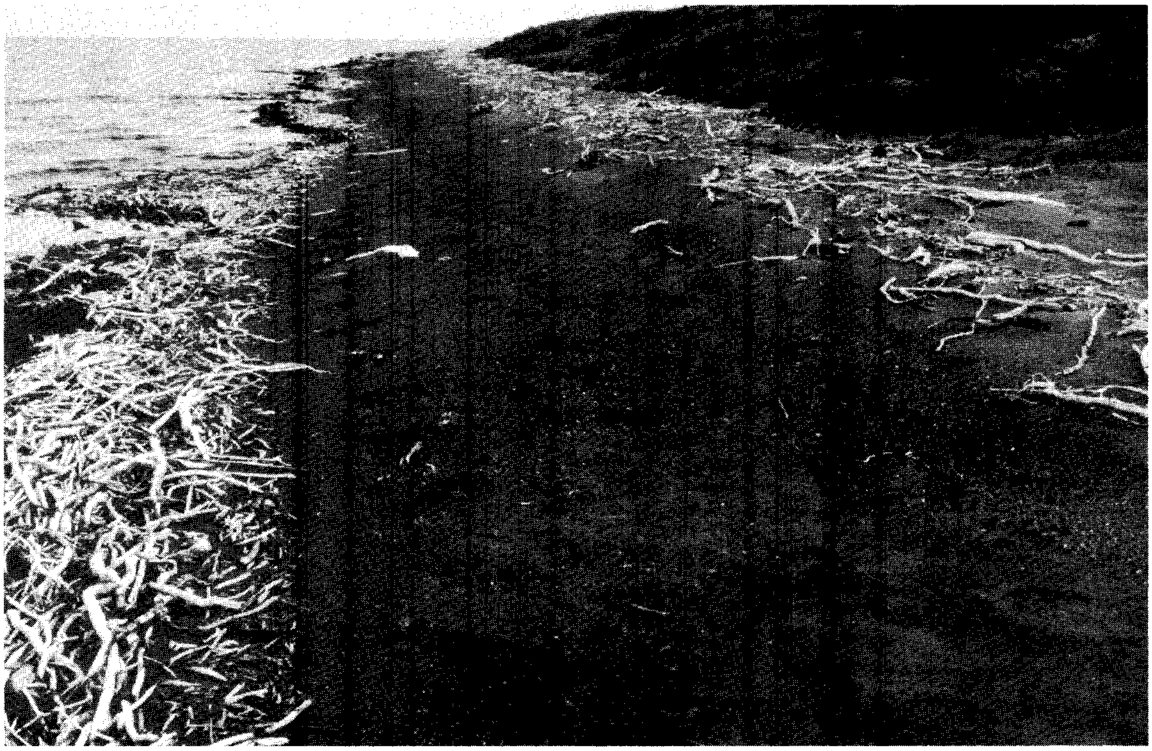

Fig. A. 27. Retention Index: 5. Eastern shore of Harrison Bay at station BE 67.

Fig. A. 28. Retention Index: 5. Shore of Prudhoe Bay near the ARCO dock.

Fig. A. 29. Retention Index: 5. Lagoonal shore at Flaxman Island. Station BE 20.

Fig. A. 30. Retention Index: 5. Mainland shore at Tapkaurak Lagoon. Station BE 6.

Fig. A. 31. Retention Index: 6. Peat-rich embayment at Simpson Cove in Camden Bay. Station BE 14.

Fig. A. 32. Retention Index: 6. Peat-rich outcrop at Tolaktuvuk Point in Harrison Bay. Station BE 70.

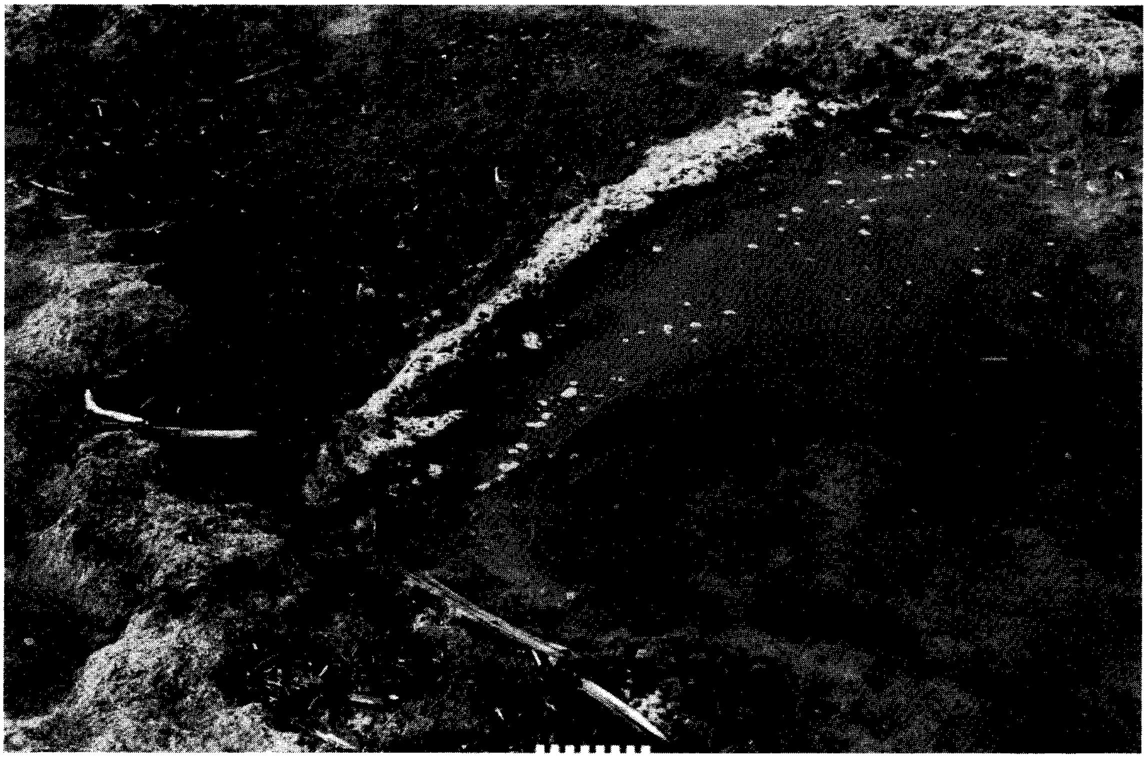

Fig. A. 33. Retention Index: 6. Floating peat trapped in small embayment along the mainland shore of Simpson Lagoon at station BE 65.

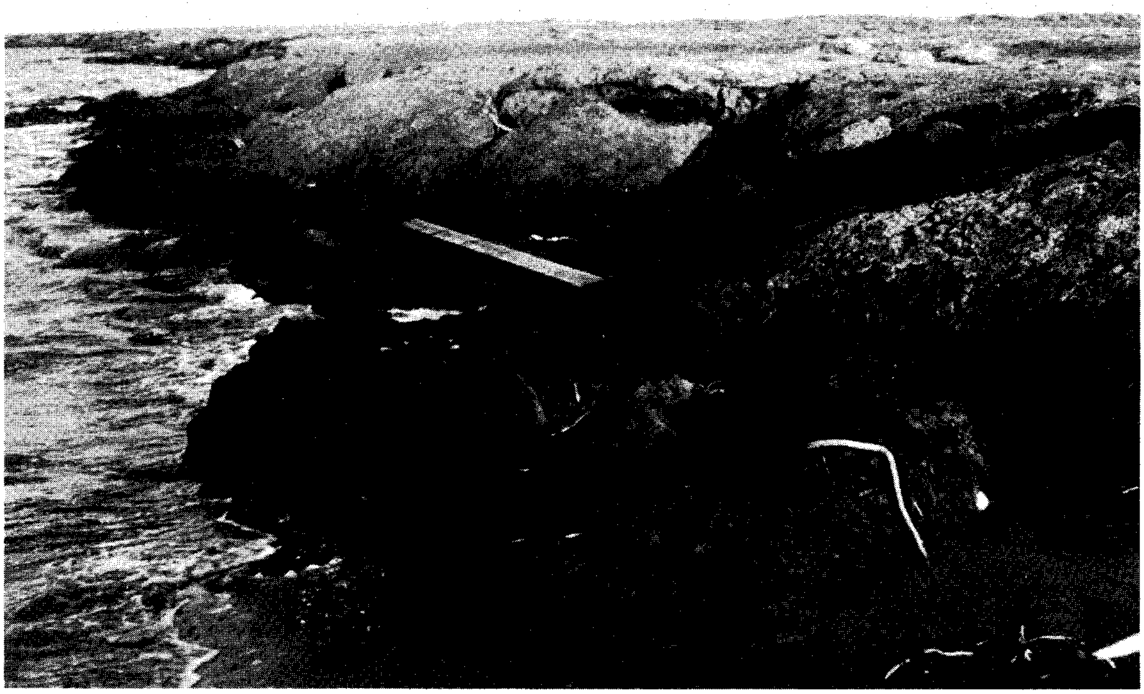

Fig. A. 34. Retention Index: 6. Low tundra mat along south shore of Prudhoe Bay.

Fig. A. 35. Retention Index: 6. "Coffee-grounds" shoreline at Simpson Cove in Camden Bay. Station BE 14.

Fig. A. 37. Retention Index: 7. This view upstream of the Konganevik River delta demonstrates the ice-covered delta with a widespread mud deposit from the spring flood. Photo taken on August 23, 1977.

Fig. A. 38. Retention Index: 7. Margin of the Colville River delta at station BE 69

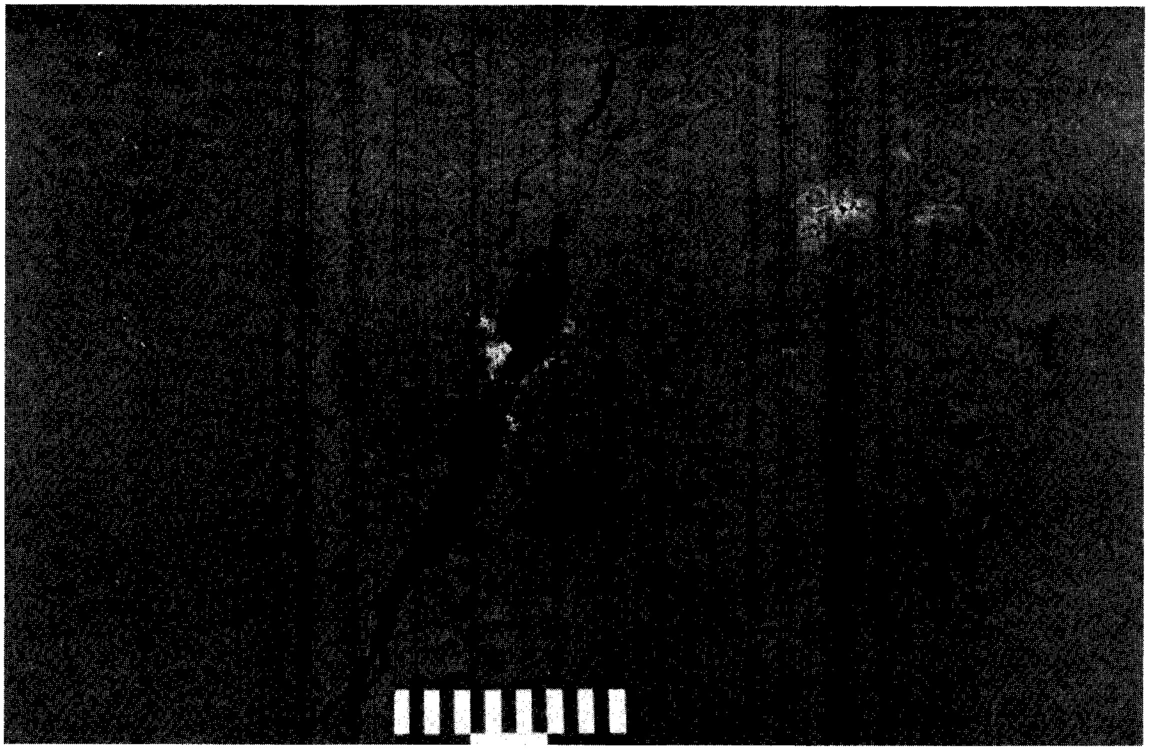

Fig. A. 39. Retention Index: 7. Tracks and trails on recently emergent mudflat at the margin of the Colville River delta. Station BE 68.

Fig. A. 40. Retention Index: 7. Tidal flats at the margin of the Sagavanirktok River delta.

Fig. A. 41. Retention Index: 7. Tidal flats at the margin of the Kangikat River delta. Station BE 2.

Fig. A. 42. Retention Index: 8. Low marsh in areas of polygonal ground at the margin of the Kuparuk River delta.

POTENTIAL OILED ICE TRAJECTORIES IN THE BEAUFORT SEA

by

D. R. Thomas

Flow Industries, Inc.
Research and Technology Division

Final Report
Outer Continental Shelf Environmental Assessment Program
Research Unit 252

January 1983

Foreword

This study was supported by the Bureau of Land Management through interagency agreement with the National Oceanic and Atmospheric Administration, under which a multiyear program responding to needs of petroleum development of the Alaskan Continental Shelf is managed by the Outer Continental Shelf Environmental Assessment (OCSEAP) Office.

TABLE OF CONTENTS

LIST OF FIGURES

LIST OF TABLES

1. Introduction

To perform oil spill risk analysis, it is necessary to describe the behavior and fate of the spilled oil from the time of the spill until it is no longer a threat to the environment. This description takes the form of a prediction of the most likely set of events that will follow an oil spill. This prediction may be partly based upon past experience, but more often than not it will have to be based upon an understanding of the processes that take place and a predictive model of those processes. This is especially true in the Beaufort Sea off the north coast of Alaska. There has been no practical experience with large oil spills in this region, especially during the winter when the sea surface is ice covered. Since a great deal of exploration activity takes place offshore during the ice season, it is necessary to predict the behavior and consequences of an accidental oil spill by means other than observations of actual spills.

There have been several experimental studies of oil spill behavior in ice-covered waters (NORCOR, 1975; Comfort and Purves, 1980; Buist et al., 1981), as well as laboratory studies of the interaction of oil and ice (Cox et al., 1980; Cox and Schultz, 1981; Martin, 1977). Several studies have looked at the available data in an attempt to synthesize oil spill scenarios for the nearshore Beaufort Sea (Lewis, 1976; NORCOR, 1977; Thomas, 1980). The conclusion has been that in the case of an oil spill during the ice growth season, from October through May, the spilled oil becomes trapped in, on top of or under the ice. It is partly or wholly protected from much of the weathering that normally takes place when oil is exposed to the atmosphere until springtime, when the oil, even that frozen into place beneath the ice cover, collects on the surface of the ice. As the weather warms later in the spring, accelerated melting takes place, which results in oil, somewhat weathered by now, floating on the sea surface surrounded by individual ice floes. At this time, the oil can have a particularly severe effect upon biological activity in and on the open water. It is also possible after breakup for oil slicks to be driven up onto beaches.

One important conclusion of the scenario outlined above is that an offshore oil spill during the ice season will probably not have significant effects on the environment until breakup the following spring. Since most of the Beaufort

Sea ice cover is in continual motion, the effective springtime spill site can be far removed from the site of the accidental spill. To predict the possible consequences of an oil spill occurring at any location, it is necessary then to be able to predict the motion of the ice cover between the time of the spill and spring breakup.

The purpose of this study has been to predict typical wintertime ice motions for ice passing over potential oil spill sites for the continental shelf region of the Beaufort Sea off the north coast of Alaska. A limited amount of ice motion data does exist for the Beaufort Sea, but these data are insufficient for computing meaningful statistics of ice motions. Our strategy has been to develop an ice trajectory model that accounts for the essential physical processes of the ice cover and that uses environmental data for the driving forces. Available ice motion data are used to tune the trajectory model, thus the results are at least consistent with the observed motions.

2. Technical Approach

2.1 General Approach

The most reliable method of predicting typical oiled ice trajectories and expected variations in trajectories would be to perform a statistical analysis on a large sample of observed ice motions. Unfortunately, the sample size of observed ice motions in the Beaufort Sea is nowhere near large enough to give reliable statistics. An alternative approach was decided upon whereby a model of large-scale sea ice behavior was used to predict ice motions from observed winds. This approach also has difficulties in that little real time data exist on ice conditions and ocean currents, which are also important in determining ice motions. These difficulties were resolved in the following manner.

Ice response (motion) fields were computed for a range of driving forces and ice conditions. Ice conditions were varied from free-drift conditions (zero strength) to very high strength conditions (zero motion). Ocean currents were assumed to be the long-term mean geostrophic velocity field derived from the dynamic topography of Newton (1973). From previous model studies, we were able to estimate the approximate error in daily velocities due to variations in the currents. Real wind data were used, but to reduce the number of model calculations to a manageable number, the daily wind fields were clustered into 16 groups with the winds within each group being similar in speed and direction in the region of interest near shore.

These ice response fields were then combined to form typical ice trajectories. The ice response fields due to winds were combined so that the statistics of the sequence of winds used matched those of the data. The ice conditions for each wind pattern were determined by choosing proportions of different ice strengths so that the resulting trajectories best matched the limited number of observed trajectories.

A complete description of the procedure outlined here is contained in the following sections.

2.2 Ice Model

2.2.1 Quasi-steady Ice Model

The mathematical model of ice dynamics used in this work incorporates a momentum equation which balances the forces due to air and water traction, Coriolis effects, sea surface tilt, and internal ice stress divergence. The model also requires a constitutive law relating the internal ice stress to deformations. For this study, quasi-steady calculations were done in which ice strength is constant and no ice redistribution or thermal growth is allowed. The strength of the ice is varied as a parameter in different simulations. It has been shown that this quasi-steady form of the ice model will, when given accurate daily average winds and currents, accurately model daily average ice velocities and motions (Pritchard et al., 1977).

The ice model used in this study is basically the one developed and tested during AIDJEX (Arctic Ice Dynamics Joint Experiment), and it has been described in detail many times (Coon, 1980; Pritchard, 1981). The quasi-steady form of the model and results of quasi-steady calculations are given by Reimer et al. (1980) and Pritchard et al. (1977). A brief description of this form of the model follows.

In the plane of motion of the sea ice, the momentum balance is expressed as

$$m\dot{\underset{\sim}{v}} = \underset{\sim}{\tau}_a + \underset{\sim}{\tau}_w - mf\underset{\sim}{k} \times \underset{\sim}{v} - mg\nabla H + \nabla \cdot \underset{\sim}{\sigma}$$

where

- m is mass per unit area of ice,
- $\underset{\sim}{v}$ is velocity in the horizontal plane,
- $\dot{\underset{\sim}{v}}$ is horizontal acceleration,
- $\underset{\sim}{\tau}_a$ is traction exerted by the atmosphere on the upper ice surface,
- $\underset{\sim}{\tau}_w$ is traction exerted by the ocean on the lower ice surface,
- f is the Coriolis parameter,
- $\underset{\sim}{k}$ is the unit vector in the vertical direction,
- g is gravitational acceleration,
- H is the height of the sea surface, and
- $\underset{\sim}{\sigma}$ is the Cauchy stress resultant in excess of hydrostatic equilibrium (two-dimensional).

The air stress is determined from the geostrophic wind in the atmosphere as

$$\underset{\sim}{\tau}_a = \rho_a c_a |\underset{\sim}{U}_g| \underset{\sim}{B}_a \underset{\sim}{U}_g$$

where $\underset{\sim}{B}_a$ is a rotational operator, turning the air stress an angle from the geostrophic wind, ρ_a is air density, and c_a is the drag coefficient. Since wind speeds are generally orders of magnitude larger than ice speeds, the geostrophic wind, $\underset{\sim}{U}_g$, is used rather than the wind velocity relative to the ice. Values of the parameters used in this study were:

$$\rho_a = 0.00143 \text{ gm/cm}^3$$
$$c_a = 0.008$$
$$f = 2\,\Omega \sin(\text{latitude}),\ \Omega = 7.29 \times 10^{-5}$$

The water stress is modeled as a function of the relative velocity between the ice and the geostrophic ocean current, but the relationship is not quadratic. A three-layer ocean consisting of surface and bottom logarithmic layers and an interior Ekman layer is assumed. In shallow, well-mixed waters, the presence of the bottom modifies the turbulence and velocity structures in the boundary layer. In general, the bottom effects result in an increased ice speed relative to the bottom for the same surface stress. In deeper waters, the bottom effects are not important for typical winds and ice motions, and the surface stress/velocity relationship is approximately quadratic. McPhee (1982) has described this drag law in detail. A similar drag law development is described in Overland and Pease (1982).

The sea surface tilt defines the ocean geostrophic current, $\underset{\sim}{v}_g$, in the form

$$mg\nabla H = -mf\underset{\sim}{k} \times \underset{\sim}{v}_g \quad .$$

The last term in the momentum balance is the divergence of internal ice stress. The stress state is related to the deformation history by material constitutive laws. An elastic-plastic model is assumed which is made up of the following three elements: (1) a yield surface, (2) a flow rule, and (3) an elastic response. No plastic hardening occurs since a constant strength is assumed for each simulation.

The stress state, $\underset{\sim}{\sigma}$, in a plastic model is constrained to lie within a function called the yield surface. For an isotropic model, this function depends only on the stress invariants and not on the principal direction. This constraint is

$$\phi \quad \sigma_I,\ \sigma_{II},\ p^* \le 0 \quad ,$$

where $\sigma_I = \frac{1}{2}$ tr $\underset{\sim}{\sigma}$ (negative pressure), $\sigma_{II} = \frac{1}{2}$ tr $\underset{\sim}{\sigma}'\underset{\sim}{\sigma}'^{1/2}$ (maximum shear), and $\underset{\sim}{\sigma}' = \underset{\sim}{\sigma}_I \underset{\sim}{1}$. The yield constraint may depend on other state parameters, in particular, the isotropic compressive strength, p*. The yield surface preferable for sea ice (Pritchard, 1978) is shown in Figure 1. The stress invariants are constrained to be within the triangle for a given value of p*. Along the straight-line portion of $\phi = 0$ passing through the origin, the stress state is that of uniaxial compression. The other straight line used to complete the yield surface is chosen for simplicity.

When the stress state in the ice lies inside the yield surface, then the stress, $\underset{\sim}{\sigma}$, is an isotropic function of the elastic strain, $\underset{\sim}{e}$:

$$\underset{\sim}{\sigma} = M_1 - M_2 \; \underset{\sim}{1} \; \mathrm{tr} \; \underset{\sim}{e} + 2 \, M_2 \, \underset{\sim}{e}$$

where M_1 and M_2 are elastic moduli set at 2.0×10^9 and 1.0×10^9 dyn/cm, respectively. The elastic strain satisfies the kinematic relation

$$\dot{\underset{\sim}{e}} = \underset{\sim}{W}\underset{\sim}{e} + \underset{\sim}{e}\underset{\sim}{W} = \underset{\sim}{D} - \underset{\sim}{D}_p$$

where the stretching $\underset{\sim}{D} = \frac{1}{2} \; \underset{\sim}{L} + \underset{\sim}{L}^T$, the spin $\underset{\sim}{W} = \frac{1}{2} \; \underset{\sim}{L} + \underset{\sim}{L}^T$, and the velocity gradient $\underset{\sim}{L}$ = grad $\underset{\sim}{v}$.

When the stress state is on the yield surface $\phi = 0$, plastic stretching occurs. As plastic flow occurs, the stress is constrained to the loading surface by the occurrence of plastic stretching $\underset{\sim}{D}_p$. The associated flow rule $\underset{\sim}{D}_p = \lambda \frac{\partial \phi}{\partial \underset{\sim}{\sigma}}$, $\lambda > 0$ requires that plastic stretching be orthogonal to the loading function at the instantaneous stress state.

The model equations are integrated using a finite difference scheme described by Pritchard and Colony (1976). The finite difference grid used in the calculations is shown in Figure 2.

2.2.2 Free-Drift Ice Model

During free-drift, motion of the ice cover may be determined by considering momentum balance locally. The forces acting on the ice cover are air stress,

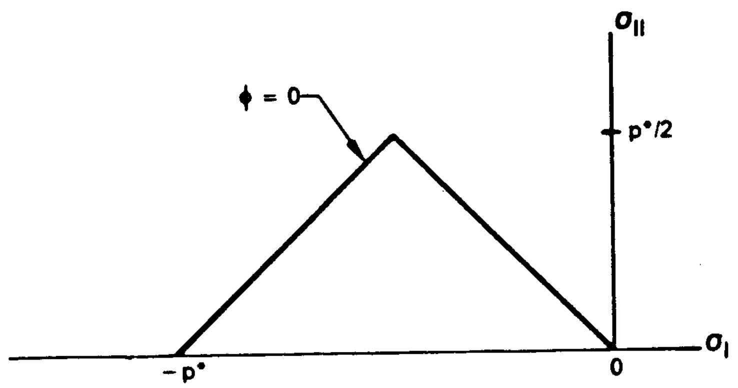

Figure 1. Diamond Yield Surface for Large-Scale Sea Ice Model

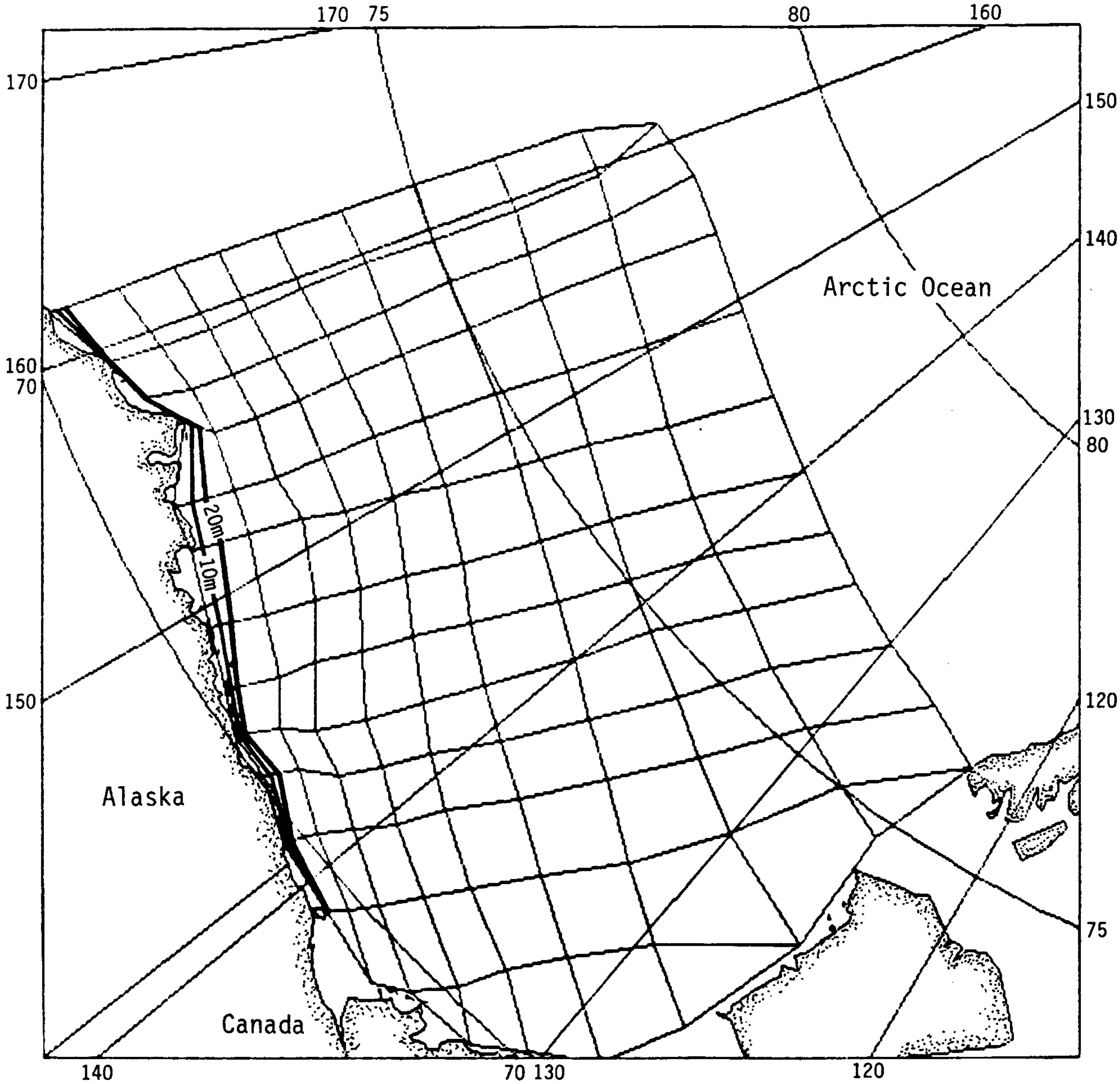

Figure 2. Computational Grids Used in the Calculations. The Approximate Locations of the 10-m and 20-m Isobaths are Also Indicated. These Contours were Used to Approximate the Seaward Extent of Fast Ice on 1 December and 1 March, Respectively.

τ_a; water stress, τ_w; Coriolis force, $-mfk \times v$; and sea surface tilt, $-mg\nabla H$. Momentum changes then occur as

$$m\dot{v} = \tau_a + \tau_w - mfk \times v - mg\nabla H \quad .$$

The ice velocity may be determined at each point as a function of time whenever the barometric pressure field history is prescribed. The results sought have a time resolution of one day. For this case, inertia is negligible. Therefore, the analysis is performed for steady-state conditions.

A more complete description of the free-drift model and comparisons of model results with observations may be found in many sources. A partial list includes McPhee (1980), Thomas and Pritchard (1979), and Pritchard and Kollé (1981).

2.3 Driving Forces

2.3.1 Winds

One of the important forces that acts on floating sea ice is that exerted by the winds. The winds, due to their day-to-day and seasonal variability, are also the major source of variability in ice motion.

To drive the ice model, the average daily atmospheric pressure fields for the years 1979 and 1980 as reported by Thorndike and Colony (1980, 1981) were used. From the pressure fields, P the geostrophic and surface winds for the Beaufort Sea were computed:

$$U_g = \frac{-1}{\rho_a f} k \times \nabla P \quad .$$

While only two years of data were used, these data were accurate, which may not be the case for other historical data for the Beaufort Sea. To assure ourselves that these two years of data were sufficient to derive reliable statistics, we compared the derived surface winds at 150° W, 71° N with the wind statistics for Lonely (in Brower et al., 1977). The winds at Lonely were used for comparison instead of those at the closer station at Oliktok because the Lonely winds are affected less by the mountain barrier baroclinity effect (Kozo, 1980). The wind speed and direction histogram for Lonely is the average of the 12 monthly histograms from Brower et al. (1977). The comparison of derived surface winds with these annual statistics is shown in Figure 3. A comparison by season showed slightly more differences than is apparent in the annual statistics. While some of the differences are undoubtedly due to real differences in the samples, there are also differences due to geographical location and due to the difference between measured surface winds and winds calculated from daily average pressure fields. The 1979 and 1980 winds were thought to be sufficiently representive of recent historical winds, so no further effort was spent on improving the wind sample. It should be pointed out that since this study began, the 1981 sea level pressure data from the Arctic Ocean Buoy Program have become available (Thorndike et al., 1982) and more data are being collected during 1982. In addition, historical sea level pressure fields for the northern hemisphere are now available though the National Center for Atmospheric Research (Jenne, 1975). Though the data are available to improve the wind statistics we used, the improvement would be insignificant, and differences in the resulting ice trajectories would be masked by uncertainties in ice conditions. Further refinement of our wind statistics would, however, be useful for observing any long-term trends or cycles. The estimation of year-to-year variability in ice motions might also be improved if the more unusual periods were included, such as during the summer of 1975 and again the following winter when extreme ice conditions and motions were observed.

The ice model described above determines the response of sea ice to winds. This response is nonlinear, both in speed and direction. Therefore, it is desirable to retain as much variation as possible in the winds used to drive the model. On the other hand, an infinite variety of wind patterns and speeds occurs in the Beaufort Sea, making it impossible to model the ice response to every possible wind. We decided to form groups of similar wind patterns rather than to use an overall mean wind field or monthly mean wind fields. An attempt was first made to cluster the winds according to the pressure pattern over the Beaufort Sea, but the results indicated that either a very large number of groups must be used, or that each of a smaller number of groups must contain some within-group variability. The final clustering of winds was done according to the speed and direction of the surface winds near the north coast of Alaska at 71° N and 150° W. Wind direction was grouped into eight equal

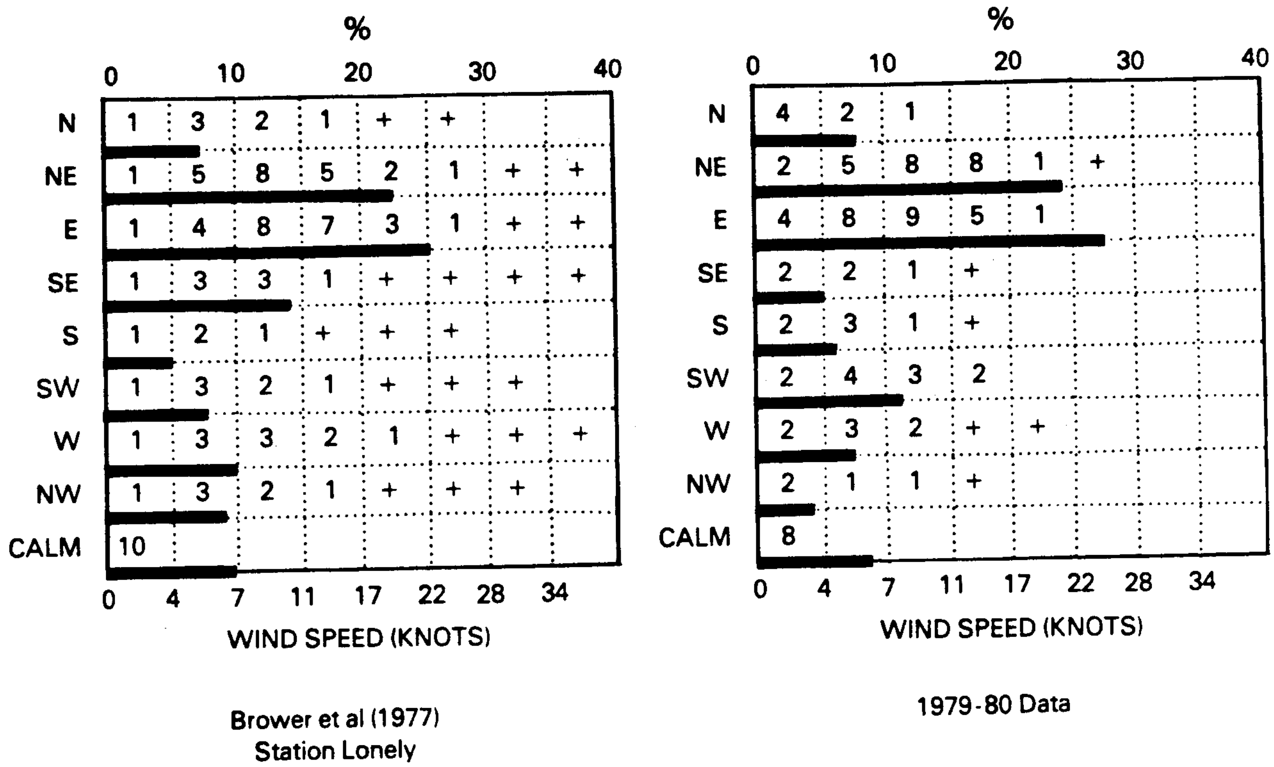

Figure 3. Annual Wind Speed and Direction Summaries for the North Alaskan Coast. The Information for Lonely was Taken from Brower et al. (1977). The Offshore Winds Were Computed from the 1979-80 Artic Buoy Program Pressure Data as Used in the Trajectory Calculations.

direction categories, and wind speed was grouped into six intervals of 2 m/s: 0-2, 2-4, 4-6, 6-8, 8-10, and greater than 10 m/s. The resultant wind groups had reasonably small within-group variances in the region of interest near the Alaskan coast. Further away from shore, the within-group variability was relatively large but still acceptable, since the means were still consistent with the mean winds near shore and the more variable winds were far enough from the region of interest to have only minimal effects on computed ice motions.

Of the 48 possible wind groups (8 directions by 6 speeds), many groups contained none or only a fraction of a percent of the observations. It was decided to ignore these groups, since the effect of including them in the model would be insignificant in comparison with the uncertainties that would result from lack of data on other parameters. Furthermore, all the winds less than 2 m/s were combined into one group without regard to direction, since those winds would have little influence on ice motions. The final result was 16 groups of wind patterns as shown in Figure 4. After classifying each daily wind field into one of these 16 patterns (neglecting the small number of days which did not fit into these 16 patterns), the mean wind field for each group was computed. In Figure 5 we show the mean wind field and 50 percent equiprobability ellipses for the 16 groups. We note that near shore the variability is quite small, while in the northern Beaufort Sea the mean winds are relatively small and the variability is large.

There are several sources of error inherent in the wind grouping we have used. First, we chose to not use the total mean wind because of the nonlinear ice model. While each of the 16 groups selected to drive the model are considerably less variable than all winds are, the within-group variability does mean that a nonlinear model will not give the correct response. Thomas and Pritchard (1979) showed that free drift (which causes a majority of the ice motion) is nonlinear but that for larger wind speeds (greater than about 4 m/s), ice speed is nearly linearly related to wind speed, although the direction of ice motion during free drift continues to change with wind speed. Thorndike and Colony (1982) have estimated that over 70 percent of the variance in ice drift can be explained by a linear relationship between geostrophic winds and ice motion. Thus, the relatively small variability within each wind

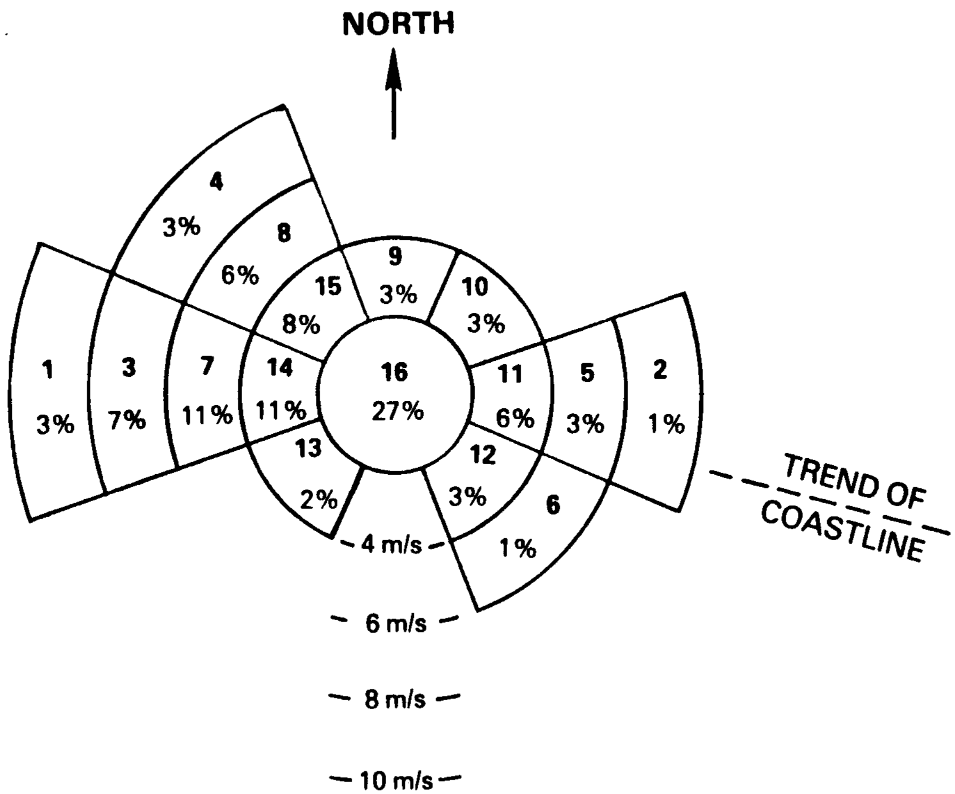

Figure 4. Wind Rose Showing the Distribution of all Winds for 1979-80 for the Nearshore North-Central Alaskan Coast. The 16 Wind Categories are Those Used in the Trajectory Calculations.

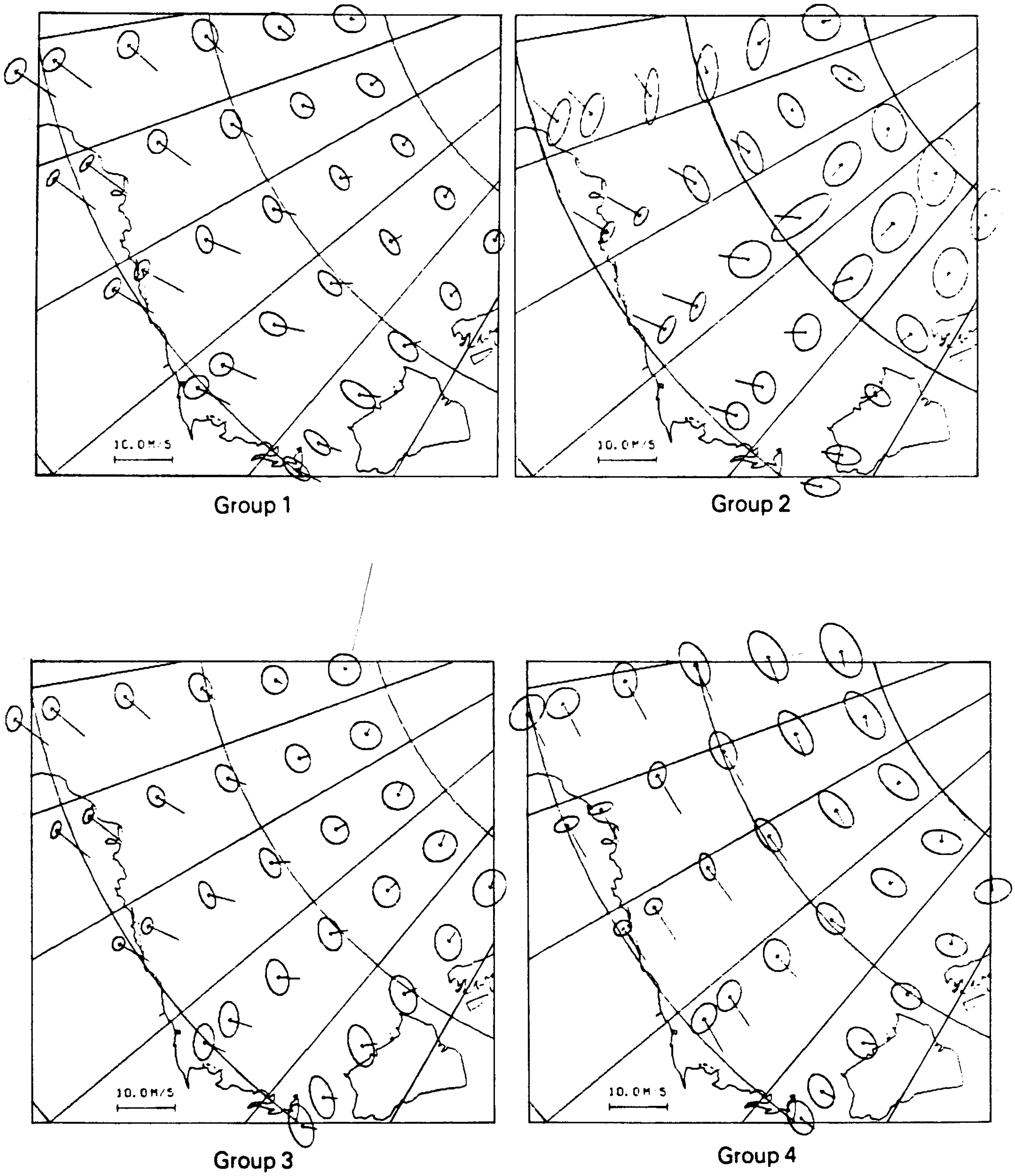

Figure 5. Mean Wind Fields and 50% Equiprobability Ellipses for the 16 Wind Groups Shown in Figure 4.

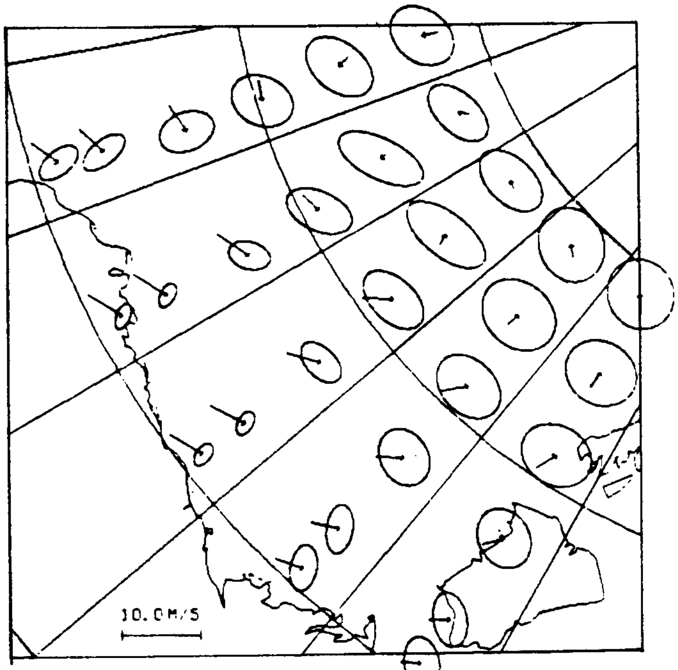

Group 5

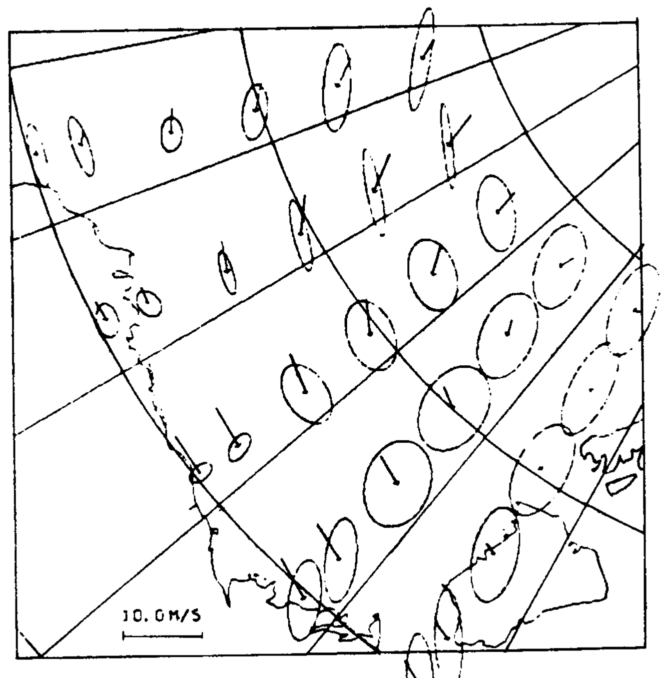

Group 6

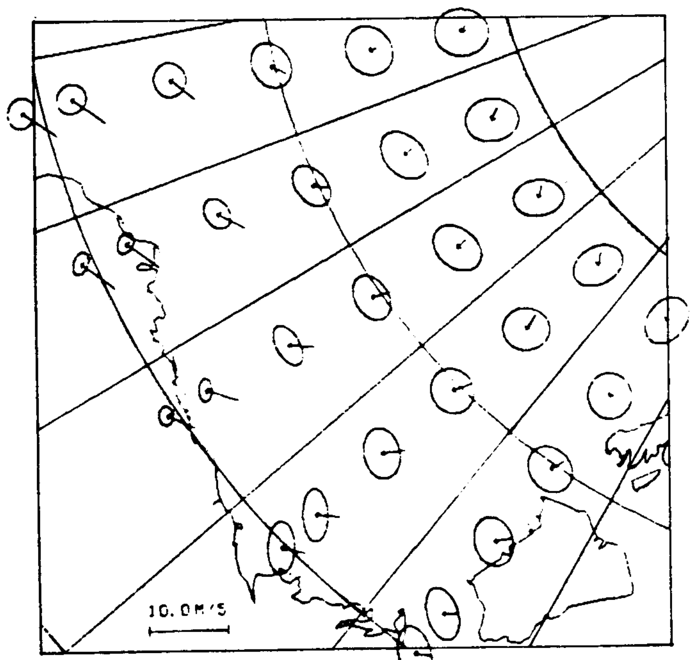

Group 7

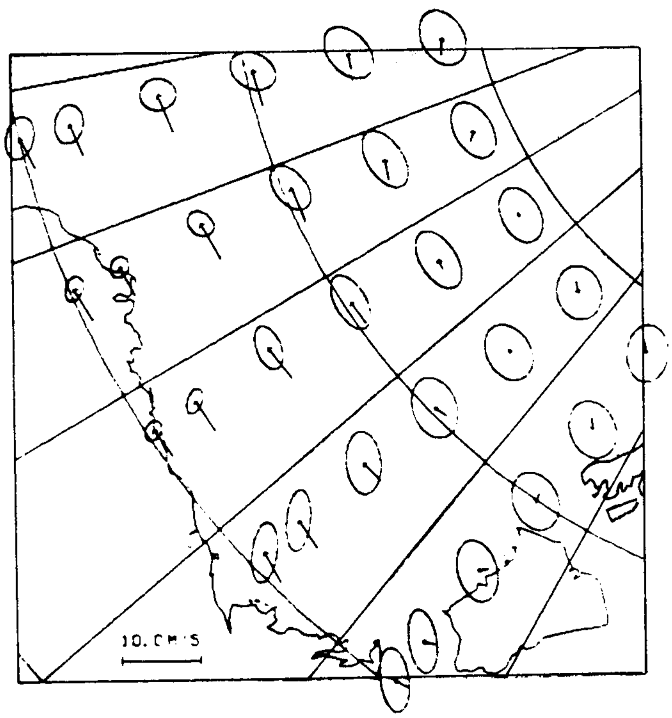

Group 8

Figure 5. Mean Wind Fields and 50% Equiprobability Ellipses for the 16 Wind Groups Shown in Figure 4 (Continued).

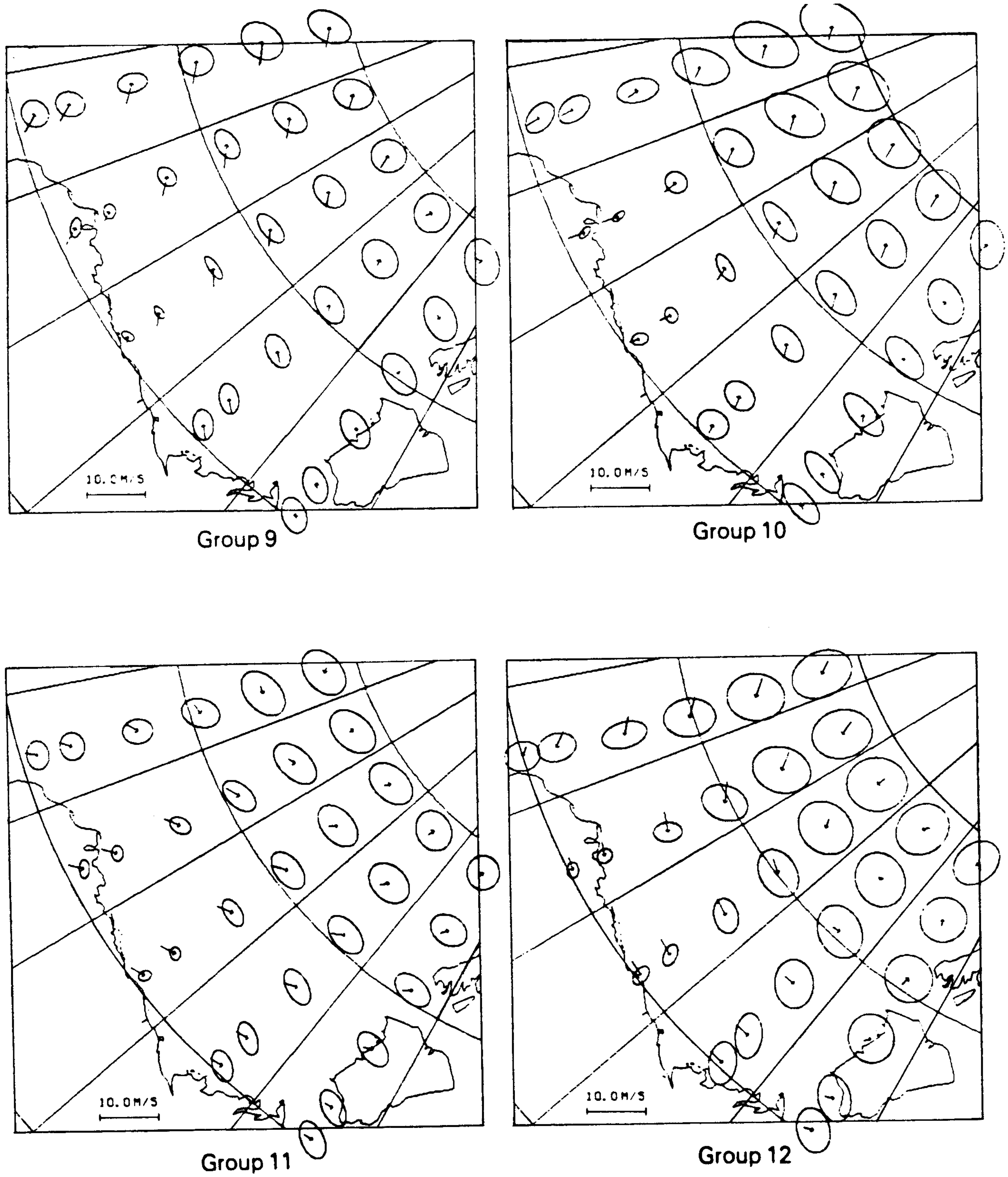

Figure 5. Mean Wind Fields and 50% Equiprobability Ellipses for the 16 Wind Groups Shown in Figure 4 (Continued).

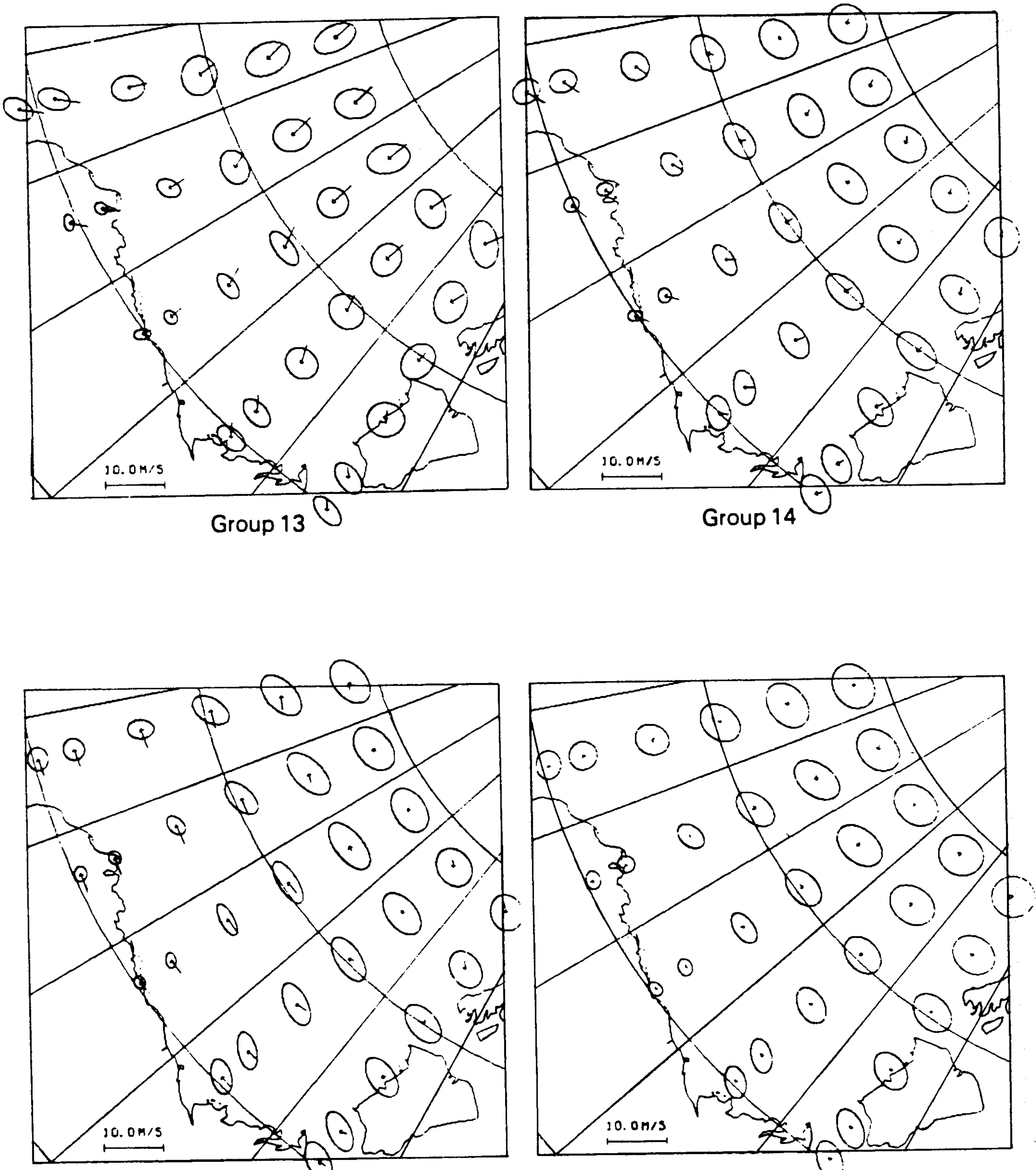

Group 13

Group 14

Group 15

Group 16

Figure 5. Mean Wind Fields and 50% Equiprobability Ellipses for the 16 Wind Groups Shown in Figure 4 (Concluded).

group, combined with a nearly linear relationship (in speed), will result in insignificant errors in ice speed and only a few degrees of error in direction. In a later section of this report, we present the results of an analysis of the effect of the within-group variability in winds on ice motions for one of the wind groups.

Another possible source of error in the mean wind fields is that we neglected a few cases where the winds were very large in magnitude because of their low probability of occurrence. These large winds can cause a significant amount of ice motion. Part of this motion would be canceled because of the variability in direction of the larger winds, and the remainder, while significant as a daily motion, would only contribute an average of a few kilometers per month to the ice motions. Over an ice season, the motion caused by large winds would likely be noticeable in the ice trajectories, but the same effect on ice motions can be achieved with smaller wind magnitudes and lower ice strength. Since we can only approximate ice strength very coarsely, the effect of neglecting high wind speeds will not be observable in our results.

An important and real source of variation in sea ice motions caused by winds results from the temporal variation in the percentage of winds occurring from each group. The sequence of the wind patterns will also affect ice motions due to the spatial variation in the wind fields. These effects were accounted for in the computations of ice trajectories by using wind transition matrices. Four transition matrices were developed, one for each season. The division into seasons was done according to the similarity of the occurrence of winds during each month over the two years of our sample. These transition matrices show the probability of occurrence of each wind group following the occurrence the day before of every other wind group. That is, given that today the wind falls in group 1, the matrices give the probability of tomorrow's winds being in group 1, 2, 3, etc. Thus, it is possible to generate a sequence of random numbers with the same statistics as the observed sequence of wind patterns. To initiate the sequence of random numbers, another random number can be generated with the same probability of occurrence as the proportion of winds in each group during a season. Assuming that 1979 and 1980 were representative years as far as the winds in the Beaufort Sea are concerned, we were able to generate random sequences of wind patterns with the same statistics as the real winds. The seasonal wind transition matrices are presented in Tables 1, 2, 3, and 4. Since we are sampling a uniformly distributed random number for the proportion of winds in each group, the sampled proportions will have some variation about the true proportion. For a sample of size 30 (one month's sequence of winds) the standard deviation of the sample proportions will be 0.09 [when $p=(1-p)=0.5$] or smaller. For trajectory calculations lasting several months, the standard deviation, computed as $SD = p(1-P)/n$, will be smaller. This variation between samples (trajectories) of the proportions of winds from each group is acceptable since the proportion of actual winds will also vary from year to year.

2.3.2 Model Boundary Conditions

When the ice strength is zero, i.e., during free-drift conditions, ice motions are determined solely by a balance of forces acting locally on the ice. When ice conditions are such that the large-scale ice strength is significantly different from zero (greater than about 1.0×10^7 dyn/cm), the far-field winds and resulting ice motions can have an increasing effect on ice motions in the region of interest. Ice conditions near shore will also affect ice motions away from shore when the motions have an onshore component. To account for these far-field and fixed-boundary effects, the ice model uses a prescribed boundary condition, the velocity of the boundary in the present case. These prescribed boundary motions were taken from the same data set as the winds used to drive the model, namely, the drifting buoys deployed during 1979 and 1980 as part of the Arctic Ocean Buoy Program (Thorndike and Colony, 1980, 1981). Average daily boundary velocities were interpolated from the average daily velocities of the same set of buoys that measured the sea level atmospheric pressure used to derive the wind fields. These daily boundary velocities were grouped and averaged in the same 16 groups as the winds were. The mean and 50 percent equiprobability ellipses of the boundary velocities for the 16 groups are shown in Figure 6. The boundary velocities interpolated from the buoy data were not as accurate as the winds used, but they have the important advantage of being consistent with the winds. The boundary motions also take into account to some degree the actual large-scale ice strengths effective from day to day. One of the major reasons for using only the 1979

Table 1. Fall Wind Group Transition Matrix

Probability of group A winds occurring.

A	1	2	3	4	5	6	7	8	9	10	11	12	13	14	15	16
P(A)	.17	.09	.12	.05	.01	.03	.03	.03	.08	.15	.01	.03	.05	.12	.00	.04

Probability of group A winds occurring given that group B last occurred.

B \ P(A,B)	1	2	3	4	5	6	7	8	9	10	11	12	13	14	15	16
1	.37	.00	.21	.05	.00	.05	.00	.00	.11	.16	.00	.00	.05	.00	.00	.00
2	.10	.10	.10	.10	.00	.10	.00	.00	.10	.10	.10	.00	.20	.00	.00	.00
3	.15	.15	.08	.00	.00	.00	.00	.00	.08	.23	.00	.08	.08	.15	.00	.00
4	.00	.00	.17	.33	.17	.00	.00	.00	.00	.17	.00	.00	.00	.17	.00	.00
5	.00	.00	.00	1.00	.00	.00	.00	.00	.00	.00	.00	.00	.00	.00	.00	.00
6	.33	.00	.00	.00	.00	.00	.33	.00	.00	.00	.00	.33	.00	.00	.00	.00
7	.00	.00	.00	.33	.00	.00	.00	.00	.00	.00	.00	.00	.33	.33	.00	.00
8	.33	.00	.00	.00	.00	.00	.33	.33	.00	.00	.00	.00	.00	.00	.00	.00
9	.22	.33	.22	.00	.00	.00	.00	.11	.11	.00	.00	.00	.00	.00	.00	.00
10	.19	.06	.19	.00	.00	.00	.00	.00	.00	.25	.00	.00	.00	.25	.00	.06
11	.00	.00	1.00	.00	.00	.00	.00	.00	.00	.00	.00	.00	.00	.00	.00	.00
12	.00	.00	.00	.00	.00	.00	.00	.33	.33	.00	.00	.33	.00	.00	.00	.00
13	.00	.00	.00	.00	.00	.17	.17	.00	.33	.00	.00	.00	.17	.00	.00	.17
14	.15	.15	.00	.00	.00	.00	.00	.00	.08	.31	.00	.00	.00	.15	.00	.15
15	.00	.00	.00	.00	.00	.00	.00	.00	.00	.00	.00	.00	.00	.00	.00	.00
16	.00	.00	.00	.00	.00	.00	.00	.00	.00	.00	.00	.00	.00	1.00	.00	.00

Table 2. Winter Wind Group Transition Matrix

Probability of group A winds occurring.

A	1	2	3	4	5	6	7	8	9	10	11	12	13	14	15	16
P(A)	.26	.03	.11	.03	.07	.09	.05	.03	.05	.07	.03	.05	.03	.05	.01	.02

Probability of group A winds occurring given that group B last occurred.

B \ P(A,B)	1	2	3	4	5	6	7	8	9	10	11	12	13	14	15	16
1	.35	.08	.10	.00	.10	.04	.04	.02	.04	.10	.04	.08	.00	.02	.02	.00
2	.43	.00	.14	.00	.00	.00	.14	.00	.00	.00	.00	.00	.29	.00	.00	.00
3	.48	.00	.22	.04	.04	.00	.00	.04	.00	.13	.00	.00	.00	.00	.00	.04
4	.17	.00	.33	.00	.00	.17	.00	.00	.00	.00	.00	.00	.00	.17	.00	.17
5	.29	.00	.07	.00	.14	.07	.14	.00	.07	.00	.14	.00	.00	.00	.07	.00
6	.16	.00	.00	.11	.11	.16	.11	.11	.00	.05	.05	.11	.00	.00	.05	.00
7	.30	.00	.00	.00	.10	.30	.10	.10	.10	.00	.00	.00	.00	.00	.00	.00
8	.57	.00	.00	.00	.00	.00	.29	.00	.14	.00	.00	.00	.00	.00	.00	.00
9	.10	.00	.00	.00	.00	.10	.00	.00	.30	.20	.00	.00	.20	.10	.00	.00
10	.14	.00	.21	.21	.00	.07	.00	.00	.07	.07	.00	.00	.00	.14	.00	.07
11	.00	.00	.00	.00	.17	.33	.00	.17	.17	.00	.17	.00	.00	.00	.00	.00
12	.10	.00	.00	.00	.10	.40	.00	.10	.00	.10	.00	.20	.00	.00	.00	.00
13	.33	.17	.17	.00	.00	.00	.00	.00	.00	.00	.00	.00	.17	.00	.00	.17
14	.00	.09	.36	.00	.09	.00	.00	.00	.00	.09	.00	.00	.09	.18	.00	.09
15	.00	.00	.00	.00	.00	.33	.00	.00	.00	.00	.00	.67	.00	.00	.00	.00
16	.00	.20	.20	.00	.00	.00	.00	.00	.00	.00	.00	.00	.00	.60	.00	.00

Table 3. Spring Wind Group Transition Matrix

Probability of group A winds occurring.

A	1	2	3	4	5	6	7	8	9	10	11	12	13	14	15	16
P(A)	0.11	0.05	0.15	0.00	0.00	0.01	0.02	0.03	0.07	0.23	0.00	0.01	0.05	0.17	0.02	0.08

Probability of group A winds occurring given that group B last occurred.

B	P(A.B)															
1	.54	.00	.23	.00	.00	.08	.00	.08	.08	.00	.00	.00	.00	.00	.00	.00
2	.33	.00	.00	.00	.00	.00	.00	.00	.17	.50	.00	.00	.00	.00	.00	.00
3	.06	.06	.35	.00	.00	.00	.00	.00	.06	.47	.00	.00	.00	.00	.00	.00
4	.00	.00	.00	.00	.00	.00	.00	.00	.00	.00	.00	.00	.00	.00	.00	.00
5	.00	.00	.00	.00	.00	.00	.00	.00	.00	.00	.00	.00	.00	.00	.00	.00
6	1.00	.00	.00	.00	.00	.00	.00	.00	.00	.00	.00	.00	.00	.00	.00	.00
7	.50	.00	.00	.00	.00	.00	.00	.50	.00	.00	.00	.00	.00	.00	.00	.00
8	.00	.00	.00	.00	.00	.00	.00	.25	.50	.00	.00	.25	.00	.00	.00	.00
9	.12	.12	.25	.00	.00	.00	.12	.00	.12	.12	.00	.00	.12	.00	.00	.00
10	.04	.12	.15	.00	.00	.00	.04	.00	.04	.35	.00	.00	.00	.23	.00	.04
11	.00	.00	.00	.00	.00	.00	.00	.00	.00	.00	.00	.00	.00	.00	.00	.00
12	.00	.00	.00	.00	.00	.00	.00	.00	.00	.00	.00	.00	.00	.00	1.00	.00
13	.00	.17	.00	.00	.00	.00	.00	.00	.17	.00	.00	.00	.33	.00	.00	.33
14	.00	.00	.10	.00	.00	.00	.00	.00	.00	.15	.00	.00	.10	.50	.00	.15
15	.00	.00	.00	.00	.00	.00	.00	.50	.00	.00	.00	.00	.00	.00	.50	.00
16	.00	.00	.00	.00	.00	.00	.00	.00	.00	.11	.00	.00	.11	.44	.00	.33

Table 4. Summer Wind Group Transition Matrix

Probability of group A winds occurring.

A	1	2	3	4	5	6	7	8	9	10	11	12	13	14	15	16
P(A)	.39	.16	.09	.01	.04	.08	.04	.02	.06	.07	.00	.04	.00	.01	.01	.00

Probability of group A winds occurring given that group B last occurred.

B	P(A.B)															
1	.57	.09	.10	.01	.04	.09	.03	.00	.03	.01	.00	.03	.00	.00	.00	.00
2	.29	.32	.18	.00	.00	.04	.04	.00	.07	.04	.00	.00	.00	.04	.00	.00
3	.35	.24	.18	.00	.00	.00	.00	.00	.06	.12	.00	.00	.00	.06	.00	.00
4	.00	.00	.00	.00	.00	.00	.00	.00	.00	1.00	.00	.00	.00	.00	.00	.00
5	.43	.00	.00	.00	.00	.14	.14	.00	.00	.00	.00	.29	.00	.00	.00	.00
6	.43	.00	.00	.00	.14	.21	.14	.00	.00	.00	.00	.07	.00	.00	.00	.00
7	.14	.00	.00	.00	.00	.14	.14	.29	.14	.00	.00	.14	.00	.00	.00	.00
8	.67	.33	.00	.00	.00	.00	.00	.00	.00	.00	.00	.00	.00	.00	.00	.00
9	.18	.55	.00	.00	.00	.00	.00	.00	.27	.00	.00	.00	.00	.00	.00	.00
10	.17	.00	.17	.00	.00	.00	.00	.00	.17	.50	.00	.00	.00	.00	.00	.00
11	.00	.00	.00	.00	.00	.00	.00	.00	.00	.00	.00	.00	.00	.00	.00	.00
12	.14	.14	.00	.00	.00	.29	.00	.14	.00	.00	.00	.14	.00	.00	.14	.00
13	.00	.00	.00	.00	.00	.00	.00	.00	.00	.00	.00	.00	.00	.00	.00	.00
14	.00	.50	.00	.00	.00	.00	.00	.00	.00	.50	.00	.00	.00	.00	.00	.00
15	.00	.00	.00	.00	1.00	.00	.00	.00	.00	.00	.00	.00	.00	.00	.00	.00
16	.00	.00	.00	.00	.00	.00	.00	.00	.00	.00	.00	.00	.00	.00	.00	.00

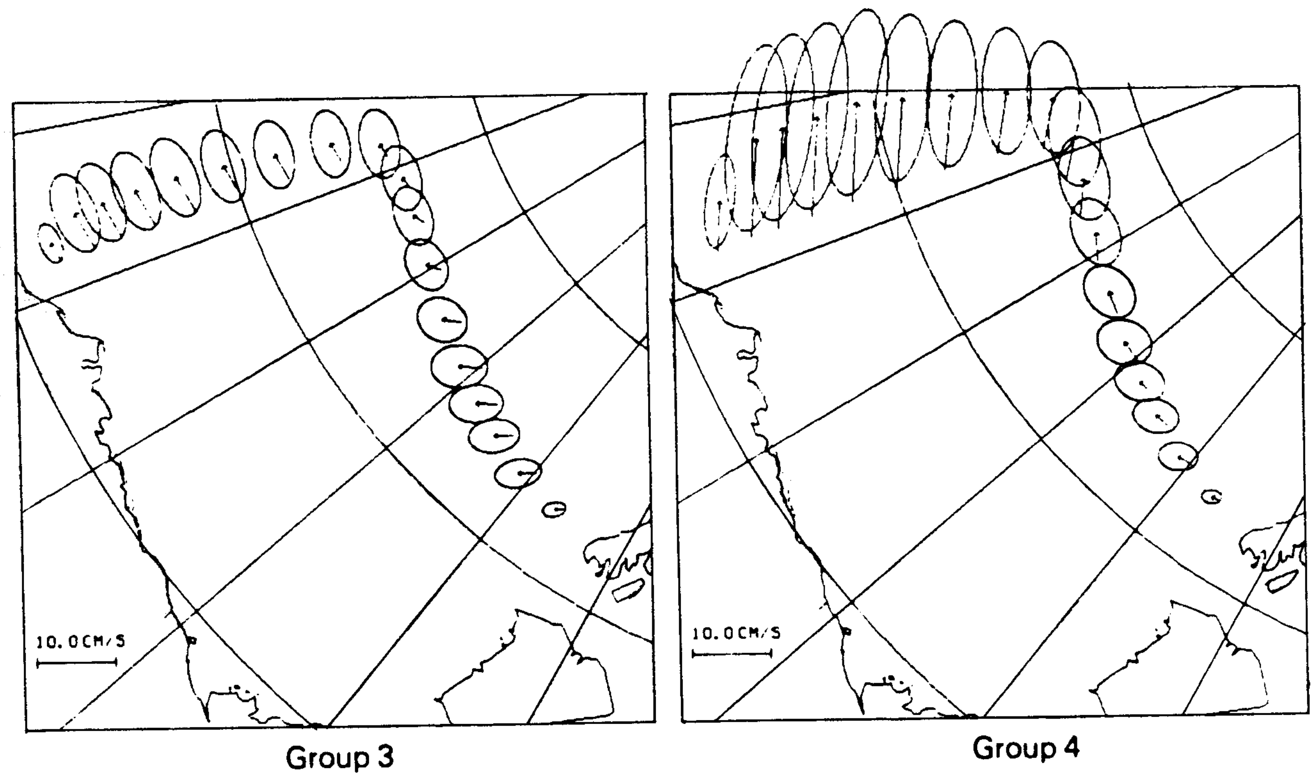

Figure 6. Mean Boundary Velocities and 50% Equiprobability Ellipses for the Same 16 Groups Shown in Figure 4.

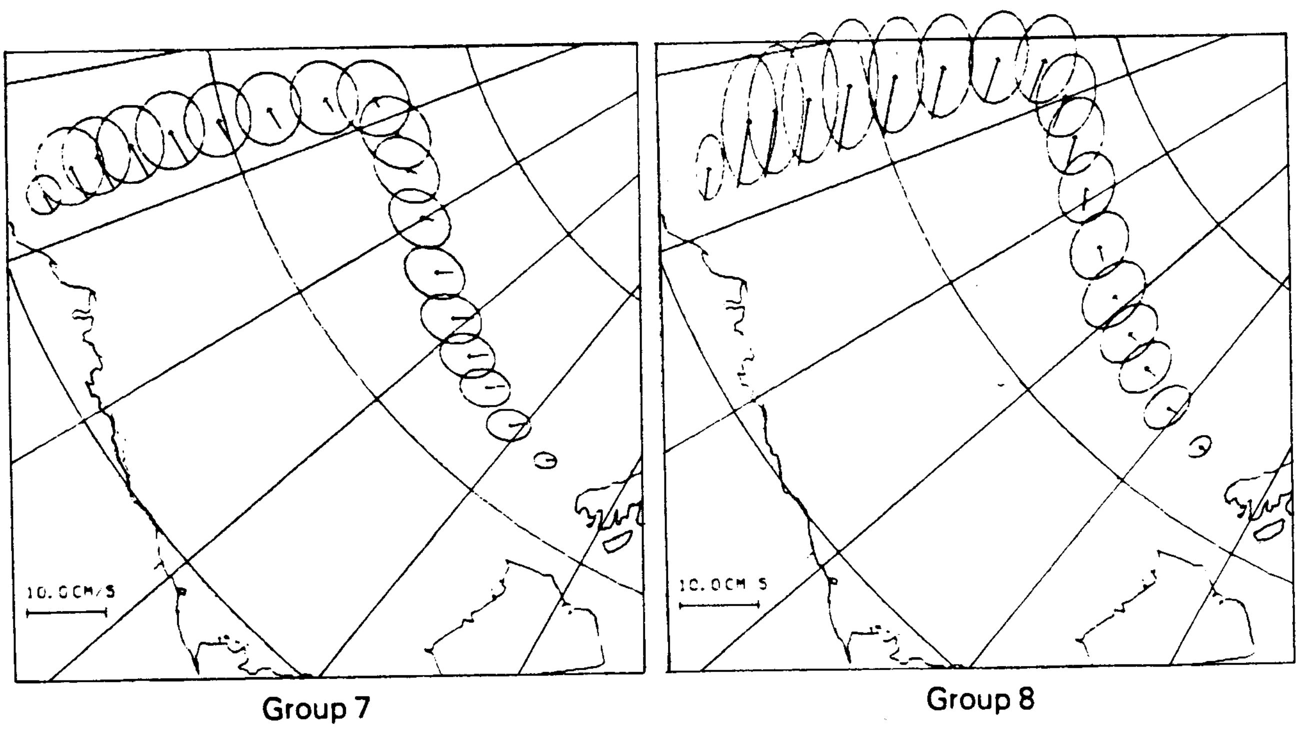

Figure 6. Mean Boundary Velocities and 50% Equiprobability Ellipses for the Same 16 Groups Shown in Figure 4 (Continued).

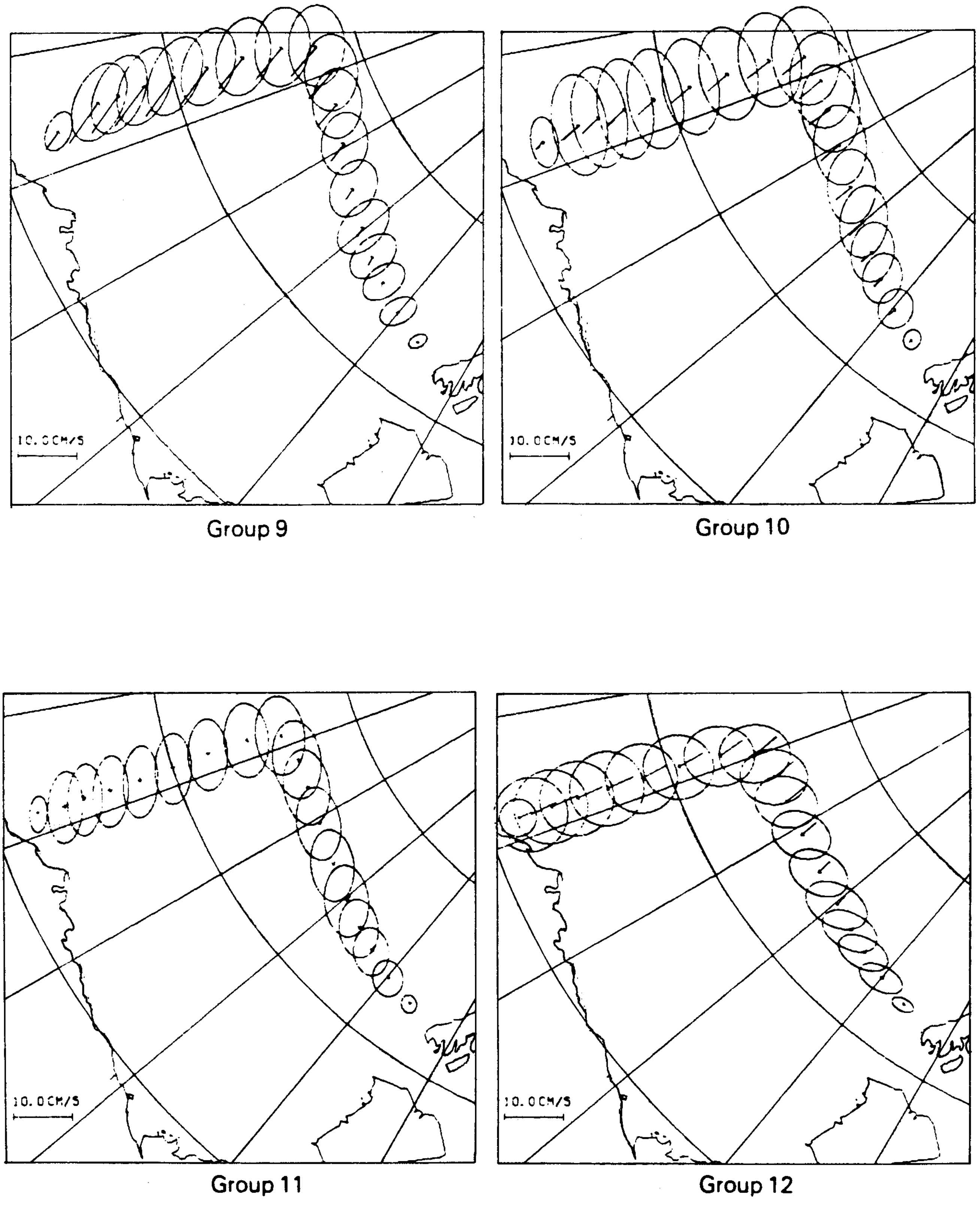

Figure 6. Mean Boundary Velocities and 50% Equiprobability Ellipses for the Same 16 Groups Shown in Figure 4 (Continued). (Concluded)

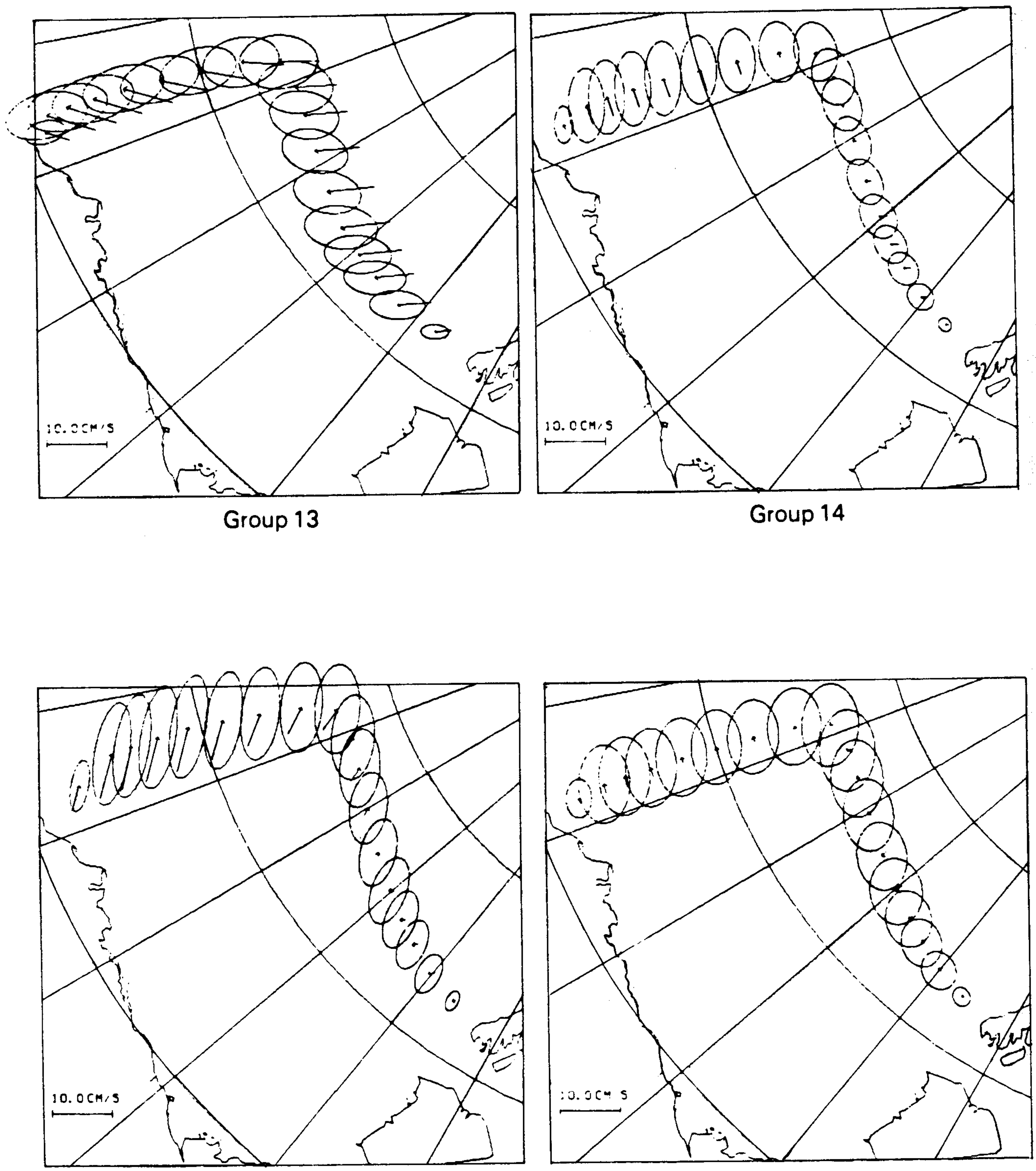

Group 13

Group 14

Group 15

Group 16

Figure 6. Mean Boundary Velocities and 50% Equiprobability Ellipses for the Same 16 Groups Shown in Figure 4 (Concluded).

and 1980 wind data instead of many more years of historical winds was the presence of these consistent ice motion data that could be used to drive the boundary of the ice model.

A zero-velocity boundary condition was used in the model for the Alaskan coast and along Banks and Prince Patrick Islands.

2.3.3 Ocean Currents

The ocean currents are also a source of variability in the computed ice trajectories. The currents used in the model calculations can be divided into two parts, a geostrophic velocity field in the Canada Basin, which was originally derived from the dynamic topography of Newton (1973), and a shelf-break current jet described by Aagaard (1983). McPhee (1982), included as Appendix A in this report, describes the inclusion of these ocean currents in the ice model. For the trajectory calculations, we included the effects of the geostrophic currents offshore as part of the long-term transport mechanism, but treated the shelf-break current jet as a source of variability in the computed trajectories.

We have considered the shelf-break current jet (called the Beaufort Current by Aagaard) as a source of error or variability in the computed trajectories rather than as a driving force. The direction of the Beaufort Current reverses frequently, having a bimodal distribution. Approximately half the time the current flows eastward with a mean speed of 15 to 25 cm/s, and the rest of the time it flows westward at a mean speed of 10 to 15 cm/s. Much of the time, during changes in direction, this current is very slow. Overall, a long-term mean of about 7 cm/s eastward results. This jet is relatively narrow, though, and does not affect ice motions away from the shelf break to any significant extent. During periods of free-drift ice motion, the current does have a pronounced effect on local ice motions. Using extreme values of the current of 40 cm/s eastward and 30 cm/s westward, a potential difference in ice velocities of 70 cm/s can exist, or about 60 km/day in ice motion. This does not mean that there is an uncertainty in long-term ice motions of 60 km/day. Obviously, since the current frequently reverses, the long-term uncertainty in ice motion will be dependent upon the variability of the current itself. The long-term mean current of about 7 cm/s to the east can affect ice motions, mostly during periods of free drift, but the effect is probably not apparent in long-term ice motions. The currents will cause ice motions under some ice conditions, but the ice motions, especially localized motions, will tend to change the ice conditions, making the compacted ice cover better able to resist further motions. That is, during the winter ice season, the ice cover itself tends to reduce the effect of any local perturbation in driving forces on the ice.

While we used a free-drift model to compute ice velocity fields to use in the trajectory calculations, it should be noted that these free-drift velocities were only an approximation to the velocities resulting from a large range of ice strengths. Ice strengths ranging from zero to about 1.0×10^7 dyn/cm result in approximately the same velocity fields. In the real world and in full time-dependent model calculations, however, this range of ice strengths results in different long-term ice motions. The higher strength ice cover will, under conditions where the ice cover converges, quickly become stronger with a resulting reduction in ice motion.

The Beaufort Current will play a more important role in the motion of oil slicks during the summer when open water and/or a loose, unconsolidated ice cover is present.

2.4 Ice Conditions

The response of an ice cover to the winds depends upon some ice strength parameter (p^*) that is a function of the thickness distribution of the ice cover. The ice strength is particularly sensitive to the amount of thin ice and open water present. It is generally assumed that sea ice has no large-scale tensile strength.

During periods when a great deal of thin ice and open water is present, the large-scale ice strength is small, the ice cover will not support stresses, and the ice responds to the winds and currents freely. This condition only occurs during the summer when the ice concentration is low (floes do not touch) and open water exists in the leads. During the ice season, when open water quickly freezes into thin ice, periods of zero ice strength occur only rarely, but model runs with ice strengths of up to about 1.0×10^7 dyn/cm show that the ice response (velocities) differs insignificantly from the response at a strength of zero. For a wide range of ice conditions, then, the effects of ice conditions on ice motion are minimal. Data seem to support this observation. Thorndike and Colony (1982) found that for the central Arctic Ocean, over 70 percent of the variance of ice velocities is explained by the geostrophic winds through a linear relationship, which is an approximation to free drift for larger wind speeds. It is assumed that part of the remaining variance is due to stress gradients within the ice cover.

There have also been times when the ice cover was observed to remain motionless even though strong winds were blowing over a large fetch. Pritchard (1978) estimated that the ice strength during one such event must have been at least 1.0×10^8 dyn/cm. Although larger winds than those observed during that period (about 10 m/s) may have caused additional ice motion, those larger winds are relatively rare. For the range of wind speeds used in the present study, we assumed that an ice strength of greater than 1.0×10^8 dyn/cm would result in no ice motion.

We therefore have essentially three ranges of ice conditions which result in different responses to applied wind loads. The first set of ice conditions results in large-scale ice strengths of from zero to 1.0×10^7 dyn/cm, and the ice response is essentially free drift. For strengths above about 1.0×10^8 dyn/cm, the ice is assumed to be able to almost completely resist wind forces, with little motion resulting. It is in the strength range from 1.0×10^7 to 1.0×10^8 dyn/cm that ice response is most affected by changes in ice conditions. Since there have been very few measurements made of actual ice thickness distributions over the Beaufort Sea, it is difficult to predict the spatial and temporal variations in ice conditions in sufficient detail to describe the distribution of ice strengths in the critical range.

Our strategy has been to assume an ice strength of 5.0×10^7 dyn/cm as representative of the range from 1.0×10^7 to 1.0×10^8 dyn/cm, and to let the differences in ice response at low, medium, and high ice strengths be the residual uncertainty in ice response due to variations in strength. This uncertainty is actually a range of possible ice responses, though, and probably represents only extreme events. The winter of 1975-76 appears to be such an extreme event where, for several months, ice motions were much smaller than for other years. This is unfortunately the time of the AIDJEX experiment, when most of the available data on ice motion was collected concurrent with accurate wind fields and ice thickness information.

2.5 Procedure for Calculating Trajectories

The procedure used for calculating ice trajectories was to first calculate a set of ice responses for each of a set of combinations of ice conditions and wind fields. For each trajectory to be computed, a sequence of randomly chosen numbers corresponding to the different wind fields was chosen in such a way that the sequence had the same statistics as the sequence of winds during 1979-80. Different statistics were used for each season. This set of numbers determined the sequence of wind fields and thus partly determined the ice response. To choose between different ice conditions that might exist for each wind field, and thus complete the determination of ice response, a separate sequence of random numbers was chosen representing different ice conditions. This sequence was not chosen to satisfy some a priori condition or statistic, but was the result of a trial and error process. For each season, a set of ice conditions was chosen so that the statistics of computed monthly displacements best fit the observed monthly displacements. This "best fit" was done in a subjective manner, since few data were available in the area of interest near the coast and we knew that our calculated trajectories were more unreliable further from shore. Finally, some of the ice response fields were modified to better account for the effects of the coast and the developing fast ice zone. These modifications were seen to also improve the comparison between computed and observed displacements.

The following ice response fields were used to compute anticipated ice trajectories:

1) Quasi-steady velocity fields, one for each of the 16 wind patterns for ice with thickness of 300 cm and a strength of 5.0×10^7 dyn/cm. These 16 velocity fields are shown in Figure 7.
2) Free-drift velocity fields, one for each combination of the 16 wind patterns and ice thicknesses of 50, 150, and 300 cm. The 16 velocity fields for an ice thickness of 300 cm are shown in Figure 8. The velocity fields for other thicknesses are similar to these.
3) Velocity field of zero velocity representing ice conditions where strength is so high (greater than about 1.0×10^8) that the ice is essentially motionless.

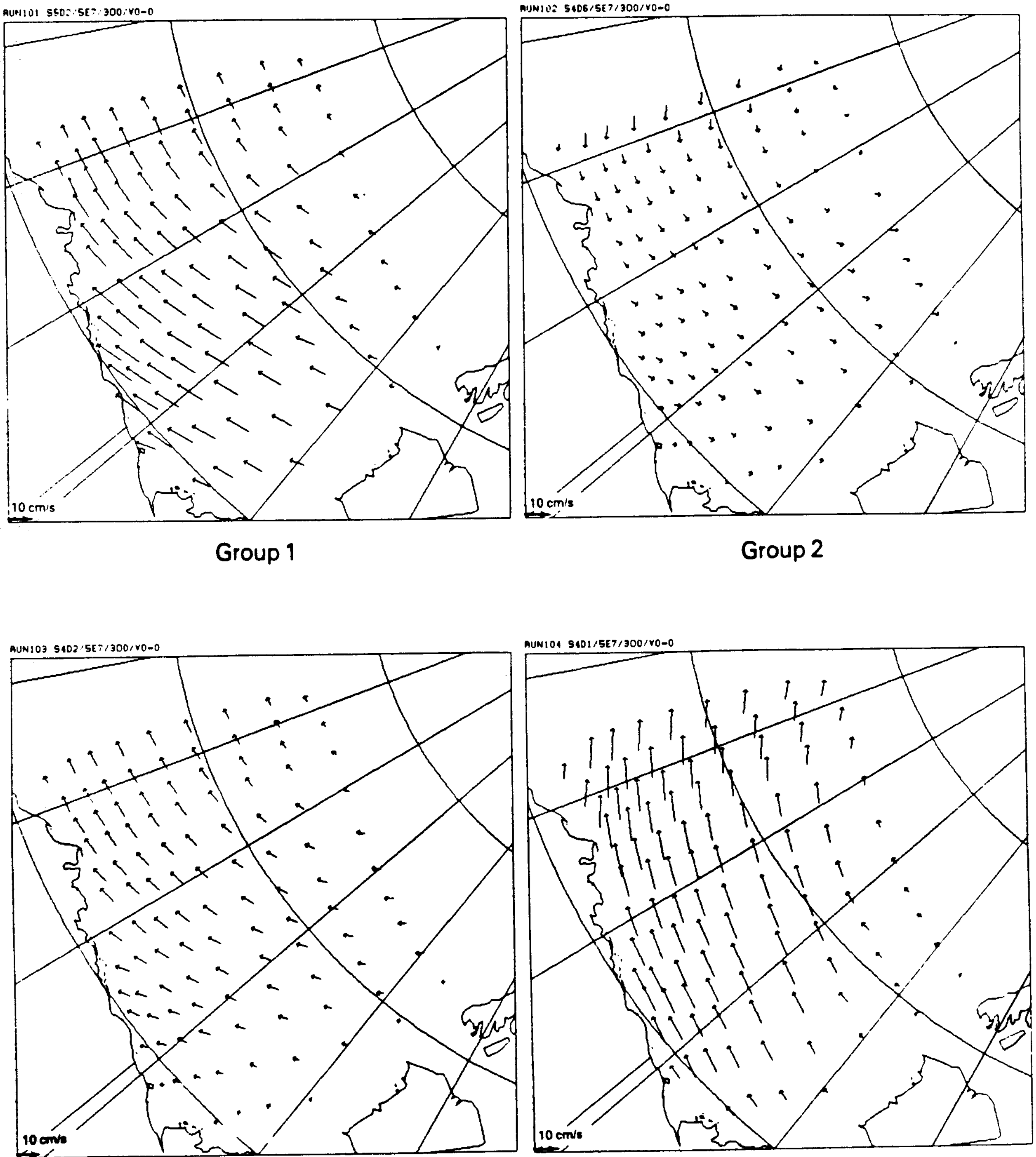

Figure 7. **Ice Velocity Fields Resulting from Model Calculations Using the 16 Mean Wind Fields and Boundary Velocities. An Ice Strength of 5E7 dyn/cm and Average Ice Thickness of 300 cm were used in the Model. Geostrophic Currents were Used Beyond the Shelf Break, and the Beaufort Current Jet was Set to Zero.**

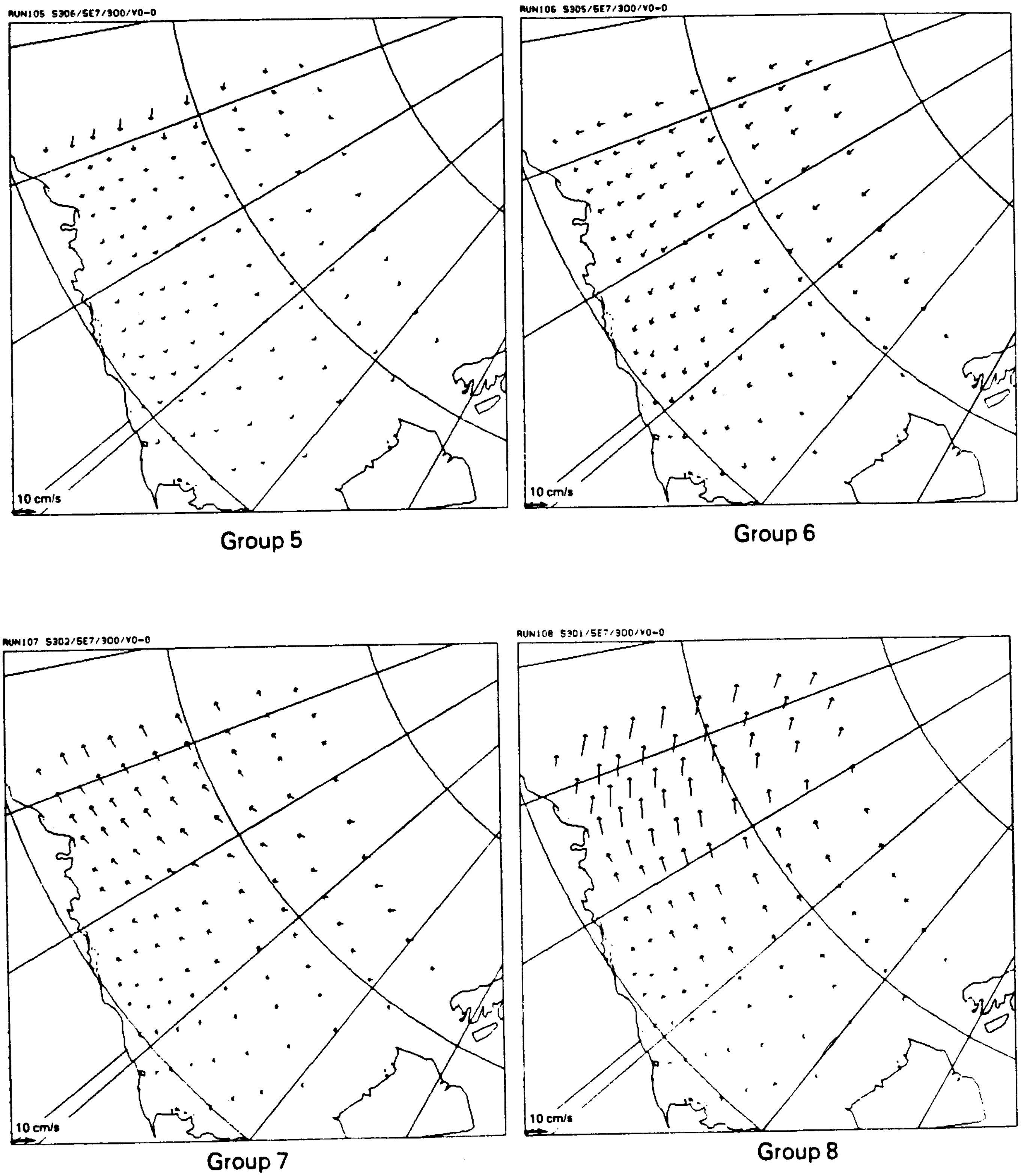

Figure 7. Ice Velocity Fields Resulting from Model Calculations Using the 16 Mean Wind Fields and Boundary Velocities. An Ice Strength of 5E7 dyn/cm and Average Ice Thickness of 300 cm were used in the Model. Geostrophic Currents were Used Beyond the Shelf Break, and the Beaufort Current Jet was Set to Zero (Continued).

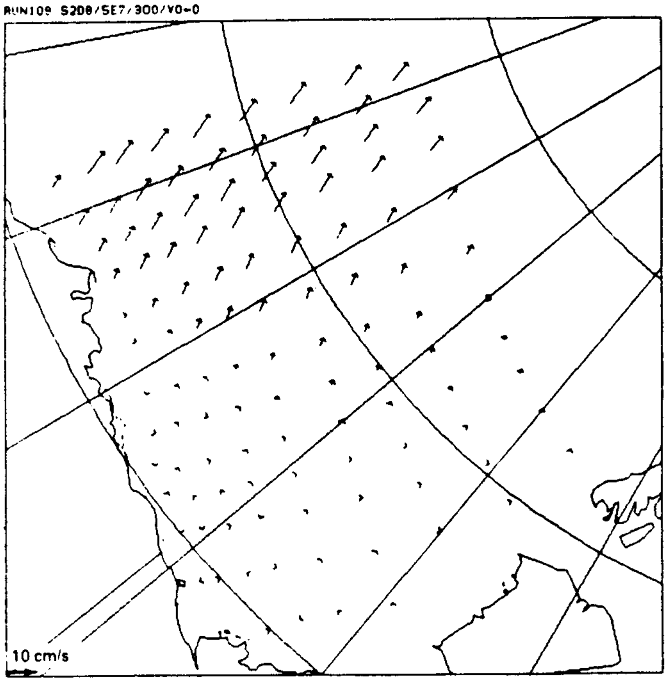

Group 9

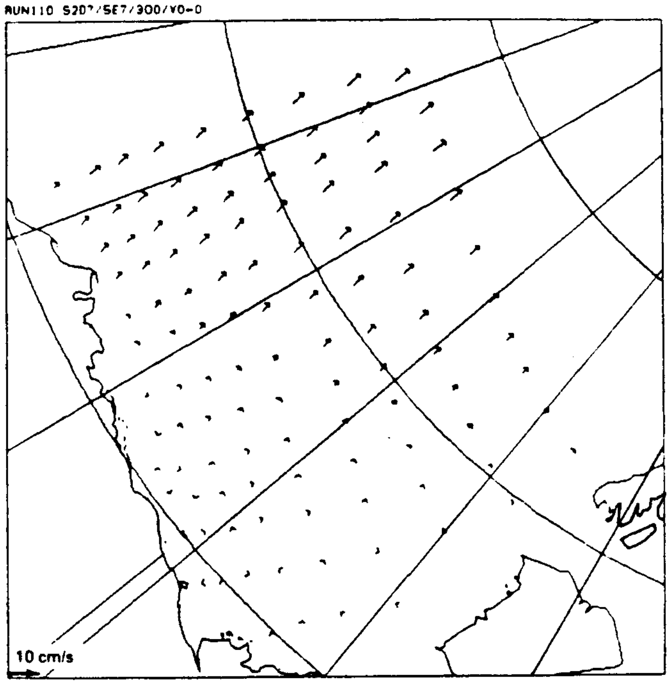

Group 10

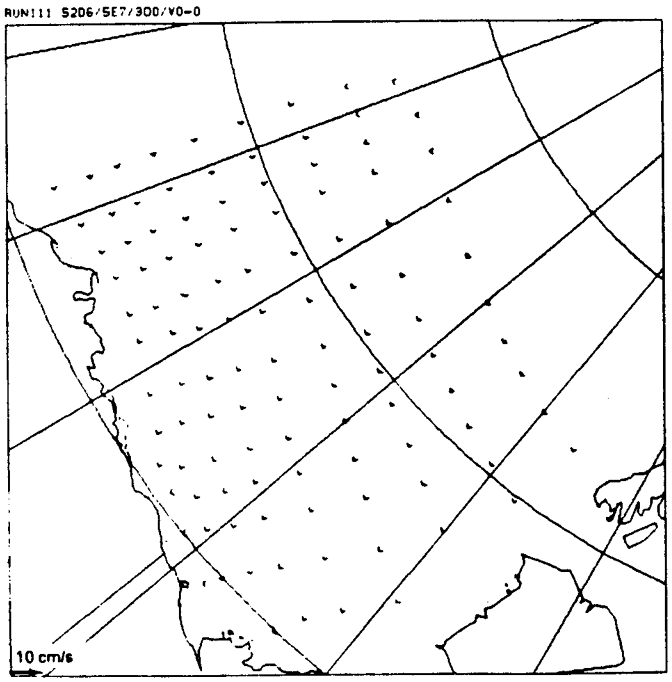

Group 11

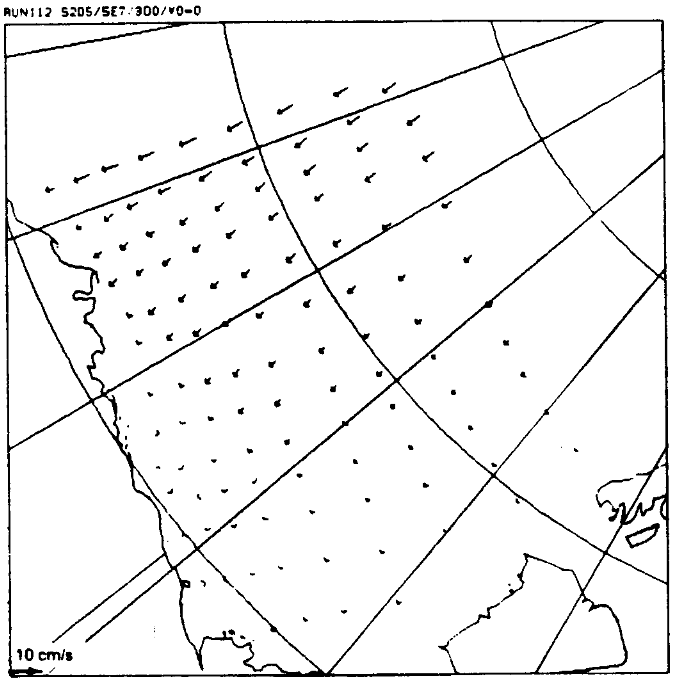

Group 12

Figure 7. Ice Velocity Fields Resulting from Model Calculations Using the 16 Mean Wind Fields and Boundary Velocities. An Ice Strength of 5E7 dyn/cm and Average Ice Thickness of 300 cm were used in the Model. Geostrophic Currents were Used Beyond the Shelf Break, and the Beaufort Current Jet was Set to Zero (Continued).

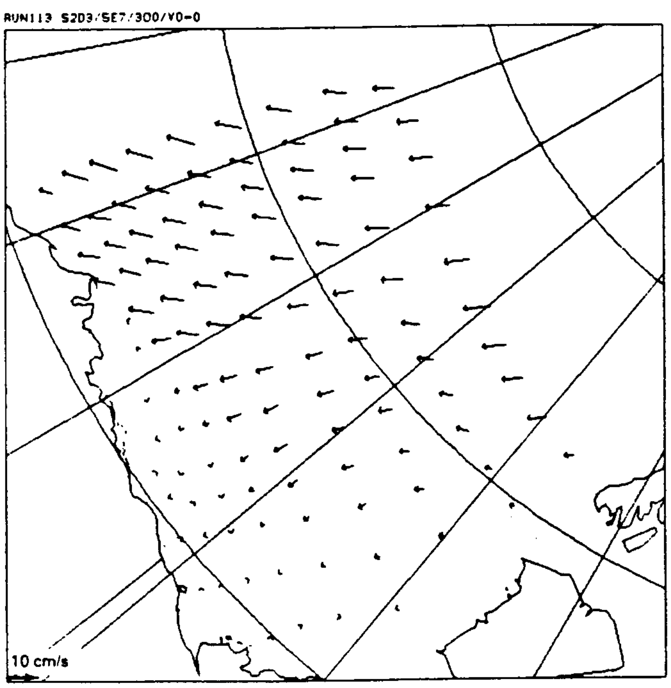

Group 13

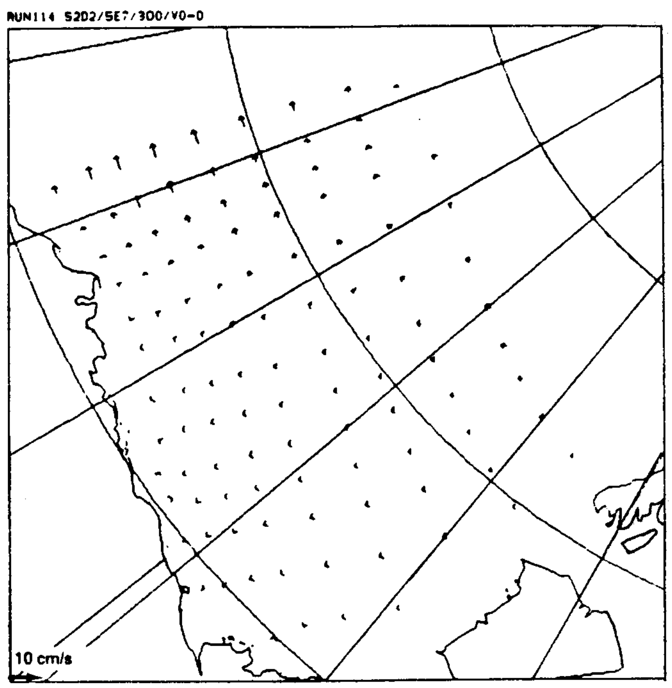

Group 14

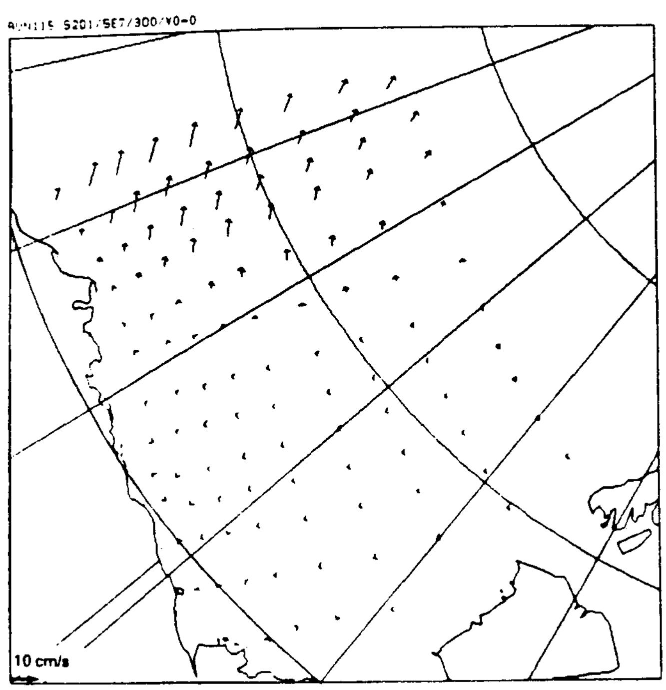

Group 15

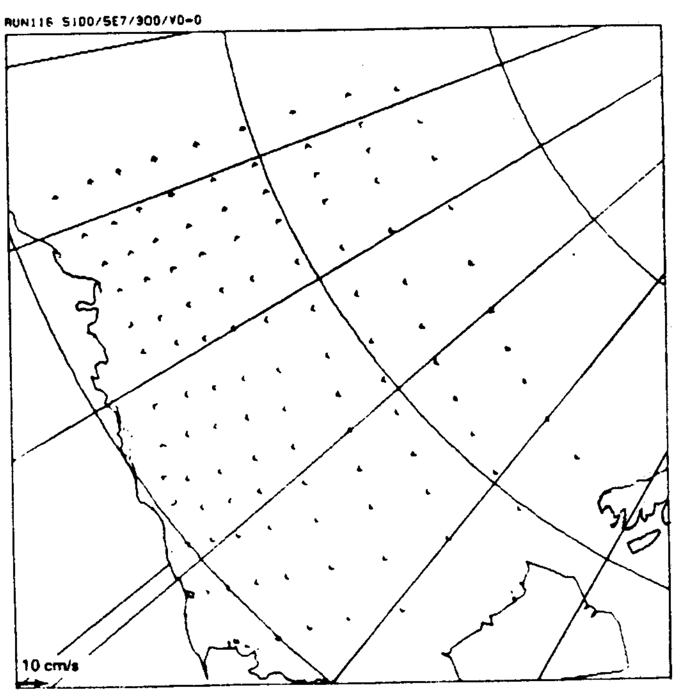

Group 16

Figure 7. Ice Velocity Fields Resulting from Model Calculations Using the 16 Mean Wind Fields and Boundary Velocities. An Ice Strength of 5E7 dyn/cm and Average Ice Thickness of 300 cm were used in the Model. Geostrophic Currents were Used Beyond the Shelf Break, and the Beaufort Current Jet was Set to Zero (Concluded).

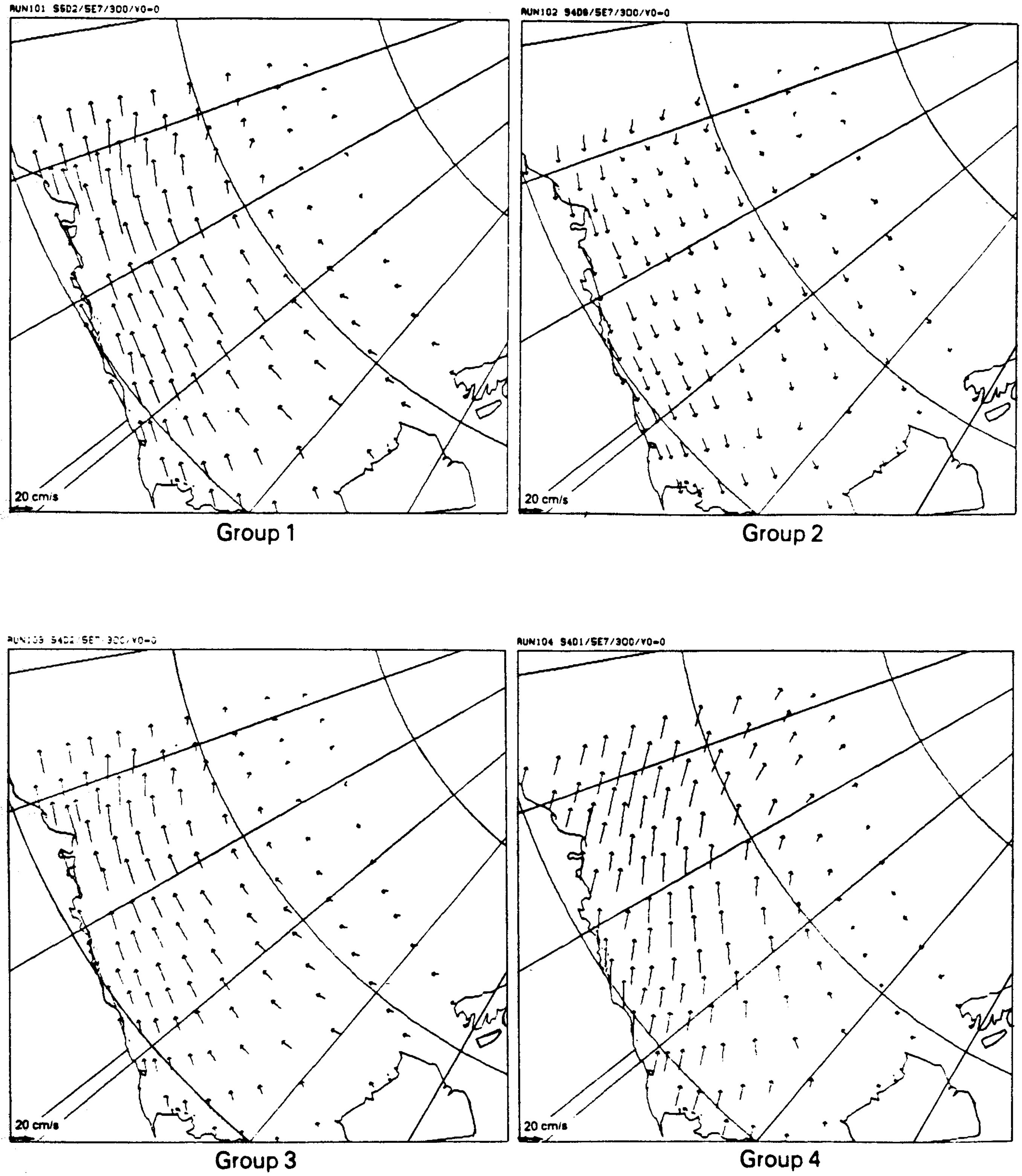

Figure 8. Free-Drift Velocity Fields Resulting from Model Calculations Using the 16 Wind and Boundary Velocity Fields. An Ice Strength of Zero and Average Ice Thickness of 300 cm were Assumed. Geostrophic Currents were Used Beyond the Shelf Break, and the Beaufort Current Jet was Set to Zero.

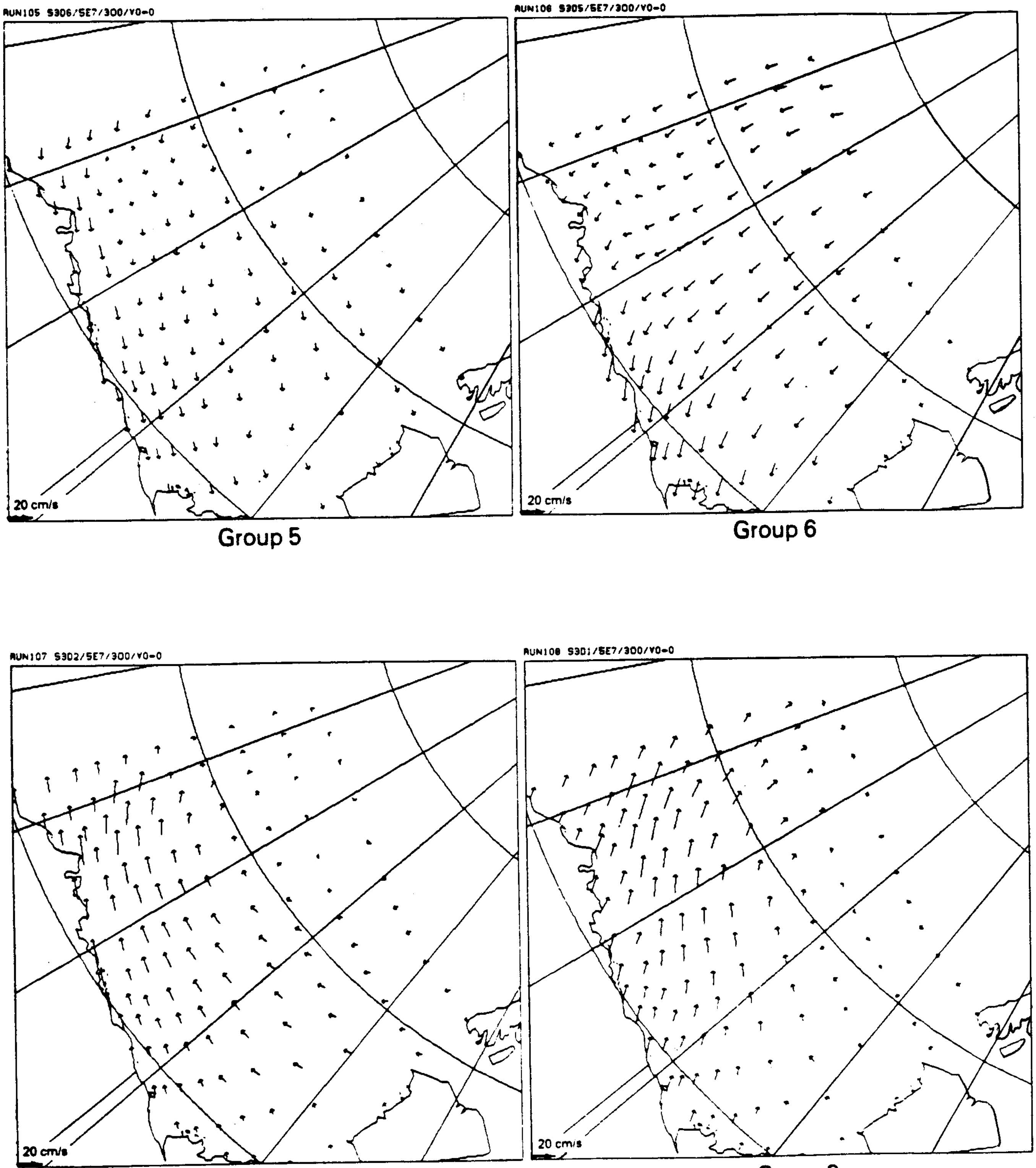

Figure 8. Free-Drift Velocity Fields Resulting from Model Calculations Using the 16 Wind and Boundary Velocity Fields. An Ice Strength of Zero and Average Ice Thickness of 300 cm were Assumed. Geostrophic Currents were Used Beyond the Shelf Break, and the Beaufort Current Jet was Set to Zero (Continued).

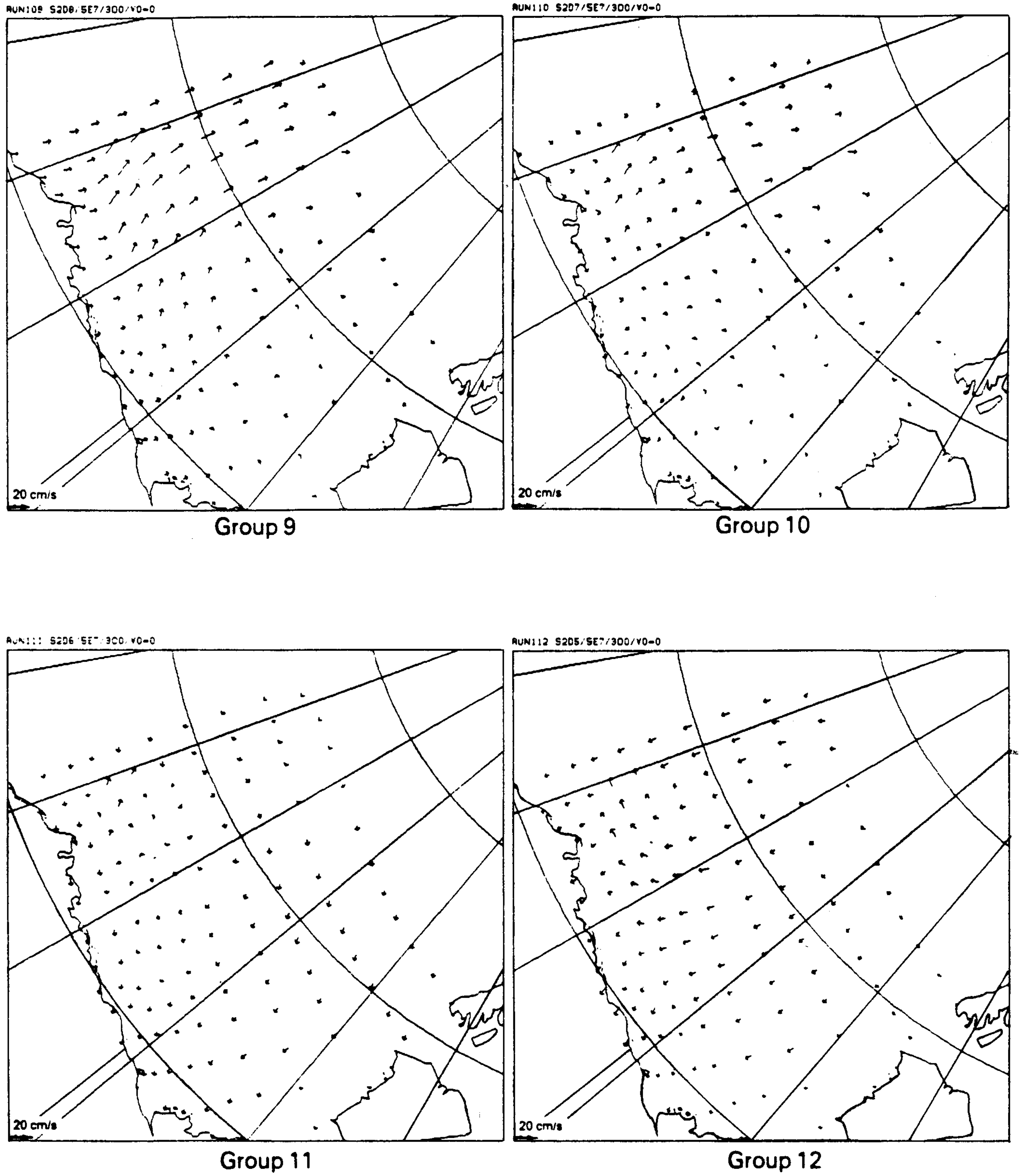

Figure 8. Free-Drift Velocity Fields Resulting from Model Calculations Using the 16 Wind and Boundary Velocity Fields. An Ice Strength of Zero and Average Ice Thickness of 300 cm were Assumed. Geostrophic Currents were Used Beyond the Shelf Break, and the Beaufort Current Jet was Set to Zero (Continued).

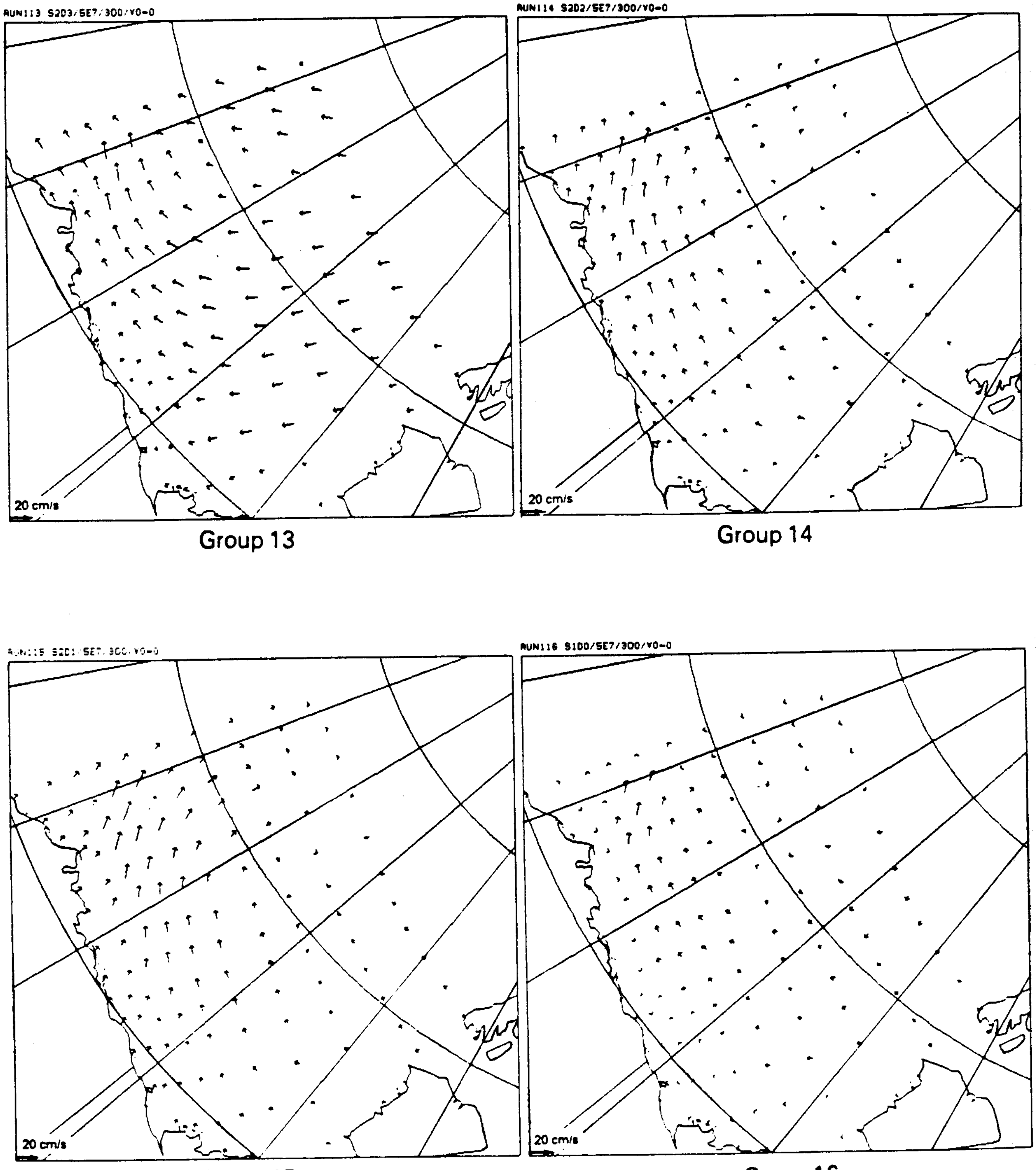

Figure 8. Free-Drift Velocity Fields Resulting from Model Calculations Using the 16 Wind and Boundary Velocity Fields. An Ice Strength of Zero and Average Ice Thickness of 300 cm were Assumed. Geostrophic Currents were Used Beyond the Shelf Break, and the Beaufort Current Jet was Set to Zero (Concluded).

To account for a varying average ice strength through the ice season, we combined various proportions of the low-strength (free-drift), medium-strength (5.0×10^7 dyn/cm) and high-strength (zero motion) ice velocity fields so that the resulting statistics of ice motion best agreed with the limited amount of observed ice motions. For the fall period (October and November) 80-percent free drift and 20-percent medium strength were found to give the best fit. For the winter (December through March), 70-percent free drift and 30-percent medium strength were used. In the spring, (April and May), 20-percent free drift and 80-percent medium strength were used. In the summer (June through September) 100-percent free drift was used. The inclusion of high-strength ice responses was a modification made to some of the ice response fields to account for an increasing ice strength when the winds blow toward shore.

To simulate the effect of increasing ice strength near the coast when winds blow onshore, we arbitrarily increased the ice strength one category whenever ice motions were toward shore. That is, in place of free-drift motion, a motion corresponding to a strength of 5.0×10^7 dyn/cm was used, and when the medium-strength (5.0×10^7 dyn/cm) motion was called for, the high-strength motion (zero motion) was used. This procedure tended to reduce the ice motion, but the majority of the reduction was in the shoreward component. Not only did the results conform more closely to our notions of how the ice behaves near shore, the agreement with observed ice motions improved considerably. During the months of October and November, this increase in ice strength is probably not justified, since the thin ice during this period is less able to resist shoreward motion. We did not treat these months differently, however, since the occurrence of onshore winds was low during the fall.

Ice thickness was not varied for ice strengths greater than zero (free drift) since it was determined that doing so would result in insignificant changes in ice motion. For free-drift velocities, ice mass has a small effect on the angle between the ice motion and the wind, so thickness was allowed to vary seasonally. During October and November, a thickness of 50 cm was used, representing mostly thin ice with some multiyear ice and ridges present. A value of 150 cm was used during December through March, representing the increasing thickness through thermal growth and deformation. In the spring, a value of 300 cm was used for the same reason. One can reasonably argue that these values are wrong, especially since no spatial variation was allowed; however, they are approximately correct for the southern Beaufort Sea, assuming growth rates of 1 cm/day and that about 5 percent of the area is always open water or very thin ice and about 5 percent of the area is ridges. More importantly, the effect of small changes in ice mass on ice velocity fields is small and, while seasonal changes may be important, monthly changes or errors of a few tens of centimeters are accounted for in the overall error of the ice model.

On the fixed boundary along the north coast of Alaska, ice velocities were assumed to be zero, except in one case. During the fall, when the ice cover near the coast is generally thin, it may be moved about by the winds. To account for this, we computed free-drift velocities for the region nearshore for the months of October and November and assumed that the nearshore ice could drift as freely as the ice further offshore.

After November, though, all ice velocities were assumed to be zero at the shoreline. At the first row of computational nodes, about 50 km offshore, the computed ice velocities were assumed to hold. Between the shore and this first row of computed velocities, we linearly interpolated velocities. One result of this is that, after the fall season, the ice near shore moves slower than ice further from shore. Observations of nearshore ice indicate that generally the ice remains in contact with the shore through most of the ice season, and that a great deal of shearing takes place seaward of the shorefast ice. Ice motions measured by the few buoys deployed on the ice in this region indicate that motions near the Alaskan coast tend to be small during most of the year. So, in general, we feel the method we used to treat motions near shore approximates reality. Some improvement could be made by using a finer scale grid near shore and by using a more detailed division of ice strengths, but on the basis of several test runs using a finer grid or different ice strengths, the improvement was hardly noticeable.

The method of accounting for shorefast ice in the trajectory model was also somewhat arbitrary, but was based upon what is presently known about the development of the fast ice zone. The following scenario is typical of the formation and growth of the fast ice zone.

Early in the fall, the area near shore is usually nearly ice free, with the ice edge (area with more than 50 percent ice cover) lying from 100 to 200 km offshore (Webster, 1982). During the first two weeks of October, temperatures drop enough to cause ice to begin to form on the surface. This early ice cover is thin and subject to movement and deformation by moderate winds. Some of the ridges that are formed near shore become grounded in the shallow water. These grounded ridges tend to anchor the surrounding ice and to protect the inshore ice from forces exerted by the moving pack ice. The thickening ice sheet near the shore also becomes strong enough so that eventually it is not moved by the winds acting over a fetch limited by the shore, by barrier islands, and by grounded ridges. By early December, there is usually a region of fast ice near shore that does not move until breakup (Barry, 1979). As the winter progresses, more ridges are built in the region where the moving pack ice interacts with the motionless fast ice. Some of these new ridges also become grounded, extending the fast ice region seaward. Studies using satellite images show that this system of large grounded ridges extends out to about the 20-m isobath (Stringer, 1978, 1982). Studies of the scour marks on the sea floor (Reimnitz et al., 1978) also indicate that the 20-m isobath is approximately the limit of the bottom-anchored fast ice zone.

The development of the fast ice zone is more or less a sporadic process that continues throughout the winter. It is not continuous since individual storms that cause ice motion and deformation are responsible for a large part of the fast ice extension. There is also a great deal of geographical variation in the extent of the fast ice zone, as well as variations from year to year.

For the trajectory model, we included the extension of the fast ice zone in the following manner. During October and November, there is assumed to be no fast ice. Ice near shore is allowed to move, but the motions are generally small for reasons mentioned above. On 1 December, we assume that all ice shoreward of the 10-m isobath becomes fast due to ridges becoming grounded out to water depths of 10 m. Ice inside the 10-m isobath does not move, and ice outside cannot move into water less than 10-m deep. On 1 March, the fast ice zone is assumed to move all the way out to the 20-m isobath as new ridges are built and become grounded. Allowing for the actual variation in the extent of fast ice from year to year and from area to area, our method, while only a coarse approximation, is a reasonable one. The approximate locations of the 10- and 20-m isobaths used are shown in Figure 2.

3. Results

3.1 Seasonal Ice Trajectories

The final results of this study consist of a set of 2250 ice trajectories. These trajectories are divided among 30 different launch sites and three different ice seasons. The 30 launch sites are shown in Figure 9. Beginning on 15 October, 30 trajectories were computed originating from each launch site. These 900 trajectories were continued until 1 August if possible. Trajectories that left the computational grid at the western boundary before 1 August were ended at that date and location. A tracked ice particle that lay within the 10-m isobath by 1 December or the 20-m isobath by 1 March was considered to have become incorporated into the shorefast ice, and the trajectory was terminated at that point.

On 1 December, another 30 trajectories were begun at each of the 26 launch sites that lay outside the 10-m isobath. Ice located at the remaining four sites in shallow water was assumed to be within the fast ice zone, remaining motionless until spring breakup. The 780 trajectories beginning in winter were also continued until 1 August, except for those that left the computational grid before then or lay inside the 20-m isobath by 1 March.

At the start of the spring season on 1 April, the fast ice zone includes all ice inside the 20-m isobath; at this time, 11 of the launch sites lay within this zone. Another 30 trajectories were begun at each of the remaining 19 launch sites and were continued until 1 August, except, again, for those trajectories that left the computational grid. None of these 570 trajectories were incorporated into the fast ice since the model assumed that the fast ice had reached its outermost extent by 1 March.

The distribution of trajectory end points for each of the three starting seasons, fall, winter, and spring, is shown in Figures 10, 11, and 12, respectively. The locations of each ice particle at 1-day intervals along the trajectories were also computed, but are not displayed.

Several general observations can be made regarding the distribution of trajectory end points and the typical trajectory path. The general trend of ice motions in the southern Beaufort Sea is westward, following the direction of the Beaufort Gyre and the modal winds. The long-term ice displacements seem to have an onshore component along the Alaskan coast except near

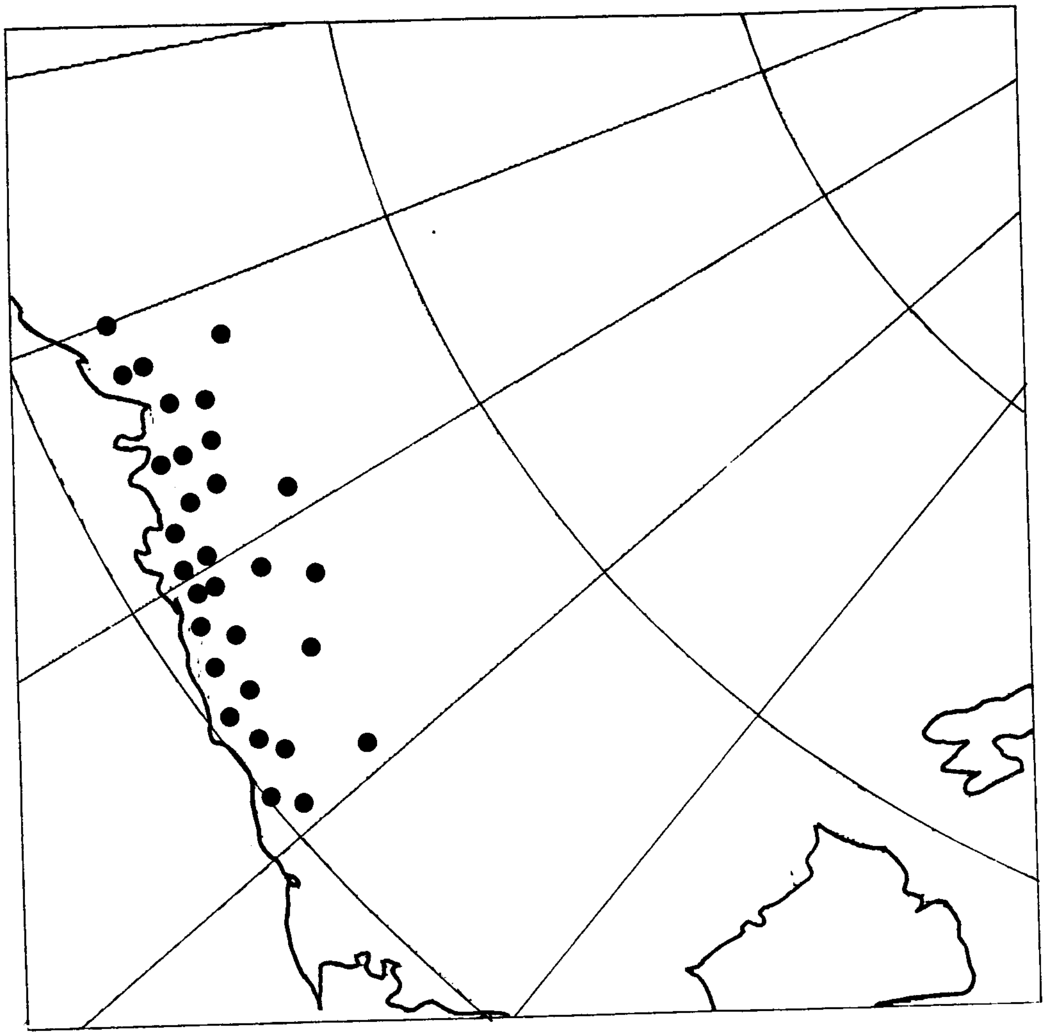

Figure 9. Locations of the 30 Launch Sites Where Seasonal Ice Trajectories were Assumed to Begin.

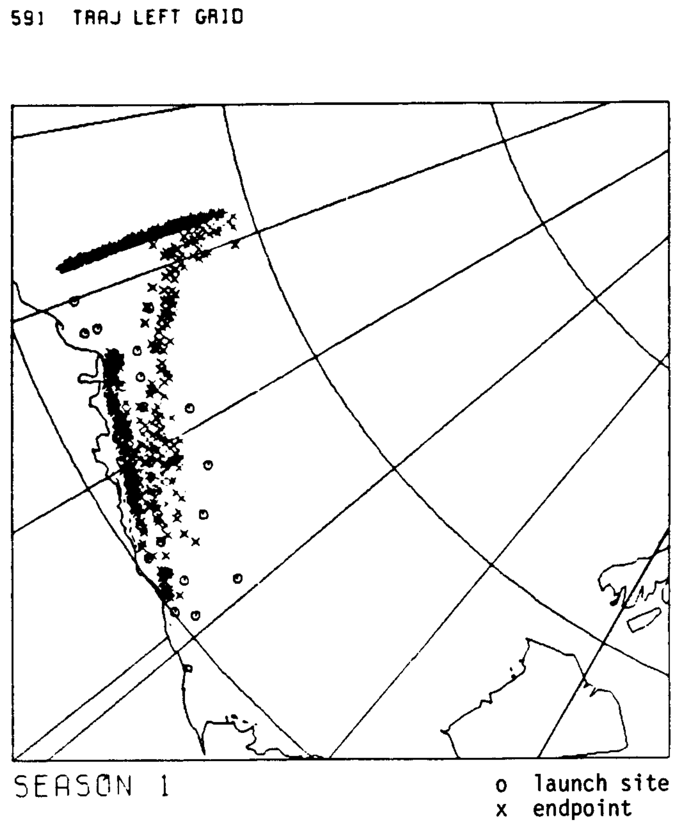

Figure 10.
Distribution of End Points on 1 August for 30 Trajectories Originating from Each of the 30 Launch Sites on 15 October. The Cluster of Points to the West is Where Individual Trajectories Crossed the Computational Grid Boundary Before 1 August.

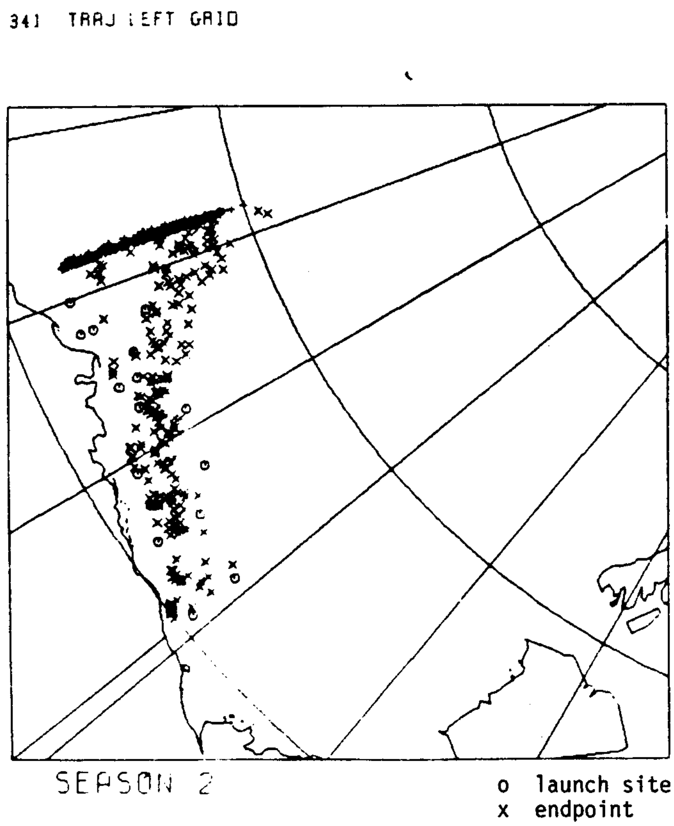

Figure 11.
Distribution of End Points on 1 August for 30 Trajectories Originating from Each of the 30 Launch Sites on 1 January. The Cluster of Points to the West is Where Individual Trajectories Crossed the Computational Grid Boundary Before 1 August.

225 TRAJ LEFT GRID

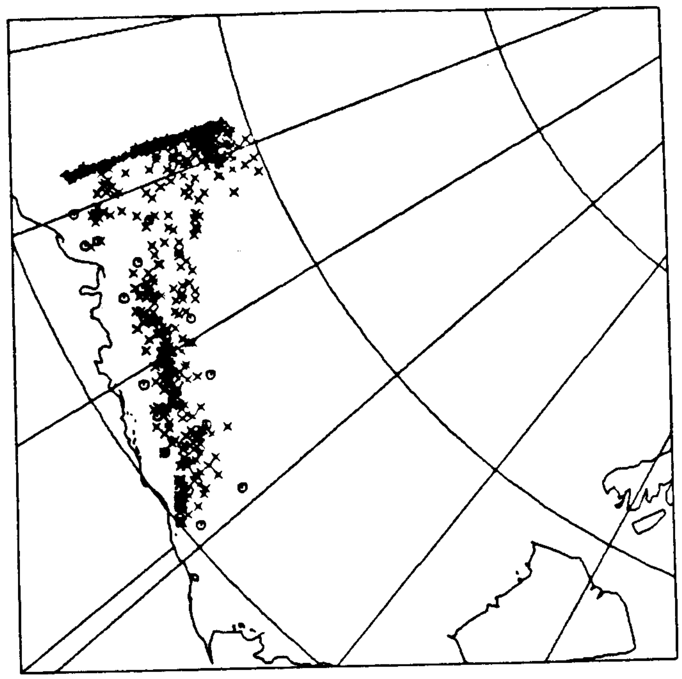

Figure 12. Distribution of End Points on 1 August for 30 Trajectories Originating from Each of the 30 Launch Sites on 1 April. The Cluster of Points to the West is where Individual Trajectories Crossed the Computational Grid Boundary Before 1 August.

Point Barrow where a northward, offshore component is evident. These modeled motions agree with observed ice motions. A full range of ice motions is displayed by the modeled trajectories, from no motion or even a slight net eastward motion during a month to about 300 km of westward motion. This is also about the range of observed monthly displacements.

3.2 Variability in Modeled Trajectories

If one were to place a buoy on the sea ice every year at the same geographical location and at the same time, the buoy would in general describe a different trajectory each year. By doing this enough times at enough different locations, one could calculate the mean and variability of the ice motion field for the Beaufort Sea. The confidence limits of these statistics would depend upon the number of repetitions of the experiment, assuming that the errors in locating the buoy's position is small. While a great deal of buoy data has been collected in the Beaufort Sea, the total number of buoys passing through each small region of the Beaufort Sea during each small time segment of the year is too small to provide accurate statistics of ice motion.

Another method of getting ice trajectories from which statistics of ice motion can be estimated is to use an ice model and real environmental data to hindcast historical ice motions. Unfortunately, no perfect model of sea ice exists and, more importantly, a complete environmental data set for driving an ice model does not exist. The only realistic approach, then, is to use the data that exist to drive the best model available, and then to estimate the total error due to variations in the driving forces and incorrectly modeled processes.

The best model available is the one developed during AIDJEX, which is described in Section 2. Typical errors in ice motion using this model have been shown to have a standard deviation of about 3 km/day with a mean daily error of about 1 km/day for daily motions (Pritchard and Kollé, 1981). Over a period of N days, the mean error accumulates as N times the mean and the standard deviation according to N times the standard deviation. Over a period of six months, substantial errors can occur. The mean difference in modeled versus actual trajectory end points would be 180 km, with a standard deviation of about 40 km. Of course, accumulating the mean in this manner assumes that the error in direction is constant each day. It is probable that, while the magnitude of the daily velocity error averages 1 km/day, the direction may vary so that over long periods of time, the total error in displacement will be much smaller than N days times 1 km/day. Insofar as possible with the limited number of observed ice trajectories available, we adjusted our trajectory model so that for periods of one month, the mean of computed monthly trajectories nearly matched the mean of observed motions. While we do not claim to be 100 percent successful in this, we do feel that the standard deviation does more nearly represent the actual variation between computed and actual ice motions due to inaccuracies in the model. It might be noted that some of this variability will be due to inaccuracies in the data used to drive the model, so a standard deviation of 3 km/day is probably a maximum error due to the sum of errors in the model, the errors in the daily winds, and errors in the mean ocean current field.

Another source of variation that we are able to account for in the trajectory model is that due to the use of mean winds rather than daily winds to calculate the daily ice motions. Due to ice strength, and the ability of ice to transmit stresses when strength is high, the ice cover may at times be determined more by the boundary motions than by the local winds. We also used mean boundary motions in the model, so, while we discuss the error due to the use of mean wind fields, the errors are partly due to using the corresponding mean boundary motions.

For one wind group, that with the largest magnitudes, we examined the variability in ice motions due to within-group wind variability and the nonlinear ice model. Both the quasi-steady and free-drift models were run using each of the daily wind fields that made up the group, as well as the group mean wind field. In Figure 13, we show the mean and 50 percent equiprobability ellipses of the daily ice motions for a strength of 5.0×10^7 dyn/cm and, in Figure 14, the ice motion field computed from the mean wind field is shown. Daily and mean boundary motions were used along with the daily and mean winds. In Figure 15 we show the mean and 50 percent equiprobability ellipses of the daily ice motions for a strength of zero (free drift) and, for comparison, the ice motion field computed using the mean wind field is shown in Figure 16. Again, the appropriate daily or mean boundary

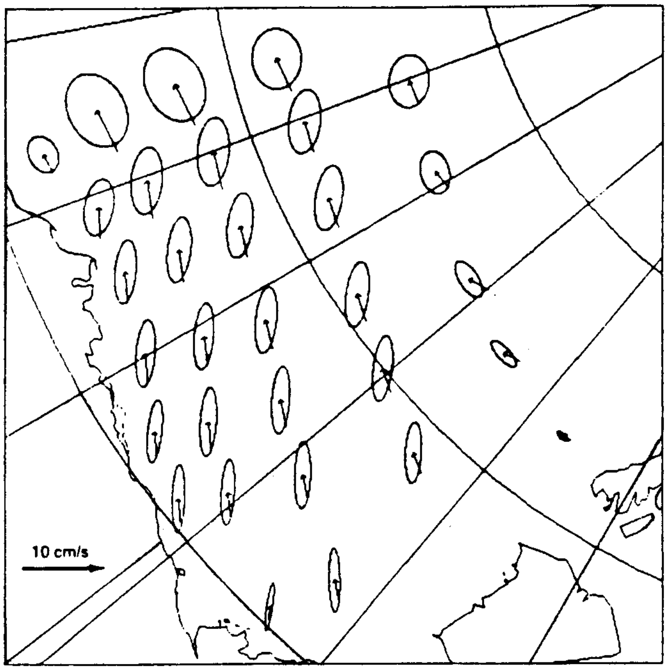

Figure 13.

Mean and 50% Equiprobability Ellipses of Modeled Ice Velocities for the 20 Days Classified as Group 1. Daily Wind Fields and Boundary Velocities were Used. An Ice Strength of 5E7 dyn/cm and Average Ice Thickness of 300 cm were Used. The Winds Used in These Calculations were Inadvertently Rotated.

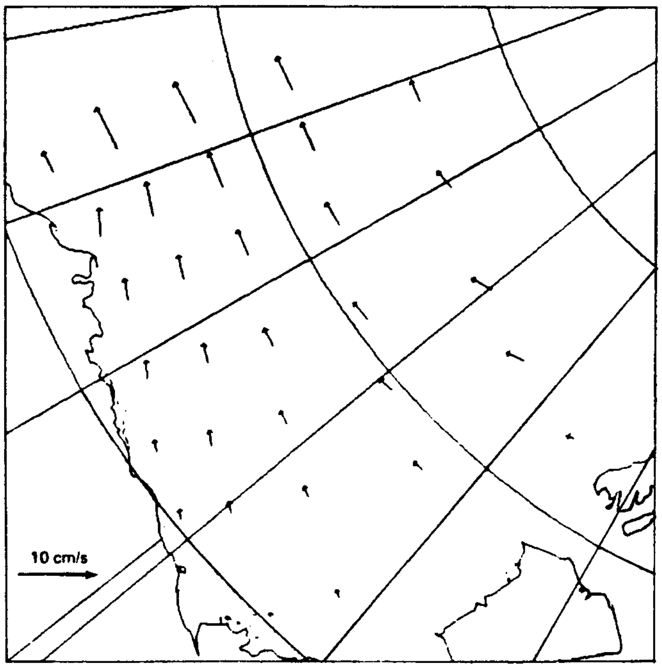

Figure 14.

Modeled Ice Velocity Field Using the Mean Winds and Boundary Velocities for Group 1. An Ice Strength of 5E7 dyn/cm and Average Ice Thickness of 300 cm were Used. The Winds Used in this Calculation were Inadvertently Rotated.

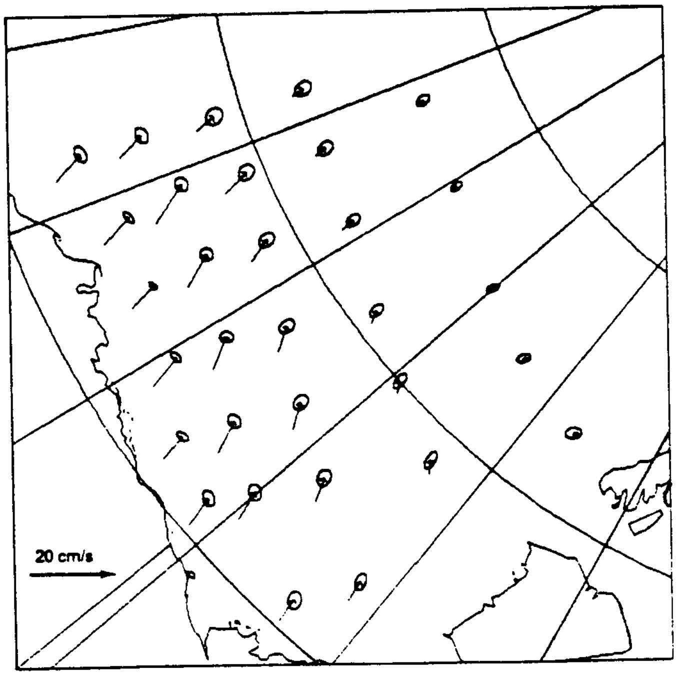

Figure 15.
Mean and 50% Equiprobability Ellipses of Free-Drift Ice Velocities for the 20 Days Classified as Group 1. Daily Wind Fields and Boundary Velocities were Used. The Winds Used in These Calculations were Inadvertently Rotated.

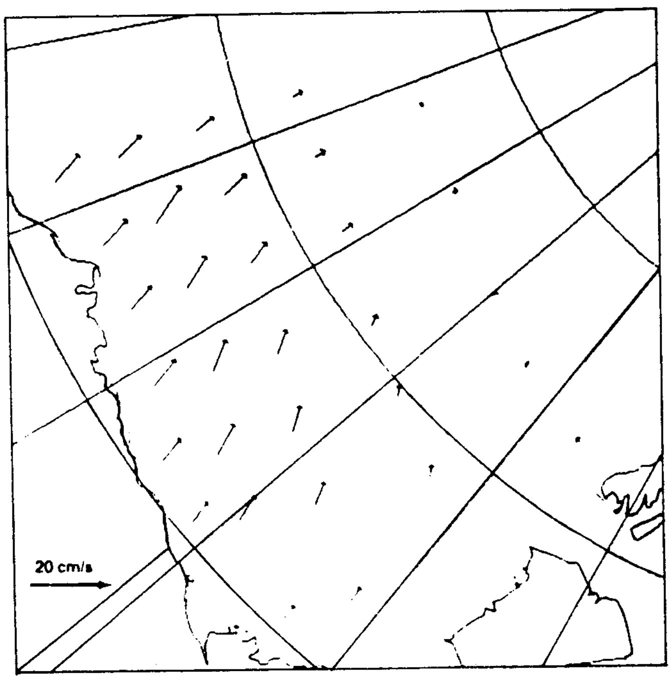

Figure 16.
Free-Drift Ice Velocity Field Using the Mean Winds and Boundary Velocities for Group 1. An Ice Strength of Zero and Average Ice Thickness of 300 cm were Used. The Winds Used in This Calculation were Inadvertently Rotated.

motions were used. The model results shown in Figures 13 through 16 contain a constant angular error, which caused these results to not conform to any of the other modeled motions; however, this error does not affect the comparison illustrated in Figures 13 through 16. The within-group standard deviation of daily displacement for this wind group is approximately 3 km/day for both ice strengths. A small difference between the mean of 20 daily displacements and the displacement calculated using the mean wind is evident, but the difference is relatively small and can be assumed to be partly canceled when all 16 wind groups are considered. The within-group variation for the other 15 groups was not calculated, but would in general be smaller than that for this group since the ice motions are generally smaller. We therefore considered 3 km/day to be the standard deviation of daily ice motions resulting from the use of group mean winds instead of daily winds. The standard deviation of errors resulting from the model itself and inaccuracies in daily driving forces was also shown to be about 3 km/day. Combining the two standard deviations, each equal to 3 km/day, we get a standard deviation of $3\sqrt{2}$ or about 4.25 km/day. Over a six-month period, this will accumulate to about 57 km. The uncertainty will likely be greater than this in the east-west direction and smaller in the north-south direction, but resolutions of these kinds of differences do not seem appropriate.

There are other uncertainties in the calculated trajectories that we are not able to estimate reliably. The two major ones arise from variations in the ocean currents and from unknown statistics of ice strength. Theoretically, there may be "extreme event" situations where the extreme range of these conditions is felt. During periods of low ice concentration, the range of velocities that the Beaufort Current jet experiences can cause differences in daily ice motions of as much as 60 km. These differences are not to be expected, however, during the ice season. The occasional reversing of the Beaufort Current itself will tend to cancel part of the ice motion it may cause. The presence of a solid ice cover, which will be able to resist forces exerted over the relatively small area of the current jet, will tend to reduce the effect of the current. Although we are not able to accurately estimate the variation in ice motion due to the Beaufort Current, we see no reason to expect that variation to be comparable with the variation caused by the winds or by ice conditions.

It is possible to estimate the range of ice motions resulting from the range of possible ice conditions. These are just free-drift motion when ice strength is low, and no motion at all when ice strength is very high. Thomas and Pritchard (1979) have calculated this range of motion for the Beaufort Sea using historical wind data. Those historical free-drift motions compare reasonably well with the trajectories computed in this present study. The historical free-drift motions were also alongshore toward the west, they were generally larger than the motions computed in this study (which were not entirely free drift), and the year-to-year variability in historical free drift is comparable to the variability found in this work. One major difference can be seen, though: the historical free-drift motions tended to be to the right of the motions found in this study. Two obvious explanations are possible. First, the historical winds were computed from sea level pressure analysis that likely to be in error for the arctic regions due to lack of input data. The pressure data available from the Arctic Ocean Buoy Program which were used in this work, were much more accurate. It is a different data set though, so some of the differences may be due to sampling. Another reason for the differences in historical free drift and the modeled trajectories reported herein, is that the ice motions in this study were not entirely free drift. Part of the motions were due to the effects of boundary motions and ice strength. The boundary motions are the result of far-field winds when ice strength is significant. This effect is minor though, when trajectories were computed using 100 percent free-drift, the motions were still to the left of those reported for historical winds.

4. Comparisons With Observations

The lack of observed ice motion data, especially in the southern Beaufort Sea, makes comparisons between observations and model results difficult. The proper statistical comparison would require many observed, long-term (month or longer) ice trajectories in one relatively small area. These are not available. The observed trajectories are spread over the entire Beaufort Sea, with the fewest observations in the area near shore where the model is most applicable. In addition, a large proportion of the nearshore observations was taken during the 1975-76 AIDJEX project. Comparison of observed motions during that ice season with observations from other years strongly suggests that anomalous winds and/or ice conditions prevailed during that ice season. It is well-known that the summer of 1975 was a bad year for shipping along the Beaufort Sea coast due to heavy ice near shore.

One method of making comparisons is to model the motion of individual buoys using an ice model and real data. This has been done in previous studies (see Pritchard and Kollé, 1981, for instance) using the same ice model used in this study, and is not repeated here.

The complete trajectory model used in this study made use of that ice model to produce ice response fields, which were then combined in a stochastic model to produce a distribution of ice trajectories. This stochastic trajectory model was "tuned" by comparing resultant ice trajectories with a subset of the observed ice motions. The comparison was done in the following manner. From the observed monthly ice motions, a sample of observations was chosen and plotted. These observations were selected to be as near the region of interest as possible, and only a limited number of observations were selected from any one ice season to avoid biasing the observations toward possibly anomalous years when, by chance, more data were available. For instance, only one observation from any month would be chosen and a random sample of spatially distributed computed trajectories would also be plotted for comparison. Seasonal comparisons could then be made. As an example, we have plotted monthly trajectories originating at each launch point used in this study. The monthly trajectories for winter, spring, summer, and fall are shown in Figures 17 through 20, respectively. The trajectories may be compared with the observed monthly trajectories plotted by season as shown in Appendix B of this report. For any one year, it will be possible to find some computed trajectories which agree with the sense of the observed motions.

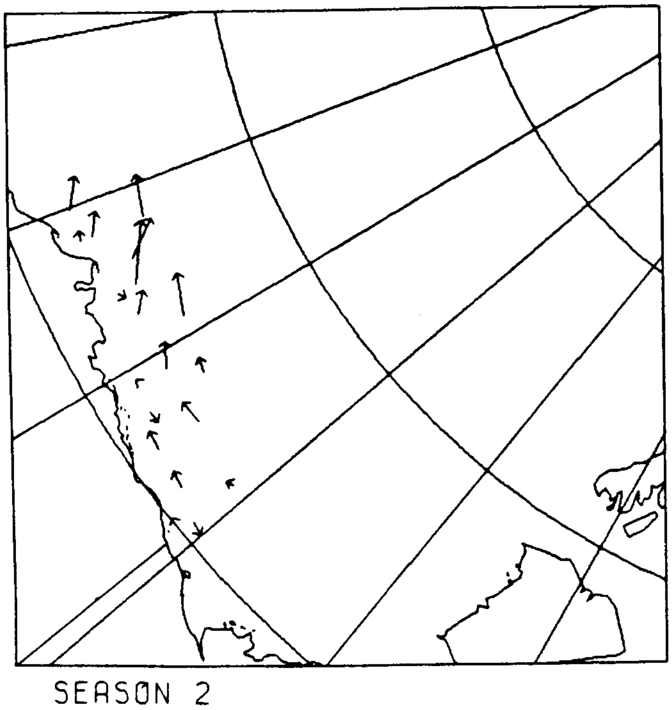

Figure 17.
Modeled Monthly Ice Motions for the Winter Season (January, February, and March). Modeled Trajectories Originate at the Launch Points Used in this Study.

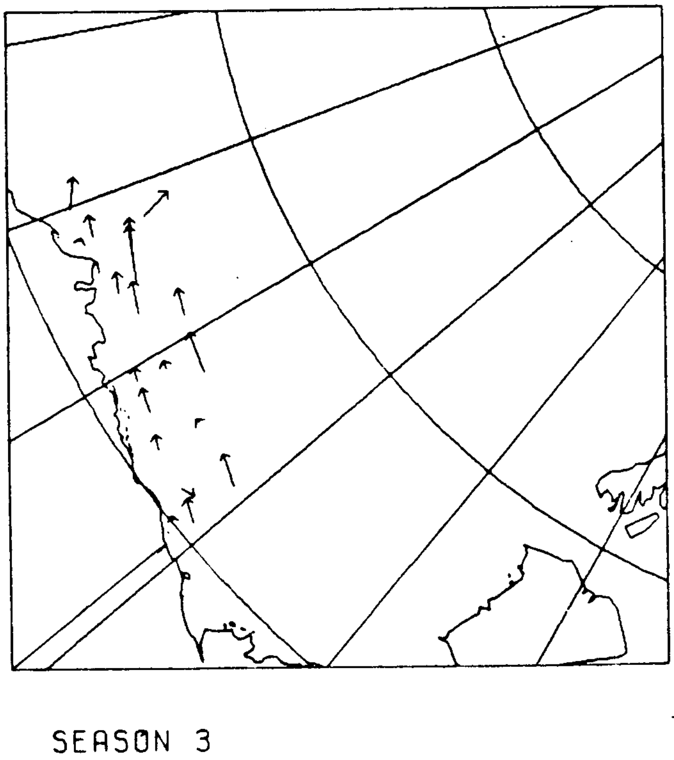

Figure 18.
Modeled Monthly Ice Motions for the Spring Season (April, May, and June). Modeled Trajectories Originate at the Launch Points Used in this Study.

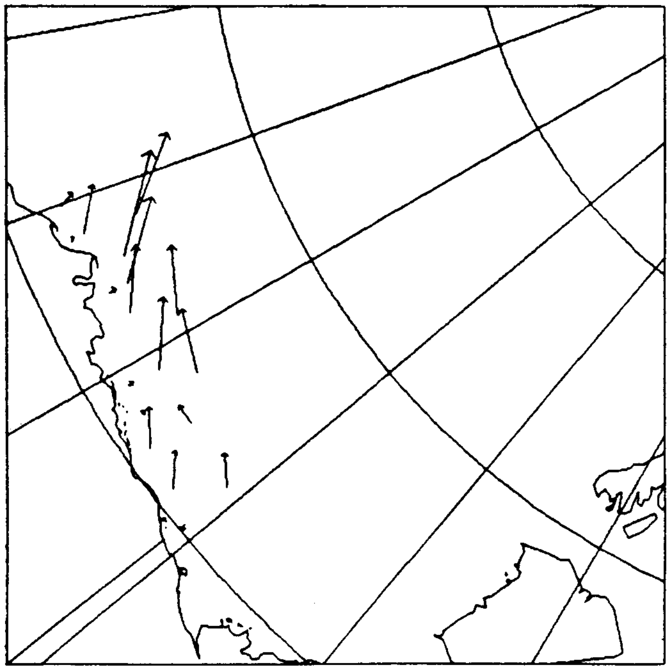

Figure 19.
Modeled Monthly Ice Motions for the Summer Season (July, August, and September). Modeled Trajectories Originate at the Launch Points Used in this Study.

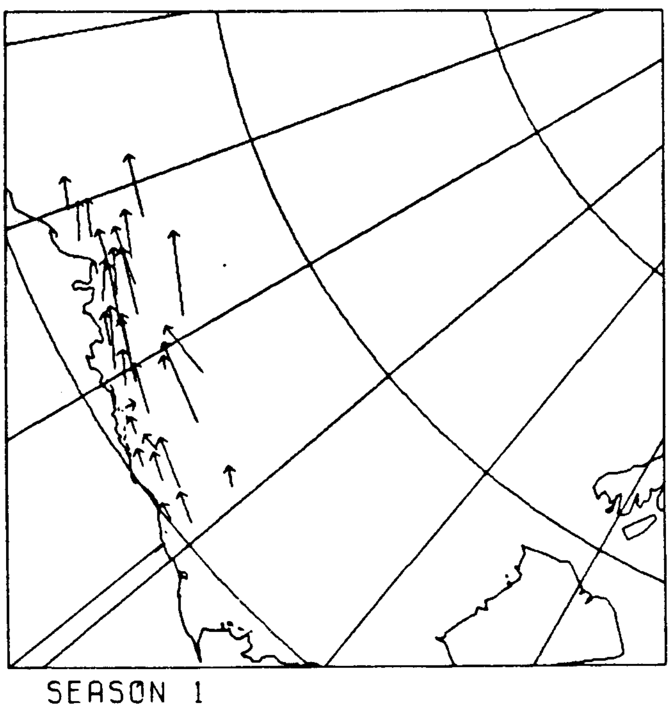

Figure 20.
Modeled Monthly Ice Motions for the Fall Season (October, November, and December). Modeled Trajectories Originate at the Launch Points Used in this Study.

5. Discussion

The results of this work are useful as an aid in predicting the ultimate fate of oil spilled during the ice season in the Beaufort Sea. Inside the fast ice zone the best prediction is that spilled oil becomes incorporated into the ice cover soon after the spill occurs, and that the oiled ice will remain in the ice with no significant ice motion occurring until spring breakup. As temperatures rise in the spring, oil is released from the ice, first onto the ice surface and then, as breakup continues and the ice melts, into the ocean. In general, wintertime oil spills in the fast ice zone become open-water spills at breakup in the same vicinity as the original spill. The primary differences are that the oil will have weathered somewhat before being released into the water and that the ice cover will be broken up.

Early in the ice season, while the fast ice zone is covered with thin, newly formed ice, significant ice motions are possible. Accounts exist of the newly formed ice cover being blown out to sea. No ice motion data have been taken for the newly formed ice in the fast ice zone early in the ice season. The modeled trajectories, however, show that there is a tendency for the ice to be held against the shore by the prevailing winds. Seaward ice motions do occur in response to specific storm events, but longer term wind patterns tend to move the ice back toward shore. Ice deformation will take place during these back and forth motions, with some possibility of oiled ice being built into ridges.

Outside the fast ice zone, the same processes of incorporation into and release from the ice take place in the event of an oil spill, but significant motion of the oiled ice will usually have occurred.. Again, very little ice motion data exist for the area between the fast ice zone and the polar pack ice zone. This area, the seasonal pack ice zone, lies within the 100 to 200 km region offshore that is mostly ice free during the late summer but is covered by a solid ice cover the rest of the year. This is the area where much of the oil exploration and development may take place, and where motions are most sparse for this area. The ice trajectory model developed during this study was designed to predict typical ice motions in this region.

The computed trajectories reported here show that the ice has a long-term motion toward the west, with occasional eastward motions for short periods of time. The average westward motion is about 3.7 km/day during the fall, 1.3 km/day during the winter, 2.1 km/day during the spring, and about 3.6 km/day during the early summer. These motions are for the launch points outside the 20-m isobath and east of Point Barrow. There is a great deal of variation in the motions, amounting to a standard deviation of daily motions of about 5 to 10 km.

The motions near shore are smaller than those further offshore, but this is mostly a result of the model design.

Along with the westward motion, the ice tends to be forced shoreward along most of the north Alaskan coast, with more northward motion occurring west of Point Barrow. This shoreward motion, combined with the westward shearing motion, will produce ice deformations, namely, ridges parallel to the shore. Observations of the ice morphology outside the fast ice zone bear this out. An active shear zone is evident throughout much of the winter, and a great many ridges, many of them grounded in shallow waters near shore, are usually evident along the Beaufort Sea coast. The present trajectory model does not allow an estimate to be made of the amount of ice that might be built into ridges. The ice strength, along with the shoreward component of the driving forces, will determine the amount of deformed ice. Ice strength was one of the parameters varied in this study and, while the general sense of the resulting motions are reasonable, errors of only a few kilometers in the amount of shoreward motion can make large differences in the amount of deformed ice. Thomas (1980) examined the motion of a buoy that was only about 30 km offshore from Cross Island during the winter of 1975-76. The net onshore motion of this buoy was about 6 km during an 80-day period, with some back-and-forth motion also probable (the positioning error of the buoy was about 2 km). Therefore, it is possible that approximately 20 percent of the ice outside the barrier islands may become built into ridges. The computed ice trajectories for this study show that shoreward trend, with a variability of computed motions large enough to allow almost any amount of deformation. To better determine the amount of ice deformed into ridges, more data on ice motions near shore are needed. The use of a full time-dependent ice model would also aid in this determination.

REFERENCES

Aagaard, Knut (1981) "The Beaufort Current," to appear in The Alaskan Beaufort Sea (P. Barnes, E. Reimnitz, and D. Schell, editors), The Academic Press, N.Y.

Barry, R. G. (1979) "Study of Climatic Effects on Fast Ice Extent and Its Seasonal Decay Along the Beaufort-Chukchi Coasts," Environmental Assessment of the Alaskan Continental Shelf, Vol. 2 Physical Science Studies, Final Reports, NOAA/OCSEAP, Boulder, Colorado, pp. 272-375.

Brower, W. A., H. F. Diaz, A. S. Prechtel, H. W. Searby, and J. L. Wise (1977) Climatic Atlas of the Outer Continental Shelf Waters and Coastal Regions of Alaska, Vol. III, Chukchi-Beaufort Sea. Arctic Environmental Information and Data Center, University of Alaska, Anchorage.

Buist, I. A., W. M. Pistruzak, and D. F. Dickins (1981) "Dome Petroleum's Oil and Gas Undersea Ice Study," Proceedings of the Fourth Arctic Marine Oilspill Program Technical Seminar, Edmonton, Alberta, pp. 647-686.

Comfort, G., and W. Purves (1980) "An Investigation of the Behaviour of Crude Oil Spilled under Multi-year Ice at Griper Bay, NWT," Proceedings of the Third Annual Marine Oilspill Program Technical Seminar, Edmonton, Alberta, pp. 62-86.

Coon, M. D. (1980) "A Review of AIDJEX Modeling," Sea Ice Processes and Models, (R. S. Pritchard, ed.), University of Washington Press, Seattle, pp. 28-33.

Cox, J. C., L. A. Schultz, R. P. Johnson, and R. A. Shelsby (1980) "The Transport and Behavior of Oil Spilled In and Under Sea Ice," Final Report of Research Unit #568 to OCSEAP Arctic Project Office, September.

Cox, J. C., and L. A. Schultz (1981) "The Mechanics of Oil Containment Beneath Rough Ice," Proceedings of the Fourth Arctic Marine Oilspill Program Technical Seminar, Edmonton, Alberta, pp. 3-44.

Jenne, R. L. (1975) "Data Sets for Meteorological Research," National Center for Atmospheric Research Technical Note NCAR-TN/IA-III, Boulder, Colorado.

Kozo, Thomas L. (1980) "Mountain Barrier Baroclinity Effects on Surface Winds Along the Alaskan Coast," Geophysical Research Letters, Vol. 7, No. 5, pp. 377-380.

Lewis, E. L. (1976) "Oil in Sea Ice," Pacific Marine Science Report 76-12, Institute of Ocean Sciences, Victoria, B.C.

Martin, S. (1977) "The Interaction of Oil with Sea Ice," OCSEAP Annual Report, Outer Continental Shelf Environmental Assessment Program, NOAA/Arctic Project Office (University of Alaska), Fairbanks.

McPhee, M. G. (1980) "An Analysis of Pack Ice Drift in Winter," Sea Ice Processes and Models, (R. S. Pritchard, ed.), University of Washington Press, Seattle, pp. 62-75.

McPhee, M. G. (1982) "The Turbulent Boundary Layer in Shallow Water," OCSEAP Annual Report for RU#567, Appendix C.

Newton, J. L. (1973) "The Canada Basin: Mean Circulation and Intermediate Scale Flow Features," Ph.D. Thesis, University of Washington, Seattle.

NORCOR Engineering and Research, Ltd. (1975) "The Interaction of Crude Oil with Arctic Sea Ice," Beaufort Sea Technical Report #27, Beaufort Sea Project, Dept. of the Environment, Victoria, B.C.

NORCOR Engineering and Research, Ltd. (1977) "Probable Behaviour and Fate of a Winter Oil Spill in the Beaufort Sea," Technical Development Report EPS-4-EC-77-5, Environmental Protection Service, Edmonton, Alberta, p. 111.

Overland, J. E., and C. H. Pease (1982) "Wind-Driven Ice Dynamics in a Shallow Sea," Submitted to Journal of Geophysical Research.

Pritchard, R. S. (1978) "The Effect of Strength on Simulations of Sea Ice Dynamics," POAC 77, Vol. I. (D. B. Muggeridge, ed.), Memorial University of Newfoundland, St. John's, pp. 494-505.

Pritchard, R. S., and R. Colony (1976) "A Difference Scheme for the AIDJEX Sea Ice Model," Numerical Methods in Geomechanics, Vol. II (C. S. Desai, ed.), American Society of Civil Engineers, New York, pp. 1194-1209.

Pritchard, R. S., M. D. Coon, M. G. McPhee, and E. Leavitt (1977) "Winter Ice Dynamics in the Nearshore Beaufort Sea," AIDJEX Bulletin No. 37, University of Washington, Seattle, pp. 37-94.

Pritchard, R. S., and J. J. Kollé (1981) "Modeling Sea Ice Trajectories for Oil Spill Tracking," Final report to U.S. Department of Transportation, United States Coast Guard, Office of Research and Development, Washington, D.C. Also, Flow Research Report No. 187, Flow Industries, Kent, Washington.

Pritchard, R. S. (1981) "Mechanical Behavior of Pack Ice," Mechanics of Structured Media (A. P. S. Selvaduri, ed.), Elsevier Scientific Publishing Company, Amsterdam, Part A, pp. 371-405.

Reimer, R. W., J. C. Schedvin, and R. S. Pritchard (1980) "Ice Motion in the Chukchi Sea," Flow Research Report No. 168, Flow Industries, Kent, Washington, p. 44.

Reimnitz, E., L. J. Tomil, and P. W. Barnes (1978) "Arctic Continental Shelf Morphology Related to Sea-ice Zonation, Beaufort Sea, Alaska," Marine Geology, Vol. 18, pp. 179-210.

Stringer, W. J. (1978) Morphology of Beaufort, Chukchi and Bering Seas Nearshore Ice Conditions by means of Satellite and Aerial Remote Sensing, Vol.I, Geophysical Institute, University of Alaska, Fairbanks.

Stringer, W. J. (1982) "Ice Concentration in the Eastern Beaufort Sea," Draft report.

Thomas, D. R. (1980) "Behavior of Oil Spills Under Sea Ice-Prudhoe Bay. Flow Research Report No. 175, Flow Industries, Kent, Washington.

Thomas, D. R., and R. S. Pritchard (1979) "Beaufort and Chukchi Sea Ice Motion, Part 1, Pack Ice Trajectories," Flow Research Report No. 133, Flow Industries, Kent, Washington.

Thorndike, A. S., and R. Colony (1980) "Arctic Ocean Buoy Program Data Report, 19 January 1979 to 31 December 1979," Polar Science Center, University of Washington, Seattle, pp. 131.

Thorndike, A. S., and R. Colony (1981) "Arctic Ocean Buoy Program Data Report, 1 January 1980 to 31 December 1980," Polar Science Center, University of Washington, Seattle, pp. 127.

Thorndike, A. S., and R. Colony (1981) "Sea Ice Motion in Response to Geostrophic Winds," Journal of Geophysical Research, Vol. 87, No. C8, July 20, 1982.

Thorndike, A. S., R. Colony, and E. A. Munoz (1982) "Arctic Ocean Buoy Program Data Report, 1 January 1981 to 31 December 1981," Polar Science Center, University of Washington, Seattle, pp. 137.

Webster, B. D. (1982) "Empirical Probabilities of the Ice Limit and Fifty Percent Ice Concentration Boundary in the Chukchi and Beaufort Seas," NOAA Technical Memorandum NWS AR-34, National Weather Service, Regional Headquarters, Anchorage, Alaska.

APPENDIX A:

A MODEL FOR CURRENTS ON THE ALASKAN BEAUFORT SHELF

APPENDIX A

A MODEL FOR CURRENTS ON THE ALASKAN BEAUFORT SHELF

Miles G. McPhee

3 June 1982

1. Introduction

The intent of this report is to describe a method for estimating oceanic currents on the Beaufort shelf north of Alaska to be used as one of the input driving force fields for a model of nearshore sea ice drift. The report presents an outline of a definitive summary of work done in the past decade on the Beaufort shelf, prepared by Aagaard (1981), and then extrapolates the results from that work to surface geostrophic currents. Not a great deal is known about currents in this region, especially near the surface where sea ice interacts with the geostrophic current, so it should be stressed that the proposed current regime is speculative.

There are two principles to be kept in mind in what follows. First, results of OCSEAP current meter studies on the Beaufort shelf show that there is often a strong current flowing along the isobaths near the shelf break (i.e., where the offshore gradient in depth suddenly increases), and that this current reverses from east-setting to west-setting frequently. Most of the measurements have been made at mid-depth or lower in the water column, so there is no clear picture of what the surface manifestation of the current is, nor how it interacts with the ice. There is evidence, however, that the current is confined to a rather narrow band, following the bathymetry of the shelf break. We thus have a "river" embedded within the oceanic flow that coincides roughly with the pack ice shear zone.

The second principle is that our proposed treatment of currents in the shallow part of the shelf (as a rough guide, inshore from the 40-m isobath) is predicated on using ice-water drag as modified by the shallow boundary layer effects described by McPhee (1982). It would thus be mistaken to assume that the absence of geostrophic current in the nearshore region means that a drag law appropriate for deep water ice drift can be used with no modification by ocean currents. Instead, currents exist in the water column that are driven by stress between ice and water, but that are different from currents which would be observed at corresponding levels under ice far offshore because the bottom has a pronounced effect on turbulence, provided the water column is well mixed.

2. Background

This section summarizes a review prepared by Aagaard (1981), especially as it pertains to current/ice interactions on the Beaufort shelf north of Alaska.

Aagaard describes the Beaufort shelf as relatively narrow with numerous embayments and several lagoon/barrier island systems. There is comparatively little fresh runoff--the discharge of the Colville, the largest of the rivers west of the Canadian Beaufort, is estimated to be about 5 percent of the discharge from the Yukon. Astronomical tides are small, with mean ranges of from 10 to 30 cm. Storm surges occur when wind systems move the shelf waters around, and have been observed to be an order of magnitude larger than astronomical tides. Except where topographic constrictions occur near shore, it is thus probable that tidal currents are relatively small over most of the shelf, which is borne out in most of the measurements. Surface winds, as measured at shore locations, are predominantly ENE in the western portion of the Beaufort and are bimodal ENE and WSW in the eastern part.

The measurements from which Aagaard's report was derived consist of hydrographic surveys totaling 110 CTD stations from October 1975 through March 1977, and a total of 2335 days of current meter records, mostly from bottom-moored instruments. This represents by far the most extensive data set for Beaufort shelf processes, and is particularly notable in that the hydrography spans the winter season--previous studies have been heavily weighted to summer (melt season) measurements.

As it pertains to ice drift analysis, perhaps the most important result of the hydrography is the seasonal change in water column structure. By the end of the melt season, a low-salinity mixed layer roughly 20 m thick has developed, which is separated from the deeper water by a sharp vertical density gradient. Sections from November 1975 showed that mixed-layer salinity increased in the offshore direction from 27 to 29 ppt. A survey three months later showed a decrease in the offshore direction from 30.7 to 29.9 ppt. The winter profile was still stratified vertically, but with much less total density difference. Because the salinity of the water column increased dramatically at all depths, and the entire column was near its freezing point in the winter (February) section, Aagaard argues that the winter structure results more from horizontal advection of water that has been exposed to freezing at various salinities than to direct, one-dimensional mixing processes. With this in mind, it seems likely that during the intense freezeup period before the sea ice has become fast, the water column is often well mixed from top to bottom; consequently, the turbulent structure will be quite different from the highly stratified summer situation.

Another important aspect of the hydrography traces the influx of Alaska coastal and Bering Sea waters flowing eastward along the shelf seaward of the 40- to 50-m isobaths. During summer this shows up as a distinct subsurface tongue of warm water hugging the shelf break. Combined with the current meter records described later, the temperature structure delineates a current jet flowing mainly eastward. Unfortunately, near the surface, the Alaska coastal water mixes rapidly with the ambient shelf water and loses its utility as a tracer.

Very few data exist on currents over the inner shelf, which is the region landward of the 40- to 50-m depth zone. Summertime measurements imply that the circulation is more or less directly wind driven, with the net motion westward in keeping with the prevailing easterly winds. Two current meters, suspended at 10 m in water of 30-m and 40-m depths, also implied a wind-driven current regime in winter, although the energy levels were much reduced from summer levels. In each case, there was negligible mean current in the three-week records. What forces wind-associated currents under fast ice is not immediately obvious: Aagaard mentions horizontal entrainment, but pressure gradients associated with water transport under mobile ice just outside the fast ice zone might also be a factor. Regardless of the mechanism, Aagaard's work suggests that no organized alongshelf motion exists on the inner shelf in the absence of wind forcing, so any currents affecting the ice motion would be caused mainly by the recent wind history.

On the outer shelf, which is essentially the shelf-break zone, the situation is quite different. Most of the current records were obtained from fixed moorings positioned along the shelf break between the 100-m and 200-m isobaths. Exceptions were the OL-1 and FLAX-1 sites, which were in 60-m-deep water. At OL-1 the bottom slope is so steep that the distance to the 200-m isobath is only a few kilometers. Heavy ice conditions precluded mooring current meters above the 40-m depth in the water column. This is well down into the pycnocline, and is not necessarily indicative of near-surface conditions, a fact which should be kept in mind in the following discussion.

The main features of the current jet along the shelf break are shown in Figure 3 of Aagaard's report. The current is clearly steered by the topography, with by far the most frequent current directions being generally eastward or westward along the local isobaths. In the mean, the current appears to be eastward at about 7 cm/s, but the mean apparently represents an infrequent realization since it is a vector sum of generally larger eastward and westward flows. The mean eastward flow varies among the various sites somewhere in the range of 15 to 25 cm/s, with the secondary mode (westward) being perhaps two-thirds of the primary.

One item of note is that the geostrophic shear between the surface and 40 dbar indicates a mean westward shear of about 7 cm/s. Based on this, Aagaard reasons that the mean surface flow may be close to zero or slightly westward.

Aagaard speculates that the overall driving force behind the mean eastward motion is the climatological factors, which cause the sea level in the Pacific to be about 1 m higher than in the Atlantic, and that the current jet persists eastward into the Canadian Beaufort, then north along Banks Island, through M'Clure Strait and into the Canadian Archipelago.

What causes the frequent flow reversals from east-setting to west-setting is not well understood. Statistical treatment in Aagaard's report tends to give somewhat contradictory indicators. There is a moderate coherence between current and both geostrophic and surface winds measured at Barter Island, yet there are also cases in which a reversal occurs with no obvious connection with the wind over the shelf. Visual comparison of currents at two moorings separated by 65 km in the alongshore direction indicates that most of the major current events are similar with little time lag, but coherence statistics for the same current meters indicated rather low average coherence.

To confuse matters further, an example is shown where two major flow reversals observed in the Chukchi, some 650 km "upstream", show up about 106 days later in a current meter record from the Beaufort shelf. If the features are related, the implication is that momentum associated with the disturbance is advected downstream at about the long-term mean velocity. On the other hand, certain reversals coincide almost exactly with reversals in the wind, and persist pretty much in phase along the entire shelf, so if the mechanism described above operates, it is probably not a dominant factor.

Aagaard's conclusion regarding the importance of wind forcing is that "the longshore (sic) wind plays an important, but not all-prevailing, role in the low-frequency variability of the subsurface longshore flow." He goes on to state that when winds along the shelf are easterly at 8 to 10 m/s, currents will normally reverse and set westerly.

There is little predictable seasonal variation in the current meter records. The presence of ice apparently has little impact on the strength of the current signal; analysis of current records from two different years showed the strongest east and west three-week-mean currents to be in the January-February period. Random fluctuations on a one- to two-month time scale appear to dominate the low-frequency variability.

From the bathymetry it appears that the current jet follows closely the 200-m isobath, which marks the shelf break along the Beaufort coast, since the offshore slope is consistently large there. The width of the jet is not well known; however, there are indications that it is confined to a rather narrow zone. The tongue of warmer water observed during the summer appears to extend across about half a degree of latitude (see Aagaard's Figures 5 and 6). Current meters at the FLAX-1 site, which was moored in 59 m of water, show decreased bimodality and generally lesser current speeds. Aagaard suggests that FLAX-1 is in a transition zone between the outer and inner shelf regions. The jet has not been observed inside the 40-m isobath, which is on the average about 30 km inshore from the 200-m isobath. The only evidence for the off-shelf limits of the feature that I am aware of comes from comparing AIDJEX met-ocean buoy records with concurrent OCSEAP "OL" mooring records. The moored current meter at 100 m showed sizable eastward motion near the 150-m isobath, but a current meter about 50 km farther offshore, suspended at 30 m below the met-ocean buoy, indicated very small currents . The met-ocean buoys were originally deployed over the 1000-m isobath, and most of the resolvable currents they measured were westward following the main sense of the Beaufort Gyre.

3. Current Model

The intent here is to include the shelf current features discussed in the previous section and in McPhee (1982) in a way that can be easily included in a numeric model for sea-ice drift.

The interaction between the sea ice and the ocean is divided into three zones: the shelf-current jet, as described in the previous section, in which the geostrophic current is a function of position relative to the core of the jet, which is assigned a particular velocity; an outer zone seaward of the current jet, which uses the same geostrophic velocity field as the AIDJEX model, derived originally from the dynamic topography of Newton (1973); and a shallow zone in which the geostrophic current is zero, but the drag relation between sea ice and water is modified by the effect of bottom turbulence. The geostrophic velocity field, interpolated at the nodes of the large computational grid, is shown in Figure A1.

The approach is keyed to the large- and small-scale grids of the Flow Nearshore Model. The main tasks for each grid point are (1) determine the water depth at the grid location from a bathymetric chart; (2) determine the position relative to the 200-m isobath, which is taken to be the core axis of the alongshelf jet; and (3) determine the geostrophic velocity according to which zone the grid point belongs.

The depth of each grid point is estimated by interpolating between known positions of depth contours obtained from an OCSEAP bathymetric chart of the Beaufort Sea. The interpolation grid was set up by determining the latitude of the 20-, 40-, 80-, 120-, 200-, and 2000-m isobaths along meridians for each half degree in longitude from 142°W to 155°W. The "shore" contour skirts the barrier islands in keeping with the grid, and for the sake of interpolation between it and the 20-m isobath, is assigned a depth of 3 m. The depth of a particular grid point is found from the latitude and longitude of the grid location by interpolating between contour latitudes on adjacent meridians.

The current jet is modeled under the following assumptions:

(1) The center of the jet follows the 200-m isobath and is characterized by one core velocity, V0, which is positive if eastward and negative if westward.

(2) The width of the jet is taken to be 60 km, and velocities within the jet fall off to zero at the inshore boundary. Velocity is also zero for all points shoreward of the inner jet boundary (again, with the caveat that the shallow boundary layer drag law is used). Offshore, the jet blends into the long-term geostrophic flow of the AIDJEX model at a distance of 30 km from the core.

(3) The strength of the jet varies sinusoidally from the maximum at the center (200-m isobath) to zero at the inner boundary and to the geostrophic velocity at the outer boundary.

The algorithm for computing the velocity at a given grid point is set up so that the core strength, V0, of the jet can be varied without having to recalculate its position relative to the jet each time. The velocity is given by the complex equation

This is accomplished by preparing an array with the following variables for each grid point:

Depth, V1(x), V1(y), ,

Figure A2 shows examples for a segment of the shelf current from about 153°W to 149°W. Current vectors are plotted along each half-degree meridian at 10-km spacings. In the upper plot, V0 is 20 cm/s to the east (positive), while in the lower plot it is 20 cm/s to the west or -20 cm/s. In the upper plot, the construction lines along the 150°W meridian show how the cosine fairing smoothes the jet from the core to the boundaries. When the current is in its predominant east-setting mode, there is an intense zone of current shear near the 72nd parallel.

Figures A3, A4 and A5 show examples of the shelf current plotted for each grid point of the small-scale grid for values of V0 of 0, +20 cm/s (eastward flow), and -14 cm/s (westward flow), respectively.

The bathymetry near the mouth of the Barrow Submarine Canyon leads to rapid changes in the current direction, which may not be realistic. Farther east, the current settles into a fairly well-behaved pattern. One thing that shows up from these plots is that the spatial coverage of the small-scale array is not very dense in the vicinity of the jet, which may distort its effect somewhat.

References

Aagaard, K. (1981) "The Beaufort Current," to appear in the <u>The Alaskan Beaufort Sea</u> (P. Barnes, E. Reimnitz, and D. Schell, editors), the Academic Press, N.Y.

McPhee, M. G. (1982) "The Turbulent Boundary Layer in Shallow Water," Appendix C of Annual Report to OCSEAP, RU#567, March.

Newton, J. L. (1973) "The Canada Basin: Mean Circulation and Intermediate Scale Flow Features," Ph.D. Thesis, University of Washington, Seattle.

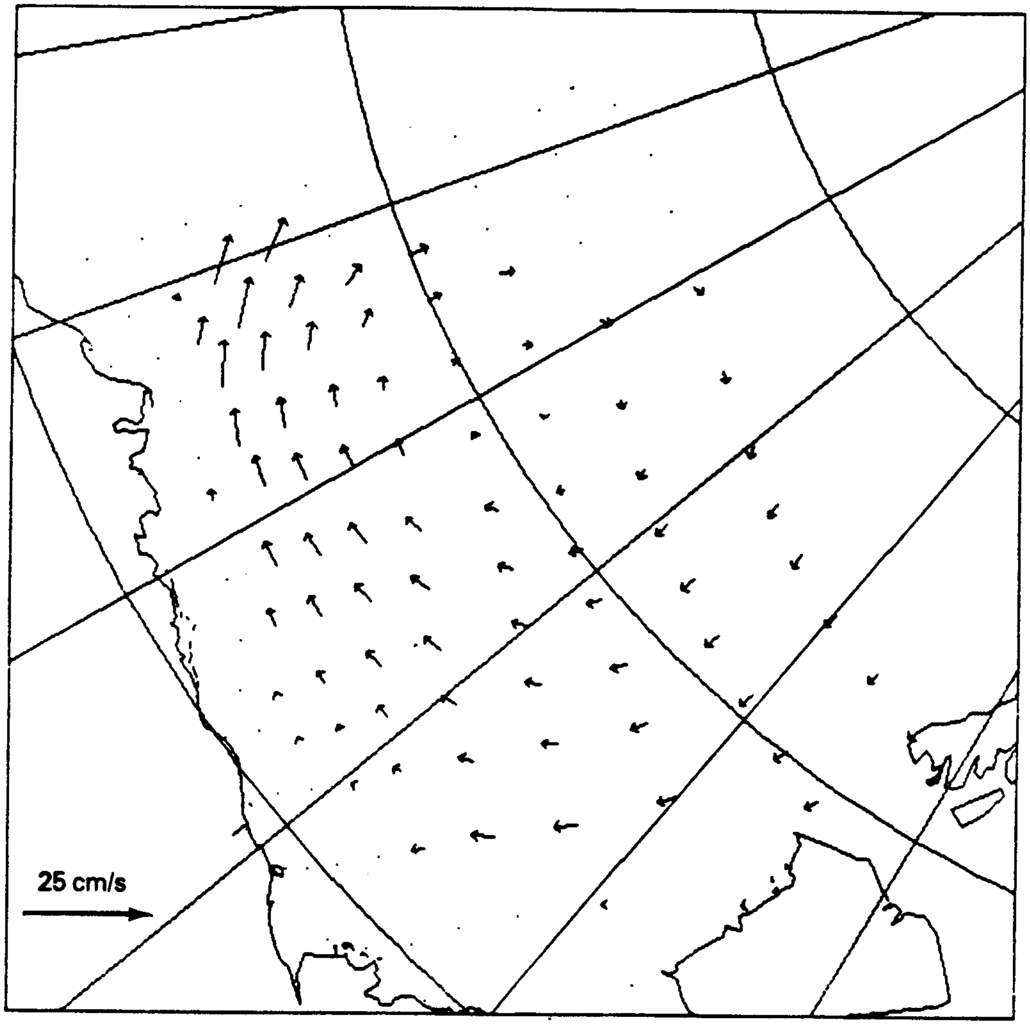

Figure A1. Geostrophic Velocity Field

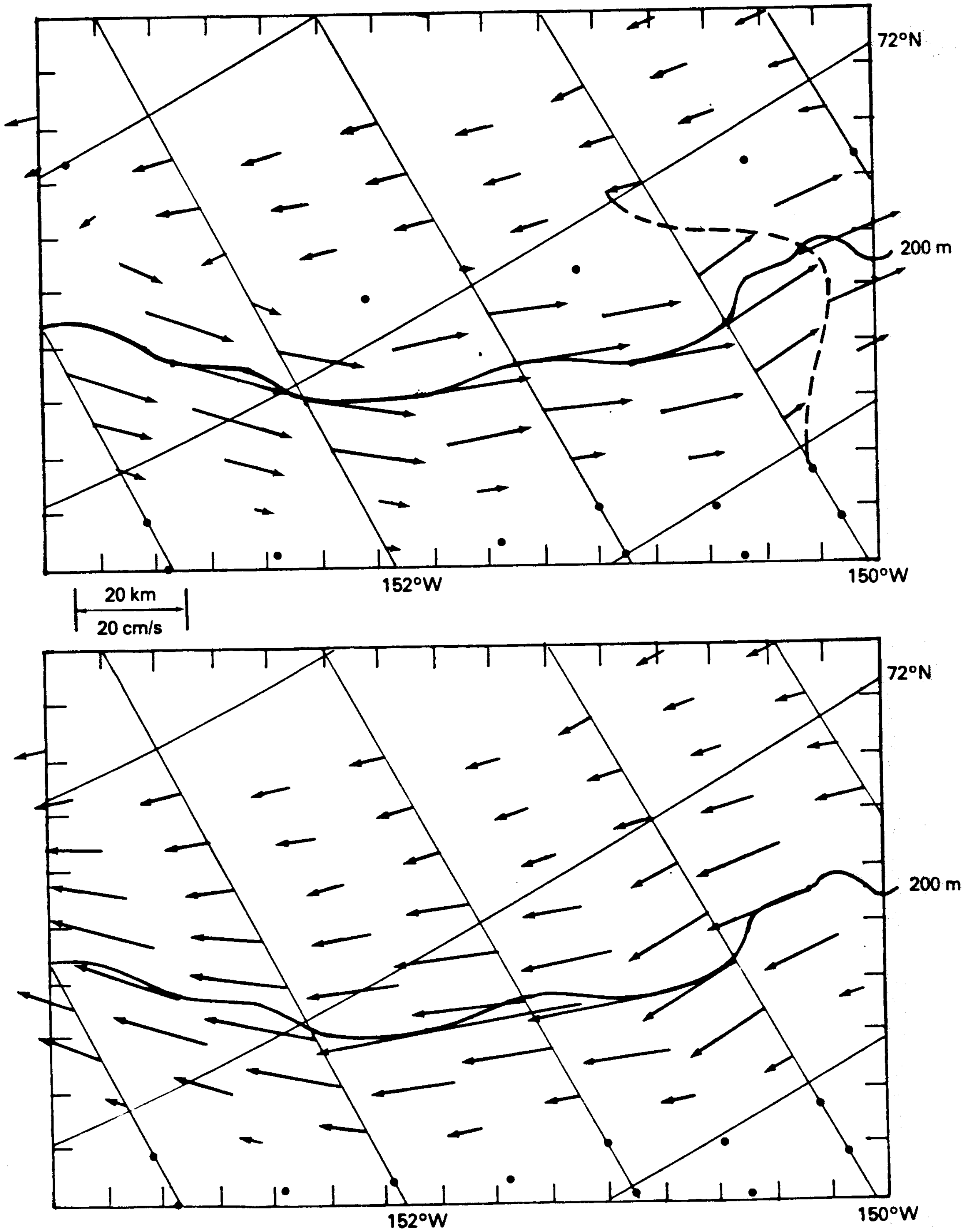

Figure A2. Segment of Modeled Beaufort Current Velocity Field for 20 cm/s Current Jet Flowing East (Above) and West (Below).

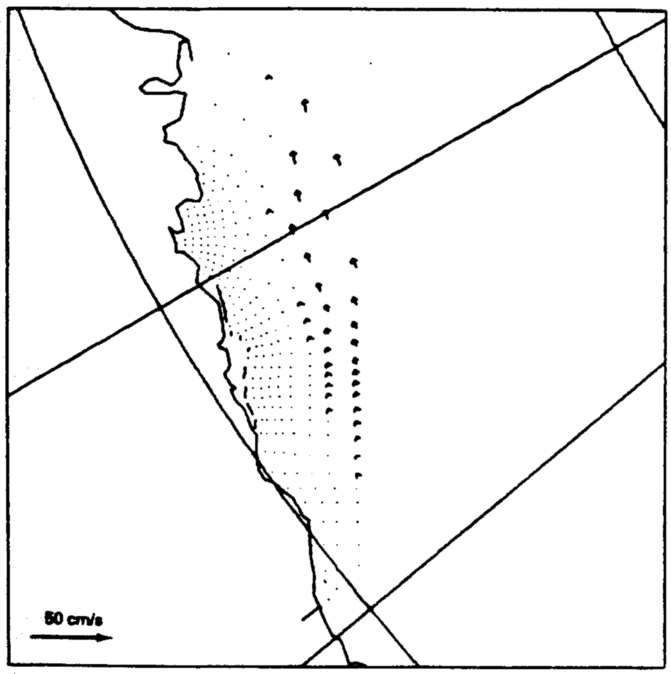

Figure A3. Modeled Beaufort Current Velocity Field for Jet with Zero Velocity.

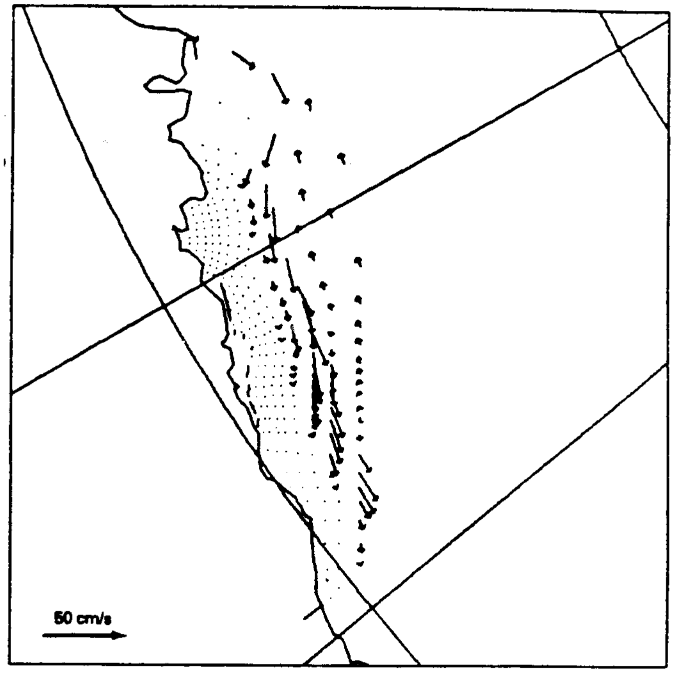

Figure A4. Modeled Beaufort Current Velocity Field for Jet with 20 cm/s Eastward Velocity.

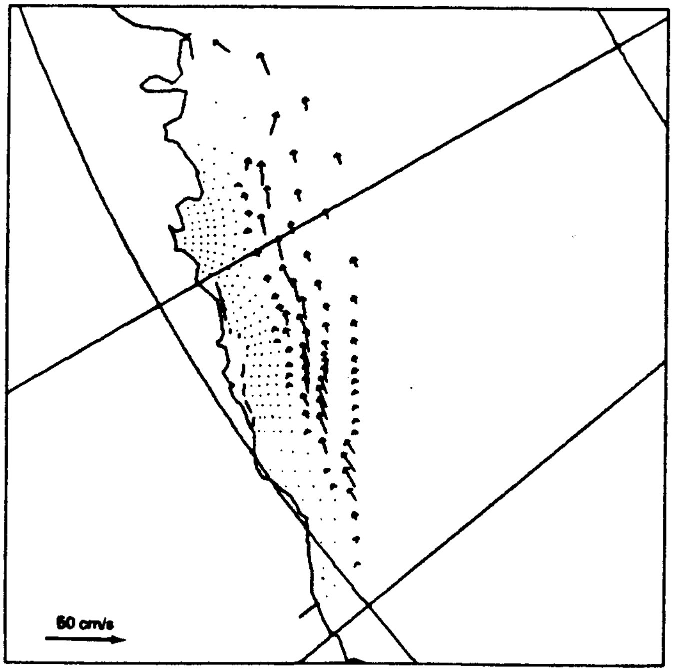

Figure A5 Modeled Beaufort Current Velocity Field for Jet with 14 cm/s Westward Velocity.

APPENDIX B:

OBSERVED MONTHLY ICE MOTIONS

APPENDIX B

OBSERVED MONTHLY ICE MOTIONS

The drift of Arctic sea ice has long been of interest to Arctic explorers and researchers. They have all recognized that the ice moves in response to winds and underlying ocean currents, and that knowledge of ice motions gives knowledge of the circulation of Arctic air and water masses. Early information on long-term ice motion came from ships that were either accidentally or intentionally caught in the ice pack. Later, manned camps, using celestial navigation, tracked the ice motion. Although enormous efforts were involved in those studies, the amount of motion data collected remained small. In recent times, though, the use of automated data buoys dropped or placed upon the ice and located by satellites has greatly increased the amount of ice motion data from areas throughout the Arctic.

The primary use of most of the recent ice motion data has been to aid in understanding how the ice cover moves and deforms in response to winds and ocean currents. In addition, we now have a general understanding of the circulation of the atmosphere and the ocean in Arctic regions. Not enough data exist, however, to adequately describe the spatial and temporal variability of ice motions throughout the Arctic.

The Beaufort Sea is of particular interest to the U.S. and there is more ice motion data available on it than on most areas of the Arctic. While the amount of data is small in a statistical sense, it can give a suggestion of the interannual variability of large-scale ice motions, as well as suggest the need for further data collection. We have collected the readily available ice motion data and present here monthly ice motions based on those data.

Due to resource limitations, we restricted the area of study to the Beaufort Sea, between 125° W and 165° W longitude, and south of about 80°N. The actual criterion was that the monthly displacement vector must fall within the area plotted. Only monthly locations and motions are presented here, although location data exist for most stations and buoys for much shorter intervals (several times a day). All the data presented here came from only a few sources, those taken during AIDJEX (Arctic Ice Dynamics Joint Experiment) from 1971 through 1976, earlier historical data collected by the AIDJEX data bank, data from OCSEAP (Outer Continental shelf Environmental Assesment Program) buoy programs, and the Arctic Ocean Buoy Program data taken by the Polar Science Center at the University of Washington. Although this data set may not be complete, only a few buoy month's worth, at the most, are missing.

The data are presented in the form of maps showing monthly ice motions as vectors at the same scale as the map. Each map shows all the monthly ice motions for a three-month period, beginning with January, February, and March 1959, and continuing through October, November, and December, 1981. Many maps show no ice motions, and where a full 12 months occur without data, the maps were left out to conserve space. The vectors are labeled with an ID number which is internal to this report and which must be cross-referenced to the actual ID in the accompanying tables to identify the data source. The ID number for a buoy will be different each ice season. The ice season is considered to begin in October and end in September; the data are broken up by ice season rather than by year or by buoy. Some buoys or stations have data available for only one or two months of the three months presented on each map; the tables must again be consulted to identify the month(s) present.

The monthly trajectories are presented in Figure B1. The map scale is 188 km/cm. The map is an azimuthal equidistant projection tangent at the pole.

In Table B1 we present the location of each buoy or station in decimal degrees of latitude and longitude on the first day of each month. Internal and external identification numbers or names are also given. A list of data sources is given at the end of the report.

A total of 366 monthly displacements are presented here. These data cover a span of 25 years (from 1958 through 1982), with 17 of those years having some data available. Satellite-transmitted buoy data were first available in 1972.

The data are basically self-explanatory, and only a few comments and observations need to be made. Much of the early data, prior to 1967, comes from ice island T-3 and may not be representative of pack ice motion. Since a deep-draft ice island experiences a different set of driving forces than a flat ice sheet, it can at times move relative to the pack, especially during the summer when it is less likely to be frozen into the pack.

A majority of the data were taken during the AIDJEX main experiment. This is unfortunate in a way, since it appears that the 1975-76 ice season was an anomalous one and possibly represents an extreme event. Not enough years of data exist yet to be sure of this. Nevertheless, one must not assume that, since a majority of the buoy data shows one pattern of ice motion, this is the typical motion. If one gives the motion data collected during 1975-76 equal weight with that from other years, we see that (1) typical motions are much larger than the mean using all buoy data would indicate, and (2) the useful data set is very small.

It should also be noted that a few of the buoys appeared to be caught in the fast ice near the Alaskan coast. Little or no motion near the coast does not imply much about the motion further away from the coast. It is generally assumed that a velocity discontinuity exists between the fast ice and the pack ice. Only during the winter of 1975-76, however, is this discontinuity evident from the data.

References

AIDJEX Staff (1972) "Station Positions, Azimuths, Weather - 1972 AIDJEX Pilot Study, Preliminary Data," AIDJEX Bulletin No. 14, University of Washington, Seattle, July.

Colony, R., Personal communication. Ice Island T-3 position data are from historical ice drift data set obtained from the National Climatic Center, Asheville, N.C.

Thorndike, A. S. (1977) "Measurements of Sea Ice Motion January 1977 to September 1977," Unpublished data report to OCSEAP, Polar Science Center, University of Washington, Seattle.

Thorndike, A. S., and J. Y. Cheung (1977a) "AIDJEX Measurements of Sea Ice Motion 11 April 1975 to 14 May 1976," AIDJEX Bulletin No. 35, University of Washington, Seattle, January, 149 pp.

Thorndike, A. S., and J. Y. Cheung (1977b) "Position Data Supplement No. 1, 14 May 1976 to 30 Nov 1976," Unpublished data report, Polar Science Center, University of Washington, Seattle.

Thorndike, A. S., and J. Y. Cheung (1977c) "Measurements of Sea Ice Motion Determined from OCS Data Buoys, October 1975 to December 1976," Environmental Assessment of the Alaskan Continental Shelf, Annual Reports of Principal Investigators for the year ending March 1977, Vol. XVI Hazards, Outer Continental Shelf Environmental Assessment Program, Boulder, Colorado, pp. 179-251.

Thorndike, A. S., and R. Colony (1980) "Arctic Ocean Buoy Program Data Report, 19 January 1979 to 31 December 1979," Polar Science Center, University of Washington, Seattle, 131 pp.

Thorndike, A. S., and R. Colony (1981) "Arctic Ocean Buoy Program Data Report, 1 January 1980 to 31 December 1980," Polar Science Center, University of Washington, Seattle, 127 pp.

Thorndike, A. S., R. Colony, and E. A. Munoz (1982) "Arctic Ocean Buoy Program Data Report, 1 January 1981 to 31 December 1981," Polar Science Center, University of Washington, Seattle, 137 pp.

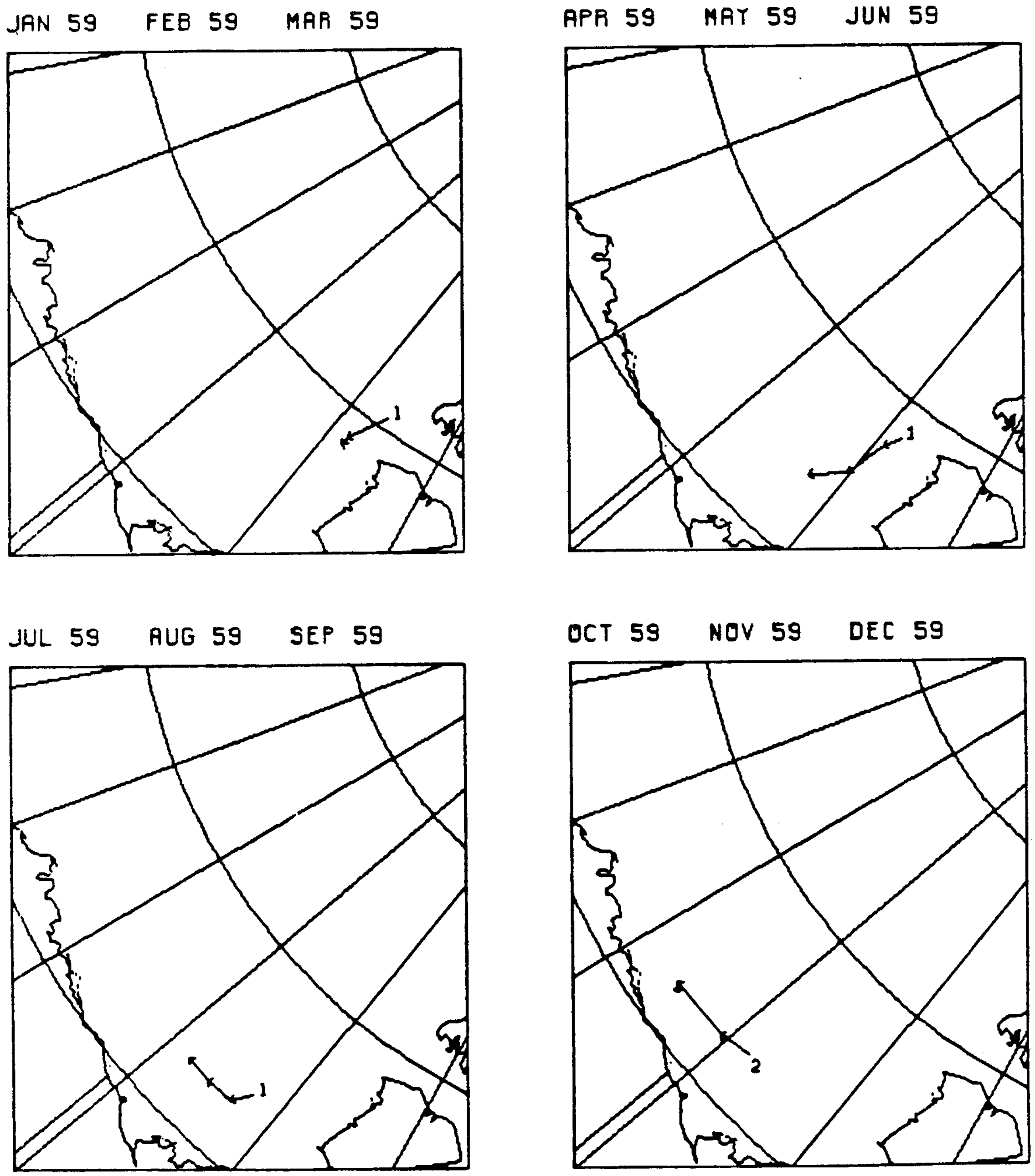

Figure B1. Observed Monthly Buoy Trajectories in the Beaufort Sea from 1959 Through 1981. Each Plot Represents a 3 Month Period.

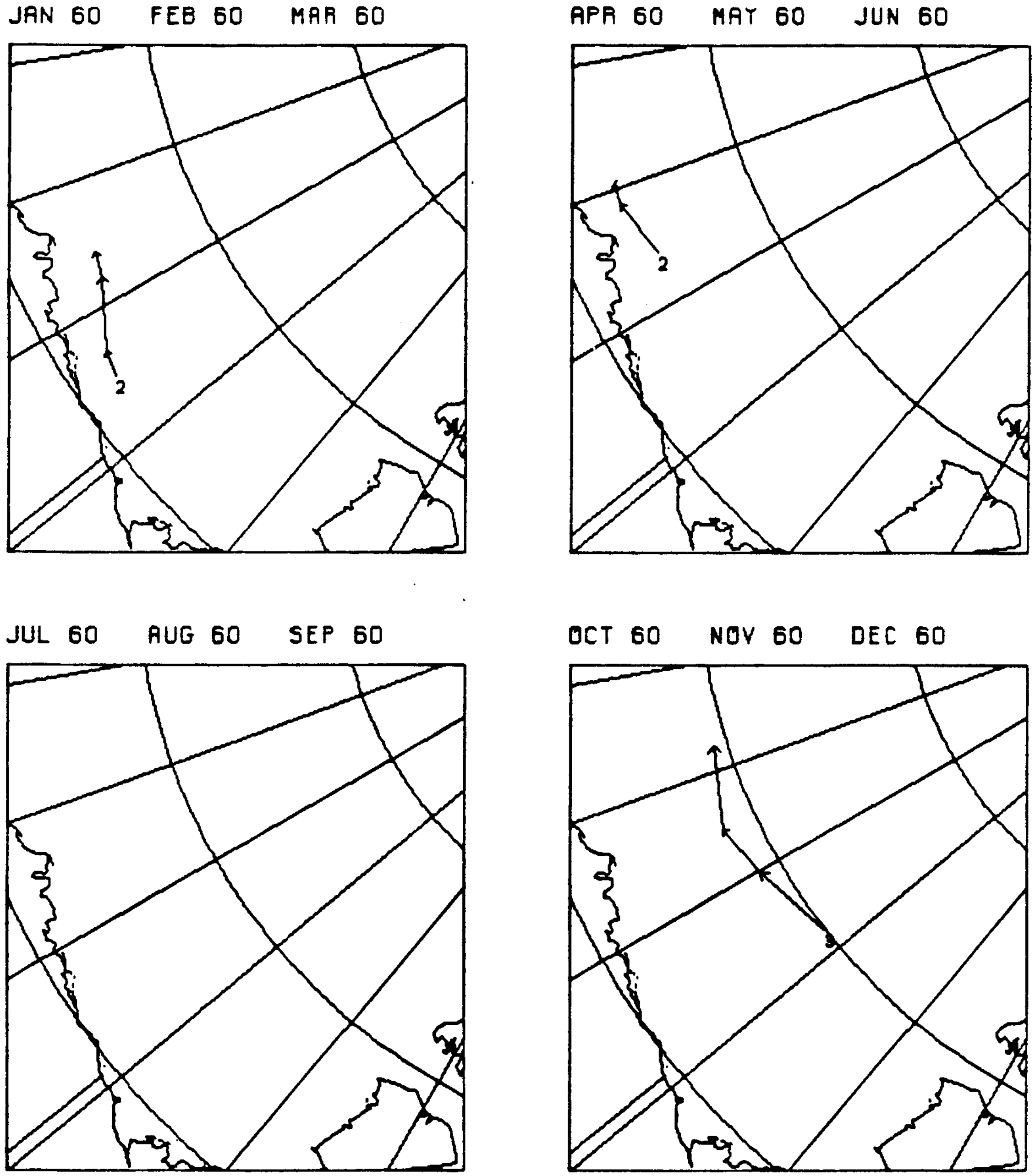

Figure B1. Observed Monthly Buoy Trajectories in the Beaufort Sea from 1959 Through 1981. Each Plot Represents a 3 Month Period (Continued).

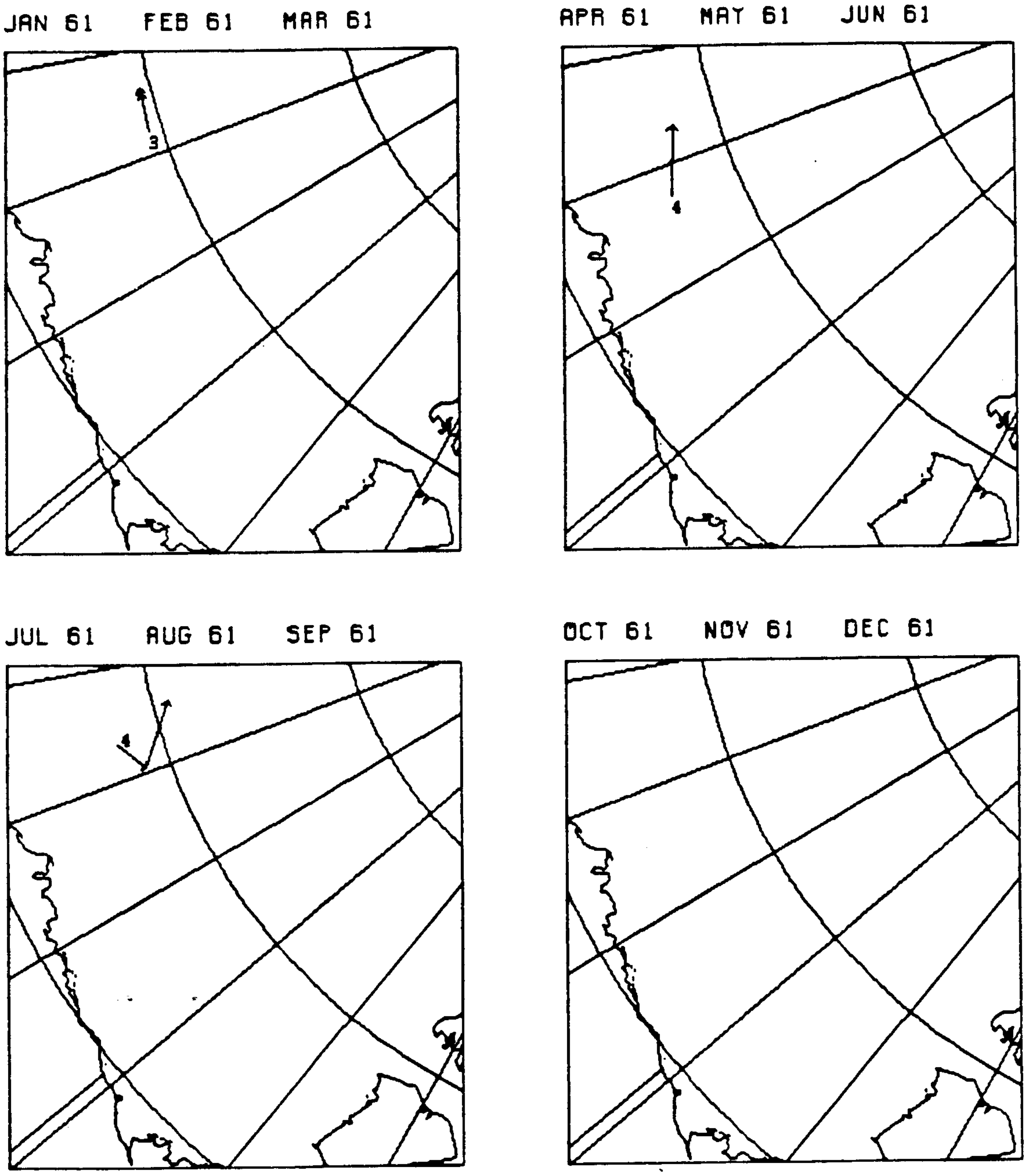

Figure B1. Observed Monthly Buoy Trajectories in the Beaufort Sea from 1959 Through 1981. Each Plot Represents a 3 Month Period (Continued).

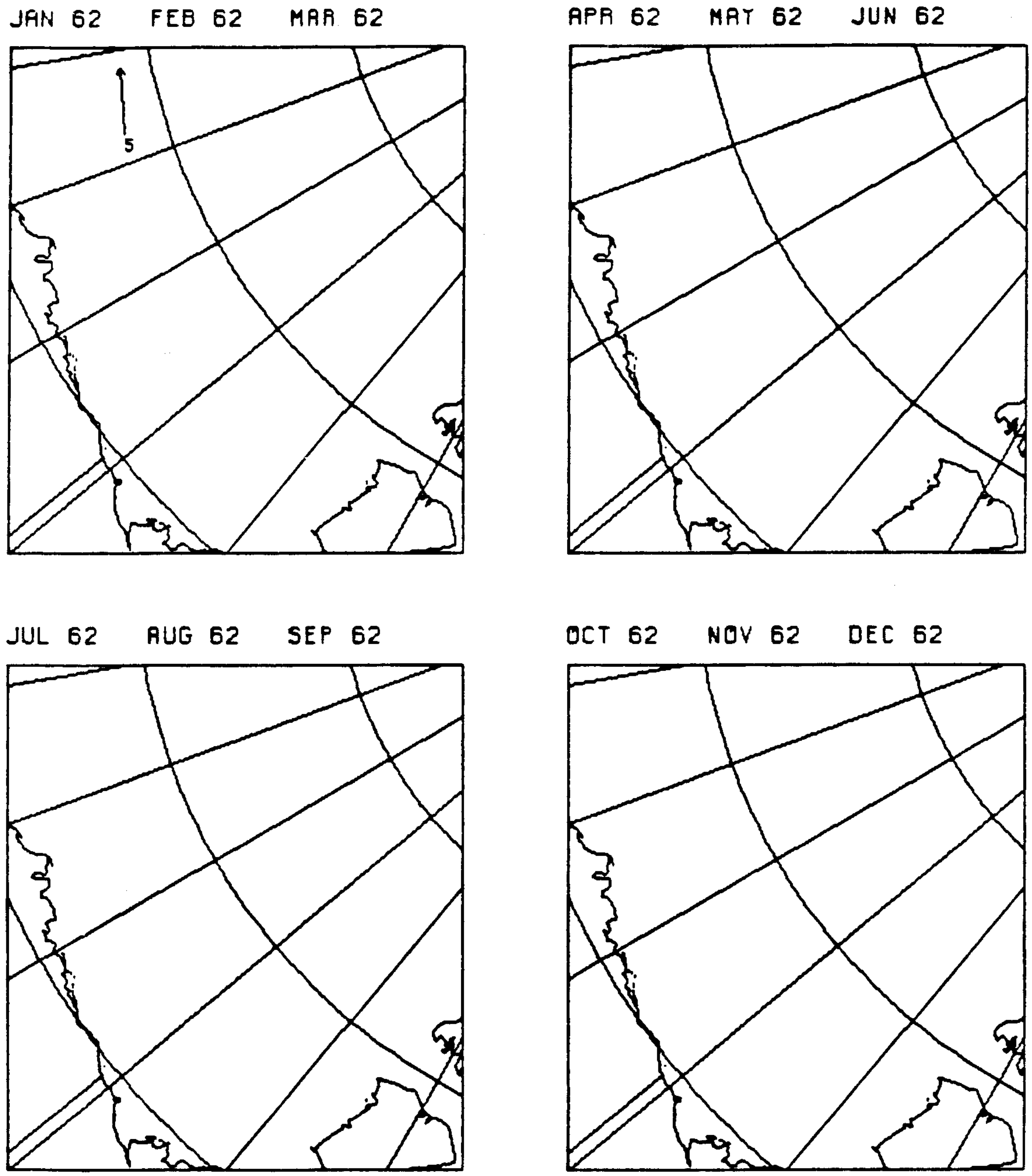

Figure B1. Observed Monthly Buoy Trajectories in the Beaufort Sea from 1959 Through 1981. Each Plot Represents a 3 Month Period (Continued).

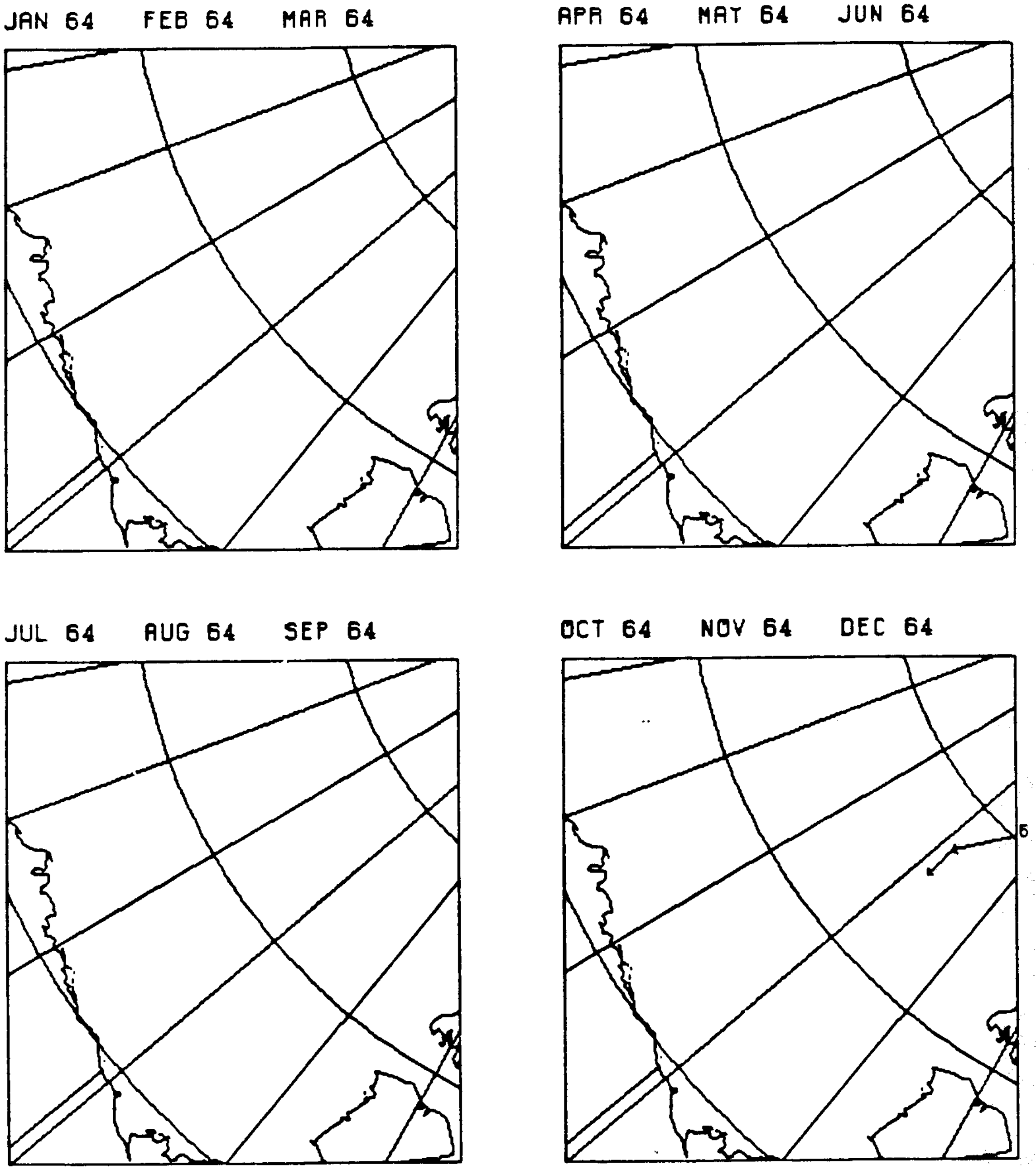

Figure B1. Observed Monthly Buoy Trajectories in the Beaufort Sea from 1959 Through 1981. Each Plot Represents a 3 Month Period (Continued).

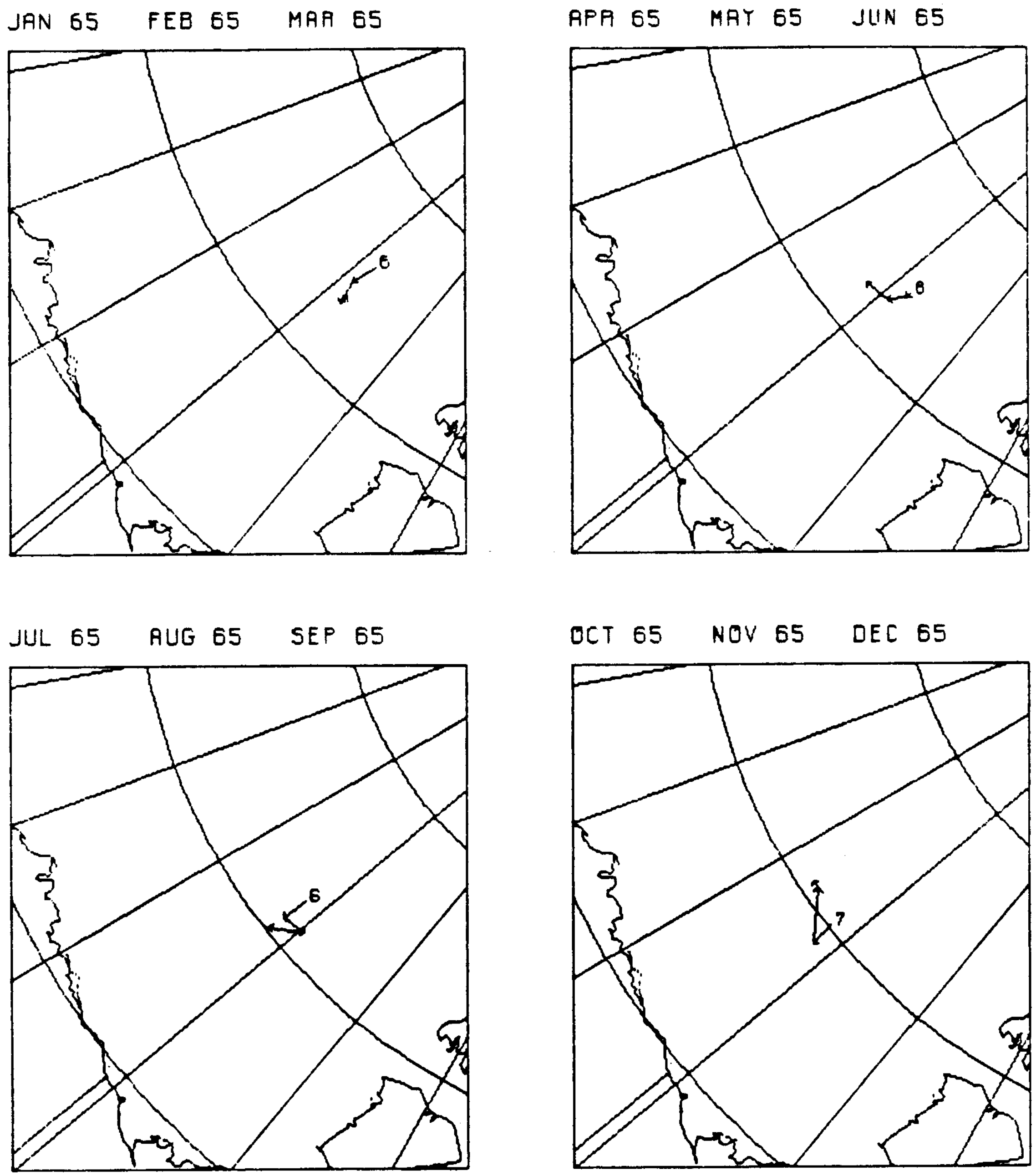

Figure B1. Observed Monthly Buoy Trajectories in the Beaufort Sea from 1959 Through 1981. Each Plot Represents a 3 Month Period (Continued).

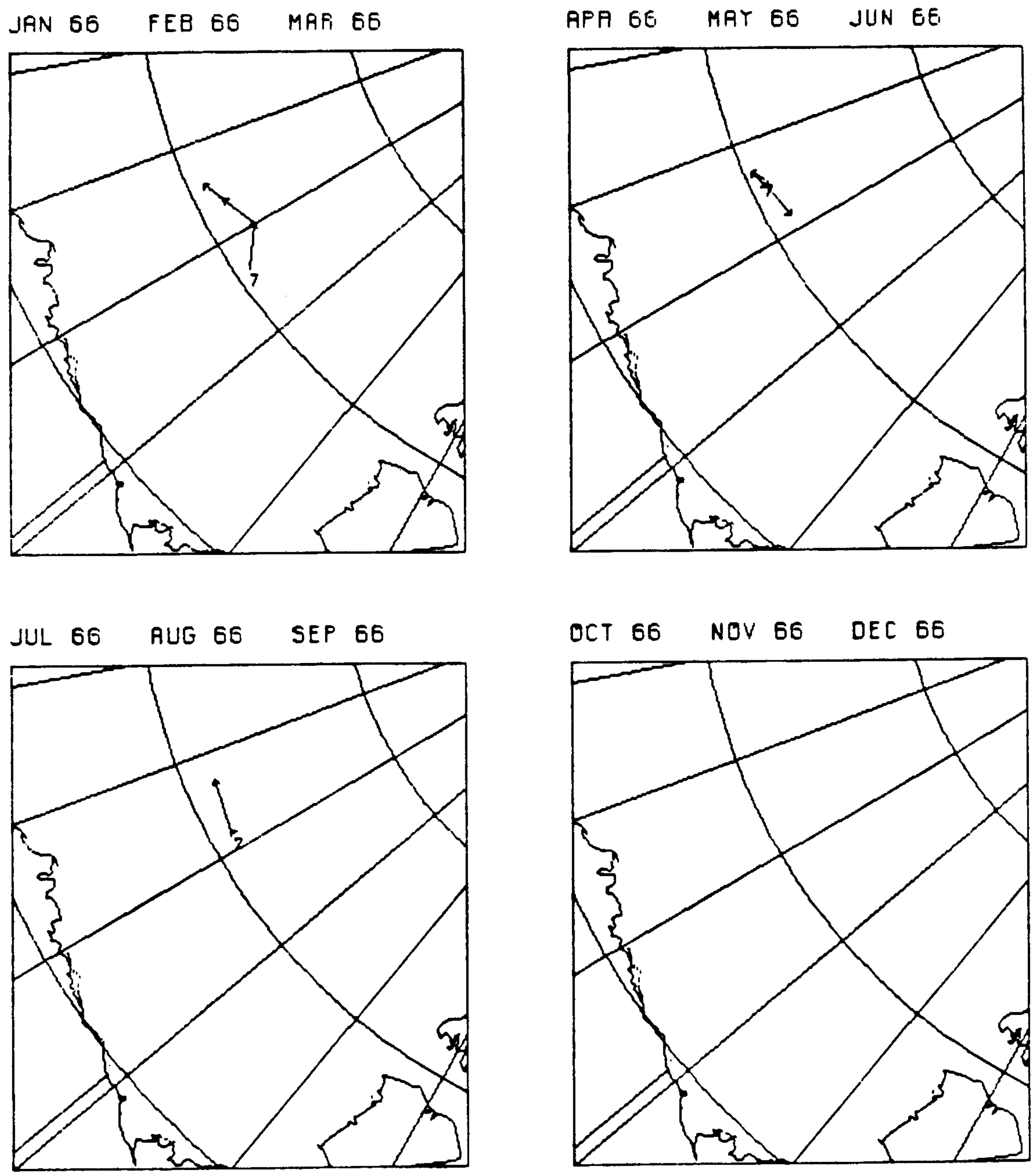

Figure B1. Observed Monthly Buoy Trajectories in the Beaufort Sea from 1959 Through 1981. Each Plot Represents a 3 Month Period (Continued).

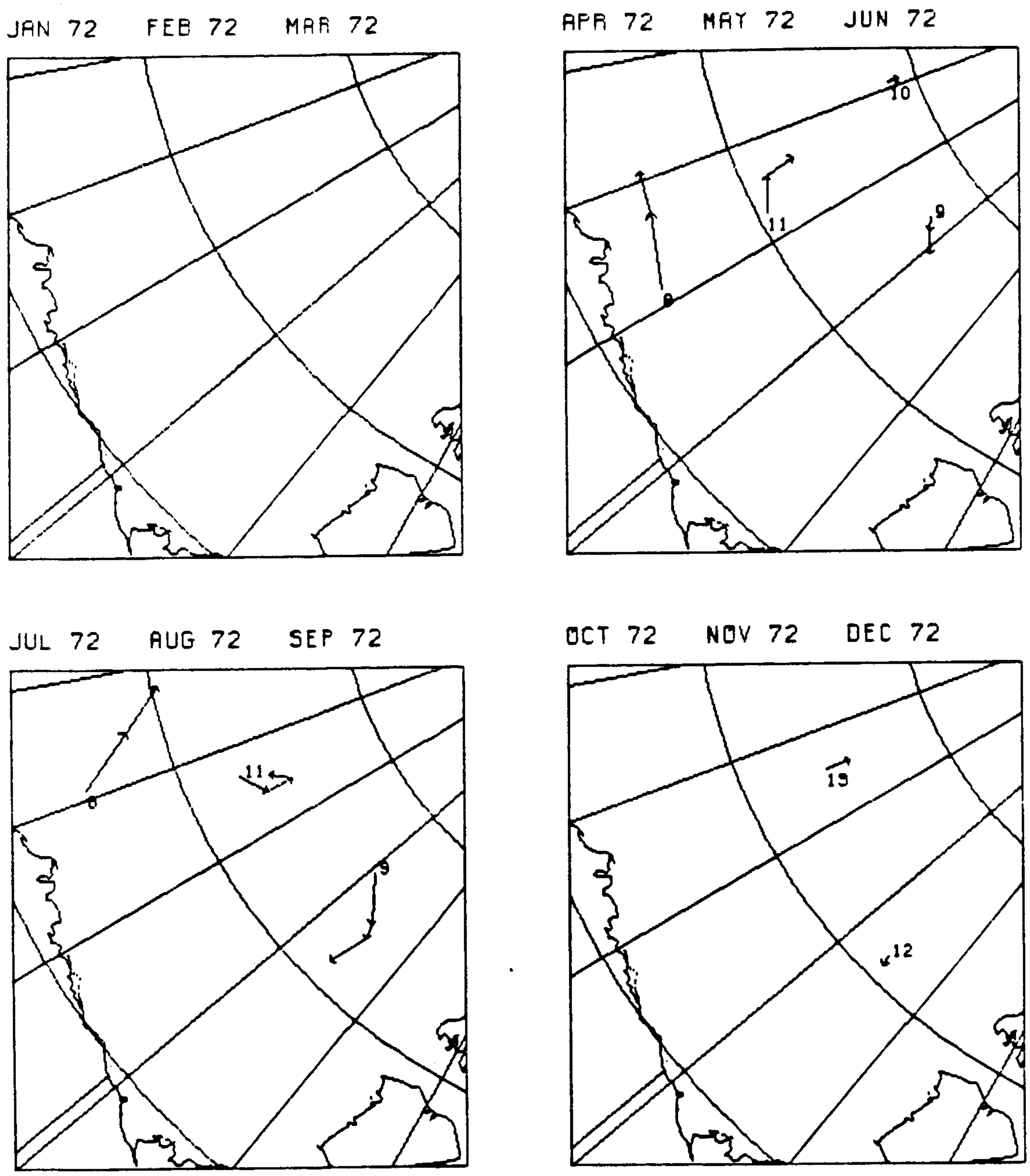

Figure B1. Observed Monthly Buoy Trajectories in the Beaufort Sea from 1959 Through 1981. Each Plot Represents a 3 Month Period (Continued).

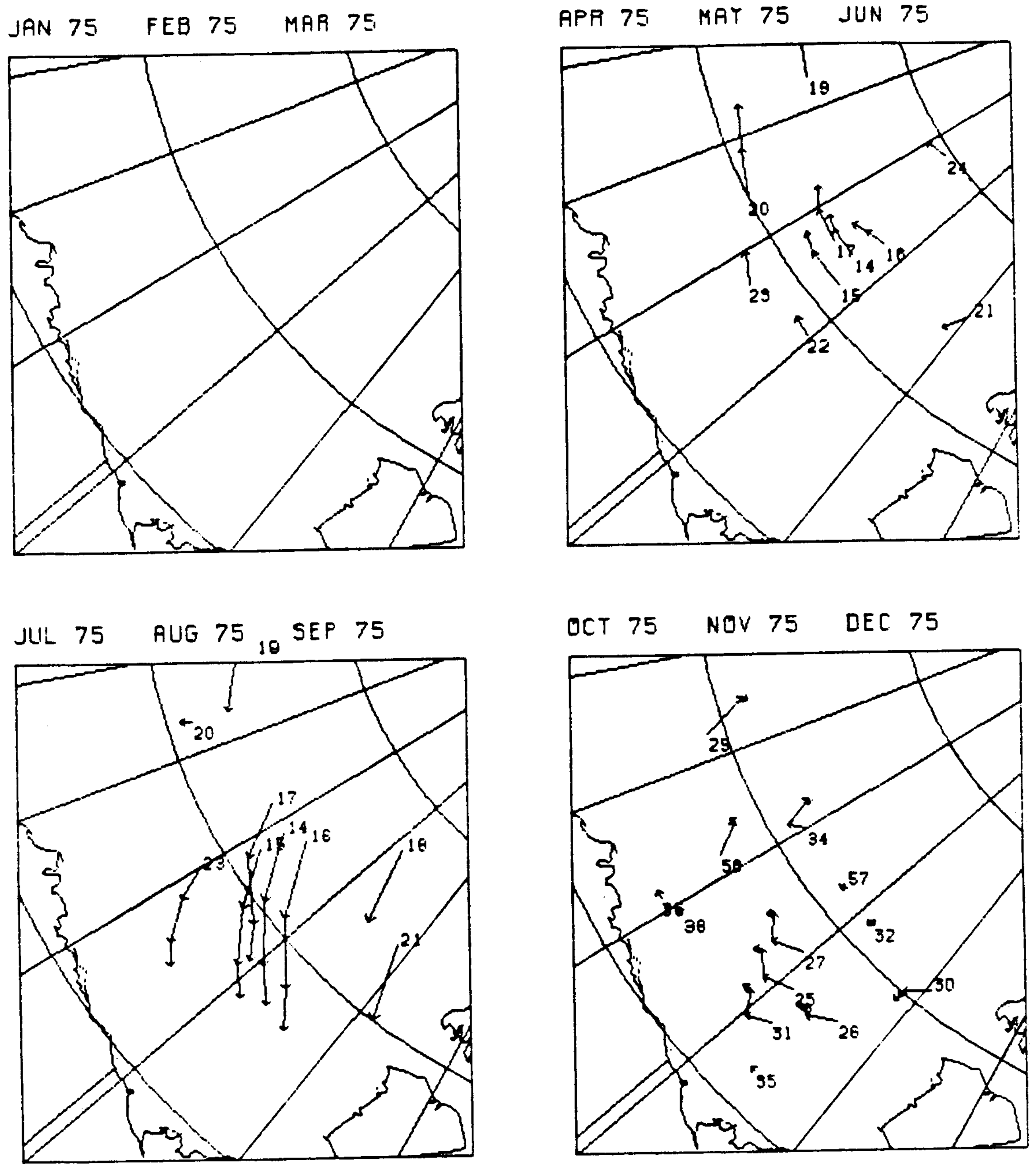

Figure B1. Observed Monthly Buoy Trajectories in the Beaufort Sea from 1959 Through 1981. Each Plot Represents a 3 Month Period (Continued).

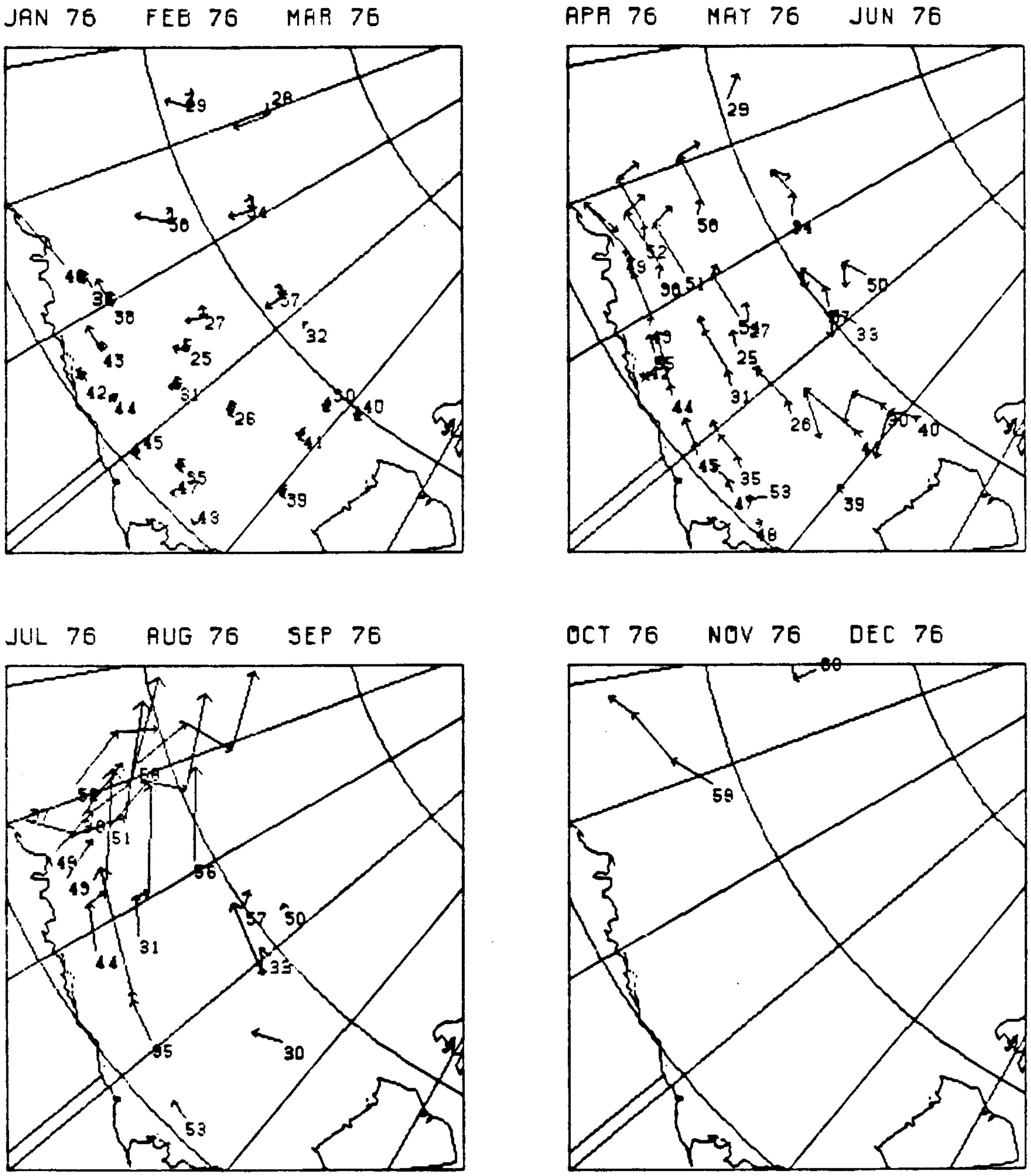

Figure B1. Observed Monthly Buoy Trajectories in the Beaufort Sea from 1959 Through 1981. Each Plot Represents a 3 Month Period (Continued).

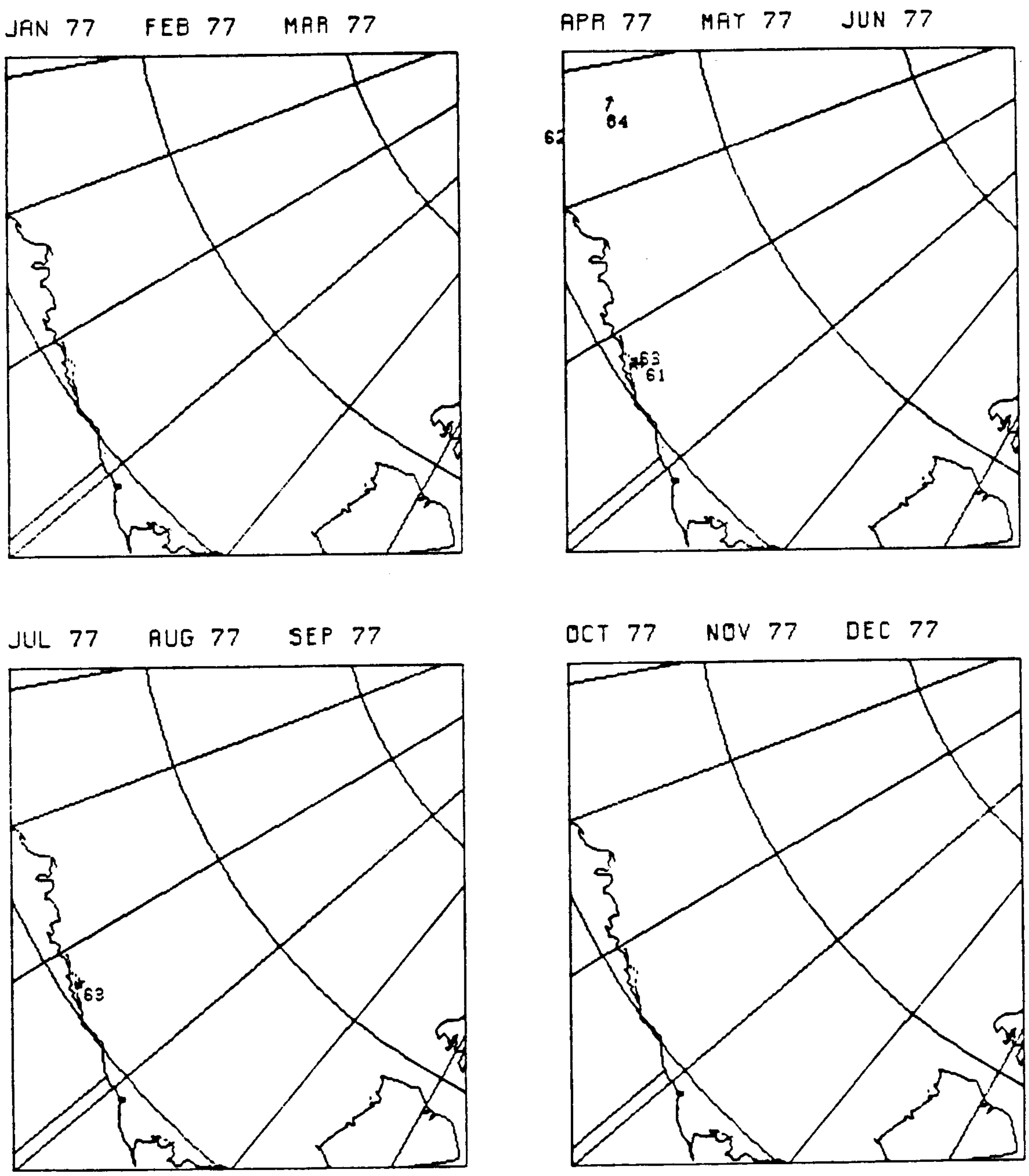

Figure B1. Observed Monthly Buoy Trajectories in the Beaufort Sea from 1959 Through 1981. Each Plot Represents a 3 Month Period (Continued).

JAN 79 FEB 79 MAR 79

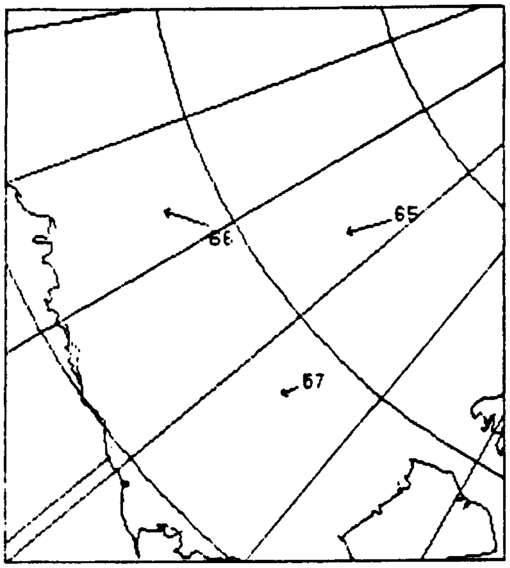

APR 79 MAY 79 JUN 79

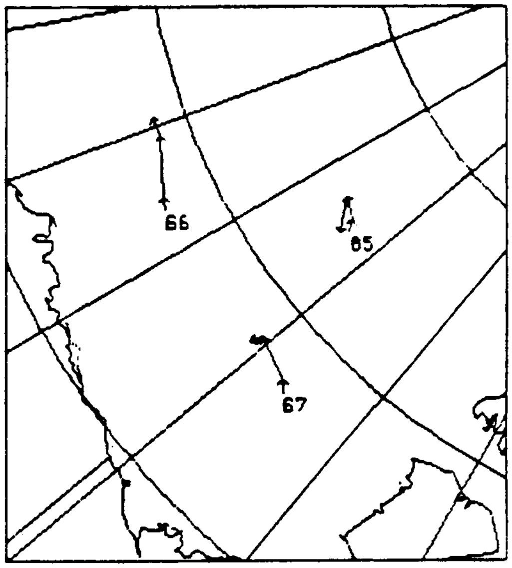

JUL 79 AUG 79 SEP 79

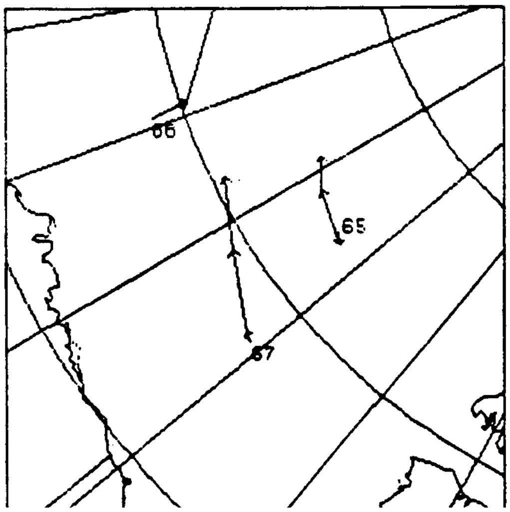

OCT 79 NOV 79 DEC 79

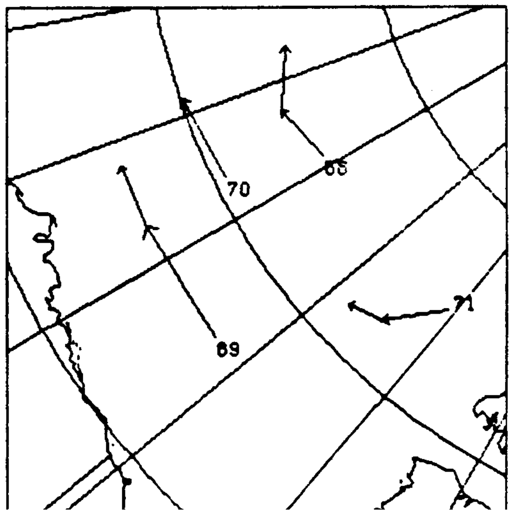

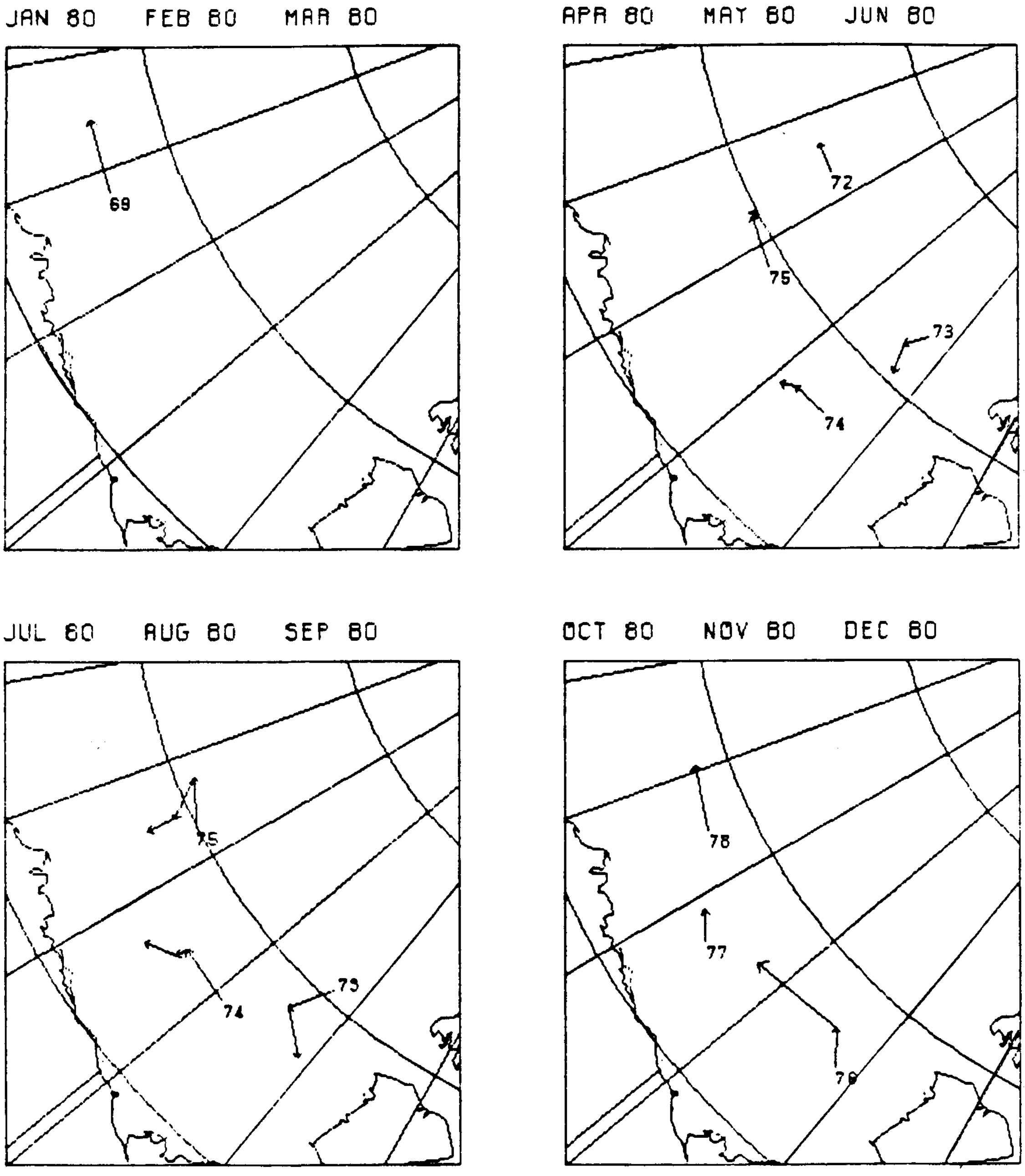

Figure B1. Observed Monthly Buoy Trajectories in the Beaufort Sea from 1959 Through 1981. Each Plot Represents a 3 Month Period (Continued).

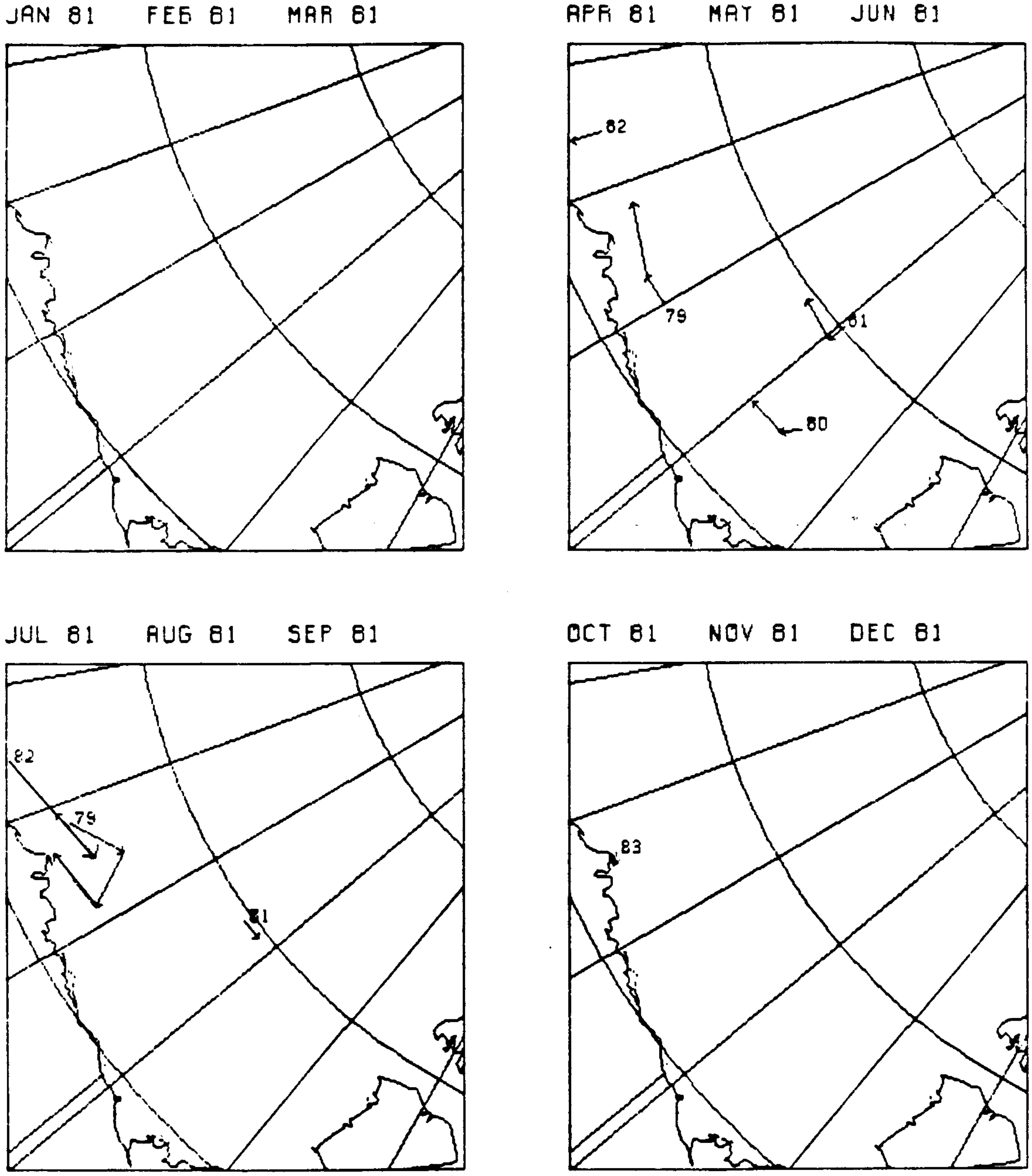

Figure B1. Observed Monthly Buoy Trajectories in the Beaufort Sea from 1959 Through 1981. Each Plot Represents a 3 Month Period (Concluded).

1958-1959 ICE SEASON		1	10
#1 ICE ISLAND T-3			10
JAN 59	75.302	126.375	
FEB 59	74.297	128.308	
MAR 59	74.089	128.333	
APR 59	74.087	128.396	
MAY 59	73.680	129.328	
JUN 59	72.602	130.174	
JUL 59	71.940	132.482	
AUG 59	71.430	133.471	
SEP 59	71.420	135.836	
OCT 59	71.465	137.945	

1959-1960 ICE SEASON		1	10
#2 ICE ISLAND T-3			10
OCT 59	71.465	137.945	
NOV 59	71.270	140.610	
DEC 59	71.168	145.713	
JAN 60	71.052	145.051	
FEB 60	71.219	146.959	
MAR 60	72.049	152.047	
APR 60	72.181	154.046	
MAY 60	71.808	158.656	
JUN 60	71.822	160.220	
JUL 60	71.789	160.230	

1960-1961 ICE SEASON		2	10
#3 ARLIS 1			6
OCT 60	74.965	142.127	
NOV 60	74.470	149.759	
DEC 60	74.136	154.859	
JAN 61	74.663	162.174	
FEB 61	74.741	165.731	
MAR 61	74.735	166.246	
#4 ARLIS II			4
JUN 61	73.276	157.435	
JUL 61	73.894	163.139	
AUG 61	74.403	160.348	
SEP 61	75.397	165.869	

1961-1962 ICE SEASON		1	2
#5 ICE ISLAND T-3			2
MAR 62	73.928	162.652	
APR 62	74.242	168.241	

1964-1965 ICE SEASON		1	12
#6 ICE ISLAND T-3			12
NOV 64	80.063	133.918	
DEC 64	78.704	138.428	
JAN 65	77.840	138.252	
FEB 65	77.176	138.679	
MAR 65	76.599	138.035	
APR 65	76.870	137.982	
MAY 65	76.708	137.941	
JUN 65	76.335	139.188	
JUL 65	76.196	141.809	
AUG 65	75.508	141.867	
SEP 65	75.680	139.388	
OCT 65	75.096	142.056	

1965-1966 ICE SEASON		1	12
#7 ICE ISLAND T-3			12
OCT 65	75.096	142.056	
NOV 65	74.451	141.724	
DEC 65	75.375	145.610	
JAN 66	75.369	146.478	
FEB 66	76.064	150.060	
MAR 66	75.667	153.684	
APR 66	75.396	155.800	
MAY 66	75.199	157.055	
JUN 66	75.406	155.096	
JUL 66	75.594	151.552	
AUG 66	75.571	151.858	
SEP 66	75.773	157.168	

1971-1972 ICE SEASON		4	19
#8 AIDJEX PILOT NO. 2			5
MAY 72	72.064	151.301	
JUN 72	72.636	157.187	
JUL 72	72.758	160.747	
AUG 72	74.128	164.497	
SEP 72	75.176	167.950	
#9 AIDJEX PILOT NO. 3			6
MAY 72	78.603	142.650	
JUN 72	78.365	141.559	
JUL 72	78.004	139.319	
AUG 72	77.062	135.299	
SEP 72	76.691	134.655	
OCT 72	75.687	135.696	
#10 AIDJEX PILOT NO. 4			2
MAY 72	79.301	160.851	
JUN 72	79.588	160.742	

Table B1. Observed Monthly Buoy Location and Motion in the Beaufort Sea from January 1959 Through December 1981.

1971-1972 ICE SEASON			(Cont)
#11 AIDJEX PILOT NO. 6			6
MAY 72	75.226	152.748	
JUN 72	75.627	155.993	
JUL 72	76.429	156.716	
AUG 72	76.920	153.944	
SEP 72	77.601	154.001	
OCT 72	77.117	155.676	
1972-1973 ICE SEASON		2	4
#12 AIDJEX PILOT NO. 3			2
OCT 72	75.687	135.696	
NOV 72	75.424	135.358	
#13 AIDJEX PILOT NO. 6			2
OCT 72	77.117	155.676	
NOV 72	77.744	155.424	
1974-1975 ICE SEASON		11	46
#14 AIDJEX STATION 0			6
MAY 75	76.4698	143.7276	
JUN 75	76.4252	147.0536	
JUL 75	76.5534	148.6963	
AUG 75	75.1930	144.0633	
SEP 75	74.1563	139.4025	
OCT 75	73.5138	136.6657	
#15 AIDJEX STATION 1			6
MAY 75	75.7393	142.0811	
JUN 75	75.6844	146.3603	
JUL 75	75.8421	148.4573	
AUG 75	74.6543	144.7962	
SEP 75	73.6711	141.0793	
OCT 75	73.1731	138.7017	
#16 AIDJEX STATION 2			6
MAY 75	77.2552	142.7120	
JUN 75	77.1068	144.9446	
JUL 75	76.9153	146.4378	
AUG 75	75.3122	141.5880	
SEP 75	74.1590	136.5076	
OCT 75	73.3718	134.0584	
#17 AIDJEX STATION 3			6
MAY 75	76.2909	146.0974	
JUN 75	76.3822	149.8458	
JUL 75	76.6779	152.0180	
AUG 75	75.4868	148.4580	
SEP 75	74.6227	142.8819	
OCT 75	73.9821	140.5618	
#18 AIDJEX STATION 5			2
JUL 75	78.6467	138.6580	
AUG 75	76.8112	135.5264	
#19 AIDJEX STATION 7			4
JUN 75	77.5096	163.6679	
JUL 75	77.5839	168.5818	
AUG 75	77.0887	168.2809	
SEP 75	76.5638	163.1204	
#20 AIDJEX STATION 8			4
MAY 75	74.9782	154.2100	
JUN 75	75.3770	158.9122	
JUL 75	75.6493	163.1167	
AUG 75	75.3531	163.5152	
#21 AIDJEX STATION 9			3
JUN 75	77.5419	129.8530	
JUL 75	76.8421	131.3362	
AUG 75	75.0190	128.5141	
#22 AIDJEX STATION 10			2
JUN 75	74.3114	140.3895	
JUL 75	74.3872	142.2449	
#23 AIDJEX STATION 11			5
JUN 75	73.9268	147.2620	
JUL 75	74.2863	149.8883	
AUG 75	73.5134	148.4273	
SEP 75	72.684	145.965	
OCT 75	72.322	144.356	
#24 AIDJEX STATION 12			2
JUN 75	79.8474	146.8590	
JUL 75	79.6081	149.9589	
1975-1976 ICE SEASON		34	221
#25 AIDJEX STATION 1			8
OCT 75	73.1731	138.7017	
NOV 75	72.7924	141.1706	
DEC 75	73.2040	143.1017	
JAN 76	73.0683	143.4680	
FEB 76	73.0853	144.2076	
MAR 76	72.9797	143.3092	
APR 76	72.7228	144.1589	
MAY 76	72.8778	145.4528	
#26 AIDJEX STATION 2			10
OCT 75	73.3718	134.0584	
NOV 75	72.9570	136.3609	
DEC 75	73.1146	136.9043	
JAN 76	72.9397	137.1979	
FEB 76	72.9547	137.7686	
MAR 76	72.8191	137.0065	
APR 76	72.7174	137.1549	
MAY 76	72.8825	138.0578	
JUN 76	72.7870	141.5580	
JUL 76	72.8680	141.7040	

Table B1. Observed Monthly Buoy Location and Motion in the Beaufort Sea from January 1959 Through December 1981 (Continued).

1975-1976 ICE SEASON		(Cont)
#27 AIDJEX STATION 3		8
OCT 75	73.9821	140.5618
NOV 75	73.5384	143.0396
DEC 75	73.9846	144.9896
JAN 76	73.8463	145.2221
FEB 76	73.8968	145.7865
MAR 76	73.7887	144.7157
APR 76	73.3683	145.3850
MAY 76	73.5482	146.7348
#28 AIDJEX STATION 7		3
FEB 76	77.6176	160.8068
MAR 76	77.4809	159.3993
APR 76	76.6684	159.5779
#29 AIDJEX STATION 8		7
NOV 75	74.579	162.427
DEC 75	75.684	164.788
JAN 76	75.757	164.410
FEB 76	75.981	164.254
MAR 76	75.7963	162.9186
APR 76	75.2410	164.3495
MAY 76	75.660	166.397
#30 AIDJEX STATION 5		11
OCT 75	75.491	129.554
NOV 75	75.024	131.557
DEC 75	74.873	131.477
JAN 76	74.711	131.638
FEB 76	74.619	131.828
MAR 76	74.523	131.347
APR 76	74.434	131.370
MAY 76	74.460	132.143
JUN 76	74.180	134.684
JUL 76	73.484	133.330
AUG 76	73.164	135.775
#31 AIDJEX STATION 10		13
OCT 75	72.194	137.925
NOV 75	71.831	139.702
DEC 75	72.368	140.956
JAN 76	72.297	141.631
FEB 76	72.319	142.175
MAR 76	72.213	141.419
APR 76	72.048	141.947
MAY 76	72.226	142.947
JUN 76	72.307	146.736
JUL 76	72.417	147.835
AUG 76	72.864	150.709
SEP 76	73.190	150.440
OCT 76	74.342	158.850
#32 AIDJEX STATION 12		4
NOV 75	75.732	138.157
DEC 75	75.803	138.471
JAN 76	75.610	138.385
FEB 76	75.592	138.679
#33 AIDJEX STATION 12		6
MAY 76	75.400	139.134
JUN 76	75.143	141.535
JUL 76	74.713	139.720
AUG 76	74.664	140.835
SEP 76	74.296	138.781
OCT 76	74.814	145.609
#34 AIDJEX STATION 13		10
OCT 75	75.833	149.959
NOV 75	75.485	151.233
DEC 75	76.260	152.608
JAN 76	76.171	152.134
FEB 76	76.373	152.045
MAR 76	76.220	150.869
APR 76	75.606	151.388
MAY 76	75.917	153.293
JUN 76	75.648	156.214
JUL 76	76.031	154.847
#35 AIDJEX STATION 14		11
DEC 75	71.057	136.077
JAN 76	71.064	136.451
FEB 76	71.049	137.136
MAR 76	70.944	136.571
APR 76	70.884	136.668
MAY 76	71.035	137.450
JUN 76	71.053	139.530
JUL 76	71.144	140.674
AUG 76	71.371	143.843
SEP 76	71.520	144.484
OCT 76	72.424	154.129
#36 AIDJEX STATION 15		4
DEC 75	71.833	151.110
JAN 76	71.809	151.699
FEB 76	71.803	153.019
MAR 76	71.678	152.349
#37 AIDJEX STATION 15		4
JUL 76	71.183	159.778
AUG 76	72.231	157.254
SEP 76	73.505	157.035
OCT 76	74.799	166.406
#38 AIDJEX STATION 16		9
DEC 75	72.086	149.034
JAN 76	72.047	149.715
FEB 76	72.169	150.670
MAR 76	72.014	149.789
APR 76	72.011	152.082
MAY 76	72.186	152.906
JUN 76	71.945	157.815
JUL 76	72.536	158.541
AUG 76	73.892	161.565
#39 AIDJEX STATION 17		5
JAN 76	72.346	129.629
FEB 76	72.330	129.990
MAR 76	72.216	129.441

Table B1. Observed Monthly Buoy Location and Motion in the Beaufort Sea from January 1959 Through December 1981 (Continued).

1975-1976 ICE SEASON		(Cont)
#39 AIDJEX STATION 17		(Cont)
APR 76	72.171	129.612
MAY 76	72.203	130.220
#40 AIDJEX STATION 18		7
JAN 76	74.968	128.895
FEB 76	74.906	128.983
MAR 76	74.830	128.629
APR 76	74.751	128.677
MAY 76	74.750	128.966
JUN 76	74.476	131.112
JUL 76	73.364	129.388
#41 AIDJEX STATION 19		7
JAN 76	73.712	131.613
FEB 76	73.680	131.843
MAR 76	73.558	131.401
APR 76	73.488	131.468
MAY 76	73.548	132.113
JUN 76	73.373	137.786
JUL 76	72.802	133.941
#42 AIDJEX STATION 20		7
JAN 76	70.470	145.962
FEB 76	70.548	146.643
MAR 76	70.445	146.984
APR 76	70.440	146.197
MAY 76	70.438	146.194
JUN 76	70.444	146.250
JUL 76	70.439	146.206
#43 AIDJEX STATION 21		8
JAN 76	71.269	147.291
FEB 76	71.333	147.751
MAR 76	71.206	147.110
APR 76	71.252	149.274
MAY 76	71.397	149.711
JUN 76	71.506	153.266
JUL 76	71.597	154.549
AUG 76	72.503	156.414
#44 AIDJEX STATION 22		10
JAN 76	70.827	143.842
FEB 76	70.820	144.074
MAR 76	70.769	143.555
APR 76	70.736	144.038
MAY 76	70.857	144.738
JUN 76	71.088	146.811
JUL 76	71.314	148.562
AUG 76	71.765	151.973
SEP 76	72.245	152.124
OCT 76	73.604	161.337
#45 AIDJEX STATION 23		6
JAN 76	70.513	139.812
FEB 76	70.409	139.898
MAR 76	70.354	139.451
APR 76	70.325	139.535

#45 AIDJEX STATION 23		(Cont)
MAY 76	70.474	140.251
JUN 76	70.642	142.092
#46 AIDJEX STATION 24		2
JAN 76	71.466	154.265
FEB 76	70.151	164.333
#47 AIDJEX STATION 26		4
MAR 76	70.387	135.619
APR 76	70.340	135.744
MAY 76	70.455	136.556
JUN 76	70.455	138.089
#48 AIDJEX STATION 27		3
MAR 76	70.208	133.070
APR 76	70.173	133.015
MAY 76	70.302	132.745
#49 AIDJEX STATION 28		7
APR 76	71.522	154.845
MAY 76	71.641	155.132
JUN 76	71.121	159.626
JUL 76	71.586	156.745
AUG 76	72.766	158.515
SEP 76	73.916	159.645
OCT 76	75.303	168.336
#50 AIDJEX STATION 29		4
MAY 76	76.370	142.411
JUN 76	76.062	144.672
JUL 76	75.775	142.540
AUG 76	75.805	142.773
#51 AIDJEX STATION 33		6
MAY 76	72.633	151.570
JUN 76	72.492	156.147
JUL 76	73.041	156.794
AUG 76	74.323	159.220
SEP 76	75.134	157.202
OCT 76	76.357	165.676
#52 AIDJEX STATION 36		6
APR 76	72.127	155.244
MAY 76	72.279	156.330
JUN 76	72.079	160.611
JUL 76	72.687	161.167
AUG 76	73.997	164.363
SEP 76	74.968	163.547
#53 AIDJEX STATION 37		3
JUN 76	70.822	133.723
JUL 76	70.439	134.694
AUG 76	70.514	136.199
#54 AIDJEX STATION 38		3
MAY 76	73.232	146.185
JUN 76	73.218	150.271
JUL 76	73.421	150.717
#55 AIDJEX STATION 39		2
JUN 76	70.969	147.418
JUL 76	71.122	148.673

Table B1. Observed Monthly Buoy Location and Motion in the Beaufort Sea from January 1959 Through December 1981 (Continued).

1975-1976 ICE SEASON (Cont)

#56 AIDJEX STATION 41			2
SEP 76	74.547	150.973	
OCT 76	75.565	158.916	
#57 AIDJEX STATION 44			9
DEC 75	75.816	143.061	
JAN 76	75.695	142.801	
FEB 76	75.763	143.019	
MAR 76	75.645	142.035	
APR 76	75.152	142.183	
MAY 76	75.373	143.814	
JUN 76	75.129	146.466	
JUL 76	74.996	144.819	
AUG 76	75.290	145.856	
#58 AIDJEX STATION 66			12
NOV 75	73.637	151.831	
DEC 75	74.351	153.937	
JAN 76	74.301	154.347	
FEB 76	74.454	154.607	
MAR 76	74.313	153.429	
APR 76	73.554	155.398	
MAY 76	73.788	156.428	
JUN 76	73.673	160.552	
JUL 76	74.261	161.140	
AUG 76	75.684	163.346	
SEP 76	76.530	159.231	
OCT 76	77.649	166.840	

1976-1977 ICE SEASON 6 20

#59 AIDJEX STATION 10			4
OCT 76	74.342	158.850	
NOV 76	73.612	162.119	
DEC 76	73.010	166.813	
JAN 77	72.514	168.540	
#60 AIDJEX STATION 66			4
OCT 76	77.649	166.840	
NOV 76	77.053	166.307	
DEC 76	77.096	168.545	
JAN 77	76.705	169.097	
#61 AIDJEX STATION R632			2
APR 77	70.716	146.937	
MAY 77	70.723	146.924	
#62 AIDJEX STATION R1052			2
MAY 77	70.835	166.271	
JUN 77	71.266	168.813	
#63 AIDJEX STATION R1601			6
APR 77	70.525	147.271	
MAY 77	70.527	147.252	
JUN 77	70.520	147.299	
JUL 77	70.520	147.290	
AUG 77	70.493	147.496	
SEP 77	70.331	147.327	
#64 AIDJEX STATION R1617			2
APR 77	72.433	166.303	
MAY 77	72.620	167.300	

1978-1979 ICE SEASON 3 24

#65 AOBP 1906			8
MAR 79	77.950	141.483	
APR 79	77.006	143.276	
MAY 79	77.228	143.956	
JUN 79	77.432	146.256	
JUL 79	76.832	143.738	
AUG 79	76.704	142.680	
SEP 79	77.052	148.024	
OCT 79	77.468	151.176	
#66 AOBP 1913			8
MAR 79	74.463	150.681	
APR 79	73.726	153.398	
MAY 79	73.810	154.413	
JUN 79	74.312	159.120	
JUL 79	74.295	160.754	
AUG 79	75.146	161.094	
SEP 79	76.381	169.485	
OCT 79	77.132	174.518	
#67 AOBP 1914			8
MAR 79	73.893	135.767	
APR 79	73.516	136.187	
MAY 79	73.722	136.883	
JUN 79	73.999	140.573	
JUL 79	73.767	140.921	
AUG 79	73.811	141.731	
SEP 79	74.627	147.847	
OCT 79	75.293	153.679	

1979-1980 ICE SEASON 8 31

#68 AOBP 1906			3
OCT 79	77.468	151.176	
NOV 79	77.069	157.145	
DEC 79	77.627	163.168	
#69 AOBP 1908			4
NOV 79	73.184	142.935	
DEC 79	73.192	153.055	
JAN 80	73.205	157.998	
FEB 80	73.342	164.420	
#70 AOBP 1914			2
OCT 79	75.293	153.679	
NOV 79	75.051	161.360	
#71 AOBP 1918			3
OCT 79	77.423	130.562	
NOV 79	76.257	134.694	
DEC 79	75.975	137.990	

Table B1. Observed Monthly Buoy Location and Motion in the Beaufort Sea from January 1959 Through December 1981 (Continued).

1979-1980 ICE SEASON (Cont)

#72 AOBP 1938			2
	MAY 80	77.079	153.259
	JUN 80	77.137	156.568
#73 AOBP 1939			5
	MAY 80	76.497	132.363
	JUN 80	75.956	133.773
	JUL 80	75.277	132.698
	AUG 80	74.172	134.583
	SEP 80	73.424	130.986
#74 AOBP 1940			6
	MAY 80	73.377	134.794
	JUN 80	73.318	138.036
	JUL 80	73.096	138.999
	AUG 80	73.197	144.163
	SEP 80	72.923	144.419
	OCT 80	72.448	146.653
#75 AOBP 1941			6
	MAY 80	74.576	147.918
	JUN 80	74.847	152.745
	JUL 80	74.967	153.037
	AUG 80	75.450	157.488
	SEP 80	74.598	154.672
	OCT 80	73.886	154.723

1980-1981 ICE SEASON 7 24

#76 AOBP 1939			3
	OCT 80	72.821	131.862
	NOV 80	73.567	134.056
	DEC 80	73.214	142.680
#77 AOBP 1940			2
	OCT 80	72.448	146.653
	NOV 80	72.879	148.822
#78 AOBP 1941			2
	OCT 80	73.886	154.723
	NOV 80	74.194	160.567
#79 AOBP 2577			6
	MAY 81	71.774	149.964
	JUN 81	71.726	152.607
	JUL 81	72.180	158.231
	AUG 81	73.085	154.417
	SEP 81	71.854	151.509
	OCT 81	71.498	156.486
#80 AOBP 2578			3
	MAY 81	72.619	135.401
	JUN 81	72.167	136.409
	JUL 81	72.178	139.703
#81 AOBP 2579			4
	MAY 81	75.087	139.612
	JUN 81	74.598	139.541
	JUL 81	74.779	143.698
	AUG 81	74.786	141.643

#82 AOBP 3813			4
	JUN 81	72.024	164.369
	JUL 81	71.229	164.223
	AUG 81	72.417	154.969
	SEP 81	71.950	159.348

1981-1982 ICE SEASON 1 3

#83 AOBP 2577			3
	OCT 81	71.498	156.486
	NOV 81	71.334	155.886
	DEC 81	71.296	155.783

Table B1. Observed Monthly Buoy Location and Motion in the Beaufort Sea from January 1959 Through December 1981 (Concluded).

INTERACTION OF OIL WITH ARCTIC SEA ICE

by

D. R. Thomas

Flow Industries, Inc.
Research and Technology Division

Final Report
Outer Continental Shelf Environmental Assessment Program
Research Unit 258

February 1983

FOREWORD

This study was supported by the Bureau of Land Management through interagency agreement with the National Oceanic and Atmospheric Administration, under which a multiyear program responding to needs of petroleum development of the Alaskan Continental Shelf is managed by the Outer Continental Shelf Environmental Assessment (OCSEAP) Office. The report will also appear in The Alaskan Beaufort Sea (edited by P. Barnes, E. Reimnitz and D. Schell; published by Academic Press, New York), which will be published in 1983.

TABLE OF CONTENTS

Interaction of Oil with Arctic Sea Ice

D. R. Thomas

Research and Technology Division
Flow Industries, Inc.
Kent, Washington

I. INTRODUCTION

Worldwide, about 1 in 3000 offshore oil wells experiences some kind of blowout. Many of these are relatively harmless in terms of environmental damage. It has been estimated that the chance of a "serious" blowout incident is less than 1 in 100,000 wells drilled. Although this is a very low probability, it happens often enough (for example, the Santa Barbara and the IXTOC 1 blowouts) that the consequences must be considered.

During the next few years, many exploratory and possibly production oil wells will be drilled on the continental shelf in the Beaufort Sea off the north coast of Alaska. Drilling will initially be from natural or artificial islands in relatively shallow waters. While this procedure will reduce the probability of blowouts and provide a stable base for control efforts and spill containment, it is possible for a blowout to occur away from the drill hole. The 1969 blowout in the Santa Barbara Channel occurred through faults and cracks in the rock as far as 0.25 km from the drill site.

Previous regulations required that any offshore drilling in the Beaufort Sea be done during the period from November through March. Present regulations allow exploratory drilling year-round in some areas of the Beaufort, while drilling is prohibited during September and October in other areas. Due to logistic considerations and site-specific environmental concerns, much of the exploratory drilling will still be done during the ice season. The entire sea surface is covered by a floating ice sheet during that time, except for occasional leads of open water. Thus, sea ice will have an important bearing on the fate of oil spilled by a blowout.

There has been little practical experience with oil spills in ice-covered waters. Accidental surface spills that have occurred in ice-covered waters in subarctic regions, as in Buzzards Bay, Massachusetts, in 1977, have not been in arctic-type ice, which generally continues to build throughout the winter and is thicker and more continuous than subarctic ice.

Recently, several experimental oil spill studies involving arctic sea ice have been performed. The Canadian government sponsored an oil spill experiment at Balaena Bay, N.W.T., during the winter of 1974-75, as part of the Beaufort Sea Project. The initial spreading of the oil and incorporation into the ice sheet were studied. The effects of oil on the thermal regime of the ice was also studied, as were weathering of the oil and clean-up techniques. An experimental spill was performed in 1978 by Environment Canada in Griper Bay, N.W.T., to study the fate of oil spilled beneath multi-year ice. During the winter of 1979-80, Dome Petroleum carried out an experimental oil spill in McKinley Bay, in the Canadian Beaufort. Plume dynamics under the ice, the effects of gas on under-ice spreading, the formation of emulsions, and the surfacing of oil in the spring were some of the topics studied.

The purpose of this paper is to summarize relevant knowledge about the interactions between arctic sea ice and oil. Previous works by Lewis (1976), NORCOR (1977), and Stringer and Weller (1980) have also addressed this topic. The completion of further experimental oil spill studies, along with recent laboratory studies of the interaction of oil and sea ice and studies of environmental conditions, makes an updating of those works desirable. An attempt is made to identify the major factors in the interaction between oil and arctic sea ice and to present them in a way that defines the scope of the problem. Generally, this paper is restricted to factors that can be expected to play a major role in the sequence of events following a large under-ice blowout in the Beaufort Sea during winter. Blowouts that occur during the summer, in subarctic waters, or beyond the continental shelf are not considered here.

II. THE INTERACTION OF OIL AND SEA ICE

If an underwater blowout occurs, releasing large quantities of crude oil and gas into the water beneath the arctic ice cover, one can expect a different chain of events than from an open-water blowout. No such under-ice blowout has occurred yet, but from experimental work (NORCOR, 1975; Martin, 1977;

Topham, 1975; Topham & Bishnoi, 1980; Cox *et al.*, 1981; Buist *et al.*, 1981) and from observations made at accidental surface spill sites in icy waters (Ruby *et al.*, 1977; Deslauriers, 1979), one can predict the course of events for an under-ice blowout with reasonable confidence. In general, an under-ice blowout in the winter will follow the course outlined below:

(1) Initial Phase -- the underwater release of oil and gas and their subsequent rise to the surface.
(2) Spreading Phase -- the spreading of oil due to water currents and buoyancy.
(3) Incorporation Phase -- the incorporation of oil into the ice cover.
(4) Transportation Phase -- the motion of the oiled ice.
(5) Release Phase -- the release of the oil from the ice.

Three areas and types of ice cover must be accounted for when considering blowouts on the Beaufort Sea continental shelf of Alaska. These are the fast ice zone, the pack ice zone, and the area of interaction between the moving pack ice and the stationary fast ice.

The fast ice zone includes ice that forms nearshore each year, although occasional multiyear floes (ice that has survived one or more melt seasons) or remnants of grounded ridges may be incorporated. The ice begins to form in early October and for a month or two it is susceptible to movement and deformation by the winds. Eventually, this nearshore ice becomes immobilized, protected by the shore on one side and barrier islands or grounded ridges on the other. Since motions and deformations occur for only a short period of time, the fast ice tends to be relatively flat and undeformed. This ice begins to melt in place in late May or June and is mostly gone by the end of July.

Further offshore is the pack ice zone. The ice in this zone is a mixture of multiyear ice and seasonal ice. Winds and currents cause the ice to be in almost constant motion. Cracks open to form leads that quickly freeze, developing a layer of thin ice. Some leads are closed by moving ice, which breaks and piles up the thin ice to form ridges and rubble piles.

Where the moving pack ice interacts with the stationary fast ice, a great deal of ice deformation takes place. The winds tend to move the pack ice westward and toward shore causing much shearing deformation. Many large ridges form in this area. Water depths here are from 10 to 30 m. Since many ridge keels are deeper than that, a band of grounded ridges often forms. Following Reimnitz *et al.* (1977), this is called the Stamukhi zone (after the Russian word stamukhi, meaning grounded ice rubble piles).

In the rest of this section, the five sequential phases of interaction between crude oil and sea ice are discussed separately.

A. *Initial Phase*

The blowout is assumed to consist of the continuous release over a minimum of several days of large quantities of crude oil and many times that amount of gas. The blowout occurs under an ice cover in the period from November through March. The blowout is also assumed to occur on the Beaufort Sea continental shelf in relatively shallow waters (less than about 200 m deep).

1. Effects of Gas. Topham (1975) reports the results of experimental releases of oil and compressed air underwater. The experiments were simulations of small well blowouts in open-water conditions. As gas is released in shallow water, it breaks up into small bubbles and rises to the surface, carrying oil and part of the surrounding water along to form an underwater plume. This plume is initially conical in shape, but becomes nearly cylindrical as it rises above the release point. The centerline velocities of experimental plumes did not vary significantly with the depth or air flow rate for the range of experimental values (flow rates of 3.6 to 40 m^3 min^{-1} at depths of 33 to 60 m).

As the plume reaches the water surface, the vertical transport changes to a radial current flowing outward. During tests in open water (Topham, 1975), a concentric wave ring was produced at some distance from the plume, marking the location of a reversal in radial surface currents. A downward current is found here, extending to a depth of about 10 m. During Dome's simulated blowout beneath sea ice (Buist *et al.*, 1981), no wave ring was observed, but downward flow did occur about 15 to 20 m from the plume. Small droplets of oil or oil-and-water emulsions will likely be carried downward, but the majority of the oil from the blowout will rise to the surface in drops with a mean diameter of 1 mm. One or two percent will be in fine droplets of approximately 0.05 mm in diameter (Topham, 1975). Drops of this size have a natural rise rate of about 0.5 mm s^{-1}. Subsurface currents could carry the very small droplets many kilometers downstream during their slow rise to the surface. However, Buist *et al.* (1981) observed that 90 percent of the oil that was released surfaced within a 50-m radius. Dissolution is generally not considered important in the Arctic (NORCOR, 1975). The formation of stable emulsions was not observed during Dome's simulated blowout.

The first interaction between the blowout and the ice cover is the collection of gas beneath the ice. Assuming that the ratio of gas to oil by volume is 150 to 1 at the surface, then gas will be released at rates near 33 $m^3\ min^{-1}$ in the case of a blowout releasing 2000 barrels per day (0.22 $m^3\ min^{-1}$) of oil. Within minutes, large pockets of gas will have accumulated beneath the ice.

Topham (1977) studied the problem of a submerged gas bubble bending and breaking an ice sheet. For thin ice, there is little doubt that a gas bubble a few centimeters in thickness and a few meters in radius will crack the ice. During Dome's simulated blowout (Buist *et al.*, 1981), air released beneath ice 0.65 m thick caused the ice to dome upward until it cracked, releasing the gas. For thicker ice (up to 2 m), the situation is not so clear. In rough ice where large, thick pockets of gas can collect, the radius needed to crack the ice is a few tens of meters. In smoother ice where the gas will collect only to a few centimeters in thickness, the critical radius can extend from a few hundred meters to several kilometers.

It is likely, nevertheless, that the gas will break the ice cover in the fast ice areas. In fast ice, natural weaknesses exist in the form of thermal cracks that probably occur every few hundred meters (Evans and Untersteiner, 1971). Thus, the gas will only spread a few hundred meters under the ice before it either cracks the ice or comes to a natural crack. Once a crack exists near the blowout site, the ice over the blowout is likely to be further fractured and broken up by turbulence or by sinking into the low-density gas-in-water mixture near the center of the plume.

A moving ice canopy may also be broken up as it passes over the gas plume. If the ice is moving at the rate of 3 km day^{-1}, this amounts to an average of about 126 m hr^{-1}. A gas flow rate of 40 $m^3\ min^{-1}$ will deposit 2400 m^3 of gas under the ice in 1 hour. If this gas collects to an average depth of 0.1 m, the under-ice bubble will cover an area of 24,000 m^2 in 1 hour. For first-year ice, the motion experienced during that hour is probably of no significance; the ice will be broken up much as stationary ice would be. If the ice is moving at several kilometers per day over a small blowout, however, it is possible that breakage will not occur.

It has been the opinion of some investigators (Logan *et al.*, 1975; Milne and Herlinveaux, n.d.) that large multiyear floes will not be broken up as they move across an underwater gas plume. Topham's work (1977) seems to support this view. Breakage of multiyear floes might occur, though, if consolidated ridge keels trap deep bubbles of gas or if thermal cracks have weakened the ice. Thermal cracks themselves provide an alternate path for releasing the gas.

2. *Thermal Effects*. A possible contributory factor in the breaking of a stationary or slowly moving sheet of first-year ice is the heat content of the oil. If hot oil escapes from the blowout outlet, it breaks up into small droplets (0.5 to 1.0 mm in diameter). Most or all of the surplus heat of the oil is transferred to the water column, which in turn is carried to the underside of the ice by the gas-induced plume. Some of the heat from the warmed water will then go into melting the ice, with the greatest part of the melting occurring directly over the blowout plume.

In addition to the heat content of the oil, the water column (except in very shallow areas) will be above freezing and can contribute to the melting of ice. The temperature above freezing of the bottom water will generally be 2 to 4 orders of magnitude lower than the temperature of the oil, but the volume of water circulated in the plume will be about 4 orders of magnitude larger than the volume of oil. The total heat transported to the bottom of the ice will thus be roughly 2 to 20 times (depending on the temperature of the water) the amount from the hot oil alone.

The specific heat of sea ice is about 2010 J (kg °K)$^{-1}$ and that of a typical crude oil is 1717 J (kg °K)$^{-1}$. The heat of fusion of water (fresh) is about 334 kJ kg^{-1}. If the ice sheet has an average temperature of -10°C, it will require 10°C x 2010 J (kg °K)$^{-1}$ + 334 kJ kg^{-1} or 354 kJ kg^{-1} to warm and melt the ice. Crude oil provides 1717 J kg^{-1} of heat for each degree of temperature above freezing. To warm and melt each kilogram of sea ice at -10°C, about 206 kg °K of crude oil is required. Since the densities of ice and crude oil are about the same, each volume of oil will melt roughly one two-hundredth that volume of ice for each degree above freezing of the oil temperature.

Oil at a temperature of 100°C, corresponding to a reservoir depth of about 4000 m, would therefore melt about 0.5 m^3 of ice for each 1.0 m^3 of oil released. At least an equivalent amount will be melted by water circulation. However, some of this heat will be spread over a large area by existing currents and by plume-induced circulation. The result will be a small area where significant ice melt takes place and a much larger area with only a slightly reduced ice thickness or a decrease in growth rates.

One would expect the ice directly over the blowout to receive a major proportion of the heat from the oil. In stationary ice or very slowly moving first-year ice, melting will tend to weaken the ice over the blowout, making it more probable that gas bubbles trapped beneath the ice will fracture it and escape. For very large blowouts, a significant amount of ice may be melted, leaving a pool of open water directly over the blowout. Large amounts of oil could collect in this open-water pool, and some of the oil could spill over onto the surrounding ice surface.

The density of sea water is about 1020 kg m^{-3} and the density of sea ice is about 910 kg m^{-3}. Densities of fresh crude oils may range from about 800 to 900 kg m^{-3}. Thus, if one tries to fill a hole through the ice with crude oil, the oil will overflow the top of the hole before it is filled to the bottom. However, during much of the ice season, the air temperature is so low that crude oil exposed to the atmosphere behaves more like a solid than a liquid. The oil will therefore be limited to a small area on the surface until it pools deep enough to begin spreading beneath the ice. Even during the spring, when the air temperature is above the oil's pour point, the snow cover and natural roughness of the ice surface will limit the spread of oil on the surface, so that spilled oil will still tend to spread beneath the ice.

B. Spreading Phase

Once oil gets underneath an ice sheet, several factors, such as the bottom roughness of the ice, the presence of gas under the ice, the magnitude and direction of ocean currents, and movement of the ice cover, will control the concentration and areal extent of the oil spread. Of secondary importance are oil properties such as density, surface tension, equilibrium thickness, and viscosity. The effects of these latter properties are fairly well understood (NORCOR, 1975; Cox *et al.*, 1981; Rosenegger, 1975; Malcolm and Cammaert, 1981) and, while important to understanding the basic mechanisms of oil-water-ice interactions, they will not be as influential on the extent of oil coverage as the grosser, more variable factors.

1. Bottom Roughness and Oil Containment. The bottom roughness of the ice will vary significantly between the fast ice, the pack ice, and the Stamukhi zones. The fast ice zone will have roughness determined chiefly by spatial variations in snow cover causing differences in ice growth rates (Barnes *et al.*, 1979). The Stamukhi zone will be dominated by deep ridge keels. In the pack ice zone, both the above types of roughness are present along with frequent refrozen leads and a high percentage of multiyear floes that have exaggerated underside relief. In addition, all ice growing in sea water has a microscale relief due to the columnar nature of new ice growth.

If oil alone is released under sea ice, or if any accompanying gas is vented, the oil begins filling under-ice voids near the blowout. As a void fills downward with oil, the oil eventually reaches a depth where it can begin escaping over neighboring summits of ice or through "passes" to the next void. If the ice itself is moving over the site of the blowout, the voids may not be completely filled, and only that ice passing directly over the blowout plume will collect oil.

If new ice forms in calm conditions, the underside of the ice will have an essentially flat, smooth surface. Oil will spread underneath this ice to some equilibrium thickness, depending upon a balance between surface tension and buoyancy. Cox *et al.* (1980) report test results for oil of various densities. The equilibrium slick thickness ranged from 5.2 to 11.5 mm for oils with densities in the range of crude oils. For a constant surface tension, a good approximation of slick thickness can be made using the empirical relationship (Cox *et al.*, 1980)

$$\delta = -8.50\ (\rho_w - \rho_o) + 1.67,$$

where δ is the slick thickness in centimeters and $(\rho_w - \rho_o)$ is the density difference between oil and water. The minimum stable drop thickness for crude oil under ice has generally been reported to be about 8 mm (Lewis, 1976). Using this value, we see that 8000 m^3 (50,000 bbl) of oil will spread under each square kilometer of smooth ice. This is the minimum volume of oil that can spread under 1 km^2 of ice in the absence of currents or ice motion. Generally, sea ice, even smooth new ice, will not be perfectly smooth, so each square kilometer will actually hold more oil than that.

During October and November, a snow cover accumulates in drifts parallel to the prevailing wind direction. Barnes *et al.* (1979) found these snow drifts to be fairly stable throughout the ice season. The drifts insulate the ice from the low atmospheric temperatures, causing reduced ice growth beneath. The underside of the ice takes on an undulating appearance and, as ice continues to grow throughout the winter, these undulations become more pronounced, increasing the oil containment capacity.

NORCOR (1975), reporting on the Balaena Bay experiment, found ice thicker than about 0.5 m to have a thickness variation of about 20 percent the mean ice thickness. Not all of this variation will be available for oil containment. Because of natural variations in the snow cover and drift patterns, voids under the ice will tend to be interconnected by passes. These passes may be at any depth within the range of ice drafts, but presumably the most likely depth will be the mean ice draft.

Kovacs (1977, 1979) and Kovacs *et al.* (1981) have mapped the underside relief of the fast ice at various places near Prudhoe Bay in the early spring using an impulse radar system that "sees" the ice water interface. From the contour maps of the ice bottom, they calculated the volume of the voids that lie above the mean ice draft. This volume (the oil containment potential) varied from 10,000 to 35,000 m^3 km^{-2} for areas of undeformed fast ice with no large slush-ice accumulations. The variation seemed to be related mostly to variations in the snow cover. For areas of slightly deformed ice, the containment potential was observed to be as high as 60,000 m^3 km^{-2}. While these numbers seem large, they are only a few times the containment potential of perfectly flat ice (8000 m^3 km^{-2}).

If deformation occurs in the inner fast ice zone, it takes place in the fall when the ice is thin. Most of this deformation is minor in character: raised rims on edges of individual floes, rafting, and a few small ridges or rubble fields. The relief is generally only a few centimeters deep, which will tend to increase the oil containment capacity. As the ice grows thicker and stronger, deformation ceases, and the existing deformed features below the ice tend to be leveled out by differential ice growth between thicker and thinner ice.

Kovacs and Weeks (1979) have observed major deformations occurring inside the barrier islands. A severe storm in early November 1978, with winds at 55 to 65 km hr^{-1} (30 to 35 knots) gusting to 110 km hr^{-1} (60 knots), broke up the fast ice, produced ice motions greater than 1 km, and built ridges up to 4 m high. During the three previous years, such events had not been observed but, obviously, they must be considered. In terms of the spreading of oil under the ice, the increased roughness created by the deformations should limit the spread by creating more voids for the collection of oil. If frequent enough and intersecting, the ridges would limit the directions in which oil could spread or possibly trap deeper pools of oil.

Outside the inner fast ice zone, in the Stamukhi zone, deformational events continue to occur throughout the winter, creating a bottomside relief many meters deep. Tucker *et al.* (1979) observed a maximum of 12 ridges per kilometer in the 20 km just north of Cross Island. If the average sail height is 1.5 m (Tucker *et al.*, 1979) and keels are 4 times as deep as sails (Kovacs and Mellor, 1974), then the potential exists for pools of oil to collect that are several meters deep and from one to a few hundred meters across, assuming that ridges frequently intersect each other. Whether the oil can actually collect in pools that deep is another matter. The only direct evidence we have of the interaction of oil and ridges occurred in Buzzards Bay, Massachusetts, in 1977. Deslauriers (1979) observed that the spilled oil tended to be trapped between the ice blocks making up the ridges, with some oil appearing on the surface. These observations may not be applicable to large arctic pressure and shear ridges that can be several tens of meters in width with a lower probability of interconnecting voids extending through the ridges at shallow depths. This is even more unlikely as the ridges age and some of the interior voids freeze.

If oil collects in deep pools surrounded by ridge keels, buoyancy could force significant amounts of oil onto the surface through openings that exist. Large volumes of gas could remain trapped by the ridges in the Stamukhi zone; however, it is unlikely that enough large areas will be impermeable to cause a significant volume of gas to be contained.

Further out, in the pack ice zone, the variety of under-ice relief increases. Not only are there first-year ice floes and pressure ridges, but variable amounts of multiyear ice and refrozen leads.

Underneath multiyear ice, there is an order of magnitude increase in the quantity of oil or gas that may be contained. Kovacs (1977) profiled the bottom of a multiyear floe and estimated that 293,000 m^3 km^{-2} of space existed above the mean draft of 4.31 m. Other investigators (Ackley *et al.*, 1974) also report greater relief under multiyear ice than under first-year ice.

Refrozen leads also hold large amounts of oil or gas. The ice in a lead is relatively thin and smooth, while the ice of the original floe will have a draft up to 3 m deeper than the ice in the lead. A large lead may be several kilometers wide and many kilometers long, limiting the direction of spreading of the oil but not the area covered. A large flaw lead often forms along the Alaskan coast at the southern boundary of the moving pack. However, most leads will be quite narrow, less than 50 m wide (Wadhams and Horne, 1978). Since leads do not form as perfectly straight lines but, rather, follow meandering floe boundaries or recent thermal cracks, there will generally be many points of contact along a lead. Thus, if oil or gas does come up beneath a refrozen lead, or flows into it from the surrounding ice, it will usually be collected in an elongated pool rather than spreading indefinitely along the lead. The oiled ice in a refrozen lead has a high probability of being built into a ridge.

There is also some probability of oil from a blowout coming up in open water in a newly opened lead. Throughout most of the ice season in the Beaufort Sea, this probability must be fairly low. New ice begins to form immediately and, within one day, a solid ice cover will exist in new leads. Oil beneath thin ice in leads will have a higher probability of appearing on the surface than oil beneath thicker ice. The ice motion that produces leads will also make leads wider or close leads by rafting or ridging the thin ice. Gas collecting under a lead can also break the ice.

2. Currents. A possible contribution to the spread of oil beneath sea ice is ocean currents. Until the oil is completely encapsulated by new ice growth, currents of sufficient magnitude can move the oil laterally beneath the ice until either an insurmountable obstruction is reached or the currents cease.

NORCOR (1975) performed some oil spill experiments near Cape Parry in March 1975 in the presence of currents about 0.1 m s^{-1} in magnitude. In one test, the ice appeared to be perfectly flat with roughness variations of 2 to 3 mm. Oil discharged under this ice spread predominately downstream to a thickness of about 6 mm. After all the oil had been discharged, movement of the oil lens appeared to stop.

A second test was performed nearby in the same current regime, but in ice with more underside relief. Troughs of up to 0.5 m in depth were present, as well as a small ridge keel downstream from the test site. This time, the oil spread downstream until one of the depressions was reached. At that point, the oil collected in a stationary pool averaging about 0.1 m in depth.

Evidently, currents of only 0.1 m s^{-1} may influence the direction of the spread of crude oil under ice, but will not greatly affect the amount of spreading.

More recently, the relationship between current speed, bottom roughness, and the movement of oil under ice has been quantified (Cox *et al.*, 1981). From flume experiments, it was determined that, for smooth ice or ice with roughness less than the equilibrium slick thickness, there is a threshold water velocity below which the oil does not move. For smooth ice, the threshold velocity was about 0.035 m s^{-1}; for ice with roughness scales of 1 mm, the threshold was 0.10 to 0.16 m s^{-1} (depending upon oil density); and for roughness scales of 10 mm, the threshold velocity was 0.20 to 0.24 m s^{-1}. For currents above the threshold velocity, the oil moved at some fraction of the current speed.

For bottom roughness elements with depths several times the slick equilibrium thickness, a boom-type containment/failure behavior was observed. The oil collected upstream of the obstruction to some equilibrium volume, after which additional oil flowed beneath the obstruction. The size and shape of the obstruction had little effect on oil containment. Thus, even mild slopes act as barriers to oil movement.

As the water velocity increases beneath the ice, a Kelvin-Helmholtz instability eventually occurs, in which case the entire slick is flushed from behind the obstruction. For the range of oil densities tested, the failure velocities ranged from about 0.14 to 0.22 m s^{-1}.

When roughness elements are spaced closer than the slick length for a given current speed and oil density, cavity trapping rather than boom containment occurs (Cox and Schultz, 1981). Cavities have the potential for containing more oil in the presence of currents than do simple barriers, and they retain oil at higher current speeds. Some oil was observed to remain in cavities at current speeds of 40 cm s^{-1}.

Measurements of nearshore under-ice currents reported in the literature (Kovacs and Morey, 1978; Weeks and Gow, 1980; Matthews, 1980; and Aagaard, 1981) indicate that the current speed is generally small, less than about 0.1 m s^{-1}, and will not cause significant oil spreading.

3. Ice Motion. The motion of the ice cover over a blowout is another mechanism by which oil can be spread beneath the ice. As ice motion increases, the containment potential of the ice decreases, leading to potentially larger contamination areas. High ice velocities also increase the possibility that gas concentrations under the ice will not be sufficient to crack thick ice and will increase oil spread.

Motions of the ice in the fast ice zone are largely confined to the fall just after freezeup or after breakup in the spring. Kovacs and Weeks (1979) have observed that motions several kilometers in magnitude can occur in the fast ice soon after freezeup while the ice is thin and weak. Motions of this magnitude are due to severe storms, which are not uncommon in the fall. During the majority of the ice season, motions of the fast ice amount to a few meters (Tucker *et al.*, 1980).

A blowout in the pack ice zone is most likely to occur under a moving ice cover. The area of ice under which oil spreads will depend upon many factors: the velocity of the ice; the discharge rate of oil and gas from the blowout; the amount of gas that can escape; the diameter of the blowout plume; the roughness of and amounts of different ice types and thicknesses; and the duration of the blowout. It is possible, however, to estimate the area of moving ice that would collect oil in a typical blowout situation.

Assume that a blowout releases 5000 bbl of oil during one day. If the ratio of gas to oil is 150 to 1, then a total of 120,000 m^3 of oil and gas is released during one day. If the containment potential of the ice passing over the blowout is 30,000 m^3 km^{-2}, then 4 km^2 would be contaminated if all the gas remains beneath the ice. The length and width of the swath of oiled ice will depend upon the speed at which the ice is moving. The minimum width will be roughly the diameter of the radial currents above the plume. If this diameter is 100 m, then the ice would have to be moving faster than 40 km day^{-1} for more than 4 km^2 day^{-1} to be contaminated. Therefore, 4 $km^2 day^{-1}$ can be considered a maximum for this example. The actual area would probably be much smaller, since much of the gas would be released through thermal cracks or broken ice.

4. Ice Growth. During the fall and winter, the first-year ice over the inner continental shelf is increasing in thickness up to 10 mm day^{-1}. For a blowout lasting several days under a stationary ice cover and in the absence of large currents, this ice growth may be significant in limiting the spread of the oil. When an area of ice contains a layer or pools of gas and oil, the ice does not immediately begin growing beneath the oil. In the region near the blowout site, the heat from the warm oil or from bottom water circulated by the blowout plume will reduce ice growth or actually melt ice. Meanwhile, unoiled ice outside this region will continue growing, increasing its oil containment potential.

C. Incorporation Phase

Oil incorporated into the ice cover will vary with the ice morphology and the season. The oil may be incorporated into the new ice forming in leads, may appear on the ice surface through cracks or unconsolidated ridges to be soaked up by any snow cover, and may be frozen into existing ice by new ice growth. As a secondary form of incorporation, oiled ice may be built into ridges.

1. Oil on the Ice Surface or in Open Water. In the fall, new ice forms as a highly porous layer of ice crystals. Oil spilled underwater will rise to the surface through this porous ice and, within a few days, the ice will solidify beneath the oil, trapping it on the surface. Snow will cover most of the oil through the remainder of the ice season.

There are two differences between oil trapped above and below thin ice. The first is the presence of suspended sediments in the water during the fall freezeup period. Barnes *et al*. (1982) documented the presence of sediment-laden ice within the fast ice zone. Sediment concentrations ranged from 0.003 to 2 kg m^{-3} of ice with considerable variations in regional distribution and yearly amount. Oil in the water beneath the ice cover will have an opportunity to adhere to this suspended matter. Second, the oil on the ice surface, even when covered by snow, is subject to evaporation. The evaporation rate varies considerably, depending upon the constituent hydrocarbon fractions of the crude oil, the temperature, and exposure to the atmosphere. NORCOR (1975) measured evaporation rates as high as 25 percent within one month. This was for a Norman Wells crude on the surface during the winter with a few centimeters of snow cover. Rates decreased sharply after the first month, but a total of 30 percent or more of the oil could have evaporated by spring.

Oil that surfaces in newly opened leads or in the broken ice directly over a blowout will also have new ice growing beneath it and will be subject to weathering throughout the remainder of the winter. Oil, being less dense than sea ice, will tend to overflow the tops of cracks. Cold temperatures and an absorbent snow cover will limit the spread of the oil to a distance of approximately 1 m (NORCOR, 1975). Thereafter, the oil will spread beneath the ice.

2. *Oil Under Undeformed Ice*. Most of the oil from a winter blowout will end up beneath the ice. Gas trapped under the ice will probably escape within a day. Observations made by divers beneath first-year ice in late February and early March confirm this (Reimnitz and Dunton, 1979). In the spring, trapped air has been observed to escape through open brine channels within minutes (Barnes *et al.*, 1979).

The majority of the oil will end up as films, drops, or pools beneath the sea ice. In the absence of strong ocean currents, the oil becomes encapsulated by new ice growth. NORCOR (1975) found that the time needed to form an ice sheet below an oil lens is a function of the thermal gradient in the ice and the thickness of the oil. In the fall, a layer of new ice will completely form beneath the oil within 5 days. During the winter, that time increases to 7 days, and in the spring, 10 days.

Martin (1977) observed no traces of oil in the ice that forms beneath an oil lens. The skeletal layer in the ice above an oil lens does appear to become heavily oiled 0.04 to 0.06 m into the ice, but has been found to contain less than 4 percent (volume) of oil (Martin, 1977; NORCOR, 1975). This is equivalent to an oil film about 2 mm in depth, or about 25 percent of the equilibrium thickness of oil under thin, smooth ice.

A layer of oil beneath sea ice tends to raise the salinity of the ice above the oil and lower the salinity of the new ice directly below the oil (NORCOR, 1975). The oil layer may trap rejected brine in the ice above, or, by insulating the ice from the sea water, lower the ice temperature above the oil lens. This insulating effect also causes slow initial ice growth below the oil, which results in lower salinity ice. The high-salinity ice directly above the oil will likely accelerate the migration of oil into brine channels when the ice begins to warm, but the effect on ice growth appears to be minimal beyond the first few days (NORCOR, 1975).

The incorporation of oil into multiyear ice presumably will occur much as it does in first-year ice. Growth rates are lower under thick multiyear ice than under thinner first-year ice, but it has been postulated that a thick oil lens, as would collect under multiyear ice, will actually enhance ice growth due to convective heat transfer through the oil.

3. Oil Incorporated in Deformed Ice. Oil spilled in the fall under thin ice, or in newly refrozen leads, may be incorporated into pressure or shear ridges. Some of the oil may remain in these ridges in an unweathered state through several melt seasons. The oiled ridges can travel great distances releasing the oil along their paths, which may be advantageous since the oil would be released slowly over a greater area. This would remove the oil from the sensitive coastal regions and release it in lower concentrations elsewhere, which is desirable.

The building of large ridges does not generally occur in the fast ice zone because of the barrier islands along this part of the coast, which, along with grounded ridge systems, serve to protect the fast ice zone from effects of the pack ice. Exceptions certainly occur, especially in the Harrison Bay or Camden Bay regions during early freezeup before protective ridges become grounded.

The most common deformation in newly formed ice is rafting. Rafting will halve the area of oiled ice and double the average oil concentration under the ice. The effect of rafting will be hardly noticeable at breakup, and, due to ice growth through the winter, rafted and undeformed ice will be approximately the same thickness. Thus, in the fast ice zone, all the ice will break up and release oil at about the same time.

Outside the fast ice zone and the barrier islands lies the Stamukhi zone. This zone comprises the past, present, and future position of the active shear zone between the moving pack ice and the stationary fast ice. All observations indicate that this zone is the most heavily ridged area in the southern Beaufort Sea with ridge densities as high as 12 ridges per kilometer (Tucker et al., 1979). If, during the fall, the ice in the Stamukhi zone becomes contaminated with oil, then there is a good chance of the oiled ice becoming incorporated into a ridge. Using some typical values (an average sail height of 1.5 m; an average keel depth of 4 times the sail height; average sail and keel slopes of 24° and 33°, respectively; and a 10-percent void volume in ridges), the area of ice in a typical ridge profile is computed to be about 54 m^2. If the ice blocks in a ridge are 0.5 m thick, then to get 12 ridges in 1 km, a 2.3-km lateral extent of ice must have been deformed to a 1 km width. As a first approximation, then, more than one-half the area of ice in the Stamukhi zone becomes ridged. Of course, the problem is much more complicated than this. Many of the ridges are built from new ice grown in leads that have opened. Many ridges are much larger than the typical ridge described and are built from thinner ice. Nevertheless, the possibility of oiled ice becoming incorporated into a ridge is significant in the Stamukhi zone.

Proceeding from the Stamukhi zone out to the pack ice zone, we can make a rough estimate of the probability of oiled ice being built into a ridge. First, if the oil comes up under a large multiyear floe, there is only a small chance of it later becoming part of a ridge. Most of the ice involved in ridging has been observed to be young ice, thinner than 0.5 m (R. M. Koerner, personal communication, in Weeks *et al.*, 1971). It is possible that, when a lead opens across a multiyear floe, oil trapped in the ice nearby could drain into the open lead and later be incorporated into a ridge if the lead closes up. Kovacs and Mellor (1974) state that there is 1 to 5 percent open water in the seasonal pack ice zone. Wadhams and Horne (1978) report from 0.1 to 3.5 percent thin (ridging-prone) ice (less than 0.5 m), with a mean value of 0.9 percent. These percentages certainly vary with the time of year, especially in the fall, and also vary with the distance from shore. If we use the value of 1 to 5 percent open water and thin ice as the measure of ice available for ridging, then this is the probability of oiled ice being built into a ridge at any one time. The cumulative probability over the entire ice season will be higher, but the increasing thickness of the oiled ice will eventually reduce the possibility of its being ridged.

In the fall, a much larger percentage of the seasonal pack ice zone is covered by thin ice. While not all of this thin ice will be involved in ridging, the probability will certainly be larger than later in the winter.

D. Transportation Phase

Estimating possible motions of oiled ice in the southern Beaufort Sea is difficult due to the lack of data. Only a few buoy observations made by AIDJEX during the winter and spring of 1976 (Thorndike and Cheung, 1977) and some radar ranging by Tucker *et al.* (1980) during 1976 and 1977 in and near the fast ice exist in the public domain. These data are insufficient for making reliable predictions of ice motions. Statistics might be formulated using historic winds and ice motion models, but ice motions are strongly dependent on the strength of the ice sheet, and data on ice strength are very limited. However, the *range* of possible motions can be computed.

The fast ice lies motionless throughout most of the ice season. Measurements of fast ice motions (Tucker *et al.*, 1980) confirm its wintertime rigidity within barrier islands or grounded ridge systems. In October and November, strong winds are able to move nearshore ice. Large motions are probably not common, but one case has been reported in the literature (Kovacs and Weeks, 1979) where motions of a few kilometers were observed near shore in early November as the result of high winds. By December, the fast ice is thick enough to resist typical storms and it will remain so until breakup in June or July.

Rivers begin flooding the nearshore fast ice in late May or early June. Shore polynyas form and spread from mid-June through early July. The ice sheet becomes thinner and rotten. Sometime during July, the ice becomes weak enough that winds will cause it to move. At first, the most likely direction of motion is towards the shore polynyas, as the ice is weakest in that direction. Soon, enough open water exists that the ice can move in any direction. The winds during the summer are predominantly from the east or northeast, so typically, the ice will be driven westward and alongshore. Maximum motions are probably comparable to pack ice motions.

Grounded ridges along the outer boundary of the fast ice, in the Stamukhi zone, will sometimes remain stranded throughout the summer. If not securely grounded, they will be driven by the winds and currents. Ridged ice driven out to sea into the pack may last for several years and travel great distances.

The pack ice motion has a long-term westward trend. During the winter, there are often periods of days or weeks when no significant pack ice motion occurs. This happens when the pack is very consolidated and light winds have blown from the north or west for long periods. When the pack is unconsolidated, the ice has little or no internal resistance to wind and water forces, and it moves about freely. This condition, known as free drift, represents the maximum extreme of possible ice motion. In between the extremes of no motion and free drift, the motion depends upon the atmospheric and oceanic driving forces, the sea surface tilt, the Coriolis effect, and internal stresses transmitted through the ice. This last term is difficult to model for long periods of time, since small errors in velocity affect the distribution of ice and, thus, the ice strength, which in turn affects future velocities.

Thomas (1983) computed typical pack ice motions and standard deviatons of daily motions using historical wind data, a range of ice conditions and ocean currents, and an ice model. The model was "tuned" so that average motions corresponded to the limited observations of ice motions.

The computed trajectories showed an average westward motion of about 3.7 km day^{-1} during the fall, 1.3 km day^{-1} during the winter, 2.1 km day^{-1} during the spring, and 3.6 km day^{-1} during the summer. The standard deviation of daily motions was more than 5 km. The motions near the shore tend to be smaller than those further offshore. Along the Alaskan coast, the ice has a shoreward component of motion, but west of Point Barrow the motion turns toward the north. While the westward trend persists from month to month over many years, daily motions exhibit a great deal of meandering and back-and-forth motion in all directions.

E. Release Phase

Oil spilled in the winter beneath the sea ice is not seen to be an immediate threat to the environment. This is due to the ice itself, which contains the spill in a relatively small area away from land and insulates the oil from interacting with the ocean and the atmosphere. Eventually, the oil is released from the ice and begins to interact with and become a danger to its environs.

For first-year sea ice, this release is well understood and has been documented by NORCOR (1975), Martin (1977), and Buist *et al.* (1981). The oil trapped in first-year ice may be released by two major routes: by rising to the ice surface through brine drainage channels or by having the ice melt completely. Some oil will be released from newly opened cracks or leads. The release of oil from beneath multiyear ice probably occurs more slowly. Comfort and Purves (1980) report that, of the oil placed beneath multiyear ice in Griper Bay (Melville Island, N.W.T.), over 90 percent had surfaced at the end of two melt seasons.

1. Brine Drainage Channels. In late February or early March, the mean temperature begins to rise in the southern Beaufort Sea. As the ice begins to warm up, brine trapped between the columnar ice crystals begins to drain. Oil trapped beneath the ice will probably accelerate this brine drainage by raising the ice salinity directly over the oil. Martin (1977) observed that oil released beneath the ice during the winter migrated 0.16 m upward through brine channels by 22 February. Once the air and ice temperature approach the freezing point, the brine channels will have extended through the ice. This occurs in late April or May. Once the channels are extended to the surface and are of sufficient diameter, oil will begin appearing on the ice surface. Oil released under ice with top-to-bottom brine channels also begins to appear on the surface within an hour (NORCOR, 1975).

Flow rates must be fairly low, since it has been observed that not all the oil is released until the ice has melted down to the initial level of the oil lens (NORCOR, 1975; Buist *et al.*, 1981). An upper bound can easily be set. Oil has been observed to take about 1 hour to migrate up through about 2 m of ice with open brine channels. The brine channels were about 4 mm in diameter, so each brine channel had a maximum volume flow of 8×10^{-6} m^3 hr^{-1}. The brine channels were spaced from 0.2 to 0.3 m apart, so each square meter of ice contained about 16 brine channels, and the flow rate per square meter was about 0.0004 m^3 hr^{-1}. This is equivalent to an oil film 0.4 mm thick being released each hour. The actual flow rate probably is smaller.

Oil that surfaces through brine channels will primarily be found floating on the surfaces of melt pools. If melt pools do not exist when the oil surfaces, they soon form due to the lowering of the surface albedo. Snow forms an effective barrier to the spread of the oil, but wind and waves will splash oil onto surrounding snow, causing pools to grow in size. Oil-in-water emulsions were observed to form in the melt pools when winds were over 25 km hr^{-1}. As much as 50 percent of the oil in a melt pool could be in the form of emulsions but, generally, emulsions break down within a day after winds subside (NORCOR, 1975; Buist *et al.*, 1981).

The rates at which the oil evaporates, emulsifies, or dissolves will be considerably lower in arctic regions than they would be in lower latitudes. Not only does the ice serve to protect the oil during the winter, but, as it melts in the spring, it releases the oil slowly over periods of weeks. The ice also acts to moderate wind effects, so smaller waves and less mixing occur in melt pools and open leads. The lower temperatures also increase the stability of the oil. In general, the process that has the most significant effect on oil quantity during spring release is evaporation.

NORCOR (1975) estimated that by early June, at some test sites of the Balaena Bay experiment, 20 percent of the oil had evaporated. By 16 June, it was reported that "the flow of oil from the ice had almost completely stopped," since the ice had melted down to the trapped oil lens in most cases. More than 50 percent of the oil had evaporated by late June.

2. Surface Melting. Most of the undeformed first-year ice near shore will melt down to the oil layer during the summer months. Any oil that does not reach the ice surface through open brine drainage channels will then be released. Typically, the nearshore area first begins to open and break up around the end of June and is mostly ice free by the end of July (Barry, 1979). Oil on the ice surface (via brine channels) will accelerate ice melting and breakup by lowering the albedo. NORCOR (1975) estimated that ice contaminated by oil would break up about two weeks earlier than unoiled ice.

III. FATE OF OIL

We have seen that the vast majority of oil spilled in the Beaufort Sea during the ice season would be held in abeyance by the ice until spring, when it would begin to appear on the ice surface. The surfaced oil begins to weather and to cause accelerated melting of the ice. Typically, all the ice in the contaminated area will have melted by mid-July, at which time about 50 percent of any remaining oil will have evaporated. Emulsification, dispersion, and dissolution of the oil on the open-water surface will also occur, and silt from flowing rivers may cause the oil to become sedimented.

Until all the ice has melted, the rates at which natural processes degrade and disperse the weathered oil will be low. The release of the oil over a period of time, the reduced surface area because of confinement by the ice, and small fetches for wind energy input all contribute to the low rates. The amounts of oil removed by natural processes will be insignificant, but may have a critical effect on the ecology of the area.

Once the area becomes free of ice, conditions parallel an open-water spill. The major difference is the evaporative losses of the oil by this time. Because of prevailing winds in the southern Beaufort Sea, an open-water slick will likely be driven onshore to the west or southwest. Since the oil is partially weathered, the slick will tend to be more concentrated than a recent spill from a blowout. Southerly or easterly winds will drive the slick offshore, breaking it up and spreading oil over larger areas. Eventually, the winds will reverse, and an even larger stretch of coast is in danger of contamination.

Oil deposited upon beaches will probably be the second largest sink for hydrocarbons (after evaporation). Sedimentation to the sea bottom will also be important. Over much longer time periods, oxidation and biodegradation will dispose of small percentages of the oil.

IV. THE EFFECTS OF ICE ON CLEANUP

It is not the purpose of this report to propose or evaluate methods of oil spill cleanup in Arctic waters. It is worthwhile, however, to review the characteristics of the ice cover and oil-ice interactions that will affect cleanup activities. Again, we are only considering a major blowout and release of large quantities of oil during the ice season.

A. Pack Ice Zone

Oil from a blowout under temporarily stationary pack ice might be partially collected from the blowout site if the blowout occurs near an island or other facility that could allow pumping and storage of the oil. Burning of oil and gas during the blowout could also be partially useful if recovery is impractical. If the pack ice is moving more than a few hundred meters per day, recovery would probably be impossible and even burning would be difficult. In this case, it would be most important to ensure gas release over or near the blowout to reduce oil spread under the ice. To help locate the oiled ice in the spring when the oil begins to surface, markers and beacons could be placed near the blowout site. Then, the oiled melt pools could be ignited, probably by air-dropped incendiary devices, to dispose of some of the oil. Most of the oil and the residue from burning would remain on the ice surface or in newly opened leads. Dispersants could be used as soon as oil appears in open-water leads and polynyas. As summer proceeds and the lighter, more-toxic components evaporate, seeding with petroleumlytic microbes and fertilization could enhance biodegradation. Since the long ice season halts or slows the natural processes acting to degrade and disperse the spill, summertime activities would be important for reducing the chances of harm in future years. The environmental contamination would probably persist for several years in any case, especially since oiled ridges may be capable of retaining some oil through the summer.

B. Fast Ice Zone

A blowout and oil spill in the fast ice zone could potentially be the most harmful because this is the area in which open water first appears in the spring, but effective cleanup may be possible. The ice will not move between November or December and the following June; currents are low, so the oil will not be moved about under the ice; and the ice provides a stable work platform. Nevertheless, a large spill could cover several square kilometers. The spill area could be reduced considerably by early ice season preventive measures. These measures would be as simple as cleaning the snow from narrow strips surrounding possible blowout sites to promote faster ice growth and more under-ice containment potential. Other methods of increasing oil containment under the ice can be postulated (skirts frozen into the ice, air-bubble systems to reduce ice growth), but none of these methods are feasible until after the ice has become thick and strong enough to resist movement by the winds. Another requirement is that the ice be safe for surface travel.

The blowout will likely create an area of open water in the fast ice directly above it. Gases will escape through this opening, and a great deal of oil trapped on the water surface will be contained by the surrounding ice. This area of open water could be enlarged by blasting. If storage facilities are available, oil could be pumped directly from the pool during the blowout.

Oil from a large blowout that has been allowed to spread beneath the ice, especially early in the ice season when bottomside relief is small, will be more difficult to collect during the winter. The oil can cover a large area and will collect in many small pools beneath the ice. At the moment, no proven technology exists for locating these pools other than trial and error drilling. The negative correlation between depth of snow cover and ice thickness (Barnes *et al.*, 1979) would aid in the search. Other possibilities are being developed, but they will probably also be very labor intensive. Even when pools of oil are found, it would be virtually impossible to remove all of the oil from the ice. After new ice growth has completely encapsulated the oil lens, it will be even more difficult to remove oil from beneath the ice.

When oil begins to appear on the ice surface in the spring, concentrations will still be so low that removing the oil would be difficult. Burning the oil at this time would be much simpler and, for small spills or remnants of large spills, a significant proportion might be disposed of in this fashion. Since the oil is released from the ice over a period of weeks, burning of the oil on each melt pool will have to be done several times. It is unlikely that all the oil will surface to be burned before breakup.

C. *Stamukhi Zone*

Oil spill cleanup in this region depends on many factors. A large amount of ridge building takes place, but a grounded ridge can extend the fast ice boundary seaward. The greater bottomside relief will tend to concentrate the oil in the region inside grounded ridge systems. Oil within ridges may be impossible to clean up, since ridges may be able to hold oil for several years. This could be advantageous, since the oil would be released slowly over several seasons and over a large area as the ridges drift with the pack, reducing contamination at any one place and time. Oil trapped in deep pools behind ridge keels should be recoverable, but would require considerable effort. In this case, the distance from shore and the difficulty of surface travel would be obstacles to cleanup.

The most successful cleanup would involve concentrating oil in a small area. Since it would be difficult to enhance the bottomside relief in the Stamukhi zone, one could only hope that ridges are located to provide this concentration. If the oil is not contained by natural features, or cannot be collected directly from the blowout site, springtime burning of surfaced oil must be considered. For small amounts of oil this can be effective, but for very large spills the majority of the oil will remain. Even after cleanup and evaporation, as much as 40 to 50 percent of a large spill will remain in ridges, on unmelted ice floes, or on the water surface. If the pack retreats northward, conventional open-water cleanup methods and dispersants might remove more of the oil. If the pack remains near shore through the summer, cleanup will have to concentrate on the beaches and open-water lagoons behind the barrier islands. Release of oil from the ice is likely to occur in subsequent summers making cleanup a long-term, wide-area project.

V. SUMMARY

The events following an under-ice blowout may be divided into five phases: (1) initial, (2) spreading, (3) incorporation, (4) transportation, and (5) release. Depending upon the season, location, and duration of the blowout, several of these phases may occur simultaneously or not at all.

The initial phase of an under-ice blowout consists of the release of oil and gas from the sea floor, the rise of the oil and gas to the surface, and the initial interaction of the oil and gas with the existing ice cover. The buoyant gas and oil entrain large amounts of water while rising to the surface.

This plume and the resulting surface currents are only marginally important to the eventual fate of the oil. The turbulence at the surface may play some part in breaking up the ice over the blowout, especially when the ice cover is moving. A much more important factor is the buoyancy of the gas from the blowout. Under a stationary ice cover, this gas is almost certain to rupture the ice, allowing gas to escape to the atmosphere. Under a moving ice cover, especially for thicker multiyear ice, it is not certain that gas trapped beneath the ice will cause the ice to break. Large amounts of gas trapped beneath the ice will have a significant effect on the spread of oil under the ice. Only a limited quantity of gas is likely to remain trapped, however, due to the presence of naturally occurring thermal cracks. From theoretical studies and casual observations, these thermal cracks appear to occur frequently enough that only a small percentage of the gas from a blowout will be trapped under the ice.

The heat from the oil and bottom water circulated by the blowout plume can also be instrumental in producing an ice-free area directly over the blowout. Oil will replace the melted ice, although this may be a fairly small percentage of the total oil released. This melt hole could, however, act as a reservoir from which oil could be pumped.

It is unlikely that much oil will be deposited on the ice surface during a winter under-ice blowout. The oil will tend to overflow onto the ice wherever an opening occurs, but low air temperatures and snow on top of the ice will act to restrict the horizontal spread.

A spreading phase follows the initial phase of the blowout. This phase depends on the relative motion and concentration of oil beneath the ice layer. Factors that are particularly important during the spreading phase are the bottom roughness of the ice, ice growth, ocean currents, existing ridge keels, and the motion of the ice cover. The roughness of the underside of the ice generally provides an upper limit to the size of the under-ice slick, except under very smooth, new ice where the size of the slick is determined by the equilibrium thickness of oil under ice.

For blowouts lasting more than a few days, the spread of oil beneath the ice may be significantly restricted by the increasing thickness of the ice outside the immediate blowout vicinity. For very large blowouts, and in the absence of ice motion or large under-ice currents, this mechanism would tend to collect much of the oil in a single, relatively small, deep pool.

In the nearshore area of the Beaufort Sea, currents are generally too small during the ice season to affect oil spread. Tidal channels between barrier islands (and possibly grounded ridges) are an exception, but probably not significant in terms of area since the tidal currents are oscillatory.

Ridge keels can have a major effect on the direction and extent of oil spread. In the Stamukhi zone, ridges may be frequent enough to control the size of the under-ice slick.

Motions of the ice cover may also control the size of the slick by allowing some gas to be trapped. The amount will depend upon ice speed and thermal crack spacing.

An incorporation phase will follow the spreading phase. Oil spilled under sea ice during the winter will generally become encapsulated within the ice. This oil is protected from weathering until the ice begins to warm in the spring, releasing the oil. This is probably the most important aspect of under-ice oil spills in the Arctic. It means that spills that occur from October through May will, in effect, occur at the beginning of ice breakup. Oil is released into a limited amount of open water at a time critical to all levels of biological activity. This delay also allows time for cleanup activities between the actual and effective release of the oil.

Oil spilled outside the grounded ridges that delineate the protected fast ice zone has a relatively high chance of being incorporated into a ridge. Due to ice motion relative to a fixed boundary, a large amount of ridge building occurs in this area during periods of pack ice motion. The amount of oil and the length of time it can be held within a ridge are important questions when considering the possibility of a blowout in the Stamukhi zone.

During the transportation phase, oil trapped by bottom roughness or frozen into the ice moves with the ice cover. In the fast ice zone, transport occurs early in the ice season when the ice is thin and weak or late in the season as the ice breaks up and begins to move. Even during these times, the amount of ice motion is usually less than a few kilometers.

Significant transportation of oil by the ice takes place in the pack ice zone. The pack generally meanders to the west, and oil from a blowout will be spread over large areas in low concentrations. Differential motions of individual floes within the pack will tend to further separate oiled areas of ice.

The release phase occurs in the spring, when all the oil except possibly that trapped within ridges begins to be released from the ice. The oil is released by two means: through brine drainage channels and by the melting of the ice cover. By mid to late July, most of the oil-contaminated ice will have melted, leaving partially weathered oil on the water surface. Open-water areas and shorelines to the west, possibly as far as the Chukchi Sea, may be contaminated with oil during the summer. During the period when the oil is being released and the ice is melting and breaking up, the motion of the oil already on the water is unpredictable. The concentration of the ice cover and the motion of the ice would undoubtedly influence the motion of the oil.

Cleanup of large under-ice oil spills will be difficult in the spring, because oil will surface slowly in many separate melt pools. As soon as the oil surfaces, it begins to weather, making it difficult to burn. The continuous release and weathering of the oil makes it necessary to burn each melt pool containing surfaced oil several times. The surfaced oil also accelerates the deterioration of the ice cover, decreasing the time interval when the ice is safe for surface work. A spill covering several square kilometers will surface in thousands of separate pools. In the pack ice, these pools are likely to be spread over many kilometers.

Cleaning the oil from the water surface as the ice melts will also be difficult. Conventional open-water cleanup methods will be difficult to use until the ice concentration is low, which may be too late to prevent widespread dispersion of the oil. For small spills or remnants of large spills, a combination of burning and open-water cleanup methods might be practical.

A much safer cleanup strategy involves pumping the oil from beneath the ice during the winter or early spring. Logistically, this would be extremely difficult, unless the oil was pooled in large concentrations beneath the ice. It is unlikely that this would occur naturally, except perhaps in the fast ice zone, where ice growth can outpace oil accumulation, or in heavily ridged areas of the Stamukhi zone. However, in the fast ice zone, an effective preventive measure would be to create under-ice reservoirs by artificially redistributing snow in areas where blowouts might occur. In the pack ice, this procedure would be impractical due to ice motion.

REFERENCES

Aagaard, K. (1981) "Current Measurements in Possible Dispersal Regions of the Beaufort Sea," *Environmental Assessment of the Alaskan Continental Shelf, Final Reports of Principal Investigators, Vol. 3, Physical Science Studies*, NOAA/OSCEAP, Boulder, Colorado, pp. 1-74.

Ackley, S. F., Hibler W. D. III, Kugzruk, F. K., Kovacs, A., and Weeks, W. F., (1974) "Thickness and Roughness Variations of Arctic Multi-Year Sea Ice," *AIDJEX Bulletin No. 25*, University of Washington, Seattle, pp. 75-96.

Barnes, P., Reimnitz, E., Toimil, L., and Hill, H. (1979) *Fast Ice Thickness and Snow Depth in Relation to Oil Entrapment Potential, Prudhoe Bay, Alaska*, U.S. Geol. Survey Open-File Report 79-539, Menlo Park, California.

Barnes, P. W., Reimnitz, E., and Fox, D. (1982) "Ice Rafting of Fine-Grained Sediment, a Sorting and Transport Mechanism, Beaufort Sea, Alaska," *J. Sedimentary Petrology* 52 (2), 493-502.

Barry, R. G. (1979) "Study of Climatic Effects on Fast Ice Extent and its Seasonal Decay Along the Beaufort-Chukchi Coasts," *Environmental Assessment of the Alaskan Continental Shelf, Final Reports*, NOAA/OCSEAP, Boulder, Colorado, Vol. 2. Physical Science Studies, pp. 272-375.

Buist, I. A., Pistruzak, W. M., and Dickins, D. F. (1981) "Dome Petroleum's Oil and Gas Undersea Ice Study," *Proceedings of the Fourth Arctic Marine Oilspill Program Technical Seminar*, Edmonton, Alberta, June 16-18, 1981, pp. 647-686.

Comfort, G. and Purves, W. (1980) "An Investigation of the Behavior of Crude Oil Spilled under Multi-year Ice at Griper Bay, N.W.T.," *Proceedings of the Third Annual Marine Oilspill Program Technical Seminar*, Edmonton, Alberta, June 3-5, 1980, pp. 62-86.

Cox, J. C., and Schultz, L. A. (1981) "The Mechanics of Oil Containment Beneath Sea Ice," *Proceedings of the Fourth Arctic Marine Oilspill Program Technical Seminar*, Edmonton, Alberta, June 16-18, 1981, pp. 3-44.

Cox, J. C., Schultz, L. A., Johnson, R. P., and Shelsby, R. A. (1981) "The Transport and Behavior of Oil Spilled In and Under Sea Ice," *Environmental Assessment of the Alaskan Continental Shelf, Final Reports of Principal Investigators*, NOAA/OCSEAP, Boulder, Colorado, Vol. 3, Physical Science Studies, pp. 427-597.

Deslauriers, P. C. (1979) "The *Bouchard No. 65* Oil Spill in the Ice-Covered Waters of Buzzards Bay," *J. Petroleum Technology, 31*, 1092-1100.

Evans, R. J., and Untersteiner, N. (1971) "Thermal Cracks in Floating Ice Sheets," *J. Geophys. Res.* 76 (3), 694-703.

Kovacs, A. (1977) "Sea Ice Thickness Profiling and Under-Ice Oil Entrapment," *Proceedings 1977 Offshore Technology Conference*, Houston, Texas, Vol. III, pp. 547-554.

Kovacs, A. (1979) "Oil Pooling Under Sea Ice," *Environmental Assessment of the Alaskan Continental Shelf, Annual Reports*, Vol. VIII. Transport, pp. 310-353.

Kovacs, A., and Mellor, M. (1974) "Sea Ice Morphology and Ice as a Geologic Agent in the Southern Beaufort Sea," *The Coast and Shelf of the Beaufort Sea*, (C. Reed and E. Slater, eds.), Arctic Institute of North America, Arlington, Virginia, pp. 113-162.

Kovacs, A., and Morey, R. M. (1978) "Radar Anisotropy of Sea Ice Due to Preferred Azimuthal Orientation of the Horizontal C Axes of Ice Crystals," *J. Geophys. Res.* 83 (C12), 6037-6046.

Kovacs, A., Morey, R., Cundy, D. and Dicoff, G. (1981) "Pooling of Oil Under Sea Ice," *Proceedings Port and Ocean Engineering Under Arctic Conditions*, Quebec, Canada, Vol. II, pp. 912-922.

Kovacs, A., and Weeks, W. F. (1979) "Dynamics of Near-Shore Ice," *Environmental Assessment of the Alaskan Continental Shelf, Annual Reports*, NOAA/OCSEAP, Boulder, Colorado, Vol. VII, Transport, pp. 181-207.

Lewis, E. L. (1976) *Oil in Sea Ice*, Pacific Marine Science Report 76 12, Institute of Ocean Sciences, Patricia Bay, Victoria, B.C.

Logan, W. J., Thornton, D. E., and Ross, S. L. (1975) *Oil Spill Counter Measures for the Beaufort Sea*, Appendix, Beaufort Sea Technical Report No. 31b, Beaufort Sea Project, Dept. of the Environment, Victoria, B.C.

Malcolm, J. D., and Cammaert, A. B. (1981) "Movement of Oil and Gas Spills Under Sea Ice," *Proceedings Port and Ocean Engineering Under Arctic Conditions*, Quebec, Canada, Vol. II, pp. 923-936.

Martin, S. (1977) *The Seasonal Variation of Oil Entrainment in First Year Sea Ice: A Comparison of NORCOR/OCS Observations*, Dept. of Oceanography, Spec. Report #71, University of Washington, March.

Matthews, J. B. (1980) "Observations of Surface and Bottom Drifter Movements in the Beaufort Sea Near Prudhoe Bay, Alaska," Submitted to *J. Geophys. Res.*

Milne, A. R., and Herlinveaux, R. H. (n.d.) *Crude Oil in Cold Water* (R. J. Childerhose, ed.), Beaufort Sea Project, Institute of Ocean Sciences, Sidney, B.C.

NORCOR Engineering and Research, Ltd. (1975) *The Interaction of Crude Oil with Arctic Sea Ice*, Beaufort Sea Technical Report #27, Beaufort Sea Project, Dept. of the Environment, Victoria, B.C.

NORCOR Engineering and Research, Ltd. (1977) *Probable Behavior and Fate of a Winter Oil Spill in the Beaufort Sea*, Technology Development Report EPS-4-EC-77-5, Environmental Impact Control Directorate.

Reimnitz, E., and Dunton, K. (1979) "Diving Observations on the Soft Ice Layer Under the Fast Ice at DS11 in the Stefansson Sound Boulder Patch," *Environmental Assessment of the Alaskan Continental Shelf, Annual Reports*, NOAA/OCSEAP, Boulder, Colorado, Vol. IX. Hazards, pp. 210-230.

Reimnitz, E., Toimil, L. J., and Barnes, P. (1977) "Arctic Continental Shelf Processes and Morphology Related to Sea Ice Zonation, Beaufort Sea, Alaska," *AIDJEX Bulletin No. 36*, University of Washington, Seattle, pp. 15-64.

Rosenegger, L. W. (1975) *Movement of Oil Under Sea Ice*, Beaufort Sea Technical Report No. 28, Beaufort Sea Project, Dept. of the Environment, Victoria, B.C.

Ruby, C. H., Ward, L. G., Fischer, I. A., and Brown, P. J. (1977) "Buzzards Bay Oil Spill - An Arctic Analogue," *Proceedings Fourth International Conference on Port and Ocean Engineering Under Arctic Conditions*, St. John's, Newfoundland, pp. 844-855.

Stringer, W., and Weller, G. (1980) "Studies of the Physical Behavior of Oil in Ice," *Proceedings of the Third Annual Marine Oilspill Program Technical Seminar*, Edmonton, Alberta, June 3-5, pp. 31-44.

Thomas, D. R. (1983) "Potential Oiled Ice Trajectories in the Beaufort Sea," Flow Research and Technology Report No. 252, Flow Industries, Kent, Washington.

Thorndike, A. S., and Cheung, J. Y. (1977) "AIDJEX Measurements of Sea Ice Motion, 11 Apr 1975 to 14 May 1976," *AIDJEX Bulletin No. 35*, January, University of Washington, Seattle.

Topham, D. R. (1975) *Hydrodynamics of an Oil Well Blowout*, Beaufort Sea Technical Report No. 33, Beaufort Sea Project, Dept. of the Environment, Victoria, B.C.

Topham, D. R. (1977) "The Deflection of an Ice Sheet by a Submerged Gas Source," *J. Appl. Mech.*, June, 279-284.

Topham, D. R., and Bishnoi, P. R. (1980) "Deep Water Blowouts," *Proceedings of the Third Annual Marine Oilspill Program Technical Seminar*, Edmonton, Alberta, June 3-5, 1980, pp. 87-95.

Tucker, W. B., Weeks, W. F., and Frank, M. (1979) *Sea Ice Ridging Over the Alaskan Continental Shelf*, CRREL Report 79-8, Hanover, New Hampshire.

Tucker, W. B., Weeks, W. F., Kovacs, A., and Gow, A. J. (1980) "Nearshore Ice Motion at Prudhoe Bay, Alaska," *Sea Ice Processes and Models*, (R. S. Pritchard, ed.), University of Washington Press, Seattle, pp. 261-272.

Wadhams, P., and Horne, R. (1978) *An Analysis of Ice Profiles Obtained by Submarine Sonar in the AIDJEX Area of the Beaufort Sea*, Scott Polar Research Institute Technical Report 78 1, Cambridge.

Weeks, W. F., and Gow, A. J. (1980) "Crystal Alignment in the Fast Ice of Arctic Alaska," *J. Geophys. Res.* 85 (C2), 1137-1146.

Weeks, W. F., Kovacs, A., and Hibler W. D. III, (1971) "Pressure Ridge Characteristics in the Arctic Coastal Environment," *Proceedings 1st International Conference on Port and Ocean Engineering under Arctic Conditions*, Trondheim, Norway, Vol. I, pp. 152-183.

ACTIVITY-DIRECTED FRACTIONATION
OF PETROLEUM SAMPLES

by

J. S. Warner and W. L. Margard
Battelle Columbus Laboratories

and

J. W. Anderson

Battelle Pacific Northwest Laboratories
Marine Research Laboratory

Final Report
Outer Continental Shelf Environmental Assessment Program
Research Unit 500

October 1979

TABLE OF CONTENTS

LIST OF FIGURES

LIST OF TABLES

SUMMARY

A fractionation and bioassay scheme was developed that can be applied to oil samples to assess the potential biological hazards of the various components that remain after an oil spill. The fractionation procedure involves solvent partitioning between heptane and acetonitrile, gel permeation chromatography using Bio-Beads S-X8, and silica gel chromatography. The first two steps are effective in removing intractable components that otherwise interfere with bioassay studies. Two *in vitro* bioassay tests and an *in vivo* test were studied to assess toxicity and mutagenicity of oil fractions. These were (1) the Ames bacterial mutagenicity test, (2) a mammalian-cell toxicity test, and (3) a mysids toxicity test. All three tests can be run using no more than a total of 30 mg of material.

In the course of developing the fractionation and bioassay protocol, samples of fresh Prudhoe Bay crude oil, weathered Prudhoe Bay crude oil, and shale oil were fractionated and bioassayed. The bioassay data obtained indicated that the aromatic hydrocarbon fractions are the most toxic fractions and probably represent the greatest biological hazard of any fraction in an oil spill situation. Some of the aromatic hydrocarbon fractions had toxicities comparable to those of phenanthrene and 1-methylpyrene used as reference materials. Some of the polar oil fractions were also shown to be toxic and slightly mutagenic. The shale oil fractions were often more toxic or mutagenic than the crude oil fractions. The weathered crude oil contained less volatiles and somewhat more polar components than the fresh crude oil. The fractionation and bioassay protocol that finally evolved from the study needs to be applied to the three oils to obtain more definitive information on the potential biological hazard of the polar fractions.

INTRODUCTION

A. General Nature and Scope of Study

Studies on the biological effects of petroleum and the associated chemical analyses have generally concentrated on the hydrocarbon components that can be readily analyzed by gas chromatography. The aromatic hydrocarbons have been of major interest interest because many of them, e.g. benzenes, naphthalenes, and phenanthenes, are quite toxic while others, e.g. benzo(a)pyrene, are mutagenic and carcinogenic. Petroleum, however, is comprised of many other components including nonvolatile and polar components that can not be analyzed for by the usual GC procedures.

In a highly weathered crude oil major amounts of the hydrocarbons have been lost by dissolution. evaporation, microbiological degradation, or photochemical degradation. Many of the components that remain are not amenable to analysis by gas chromatography because they are too nonvolatile or too polar. Nevertheless, any program concerned with the long-term biological effects of oil spills ought to consider such components. Perhaps some of the nonvolatile or polar components are toxic or mutagenic and should be studied in monitoring programs. On the other hand such components may have no significant biological effects and should be ignored. However they should not be ignored until there is experimental evidence indicating that they are indeed inactive. They shouldn't be ignored simply because they are not detectable by the usual analtyical methods.

This research program was undertaken as an effort to determine whether any of the nonvolatile and polar nonhydrocarbon components are toxic or mutagenic and thus represent a biological hazard in an oil spill situation. The program plan involved fractionation of oil into various hydrocarbon fractions and nonhydrocarbon fractions followed by bioassays to detect any toxicity or mutagenicity. Those fractions exhibiting activity would be subfractionated and the subfractions checked by bioassays. More extensive bioassay and chemical characterization studies would be directed to the active subfractions, hence, the term "activity-directed" fractionation. The program involved primarily a study of fresh and weathered Prudhoe Bay crude oil.

B. Specific Objectives

1. Develop procedures for fractionating and isolating the nonhydrocarbon components of crude oil.

2. Determine the toxicity and mutagenicity of nonhydrocarbon oil fractions using bioassay screening procedures amenable to small amounts of sample.

3. Characterize the active nonhydrocarbon oil fractions.

C. Relevance

The program involved the use of Prudhoe Bay crude oil, the oil most apt to be involved in any oil spill in the Alaskan environment. The weathering was performed in an Alaskan environment to simulate the weathering processes that would occur in an Alaskan oil spill. Since the possible biological activity of nonhydrocarbon components in oil has been largely ignored in the OCSEAP program, demonstration of significant toxicity or mutagenicity in nonhydrocarbon fractions associated with Alaskan-weathered Prudhoe Bay crude oil would need to be considered in the design of any continuing OCSEAP monitoring programs.

EXPERIMENTAL APPROACH

The original design of the program was based on the concept of activity-directed fractionation. Oil was to be fractionated into a dozen fractions or so, bioassay tests would be run to determine which fractions were toxic or mutagenic, those fractions that showed activity would be subfractionated, bioassay tests would be run on the subfractions, and the process of subfractionation of active fractions followed by bioassay would be continued until subfractionation no longer increased the activity per unit weight. The inactive fractions and hydrocarbon fractions obtained would be ignored and the final active nonhydrocarbon fractions would be characterized chemically as well as for biological activity. An effort would be made to account for all of the oil, i.e. obtain a mass balance, so that no potentially active fractions would be overlooked.

Three major inherent problems seriously interfered with the success of the original program design. One problem involved solubility — the problem of how to get highly water-insoluble components of oil into an aqueous medium required for bioassay. A second problem was the partial volatility of the oil which made it difficult to obtain reliable residue weights and therefore prevented a good mass balance from being achieved. The third problem was the insensitivity of the bioassay screening methods, especially the Ames mutagenicity assay, which meant that in the initial fractionation even those fractions containing active components would be so diluted by inactive components that no activity would be detected. This meant that all of the fractions would appear inactive and no direction would be given to the subfractionation.

Solubility Problem

The solubility problem was not an unexpected problem but one which had to be dealt with somehow. The problem had three facets. A medium was needed that would (1) dissolve or disperse the oil fraction (2) keep the oil fraction dispersed in the aqueous bioassay media, and (3) be nontoxic to the bioassay organisms.

Organic solvents such as tetrahydrofuran, benzene, pyridine, and methylene chloride were found to be good solvents for the oil fractions and were sufficiently water soluble but were too toxic. Dimethyl sulfoxide and acetone were not toxic and therefore were satisfactory for the bioassay but would not dissolve many of the oil fractions. Numerous other solvents, mainly alcohols and ketones, were investigated and the best ones found were cyclohexanone and cyclohexanol. These two were good oil solvents, sufficiently water-soluble, and less toxic than tetrahydrofuran. However, they were still too toxic and although the oil fractions dissolved in the solvents as soon as the solutions were mixed with aqueous bioassay media the oil fractions separated out.

Several dispersants were studied in an effort to keep the oil fractions dispersed in the bioassay media. The dispersants were selected for low toxicity and included glyceryl monooleate, lecithin, nonylphenoxypolyethoxyethanol, and Corexit. None was effective in the *in vitro* bioassays. In addition to being ineffective, the dispersants interfered with the mammalian cell toxicity assay by causing the cells to become detached from the assay plate.

Because of the problem of at least partial insolubility of some of the oil fractions and the inability to disperse them completely, the plan of attempting to account for the potential biological activity of all fractions was changed to a plan for studying only those fractions that would dissolve in dimethyl sulfoxide (DMSO). This change was justified on the basis that practically all known biologically-active organic compounds are at least slightly soluble in DMSO, or, from a more fundamental standpoint, if a component does not dissolve at least slightly in DMSO it is unlikely that it can pass into a cellular system to exert a biological effect.

Volatility Problem

The partial volatility of crude oil affects the accuracy of residue weights and therefore interferes with efforts to achieve a mass balance. In evaporating oil solutions, the oily residue acts as a keeper for the solvent as well as a keeper for the more volatile oil components. The ideal case would be one in which the amount of solvent remaining after evaporation were equal to the amount of volatile oil components lost so that the residue weight observed would fortuitously be equal to what might be called the true residue weight. However as the viscosity and volatility of the oil components vary from fraction to fraction the errors in residue weight determinations will vary considerably. In most cases the residue weight observed was less than the expected true residue weight.

In an effort to decrease the amount of volatile oil components lost during residue weight determinations and thereby improve the mass balance, some of the more volatile components were removed by reduced pressure distillation. The percent of total oil removed in this manner was quite arbitrary and depended upon the distillation conditions. This approach helped considerably in obtaining residue weights that were closer to the expected values but even so they could only be considered as approximations. In most of the fractionation steps prior removal of volatiles was not used and recoveries based on residue weights were frequently about 85 percent. The 15% discrepancy could represent material that was not recovered or could simply represent errors in the residue weight determinations.

Insensitivity of Ames Test

The problem of the insensitivity of the Ames test can be evaluated on the basis of its theoretical ability to detect benz(a)pyrene (BaP) in crude oil. The detection limit for BaP in the Ames test is about 1 μg. The amount of BaP that can be expected in crude oil is about 1 μg/g. If BaP were the only mutagen present in the crude oil, all of the BaP in one gram of oil would need to be added to an Ames test plate in order for any mutagenicity to be detected. However, the maximum amount of sample that can be accommodated by an Ames plate is about 1 mg (0.1 ml of a 1% solution in DMSO). This means that the 1 μg of BaP in 1 g of oil has to be concentrated by a factor of 1000 before it can be detected by the Ames test. If all fractions contained equal amounts of material, the crude oil would have to be fractionated into at least 1000 fractions and all of the BaP would have to be in just one of those fractions before any mutagenicity would be detected. These quantitative considerations are summarized in Table 1.

TABLE 1. QUANTITATIVE CONSIDERATIONS OF THE AMES TEST

PREMISE 1:	BaP Concentration In Crude Oil = 1 μg/g
PREMISE 2:	BaP Is Only Mutagen In Crude Oil
PREMISE 3:	Limit Of Detection of BaP In Ames Test = 1 μg
CONCLUSION 1:	All Of The BaP In 1 g Of Crude Oil Must Be Added To Ames Test To Be Detectable
PREMISE 4:	Maximum Amount Of Sample Accommodated By Ames Test = 100 μl Of 1% Solution = 1 mg
CONCLUSION 2:	Crude Oil Must Be Fractionated In A Manner That Gives A 1000-Fold Concentration Factor for BaP
PREMISE 5:	All Fractions Contain Equal Amounts Of Material
CONCLUSION 3:	Crude Oil Must Be Fractionated Into At Least 1000 Fractions And All Of The BaP Must Be In One Of Those Fractions Before Any Mutagenicity Will Be Detected

The above considerations demonstrated that the concept of initially fractionating the oil into only a dozen or so fractions and using bioassay activity to direct subsequent subfractionations could not be applied successfully. Therefore, the approach was changed to provide for a number of fractionations before applying bioassay tests. Most of the final fractions contained only 1-2 mg of residual material per gram of oil. Much of the total oil was discarded in DMSO-insoluble fractions, high-molecular-weight fractions, or hydrocarbon fractions. A few fractions contained 5-25 mg of residual material per gram of oil. Because of the fractions discarded and the few fractions containing relatively large amounts of material, the total number of fractions obtained was only bout 45 instead of 1000.

A problem associated with the insensitivity of the bioassay tests was that of scaling up fractionation procedures to provide enough of a fraction for replicate bioassays under different conditions. The scaled up procedures used permitted 10 g of oil to be processed. Fractions which contained only 10-20 mg of material could only be assayed once. More attention was therefore given to fractions containing 50-250 mg of total residual material.

Fractionation Scheme

Several different fractionation schemes were investigated during the course of the program. Initial fractionation schemes involved vacuum-stripping of volatiles as discussed above, separation of pentane-insolubles (asphaltenes), and silica gel chromatography of the pentane solubles. Subsequent subfractionation was to be achieved by gel permeation chromatography and HPLC using reverse-phase systems. The eluting solvents used for successive elutions in the silica gel chromatography were petroleum ether, 20 percent methylene chloride in petroleum ether, methylene chloride, and acetonitrile. This elution scheme suffered from the fact that acetonitrile, like DMSO, is not a very good solvent for many of the oil fractions and thus retarded rather than accelerated the elution of components from silica gel.

Tetrahydrofuran (THF), a highly polar solvent and an excellent solvent for all oil fractions, was substituted for acetonitrile. Ideally, the fractions eluted with THF could be concentrated and assayed directly. However, as described above, THF was too toxic to the assay organisms. It was also found that concentration of fractions and blanks to an oil for solvent exchange resulted in relatively large amounts of residual material that could be attributed to the THF. This material contained peroxides and peroxide decomposition products. Its presence could be avoided by the use of THF containing an antioxidant, usually a phenolic compound, or by redistillation immediately before use. The addition of an antioxidant to the system was not at all desirable. Redistillation would help; however the chromatographic process took several days and significant peroxide formation can occur during that length of time. Because of these various problems, THF was discontinued as an eluting solvent.

The fractionation scheme that finally evolved from the program is summarized in Figure 1. The scheme involved solvent partitioning to remove the bulk of the nonpolar material that is not soluble in DMSO, gel permeation chromatography to remove polymeric material, and silica gel chromatography to fractionate on the basis of polarity.

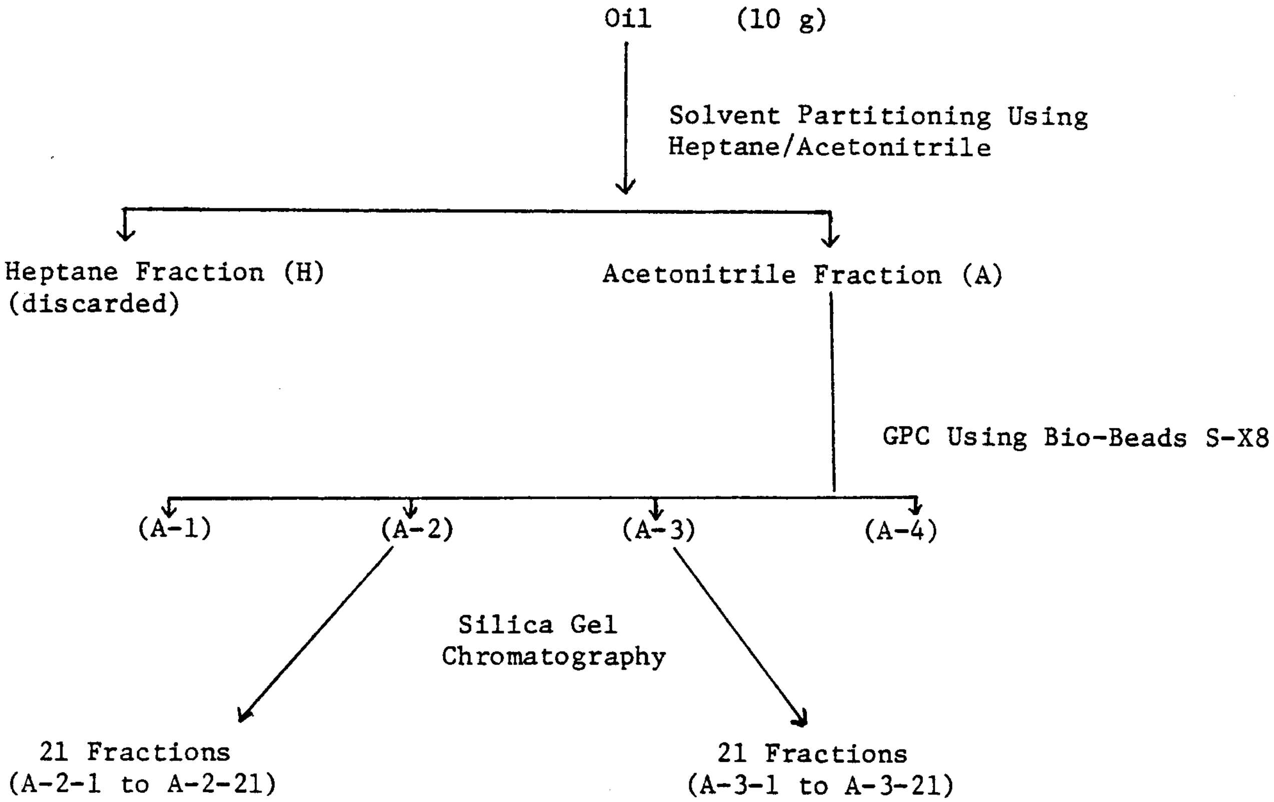

FIGURE 1. OIL FRACTIONATION SCHEME

Heptane/acetonitrile partitioning was found to simulate heptane/DMSO partitioning very well and had the added advantage of giving an extract (acetonitrile) that could be readily concentrated directly. The partitioning step removed about 75% of the oil as acetonitrile-insoluble material and thus reduced considerably the amount of material to be processed by the next step. Of even greater importance, the partitioning removed most of the DMSO-insoluble material that could not be accommodated by the bioassays.

The gel permeation chromatography (GPC), also referred to as size exclusion chromatography, separates components primarily on the basis of molecular size. Sephadex LH-20, a modified dextran material, was tried initially for this step with various solvent systems, e.g. isopropanol and methylene chloride, but so much irreversible adsorption resulted that the column could not be reused. Bio-Beads S-X8, a styrene-divinylbenzene copolymer, worked very well with methylene chloride as the eluting solvent. The oil extracts were fractionated into four fractions. The first fraction contained the long-chain and polymeric material which accounted for most of the dark color. The last fraction contained small compact polynuclear compounds. The bulk of the material was in the two center fractions which accounts for the molecular-size range of most biologically-active organic compounds.

The final fractionation step, adsorption chromatography, used silica gel that was partially deactivated by 10% methanol in ethylene dichloride. This solvent in addition to deactivating the column served as a highly polar wash solvent for removing contaminants from the silica gel. Prior to use the column was partially reactivated by stepwise elution with ethylene dichloride followed by hexane. The elution scheme used is shown in Table 2.

TABLE 2. ELUTION SCHEME FOR SILICA GEL FRACTIONATION

Fraction No.	Eluting Solvent
1-7	Hexane
8-12	10% Ethylene Dichloride in Hexane
13-16	Ethylene Dichloride
17-21	10% Methanol in Ethylene Dichloride

25 mm ID x 1200 mm upward flow column
350 g silica gel, Davison Grade 923
10 ml/min elution rate
250 ml fractions

The column could be regenerated and used a number of times for fractions that had been cleaned up by solvent partitioning and GPC. The elution solvents used in the scheme are stable materials that can be readily obtained in high purity and readily concentrated.

The above fractionation scheme was applied to both fresh and weathered Prudhoe Bay crude oil. Shale oil* from a simulated in situ process was generously supplied by Dr. Richard Poulson of the Laramie Energy Technology Center and was

* The designation by LETC was ES-77-209, Run 16, dry.

fractionated for comparison. The major fractions obtained were evaluated by bioassay tests, namely the Ames mutagenicity test, a mammalian cell toxicity test, and/or a mysids toxicity test.

METHODS

Weathering

The weathered crude oil used in the program was prepared by Dr. Stanley Rice of Auke Bay Fisheries Laboratories in Auke Bay, Alaska. A 9.5-liter sample of Prudhoe Bay crude oil was poured into a 1.2 m x 1.2 m pine board open retainer moored in Auke Bay from July 12, 1976, to September 14, 1976. The exposure permitted weathering by evaporation, dissolution, photochemical oxidation, and microbiological degradation and thus simulated oil spill conditions in an Alaskan environment.

The depth of the oil slick was initially 6 mm. A 1-liter sample was taken on August 16 and used for all fractionation studies involving weathered oil. Small samples, 100 ml each, were also collected on August 2, August 13, August 31, and September 14. All samples were stored at -20°C.

Pentane Solubility

Twelve grams of crude oil was mixed with 600 ml of n-pentane and the resulting suspension was centrifuged at 1500 rpm. The supernatant, pentane soluble fraction, was saved and the precipitate was resuspended in 50 ml of n-pentane and centrifuged. The supernatant from this wash was combined with the previous supernatant. The precipitate, pentane insolubles, was dried in a vacuum desiccator and weighed. Fresh crude oil gave 3.0% pentane insolubles and the weathered oil gave 4.6% pentane insolubles.

Vacuum Stripping

Rotating Evaporator Procedure

Twenty grams of fresh crude oil was placed in a 100-ml round-bottom flask and attached to a rotating evaporator that was fitted with a receiving trap cooled in a Dry Ice-acetone bath. Stripping of volatiles was achieved by heating the rotating flask in a water bath at 90°C for a 10-hour period while applying a reduced pressure of about 25 mm using a water aspirator. The volatiles collected amounted to 17% of the starting oil. GC analysis of the volatiles and the residual oil indicated that most of the components with boiling points up to the C_3-benzenes had been stripped off but most of the naphthalene and alkylnaphthalenes remained in the residue oil.

Distillation Column Procedure

Fifty grams of fresh crude oil was placed in a 100-ml distillation flask fitted with a thermometer, a magnetic stirrer, and a 150 mm x 9 mm O.D. Vigreaux column having a distilling head that led to a receiving trap cooled in a Dry Ice-acetone bath. The flask was heated with a heating mantle and reduced pressure was applied using a vacuum pump. Distillation was achieved at 0.06 mm by heating to give a pot temperature of up to 150°C. The head temperature rose to 100°C under these conditions and then dropped when no more distillate was obtained. The distillate collected amounted to 32% of the starting oil. GC analysis indicated that although the majority of the methylnaphthalenes appeared in the distillate, a significant amount still remained in the residual oil.

Acid Extraction

One hundred grams of fresh crude oil in 400 ml of hexane was stirred with 500 ml of 2N H_2SO_4 for 20 hours. The mixture was then transfered to a separatory funnel and allowed to settle for 3 hours. The aqueous layer was withdrawn, washed with 100 ml of hexane, neutralized to pH 7.2 with 4N NaOH and back extracted three times with 200-ml portions of methylene chloride. The combined methylene chloride extracts were dried with anhydrous sodium sulfate and concentrated to 5 ml on a rotating evaporator. Residue weights obtained on 100-μl aliquots of the concentrated extract indicated that the total acid extractable components amounted to about 0.04% of the starting oil.

Solvent Partitioning

Ten grams of oil was placed in a 1.8 l glass jug with 100 ml of heptane and 500 ml acetonitrile. The heptane was equilibrated with acetonitrile and the acetonitrile equilibrated with heptane prior to use. The mixture was shaken vigorously on a mechanical for one hour and transfered to a 1-liter separatory funnel with a Teflon stopcock for separation of the phases. The acetonitrile layer was withdrawn and the heptane layer was reequilibrated with another 500 ml of acetonitrile. This was repeated three more times to give five successive acetonitrile extracts. Each extract was concentrated to an oil using a rotating evaporator and taken up in 10 ml of methylene chloride. A 0.05 ml aliquot of each methylene chloride solution was evaporated to determine the residue weight. The solutions were then combined and concentrated to 5-10 ml for subsequent GPC fractionation.

Partitioning using other solvents was performed in a similar manner.

Solvent Exchange

Solvent exchange with a higher-boiling volatile solvent was accomplished using a vortex evaporator by simply concentrating to a small volume, adding a 5-fold volume of the higher boiling solvent and reconcentrating to a small volume. This work well, for example, for replacing ethylene dichloride with heptane prior to silica gel fractionation.

Solvent exchange of a volatile solvent with a nonvolatile solvent was not very complete because the nonvolatile solvent did not distil to permit removal of the last traces of the volatile solvent by codistillation. However, the complete removal of the relatively toxic volatile solvent, ethylene dichloride, from solutions in a nonvolatile solvent, DMSO, was very important in preparing solutions for bioassay. To avoid the presence of ethylene dichloride in DMSO solutions, the ethylene dichloride was exchanged with heptane, a much less toxic solvent, prior to the addition of DMSO. The heptane was then stripped from the DMSO on a vortex evaporator at 60°C with the full vacuum of an aspirator. GC analysis showed that the resulting DMSO solutions contained less than 10 ppm of ethylene dichloride.

GPC Fractionation

Gel permeation chromatography (GPC) was used to fractionate oil primarily on the basis of molecular size. The GPC column was prepared by packing a 750 mm x 25 mm I.D. upward flow chromatography column with 150g of Bio-Beads S-X8 that was preswelled in methylene chloride. The inlet end (bottom) of the column was connected to a Rheodyne Model 7105 injector valve with a 1-ml sample loop and to an Altex Model 110 pump that maintained the solvent flow at 2 ml/min. The column inlet pressure was 15 psi at that flow rate. The void volume of the column was 116 ml. The efficiency of the column was shown to be about 2500 theoretical plates by injecting 0.15 mg of di-n-octyl phthalate and monitoring with a UV detector at 254 nm.

Up to 500 mg of oil in 1 ml of ethylene dichloride solution was fractionated in a single run. All components were eluted within 175 minutes (350 ml). In most cases four fractions were collected, 0-70 min, 70-110 min, 110-130 min, and 130-175 min. Most of the color eluted in the first fraction. The column was used repeatedly and no significant change in column efficiency or retention time for di-n-octyl phthalate was observed.

Silica Gel Fractionation

A 1.2 m x 25 mm I.D. chromatography column set up for upward flow operation was slurry-packed with 350g of Davison Grade 923 silica gel that was activated by heating at 150°C overnight and deactivated by shaking with 1000 ml of 1:9 methanol:ethylene dichloride. The column was fitted with a Rheodyne Model 7105 injection valve that had a 5-ml sample loop. A constant solvent flow rate was achieved by using an Altex Model 110 pump.

The column was rinsed and equilibrated with 1:9 methanol:ethylene dichloride at a flow rate of 1 ml/min for 20 hours. It was then equilibrated with ethylene dichloride for two hours at 5 ml/min, with 1:9 ethylene dichloride:hexane for two hours at 5 ml/min, and finally with hexane for 20 hours at 1 ml/min.

The sample to be fractionated, up to 1.4 g, was dissolved in heptane and centrifuged to remove any insoluble components. The heptane solution was injected onto the column in two 5-ml injections with approximately one minute between injections. The injector loop outlet flow and sample container rinse combined, approximately 4 ml, was injected as a third injection. The heptane insolubles were dissolved in ethylene dichloride and injected later when elution with ethylene dichloride was begun.

The column was eluted at a flow rate of 10 ml/min with 1400 ml of hexane, followed by 1400 ml of 1:9 ethylene dichloride:hexane, followed by 900 ml of ethylene dichloride, and finally with 1400 ml of 1:9 methanol:ethylene dichloride. Fractions were collected every 25 minutes (250 ml each).

Each fraction was concentrated to an oil in a rotating evaporator at 30°C and taken up in several portions of methylene chloride to a volume of 10 ml. A 50-μl aliquot of each fraction was used for residue weight determinations.

Salmonella Mutagenicity Assay

Mutagenicity was determined by the Ames test in which the sample was incubated with a histidine-dependent strain of Salmonella bacteria in a histidine-deficient culture medium. Mammalian (rat) liver microsomes containing hydroxylase systems were added in an effort to convert certain inactive compounds to active mutagens. Benz(a)pyrene is an example of a known carcinogen that requires such microsomal activation in order for it to exert a mutagenic affect. The Ames test can be run with an without microsomal activation in order to differentiate between compounds that are mutagenic as such and those that require activation. However compounds which are mutagenic in the absence of microsomes are generally also active in the presence of microsomes and therefore, in using the test as a screening procedure, microsomes were added to all of the plates in this program.

Solvent control plates treated with solvent alone and positive control plates treated with known carcinogens, e.g. benz(a)pyrene and 2-aminoanthracene, were used to provide reference data against which activity of test substances could be compared. Sterility control checks were also run for each test sample using nutrient agar.

Whenever a compound or fraction is toxic to the bacteria and kills all of the organisms at the level being tested it will not give any mutagenic activity even though it might be mutagenic at a lower dosage level. Therefore, when using the Ames test as a screening procedure at one dosage level, it is necessary to assess the toxicity of the sample in order to avoid false negatives. Salmonella toxicity tests were run on all samples screened on the program.

Three different Salmonella typhimurium tester strains were used for the program, TA-98, TA-100, and TA-1537. These are all strains that have been developed for their ability to be reverted back to the histidine-producing wild type by particular mutagens, however they differ in their sensitivity and specificity to different mutagens.

Liver Microsome Preparations

The activation system for the mutagenesis screening consisted of Arochlor 1254-induced microsomes derived from rat livers. Induction was accomplished by a single interperitoneal injection of Arochlor (200 mg/ml of corn oil) into adult male rats weighing about 200 g each, at a dosage of 0.5 mg/g of body weight, 5 days before sacrifice. The rats were deprived of food 24 hours before sacrifice. They were stunned by a blow on the head and decapitated.

The livers were aseptically removed from the rats and placed into a cold preweighed beaker containing 10 ml of 0.15M KCl. After the livers were swirled in this beaker they were removed with forceps to a second beaker containing 3 ml of the KCl solution per gram of wet liver weight. The livers were then minced with sterile scrissors, transferred to a chilled glass homogenizing tube and homogenized by passing a low-speed motor driven pestle through the livers a maximum of four times. The homogenates were then placed in cold centrifuge tubes and centrifuged for 10 minutes at 9,000 G at 4°C. The resulting supernatant microsomes were decanted, aliquoted in 3 ml amounts to small culture tubes, quickly frozen in Dry Ice, and stored at -80°C in a Revco freezer. Sufficient microsomes for use each day were thawed at room temperature and kept on ice before and during use.

Microsomal Mix

The microsomal mix was prepared according to the recommendations of Ames by mixing 2 ml of microsomes, 0.4 ml of 0.4 M $MgCl_2$, 0.4 ml of 1.65 M KCl, 0.1 ml of 1 M glucose-6-phosphate, 0.8 ml of 0.1 M NADP, 10 ml of 0.2 M sodium phosphate buffer (pH 7.4), and sterile distilled water to bring the total volume to 20 ml. Stock solutions of NADP (0.1 M) and glucose-6-phosphate were prepared with sterile water, aliquoted in appropriate amounts, and maintained in a Revco freezer. The stock salt solutions were prepared, autoclaved, and refrigerated. The microsomal mix was prepared fresh daily and maintained on ice before and during use.

Bacteria

The *Salmonella* tester strains, TA-98, TA-100, and TA-1537, were obtained directly from Ames and stock solutions of the strains were stored at -80°C. At monthly intervals, new bacterial isolates were obtained from this stock supply. Each clonal culture was checked for confirmation of biochemical activity and spontaneous reversion rate. The cultures which conformed to the specifications of Ames were streak isolated and used as master cultures. These master cultures were used as the origin of weekly preparations of working broth cultures. All broth cultures were nutrient broth (Difco) supplemented with 0.5 percent NaCl. The broth cultures were prepared by inoculating 0.1 ml of master culture into 10 ml of nutrient broth and incubating the culture in a water bath shaker for 16-20 hours. This gave a stock culture containing approximately 10^9 cells per ml. The incubation was performed the night before the assay and the cultures were kept on ice during the process of preparing the assay plates.

Bacteriological Media

The selective basal medium used in the mutagenicity assays was a 1.5 percent Bacto-Difco agar in Vogel-Bonner Medium E with 2 percent glucose. The basal medium used in the toxicity assays was nutrient agar.

The top agar for both mutagenicity and toxicity assays was 0.6 percent Difco agar in 0.5 percent NaCl. It was prepared in 100 ml aliquots, autoclaved, and stored at room temperature. Before use the top agar was melted and mixed thoroughly with 10 ml of a sterile solution of 0.5 mM L-histidine·HCl and 0.5 mM biotin. It was then aliquoted in 2-ml amounts in sterile culture tubes and maintained at 45°C in a water bath before use.

Plate Test Procedure

The toxicity determinations were made in duplicate for each sample using each of the three tester strains. The determinations were made as follows. The stock culture of each tester organism was diluted in physiological saline to give approximately 300 cells per ml. The molten top agar tubes were treated with 0.1 ml of test material, 0.1 ml of the diluted tester strain, and 0.2 ml of the microsomal mix. It was immediately mixed for a few seconds by vortexing and poured onto a nutrient agar plate. After solidification of the top agar the plates were incubated at 37°C for 72 hours and the resulting colonies counted.

The plate test procedure for mutagenicity determination was the same as that for toxicity determination except that the stock culture containing approximately 10^9 cells per ml was used instead of the diluted culture and histidine-deficient Vogel-Bonner glucose agar was used instead of nutrient agar for the basal medium.

With each set of toxicity and mutagenicity determinations solvent controls were run in which pure solvent was used instead of the test material solution, positive controls (mutagenicity determination only) were run in which solutions containing 10 μg/ml of benz(a)pyrene and 50 μg/ml of 2-aminoanthracene were used instead of the test material solution, and sterility checks were run in which no tester organisms were added. In order for a set of tests to be considered valid the following criteria had to be met: (1) the sterility checks of the test materials must give no more than two colonies per plate, (2) the solvent controls in the toxicity determination must give 100 to 300 colonies per plate, (3) the positive controls must give at least a three-fold increase in the number of revertant colonies over the average value of the respective negative control (solvent control), (4) the average number of spontaneous revertant colonies (solvent control) must be 15 to 60 for TA-98, 70 to 250 for TA-100, and 5 to 20 for TA-1537. In order for a test material to be considered mutagenic it had to give at least twice the number of revertant colonies as the respective negative control. Test materials that exhibited toxicity were assayed again at lower levels whenever possible.

Mammalian Cell Toxicity Assay

An indication of the mammalian cell toxicity of test fractions was determined by using a prescreen confluency assay. This is a single plate cell culture assay that permits a rapid determination of the toxicity of test materials in wide ranges of concentrations.

Procedure

Subconfluent monolayers of cells (embryonic fibroblasts obtained from Dr. Charles Heidelberger of the University of Southern California) were established in the individual wells of Falcon No. 3008 multiwell tissue culture plate by seeding 5 x 10^3 cells in each well and allowing them to grow for 24 hours at 37°C in a humidified 5% CO_2 incubator. The growth medium was Eagle's basal medium with Earl's salt containing 10% heat inactivated fetal calf serum with no antibiotics. At the end of the incubation period the growth medium was removed from all of the wells by aspiration. Fresh growth medium containing a desired known concentration of the test material was replaced on the cells. Three of the four wells in each of the six rows of the plates were used for triplicate samples of the test material. The last well in each row was used as a control. Thus each plate was used for six test samples or dosages in triplicate and provided six control replicates. Usually at least three dose levels were run for each fraction evaluated.

The plates were incubated again for 24 hours after which the growth medium was removed, the cells washed with phosphate buffered saline, treated with fresh growth medium, and reincubated. When all the monolayers in the control wells reached 90-100 percent confluency (generally 6 days), all of the wells in the plates were washed, fixed with methanol and the cells stained with Giemsa. After the plates were dry they were scored on a basis of percentage of the surface area covered by the cell monolayer.

Evaluation of Results

The percentage of surface area coverage (confluency) was averaged for each set of three wells treated with a specific concentration of test material and for the six control wells. The average percent confluency in the test wells was adjusted slightly by dividing by the average percent confluency for the control wells times 100. The dose level of test material that would have given 50 percent confluency, CD_{50}, was determined by extrapolation of the adjusted percent confluencies found for various levels of the test material. A comparison of CD_{50} values provide meaningful information on the relative toxicities of different test materials in the assay system.

In Vivo Toxicity Assays

Static bioassays were conducted using brine shrimp (*Artemia salina* L.) and mysids (*Neomysis awatschensis*). Brine shrimp were obtained by hatching them in the laboratory. Mysids were collected by trawl from Sequim Bay, Washington. After initial hatching the brine shrimp were maintained in two 5-gallon aquaria at room temperature with gentle aeration. The algae *Monochrysis* was used as a food source. Adult animals approximately 5mm in length were selected for use in the assay. The mysids were maintained in large flow-through tanks. They were acclimatized for at least one day prior to testing and fed a diet of *Artemia nauplii*.

All bioassays ran for 48 hours. Twenty animals were placed in each 6-liter static aquaria containing four liters of filtered seawater with gentle aeration. Ambient temperature (10°C) was maintained by water bath and the salinity and temperature of each aquarium was monitored daily.

Brine shrimp were transferred from culture tank to test aquaria using a fine mesh net. This allowed for slow draining of algal culture water with a minimum of animal stress. Mysids were captured by the use of hollow glass tubes. These tubes utilized suction to draw the animal and seawater into their chambers without direct handling. Mysids were placed in an intermediate beaker in groups of twenty and fed for one hour just prior to testing. The seawater, and remaining nauplii were drained and the beaker contents submerged in the bioassay aquarium.

The test material solutions were added via a syringe to the seawater at levels of 1 to 1000 μl/l. In the initial tests the solutions were added to 250 ml of seawater in a stainless steel Waring blendor, blended for 30 seconds and stirred into the bioassay aquaria containing the animals and 3250 ml of seawater. The blendor was rinsed twice by blending two 250-ml portions of seawater which were added to the aquaria to give a total volume of 4 liters. In later studies the test material solutions were added to a volumetric flask containing two liters of seawater and 2 1 of Corexit dispersant. This was mixed by inversion 15 times and stirred into aquaria containing the animals and another two liters of seawater.

The number of live animals remaining after 24 hours and 48 hours was recorded and the corresponding LC_{50} values determined by extrapolation.

RESULTS

Fractionation Studies

Solvent Partitioning

Solvent partitioning in heptane/acetonitrile was used to simulate heptane/DMSO partitioning. In order to assess the performance of acetonitrile relative to that of DMSO and other polar solvents in such a system, a series of reference compounds ranging from very nonpolar compounds to moderately polar compounds was used in equilibration studies. Gas chromatographic analysis was used for the quantitation. The results, given in Table 3, show that acetonitrile does perform similarly to DMSO. In these studies in which the heptane was partitioned with an equal volume of acetonitrile, moderately polar compounds such as acetylnaphthalene and quinoline are almost quantitatively partitioned into the acetonitrile in one equilibration. For the partitioning step used in fractionation scheme applied to oil a 5:1 ratio of acetonitrile to heptane was used instead of 1:1. Also the partitioning was performed five times with fresh solvent. Any compounds that would remain in the heptane under such conditions would very probably not be biologically active and could be justifiably discarded.

TABLE 3. SOLVENT PARTITIONING STUDIES

	% Extracted Into Given Solvent When Partitioned With Equal Volume of Heptane			
Compound	Acetonitrile	DMSO	Nitromethane	Methanol
C_{16}	2	2	2	2
C_{26}	2	2	2	2
Androstane	2	2	2	2
Hexaethylbenzene	17	16	20	20
2,3,6-Trimethylnaphthalene	43	48	48	49
Naphthalene	61	71	62	66
Phenanthrene	71	90	69	73
Pyrene	71	92	66	72
Dibenzothiophene	68	91	69	74
Dibenzofuran	67	82	69	72
Acetylnaphthalene	94	98	96	98
Quinoline	98	>98	>98	98

The amounts of oil extracted by each individual partitioning using 5:1 acetonitrile:heptane are shown in Figure 2. The first partitioning accounted for the major amount of the extractable material. The total amount extracted into the acetonitrile was about 23 percent of fresh and weathered Prudhoe Bay crude oil and about 45 percent of the shale oil.

GPC Fractionation

The second step in the fractionation scheme was GPC fractionation using Bio-Beads S-X8 with methylene chloride as the eluting solvent. A representative elution profile was obtained using a small amount of an acetonitrile extract of weathered oil. The amount present in each five-minute (10-ml) fraction was determined by residue weight measurements. The elution profile obtained is shown in Figure 3. For comparison the elution ranges found for various reference compounds are indicated. Long-chain compounds eluted early and the compact aromatic compounds eluted considerably later. Polar aromatics eluted earlier than less-polar aromatics.

The acetonitrile extracts of 10-gram samples of the three oils were fractioned into four fractions designated as A-1 through A-4 in Figure 3. The elution profiles obtained for the oils in this manner are shown in Figure 4. The shale oil eluted somewhat earlier than the crude oils possibly becuase of a higher content of heterocyclic more polar components.

The effectiveness of the GPC fractionation system is indicated by the gas chromatograms of weathered oil fractions shown in Figures 5 and 6. The main individual peaks in A-2 (Figure 5) are trace amounts of normal paraffins; most of the material does not elute from the GC column. Fraction A-3 (Figure 6) on the other hand gives the usual pattern of aromatic hydrocarbons, the methylnaphthalenes (MN), dimethylnaphthalenes (DMN), and trimethylnaphthalenes (TMN), etc. No significant overlap of the two fractions is noted.

Silica Gel Fractionation

Silica gel fractionation was applied to the A-2 and A-3 fractions from each of the three oil samples. The elution profiles obtained are given in Figure 7. The largest amounts of material were in the first six fractions, the hydrocarbon fractions. However at about fractions 9, 13, and 18 when elution with progressively more polar solvents was begun, significant amounts of more polar components were obtained, especially in the larger-molecule or more polar A-2 fractions. The shale oil and to a lesser extent the weathered oil had more polar material than the fresh oil.

The efficiency of the silica gel fractionation, which used silica gel that had been previously deactivated with 10% methanol in ethylene dichloride, is indicated by the gas chromatograms of hydrocarbon fractions shown in Figures 8 and 9. Fraction 4 from A-3 from fresh crude oil (Figure 8) gives a GC pattern indicative primarily of naphthalene (N), methylnaphthalenes (MN), dimethylnaphthalenes (DMN), and trimethylnaphthalenes (TMN). The next fraction, fraction 5 (Figure 9) contains very few naphthalenes but mainly the phenanthrenes, fluorenes, pyrenes, and fluoranthenes.

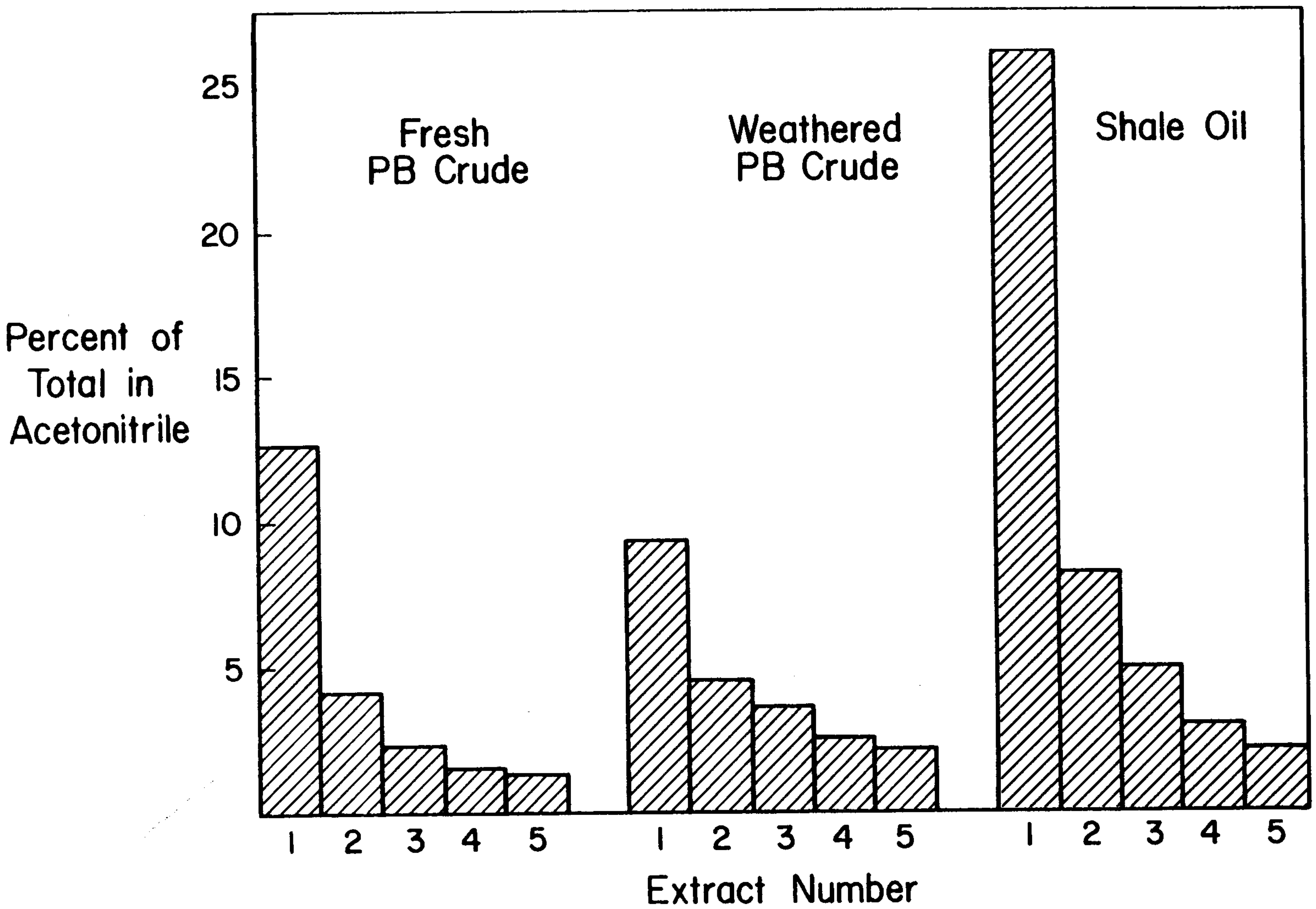

FIGURE 2. HEPTANE/ACETONITRILE PARTITIONING

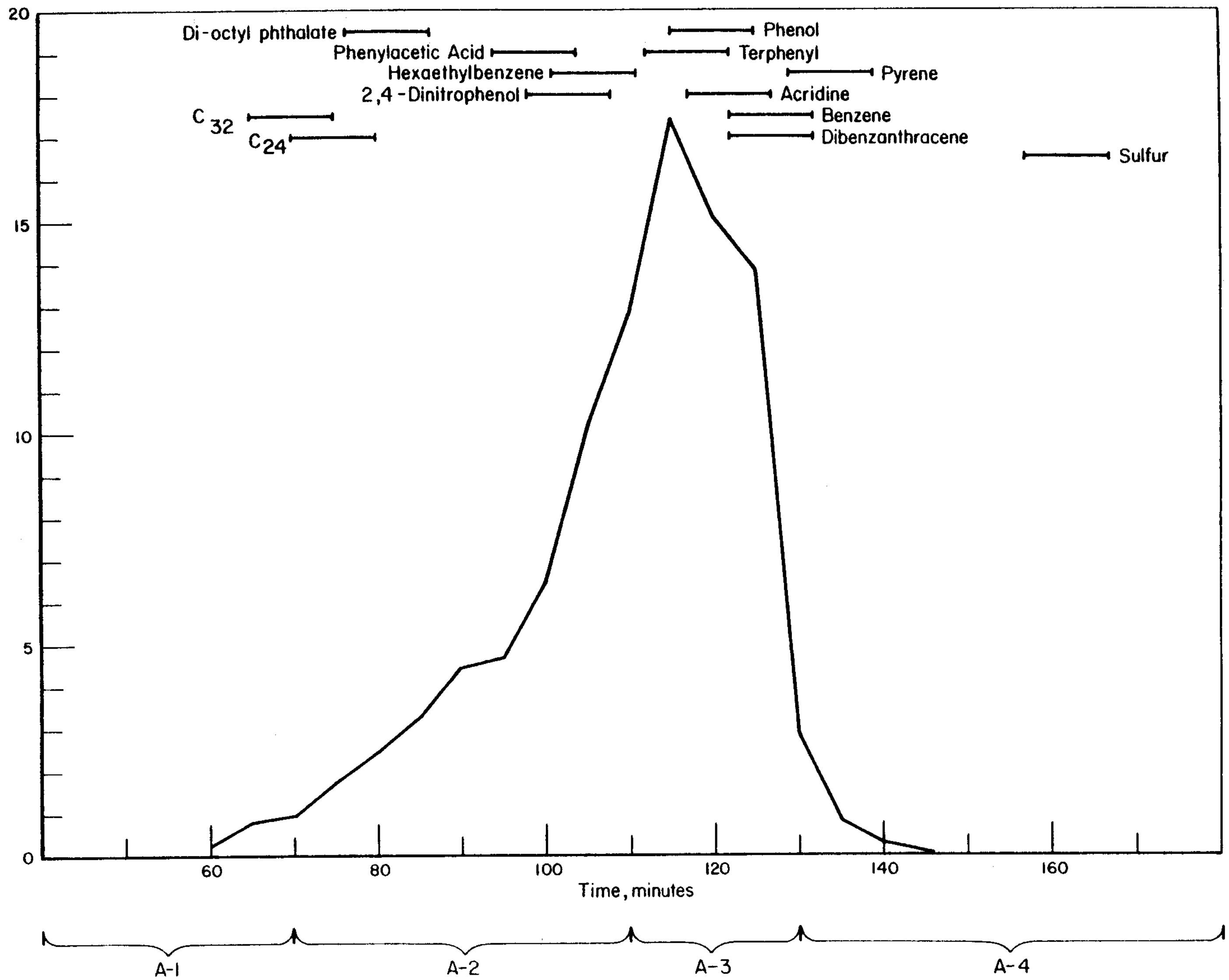

FIGURE 3. ELUTION PROFILE OF ACETONITRILE EXTRACT OF WEATHERED PB CRUDE OIL USING BIO-BEADS S-X8

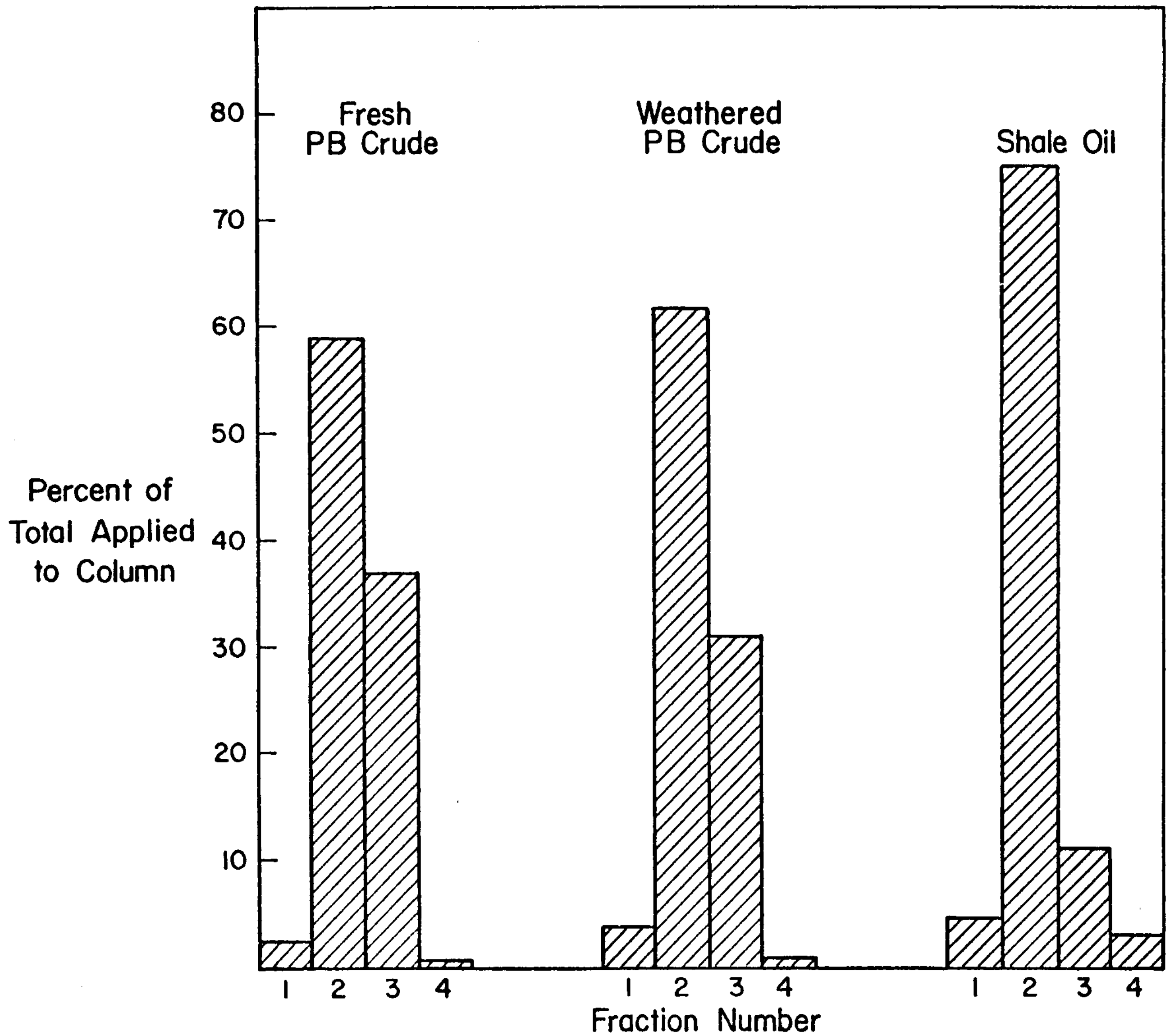

FIGURE 4. ELUTION PROFILES FROM FRACTIONATION USING BIO-BEADS S-X8

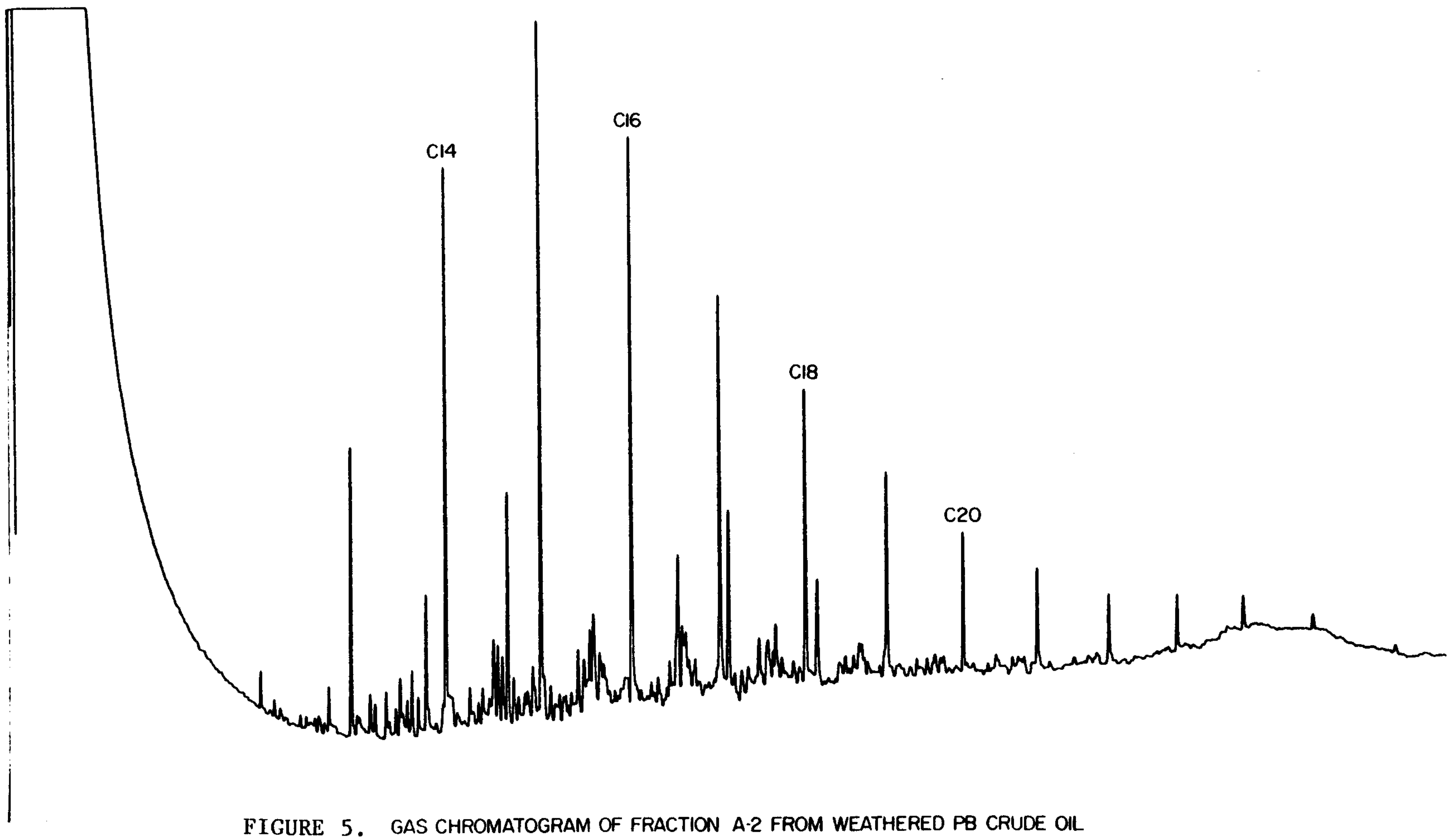

FIGURE 5. GAS CHROMATOGRAM OF FRACTION A-2 FROM WEATHERED PB CRUDE OIL

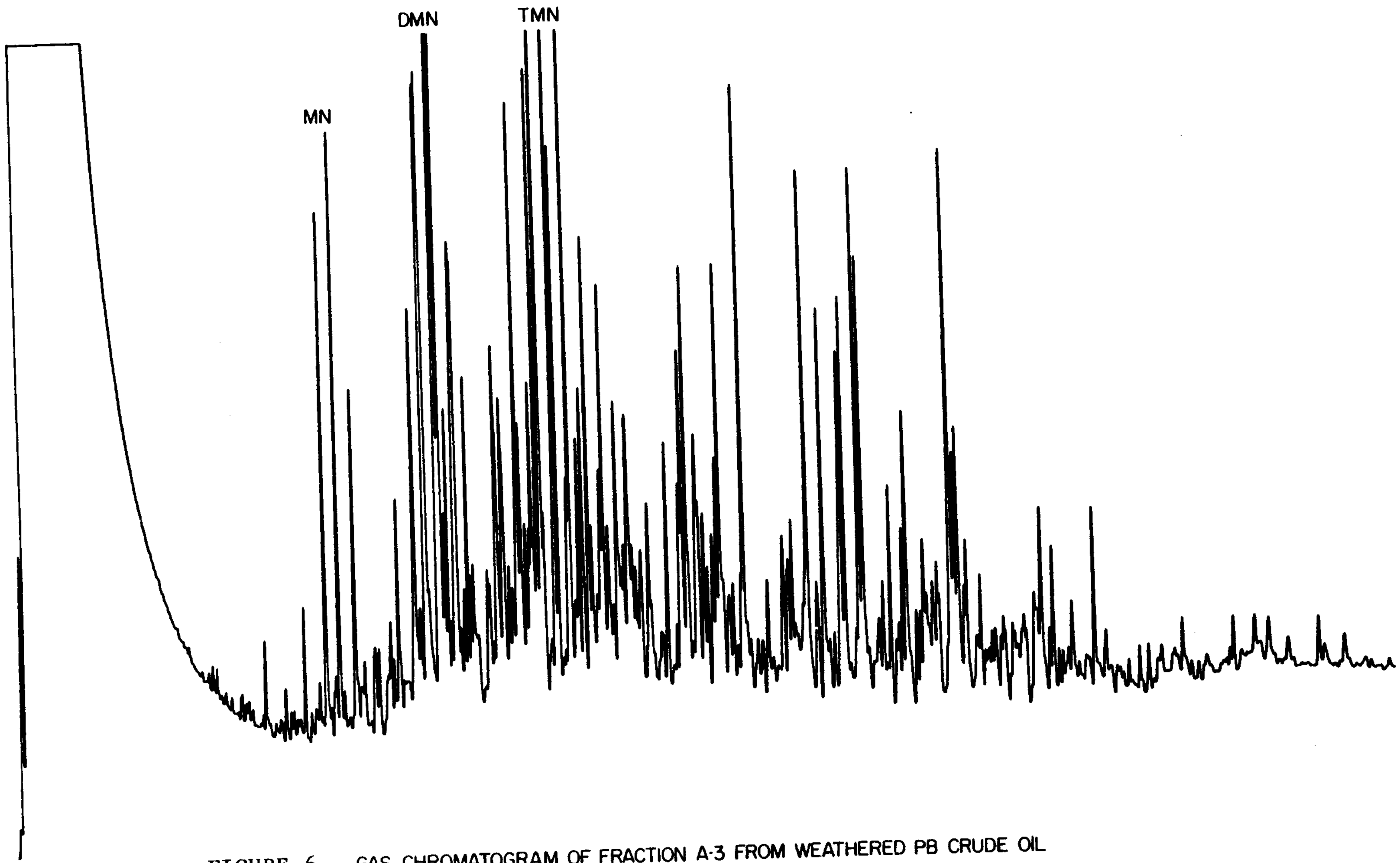

FIGURE 6. GAS CHROMATOGRAM OF FRACTION A-3 FROM WEATHERED PB CRUDE OIL

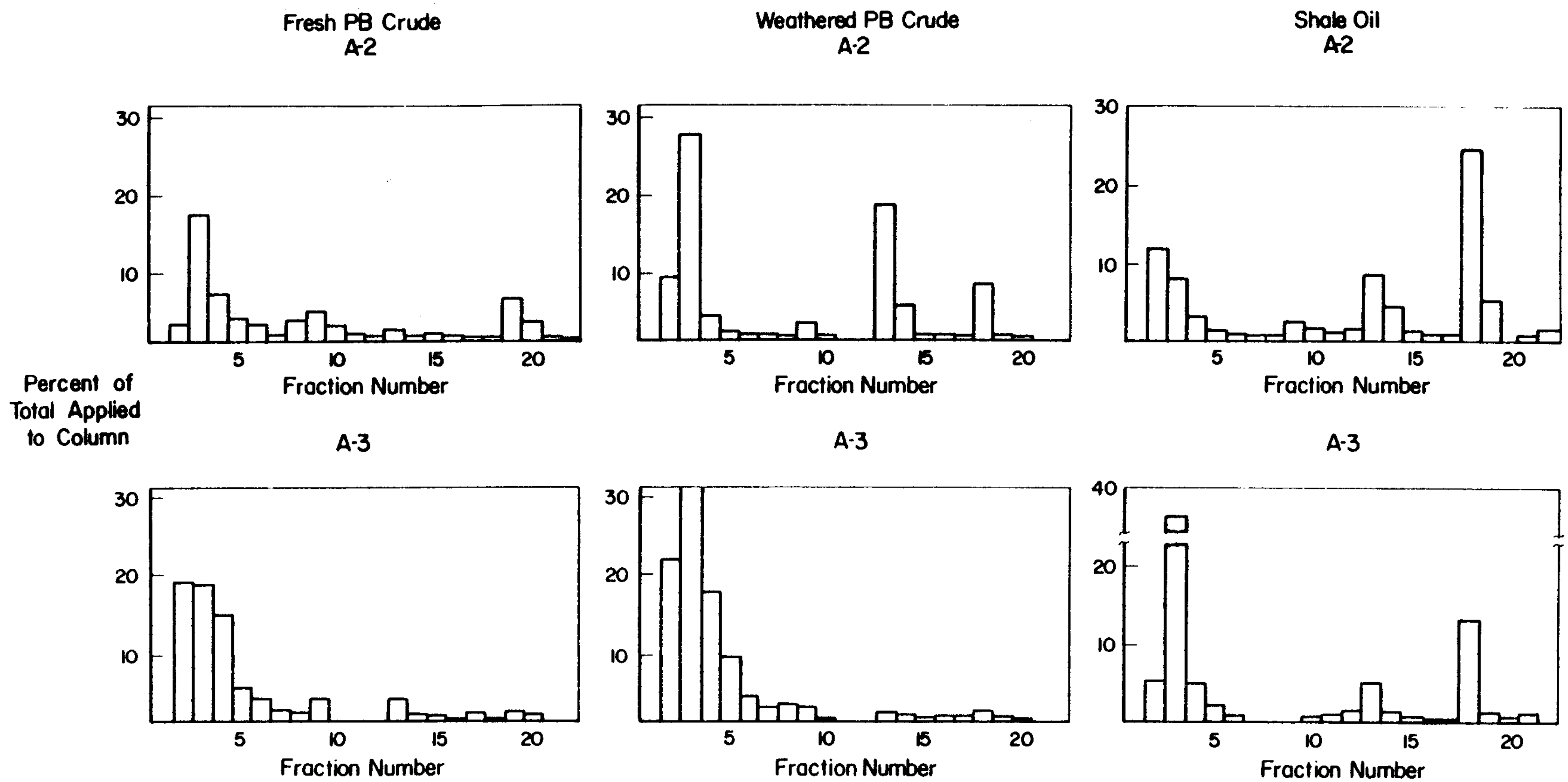

FIGURE 7. ELUTION PROFILES FROM FRACTIONATION USING SILICA GEL

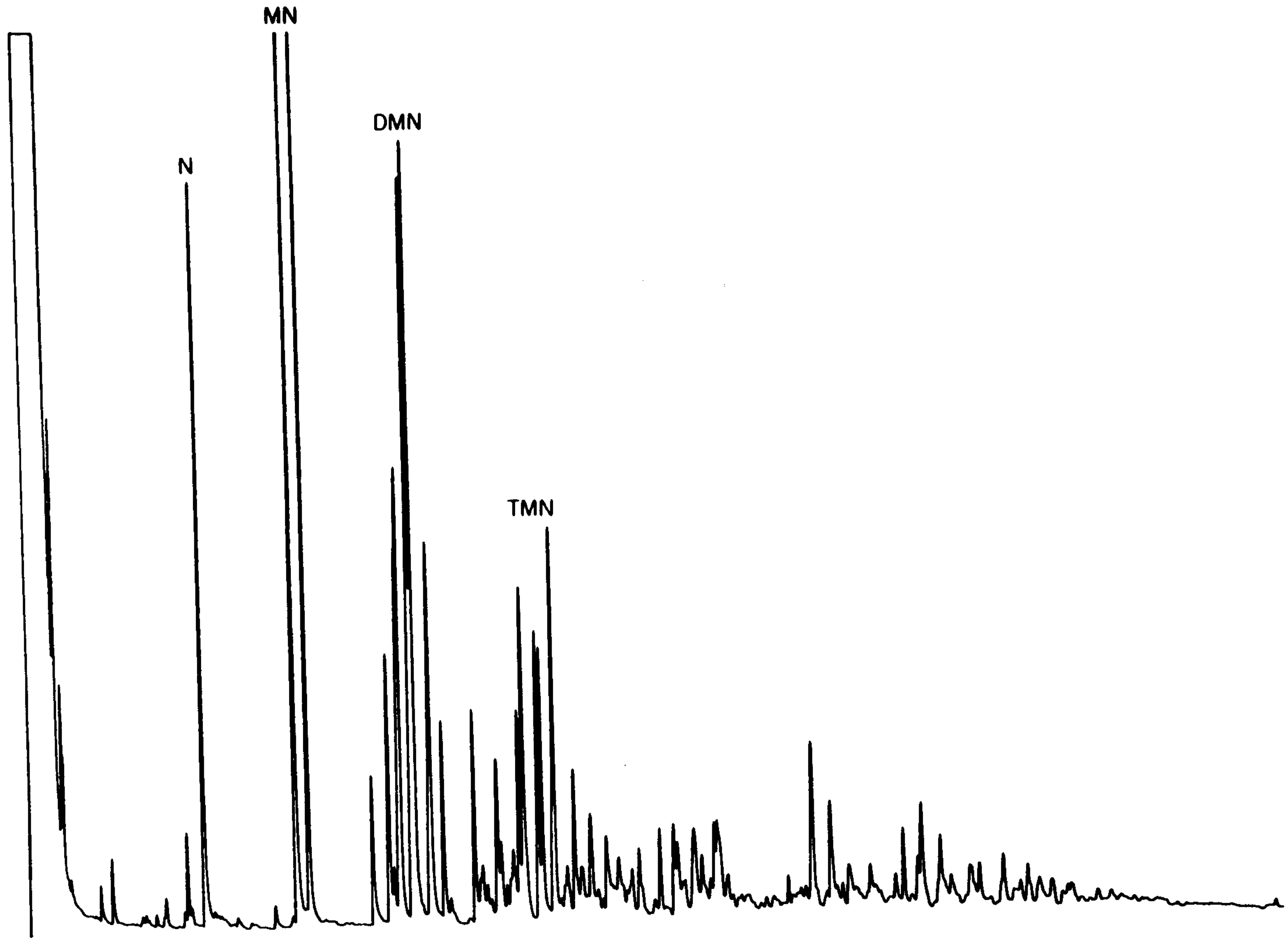

FIGURE 8. GAS CHROMATOGRAM OF FRACTION A-3-4 FROM FRESH PB CRUDE OIL

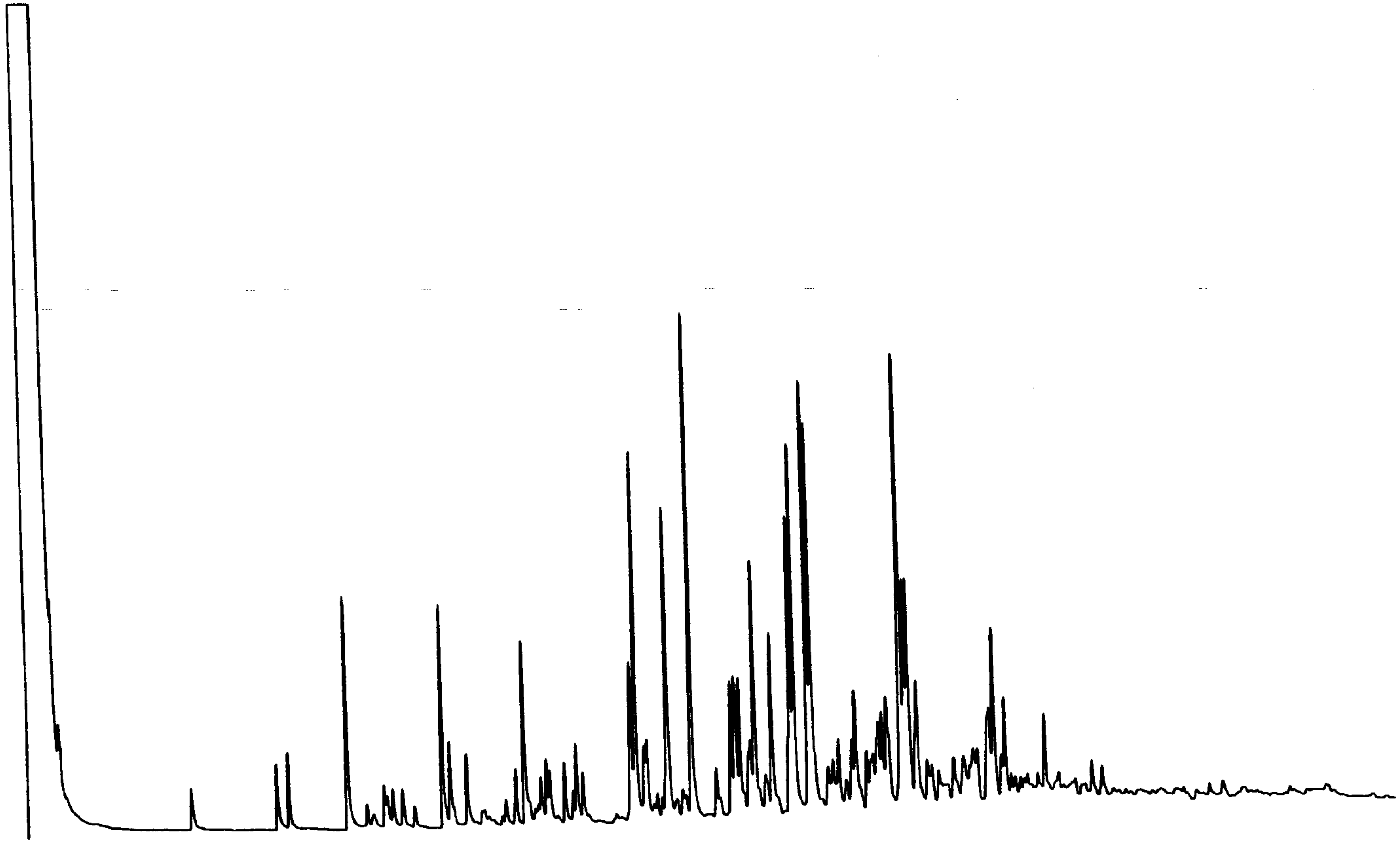

FIGURE 9. GAS CHROMATOGRAM OF FRACTION A-3-5 FROM FRESH PB CRUDE OIL

Bioassay Studies

In Vitro Studies

Various fractions of crude oil and shale oil as well as reference compounds were subjected to *in vitro* biological screening tests, namely the Ames *Salmonella* mutagenicity test and a prescreen confluency mammalian cell toxicity assay. The results obtained are summarized in Table 4.

Many of the oil fractions were as toxic or somewhat more toxic than reference compounds such as naphthalene, carbazole, 4-methylphenol, and 2-naphthol. The shale oil fractions were more consistently toxic than the crude oil fractions. The A-2 and A-3 series of silica gel fractions, which had the benefit of cleanup by solvent partitioning and GPC, were more toxic than silica gel fractions from whole oil.

No mutagenicity was exhibited by the various fractions except for a slight mutagenicity from some of the shale oil fractions. Very likely significantly greater mutagenicity would have resulted from modifying the bioassay protocol.

Salmonella toxicity tests were run concurrently with the mutagenicity tests to determine whether the number of revertants might be influenced by a toxicity effect. In many cases very significant toxicity, 90% kill or greater, occurred in the Salmonella toxicity tests while no toxicity was observed in the mutagenicity tests as indicated by a heavy background lawn. Observation of a background lawn was therefore chosen as a more reliable indicator of no significant toxicity in the mutagenicity assay.

In Vivo Studies

Initial *in vivo* studies were conducted using both brine shrimp and mysids. Phenanthrene was used as a standard toxicant to provide an index of the sensitivity of the animals. Cyclopentanone and tetrahydrofuran, initially considered for use as solvents for oil fractions, as well as fresh crude oil in cyclopentanone were also bioassayed using mysids. The results are given in Table 5. Mysids were found to be much more sensitive than brine shrimp to exposure of phenanthrene. Mysids are also a much more realistic indicator species than brine shrimp for determining the ecological damage of an oil spill. For these reasons, mysids were selected for all subsequent studies.

Cyclopentanone was less toxic than THF by a factor of about two. The results indicated that it could be used at a concentration of 100 µl/l with little effect on mysids. A solution of 1 ml of Prudhoe Bay crude oil in 9 ml of cyclopentanone could therefore be used in the bioassay to give crude oil levels up to 10 µl/l without interference by the cyclopentanone. Bioassay at this maximum level resulted in no significant toxic effects from the crude oil. Phenanthrene was at least 100 times more toxic than the crude oil. This indicated that all of the different components in the crude oil that have toxicities as great as phenanthrene comprise altogether no more than one percent of the total unless there are also protective components present. Therefore, in order to provide toxic fractions, the fractionation process used must concentrate

TABLE 4. IN VITRO BIOLOGICAL SCREENING STUDIES

No.	Sample	Relative Mutagenicity[a] at Given Dosage, μg/plate 1000	500	200	Mammalian Cell Toxicity, CD_{50}[b], μg/ml
1.	Benzo(a)pyrene		7 at 1 μg/plate		--
2.	2-Aminoanthracene		20 at 5 μg/plate		--
3.	Benzene	1			>100
4.	1,2,4-Trimethylbenzene	1			80
5.	Naphthalene	1			100
6.	2-Methylnaphthalene	1			70
7.	Phenanthrene	c			>100
8.	2-Naphthol	c			75
9.	4,4'-Methylbiphenyl	1			>100
10.	1-Methylpyrene	1			40
11.	4-Methylphenol	1			>100
12.	Carbazole	1			>100
13.	Fresh PB Fraction SG-21[d]	1			>100
14.	Fresh PB Fraction SG-22	1			>100
15.	Fresh PB Fraction SG-23	1			>100
16.	Fresh PB Fraction SG-24	1			>100
17.	Fresh PB Fraction SG-25	1			>100
18.	Fresh PB Fraction SG-26	1			>100
19.	Weathered PB Fraction SG-51	1			>100
20.	Weathered PB Fraction SG-52	1			>100
21.	Weathered PB Fraction SG-53	1			>100
22.	Weathered PB Fraction SG-54	1			>100
23.	Weathered PB Fraction SG-55	1			>100
24.	Weathered PB Fraction SG-56	1			>100
25.	Fresh PB Acid Extractables		1	1	--
26.	Fresh PB DMSO Extractables		1		--
27.	Fresh PB Extract AN-1[e]		1	1	35
28.	Fresh PB Extract AN-3			1	35
29.	Fresh PB Extract AN-5			1	>40
30.	Weathered PB Extract AN-1			1	>40
31.	Weathered PB Extract AN-3			1	>40
32.	Weathered PB Extract AN-5			1	>40
33.	Fresh PB Extract M-5[f]			1	>40
34.	Fresh PB Extract M-6			1	>40
35.	Fresh PB Fraction A-2-6[g]	1	1		>100
36.	Fresh PB Fraction A-2-9	1	1		>100
37.	Fresh PB Fraction A-2-13	1	1		75
38.	Fresh PB Fraction A-2-19	1	1		60
39.	Fresh PB Fraction A-3-6[h]	1	1		30
40.	Fresh PB Fraction A-3-9	2	2		>100
41.	Fresh PB Fraction A-3-13	1	1		50
42.	Weathered PB Fraction A-2-3	1	1		60
43.	Weathered PB Fraction A-2-9	1	1		>100
44.	Weathered PB Fraction A-2-13	1	1		70
45.	Weathered PB Fraction A-2-18	1	1		60
46.	Weathered PB Fraction A-3-4	1	1		30

TABLE 4. (Continued)

No.	Sample	Relative Mutagenicity[a] at Given Dosage, μg/plate 1000	500	200	Mammalian Cell Toxicity, CD_{50}[b], μg/ml
47.	Weathered PB Fraction A-3-6	1	1		35
48.	Weathered PB Fraction A-3-8	1	1		>100
49.	Shale Oil Fraction A-2-4	1	1		70
50.	Shale Oil Fraction A-2-6	1	1		35
51.	Shale Oil Fraction A-2-9	1	1		30
52.	Shale Oil Fraction A-2-11	1	1		30
53,	Shale Oil Fraction A-2-13	1	1		40
54.	Shale Oil Fraction A-2-15	1	2		45
55.	Shale Oil Fraction A-2-18	1	2		40
56.	Shale Oil Fraction A-2-21	c	1		20
57.	Shale Oil Fraction A-3-3	1	1		30
58.	Shale Oil Fraction A-3-4	2	1		10
59.	Shale Oil Fraction A-3-13	c	1		40
60.	Shale Oil Fraction A-3-18	c	2		>100

a. $\frac{\text{Revertants in Sample Plate}}{\text{Revertants in Control Plate}}$

b. The dosage level that would result in only 50% confluency.

c. Toxic at this dosage.

d. PB refers to Prudhoe Bay crude oil
SG refers to silica gel chromatographic fractions from whole oil.

e. AN indicates an acetonitrile extract of oil in heptane.

f. M indicates a methanol extract.

g. A-2 fractions are silica gel chromatographic fractions from the second GPC fraction.

h. A-3 fractions are silica gel chromatographic fractions from the third GPC fraction.

TABLE 5. IN VIVO BIOASSAY EVALUATION STUDIES

Concn, mg/l	Animals	No. of Test Animals Surviving After Given Exposure Time				LC_{50}, mg/l, for Given Exposure Time	
		24 hr		48 hr		24 hr	48 hr
		Phenanthrene/Mysids					
0.050	30	25	83%	23	77%		
0.100	30	14	47%	8	27%	0.096	0.076
0.200	30	1	3%	0	0%		
0.500	30	1	3%	0	0%		
Control	30	27	90%	18	60%		
		Phenanthrene/Brine Shrimp					
0.025	20	20	100%	18	90%	>0.200	>0.200
0.050	20	19	95%	17	85%		
0.100	20	20	100%	17	85%		
0.200	20	20	100%	18	90%		
Control	20	20	100%	19	95%		
		Cyclopentanone/Mysids					
10	20	20	100%	20	100%	800	420
100	20	20	100%	17	85%		
500	20	14	70	9	45%		
1000	20	9	45%	2	10%		
Control	0	19	95%	19	95%		
		THF/Mysids					
10	20	20	100%	20	100%	570	240
100	20	20	100%	18	90%		
500	20	12	60%	3	15%		
1000	20	1	5%	0	0%		
Control	20	20	100%	19	95%		
		Prudhoe Bay Crude Oil in Cyclopentanone/Mysids					
0.5	20	20	100%	20	100%	>10	>10
1.0	20	20	100%	19	95%		
5.0	20	19	95%	19	95%		
10.0	20	19	95%	16	80%		
Control	20	19	95%	18	90%		

the toxic components of oil at least 100-fold.

The mysids toxicity assay was applied to various reference compounds and a number of oil fractions. The results are given in Table 6. The majority of the oil fractions were not toxic at the levels assayed. The shale oil fractions in general were more toxic than the crude oil fractions. The most toxic fractions were A-3-4 and A-3-5 from weathered crude oil. Fraction A-3-4 is the fraction that contains the naphthalenes and A-3-5 is the fraction that contains the phenanthrenes and pyrenes, etc. All of the components present in A-3-5 are apparently as toxic as the phenanthrene and 1-methylpyrene included as reference compounds. The fairly large polar compounds, fraction A-2-18 from both weathered PB and shale oil, are also significantly more toxic than whole crude oil.

Dimethyl sulfoxide was shown to be less toxic than oil solvents such as THF or cyclopentanone by a factor of 20 or more. A concentration of at least 0.1% can be used with very little chance of toxic effects appearing. This means that a 1% solution of an oil fraction in DMSO can be used to administer the oil at levels up to 10 mg/l without solvent effects.

Corexit, a dispersant that is highly effective in oil spill situations, was also included in the assay. It was relatively nontoxic in that the 48 hour LC_{50} was 100 mg/l. This shows that the level of 1 mg/l that is commonly used in practice would have no biological effect detectable by the mysids test.

TABLE 6. *IN VIVO* BIOLOGICAL SCREENING STUDIES USING MYSIDS

No.	Sample	LC_{50} For Given Exposure Time, mg/l 24 Hr	48 Hr
1.	Phenanthrene	0.2	0.2
2.	1,2,4-Trimethylbenzene	8	7
3.	2-Methylnaphthalene	0.6	0.7
4.	1-Methylpyrene	0.4	0.2
5.	4-Methylphenol	9	4
6.	Dibenzothiophene	2	2
7.	Fresh PB Volatiles[a]	>10	>10
8.	Fresh PB Residuals	>10	>10
9.	Fresh PB Fraction SG-16[b]	>10	>10
10.	SG-21	>10	>10
11.	SG-22	>10	>10
12.	SG-23	>10	>10
13.	SG-24	>10	>10
14.	SG-25	>10	>10
15.	SG-26	>10	>10
16.	Weathered PB Fraction SG-44	>10	>10
17.	SG-46	>10	>10
18.	SG-51	>10	>10
19.	SG-54	>10	>10
20.	SG-56	>10	>10
21.	Fresh PB Fraction A-2-9[c]	>20	>20
22.	A-2-19	>10	10
23.	Weathered PB Fraction A-2-3	>10	>10
24.	A-2-13	>40	29
25.	A-2-18	15	5
26.	A-3-4[d]	2	1
27.	A-3-5	0.8	0.5
28.	Shale Oil Fraction A-2-4	5	2
29.	A-2-9	>10	3
30.	A-2-13	4	1
31.	A-2-18	5	2
32.	A-3-18	4	1
33.	Dimethyl sulfoxide	>10,000	10,000
34.	Corexit	500	100
35.	Fresh PB Crude Oil[e]	>10	>10

a. PB refers to Prudhoe Bay crude oil.

b. SG refers to silica gel chromatographic fractions from whole oil.

c. A-2 fractions are silica gel chromatographic fractions from the second GPC fraction.

d. A-3 fractions are silica gel chromatographic fractions from the third GPC fraction.

e. 1 mg/l of Corexit was used to aid dispersion.

DISCUSSION

Many of the concerns and problems associated with developing a sound program have already been discussed in the Experimental Approach section. A key aspect in the development of the program was accepting the premise that major portions of petroleum are intractable in terms of being available to biological systems and such intractable nonavailable portions need not be accounted for in the bioassay program. The fractionation scheme that evolved, using solvent partitioning, GPC fractionation, and silica gel fractionation, worked very well and was quite effective in removing intractable components. Most of the intractable components stayed in the heptane layer during the solvent partitioning. These components were probably comprised mainly of the paraffin waxes and other highly paraffinic material. The GPC fractionation removed most of the colored and polymeric intractable components that remained.

Many of the final fractions did not contain enough material for bioassaying. The fractions that were studied indicated that most of the toxicity was associated with the aromatic hydrocarbon fractions. Some of the more polar fractions exhibited toxicity and also a hint of mutagenicity. Subfractionation and mutagenicity assays employing a more sensitive system would be needed to demonstrate any very significant mutagenic or potential carcinogenic effects.

Because of the strong parallel between mutagens and carcinogens, the mutagenicity assay is of major interest for detecting potential long-range biological effects of spilled oil. The insensitivity of the Ames mutagenicity assay as used was a serious deficiency in the program. One of the main causes of the insensitivity is the fact that an attempt was made to use the test as a screening method for all fractions using only one or two concentration levels. The number of plates per test were therefore kept to a minimum. The Ames test in a complete form can involve 5 bacterial strains, 5 levels of test material, with and without microsomal activation, in triplicate, with one set for mutagenicity and another complete set for toxicity. This complete form of the test entails the preparation and counting of 300 agar plates. Our procedure consisted of screening 3 strains, with only one level of test material in most cases, with microsomal activation using one set for mutagenicity and another complete set for toxicity. This procedure entailed the preparation and counting of only 12 plates instead of 300.

The 12-plate protocol was fully justifiable as a substitution for a 300-plate protocol as an initial screening protocol. Unfortunately, in retrospect with additional understanding and data obtained, neither protocol suffices for determining potential mutagenicity of oil fractions. Both of the above protocols work well for detecting the mutagenicity of 1 μg of BaP but they do not serve well for detecting mutagenicity in oil fractions. They are not optimized for handling a 1000-μg sample of oily matrix. Two major deficiencies were found. The first deficiency involves the separate toxicity assay which is designed to determine whether or not a low value for the number of revertants results from partial toxicity instead of from a lack of mutagenicity. The deficiency stems from the fact that about 10^8 cells are used in the mutagenicity assay but only about 10^3 cells are used in the toxicity assay. When applied to 1 to 10 μg of a pure compound the toxicity test results can be considered relevant to the mutagenicity test. However when 1000 μg of an oil fraction is used, considerable toxicity may be observed in the toxicity test when in reality there may be no significant toxicity in the corresponding mutagenicity test as indicated by a normal background lawn. This inconsistency between the toxicity test and mutagenicity test can be explained on the basis of physical adsorption effects related to the number of cells. The 1000-μg oil sample can nearly overwhelm the 10^3 cells in the toxicity test by simple physical adsorption rather than by actual cellular toxicity. When the 1000 μg is added to 10^8 cells in the mutagenicity test however, the cells are in great excess and the number of cells that become inactivated by physical adsorption of the oil is an insignificantly small proportion of the total. The toxicity of an oil fraction in the mutagenicity test can therefore best be evaluated by observing the background lawn. The use of a range of test dosages would also help factor out the toxicity effect. The effectiveness of the background lawn observation approach was demonstrated by assaying an oil fraction at levels of 500, 1000, and 2000 μg. The corresponding numbers of revertants found were 114, 18, and 5, respectively. There was a partial reduction in the background lawn at the 1000 μg level and almost complete absence of background lawn at the 2000 μg level. The separate toxicity test should therefore be deleted from any future protocols.

The second deficiency, which is a much more serious deficiency, involves optimization of the mutagenicity assay. The assay is quite sensitive to changes in the amount of microsomes added to each plate. The mutagenicity assay used for this program was optimized for use with 1 μg of BaP, a representative petroleum mutagen. The optimization involves optimizing the concentration of the microsomal fraction in the microsomal mix as well as optimizing the amount of microsomal mix added to each plate. Representative data from such an optimization study are given in Table 7. On the basis of these data, 0.15 ml of 10% microsomal mix were considered optimal in using this particular microsomal mix and TA-98 culture.

TABLE 7. OPTIMIZATION OF MUTAGENICITY TEST FOR BaP

Amount of Microsomal Mix, ml/plate	Number of Revertants Per Plate When Using Given Percent of Microsomal Fraction in the Microsomal Mix[a]		
	7.5	10	12.5
0.1	136-126[b]	136-145	247-223
0.2	179-193	231-236	54-56
0.3	73-75	62-42	49-54
0.4	73-62	38-46	45-41
0.5	54-57	36-44	39-42

a. All tests were conducted using strain TA-98 and 1 μg of BaP.
b. Individual results from duplicate plates are given. The values obtained for spontaneous reversions in the absence of BaP in triplicate plates were 28, 29, and 32.

The microsomal activation is used to convert compounds such as BaP, which are inactive as such, into hydroxylated metabolites that are mutagenic. In this manner the test simulates what happens in an actual mammalian system.

The amount of microsomes present, however, is quite critical. An insufficient amount of microsomes will result in much of the BaP staying in its original inactive form while an excess of microsomes will metabolize the active hydroxylated metabolites further to yield inactive species.

When a test is optimized for 1 μg of BaP it will not be optimized for an oil fraction. This was shown by using various different amounts of microsomal mix when assaying 1000 μg of one of the oil fractions. With 0.1, 0.2, 0.3, 0.4, and 0.5 ml of 10% microsomal mix the numbers of revertants were 36, 54, 71, 125, and 205, respectively. Perhaps with a greater amount of microsomal mix an even greater number of revertants would have been obtained. The average number of spontaneous revertants in this test was 30. Therefore by using 0.15 or 0.2 ml of microsomal mix as dictated by optimization studies with BaP, the number of revertants is less than two times background and not considered significant. By using greater amounts of microsomes a number of revertants of at least 7 times background can be achieved which indicates very definite mutagenicity.

The need for greater amounts of microsomes when assaying 100 to 1000 μg of an oil fraction can be readily understood by considering that there are many more molecules competing for microsomal action than when only 1 g of BaP is present. Therefore in order for traces of BaP-type molecules to be optimally converted to active metabolites many more microsomes are required. This effect can also affect the amount of oil fraction that is optimal for the assay. For a given amount of microsomal mix, the mutagenicity of 200 μg of a given oil fraction may be much greater than that of 500 μg or 1000 μg simply because at the higher levels the ratio of microsomes to oil molecules is not great enough to give optimal conversion of BaP-type molecules. There may be many components that preferentially interact with the microsomes without being converted to active metabolites.

It can be concluded from the above considerations that the amount of microsomes used in the mutagenicity assay must be optimized for each individual oil fraction. This conclusion, of course, suggests quite profound changes in any protocol intended as a screening test. Variations in both the amount of microsomes per plate and the amount of test material per plate must be studied. One approach would be to use four different amounts of microsomes, e.g. 0.2, 0.4, 0.8, and 1.6 ml, with each of four different levels of oil fraction, e.g. 800, 400, 200, and 100 μg. If run in duplicate, this would require 32 plates per sample per test strain used. Our experience and that of other workers, however has indicated that the use of TA-98 alone is satisfactory for detecting all mutagenic components of petroleum materials. Therefore a satisfactory screening protocol could involve 32 plates per sample which is considerably more than the 12 plates per sample used in this program but is still a reasonable number. Most important, of course, is the fact that such a protocol would have a much greater chance of detecting the mutagenicity of an oil fraction.

Because of the very limited amount of material available in many of the oil fractions, the amount required by the mutagenicity protocol is an important consideration. It is of interest to note that the 32-plate protocol described above requires 12 mg, exactly the same amount as the 12-plate protocol used at the 1000 μg/plate level. If the 800 μg level were deleted, the 32-plate protocol would become a 24-plate protocol and only 5.6 mg of test material would be required. This is about the same as required for the 12-plate protocol at the

500 μg/plate level. Thus the protocol described above is a reasonable screening protocol in terms of sample requirements as well as effectiveness.

It was indicated earlier that either further subfractionation or a more sensitive mutagenicity assay system would be required to demonstrate significant biological effects of oil fractions. It is very likely that the screening protocol described above would be at least 10 times more sensitive than the 12-plate protocol used and thus would achieve the requirements of an activity-directed fractionation program.

One of the problems associated with using the mysids toxicity test has been the relatively large amount of sample required. In order to test an oil fraction at levels of 10, 4, 1, 0.4, and 0.1 mg/l in duplicate at least 62 mg is needed. Most of the fractions obtained didn't contain that much material. However if the highest dose were deleted from the assay only 11.2 mg would be needed. Since the aromatic hydrocarbon fractions gave LC_{50}s in the range of 0.4 to 2 mg/l and since they represent a major fraction of the oil, it is reasonable to consider that any of the minor fractions that is not toxic at a level of 4 mg/l will not be significant in an oil spill situation and can justifiably be ignored. On this basis, the mysids test could be used to assay even minor fractions that show toxicity in *in vitro* assays.

CONCLUSIONS

Major components of petroleum are so intractable that they can not be evaluated in bioassay tests. However such components are so water insoluble and even insoluble in dimethyl sulfoxide that it is unlikely that they would ever exert any biological effect. Fractionation of oil using solvent partitioning between heptane and acetonitrile in conjunction with gel permeation chromatography can be used effectively to remove the intractable components that otherwise interfere with bioassay studies. Subsequent subfractionation using silica gel chromatography serves very well for obtaining a series of 20 fractions having increasing polarities.

An *in vivo* test involving toxicity to mysids, an *in vitro* mammalian-cell toxicity test based on confluency of growth, and the Ames bacterial mutagenicity test all work well to assess the biological activity of oil fractions that have had intractable components removed. The total sample requirement for running all three tests is less than 30 mg. In applying the Ames mutagenicity test to an oil fraction, varying amounts of microsomes need to be added to each of several concentrations of the oil fraction in order to optimize the test for that particular fraction. By using such an optimization protocol the test should be much more sensitive than the protocol actually used for this program.

On the basis of the limited bioassay results obtained on the program, the main petroleum fractions from an oil spill, that would represent a biological hazard are those that contain the aromatic hydrocarbons. However some of the polar fractions are toxic and mutagenic to a lesser extent and may also be significant biological hazards. The polar fractions from shale oil are more toxic and mutagenic than those from Prudhoe Bay crude oil.

The final bioassay scheme that evolved from the program has not been applied to the oil samples. The complete fractionation and bioassay scheme is based on experimental evidence that indicates that it will work very well. It should be applied in a somewhat scaled-up mode to fresh crude oil, weathered crude oil, and shale oil to obtain more complete and more definitive data on the potential biological hazards of polar petroleum components.

NEEDS FOR FUTURE STUDY

The knowledge gained in this research program now permits a proven fractionation-bioassay scheme to be applied to the determination of biologically-active nonhydrocarbon fractions of petroleum or petroleum-like materials, e.g. shale oil. It is unfortunate that some of the key factors in the scheme were not obtained until the end of the program. Therefore the total data obtained give a very incomplete picture of what are the potential biological hazards of the nonhydrocarbon components of weathered oil remaining after an oil spill.

The limited data that were obtained confirm the fact that the aromatic hydrocarbons represent the greatest environmental hazard of any of the petroleum components. At the same time, however, there were indications that some of the more polar fractions may be biologically active. It would be well worthwhile at this point to repeat the fractionations with a modest scale up of 5 to 10 times and assay all of the nonhydrocarbon fractions using all three of the bioassay tests with the modifications discussed above. This would entail considerably less time and effort than has been devoted to the program so far but would result in much more definitive data that would be very important to the OCSEAP program.

ACKNOWLEDGEMENTS

We gratefully acknowledge the assistance on this program provided by Suzanne Winters and Cory Howard who performed the fractionation studies; Joan Pitman, Anne Aukerman, and Susan Gruebel who performed the *in vitro* bioassay studies; and Frances Stefan and Steven Kieser who performed the *in vivo* bioassay studies.

We thank Stanley Rice and Jeffrey Short of the NOAA Auke Bay Fisheries Laboratory for preparing the weathered Prudhoe Bay crude oil. We also thank Richard Poulson of the Environmental Sciences Division, Laramie Energy Technology Center for kindly supplying the simulated *in situ* shale oil used for comparison studies.

APPENDIX 1:

FRACTIONATION AND BIOASSAY OF WEATHERED PRUDHOE BAY CRUDE OIL

by

J. S. Warner and W. L. Margard

Battelle Columbus Laboratories
505 King Avenue
Columbus, Ohio 43201

and

J. W. Anderson

Battelle Pacific Northwest Laboratories
Route 5, Box 1000
Marine Research Laboratory
Sequim, Washington 98382

June 1979

ABSTRACT

The less volatile and nonhydrocarbon components of weathered petroleum that remain after an oil spill are generally overlooked in biological studies and associated gas chromatographic analyses. In an effort to determine whether such components present a potential environmental hazard weathered Prudhoe Bay crude oil was fractionated by solvent partitioning, gel permeation chromatography, and adsorption chromatography. Fractions were assayed for mutagenicity and toxicity by using the Ames *Salmonella* mutagenicity assay and a mammalian-cell prescreen confluency assay. The toxicity of selected fractions was also determined by *in vivo* studies using mysids as the test organism. Fresh Prudhoe Bay crude oil and shale oil were included in the study for comparison purposes.

FRACTIONATION AND BIOASSAY OF WEATHERED PRUDHOE BAY CRUDE OIL

by

J. S. Warner and W. L. Margard
Battelle Columbus Laboratories, Columbus, Ohio

and

J. W. Anderson
Battelle Pacific Northwest Laboratories
Marine Research Laboratory, Sequim, Washington

June 13-15, 1979

The program that I'll discuss here can be considered as stemming from a concern about oil spills -- a concern about what environmentally harmful components may be left by an oil spill.

As we are all well aware, a great deal of effort has been devoted in recent years to studying the biological effects of oil spills, i.e., the biological effects of petroleum. The biological studies are frequently supported by chemical analyses in an effort to determine which petroleum components are causing the effects observed.

We've been involved in the chemical analysis end of programs, including methods development, for the past 6 or 7 years. Generally chemical analyses are limited to those components that can be detected most easily, the volatile and semivolatile hydrocarbons that are easily determined by gas chromatography. These include the saturated hydrocarbons n-paraffins, isoprenoids, and naphthenes which are essentially nontoxic, but which are sometimes considered as indicators of petroleum, as well as aromatic hydrocarbons such as benzenes, naphthalenes, and phenanthrenes which are of interest because of their toxicity, and polynuclear aromatics, such as benzo[a]pyrene and dibenzanthracene which are of interest because of their carcinogenicity.

Petroleum however is comprised of many other components including nonvolatile and polar components. In a highly weathered oil, 80 or 90 percent of the oil may be nonGC-able components. This is because many of the GC-able hydrocarbons found in a fresh oil are degraded by microorganisms, photochemically degraded, or lost from an oil slick by dissolution and evaporation. It therefore seemed that any program concerned with the long-term biological effects of an oil spill ought to consider components other than the GC-able hydrocarbons. Perhaps some of the nonvolatile and polar components are toxic or mutagenic and should be studied in monitoring programs. On the other hand such components may have no significant biological activity and we should continue to ignore them. However we should not ignore them until we have experimental evidence indicating that they are indeed not important. We should'nt ignore them simply because they're not detectable by the analytical methods usually employed.

We therefore initiated a program, sponsored by NOAA as part of its Alaskan Outer Continental Shelf Environmental Assessment Program, to study nonhydrocarbon components of weather oil. The plan called for what we termed activity-directed fractionation. This meant that we would fractionate the oil into a dozen fractions or so, run bioassay tests to determine which ones were toxic or mutagenic, subfractionate those active fractions, run bioassay tests on the subfractions, and continue in that manner until subfractionation no longer increased the activity per unit weight. We would ignore the inactive fractions, ignore the hydrocarbon fractions, and chemically characterize the active nonhydrocarbon fractions. We hoped to end up with all of the oil accounted for, i.e., a mass balance, so we wouldn't miss any potentially active fraction.

In discussing the program here I'll describe some of the things we did that didn't seem to work out very well; I'll describe some of the approaches that did seem to work and put us on the right track; and I'll discuss some of the problems involved. I won't be giving the answers, in terms of what are the nonhydrocarbon toxic components, not because I'm holding out but because we just haven't gotten that far along with the program.

There were several problems that seriously interfered with the success of the plan. One major problem was the basic phenomenon that oil and water don't mix. This presented the problem of how to get a highly water-insoluble component into an aqueous medium required for bioassay. A second problem was the partial volatility of the oil which made it difficult to obtain very reliable residue weights and therefore prevented a good mass balance from being achieved. A third problem was the insensitivity of the bioassay methods which meant that in the initial fractionation all of the fractions might appear inactive and no direction would be given to the subfractionation.

The solubility problem was one that hit us right off the bat. I don't mean to imply that we didn't expect it but we just had to deal with it somehow. There were really two problems -- one was finding a water-soluble or water-dispersible organic solvent that would dissolve the oil fraction but not be toxic in the bioassay; and the other was how to keep the oil fraction dispersed in the aqueous bioassay medium. Solvents such as tetrahydrofuran, benzene, and methylene chloride are good solvents for the oil fractions and are sufficiently water soluble, but are too toxic in the bioassay. Dimethyl sulfoxide and acetone are not toxic in the bioassay but are not satisfactory solvents for many of the oil fractions. We investigated various other solvents and found cyclohexanone and cyclohexanol to be good oil solvents, sufficiently water-soluble and less toxic than THF; but even so they really weren't satisfactory. They were still too toxic and although the oil fractions were soluble in the solvents, as soon as the solutions were added to the aqueous bioassay medium the oil fraction separated out. We tried several dispersants but they didn't work very well either.

At about that point we decided to take the sour grapes approach. We decided to go ahead and use dimethyl sulfoxide and if an oil component didn't dissolve in the DMSO we just wouldn't be interested in it after all. We rationalized the decision on the basis that just about every biologically-active organic compound we could think of was at least slightly soluble in DMSO -- or to put it more basically, if a component wouldn't dissolve at least slightly in DMSO it was unlikely that it could get into a cellular system to exert a biological effect. So, despite the sour grapes aspect of the decision we felt we actually were on pretty firm ground.

The partial volatility problem affected residue weights and therefore the mass balance. In evaporating oil solutions, the oily residue acts as a keeper for the solvent as well as a keeper for the more volatile oil components. The ideal case would be one in which the amount of solvent remaining after evaporation is equal to the amount of volatile oil components lost so that the residue weight observed is equal to what might be called the true residue weight. However, as the viscosity and volatility of the oil components vary from fraction to fraction the errors in residue weight determinations will vary. In most cases the residue weight observed is probably less than the true residue weight. Working with oil that had the more volatile components removed by reduced pressure distillation helped considerably but even so the residue weights obtained could only be considered approximations. In most of our fractionation steps, recoveries based on residue weights varied between 85 and 95 percent. However, when we got a recovery of 85% we could never be sure whether the 15% discrepancy actually represented material that was not recovered or simply represented errors in residue weight determinations.

The problem of insensitivity of the bioassay methods was particularly true for the Ames mutagenicity assay. Fractionation into a large number of fractions prior to bioassay was necessary. I'll discuss that some more a little later.

At this point I think it would be helpful if I would summarize (see Figure 1) the scope of our program as it evolved after studying the problems that I've described so far. We studied 3 different oils. Although we were primarily concerned with weathered Prudhoe Bay crude oil, we used fresh crude oil and shale oil for comparison. The shale oil was from a simulated in situ process of the Laramie Energy Research Center. The weathered crude oil was provided by Dr. Stan Rice of the National Marine Fisheries Auke Bay Laboratory in Alaska. He exposed the oil during the summer for 2 months in a pine frame attached to a floating dock. The oil was therefore subjected to dissolution into the water, evaporation into the air, photochemical degradation, and microbiological degradation, thus simulating in many respects an oil spill situation in an Alaskan environment.

The fractionations involved solvent partitioning, gel permeation or size-exclusion chromatography, and adsorption chromatography.

The bioassays included two in vitro tests, namely the Ames bacterial mutagenicity test and a mammalian-cell toxicity test, and an in vivo assay using mysids. The in vivo studies are being directed by Dr. Jack Anderson at Battelle Northwest's Sequim Marine Biology Laboratory.

STARTING OIL SAMPLES

Fresh PB Crude Oil
Weathered PB Crude Oil
Shale Oil

FRACTIONATION METHODS

Heptane/Acetonitrile Equilibration
Gel Permeation Chromatography — Bio-Beads S-X8
Adsorption Chromatography — Silica Gel

BIOASSAY METHODS

Ames Salmonella Mutagenicity Test
Mammalian-cell Prescreen Confluency Test
Mysid Toxicity Test

FIGURE 1. PROGRAM SCOPE

To give an appreciation for the problems associated with the sensitivity of the Ames mutagenicity test, lets look at some of the quantitative considerations (see Figure 2) in applying the Ames test to the detection of mutagenicity of BaP in crude oil. If we consider that the BaP concentration in a crude oil is 2 μg/g, and the detection limit for BaP in the Ames test is 2 μg, and assume that BaP is the only mutagen present, then we can conclude that all of the BaP in 1g of crude oil has to be added to the Ames test plate in order for any mutagenicity to be detected. Furthermore, since the maximum amount of sample that can be accommodated by an Ames test plate is about 1 mg, the crude oil must be fractionated in a manner that gives a 1000-fold concentration factor for BaP. If all fractions contained equal amounts of material, the crude oil would have to be fractionated into at least 1000 fractions and all of the BaP would have to be in just one of those fractions before any mutagenicity would be detected. Fortunately, the situation is probably not quite that dismal. In the first place fractions that contain BaP undoubtedly contain other mutagens and secondly a major inactive portion of the oil can be removed by solvent partitioning.

The fractionation scheme that we used is shown in Figure 3. The scheme involved solvent partitioning to remove the bulk of the nonpolar material, size exclusion chromatography using Bio Beads S-X8 to remove polymeric material, and silica gel chromatography to fractionate on the basis of polarity.

The heptane/acetonitrile partitioning was used to simulate a heptane/DMSO partitioning. Acetonitrile has a big advantage over DMSO in that it is quite volatile and extracts can be readily concentrated directly. When DMSO is used, the extract has to be diluted with water and the oil components back extracted into a solvent such as cyclopentane. In order to assess how well acetonitrile might work as a DMSO substitute we ran solvent partitioning studies with various reference compounds. The results are shown in Table 1. The values given are the percent of the compound extracted into the polar solvent when partitioned with an equal volume of heptane. The very nonpolar saturated hydrocarbons stayed almost entirely in the heptane, significant or major amounts of aromatic hydrocarbons went into the polar solvents, and essentially all of the more polar compounds went into the polar solvents. In the heptane/acetonitrile partitioning that we used for the oil fractionation we used a 5:1 ratio of acetonitrile

PREMISE 1:	BaP Concentration In Crude Oil = 2 μg/g
PREMISE 2:	BaP Is Only Mutagen In Crude Oil
PREMISE 3:	Limit Of Detection Of BaP In Ames Test = 2 μg
CONCLUSION 1:	All Of The BaP In 1 g Of Crude Oil Must Be Added To Ames Test To Be Detectable
PREMISE 4:	Maximum Amount of Sample Accommodated By Ames Test = 100 μl Of 1% Solution = 1 mg
CONCLUSION 2:	Crude Oil Must Be Fractionated In A Manner That Gives A 1000-Fold Concentration Factor For BaP
PREMISE 5:	All Fractions Contain Equal Amounts Of Material
CONCLUSION 3:	Crude Oil Must Be Fractionated Into At Least 1000 Fractions And All Of The BaP Must Be In One Of Those Fractions Before Any Mutagenicity Will Be Detected

FIGURE 2. QUANTITATIVE CONSIDERATIONS OF AMES TEST

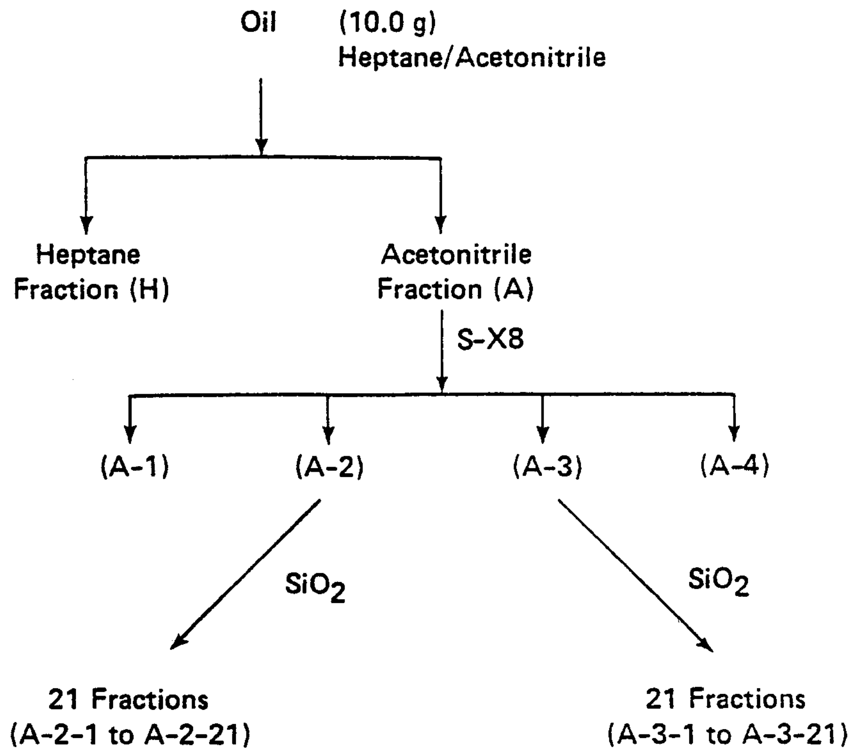

FIGURE 3. FRACTIONATION SCHEME

TABLE 1. SOLVENT PARTITIONING

Compound	% Extracted Into Given Solvent When Partitioned With Equal Volume of Heptane			
	Acetonitrile	DMSO	Nitromethane	Methanol
C_{16}	<2	<2	<2	<2
C_{26}	<2	<2	<2	<2
Androstane	<2	<2	<2	<2
Hexaethylbenzene	17	16	20	20
2,3,6-Trimethylnaphthalene	43	48	48	49
Naphthalene	61	71	62	66
Phenanthrene	71	90	69	73
Pyrene	71	92	66	72
Dibenzothiophene	68	91	69	74
Dibenzofuran	67	82	69	72
Acetylnaphthalene	94	98	96	98
Quinoline	98	>98	>98	98

to heptane instead of 1:1 and repeated the extraction 5 times. Any components that would remain in the heptane under such conditions would probably not be biologically active and were therefore discarded. The amounts extracted by each individual partitioning are shown in Figure 4. The first partitioning, of course, accounted for a major amount of the extractable material. The total amount extracted into the acetonitrile was about 23% of fresh and weathered Prudhoe Bay crude oil and about 45% of the shale oil. This step thus reduced considerably the amount of material to be processed by the next step, the gel permeation chromatography, and, of even greater importance it removed most of the DMSO-insoluble material that could not be accommodated by the bioassay methods anyway.

The next step in the fractionation scheme was gel permeation chromatography also referred to as size exclusion chromatography. We originally tried Sephadex LH-20 for this step but got so much irreversible adsorption that we couldn't reuse the column. Bio-Beads S-X8, a styrene-divinylbenzene copolymer, worked quite well with methylene chloride as the eluting solvent. It's a system that we've used quite successfully for cleaning up extracts of environmental samples. An elution profile obtained for the acetonitrile extract of weathered crude oil is shown in Figure 5. For comparison I've also indicated the elution ranges of various reference compounds. Long-chain compounds elute early and the compact aromatic compounds elute considerably later. Polar aromatics elute earlier than less-polar aromatics. It's also of interest to note that elemental sulfur elutes even later than aromatic compounds and although that's not of concern to this program it provides a very useful technique for removing sulfur from hydrocarbon-containing sediment extracts.

The oil extracts were fractionated into four fractions designated as A-1 to A-4. The first fraction contained a major portion of the dark color, presumably polymeric material. This is material that would be largely irreversibly retained during subsequent silica gel chromatography. The fourth fraction contained the very small molecules especially compact polynuclear aromatics having strong pi-bonding characteristics. The bulk of the material was in the two center fractions A-2 and A-3.

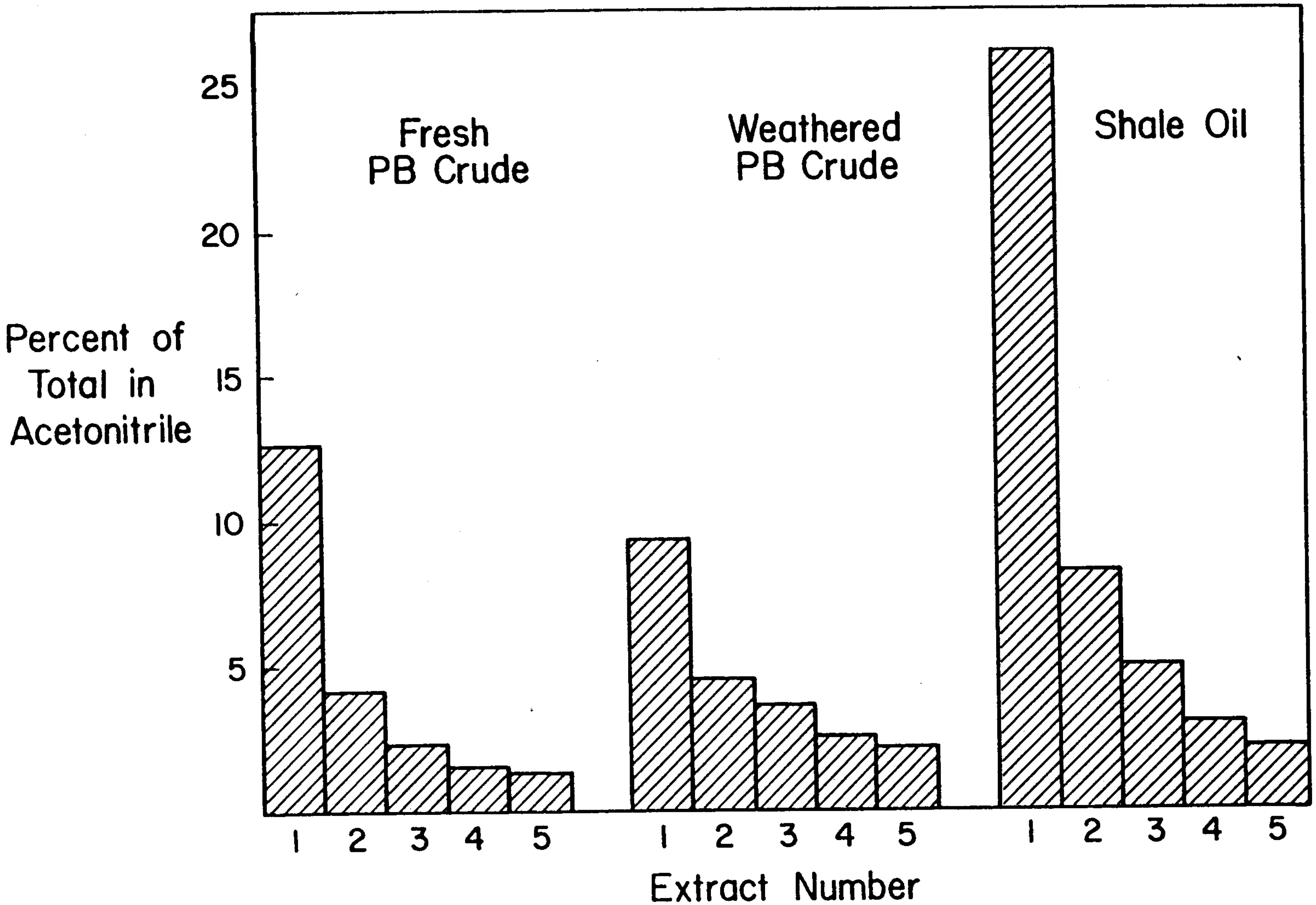

FIGURE 4. HEPTANE/ACETONITRILE PARTITIONING

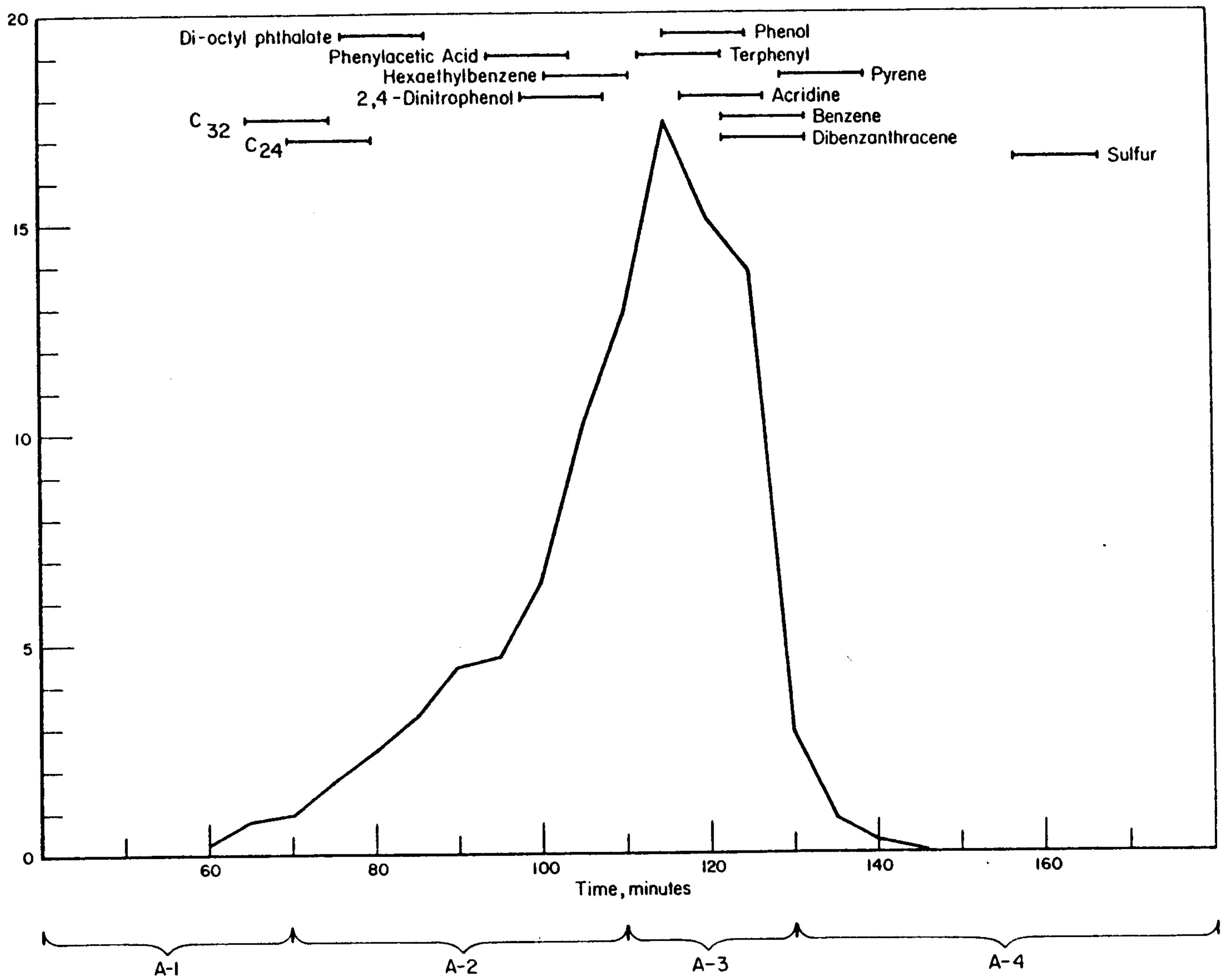

FIGURE 5. ELUTION PROFILE OF ACETONITRILE EXTRACT OF WEATHERED PB CRUDE OIL USING BIO-BEADS S-X8

The elution profiles obtained for the three oils in this manner are shown in Figure 6. The shale oil eluted somewhat earlier than the crude oils possibly because of a higher content of heterocyclic more polar components.

The effectiveness of this Bio-Beads fractionation system is indicated by the gas chromatograms shown in Figures 7 and 8. The main individual peaks in A-2 (see Figure 7), are trace amounts of normal paraffins; most of the material does not elute from the GC. Fraction A-3 (see Figure 8) on the other hand gives the usual pattern of aromatic hydrocarbons, the methylnaphthalenes, dimethylnaphthalenes, trimethylnaphthalenes, etc.

The next fractionation step used was adsorption chromatography using silica gel. The elution scheme used is given in Table 2. The column was prepared in 10% methanol in ethylene dichloride and was therefore somewhat deactivated. Prior to use it was washed with straight ethylene dichloride and then with hexane. In the elution process the hexane would elute any saturated hydrocarbons first, then the benzenes and naphthalenes, then phenanthrenes and higher polynuclear aromatic hydrocarbons. With the addition of ethylene dichloride, heterocyclic nitrogen- and oxygen-containing compounds would elute and later with the addition of methanol much more polar compounds would elute.

The elution profiles obtained for the A-2 and A-3 Bio-Beads fractions from the three oils are given in Figure 9. The largest amounts of material were in the first six fractions, the hydrocarbon fractions. However around fraction 9 when 10% ethylene dichloride was begun, fraction 13 when straight ethylene dichloride was begun, and fraction 19 when 10% methanol was begun, significant amounts of more polar components were obtained, especially in the larger-molecule or more polar A-2 fractions. The weathered crude oil and shale oil had significantly more polar material than the fresh crude oil. It's this polar material, which represents only about 5% of the starting oil, that we're most interested in.

The efficiency of the silica gel fractionation used is indicated by the gas chromatograms shown in Figures 10 and 11. These are chromatograms of hydrocarbon fractions that we're familiar with. Fraction 4 from A-3 from fresh crude oil (see Figure 10) gives a GC pattern indicative primarily of naphthalenes, methylnaphthalenes, dimethylnaphthalenes, and trimethylnaphthalenes. The next fraction, fraction 5, (see Figure 11) contains very few naphthalenes but mainly the phenanthrenes and fluorenes.

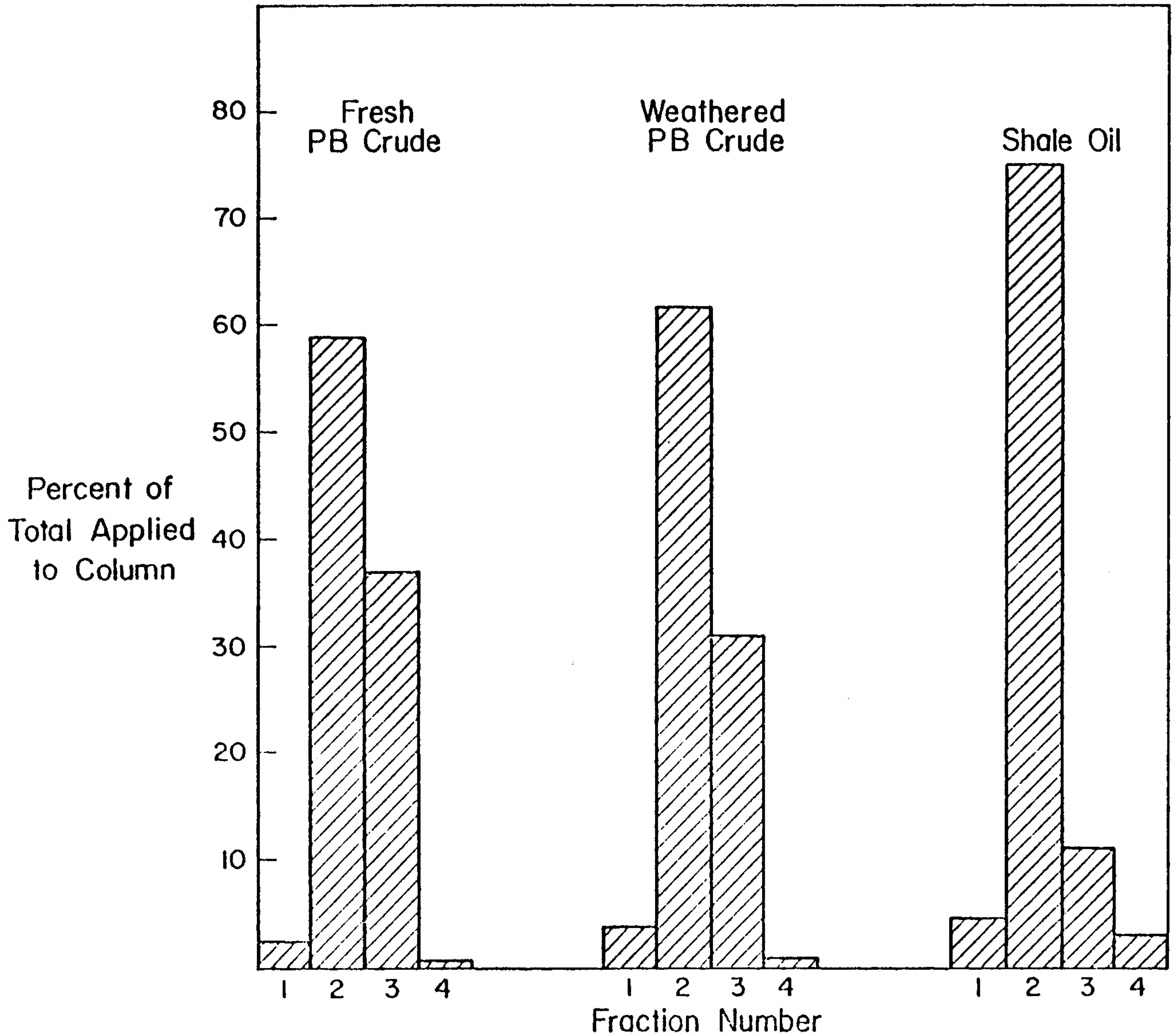

FIGURE 6. ELUTION PROFILES FROM FRACTIONATION USING BIO-BEADS S-X8

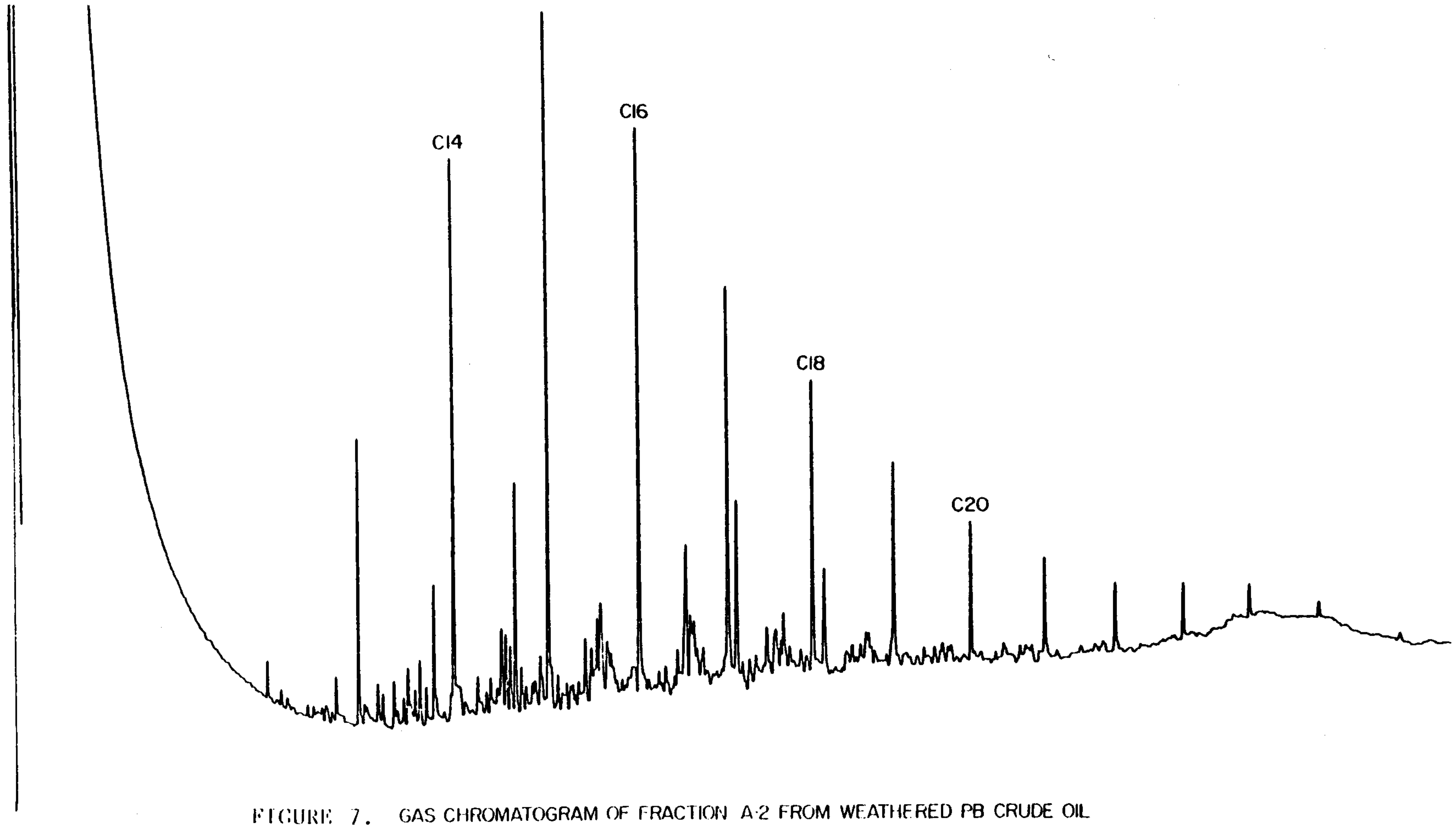

FIGURE 7. GAS CHROMATOGRAM OF FRACTION A-2 FROM WEATHERED PB CRUDE OIL

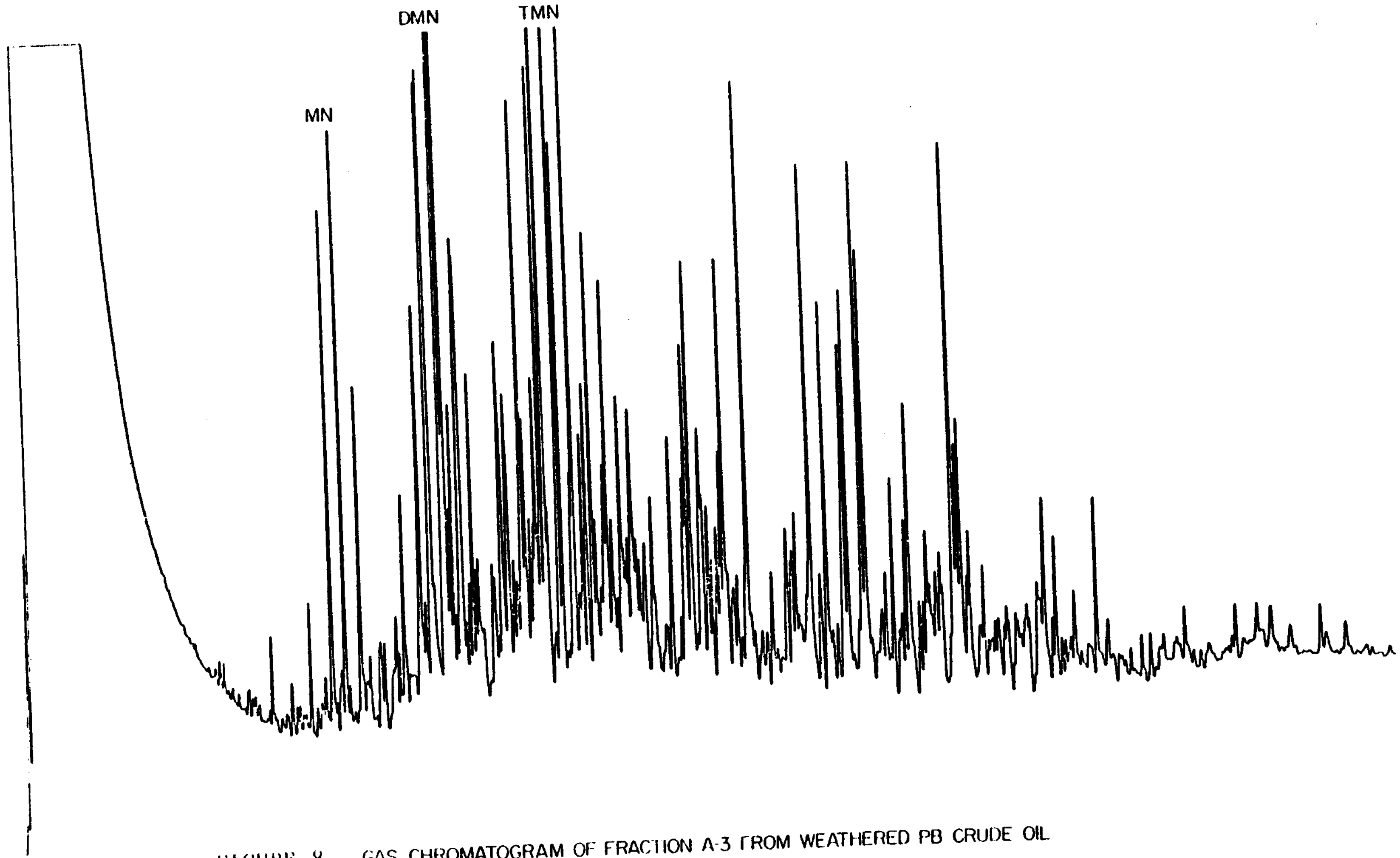

FIGURE 8. GAS CHROMATOGRAM OF FRACTION A-3 FROM WEATHERED PB CRUDE OIL

TABLE 2. SILICA GEL FRACTIONATION

Fraction No.	Eluting Solvent
1 – 7	Hexane
8 – 12	10% Ethylene Dichloride in Hexane
13 – 16	Ethylene Dichloride
17 – 21	10% Methanol in Ethylene Dichloride

25 mm ID x 1200 mm upward flow column
350 g silica gel, Davison Grade 923
10 ml/min elution rate
250 ml fractions

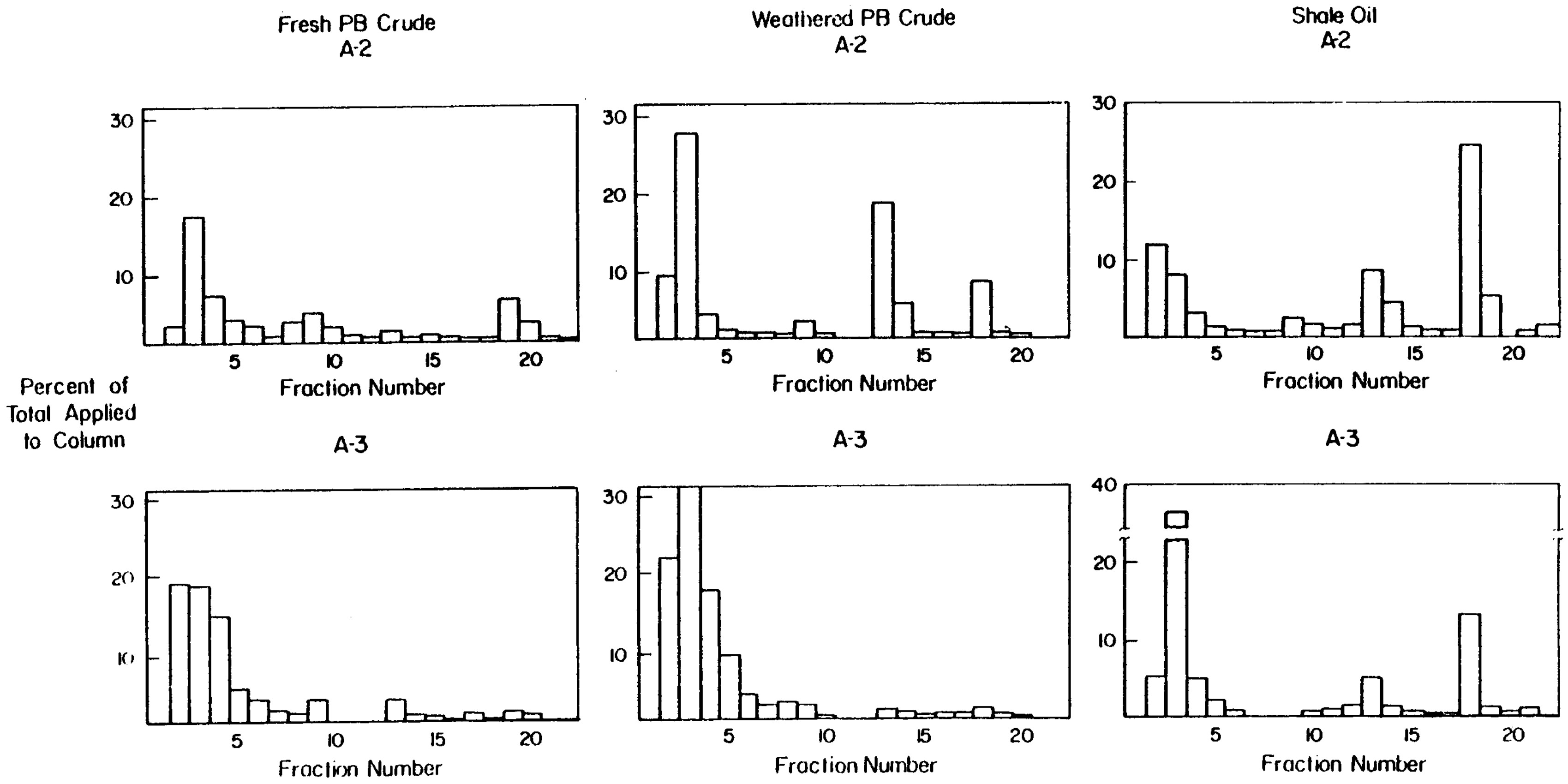

FIGURE 9. ELUTION PROFILES FROM FRACTIONATION USING SILICA GEL

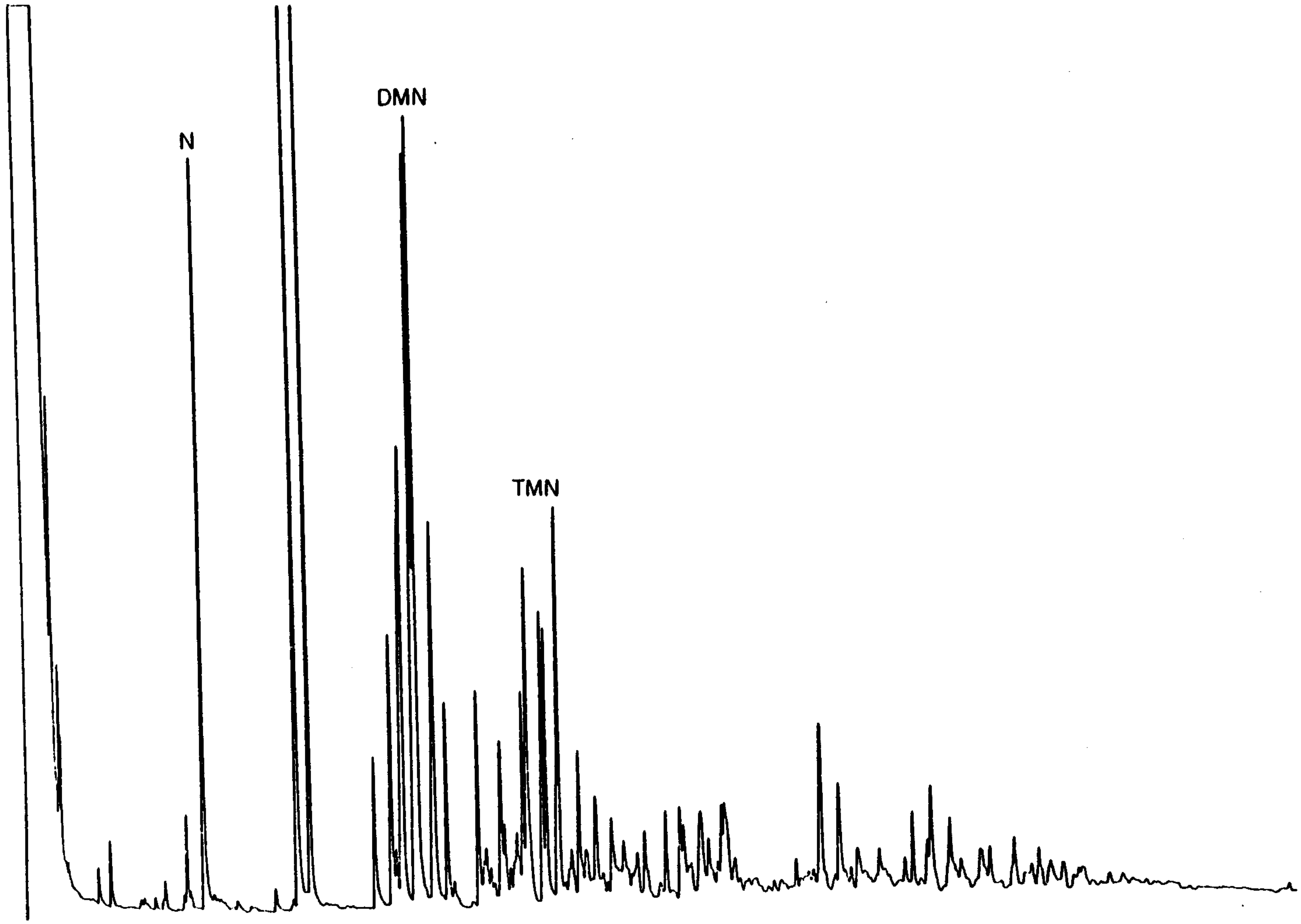

FIGURE 10. GAS CHROMATOGRAM OF FRACTION A-3-4 FROM FRESH PB CRUDE OIL

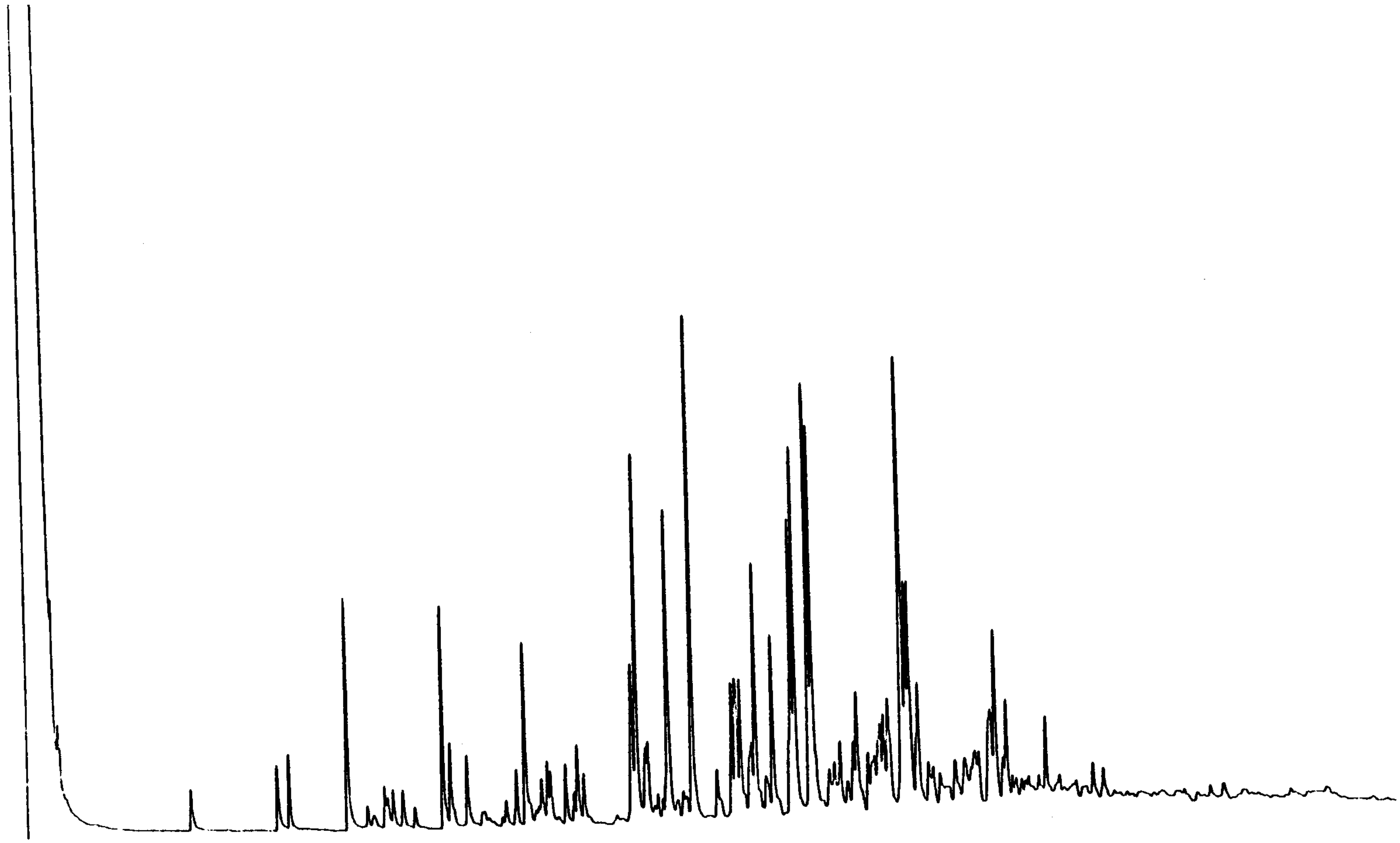

FIGURE 11. GAS CHROMATOGRAM OF FRACTION A-3-5 FROM FRESH PB CRUDE OIL

That covers the fractionation studies. I wish I could give bioassay results on all the fractions but that work is not completed. We've used various reference compounds in the toxicity assays, including 2-methylnaphthalene, phenanthene, 1-methylpyrene, 4-methylphenol, 2-naphthol, dibenzothiophene, and carbazole, and found 1-methylpyrene to be somewhat more toxic than the others. We have also found that some of the polar fractions of oil have toxicities comparable to that of 1-methylpyrene, so it will be interesting to study those fractions in greater detail.

In the Ames mutagenicity assay we have found a slight amount of activity in some of the polar fractions but further optimization studies need to be run before we can make any valid conclusions.

Although I've not been able to provide bioassay data, I hope the presentation of the approach and the discussion of the problems involved have provided some useful insights into working on this type of problem.

U.S. DEPARTMENT OF COMMERCE
NATIONAL OCEANIC AND ATMOSPHERIC ADMINISTRATION
NATIONAL OCEAN SERVICE
701 C Street
Box 56
Anchorage, Alaska 99513

OFFICIAL BUSINESS
PENALTY FOR PRIVATE USE $300

POSTAGE AND FEES PAID
U.S. DEPARTMENT OF COMMERCE
COM-210

PRINTED MATTER
CLASS OF POSTAL SERVICE

UNIV OF ALASKA/INFO SERVICES
ARCTIC ENV INFO AND DATA CTR
707 A STREET
ANCHORAGE, AK 99501 *

NOAA FORM 61-13
(9-84)